Non-linear data-driven modelling on multidimensional fields: an application to hydro-morphodynamic coastal fows

Rem-Sophia Mouradi

To cite this version:

Rem-Sophia Mouradi. Non-linear data-driven modelling on multidimensional fields: an application to hydro-morphodynamic coastal fows. Statistics [stat]. Institut national polytechnique de Toulouse (INPT), 2021. English. NNT : . tel-03405363

HAL Id: tel-03405363
https://theses.hal.science/tel-03405363

Submitted on 27 Oct 2021

THÈSE

En vue de l'obtention du

DOCTORAT DE L'UNIVERSITÉ DE TOULOUSE

Délivré par l'Institut National Polytechnique de Toulouse

Présentée et soutenue par

Rem-Sophia MOURADI

Le 16 mars 2021

Modélisation non-linéaire de champs multidimensionnels guidée par la donnée : application aux écoulements côtiers hydro-morphodynamiques

Ecole doctorale : **SDU2E - Sciences de l'Univers, de l'Environnement et de l'Espace**

Spécialité : **Océan, Atmosphère, Climat**

Unité de recherche :
CECI - Climat, Environnement, Couplages et Incertitudes / CERFACS

Thèse dirigée par
Olivier THUAL et Cédric GOEURY

Jury
M. Olivier LE MAÎTRE, Rapporteur
M. Pierre-Olivier MALATERRE, Rapporteur
M. Florent LYARD, Examinateur
Mme Hélène ROUX, Examinatrice
Mme Christine KERIBIN, Examinatrice
M. Olivier THUAL, Directeur de thèse
M. Cédric GOEURY, Directeur de thèse
Mme Clémentine PRIEUR, Présidente

M. Pablo Tassi, invité
M. Fabrice Zaoui, invité

En souvenir de mon beau père, Bernard.

Remerciements

Chers lecteurs,
Chercheurs, doctorants et étudiants, et quelques amis curieux,

Pour commencer, ces trois années de thèse n'ont pas été de tout repos, loin de là. Cela a nécessité une constance dans les efforts, et une grande part de travail introspectif. Je tiens à partager avec vous quelques "rencontres littéraires" qui m'ont marquée, vis à vis du travail de recherche scientifique, surtout dans des moments de doutes.

Sur la persévérance et la patience, ainsi que la place de la chance :

Il vaut mieux avoir de la chance. Mais je préfère être exact.
Et alors quand vient la chance, on est fin prêt.

Dans "Le vieil homme et la mer", Ernst Hemingway.

Sur les sacrifices personnels d'une part, et l'importance de l'effort collectif d'autre part :

Mon ouvrage avance, lentement
Comme une forêt qui pousse en silence.
C'est une tâche exigeante que la mienne,
Une tâche que rien ne doit venir troubler.

♣

Je ne me sens pas seule, pourtant,
Enfermée dans mon atelier.

♣

Je laisse parfois mes doigts à leur étrange ballet,
Et je songe à ces vies que je ne vivrai pas
A ces voyages que je n'ai jamais faits
A ces visages que je n'ai pas croisés.

♣

Je ne suis qu'un maillon de la chaîne,
Un maillon dérisoire, mais qu'importe,
Il me semble que ma vie est là,
Dans ces trois fils tendus devant moi,
Dans ces cheveux qui dansent
Tout au bout de mes doigts.

Dans "La tresse", Laetitia Colombani.

Sur la tourmente, le doute et puis... le dépassement de soi :

Il faut avoir du chaos en soi pour enfanter d'une étoile qui danse.

Dans "Ainsi parla Zarathoustra", Friedrich Nietzsche.

Et enfin sur la modestie, la tolérance, l'acceptation de soi et des autres :

We are human
After all
Much in common
After all
♣
Human, human, human, human

"Human after all", Daft Punk.

Chers lecteurs,
Collègues, amis et famille,

Le parcours n'a pas été que personnel. Le travail présenté dans ce manuscrit est le fruit de riches interactions scientifiques et humaines, et il serait prétentieux que je m'en attribue le mérite seule, sans gratitude envers les nombreuses personnes qui y ont contribué.

D'abord, j'ai une immense reconnaissance envers mes "co-équipiers de thèse", mon directeur **Olivier Thual** et co-directeur **Cédric Goeury**, ainsi que mes co-encadrants **Pablo Tassi** et **Fabrice Zaoui**. J'ai grandi professionnellement et humainement auprès de vous, grâce à un étroit accompagnement. Vous vous êtes montrés disponibles, patients, m'avez lancé de nombreux défis en toute bienveillance, avez encadré ma curiosité avec beaucoup de sagesse et de recul, tout en m'encourageant dans "mes élans de créativité" avec tant d'optimisme. J'ai eu une expérience de thèse épanouissante à vos côtés.

Ensuite, je remercie les membres de mon comité de suivi de thèse, **Anne-Laure Besnier**, **Sébastien Boyaval** et **Germain Antoine**, pour leur intérêt, écoute, et précieuses suggestions techniques. J'ai également beaucoup de gratitude pour mes rapporteurs de thèse **Olivier Le Maître** et **Pierre-Olivier Malaterre**, pour leur lecture attentive du manuscrit et les commentaires constructifs. Je les remercie également, ainsi que les examinateurs **Clémentine Prieur**, **Florent Lyard**, **Hélène Roux** et **Christine Kéribin**, pour la discussion scientifique qui a suivi la soutenance. Un échange, que je redoutais comme tout doctorant, et qui s'est avéré enrichissant et bienveillant, duquel je suis sortie avec plus de recul, de précieuses perspectives techniques, et plus d'admiration encore pour les chercheurs qu'ils sont.

Je souhaite remercier les collègues m'ayant soutenue techniquement pour divers aspects de cette thèse. En particulier, mes collègues du CERFACS, **Mélanie Rochoux**, **Laurent Terray**, **Sophie Ricci**, **Isabelle Mirouze**, **Corentin Lapeyre**, **Siham El Garroussi** et **Pamphile Roy**, qui ont chacun pris de leur temps pour discuter de mon sujet et me faire bénéficier de leurs expériences techniques, lors de mes visites à Toulouse. Sans oublier mes collègues du Laboratoire National d'Hydraulique et Environnement (LNHE) à EDF R&D, un grand merci à **Maria Joao** pour les discussions autour de la modélisation des vagues, **Mathieu Couplet** pour les échanges statistiques, et **Didier Rougé** pour m'avoir transmis une petite partie de sa grande expérience concernant la modélisation du chenal d'amenée étudié.

Je remercie également **Damien Violeau** (LNHE) et **Vanessya Laborie** (CEREMA) pour leurs critiques constructives de la contribution au Telemac User Conference, autour de la modélisation hydrodynamique de la marée. Bien-sûr, je n'oublie pas mes collègues d'autres départements, en particulier **Michael Baudin**, **Merlin Keller** et **Bertrand Iooss** de PRISM ainsi que **Jean-Philippe Argaud** et **Anne Dutfoy** de PERICLES pour les échanges techniques et de nombreux éléments bibliographiques. Je tiens également à remercier l'**Équipe de Mesures en milieu Naturel (EMN)** du LNHE pour m'avoir permis de participer à une campagne en 2018 (une bouffée d'air frais, entre codes, maillages et formules).

Cette thèse n'aurait pas eu lieu sans le financement d'**EDF** et d'**ANRT**, via la convention **CIFRE** 2017/1452. Je les remercie donc, ainsi que les chefs du projet **VERONA/IGUASOU** Anne-Laure Besnier et Germain Antoine, sans oublier le chef d'équipe P73 au LNHE, **Giovanni Mattarolo**, pour m'avoir confié ce travail. Je remercie également l'**Université de Toulouse**, l'école doctorale Sciences de l'Univers, de l'Environnement et de l'Espace (**SDU2E**) au sein de l'Institut National Polytechnique de Toulouse (**INPT**), et en particulier le laboratoire Climat, Environnement, Couplages et Incertitudes (**CECI**) du **CNRS/CERFACS** et son directeur Laurent Terray, pour avoir accueilli cette thèse.

Plus généralement, merci aux collègues, chercheurs, doctorants et stagiaires, des compétences sédimentaire, hydrodynamique, numérique et développement, des équipes **P73, P74** au **LNHE**, Laboratoire d'Hydraulique Saint Venant (**LHSV**), et équipe **GLOBC/CECI** du **CERFACS** pour les nombreuses interactions officielles et officieuses, dans des salles de réunions (ou par visio à partir de Mars 2020...), devant la machine à café, en marchant vers le restaurant ou le RER A (instants chers et plus rares à partir de Mars 2020...). Un grand merci pour les moments de convivialité sportifs, musicaux et gourmands !

Un énorme merci à **ma belle famille** pour leur soutien et encouragements, pour m'avoir permis de me ressourcer quand j'en avais le plus besoin, surtout au terme de ces trois ans.

Je serai éternellement reconnaissante envers **mon père, ma mère**, et les meilleures soeurs du monde (en toute subjectivité) **Siham** et **Houria**, pour avoir toujours cru en moi et pour leurs sacrifices. Cette dernière année m'a été difficile sans pouvoir les voir, mais ce n'est que partie remise.

Enfin, je n'ai pas les mots pour décrire à quel point l'apport de mon chéri **Fabien** a été important. Tu m'as soutenue dans des moments de doute et de joie, et j'ai toujours su que quoi qu'il se passe, tu seras toujours là. Ça n'a pas de prix.

Chers lecteurs,
Chercheurs, doctorants et étudiants, et quelques amis toujours aussi curieux,

Bonne lecture.

Non-linear data-driven modelling on multidimensional fields: an application to hydro-morphodynamic coastal flows

Rem-Sophia MOURADI
January 13, 2021

Contents

List of Figures

List of Tables

Introduction

Au 21ème siècle, la recherche scientifique dans de nombreux domaines de la physique implique de traiter diverses sources de données. Les observations deviennent de plus en plus nombreuses et accessibles, grâce aux avancées technologiques de mesure, stockage de données, capacité de transmission et traitement. Par ailleurs, la puissante avancée historique des ressources computationnelles, à partir de la fin des années 90, a encouragé l'usage des modèles à base de processus physiques, permettant d'améliorer notre compréhension des phénomènes observés, et de générer de la donnée supplémentaire. C'est ainsi que les approches guidées par la donnée sont devenues une des pierres angulaires de la physique, allant de l'Assimilation de Données (AD) au Machine Learning (ML).

Cette thèse se concentre sur le ML interprétable, en utilisant les techniques de Réduction de Dimension (DR) et de régression probabiliste non-linéaire et multivariée, en combinant deux approches classiques : la Décomposition en modes Propres Orthogonaux (POD), et l'Expansion par Polynômes du Chaos (PCE). La méthodologie proposée est appliquée à différentes étapes de la modélisation guidée par la donnée : (i) l'apprentissage à base de données mesurées, (ii) la Quantification des Incertitudes (UQ) efficace et (iii) l'Assimilation de Données rapide et précise.

Les contributions présentées découlent d'investigations menées au sein de la communauté scientifique des géosciences, qui connaît par ailleurs une augmentation constante des sources de données. Les méthodologies proposées ont pour but de fournir un outil prédictif dans un contexte industriel, avec des défis sous-jacents, notamment concernant les contraintes liées au temps de calcul. Plus précisement, la modélisation de la morphodynamique dans un chenal bord-de-mer de centrale électrique est visée. Des données de surveillance du chenal, collectées durant plusieurs années dans le but d'optimiser sa gestion, ainsi qu'un modèle numérique hydro-morphodynamique, sont disponibles. L'objectif principal de cette thèse est donc d'établir une méthodologie de couplage optimal entre données de terrain et modélisation numérique, en utilisant des outils statistiques adaptés. La finalité est de prédire de manière rapide et précise l'élévation du lit sous-marin, aussi appelée bathymétrie. Cette méthodologie est appliquée dans une configuration côtière, avec pour objectif de mieux comprendre la morphodynamique (évolution des bathymétries). Cet aspect est crucial pour plusieurs applications, en particulier pour la prédiction de l'écoulement résultant, ce qui peut être d'intérêt socio-économique (par exemple pour prédire des inondations), ou d'intérêt industriel comme pour l'application proposée.

In the 21st century, scientific research in many physical fields involves dealing with a variety of data sources. Observations are becoming plentiful and accessible, due to technological advances in measurement devices, data storage, transmission and treatment capacities. The powerful historical jump of computational resources since late 90's has encouraged the use of process-based models, allowing to improve our understanding of physical phenomena, and to generate additional data. This is how data-driven approaches have become one of the cornerstones of physics, from Data Assimilation (DA) to Machine Learning (ML). As an example, ML has gained interest from classical physics (fluid mechanics [32, 116, 145, 174]; aerodynamics [267, 277]; plasma physics [83, 189], astrophysics and astronomy [115, 260]) to quantum physics (particle physics [4]; quantum mechanics [164]). Perhaps, physicists nourish a hope about exploring the "chasm of ignorance" using data-based techniques, by pushing the boundaries of classical approaches [105]. Although time has not yet come for drastic change [105], and believing that data may come with added value to previously established theories, one may ask the following: what are the optimal combinations between all information sources? and how to help physical modelling advances using statistical tools? These are open research questions that we do not pretend to solve in one thesis, but represent a guideline for the presented discussions.

The thesis work focuses on interpretable ML using Dimensionality Reduction (DR) and non-linear multivariate probabilistic regression, by combining two classical approaches: POD and Polynomial Chaos Expansion (PCE). The proposed methodology is applied at various steps of the data-driven modelling: (i) pure measurement based learning; (ii) efficient UQ and (iii) fast and accurate DA. In particular, the work takes place in the geosciences community, which also registers a constant increase in data sources [109]. Some interesting programs can be cited as the new SWOT satellite mission [166, 176], or the Sentinel satellite missions (Copernicus program) [66, 147]. Consequently, the community is also keen on data-based works, with increasingly represented contributions in ML [109, 206, 217], DA [39, 72], and UQ [19, 169]. These methods are of particular interest for example, in a context of climate change, where new data constantly need to be taken into account [205].

The proposed steps of this thesis aim at providing a predictive tool in an industrial context with inherent challenges, for example concerning computational time constraints. More precisely, the modelling of *morphodynamics* in a coastal power plant's water intake was targeted. Data were collected during many years of monitoring, in order to optimize the intake's management, and a *hydro-morphodynamic* numerical model is available. The main objective of this thesis is therefore to enable an optimal coupling methodology between field data and numerical modelling using appropriate statistical tools, for fast and accurate prediction of underwater topography (also called *bathymetry* or *bottom/bed* elevation). This methodology is applied in a coastal set-up, with the goal of better understanding sea bed temporal evolution, known as *morphodynamics*. This topic is crucial for many applications, in particular for the prediction of the resulting flow, which can be of socio-economical interest (e.g floods prediction) or industrial interest (e.g. current application).

Industrial context: power plants monitoring

Water intakes are a crucial component of power plants, as they ensure their cooling process via a pumping system. The plants are therefore constructed near to natural water sources, where intakes are the link between the source and the plant. Hence, as they settle in a natural environment, water intakes are subject to diverse solicitations that can modify their cooling capacity, namely sediment arrivals, inducing changes in the stream flow. As a result, the carrying capacity of the water intake can be drastically reduced by decreasing its effective area of transport [237]. Excessive sediment depositions are commonly observed in cooling water intakes, as for the present application represented in Figure 1-a, and are also a well-known issue in harbors for example, as shown in Figure 1-b. The example of bathymetry evolution in the intake (Figure 2-a) shows that sediment depositions (in red) can occur almost everywhere from the entrance to downstream, depending on flow conditions. Therefore, effective water intake management implies frequent dredging interventions characterized by high operational costs, that are usually hindered by a tight schedule.

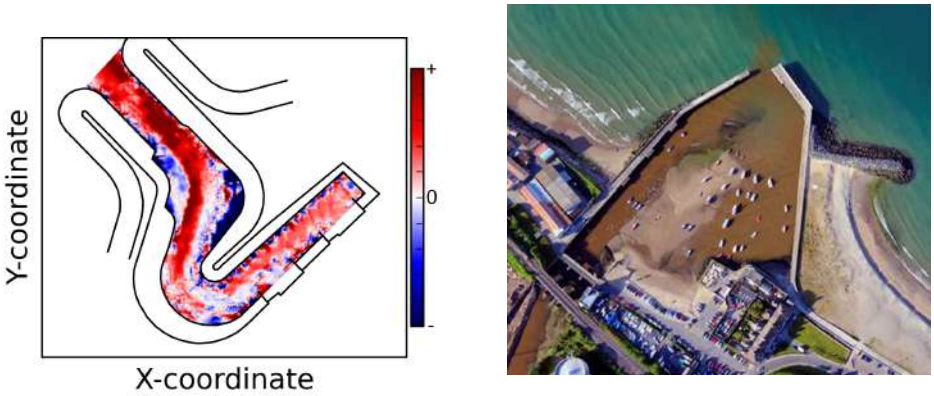

(a) Plant's intake (b) Bray Harbor

Figure 1 – Example of measured sedimentation in the intake of interest and comparison to siltation in Bray Harbor, Irish Sea (Muir Éireann, *Source: Afloat Magazine.*)

Power plants are generally constructed in river or coastal zones, each characterized with particularities concerning their ecological environments and hydro-morphodynamic properties. The geometry of the intakes and their localization are optimized prior to the construction of the plant, but sediment depositions are sometimes unavoidable. One of the challenges is therefore to better understand and characterize the sediment dynamics observed in a settled intake in order to design adapted solutions and to optimize dredging operations.

The studied plant is located in a coastal environment, and the intake's upstream is connected to the sea. Downstream, a pumping system ensures the cooling. In the studied case, there are two independent cooling stations (Figure 2-a), each characterized with a theoretical aspiration flowrate of 45 m^3/s in production regime. The studied intake is surrounded by 60 m high chalky cliffs (black lines in 2-b). It incorporates a jetty, whose angle with the shoreline, and position relative to the direction of the net longshore sediment transport, influence the amount of sediments diverted into the channel by waves and tidal current action. The jetty reduces the littoral drift, resulting in a localized sediment accretion against the shore-normal structure due to trapped longshore sediment transport [54]. This for example caused formation of a beach adjacent to the west intake dike, as shown in Figure 2-b. Additionally, a return current is prone to develop in the form of a swirling vortex at the end of the structure, that might favour the sediment deposition in the vicinity of the channel entrance, and consequently the amount of sediment delivered into the cooling water intake [46].

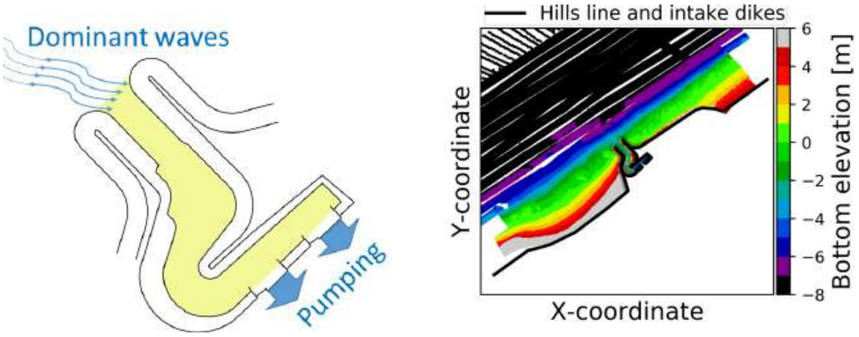

(a) Intake conditions (b) Nearshore bathymetry

Figure 2 – Schematic drawing of the interest intake.

Challenges and thesis contribution

The application takes place in an industrial context, with financial and time optimization stakes. The power plants operators are in great need of an accurate modelling tool, in order to predict the sedimentation of the intake, which would help optimize and anticipate dredging operations.

Although a numerical model is available, morphodynamics remain complex to describe. The complexity of the involved dynamics and phenomena result in uncertain modelling choices, and sometimes non-unanimity of the approaches [9, 187]. This is enhanced, in coastal cases in particular, by the complexity of the flow motion, subject to tides, waves, density currents, their interactions, etc. [234]. As a result, the use of alternative statistical techniques is encouraged, either with pure ML if enough measurements are available, or complementary to physics-based modelling [233].

In the particular case of the studied intake, the coastal environment in which it settles has been extensively observed and studied in literature. The available data have also been the subject of previous analysis and statistical investigations. Although interesting, the latter remain basic (correlations, scatter plots) or qualitative, and do not provide a satisfactory answer to the industrial needs.

Hence, the general objectives of the thesis are:

- To perform quantitative analysis of the intake dynamics from the available measurements, using advanced statistical tools;
- To apply the statistical conclusions for physical interpretation, in order to support previous analysis. The aim is to determine the phenomena that are generally responsible of sediment deposition. This is important for the monitoring of the power plant's water intake, for example to help targeting valuable measurements;
- To provide a predictive tool for operational conditions;
- To evaluate the use of available hydro-morphodynamic models under operational conditions, for further physical investigation. In particular, advanced study is

needed concerning their uncertainties, and strategies for optimal calibration on measurements.

The thesis work aims at providing robust and practical answers for this application. The objective however was to deploy strategies that could be generalized to other physical frameworks. The main achievements of this work, based on the materials provided by the application, can be summarized as:

- Quantitative analysis using POD allowed interpreting the dynamics, filtering the data and constituting a spatial basis for field predictions. Locations for optimal measurements were identified, by correlating global and spatially localized decompositions. Accurate and fast non-linear predictive tool, for multidimensional physical fields, was provided using a coupling between POD and PCE. Physical interpretation was assured using adequate ranking measures, valid at both POD patterns scale and global output scale. Robustness to noise and training-set variations was demonstrated, and the performance was successfully compared to classical NN. The proposed methodology is adapted for industrial contexts with strong time constraints and physical interpretation needs. Additionally, it gives the possibility of straightforward Uncertainty Quantificiation (UQ) from the probabilistic framework of PCE;

- Dimensionality Reduction (DR) was used for comparative study between measurements and uncertainties in physics-based models. More precisely, the patterns of measurements were compared to the patterns of the used model by performing UQ studies on the latter. Additionally, optimal parametric calibration of the model on measurements has shown to be uncertain, and variable with modelling choices;

- Optimal approaches for variational Data Assimilation (DA), based on DR and metamodelling, were studied. This provides a strategy for costly numerical models, that may help in further physical analysis and generation of synthetic data;

- UQ has been performed in a high-dimensional framework, for a numerical model where IC, BC and parameters, are all uncertain. POD helped reducing the dimensionality of the UQ problem to few components, applied independently on output field measurements to provide IC, and on synthetic data from bigger scale models to provide BC.

This thesis is consequently organized in six Chapters:

- Chapter 1 introduces the application, with a literature review of the natural environment and involved physics (nearshore dynamics). The application's data and the classically used physics-based model, consisting on a coupling between the Shallow Water Equations (SWE) and sediment mass conservation or *Exner* Equation, are described;

- Chapter 2 presents the theoretical basis behind the methods used in the presented contributions. Machine Learning (ML), Neural Networks (NN), Proper Orthogonal Decomposition (POD), Polynomial Chaos Expansion (PCE), Data Assimilation (DA) and Uncertainty Quantificiation (UQ) are detailed;

- Chapter 3 emphasizes the interest of POD in data filtering and determination of optimal measure locations. Then, the physically interpretable ML algorithm, based on POD-PCE coupling, is presented in journal paper form;

- Chapter 4 concerns the use of POD on field measurements of periodic variables, to perform UQ on a process-based model. In particular, uncertainties related to common modelling choices (domain size, closures) and resulting uncertainty in parametric calibration are studied;
- Chapter 5 compares Dimensionality Reduction (DR) and metamodelling methods for fast and accurate DA. A POD-PCE based metamodelling with three-Dimensional VARiational (3DVAR) Data Assimilation (DA), and combined state-parameters reduction with POD, are compared to classical iterative 3DVAR with numerical model;
- Chapter 6 combines previous optimal choices to perform high-dimensional UQ on a process-based model, with uncertain Boundary Conditions (BC), Initial Conditions (IC) and parameters.

Throughout the manuscript, a distinction is made between *data-based approaches* and *physically-based data-driven approaches*, as part of general data-driven methods [233]. The term "*data-based*" refers to methods and applications where only data are used as a source of information. This for example concerns pure measurement-based ML. The term "*physically-based data-driven*" refers to methods and applications where physics-based (or process-based) models are jointly used with measurements. This is for example the case with DA, where measurements can be used along with an equation-based numerical model.

Chapter 1

Nearshore processes and morphodynamics

Pour commencer, le paysage dans lequel le chenal étudié se situe, en l'occurrence la Manche orientale, est présenté. En particulier, nous nous intéressons aux phénomènes physiques permettant d'expliquer la morphodynamique observée. Ensuite, les données à notre disposition sont présentées, notamment une campagne réalisée en début de thèse. Par ailleurs, les investigations physiques liées à ces données sont décrites. Enfin, les équations à base de processus physiques, classiquement utilisées pour modéliser l'hydro-morphodynamique côtière, sont présentées. Cependant, la modélisation numérique se montre complexe, et les mesures sont partielles. Elles sont par ailleurs toutes deux entachées d'incertitudes. Ceci permet de démontrer l'intérêt des techniques statistiques mises en place, comme résumé en fin de chapitre. En effet, l'objectif est de tirer un profit simultané de toute source d'information, pouvant aider à la prédiction dans un contexte opérationnel.

To begin with, the area in which the studied intake settles, i.e. the Eastern English Channel, is presented. In particular, we focus attention on the physical processes that may explain the observed sediment transport and morphodynamics. Then, the available data are presented, namely a measurement campaign in the beginning of the thesis. Additionally, related physical investigations are described. Lastly, the process-based physical equations, classically used to model hydro-morphodynamic processes in coastal areas, are presented. On the one hand, numerical modelling shows to be complex, and on the other hand measurements are incomplete. They are besides both characterized with uncertainties. This allows demonstrating the interest of the developed statistical techniques, as summarized at the end of this chapter. In fact, the objective is to simultaneously benefit from all sources of information, which would help prediction in an operational context.

Contents

1.1 Physical context: dynamics at regional, local and intake scales

Before exploring original ideas, a literature review of the physical context is presented to emphasis relevant modelling choices. A summary of observations in the intake's natural environment, and a description of the physical phenomena implying sedimentation are given hereafter. However, it can be noted that the physical analysis of the dynamics remains relevant in other contexts, and the same modelling tools could therefore be applied to other configurations.

The interest site is located on the Eastern English Channel coast in northern France. The area has been extensively studied in literature [14, 122, 130, 137], by the geosciences community and stakeholders, both prior to construction and later for monitoring.

The nearest tidal gauge (harbor), approximately located at 10 km from the intake, has been operational since January 1945 [130]. The oldest local wave observations date back to 1911. These were simply based on visual appreciation, also registered at the nearest harbor, from 1911 to 1914 and from 1932 to 1939 by the harbor's maritime service [122].

Until 1976, literature about the characteristics of the plant's area (e.g. ecological, hydrodynamic, meteorological, etc.) were limited. The stakeholders therefore commissioned the French Institute for ocean science (*Institut Français de REcherche pour l'Exploitation de la MER*, IFREMER) for pre-construction studies, concerning the study of benthic (bottom) [136] and pelagic (water column) [137] environments. Then, the first local wave records are realized using pressure sensors from 1976 to 1978, and using a datawell waverider from 1978 to 1987 [122]. A first measurement campaign of currents is later realized on 1997 [122].

Since then, IFREMER was also commissioned to assure constant surveillance of the power plant's area, among which pre-construction campaigns [13] and future surveys [1, 14, 42, 56]. A synthesis covering the evolution from initial state prior to construction to 2008 was then described in [57]. Additionally, attempts to analyse and interpret the power plant's intake observed sedimentation, using hydro-meteorological data, were given in [122, 123].

The objective of this section is to summarize the characteristics of the study area, at the regional, local and water intake scales, as follows:

- Hydrodynamic conditions, namely tides;
- Climatology and meteorology, where the wind and waves are described, as well as less frequent events (storm surges);
- Morphology and sediment characteristics of the area;
- Physico-chemical properties, in particular turbidity that is an indicator of fine sediments suspension.
- Resulting morphodynamics caused by the previous processes;

1.1.1 Hydrodynamic conditions

Tides

In the eastern English Channel, the tide originates from the Atlantic ocean, and propagates at flood is from West to East. It is dominated by a semi-diurnal circulation, with two high tides and low tides of quasi-equal amplitudes.

The tide in the study zone is classified as macro/mega-tidal, because of the marine shelf that is funnel-shaped, substantially increasing the tidal amplitude. Additionally, reflection of the tide on Picardy coast implies an amplitude increase from the central/western Channel [122]. Consequently, the average tidal range is about 7 m, increasing to 9 m for spring tide [46, 130] (also recorded as 8.5 m and 10 m respectively in [126]). The maximal difference between the high water and the succeeding low water is about 11 m (tidal coefficient of 120), and the high tide's time delay between Brest and Dieppe is about 7 hours.

The tidal currents are alternating and globally parallel to the coast, with flood and ebb currents developed in the E-NE and W-SW directions (N, S, E and W refer to North, South, East and West respectively). They can be locally perturbed with the coastal morphology and meteorological forcing, as shown by the 1997 survey [122] where a great variability of the velocities from a coastal point to another is noticed. The currents however remain generally intense, due to the marine shelf that drives them through tight areas [130]. The maximum velocity reaches 2.05 m/s at central/western Channel, and is generally decreasing from east to west. The average currents are asymmetrical, 20 to 30 % more intense at flood (from 0.8 to 1 m/s) than at ebb (from 0.5 to 0.7 m/s) [160]. A velocity decay of 20 to 30 % is also noted from spring to neap tide [46]. Last, the velocities decrease to 0.25 m/s by the coast (at approximate water depth of 6 m) [46, 130, 136]. These intense currents imply continuous tidal mixing, particularly strong at the west coast of the Cotentin peninsula (Normano-Breton Gulf), where the currents are considerable and the depths are small [136].

Other currents

In addition to tides, other types of currents should be mentioned. A drift current from the Atlantic ocean, also called the slope current, is the result of free surface elevation gradients. The latter are either caused by the Highs and Lows (anticyclones and depressions) or by bathymetric steepness. The influence of this current is permanent, namely in shaping the shore morphology, but is hidden by tidal variations. Literature also indicates the presence of a several kilometers large "coastal river", that flows from the Seine bay to Pas-de-Calais [33]. This corridor can seemingly be noticed on satellite images, showing a strong turbidity [122]. Long-shore currents, caused by the oblique wave breaking on the coast, and wind drift currents caused by the constraint on sea surface that is transmitted to deeper layers, can also influence the velocity field in the studied area.

Extreme states

Lastly, extreme sea levels, can be mentioned. In the English Channel, these are generally due to storms associated to larger water supply from the Atlantic ocean. Positioning of depression (British islands, North sea, etc.) and its size influence the extent of zones that are affected by surge [130]. Other hydrodynamic phenomena may influence extreme tides, as the action of waves implying water accumulation by the coast (wave setup) or breaking on beaches implying local water level rise (swash run-up) [130]. At the nearest tidal gauge from the studied intake, the maximum surges for annual and decennial return periods are 0.9 and 1.13 m respectively [227], while the centennial value is around 1.32 m [24]. The highest recorded value ever registered at the nearest harbor is 1.79 m [130].

1.1.2 Climatology and meteorology

Wind

Climate is a central component of marine and coastal environments. In the English Channel, the wind has a considerable influence on the currents, as the depths are small (50 m deep on average). The area is therefore greatly subject to wind waves, and to potentially violent storms [130, 136]. Additionally, it is located between sub-tropical region of high atmospheric pressures at south and sub-polar region of low pressures at north. The wind circulation is therefore from west to east, blowing from the Atlantic to the Channel. The study area is located in a zone that is totally exposed to westerly wind, conversely to other zones that are almost boxed-in by advanced cliffs (e.g. Cotentin peninsula) [130].

The dominant wind origin can be different for a given year. For example, 1968's Dieppe data gathered and analyzed in [136] show that wind globally originated from S-E, sparing the perpendicular Normandy coast. However, half of the strongest winds (18 to 24 m/s) originated from W to N-W, resulting with water accumulation by the coast and slow-down of tidal mixing [136] (Table 1.1).

Sector Force	N	N-E	E	S-E	S	S-W	W	N-W	Total
1 - 4	42	98	66	210	104	61	85	52	718
5 - 7	21	26	3	8	24	54	62	37	235
8 - 9	1	1	0	0	1	2	3	4	12
10 - 12	0	0	0	0	0	0	0	0	0
Total	64	125	69	218	129	117	150	93	1000

Table 1.1 – Frequency (‰) of observed winds on 1968 by origin and force scale at Dieppe (France), by Loic [136].

More recent observations from 1981 to 2010 at Dieppe were analyzed in [130], showing frequent and violent wind (year average 5.2 m/s). For this period, 10 % of the wind for each year is strong and blows at least three consecutive days, implying strong marine agitation and frontal assault of the coastline. Dominance is from South quadrant (38%) and West quadrant (24 %), precisely from South-West to North-West from November to February. Westerly wind is not the most frequent, but definitely the strongest (> 8 m/s) along with Northern winds. Depending on the analyzed location, regional diversity of wind distributions is also observed (Figure 1.1) [130]. Through an investigation of 2003-2007 NCEP reanalysis data at the vicinity of the studied area (24 km off the coast), Latteux [122] shows that more frequent and violent winds originate from South-West to West, as shown in Figure 1.2.

The impact of wind on the observed waves is considerable. It forces a constraint on the free surface of the sea, which generates strong fluctuations (wind waves). Furthermore, the most frequent winds originate from the west quadrant, which means that they have large fetch to induce the development of important waves originating from the Atlantic Ocean.

Waves

The oldest wave observations (previous to 1939) confirm that the dominant waves come from the west [122]. This is also concluded by Latteux [122] using the ANEMOC database [153, 253] (hindcast with the third generation spectral wave model TOMAWAC [22]), over the 2003 – 2009 period, as illustrated in Figure 1.3.

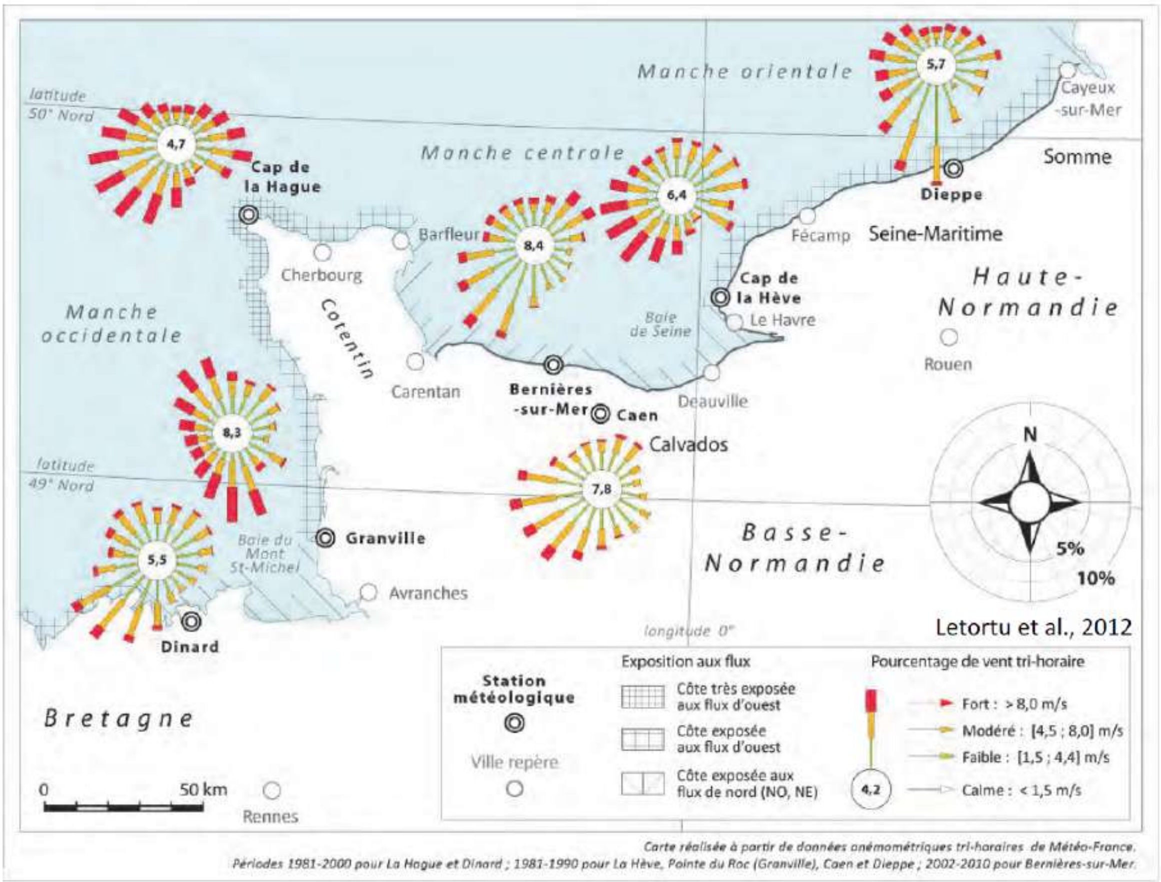

Carte réalisée à partir de données anémométriques tri-horaires de Météo-France.
Périodes 1981-2000 pour La Hague et Dinard ; 1981-1990 pour La Hève, Pointe du Roc (Granville), Caen et Dieppe ; 2002-2010 pour Bernières-sur-Mer.

Figure 1.1 – Wind exposition on the English Channel coast from 1981 to 2010, by Letortu [130]

Waves originating from N and NE are weaker, but act on longer duration implying a cumulative effect that may lead to rough sea states [130]. They have a small fetch of 100 to 160 km, implying small wave periods (compared to infinite fetch of Westerly swell), and are damped due to small water depths and refraction [130]. However, even in the absence of infinite fetch swell, wind can be sufficiently strong to locally generate important waves, called wind waves, which is often observed in the English Channel [46]. This distinction between wind waves created by local wind and infinite fetch swell originating from the ocean is important, as it implies that locally observed waves are not only generated by local wind.

An important wave intensity indicator is the *significant wave height*, denoted H_s, measuring the average of the highest third of recorded wave heights (Table 1.4 in Section 1.3.2). At the nearest harbor from the studied intake, historical data from 1978 to 1987 were analyzed in [122], to calculate H_s and its 70 % confidence interval: annual H_s is around 3.8 m with a confidence interval of $[3.7, 4.0]$ m, while decennial H_s is around 4.7 m with a confidence interval of $[4.4, 4.9]$ m. Additionally, based on the 1981-2010 data analysis in [130], it is concluded that 70 % of H_s remains lower than 1 m, and 95 % lower than 2 m.

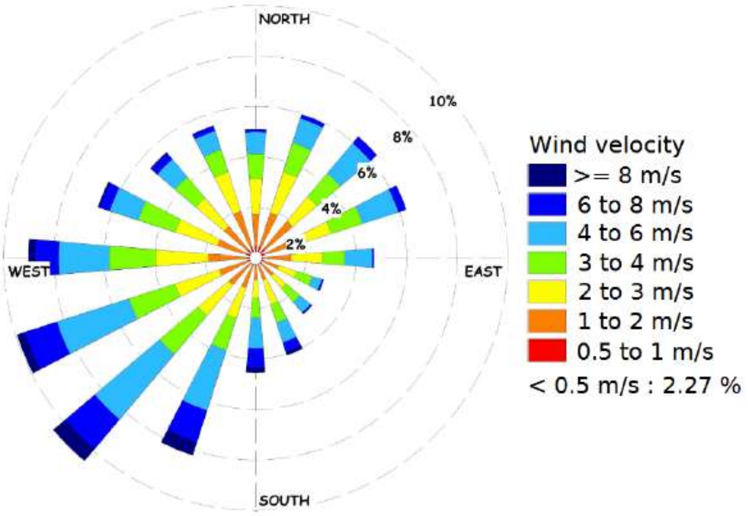

Figure 1.2 – Wind rose for 2003-2007 NCEP data at the vicinity of the power plant, by Latteux [122]

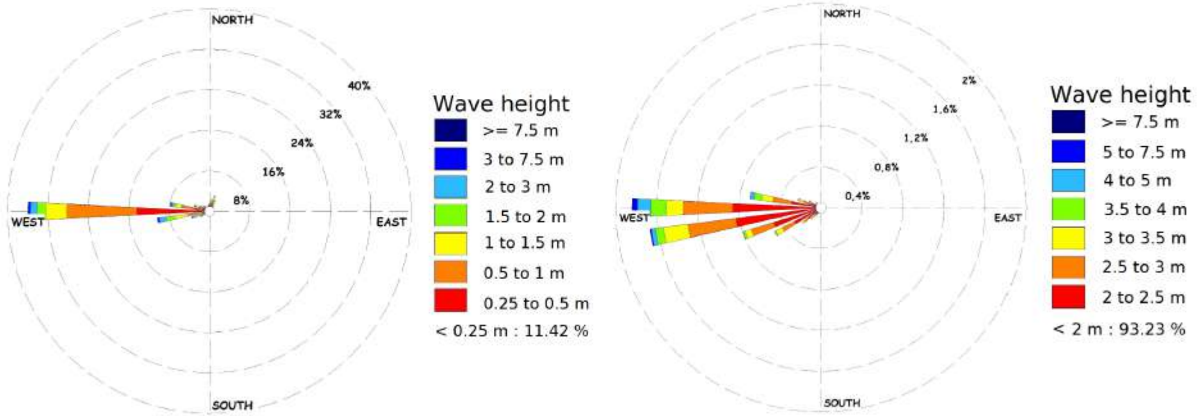

(a) Wave rose

(b) Waves higher than 2 m

Figure 1.3 – Wave rose for 2003-2009 ANEMOC data, 24 km off coast at the vicinity of the power plant, by Latteux [122]

A seasonal effect can also be noticed. For example, using 1961-1990 SHOM data, Latteux [122] concludes that the most severe sea conditions are observed from October to March. If averaged on this winter period, H_s exceeds 2.5 m for 7 days/year, oppositely to 2 days/year if averaged on the April-September summer period. Furthermore, these winter waves also mainly originate from the West, directly arriving to the Seine-Maritime coast. In particular, November is said to be the most severe month, and May and August the most calm ones [122].

Wave periods in the English Channel vary from 2 to 19 s (5 s to 7 s in average). For the strongest waves (SW to W origin), periods vary from 6 to 9 s [130]. Additionally, using ANEMOC's data, it is concluded by [122] that wave's peak period (wave period with highest energy, as defined in Table 1.4, Section 1.3.2) is strongly correlated to its height. The highest waves have longer periods.

Extreme sea states are also observed in the study area. Maximum H_s for annual return period varies between 3.5 and 4 m, while the centennial one varies from 5.5 to 7 m [130]. At the vicinity of the studied power plant's intake, annual H_s value is around 3.8 m while decennial value is around 4.7 m, and respective maximums are 4.2 and 5.8 m [46].

1.1.3 Sediment characteristics and morphology

Coastal morphology

Normandy's coastline is variable and characterized with irregularities. The Calvados coast for example is boxed-in between two advanced continental tips (Cotentin Peninsula to Etretat), which protects it from strong winds. Conversely, the study area is characterized by a relatively homogeneous coastline and is totally exposed to westerly wind [130]. Cliffs at the west of the intake and the western dike of the latter form a currents deceleration zone, favourable to sedimentation. A beach hence formed near to the west dike, as previously shown in Figure 2-b. The dike also induces vortex formation that stirs the sediments up [46], and the cliff diverts the currents towards the coastline which transports the sediments in the same direction.

Regional scale

At the regional scale of English Channel, depths are lower than 50 m, with slowly varying bottom contours. Slope is relatively low, with an average value of 0.7 %, but can locally go up to 2 %. Seabed is composed of sand and pebbles, with a thin layer (around 1 m) of mobile sediments [46]. The sediments distribution greatly depends on hydrodynamic conditions. Indeed, the coarsest sediments are generally located in zones where currents are intense. This also plays a role in the sediment distribution from deepest seas to the coast, where the sediments are finer, because of the transition between current influence zone (offshore) and wave influence zone (coast) [46]. Sediment distribution in the English Channel is shown in Figure 1.4.

Local scale

At local scale, sediment accumulations take the form of ripples, located at 15 to 30 m depths near the coast. These ripples are composed of an inferior layer of coarse sediments (pebbles, gravels, coarse-grained sand) and a superior layer of medium to fine silted sand [46]. The sediments are finer from West to East because of the previously described currents deceleration [122]. In the sub-marine area, nearshore soil consists in mega-ripples (15 to 20 m wavelength) developing parallel to the coast, and a complex succession of sandy tapes, stretching in the West-to-East direction, composed of 51.5 % sand, 46 % coarse sediments, 2 % of rock and 0.5 % finer sediments (e.g. silt) [46]. The available sediment stock has been constantly increasing from 1988 to 2000, and the mega-ripples

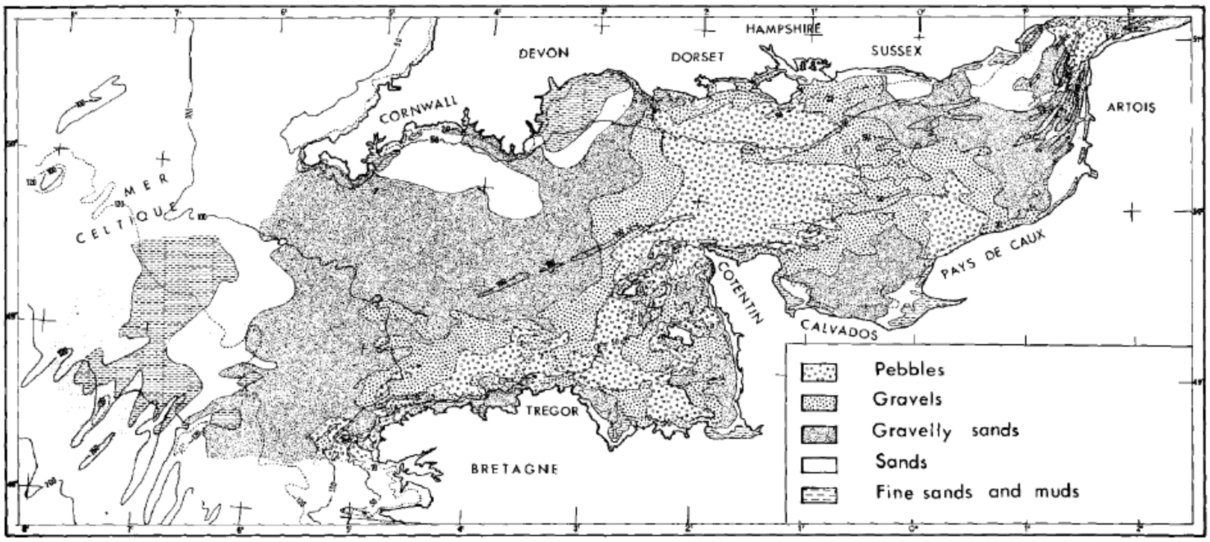

Figure 1.4 – Sediment types in the English Channel, by Larsonneur et al. [120]

zone has expanded, as can be seen in Figure 1.5. Mobile sediments layer thickness remains however low [46]. Consequently, these short term patterns evolutions are explained by hydrodynamic and meteorological events, that may increase the sediments supply from outer zones, or encourage the release of finer sediments that may be trapped inside the coarser sediments [46].

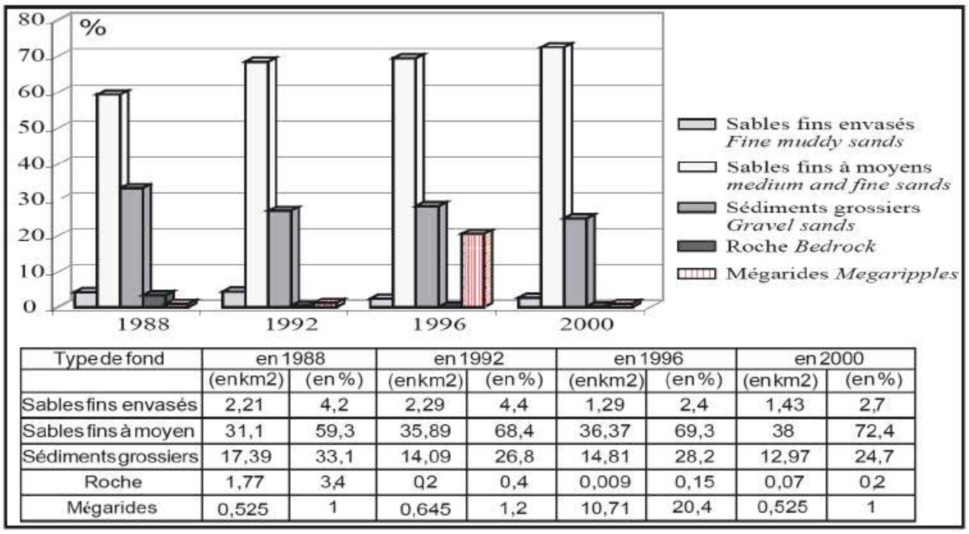

Type de fond	en 1988		en 1992		en 1996		en 2000	
	(en km2)	(en %)	(en km2)	(en %)	(en km2)	(en %)	(en km2)	(en %)
Sables fins envasés	2,21	4,2	2,29	4,4	1,29	2,4	1,43	2,7
Sables fins à moyen	31,1	59,3	35,89	68,4	36,37	69,3	38	72,4
Sédiments grossiers	17,39	33,1	14,09	26,8	14,81	28,2	12,97	24,7
Roche	1,77	3,4	0,2	0,4	0,009	0,15	0,07	0,2
Mégarides	0,525	1	0,645	1,2	10,71	20,4	0,525	1

Figure 1.5 – Bottom types evolutions in the marine zone of the intake, by Costa et al. [46]

Near the intake

Closer to the studied area, Latteux [122] indicates that: at coast's vicinity, seabed is generally rocky, or covered with gravels and pebbles. In this area, the presence of a several meters thick sedimentary prism is observed [42]. In small depths zone up to 1500 m off the cliffs, sediments are generally fine sand, with a median diameter of $[100, 150]$ μm. Beyond 1500 m, it is generally medium sand. Precise measurements prior to the plant construction show that soil was in great proportion composed of $[200, 500]$ μm grains. Nearshore, in the sub-tidal zone up to 10 m depths, fine sand and a relatively important silt fraction are observed. From 10 to 15 m depths, the sand is fine to medium, with an important coarse sand fraction. From 15 to 19 m depths, the sediments are generally coarse, with a greater fraction of fine gravels [136]. In the inter-tidal zone, sediments are homogeneous and well sorted (single mode statistical distribution). Up to 160 m off the coast, relatively large banks can be observed ($[20, 30]$ cm layer), composed of medium sand, with a principal mode around 250 μm. From 160 to 350 m from the coast, depositions consist in plating on a limestone bottom ($[5, 10]$ cm layer), with mostly fine-sized sediments (principle mode from $[125, 160]$ μm). These sand plating layers can attain a 1.5 m thickness [46], and more sand gets generally trapped inside pebble bars and is therefore hidden in this inner structure. Beyond 350 m, larger medium sand banks with finer sediments at the surface can be observed (5 to 20 cm layer), with a principle mode around 125 μm, and secondary around 63 μm) [136]. The proportion of sand varies from 25 %, 120 m from the cliffs, to 90 %, 400 m from the cliffs.

In front of the intake, seismic reflection surveys show that the thickness of mobile sediments attains 4 m, which shows a strong sand accumulation [122]. This represents a sediment stock that is inclined to be redirected inside the intake under favorable hydrodynamic forcing. A recent campaign on 2010 (Section 1.2) allowed measuring the soil granulometry at different points outside the intake and two points inside. The cumulative distribution with the diameters of sediments is shown in Figure 1.6. The sediments are generally fine sand, granulometry is well sorted, and the median diameter generally varies between 175 and 225 μm. Some exceptions are noted, where Point 4 at the east of the power plant shows finer sediments (median 125 μm), whereas Point 6 located at the intake's entrance shows coarser sediments (median 300 μm).

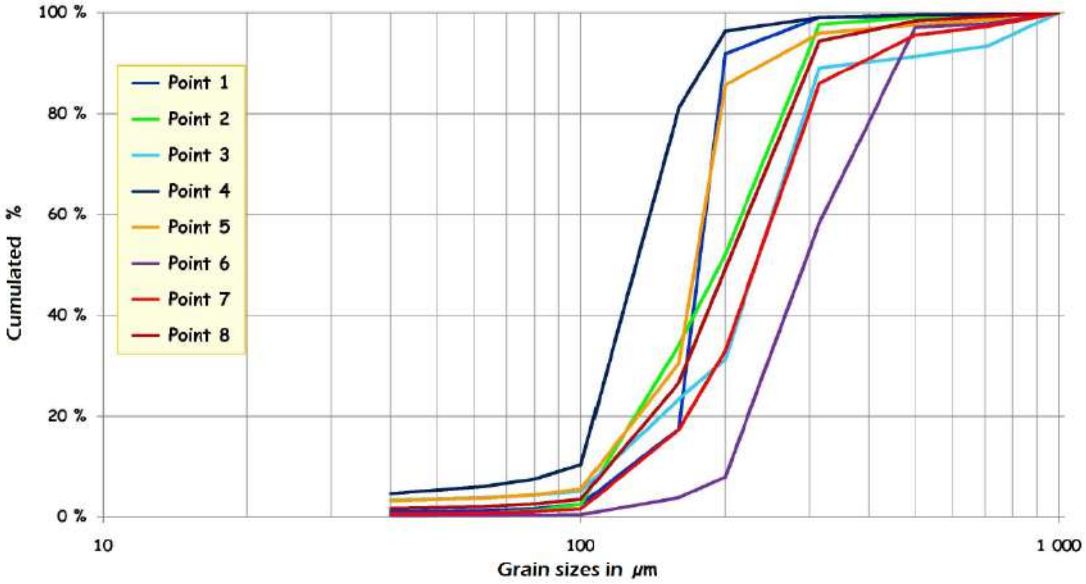

Figure 1.6 – Cumulative distributions of the sediments granulometry realized for the 2010 campaign, by Latteux [122]. Points 1 to 6 are outside the intake, points 7 and 8 are inside.

Inside the intake

Inside the intake, measurements realized on 1993 show a distribution of median sediment size in Figure 1.7. The silt proportion increases from the intake entrance to the pumps, and the median diameter of the sandy proportion decreases.

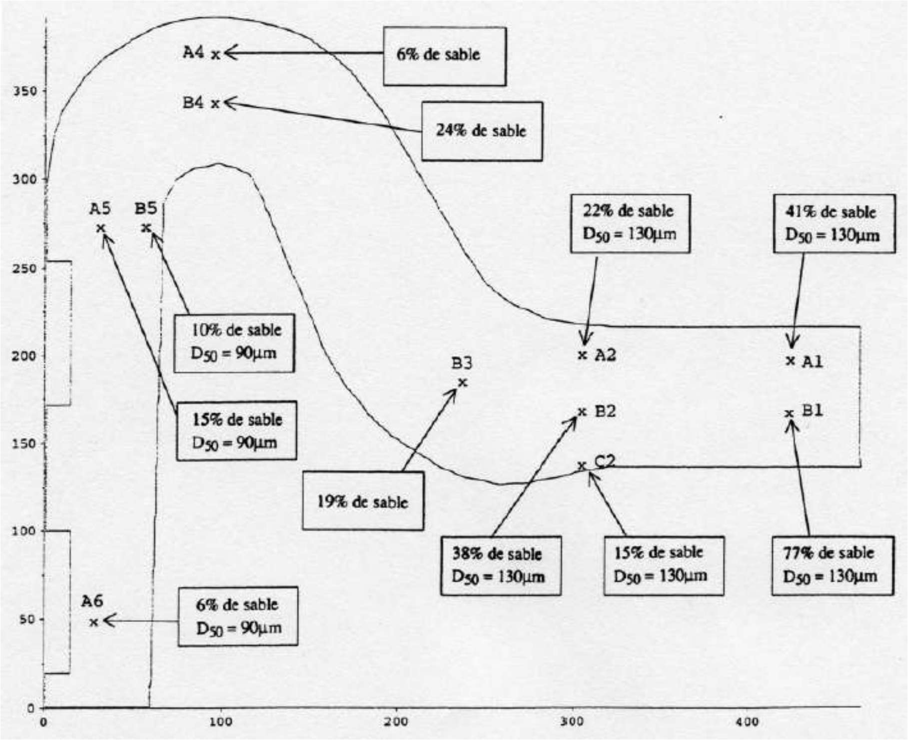

Figure 1.7 – Median sediment grains inside the intake on 1993, by Latteux [122]. *Sable* is french word for sand, and D_{50} designates the median sand grain size.

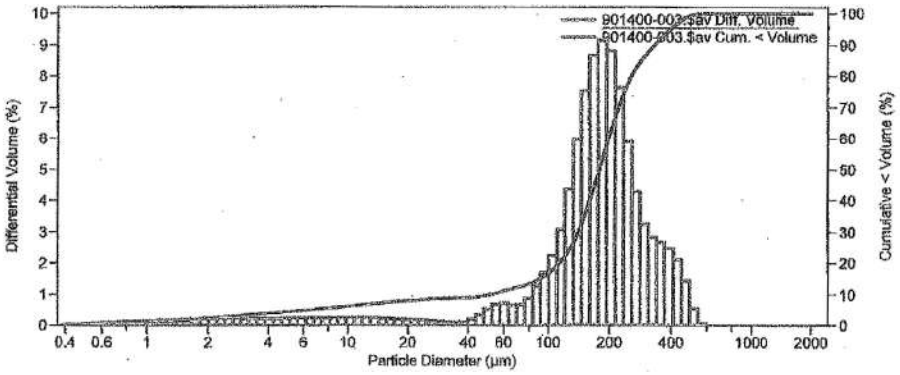

(a) Intake's entrance

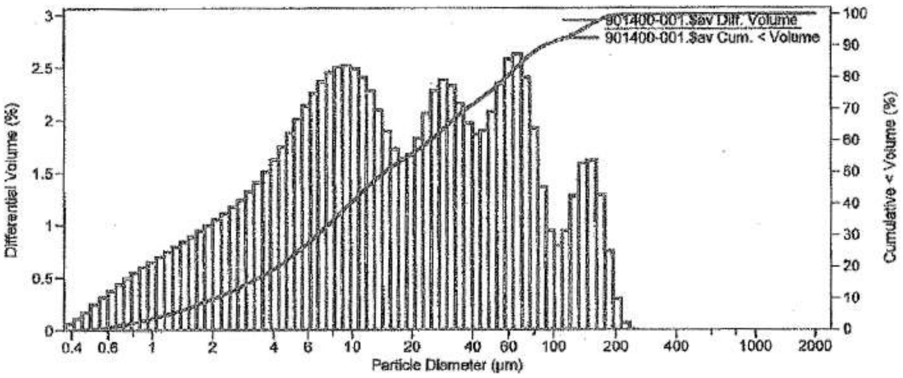

(b) Downstream

Figure 1.8 – Granulometry distributions inside the intake on 2008, by Latteux [122].

This observation is also confirmed by more recent measurement campaign on 2008 (Figure 1.8), where the sediments are shown to be homogeneous and well sorted at the intake's entrance, and very heterogeneous and poorly sorted downstream, with one sand mode and various silt modes.

1.1.4 Physico-chemical characteristics

Salinity

In the local area in which the intake settles, salinity remains lower than 35 ‰, except at autumn where it slightly increases. It varies between 32 ‰ and 34 ‰ from January to February. Right in front of the studied intake, surface and bottom salinity are both lower than 33 ‰[136]. Fluvial supplies, inducing desalinisation of the English Channel, contributing to this low salinity.

Precipitations

The climate of coastal Normandy and Picardy is temperate and oceanic. This results with relatively homogeneous precipitations throughout the year, distributed on 130 days of rain per year. It is noted that 300 mm are accumulated for Seine-Maritime (1971 to 2000 data). These are however average information and do not prevent from intra- and inter-annual variability, because of the active coastal meteorological dynamic. Indeed, in the nearest harbor from the studied intake, rain covers half of the year, from October to January. Rain is not intense, but lasts over long durations (lasting minimum 7 days over 32 % of the year) [130]. This constant water supply may result with serious increase of streams levels and consequently lead to overflow [136].

Temperature

The continental climate of eastern English Channel implies higher summer temperatures and lower winter temperatures compared to western Channel. The thermal contrasts remain however low [136]. The continuous tidal mixing of sea waters implies a low difference of temperature between sea surface and bottom [130].

Turbidity

Turbidity in the English Channel is fairly high near the coast. In fact, the continuous tidal mixing of sea waters induces a mean turbidity of 8 to 17 mg/l. Furthermore, an in-situ campaign shows for example that a maximum rate of suspended sediments is recorded in April: 16.70 mg/l measured 1 km from the shore, and 27.16 mg/l measured 4 km from the shore. This is caused by strong wind at the same period, inducing intense mixing [137]. As previously mentioned, the "coastal river" identified on satellite images is also a proof of this high turbidity [122]. Additionally, at fairly low distance from the coast, water has a white/chalky aspect extending on hundreds of meters, resulting from cliffs erosion. Water releases from the power plant are also characterized with the same visual aspects, indicating that the turbid water is aspired by the pumps and indeed transported through the intake [122]. However, it can be mentioned that turbidity measurements are generally undertaken by calm seas, and therefore underestimate its average value. To obtain a realistic value, Latteux [122] attempts to deduce turbidity from the observed nearest harbor silting. An average annual concentration is therefore estimated around 50 to 100 mg/l (much higher than the above mentioned 27.16 mg/l). In the vicinity of the interest power plant, sediment stock is always sufficient to lean great sediment supply to the intake, and turbidity increases with wave heights and is strongly influenced by the tidal levels (Section 1.4). Therefore, sedimentation of the intake only depends on meteorological and hydrodynamic conditions (wind, waves, tides, etc.) [122].

1.1.5 Morphodynamics

The morphodynamics described hereafter result from a combination of effects. On the one hand, the presence of industrial facilities (harbors, power plants, etc.) play a role in the observed dynamics. For example, a strong sediment accumulation is observed at the facilities upstream, generally followed by a decrease of sediment stock downstream [46]. On the other hand, natural forcings as the previously discussed hydrodynamic and meteorological conditions, as well as the intake's hydrodynamic functioning, influence the sediment transport, as described below.

Physical processes at regional scale

At the regional scale of the English Channel, the previously described sea conditions imply a 65 % foreshore sediment transit towards North-East, and 35 % in the opposite direction [130]. Due to the dominant west originating swell, the previously described sand plating on limestone bottom in the inter-tidal zones are very mobile, and generally transit from South-West to North-East [46]. The presence of such patterns indicates sand exchanges from offshore to the coast [46].

Waves have a considerable influence on sediment re-suspension. They have stronger effect in small depth zones, where the absence of fine sediments at the bottom indicate that waves prevent them from settling [46]. Waves threshold of action depends on the sediments size, and under storm conditions, they can create enough constraint to put a larger amount of sediments in motion [234, 258, 259]. Using semi-empirical sediment transport formulas (e.g. Soulsby [234] in Equation 1.29) with storm wave values ($H_s = 3$ m and $T_p = 8$ s), Costa et al. [46] shows that their effect is also highly dependent on tidal levels. By spring low tide levels, they easily suspend the coarsest sediments. By high tide, they only have an effect in small-depth zones (below 8 m). Tidal currents are also capital for sediment dynamics. As previously mentioned, granulometry and geographical distribution of the sediments demonstrate the offshore impact of tidal currents and their gradients. Tidal mixing stirs the sediments up, and the velocities amplitudes play a major role in the sediments mobilization, as a function of their size/weight [46]. Compared to waves, the tides act continuously by transporting major sediment patterns offshore.

However, tidal currents alone are not enough to drive the sediments towards the inter-tidal zones. In fact, the tides generally slow down (below 0.4 m/s) by low depth zones (6 m) and their transport capacity is therefore reduced. The action of tides is then took over by waves. When the patterns are close enough from the coast, storm waves act episodically, strongly re-suspending the sediments. Other more frequent and less strong waves gradually carry the sediments to inter-tidal zones. For example, wave breaking by the coast, with a given angle of approach, induce long-shore and rip currents, causing long-shore drift and mobilization of beaches sediments. This hand-off between tides and waves spatially and temporally varies, showing strong non-linearity of the dynamics [46]. Hence, for a strong sediment supply to reach industrial facilities (e.g intake), three elements are necessary: important sediment accumulations offshore, tidal currents that transport them closer to the coast, and strong waves that suspend them (preferentially at low tide) [46]. To conclude, there is an important interaction between the tidal effect and the action of waves, as well as a hand-off from waves to tide and from tide to waves depending on the situation. Morphodynamics are non-linear and represent a discontinuous function of the hydrodynamic conditions, where a threshold of movement is observed (depending on the sediments sizes). Therefore, realistic scenarios are generally not easy to model [234, 258, 259].

Physical processes at local scale

At local scale, morphological examination of the sedimentary figures nearshore [46], between the nearest harbors west and east of the intake, results with the following conclusions: west of the intake, the presence of advanced cliffs modify the direction of currents and the sedimentary transit is therefore 15° oblique as compared to the coast; east of the intake, sediment transit is parallel to the coast. At both the nearest harbors west and east of the intake, a considerable increasing sedimentation tendency has been recorded between 1989 and 1998. One of the harbors for example recorded $80,000$ m^3/year of sediment deposition from 2000 to 2002. The values can however strongly vary from a year to another, with possible peaks for specific years or months. An important peak has for example been noticed on January 2007 in both harbors and the studied intake. Seasonal aspect has also been noted, with a favourable sedimentation period between January and August, and natural erosion from September to December [122].

Physical processes at intake scale

Right in front of the intake, foreshore is formed of discontinuous levels (stairs). Bottom slopes are hence steeper compared to offshore slopes. Each foreshore level constitutes a sediment trap. Hence, for sediments to climb closer to the intake, from a level to another, strong suspension is necessary. It is therefore supposed that sediments arrival towards the intake is mainly the result of suspended transport, which is principally caused by waves [46]. This is also supported by the previously cited turbidity measurements.

Physical processes inside the intake

In the studied intake, sedimentation trends have been increasing over the last two decades [122], encouraging the power plant's operators to establish frequent surveillance (Section 1.2). Some hypothesis have been formulated to explain such behavior, among which: (i) the massive sand dropping that followed dredgings for the construction of a new harbour, located 70 km at the west of the intake; (ii) the regular sand droppings following the nearest harbors regular dredgings to assure navigation and (iii) saturation of neighbouring beaches, upstream of the intake. However, none of these hypothesis were verified.

Water aspiration through pumping systems attracts the sediments, that were resuspended by the coupled effect of tides and waves beforehand, to the intake. Additionally, currents inside the intake are lower than outside, encouraging the sediments to settle at the bottom [122]. Sands, heavy enough, tend to deposit upstream of the intake, whereas silt tends to deposit downstream. This explains the previously shown sediment distributions inside the intake, in Figure 1.7. Sand accumulation upstream forms a bump, whose size increases in time with the sediment supply, and ends up expanding downstream (example in Figure 1-a) [122]. This means that the previous state of the channel also plays an important role as the available space for the sediments deposition depends on the initial depths. These depths are increased when a dredging occurs. The dredging information can therefore be capital to understand the observed depositions.

It is probable that depositions in the intake take place in short lapse of time (few days) [122], when the tide-wave combined effects are favourable, for example by storm conditions. Erosion of the upstream bump can also occur, for example by spring low tide when the currents are strong enough. This tends to spread out the sediments through the intake. However, these strong current episodes do not last long enough to assure natural scouring of the intake, and regular dredgings are therefore necessary [122].

Conclusions

Previous analysis showed that the physical phenomena involved in sedimentation processes are highly complex and non-linear. Hydrodynamic and meteorological conditions play an important role in the observed dynamics, through wind, waves, tides, pumping, etc. Their influence on the sediment depositions was physically interpreted and supported by different observations in the studied area.

However, deeper analysis of the intake dynamics is still needed, in order to establish quantitative causality between sea/pumping conditions and sedimentation. In particular, the intake operators are in great need of a modelling tool to manage dredging operations and pumping conditions. This would be possible if a predictive model could be provided for operational conditions. To develop such a tool, two sources of data are considered hereafter: measurements, described in in Section 1.2 and process-based equations for numerical modelling presented in Section 1.3. Data can be used for pure data-based predictions, for example through Machine Learning (ML), or combined to process-based equations for physically-based data-driven modelling, for example through Data Assimilation (DA).

1.2 Available measurements for data-based and data-driven investigations

In this section, the available data for statistical investigations of the intake morphodynamics are of interest. Attention is focused on local measurements provided by the stakeholders. In particular, in order to guarantee safe and optimal functioning of the cooling intake, close supervision is assured. This consists in regular measurements of spatially distributed bathymetries, along with meteorological and hydrodynamic indicators (waves, wind, tidal levels, etc.). These data, coupled to the plant's monitoring information (dredging data, pumping flowrates), enable the operators to analyze the observed dynamics. The data collected during many years of surveillance, as well as additional casual surveys, are consequently described hereafter.

It should be noted however that other data sources, not described here, can complete the physical analysis and are kept as perspective. For example data-bases as ANEMOC [21] or the National In Situ Swell Records Center (CANDHIS) [132] can be cited.

1.2.1 Continuous monitoring

Over the last decade, close surveillance of the cooling intake consisted in regular bathymetry measurements, along with collecting hydrodynamic, meteorological and operational information that are likely to be influential (tides, waves, pumping flowrates, etc.).

Bathymetry measurements are performed using a boat that navigates through the intake, equipped with a Single-Beam Echo Sounding device. The most recent itineraries cover 39 cross-sectional profiles of the intake measured at 25 m intervals, as illustrated in Figure 1.9. The profiles are on average 100 m large with a 0.5 m spatial resolution of the bathymetric data. The latter were collected fortnightly between 2005 and 2018. However, data quality has dramatically evolved, due to the device precision evolution and to increasing need of complete information, as can be seen in Figure 1.9.

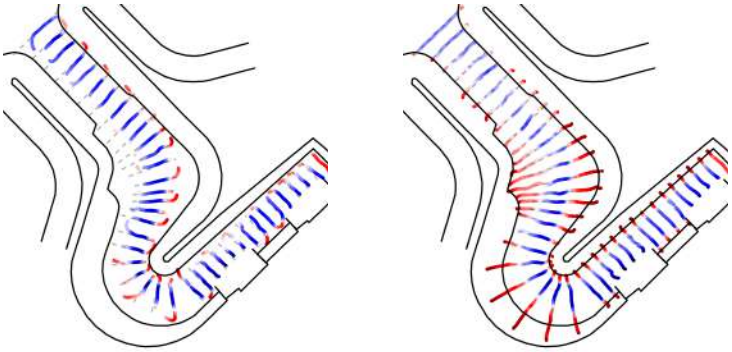

(a) 2007 measurement (b) 2018 measurement

Figure 1.9 – 2007 vs. 2018 mono-beam bathymetry measurements in the power plant's water intake. Values are near-zero when white ($0\ m\ CM$), positive when red and negative when blue.

The collected hydrodynamic and meteorological information comprise wave and wind variables, provided by the VAG prediction model of the sea state [85], using retrospective 3-hourly simulations between 2009 and 2018. Tidal water levels were obtained from the SHOM-REFerence network for Tidal observations (REFMAR) tidal gauge station located in the vicinity of the study zone, with hourly survey frequency [200]. Additional information such as the daily coolant flow rates, and channel dredging volumes and frequency, were provided by the plant operator. The measured variables, their time coverage and frequencies are summed up in Table 1.2.

An example of these measurements is shown in Figure 1.10. The instantaneous wave heights and tidal levels seem uncorrelated at first sight. Wave height peaks correspond to wind velocity peaks globally, but a difference is observed when the wind changes direction from a mean SW origin ($Wdir = 225°$) to a mean E origin ($Wdir = 90°$). This illustrates the complexity of dependencies and interactions between variables in the studied problem, in addition to the non-linear response of the morphodynamics.

Variable	**Data frequency**	**Period**	**Source**	**Spatial coverage**
Bottom elevations	2 weeks	2005 - 2018	Plant operator	intake's cross-sections
Pumping flowrate	Daily	2007-2018	Plant operator	one global information
Dredging date	6 months	2007-2018	Plant operator	one global information
Dredging volume	6 months	2007-2018	Plant operator	one global information
Tidal level	Hourly	2009-2018	REFMAR [200]	Nearest tidal gauge
Wind direction	3-hourly	2009-2018	VAG Model [85]	Nearshore grid point
Wind velocity	3-hourly	2009-2018	VAG Model [85]	Nearshore grid point
Wave period	3-hourly	2009-2018	VAG Model [85]	Nearshore grid point
Wave height	3-hourly	2009-2018	VAG Model [85]	Nearshore grid point
Wave direction	3-hourly	2009-2018	VAG Model [85]	Nearshore grid point

Table 1.2 – Summary of measurements, their frequencies, periods, sources and spatial coverage.

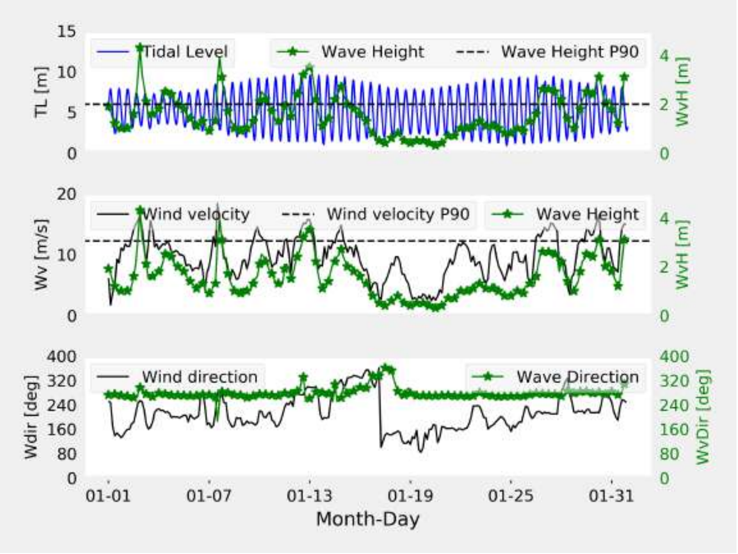

Figure 1.10 – Measurements of Tidal Level (TL), Wind velocity (Wv), Wind direction (Wdir), Wave Height (WvH) and Wave Direction (WvD) on January 2016. (P: Percentile)

Presented data are characterized with measurement uncertainties. Single-Beam bathymetries were realized with a sonar boat, by different operators throughout the years. Three elements are measured: bottom elevation and two horizontal space coordinates. Device precision was generally verified before each campaign (usually compared to pressure capture, manual probes installed in fixed heights, control of GPS coordinates on control points). Reported absolute differences did not exceed 0.01 m for both bed elevations and coordinates. Devices also improved throughout the years, where most recent bathymetry reports mention maximal errors of 0.006 m on horizontal coordinates (Ashtech

Proflex 800 GPS), and an absolute error of 0.01 m for bed elevation (TRITECH PA500 Frequency 500 kHz), for a 0.99 to 1.0 m measured value, representing an error of 1 %. Concerning tidal elevations, an absolute error of 2 cm is noted for the nearest harbor, equipped with a radar tidal gauge (Krohne Optiflex). Wave and wind data are obtained from models reanalysis, where 10 m wind data are assimilated with ARPEGE/ALADIN [197], then injected in VAG model [85] for waves reanalysis. In these models, a comparison by Campos and Guedes Soares [35] to GlobWave satellite data shows that spatial average of yearly absolute errors does not exceed 0.28 m/s for wind and 0.13 m for waves, where monthly errors can go up to 0.20 m. Previously described measurement uncertainties are summarized in Table 1.3.

1.2.2 Punctual observations

In addition to constant monitoring, punctual measurement campaigns were organized for supplementary information. In particular, a two-months survey was undertaken in 2010 to record local currents, waves and turbidity. Additionally, a new measurement campaign took place at the beginning of the thesis on 2018, with the objective of completing previous information by data inside the intake. I therefore had the opportunity to participate to the installation of necessary measurement devices in the intake, during a week time.

The 2010 field survey

Free surface elevation and velocity components were measured at the vicinity of the intake in five measurement points, as illustrated in Figure 1.11.

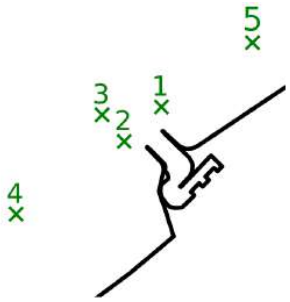

Figure 1.11 – Locations of measurement points for the two-months 2010 survey.

The targeted period is characterized with possible storms and surges. A superposition of the measured hydrodynamic variables on tidal periods is shown in Figure 1.12.

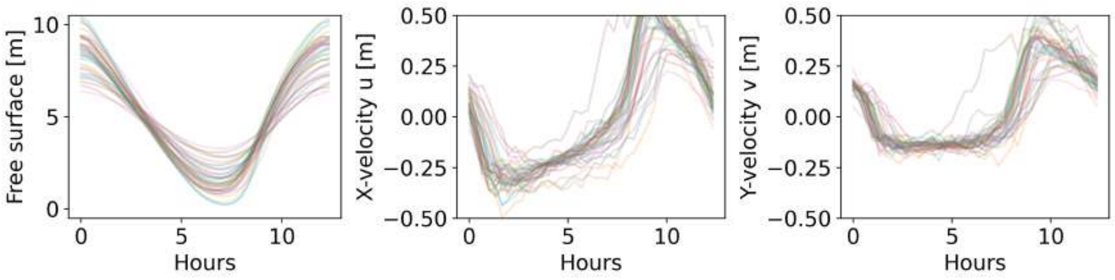

(a) Free surface (b) X-velocity u (c) Y-velocity v

Figure 1.12 – Superposition of 2010 measurements for the hydrodynamic variables on Point 1.

An example of bottom turbidity and wave heights on Point 4 is shown in Figure 1.13. As previously mentioned, data are subject to measurement errors. In particular for the 2010 campaign, Acoustic Wave And Current (AWAC) meters (1 MHz Nortek, Doppler technology) were used for offshore tidal velocities, levels (through pressure records) and wave heights (Points 3, 4, and 5). Absolute error is about 1 cm/s for tidal velocities and 5 cm for tidal levels, relative error is 1 % for wave heights, and absolute error is 2° for wave direction. For Points 1 and 2, wave heights and three-Dimensional (3D) velocity components (in the water column) were measured using Aquadopp profiler (1 MHz Nortek, Doppler) with an error of 1 % ± 5 mm/s for velocities. Turbidimeters (YSI 6136 and YSI 6126 at points 1 to 4 and multi-parameter Hydrolab MS5 for point 5) were also used with an error ranging from 2 % (YSI) to maximum 5 % (Hydrolab). Described measurement uncertainties can be found in Table 1.3.

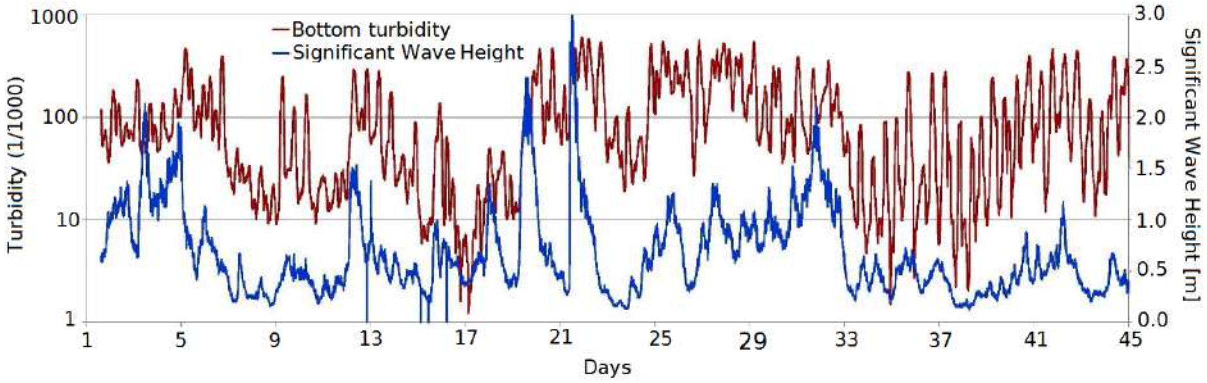

Figure 1.13 – Plots of turbidity and wave heights measurements on Point 4, by [122]

Campaigns	Data	Device	Error
Continuous	Single-beam bathymetry	Sonar boats	≤ ±0.01 m
	Tidal elevations	Krohne Optiflex	±2 cm
	Wind velocities	ARPEGE/ALADIN reanalysis	average ≤ ±0.28 m/s
	Wave heights	VAG reanalysis	average ≤ ±0.13 m
2010	Tidal velocity (Points 3 to 5)	AWAC (1 MHz)	±1 cm/s
	Tidal velocity (Points 1, 2)	Aquadopp (1 MHz)	±1 % ± 5 mm/s
	Tidal levels (Points 3 to 5)	AWAC (1 MHz)	±5 cm
	Wave heights (Points 3 to 5)	AWAC (1 MHz)	±1 %
	Wave directions (Points 3 to 5)	AWAC (1 MHz)	±2°
	Turbidity (Points 1 to 4)	Turbidimeters YSI	±2 %
	Turbidity (Point 5)	Hydrolab MS5	±2 %
2018	Velocity magnitude	RiverPro ADCP	±0.25 % ± 2 mm/s)
	Turbidity	SAMBAT buoy	≤ ±2 %

Table 1.3 – Measurements uncertainties.

The 2018 field survey

In particular, water levels, 3D velocities and turbidity were provided. Immersed pressure sensors for water depth (Figure 1.14-a) , SAMBAT autonomous multi-parametric buoy for physico-chemical water characteristics (Figure 1.14-b), and ADCP Teledyne RiverPRO (600 to 1200 kHz) for currents equipped on boat rafts (Zodiac MarkIII 30cv and Sillinger 80cv) and on an aquatic drone boat (RiverDrone, Figure 1.14-c) were used for measurements. Localisations of measurements were tracked using a Leica CS15/GS14 GPS (Figure 1.14-d).

(a) Pressure sensors fixed to anchors

(b) SAMBAT buoy

(c) RiverDrone

(d) Leica GPS

Figure 1.14 – Measurement devices for the 2018 campaign.

ADCP velocity measurements were recorded at High Tide (HT), Half Falling Tide (HFT), Low Tide (LT), and Half Rising Tide (HRT), at different intake transects schematized in Figure 1.15-a and vertically sampled each 10 cm in the water columns. Buoys were installed for approximately 6 weeks. An example of velocity magnitude profile at a transect perpendicular to pumps is also shown in Figure 1.15-b, where velocities are higher at the vicinity of the pumps.

Physico-chemical characteristics were measured with a frequency of 5 minutes, using the SAMBAT buoy immersed at the entrance of the intake. Examples of 4-day turbidity and salinity measurements are shown in Figure 1.16.

Turbidity measurements with the SAMBAT buoy are characterized by 5 % maximum error, and RiverPro ADCP technical sheet indicates 0.25 % (±2 mm/s) error for velocity magnitude. These are added to errors of previously described campaigns in Table 1.3.

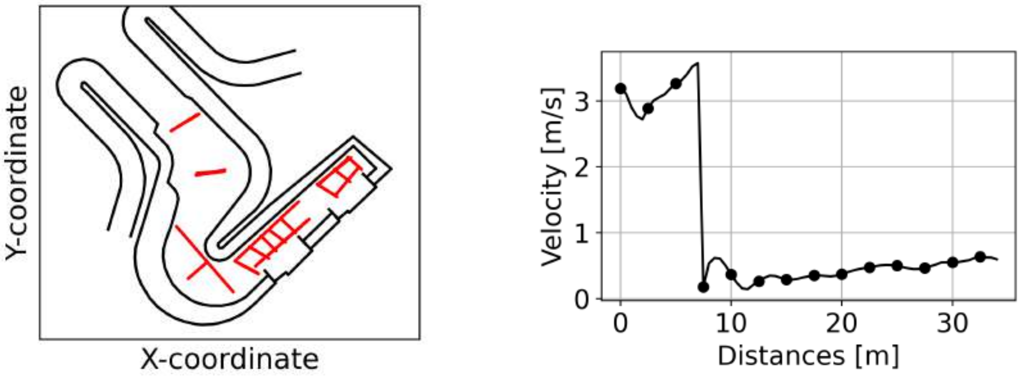

(a) Transects locations (b) Velocity profile example

Figure 1.15 – ADCP measurement transects in the intake represented in red color, and an example of velocity magnitude profile at a transect perpendicular to pumps, from left bank (pump) to right bank.

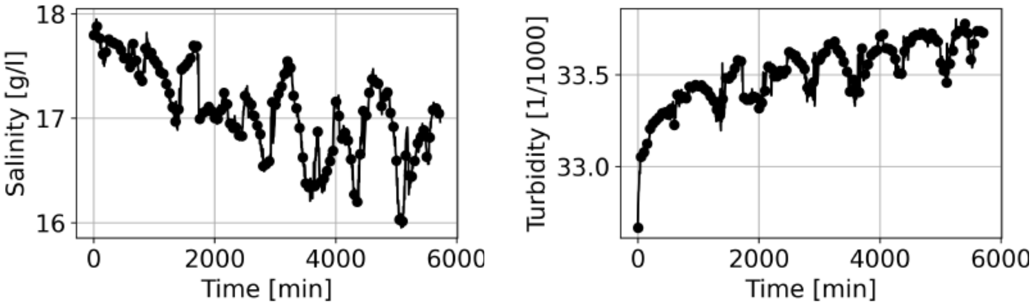

(a) Salinity (b) Turbidity

Figure 1.16 – Examples of salinity and turbidity measurements with the SAMBAT buoy.

1.3 Process-based hydro-morphodynamics for data-driven modelling

Previously presented data are a valuable source of information, that could help understanding the dynamics. It can also be completed by numerical investigations, using appropriate physics-based models, that are described hereafter.

There is a complex interdependence of water motion, sediment dynamics and bed morphology. The bottom grains are transported due to the action of the flow on the bottom. This motion is classically separated into two distinct but interacting physical processes [258, 259]. The first part is called "*suspension*", where the particles are transported in the water column at flow velocity. The second is called "*bed-load*", where the particles move due to their interactions with each other, in contact with the bottom. This sediment movement modifies the bathymetry, which implies a modification of the flow dynamics. From an Eulerian viewpoint (description of the field at given locations), this inter-dependency is usually modelled thanks to a coupled system of equations, composed of conservation laws on hydrodynamics and sediment transport [187]. Lagrangian approaches (particles tracking) exist as well [15] but are discarded in this work, principally because of the industrial constraints that highly limit simulation times.

The first part of the hydro-morphodynamic modelling system is a conservation law on the fluid mass and momentum, called the three-Dimensional Free-Surface Navier-Stokes (3D-FS-NS) equations. They consist on the classical Navier Stokes (NS) equations with a kinematic Boundary Conditions (BC) on the free surface, convenient for the modelling of flows in natural environments (river, sea, etc.). The 3D-FS-NS equations simulate the classical three velocity components (two on the horizontal plane and one the vertical), to which is added the water depth variable, or the free surface elevation (water depth + bottom elevation). However, for time constraints, a two-Dimensional (2D) system is more often preferred in industrial applications when possible. In particular, a depth averaged version of 3D-FS-NS, called 2D-Horizontal (2DH) model, is deduced by integrating the system on the vertical. This 2DH system is also called the Shallow Water Equations (SWE) or the Saint-Venant equations. A reminder of the 3D-FS-NS equations and derived SWE is proposed in Section 1.3.1, with a summary of inherent approximations and limitations. Additionally, methods to take the waves influence into account are summarized in Section 1.3.2.

The second part of the hydro-morphodynamic modelling system consists on a sediment mass balance [187]. In Eulerian approaches, the sediments are treated as a continuum, and their conservation at the bottom is represented by the *Exner* equation. Presence of sediments in the water column (suspension) is represented by a concentration of particles in the flow [9], assuming a dilute mixture of sediment and water. The concentration is modelled by an advection-diffusion equation, with source/sink terms that represent the exchange with the bottom (bed-load dominated region). These source/sink terms are also present in the Exner equation, to which a bed-load flux is added, both participating to the deformation of the bed. The bed-load and suspension processes work together through the coupling of these equations to the flow equations. The involved fluxes are generally estimated with empirical formulas that use the flow variables. A reminder of these equations and a discussion about the closures for fluxes and source terms is proposed in Section 1.3.3.

Lastly, a brief description of the used modelling system is given in Section 1.3.4.

1.3.1 Hydrodynamic equations

This section is dedicated to the equations and hypothesis behind the used numerical model, in particular the Shallow Water Equations (SWE) for free-surface flows. Before providing the formulation of SWE and underlying assumptions, we briefly recall the fundamental reasoning behind Navier Stokes (NS) equations, their closures and the free-surface version. These are indeed fundamental for the establishment of SWE. The theoretical framework and reasoning will be presented in a summarized way, and readers interested in further details can refer to [10, 219, 247, 248] .

Navier-Stokes equations

NS equations express the fluid particles motion, on the basis of two fundamental principles: the conservation of mass, and Newton's second law on a fluid particle, assuming that the latter is submitted to forces, that can be either external to the fluid continuum (e.g gravity), or internal (interactions between the fluid particles) [10, 247]. This leads to the continuity and momentum conservation system of Equations 1.1,

$$\begin{cases} \dfrac{\partial \rho}{\partial t} + \nabla \cdot (\rho \boldsymbol{U}) = 0 \\ \rho \left(\dfrac{\partial \boldsymbol{U}}{\partial t} + (\boldsymbol{U} \cdot \nabla) \boldsymbol{U} \right) = \nabla \cdot \boldsymbol{\Sigma} + \rho \boldsymbol{g} + \boldsymbol{F} \end{cases} , \tag{1.1}$$

∇ and $\nabla\cdot$ are the gradient and divergence operators respectively, $\boldsymbol{U} := [U, V, W]^T$ is the 3D velocity vector for space-coordinates $\mathbf{x} = (x, y, z)$, $\nabla \cdot \boldsymbol{\Sigma}$ are the surfacic forces expressed in terms of stress tensor $\boldsymbol{\Sigma}$, $\rho \boldsymbol{g}$ is the gravity volumic force and $\boldsymbol{F}$ are the remaining external forces (e.g. Coriolis). An approximation is introduced to express the stress tensor $\boldsymbol{\Sigma}$ in terms of deformation, which depends on the molecular structure of the fluid. This is the well known rheologic Stokes law for Newtonian fluids, expressed in Equation 1.2,

$$\boldsymbol{\Sigma} = -p\boldsymbol{I} + \lambda \ \nabla \cdot \boldsymbol{U} \ \boldsymbol{I} + \mu \left(\nabla \boldsymbol{U} + \nabla \boldsymbol{U}^T \right) \ , \tag{1.2}$$

where $\boldsymbol{I}$ is the identity tensor, p is the pressure, μ is the dynamic molecular viscosity and $\lambda \approx -\frac{2}{3}\mu$ (empirical). The coefficients λ and μ are called the Lamé coefficients and the previous relation is called the Stokes hypothesis [247]. The system 1.1 and the Stokes empirical closure for the stress tensor 1.2 constitute the NS equations for Newtonian fluids written in Equation 1.3, where Δ is the Laplacian operator, and $\nu = \mu/\rho$ is the kinematic viscosity. This is simplified for incompressible fluids as $\nabla \cdot \boldsymbol{U} = 0$.

$$\begin{cases} \dfrac{\partial \rho}{\partial t} + \nabla \cdot (\rho \boldsymbol{U}) = 0 \\ \\ \dfrac{\partial \boldsymbol{U}}{\partial t} + (\boldsymbol{U} \cdot \nabla) \boldsymbol{U} = -\dfrac{1}{\rho} \nabla p + \nu \Delta \boldsymbol{U} + \dfrac{1}{3} \nu \nabla (\nabla \cdot \boldsymbol{U}) + \boldsymbol{g} + \frac{1}{\rho} \boldsymbol{F} \end{cases} . \tag{1.3}$$

Determination of the unknown velocity components from the resolution of these equations can for example describe the full state of a fluid that is constrained in a flume, if adequate Boundary Conditions (BC) are given. However, for a range of natural flows (river, estuary, sea), it is capital to characterize the evolution of the water depth denoted $h(\mathbf{x}, t)$, which is an additional unknown. These flows, called free-surface flows, are a particular case of two-phase flows with an interface between water and air [219]. Hence, an equation $\Phi(\mathbf{x}, t) = z - \eta(x, y, t)$ is added to characterize the interface between the first fluid layer (here water) and the second fluid layer (here the air). In this equation z denotes an arbitrary elevation in the calculation domain (third spatial coordinate in $\mathbf{x}$) and $\eta(x, y, t)$ denotes the interface position, which implies that $\Phi(\mathbf{x}, t)$ is null at the interface and negative in the lower fluid layer. This equation is completed with a BC on the interface where the fluid particles are considered to have a zero normal velocity (no fluid particle leaves the interface). This gives birth to the *kinematic condition* in Equation 1.4 (free-surface condition for water-air two-phase flows).

$$\frac{\partial \Phi(\mathbf{x}, t)}{\partial t} + \boldsymbol{U} \cdot \nabla \Phi(\mathbf{x}, t) = 0 \ . \tag{1.4}$$

The system 1.1, Stokes closure 1.2 and kinematic condition 1.4 represent the three-Dimensional Free-Surface Navier-Stokes (3D-FS-NS) equations for Newtonian fluids.

Experiments on simple cases show however that the measured velocity can be much lower than the analytical solution provided with the NS equations. The overestimation is considered to be caused by unmodelled flow structures called *eddies*, that act as energy dissipators, which is also known as *turbulence*. Hence, in order to introduce additional dissipation, an eddy or turbulent viscosity, denoted ν_t, is often added to the kinematic viscosity, which allows to account, in average, for the presence of vortexes and instationnarities. Its value is usually scaled for the mean flow to correspond to measurements, either by fitting a constant value, or using more sophisticated closures as the $k-\epsilon$ model [250]. In this approach, the complex structure of eddies at various scales is not properly modelled, but only its mean effect on the flow is taken into account. This is called *Reynolds averaging*, in the sense that all modelled unknowns represent mean values of the variations caused by smaller scale flow patterns. The system's variables are considered to be a superposition of mean quantities and fluctuations representing eddies, for example written as $\mathbf{U} = \overline{\mathbf{U}} + \mathbf{U}'$ for velocity, where $\overline{\mathbf{U}}$ is the average and $\mathbf{U}'$ is the fluctuation. Incorporating this approximation to NS gives the so-called Reynolds Averaged NS (RANS) Equations.

At this step, there are already few hypothesis that should be kept in mind while using the presented 3D-FS-NS for modelling: (i) the fluid is Newtonian, and equations are usually used in incompressible form for small to medium scale environmental flows; (ii) Stokes law with Lamé coefficients is an empirical closure; (iii) introduction of an eddy viscosity partially solves the turbulence problem, as only a mean flow is represented rather than the complex structure of eddies at various scales; (iv) closures are necessary for the variations of pressure p and fluid density ρ using state laws; (v) the remaining forces $\boldsymbol{F}$ should be defined and are also often modelled using closures; (vi) kinematic condition implies that no detachment of the fluid particles from the interface is modelled; (vii) analytical solutions for NS are only defined for few particular cases. The existence and smoothness of NS solutions is still a Millennium Prize Problem [38]. Therefore, they are approximated using numerical schemes that introduce uncertainties.

Shallow Water Equations

Numerical resolution of the 3D-FS-NS equations is however costly, namely for natural flows that are contained in large domains (kilometers) and for which a fine resolution is desired (meters). A 2D version has therefore been derived to characterize horizontal flows. These are the Shallow Water Equations (SWE), and their derivation for viscous flows is demonstrated in [79]. We briefly recall assumptions and details for specific terms of interest. Readers interested in detailed demonstrations may refer to [79].

The SWE are derived from the incompressible 3D-FS-NS equations, using adimensionalization and depth-averaging (integration on the vertical). In addition to previously described NS assumptions and incompressibility ($\nabla \cdot \boldsymbol{U} = 0$), the following hypothesis are added:

- flow is studied in shallow waters. The characteristic vertical scale h_0 is negligible compared to the horizontal one L_0 ($h_0/L_0 << 1$);

- vertical accelerations are negligible, and external forces $\boldsymbol{F}$ are constant along the vertical;
- bed slope is low, i.e. no abrupt bathymetry variations;
- appropriate BC are set, namely: (i) p is equal to the atmospheric pressure p_a at the free-surface $z = \eta(x, y, t)$; (ii) horizontal velocity is null at the bottom $z = z_b(x, y, t)$, where z_b is the bed elevation; (iii) there is no vertical variation of horizontal velocities at the free-surface;
- impermeability hypothesis is considered, i.e. no particle leaves the fluid through free-surface or bottom;
- new depth-averaged quantities are introduced for the velocity components as in 1.5, where $h(x, y, t) = \eta(x, y, t) - z_b(x, y, t)$ is the water depth;

$$\begin{cases} u(x,y,t) \coloneqq \dfrac{1}{h(x,y,t)} \displaystyle\int_{z_b(x,y,t)}^{\eta(x,y,t)} U(\mathbf{x},t)dz \\ \\ v(x,y,t) \coloneqq \dfrac{1}{h(x,y,t)} \displaystyle\int_{z_b(x,y,t)}^{\eta(x,y,t)} V(\mathbf{x},t)dz \end{cases} . \tag{1.5}$$

The adimensionalization applied to the momentum equation on the vertical velocity component W, gives the hydrostatic pressure condition $\dfrac{\partial p}{\partial z} = -\rho g$, called *hydrostatic pressure hypothesis*. The latter is the result of shallow water hypothesis. Adimensionalization to the remaining equations allows to neglect some terms using the above-mentioned assumptions. Depth-averaging on the vertical, with the hydrostatic pressure and the kinematic condition that make the water depth variable appear in the system, give the SWE in 1.6.

$$\begin{cases} \dfrac{\partial h}{\partial t} + \dfrac{\partial (hu)}{\partial x} + \dfrac{\partial (hv)}{\partial y} = 0 \\ \dfrac{\partial (hu)}{\partial t} + \dfrac{\partial (hu^2)}{\partial x} + \dfrac{\partial (huv)}{\partial y} = -gh\dfrac{\partial \eta}{\partial x} - \dfrac{1}{\rho}\tau_{bx} + \dfrac{h}{\rho}F_x + \nabla \cdot (h\nu_e \nabla u) \\ \dfrac{\partial (hv)}{\partial t} + \dfrac{\partial (huv)}{\partial x} + \dfrac{\partial (hv^2)}{\partial y} = -gh\dfrac{\partial \eta}{\partial y} - \dfrac{1}{\rho}\tau_{by} + \dfrac{h}{\rho}F_y + \nabla \cdot (h\nu_e \nabla v) \end{cases} . \tag{1.6}$$

Right hand side of the system contains new quantities. Firstly, $\nu_e \coloneqq \nu + \nu_t + \nu_d$ is called effective viscosity, and accounts for diffusion caused by kinematic and eddy viscosities $(\nu + \nu_t)$, and *dispersion* expressed in ν_d. Indeed, when integrating the non-linear term $((\boldsymbol{U} \cdot \nabla)\boldsymbol{U})$ in the NS equations, velocity quantities in the form $\int U^2 dz$ appear. The latter are approximated as $\int U^2 \approx hu^2 + \int \tilde{u}^2 dz$, where $\tilde{u}$ accounts for vertical variations. Dispersive viscosity ν_d results from a linear approximation in the form $\int \tilde{u}^2 dz \approx \beta h u^2$, given the impossibility of exact calculation.

Secondly, bed shear stress vector $\boldsymbol{\tau}_b$ is introduced. The latter appears from integration of $\nabla \cdot \boldsymbol{\Sigma} = \mu \Delta \boldsymbol{U}$. Using Leibnitz rule, normal projections of $\boldsymbol{\Sigma}$ at domain boundaries (integration interval bounds) are used, i.e. $\boldsymbol{\Sigma}_b \cdot \boldsymbol{n}_b \coloneqq \boldsymbol{\Sigma}(x, y, z = z_b(x, y), t) \cdot \boldsymbol{n}_b$ and $\boldsymbol{\Sigma}_s \cdot \boldsymbol{n}_s \coloneqq \boldsymbol{\Sigma}(x, y, z = \eta(x, y), t) \cdot \boldsymbol{n}_b$ corresponding to bottom and free-surface constraints respectively. Free-surface constraint $\boldsymbol{\tau}_s$ is usually neglected for applications where wind forcing is not important (rivers mainly). This is why it does not usually appear in SWE, and is implicitly contained in the external forces as $\boldsymbol{F}_s := \frac{1}{h}\boldsymbol{\tau}_s$, considered depending on the modelled case. It can however be capital for coastal applications, as it may imply strong deformation, resulting in wind waves. However, realistic ocean waves propagation can not be fully modelled with SWE, which is discussed in Section 1.3.2. Bottom constraint (or bed shear stress) $\boldsymbol{\tau}_b$ is however capital for all environmental applications as it has considerable influence on the flow, by the energy dissipation it introduces [167]. Indeed, dissipative effects resulting from bed resistance to the flow, that take the form of near bed flow structures (small to big turbulent eddies), are represented by $\boldsymbol{\tau}_b$, and play a major role in currents moderation [167]. Its analytical expression is written in Equation 1.7.

$$\boldsymbol{\tau}_b := \boldsymbol{\Sigma}^b \cdot \boldsymbol{n}_b = \mu \left(\left.\frac{\partial U}{\partial z}\right|_{z=z_b}, \left.\frac{\partial V}{\partial z}\right|_{z=z_b} \right) . \tag{1.7}$$

Its exact formulation is unknown and needs closure. It is therefore generally approximated using theoretical plane horizontal bed resistance to parallel flow, as in Equation 1.8,

$$\boldsymbol{\tau}_b = \frac{1}{2}\rho \; C_f(\boldsymbol{\theta}_b, \boldsymbol{\theta}_f)|\boldsymbol{u}|\boldsymbol{u} \ , \tag{1.8}$$

where C_f, dimensionless, is called *friction coefficient*, depending on bed and flow/fluid characteristics denoted $\boldsymbol{\theta}_b$ and $\boldsymbol{\theta}_f$ respectively. Literature formulas for C_f are either empirical or semi-empirical [167], based on experimental setups combined to theoretical approaches on simple cases [146, 157]. One of the most widely used empirical formulas is Strickler's model in Equation 1.9 (or Manning-Strickler in the Anglo-Saxon terminology [148]), where coefficient B takes values in the range $[21.1, 26.613]$ $\mathrm{m}^{1/2}\ \mathrm{s}^{-1}$ and k_s is the bed roughness height, allowing to measure bed irregularities and texture [148]. This formula is usually written as a function of the *Strickler coefficient* $K := B/k_s^{1/6}$ (or Manning's $n := 1/K$). It is easy to implement and the orders of magnitude of K are well documented for various environmental applications, as it has been calibrated for a wide variety of rivers [16, 71].

$$C_f = \frac{2g}{B^2}\left(\frac{k_s}{h}\right)^{1/3} . \tag{1.9}$$

Nevertheless, it is admitted that bed resistance may change with turbulence regimes [148, 157], an element that empirical formulas discard. Formulas accounting for turbulence generally result from theoretical reasoning [250, 274] completed by estimations from experimental setups with different flow regimes [146, 157]. The semi-empirical Colebrook-White's formula is for example written in Equation 1.10, where $Re = U \times D_h/\nu$ is the *Reynolds number*, D_h is the hydraulic diameter often approximated by $4 \times h$, and B_1, B_2 and B_3 are dimensionless coefficients. The latter have been fitted using different flow conditions and take values in the intervals $[2, 2.14]$, $[0, 7.17]$ and $[8.888, 14.83]$ respectively [274].

$$C_f = \frac{\lambda}{4} = \frac{1}{4 \times \left(-B_1 log\left(\frac{1}{B_2}\frac{k_s}{h} + \frac{B_3}{Re\sqrt{\lambda}}\right)\right)^2} . \tag{1.10}$$

For both formulas, k_s must be defined. The roughness concept is physically complex to describe, as it results from different characteristics of the bed: i) *skin drag* (surface texture: grains); ii) *form drag* (surface geometry: bed forms) and iii) *shape drag* (overall geometry: meanders, bends) [91, 167]. All these effects must be accounted for in realistic models. Roughness height k_s is therefore usually used for calibration, as a "model of the physical processes that are omitted" near the bed [167]. Hence, it should be manipulated cautiously to avoid over-tuning and balancing numerical errors. This is not an easy task. To avoid non-physical calibration, k_s bounds should be quantified. In 2D models, using SWE for example, it is used to compensate for *form drag* in addition to *skin drag*, as resulting 3D flow structures, pressure forces acting on the bed forms, effect of small bathymetry variations on the water column, and near-bed turbulence are not modelled.

The previously cited formulas were established in experimental configurations with skin roughness only. The latter is therefore well documented in literature and generally estimated from bed materials size [91, 148, 167]. Form drag is more difficult to quantify [167] and exhibits unsteadiness, going through different regimes as bed forms change with the flow [198], illustrated in Figure 1.17.

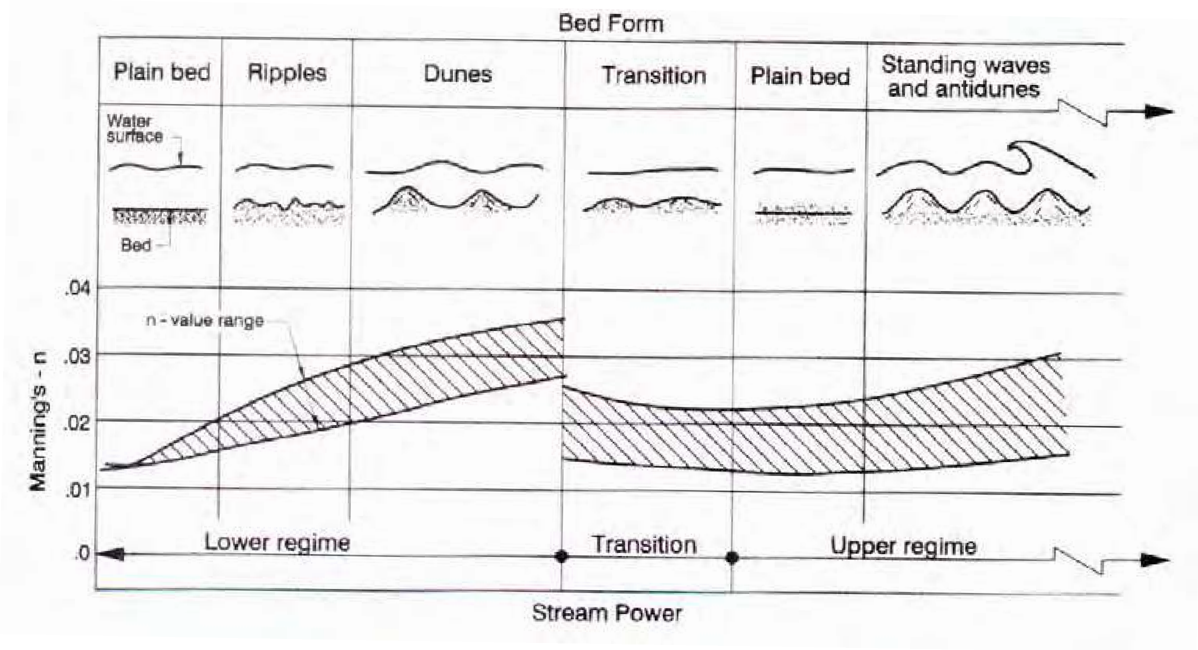

Figure 1.17 – Variation of Manning's coefficient with bed forms, by Hassanzadeh [91]

Dominant bed forms in coastal seas are ripples, followed by megaripples and dunes (Figure 1.18 from Section 1.3.3). van Rijn [258] therefore propose to quantify roughness induced by ripples k_s^r, mega-ripples $k_s^{m,r}$ and dunes k_s^d with an appropriate function of bed and flow characteristics [258]. These formulas are however also uncertain. For simpler use, bounds are also reported in [258] for each component, as $[0.00064, 0.075]$ m, $[0.002, 0.2]$ m and $[0, 1]$ m respectively. In particular, k_s^r values account for both skin and ripple friction. For these roughness types, and in the absence of alternatives, it is considered that their induced bed resistance follows the same laws as skin drag. Common practice consists on separating $\boldsymbol{\tau}_b$ to additive components [71], or calculating an equivalent roughness height as proposed by [258] using $k_s = \sqrt{(k_s^r)^2 + (k_s^{mr})^2 + (k_s^d)^2}$. Therefore, previously described bounds can be used to limit the total roughness calibration interval to $k_s \in [0.00064, 1.023]$ m. Same additivity strategies are usually used to account for bed resistance induced by other current types (e.g. wave generated near bed turbulence).

In addition, adequate Boundary Conditions (BC) should be set for numerical modelling. Solid BC commonly correspond to null fluxes (*no slip* condition). For the intake case, outflow BC are set to pumping flowrates. Inflow BC are however uncertain, depending on nearshore hydrodynamics mainly consisting in tidal and wave forcing. They can be parameterized, for example using the TPXO tidal data-base, particularly the European Shelf (ES) local model [62]. In this case, hydrodynamic unknowns at the boundary are modelled as a superposition of harmonic components, as in Equation 1.11,

$$\begin{array}{rcl} F(\mathbf{p},t) & = & \sum F_i(\mathbf{p},t) \\ F_i(\mathbf{p},t) & = & f_i(t)A_{F_i}(\mathbf{p})cos\left(2\pi t/T_i - \phi_{F_i}(\mathbf{p}) + u_i^0 + v_i(t)\right) \end{array}, \tag{1.11}$$

where the term F at point $\mathbf{p}$ and time t represents the unknown (velocity component and/or water depth), F_i a harmonic component with constant period T_i, amplitude A_{F_i}, phase ϕ_{F_i}, phase at origin of times u_i^0, and temporal nodal factors $f_i(t)$ and $v_i(t)$. In order to account for uncertainties in the tidal base, three parameters, denoted CTL (Coefficient of Tidal Level), MTL (Mean Tidal Level) and CTV (Coefficient of Tidal Velocity), can be used to calibrate BC on measurements, as in Equation 1.12. For example, MTL allows to compensate for seasonal variability (effect of thermal expansion, salinity variations, air pressure, etc.) and long-term sea level rise resulting from climate change [102]. The three coefficients MTL, CTL and CTV can also be used to compensate the effects of storm and surge (atmospheric and wave setup), as the latter are not modelled and not taken into consideration in the TPXO data-base.

$$\begin{array}{rcl} h & = & CTL \times \sum h_i(M,t) - z_f + MTL \\ u & = & CTV \times \sum u_i(M,t) \\ v & = & CTV \times \sum v_i(M,t) \end{array}. \tag{1.12}$$

In all previously used formulas, be it for friction or BC approximation, an important degree of uncertainty should be highlighted. Namely, only empirical or semi-empirical formulas are used, and a number of tuning coefficients are noted. Particularly, formulas are often ”applied to flow conditions far from those on the basis of which they have been developed” [146]. Additionally, they are often used to compensate for unmodelled physics. For example, eddy viscosity ν_t is used to model average effect of turbulence without modelling all eddies and energy cascade with Direct Numerical Simulations (DNS), and roughness height k_s is similarly used to compensate for unrepresented near bed phenomena. These approximations are indeed practical, but remain uncertain. In the absence of alternatives however, the presented formulas are used, considering that they carry a part of truth and a part of error that can be characterized with Uncertainty Quantificiation (UQ) (see Chapter 3 for theoretical details and Chapter 4 for application).

Lastly, until now, bottom elevation z_b was not discussed, even though it is present in SWE, through water depth h, and can evolve in time. This has a strong influence on flow modelling, and can be of interest in morphodynamic problems, as for the studied intake. Bathymetry evolution and sediment dynamics are dealt with in Section 1.3.3.

1.3.2 Waves modelling

Wind can be an important component of coastal applications, as it locally generates waves (*wind waves*). Once generated, waves can propagate with the flow (*swell*) and dissipate through numerous phenomena (e.g. *breaking*).

Wind effect on the free surface can be accounted for through normal shear stress in SWE, as explained in Section 1.3.1. Empirical formulas are usually used for that matter.

However, realistic waves propagation cannot be modelled with SWE in coastal configurations, since waves have different velocities and can deform [249, 250]. Indeed, as a consequence of the used hypothesis, SWE are said to be *non-dispersive*, because they only propagate waves without deformation, and only with two possible velocities (see the linearization using small perturbations [248, 250]). Therefore, other approaches are used for wave propagation and dissipation, to model free-surface spatio-temporal fluctuations around the average delivered by SWE. Additionally, waves also imply a change in the flow currents, due to the orbital motion of water particles [248]. This means that velocity values are impacted, which can be modelled in SWE by adding an external force to momentum conservation, called the wave driving force $\boldsymbol{F}^w$, or corresponding stress called *radiation stress*. This force/stress implies momentum excess in the same way friction $\boldsymbol{F}^f$ implies diffusion.

To compute the wave driving forces and free surface fluctuations, a new model is needed. Three approaches are briefly presented, but readers in need of detailed explanation and theoretical elements can refer to [30, 249].

Physical approach: spectral models

Natural waves are random and irregular in space and time. This randomness can be approximated by a finite superposition of $m \in \mathbb{N}$ independent monochromatic (or regular) wave components, with their amplitudes a_i, angular frequencies ω_i, wave numbers k_i, directions θ_i, and phases Φ_i as in Equation 1.13.

$$\xi(x, y, t) = \sum_{i=1}^{m} \xi_i(x, y, t) = \sum_{i=1}^{m} a_i \ \cos(k_i(x \sin\theta_i + y \cos\theta_i) - \omega_i t + \Phi_i) \ . \tag{1.13}$$

Firstly, for a component ξ_i, wave height is defined as $H_i = 2a_i$, frequency as $f_i := \Omega_i/2\pi$ and period as $T_i = 1/f_i$. Secondly, the wave number relates to wave length L_i as $k_i 2\pi/L_i$, and the wave number vector is defined as $[(k_i)_x, (k_i)_y]^T := [k_i sin\theta_i, k_i cos\theta_i]^T$. Furthermore, there exist a physical relation between ω_i and k_i, called the *linear dispersion relation for surface waves*, and denoted Ω, that reads $\omega_i^2 = \Omega((k_i)_x, (k_i)_y, x, y, t)^2 = (gk_i)\tanh(k_i h)$. This can be calculated by finding small perturbation solutions of the incompressible Euler equations with flat bottom [249]. Lastly, for ξ_i, the induced mechanical energy per unit of surface (potential+kinetic) is defined as $E_i := 1/2\rho g a_i^2$, whereas it is approximated as $E := \sum_{i=1}^{m} E_i$ for the superposition of waves $\xi = \sum_{i=1}^{m} \xi_i$.

In real life however, waves are not a discrete superposition of components, and their energy is not a discrete summation. They are continuous physical quantities, that can be expressed on continuous domains of frequencies $f \in [0, +\infty]$ and directions $\theta \in [0, 2\pi]$. Elementary energy, called *spectrum of wave energy* and denoted $E(f, \theta)$, can be defined for a continuous representation of E on the full frequency-direction space $[0, +\infty] \times [0, 2\pi]$ as $E = \int_0^{+\infty} \int_0^{2\pi} E(f, \theta) df d\theta$. Another variant of the same quantity, called *variance spectrum of wave energy*, is defined as $F(f, \theta) := E(f, \theta)/\rho g$. The latter is related to wave perturbation as in Equation 1.14, where the phases ϕ are randomly distributed over the range $[0, 2\pi]$.

$$\xi(x, y, t) = \int_0^{+\infty} \int_0^{2\pi} \sqrt{2F(f, \theta) df d\theta} cos\left(k(f) \times (xsin\theta + ycos\theta) - 2\pi f t + \Phi\right) \ . \tag{1.14}$$

Therefore, each amplitude a_i in Equation 1.13 can be seen as an elementary component approximated as $a_i = \sqrt{2F(f,\theta)df\,d\theta}$.

Waves can travel in space and time, which means that their characteristics may vary with their coordinates as $f = f(x,y,t)$ and $\theta = \theta(x,y,t)$.

In a uniform medium, an observer that moves with a wave sees unchanged characteristics, meaning that ω (or f) and $[k_x,k_y]^T$ (or angle k and θ) keep unchanged on this trajectory [30]. The observer follows a straight path, called the *ray* [30]. Rays therefore define paths along which frequency and wave number remain constant, which can be formally written as $\frac{d\omega}{dt} = \frac{dk_x}{dt} = \frac{dk_y}{dt} = 0$, with $\frac{d}{dt} = \frac{\partial}{\partial t} + \dot{x}\frac{\partial}{\partial x} + \dot{y}\frac{\partial}{\partial y}$. Vector $[\dot{x},\dot{y}]^T \coloneqq \left[\frac{\partial x}{\partial t},\frac{\partial y}{\partial t}\right]$ defines the celerity of the wave in the global referential, called *group velocity*, often denoted $[c_x^g,c_y^g]^T$ and calculated as in Equation 1.15.

$$[c_x^g,c_y^g]^T \coloneqq \left[\frac{\partial x}{\partial t},\frac{\partial y}{\partial t}\right]^T = \left[\frac{\partial \Omega}{\partial k_x},\frac{\partial \Omega}{\partial k_y}\right]^T \; . \tag{1.15}$$

In a non-uniform medium however, characteristics of the flow have an influence on wave trajectories and deformation. Rays are no longer straight but curved. If the flow characteristics are denoted λ, the differentials become $\frac{d\omega}{dt} = \frac{\partial\Omega}{\partial\lambda}\frac{\partial\lambda}{\partial t}$, $\frac{dk_x}{dt} = -\frac{\partial\Omega}{\partial\lambda}\frac{\partial\lambda}{\partial x}$ and $\frac{dk_y}{dt} = -\frac{\partial\Omega}{\partial\lambda}\frac{\partial\lambda}{\partial y}$ [30]. This implies that the frequency and wave number vary along the ray, with variations of the medium characteristics (e.g. flow velocity).

Consequently, modelling the sea state consists on calculating variations of frequencies and wave numbers along rays, in order to determine variations of wave amplitudes in the spatio-temporal domain. A conservation law is generally used [30], written as in Equation 1.16.

$$\frac{dN}{dt} = \frac{\partial N}{\partial t} + \frac{\partial \dot{x}N}{\partial x} + \frac{\partial \dot{y}N}{\partial y} + \frac{\partial \dot{k}_xN}{\partial k_x} + \frac{\partial \dot{k}_yN}{\partial k_y} = Q \; . \tag{1.16}$$

Conserved quantity N is called *wave action* and defined as $N(x,y,k_x,k_y,t) = F(f,\theta)/\sigma$, where σ is the relative pulsation observed from a referential moving at flow velocity $\boldsymbol{u}$. It relates to wave frequency by $\Omega(k_x,k_y,x,y,t) = \omega = \sigma + [k_x,k_y]^T \cdot \boldsymbol{u}$ (Doppler effect). Waves generation and dissipation are controlled through source terms Q. Propagation equations (or Hamilton equations) defined in 1.17 complete the system.

$$\begin{cases} \dot{x} = \frac{\partial x}{\partial t} = c_x^g = \frac{\partial\Omega}{\partial k_x} \\ \dot{y} = c_y^g = \frac{\partial y}{\partial t} = \frac{\partial\Omega}{\partial k_y} \\ \dot{k}_x = -\frac{\partial\Omega}{\partial x} \\ \dot{k}_y = -\frac{\partial\Omega}{\partial y} \end{cases} \; . \tag{1.17}$$

There are therefore three modelling steps: (i) waves generation by wind forcing, which can be accounted for in Q in Equation 1.16, (ii) waves propagation with the flow using Equation 1.16 and (iii) waves transformation due to different phenomena that induce dissipation and energy transfer (e.g. *shoaling*, *breaking*, *refraction*, *reflection*, *diffraction*, non-linear interactions between the waves, etc.), also accounted for in the source term Q of Equation 1.16.

Flow characteristics (velocity $\mathbf{u}$ and water depth h) are essential for the propagation of waves and therefore influence the sea state. Waves reciprocally influence the flow, which can be modelled by adding a source term to SWE in Equation 1.6, in the form of an external force. The latter is called *wave radiation force*, and defined in Equation 1.18,

$$\boldsymbol{F}^w = [F_x^w, F_x^w]^T = \left[\frac{1}{\rho(h+\xi)}\left(\frac{\partial S_{xx}}{\partial x} + \frac{\partial S_{xy}}{\partial y}\right), \frac{1}{\rho(h+\xi)}\left(\frac{\partial S_{yx}}{\partial x} + \frac{\partial S_{yy}}{\partial y}\right)\right] , \tag{1.18}$$

where S_{xx}, $S_{xy} = S_{yx}$ and S_{yy} are the components of a symmetrical radiation stress tensor denoted $\mathbf{S}$ and defined in Equation 1.19 with $n = \frac{1}{2} + \frac{kh}{\sinh(2kh)}$ [270].

$$\mathbf{S} = \begin{pmatrix} S_{xx} & S_{xy} \\ S_{yx} & S_{yy} \end{pmatrix} = \frac{F(f,\theta)}{2} \begin{pmatrix} 2\pi(1+\cos^2\theta) - 1 & n\sin 2\theta \\ n\sin 2\theta & 2\pi(1+\sin^2\theta) - 1 \end{pmatrix} . \tag{1.19}$$

Statistical characterization

Solving a sea state model is known to be computationally demanding, which is not acceptable industrial applications. However, when wave measurements are available, radiation forces can be directly estimated using statistical models, and injected into the SWE. This allows to replace the process-based models, for example conservation equation defined in 1.16, by a low cost estimation.

For example, an estimation of the non-directional energy density (defined for a mean direction with a frequency variable only) is defined by JONSWAP (Joint North Sea Wave Project, [92]), for limited fetch conditions, as in Equation 1.20

$$E(f) = \alpha_P g^2 (2\pi)^{-4} f^{-5} \exp\left(-\frac{5}{4}\left(\frac{f}{f_p}\right)^{-} 4\right) \gamma^{\exp\left(-\frac{(f-f_p)^2}{2\sigma_J^2 f_p^2}\right)} . \tag{1.20}$$

where α_P is the Phillips constant [193], $\gamma = 3.3$, f_p is the peak frequency, σ_J is the peak width set to $\sigma_J = 0.07$ for $f \leq f_p$ and $\sigma_J = 0.09$ for $f > f_p$ [125, 234]. The directional spreading $E(f,\theta)$ is estimated by multiplying the non-directional spectrum $E(f)$ by a spreading function $A\cos^{2n}\alpha$, where α is the direction relative to the mean direction of wave propagation [234]. The coefficient n is often set to 1 and the energy A is set so that the energy in all directions sums to the same total as the non-directional. This allows to estimate the radiation stress from measurements, at any location where wave characteristics are measured.

Parametric approach: apparent roughness

If neither spectral modelling is an option (computational cost), nor spatio-temporal wave characteristics are available for statistical spectrum calculation, then it is not possible to directly estimate the wave radiation forces. Their effect can however be indirectly considered, by a modification of the friction forces [191, 258]. This is a parametric approach, called *apparent roughness* in literature.

Apparent roughness, denoted k_a is defined as the roughness value allowing to simulate flow conditions in coastal configurations without direct wave modelling. It is used with classical friction formulas, as defined in Section 1.3.1. For example, van Rijn [258] proposes a modification of k_s in the form of Equation 1.21, to account for waves,

$$k_a = \exp\left[(0.8 + \phi - 0.3\phi^2) u_w / |\mathbf{u}_c|\right] k_s , \tag{1.21}$$

where u_w is the waves peak orbital velocity, $|\mathbf{u}_c|$ is the current-only velocity magnitude and ϕ is the angle between the wave direction and current direction in radians.

Orbital velocity u_w can be estimated assuming linear wave theory as in Equation 1.22, where H_s is the *significant wave height* and $\omega_p = 2\pi/T_p$ with T_p the *peak period*, defined in Table 1.4.

$$u_w = \frac{H_s \omega_p}{2\sinh(kh)} . \tag{1.22}$$

More sophisticated formulas also exist for real waves, as the one given by [235] in Equation 1.23, where T_z is the *zero up-crossing period* defined in Table 1.4.

$$u_w = \left(\frac{H_s}{4}\right)\left(\frac{g}{h}\right)^{1/2} \exp\left\{-\left[\frac{3.65}{T_z}\left(\frac{h}{g}\right)^{1/2}\right]^{2.1}\right\} . \tag{1.23}$$

Quantity	**Notation / Formula**	**Comments**
n−th moment of energy spectrum	$m_n = \int_0^{+\infty}\int_0^{2\pi} f^n F(f,\theta) df d\theta$	-
Moment $n = 0$	m_0	variance of the perturbed free surface elevation
Spectral significant wave height	$H_{m0} = 4m_0^{1/2}$	-
Significant wave height	$H_s \approx H_{m0}$	average of the highest third of wave heights, also denoted $H_{1/3}$
Root-mean square height	$H_{rms} = H_s/\sqrt{2}$	It is a good average of the wave energy
Mean period	$T_m = (m_0/m_2)^{1/2}$	-
Peak period	$T_p = 2\pi/\omega_p \approx 5\sqrt{H_{m0}}$;	Wave period with highest energy
Zero up-crossing period	$T_z \approx T_m$; $T_z \approx 0.710\ T_p$ (Pierson-Moskowitz); $T_z \approx 0.781\ T_p$ (JONSWAP)	Period of time between two up-crossings of the average wave height, also denoted $T_{m0,2}$

Table 1.4 – Waves characteristic quantities

It remains difficult to estimate the current-only velocity in real life configurations, where the effect of waves can not be isolated. Therefore, rugosity is often used as a calibration parameter for combined wave-current velocities, to perform fitting on measurements. In this case, orders of magnitude for k_a can help. The authors in [258] report, based on a literature review of ripple-bed experiments, that k_a/k_s ranges in the interval $[1, 15]$, depending on the relative strength of wave to current motion, the wave height and the wave direction. On the basis of a field campaign, it is also reported that k_a ranges in the interval $[0.001, 2]$ m [258].

1.3.3 Sediment transport and morphodynamic equations

As explained in Section 1.3.1, bottom elevation z_b, or bathymetry, can vary as a function of flow parameters. Sediment grains can be transported by different forcing effects (tides, waves, density, etc.), with possible interactions and non-linearities [9]. Their motion may induce bed forms changes, through different deformation scales. As an example illustrated in Figure 1.18, *bed waves* are small scale patterns, while *mega-ripples* and *dunes* are bigger. These deformations can have an impact on the flow, by increasing or decreasing bed resistance, implying changes in the drag force. Near bed hydrodynamics and turbulence can consequently be impacted, resulting on an inverse feedback on morphodynamics, and so on.

To describe morphodynamics, sediment particles motion is modelled, and distinction is usually made between *suspension* that takes place in the water column, and *bed-load*, which is the rolling, sliding and hopping of particles near the bed [9]. Both effects are accounted through a sediment mass balance equation.

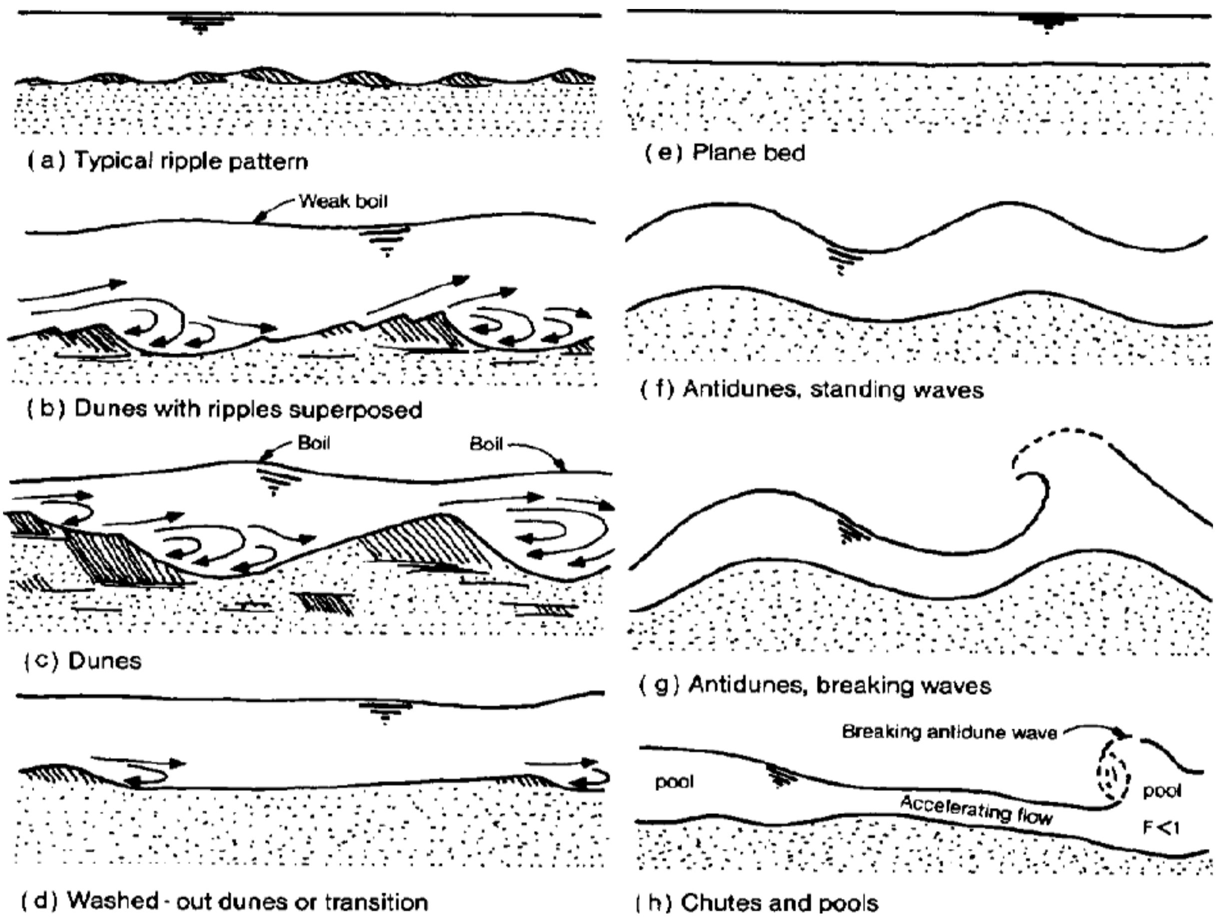

Figure 1.18 – Bed forms illustrations by Guy et al. [86]

Sediment mass balance results from conservation calculations on elementary bed surface [9], where sediments are considered as a continuum. When considering bed load and suspended sediment transport, this gives the Exner Equation 1.24,

$$(1-\lambda)\frac{\partial z_b}{\partial t} + \nabla \cdot \mathbf{q}_b + E - D = 0 \ , \tag{1.24}$$

where bed elevation z_s is transported with bed porosity λ (or volumic particle concentration $1 - \lambda$), enhanced with volumic bed-load transport rate vector per unit width $\mathbf{q}_b$ (m^2/s) and particle volumic erosion and deposition fluxes denoted $\boldsymbol{E}$ and $\boldsymbol{D}$ respectively.

This equation is the most used one in morphodynamic modelling, with both 2D and 3D hydrodynamics. Mass balance is however only applied to a near-bed layer, while other sediment balance in an arbitrary layer can be derived [186]. Furthermore, given the high degree of randomness in sediment motion, probabilistic models have been developed [74]. However, these are not considered herein, and attention is focused on the terms of Equation 1.24.

Bed-load and erosion/deposition fluxes are unknown and need closures. Morphodynamic processes are however difficult to observe and describe, making analytical deductions and process-based modelling difficult [9, 187]. Most modelling of sediment processes is therefore empirically driven, with closures generally deduced from laboratory experiments, incorporating a certain degree of simplification [9]. Hence, formulas are traditionally parameterized by sediments characteristics (e.g. grains diameter). However, natural environments are more complex, motion is greatly influenced by small scale behaviors, and variety of grain types can be found in the same location. This induces different responses to same constraints, with possible chimico-physical interactions between grains. Consequently, discrepancies between model predictions and measurements are often observed, and generally attributed to problem oversimplification [187].

While contemporary works focus on correction strategies, as the distinction between steady vs. unsteady flow, cohesive vs. non-cohesive behavior, etc., numerous open modelling questions remain difficult to tackle [187]. Suspension and bed-load parametrizations will be presented, keeping in mind that they could be highly uncertain [170].

Suspended sediment transport

Suspended load takes place in the water column, after sediments leave the bottom due to flow constraints and near bed agitation (e.g. turbulence). Indeed, when the latter generate sufficient lift force compared to grain weight, helped by turbulent eddies, erosion of bed sediment may result in resuspension. Conversely, deposition happens when grain weight attracts the sediments to the bottom. Other physical parameters also influence these processes, as sediment diffusivities, settling velocities, cohesive processes such as flocculation, etc. [9].

This alternating erosion and deposition events are modelled via the equilibrium of fluxes $\boldsymbol{E} - \boldsymbol{D}$ in Equation 1.24. Several methods for calculating those fluxes as a function of flow and sediment parameters can be found in literature, as discussed below. In general, they are estimated at each location as a function of near bed sediment concentration. Hence, it is necessary to model sediment concentration values in the flow, using an appropriate model.

Conservation of sediment concentration on elementary fluid particle volume, combined to Reynolds averaging, leads to an advection-diffusion equation. This is written in Equation 1.25,

$$\frac{\partial hc}{\partial t} + \nabla \cdot (h\mathbf{u}c) = \nabla \cdot (h\epsilon_s \nabla c) + (E - D) + S_c \ , \tag{1.25}$$

where c is the modelled depth-averaged concentration of sediments (volumic percentage), ϵ_s is the sediment diffusivity accounting for molecular and turbulent diffusion (often set to $\epsilon_s = \nu_d/\rho_c$, where $\rho_c \approx 1$), and S_c are any additional source/sink terms.

The $E-D$ term is the *net sediment flux*, which represents the rate of change of sediment concentration, between the bed and water column, due to the settling fluxes [9]. It is considered to result from an equilibrium in the near-bed concentration, and can be calculated as $E - D \approx w_s \times (c_{eq} - c_{ref})$ (or $E \approx c_{eq} \times w_s$ and $D \approx c_{ref} \times w_s$), where c_{eq} is called *equilibrium near bed concentration*, c_{ref} is the reference concentration at the interface $z = z_{ref}$ between bed-load layer and suspended load layer, and w_s is the sediments settling velocity.

Sediments settling velocity can be estimated from grain diameter as in 1.26,

$$w_s = \begin{cases} \dfrac{(\rho_s/\rho - 1) g d_{50}^2}{18\nu} & \text{if } d_{50} \leq 10^{-4} \\ \dfrac{10\nu}{d_{50}} \left(\sqrt{1 + 0.01 \dfrac{(\rho_s/\rho - 1) g d_{50}^3}{\nu^2}} - 1 \right) & \text{if } 10^{-4} < d_{50} \leq 10^{-3} \\ 1.1\sqrt{(\rho_s/\rho - 1) g d_{50}} & \text{otherwise} \end{cases} , \tag{1.26}$$

where ρ_s is the sediment density and d_n is the $n-$th percentile of grain size distribution, i.e. d_{50} denotes the median grain size.

Interface concentration c_{ref} at $z = z_{ref}$ is usually estimated at each coordinate from integration of an assumed Rouse profile for sediment concentration, as in Equation 1.27,

$$c(z) = c_{ref} \left(\frac{z - h}{z} \frac{a}{a - h} \right)^R \ , \tag{1.27}$$

where $R := w_s/\kappa u_*$ is the Rouse number, $\kappa \approx 0.4$ is the von Karman constant, $u_* := \sqrt{|\tau_b|/\rho}$ is the friction velocity and a is a reference elevation that can vary, but usually set very close to bed. Reference elevation is usually defined as a function of median grain size $z_{ref} = \alpha d_{50}$ [278], where α usually ranges in $[0.5, 3]$.

Equilibrium concentration c_{eq} can be determined using empirical formulas. For example, Zyserman-Fredsoe's formula [278] is given in Equation 1.28, where motion is defined as a function of Shield's stress $\theta := \frac{|\tau_b|}{(\rho_s - \rho) g d_{50}}$, which is the non-dimensional bed shear stress ,

$$c_{eq} = \frac{0.331(\theta' - \theta_{cr})^{1.75}}{1 + 0.72(\theta' - \theta_{cr})^{1.75}}, \tag{1.28}$$

where $\theta' = \mu\theta$ is the skin friction stress (non-dimensional), and μ, called *friction factor*, designates the proportion of friction related to grains texture (see Section 1.3.1). The parameter θ_{cr} is called *critical Shields*, and can be set to different values [75], as 0.047 in

[159].

Another formula convenient for combined wave-current action is the Soulsby and van Rijn estimation [234], in Equation 1.29,

$$c_{eq} = \begin{cases} a_{ss}\left(\sqrt{|\mathbf{u}| + \frac{0.018}{C_D}u_w} - u_{cr}\right) & \text{if } |\mathbf{u}| \geq u_{cr} \\ 0.0 & \text{otherwise} \end{cases}, \tag{1.29}$$

where u_w is the wave orbital velocity that can be estimated as in Equation 1.23 (Section 1.3.2), C_D is a drag coefficient calculated Equation 1.30 where $z_0 \approx 0.006$ m is a bed roughness value, u_{cr} is a threshold for current velocity magnitude estimated in 1.31, and a_{ss} is called *suspended transport factor* and is computed as in 1.32.

$$C_D = \left(\frac{0.4}{log(max(h, z_0)/z_0 - 1)}\right)^2, \tag{1.30}$$

$$u_{cr} = \begin{cases} 0.19(d_{50}^{0.1})log_{10}\left(\frac{4.0\ h}{d_{90}}\right) & \text{if } d_{50} < 0.0005\ m \\ 8.5(d_{50}^{0.6})log_{10}\left(\frac{4.0\ h}{d_{90}}\right) & \text{otherwise} \end{cases}, \tag{1.31}$$

$$a_{ss} = \frac{0.012hd_{50}\left(\left(\frac{g(\rho_s/\rho-1)}{\nu^2}\right)^{1/3} d_{50}\right)^{-0.6}}{((\rho_s/\rho - 1)gd_{50})^{1.2}}, \tag{1.32}$$

In addition to the previous formulas that define concentration flux Boundary Conditions (BC) at the bottom, appropriate Boundary Conditions (BC) should be set for remaining boundaries. Free surface and solid BC commonly corresponds to null fluxes or no slip condition [9]. Open BC however need to be defined, specifically in the case of intake with entering sediments upstream. In this case, BC can either be directly specified with depth averaged concentration value or indirectly imposed from near bed concentration using Equation 1.28 or 1.29 and Rouse profile 1.27.

In addition to the uncertainties inherent to parameteric closures, some modelling limitations can be noted. Firstly, previous formulas are only valid for non-cohesive sediments erosion and deposition, under reasonable/little disequilibrium. In the current work, only non-cohesive sediments are considered. However, intake and nearshore measurements (Section 1.1) also showed the presence of silt, which has cohesive behavior. We shall therefore keep this modelling limitation in mind. In particular, for cohesive sediments, erosion only occurs above a critical shear stress threshold $\theta > \theta_{ce}$ (not necessarily Shields parameter), that increases with physico-chemical effects such as cohesiveness, while porosity λ decreases [9]. Deposition conversely happens below a threshold $\theta < \theta_{cd}$. These definitions make the difference with non-cohesive sediments behavior, where erosion and deposition can simultaneously occur [9].

Secondly, absence of stress between fluid and sediment particles in the water column is assumed, considering that turbulence induced constraint is predominant. Similarly, stress between sediment particles is neglected, assuming no particles collision in the flow. These hypothesis can be questioned for highly concentrated or near bed flows [187].

Bed-load

Bed load corresponds to near bed sediment motion, limited in a thin, high sediment concentration layer, that corresponds to few centimeters depending on flow conditions [9]. Bed load is principally caused by sediment particles interactions. Once hydrodynamic driving forces are sufficient for sediments mobilization, bed stability is compromised and grains begin to move by interacting with each other, rolling, sliding and jumping [9]. This causes bed features formation (e.g. 1.18) and migration.

Oppositely to suspended load, particles are not considered dilute in the water column, and the bed load flux $\mathbf{q}_b$ is not calculated with flow equations. It is rather directly parameterized with bed and current properties, either using empirical or semi-empirical formulas, generally assuming uniform flow conditions [9, 187]. For example, the well known Meyer-Peter and Müller empirical formula [159] defined for steady uniform flow conditions and $d_{50} \in [0.4, 29]$ mm, is written in 1.33,

$$|\mathbf{q}_b| = \begin{cases} 0 & \text{if } \theta < \theta_{cr} \\ \alpha_{mpm}\sqrt{g(\rho_s/\rho - 1)d_{50}^3}(\theta - \theta_{cr})^{p_{mpm}} & \text{otherwise} \end{cases}, \tag{1.33}$$

where the critical Shields stress θ_{cr} defines a threshold of motion. Coefficient α_{mpm} was originally set to $\alpha_{mpm} = 8$ in [159], and was modified in various studies to fit on measurements as $\alpha_{mpm} \in [3, 12]$ [75, 101, 180]. Power value p_{mpm} was originally set to $p_{mpm} = 3/2$ in [159], and also took different values as $p_{mpm} = 1.6$, function of data [75].

Other formulas proposed in the literature allow to account for the effect of waves. For example Soulsby - van Rijn proposed, in addition to concentration parameterization in 1.29, a formula for combined current-wave action giving a total transport rate $\mathbf{q}_{b,s}$ accounting for both bed-load and suspension [234] in Equation 1.34,

$$|\mathbf{q}_{b,s}| = a_{b,s}|\mathbf{u}|\left[\left(|\mathbf{u}|^2 + \frac{0.018}{C_D}u_w^2\right)^{0.5} - u_{cr}\right]^{2.4}, \tag{1.34}$$

where bed load coefficient a_b and suspended load a_s can be estimated as in Equation 1.35, and critical velocity u_{cr} is calculated as previously shown in Equation 1.31.

$$\begin{cases} a_b = \dfrac{0.005h(d_{50}/h)^{1/2}}{((\rho_s/\rho - 1)gd_{50})^{1/2}} \\ \\ a_s = \dfrac{0.012d_{50}D_*^{-0.6}}{((\rho_s/\rho - 1)gd_{50})^{1/2}} \end{cases}. \tag{1.35}$$

Once bed load magnitude is estimated, the vector is set to $\mathbf{q}_b = (|\mathbf{q}_b|\cos\alpha, |\mathbf{q}_b|\sin\alpha)$, where α is the angle of sediment motion relative to the $x-$axis. It can be estimated from flow direction, and deviated as a function of bed slope, as in Equation 1.36,

$$\tan\alpha = \frac{\sin\delta - \frac{1}{f(\theta)}\frac{\partial z_b}{\partial y}}{\cos\delta - \frac{1}{f(\theta)}\frac{\partial z_b}{\partial x}}, \tag{1.36}$$

where $\delta = \tan^{-1}(v/u)$ is the flow stream angle, $f(\theta)$ is a *shape function* for example defined as $f(\theta) = 3/2\theta$ by Koch and Flokstra [114]. Bed load angle can also be influenced by other constraints such as secondary currents or spiral flows.

In addition to parametric closures uncertainties, it can be noted that these approaches, as many classical formulas, only use a single characteristic grain size (e.g. median d_{50}) for transport rate estimation. However, grain distributions can sometimes be non-gaussian or multi-modal, as shown in Figures 1.8 and 1.7. This means that the grain distribution may be poorly represented by a single statistical moment. Hence, estimation with the above formulas can result with under- or over-estimation of the transport rate [187]. Consequently, grain sizes are often calibrated to fit the morphodynamics on measurements, resulting in *representative values*, which are not necessarily the statistical estimators deduced from measurements. Author approaches to account for multi-class sediment transport can be found in literature [187], but generally increase the modelling problem dimensionality.

1.3.4 Modelling system

The previously described equations and closures are implemented within the open-source TELEMAC-MASCARET System (TMS) (`https://www.opentelemac.org/`). It is a parallelized High Performance Computing (HPC) hydro-informatic system, allowing to simulate complex flows, through independent physical modules. Namely, TELEMAC-2D [95] models 2D hydrodynamics using SWE, TOMAWAC [22] simulates wave propagation and transformation using spectral modelling, and SISYPHE [263] represents sediment dynamics using Exner equation (or new GAIA module since 2019 [12]). Numerical schemes and adequate solvers are used for modelling, as Finite Elements (FE) used for the application cases. Application Program Interfaces (API) are implemented for each TMS module, which allows a total control on simulation variables and parameters while running a case [81]. Through direct access to physical memory, user can stop a simulation at any time step, retrieve some variables values and change them if necessary through pointers (memory addresses). This is particularly convenient for data-driven approaches, such as Uncertainty Quantificiation (UQ) and Data Assimilation (DA) (see Chapter 2).

Coupling of TMS modules for complex applications is made asynchronous (time-splitting). This means that modules equations are solved independently, with an entirely decoupled system of equations. Combination of processes is then assured by communicating interest variables between the modules at a given frequency, as illustrated in Figure 1.19.

In morphodynamics, decoupling is typical in most existing 2D and 3D modelling systems, where the core is a hydrodynamic model to which waves, sediments, turbulence, etc. can be added [9, 187]. Principal hypothesis behind this approximation states that bed morphological evolution is of much lower order of magnitude than the flow changes. This is classically met in river and sea bed applications, but may fail for rapid processes. Hence, it should be kept in mind that decoupling is a simplification, with certain theoretical issues [45]. It implies that provided solutions are only approximations of the coupled modelling system solutions. Other approaches exist for coupled sediment-flow interaction, inspired by two-phase flow models [187], but are however not used in this thesis.

Lastly, general limitations inherent to the models, and resulting from previously described modelling choices, should be highlighted. Due to computational costs, only a 2D model is considered for hydrodynamics, and turbulence is not fully modelled. For the same reasons, coupling with spectral waves model is only used for schematic cases (for example in previous investigations in Section 1.4.2), and calibration of an apparent rugosity for combined current-wave flow is preferred for remaining investigations. Used models incorporate an important degree of uncertainty due to empirical closures, and approximations used for indirect modelling of important physical processes. Friction closures and sediment transport formulas use tuning coefficients (*structural uncertainty*). Rugosity height k_s and median grain diameter d_{50}, major physical information, are also highly uncertain (*epistemic uncertainty*) and are calibrated to compensate for the unmodelled. Bad considerations of spatio-temporal waves, turbulence, and 3D flow structures, are often pointed out as a limitation to morphodynamic models, since small eddies, orbital water particle motion, and flow structure may control near-bed mass exchange [9, 187]. Additionally, suspended sediments are considered dilute in the fluid, implying variations of fluid density ρ. These variations can be modelled with adequate formulas (e.g. UNESCO equations of state [257]), but without 3D modelling, resulting density currents can not be captured [9]. Proportion of suspended vs. bed-loaded sediments remains unquantified. Consequently in this thesis, as a first approximation, only suspension is taken into consideration, probably predominant according to literature review in Section 1.1. Lastly, BC and IC are also uncertain, for example tidal BC are parameterized, and incomplete IC bathymetry fields are subject to interpolation bias. Lastly, common modelling error sources should be noted, as those resulting from numerical discretizations, interpolations and solvers.

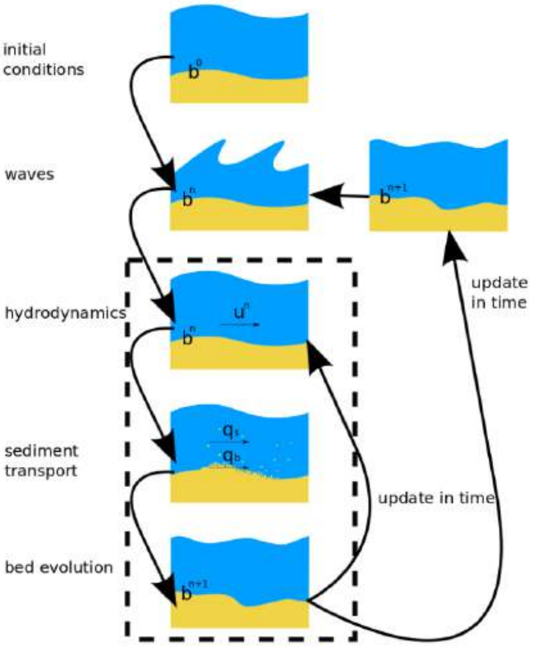

Figure 1.19 – Scheme of TMS modules coupling [246]

1.4 State of the art of the intake dynamics investigations

Some attempts to analyze the intake's sedimentation were given in previous studies, using the data described in Section 1.2 and the modelling equations introduced in Section 1.3. These are summarized below.

1.4.1 Data-based investigations

Intake's data were mainly analyzed by Latteux [122], with either qualitative analysis by comparative plots, or quantitative estimations of the dependency between sediment transport and hydrodynamic indicators, using Pearson's correlation coefficient. The latter, defined in Equation 2.8 (Chapter 2), varies in the interval $[-1, 1]$ and allows to measure linear dependencies between variables. An absolute value close to 1 indicates strong linear correlation between the studied variables and inversely, a value close to 0 shows that linear dependency can be neglected. Positive values indicate increasing relationships, and vice versa. It should be kept in mind that Pearson's coefficient can be negligible even in the case of strong dependency, if linear correlation is negligible.

Waves

Firstly, the two-months 2010 campaign data (February to March, Section 1.2) showed that W originating swell, although dominant, is closely followed by N origin swell [122]. This highlights that even though W dominance is noticed for decennial scale (as discussed in Section 1.1), it does not prevent another wave origin to be important for a punctual duration. Additionally, there are significant positive correlations (from 0.96 to 0.97) between $\boldsymbol{H_s}$ at the vicinity of the intake (Points 3, 4 and 5 in Figure 1.11) and at 7 km from the coast, and a slightly lower correlation (from 0.9 to 0.915) in front of the intake dikes (points 1 and 2 in Figure 1.11). This is probably due to the local reflection effect [122]. This study also concludes that 70% of $\boldsymbol{H_s}$ remains lower than 1 m, and 2 m lower than 96 % (also confirmed in [130], 70 % < 1 m and 95 % < 2 m as previously highlighted in Section 1.1). It is also shown that $\boldsymbol{H_s}$ generally decreases at low tide.

Turbidity

Next, analyzing turbidity shows that difference between sea bottom turbidity (30 cm above bottom) and middle of the water column (2.3 m above bottom) can be greater than 70 mg/l [122]. Turbidity at the bottom reacts to $\boldsymbol{H_s}$, namely peaks that coincide with strong wind waves. However its decrease following a strong wind is slow. Additionally, turbidity is stronger at low tide, but no effect of tidal currents intensity was noticed. Quantitative analysis of the collected data also showed strong correlations between measured turbidity, wave heights and tidal levels, with interactions between the latter two, explained by interactions of their constraints on the bottom. For deeper analysis, the bottom shear stress resulting from waves was estimated using Soulsby's formula with a rugosity of $k_s = 0.006$ m (Nikuradse's value for rippled sand bottoms). A significant positive correlation was noticed between the estimated stress and turbidity. Furthermore, adding the bottom shear stress resulting from the tidal currents (Bijker approach) to Soulsby's wave stress improves the correlation (Section 1.3 for details about the formulas). The vertical gradient of turbidity also increases with the total constraint.

Waves impact on intake's sedimentation

Secondly, the 2015-2010 bathymetries were used to analyse the intake's sedimentation. The volume of sedimentation was calculated for each two successive bathymetries that are not interrupted by dredging, and then divided by the duration to provide a daily rate (m^3/day). This rate was used as the main sedimentation indicator and correlations with the other measured variables were investigated.

Wave data from the ANEMOC data-base over the 2003 – 2009 period [21, 153] were used for comparison, on two points at 12 and 24 km off the coast. A general increasing tendency of the sedimentation daily rate with the wave height H_s is noticed (correlation of 0.81 with the 24 km point, and 0.83 with the 12 km point), but a strong dispersion of the cloud around the mean tendency is also highlighted. Correlations are greater with a power of the wave height H_s^3 (0.89 and 0.88 respectively). The westerly swell induces more sedimentation than waves with the same height but a different origin. This might be related to the sediment accumulation at the west bank of the intake (Figure 2) [122].

The area on which the daily sedimentation rate is calculated influences the previously observed correlations. Indeed, dividing the intake's area by three, Latteux [122] attempts other calculations using the the intake's upstream portion only for the volume calculations. Correlations are greater for low deposits and lower for high deposits.

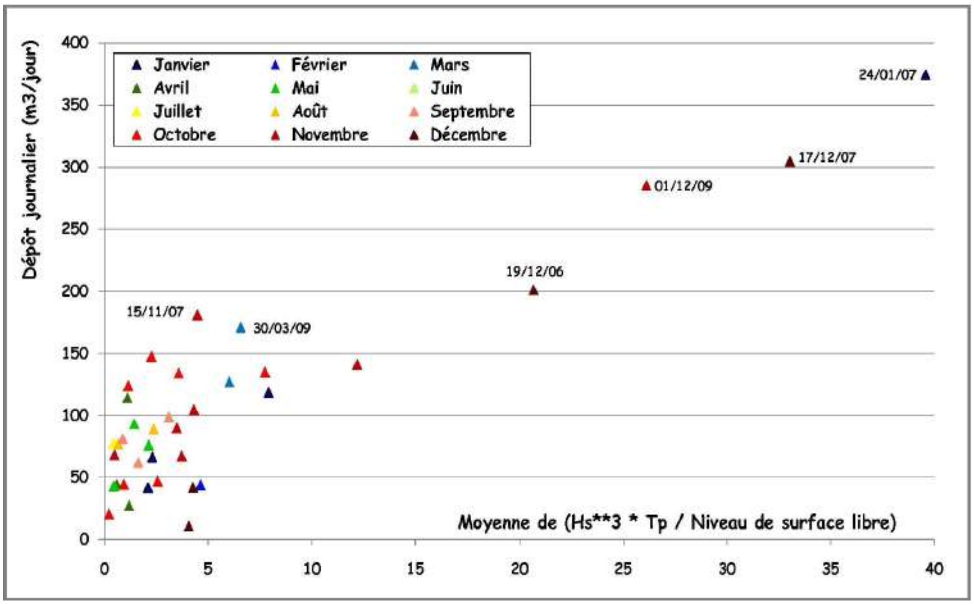

Figure 1.20 – Intake's daily deposition rate as a function of the average of $H_s^3 * T_p/z_s$ for each deposition period, colored by the sedimentation month, by Latteux [122]

Tidal levels impact on intake's sedimentation

The tidal levels, denoted z_s, were also used to deduce correlations with the daily sedimentation rates. Correlation value between the daily sedimentation rates and the average of H_s^3/z_s over the sedimentation duration was equal to 0.89 for both points located at 12 km and 24 km off the coast. Correlation with the wave period, denoted T_p, was also studied, by considering the average of $H_s^3 T_p/z_s$ instead of H_s^3/z_s. This results with almost the same correlation value (only a slight increase of 0.003 was noticed). A scatter plot of the daily sedimentation rates as a function of $H_s^3 * T_p/z_s$ is shown in Figure 1.20.

Initial state influence

The initial intake clogging can also be influencing for the sediment deposition. Indeed, the highest the intake bottom elevations, the lowest the water levels and the highest the flow velocities. Hence, the sedimentation rate should in principle be reduced with clogging. Nevertheless, no significant correlation is noticed between the daily sedimentation rates and the initial average bottom elevations of the intake.

Seasonal effects

Seasonal effects are also considered, as the silt proportion is in principle higher in winter than in summer, but no significant correlation could be deduced, as can be seen in Figure 1.20, where cloud points are colored by sedimentation month.

Pumping regimes

A positive correlation value was expected between the average plant pumping flowrate and the daily sediment deposition, as greater pumping means greater proportion of sediments diverted to the intake. This was again not observed, and the opposite was even noticed. This can be explained by higher intake velocities that aspire the sediments out through the pumps rather than allowing their deposition.

1.4.2 Process-based investigations

Preliminary numerical model investigations at the study area were attempted as well.

Hydrodynamic modelling

A hydrodynamic model, on a large domain of 33 km longshore and 15 km offshore, was used by Rougé and Tassi [207] to reproduce the 2010 campaign tidal amplitude and mean level, and maximal velocity magnitudes at flood and ebb, by calibrating three inputs: two tidal parameters and a single friction coefficient (CTL, MTL and strickler's coefficient K, as described in Section 1.3.1). It was shown after calibration that maximal velocity magnitude difference at flood remains generally lower than 5 cm/s (slight underestimation), with a temporal phase shift of 15 to 20 minutes. However, it was noted at ebb that velocity magnitude difference can go up to 10 cm/s for Point 2 (Figure 1.11).

Combined tide-wave effects

A combination of waves spectral modelling with hydrodynamic modelling, using coupled TELEMAC2D-TOMAWAC, was also attempted on the previously mentioned 33×15 km domain [207]. Waves were added to calibrated hydrodynamics, with a coupling time step of 15 minutes [207]. Three wave events (one day per event) from the 2010 campaign with different directions and height values were selected. The directions/heights were imposed as BC. Wave heights and directions are globally well represented over time. By coupling to hydrodynamics, the qualitative importance of waves for the initiation of long-shore currents was demonstrated. Indeed, at the vicinity of the beach that formed near the west dike of the intake, velocity magnitude does not exceed 30 cm/s without waves while it goes up to 1.5 m/s when waves are considered (scenario with a tidal range of 7.23 m, $H_s = 1.8$ m and NE originating swell). This behavior is particularly true for waves that arrive with a given angle to the coast.

In another example, Latteux [122] analyzed the combined tide-wave effect, with schematic westerly waves of height 3.8 m and peak period 8 s. These simulations showed that orbital velocities are higher at low tide, attaining 1.3 m/s on the rocky plateau in front of the intake and 0.5 m/s at deeper seas of −10 m CM. This means that sediment stock has greater chances being stirred to the intake at low tide [122]. At high tide, these velocities fall to 0.7 m and 0.4 m respectively. This implies four times higher bottom constraints at low tide compared to high tide (corresponding to two times higher orbital velocities). Furthermore, wave breaking induced currents are more significant at low tide.

Full wave-hydro-morphodynamic coupling

Full coupling between waves, hydrodynamics and morphodynamics was attempted by Rougé and Tassi [207] on the previously described large scale domain of 33 km longshore and 15 km offshore. In particular, Bijker formula was used to deduce combined bed-load and suspended load fluxes, with a median diameter of $d_{50} = 200\ \mu$m and a bed porosity of $\lambda = 0.375$. The sediment dynamics were greatly influenced with by presence of waves, as bed shear stress was increased by the latter. For the strongest combined tide-wave currents (scenario with a tidal range of 7.23 m, $H_s = 1.8$ m and NE originating swell), deduced solid transport rate varied in $[10^{-3}, 10^{-2}]$ m^{2}s^{-1} at the intake's entrance, and was maximal in the center. Sediment depositions over a day period reached +1 m at the entrance of the intake.

1.5 Summary

Literature review conducted in Section 1.1 shows that the physical phenomena involved in sedimentation processes are highly complex and non-linear. Hydrodynamic and meteorological conditions play an important role in the observed dynamics, through wind, waves and tides. A hand-off between tides and waves explains the particles trajectory from offshore to the intake. However, the dynamics at the vicinity of the intake need to be more deeply analyzed and in particular, a predictive tool was required by the power plant stakeholders. For this reason, two data sources were described: (i) measurements from regular monitoring and punctual campaigns in Section 1.2 and (ii) process-based equations for numerical modelling in Section 1.3.

Previously attempted investigations with the measurements and models were summarized in Section 1.4. They resulted with interesting conclusions, but the latter remain basic (linear correlations, scatter plots, qualitative analysis, manual model calibrations, etc.), and do not provide a predictive tool for operational conditions. Additionally, optimal combination of these data sources was not attempted, and their respective uncertainties not taken into consideration, in particular process-based modelling uncertainty and measurement errors.

Hence, advanced mathematical tools that allow deeper measurement-based and data-driven investigations are detailed in the following Chapter 2, namely Uncertainty Quantificiation (UQ), Machine Learning (ML) and Data Assimilation (DA), where particular focus is given to Dimensionality Reduction (DR) and probabilistic modelling. Introduced framework and techniques can be applied to a variety of non-linear physical fields. Chapter 2 is therefore kept general, without explicit mention of the physical problem.

Chapter 2

Data-driven modelling

Ce chapitre introduit les éléments théoriques nécessaires à l'établissement des résultats obtenus dans le cadre de la thèse. Les méthodes statistiques pour le traitement des données, qu'elles soient mesurées ou numériques, sont introduites. En particulier, l'apprentissage statistique, ou Machine Learning, est présenté, et les limitations des techniques classiques soulignées. Pour dépasser ces dernières, nous proposons de combiner réduction de dimension et régression probabiliste multivariée non-linéaire. Ces deux méthodes sont centrales dans le cadre de la thèse et utilisées dans les différentes contributions proposées dans les chapitres suivants. Elles sont donc également détaillées. En outre, nous introduisons les approches hybrides permettant de combiner mesures et modèles numériques, en particulier la Quantification d'Incertitudes et l'Assimilation de Données. Elles sont d'un intérêt particulier, dans la mesure où nous disposons de deux sources d'information, toutes deux entachées d'incertitudes.

This chapter introduces the theoretical elements necessary for the establishment of the thesis results. The statistical methods used for data processing, be it on measurements or numerical information, are introduced. In particular, statistical learning, or Machine Learning, is presented, and limitations of classical techniques are highlighted. To overcome the latter, we propose to combine dimensionality reduction and non-linear multivariate probabilistic regression. These two methods are central for the thesis, and used in the different contributions proposed in the following chapters. They are consequently discussed as well. In addition, we introduce hybrid approaches allowing to combine measurements and numerical models, in particular Uncertainty Quantification and Data Assimilation. They are of particular interest, as we have two sources of information, both characterized with uncertainties.

Contents

2.1 Uncertainty Quantification

Two principle sources of information are available in this thesis work: measurements and a process-based model. They are both characterized with errors, that should be taken into consideration for robust predictions, design, etc. [231]. In this context, Uncertainty Quantificiation (UQ) techniques, based on stochastic simulations, can help characterizing the model uncertainties, through *uncertainty propagation* allowing to study the propagation of uncertainties from inputs to outputs, and *sensitivity analysis* that aims at ranking the inputs by their influence [240].

Interest of the geosciences community in such methods is increasingly high. UQ examples (non exhaustive) can be found in [19] for sensitivity of storm simulations (surge and wave models) to uncertain inputs (wind and bed friction constraints, eddy viscosity, parameters for wave fluxes, etc.), in [8, 52, 268] for bed friction related uncertainties and their impact on flood simulations, and in [20, 170, 214] for sediment transport uncertainty (due to bed grains size, sediment transport formulas, etc.). A review of sensitivity analysis techniques used on environmental models can be found in [194]. These studies can sometimes be case dependent, and result in different conclusions when different frameworks, parameters and related errors/uncertainties or interest variables, are considered. As an example, an insightful literature analysis of different conclusions deduced from different uncertainty studies, regarding the ranking of most influencing sediment parameters, is given by Oliveira et al. [184] (Tables 1 and 2 [184]).

In the following, UQ is briefly presented. The probabilistic framework, with basic mathematical notations and notions for UQ studies, is introduced in Section 2.1.1. Classical UQ steps are described in Section 2.1.2, including a brief description of powerful tools for stochastic models construction, such as the Kernel Density Estimates (KDE), Maximum Entropy Principle (MEP), the *Bayes theorem*, etc., and classical methods for *sensitivity analysis* like the ANalysis Of VAriance (ANOVA) decomposition. Lastly, spectral stochastic modelling is presented in Section 2.1.6.

2.1.1 Probabilistic framework

In the following, random variables are defined and used through UQ study steps. In particular, they are characterized by PDFs and can be described using statistical moments. We therefore recall some fundamentals of the mathematical probabilistic framework, useful for the following sections.

Probability space and Probability Density Functions

First, we denote by $(\Omega, F, \mathbb{P})$ a probability space, where Ω is the event space (space of all the possible events ω) equipped with σ-algebra F (some events of Ω) and its probability measure $\mathbb{P}$ (likelihood of a given event occurrence).

A real random variable $\mathbf{Y}$ of dimension $m \in \mathbb{N}$, with support $D_{\mathbf{Y}} = \mathbb{R}^m$, defines an application $\mathbf{Y}(\omega) : \Omega \longrightarrow D_{\mathbf{Y}}$. Its components are denoted by subscripts as $\mathbf{Y} = [Y_1, \ldots, Y_m]^T$, and its realizations are denoted by lower case letter $\mathbf{y} \in D_{\mathbf{Y}}$, or collected in sample of size $n \in \mathbb{N}$ with superscript notations $\mathcal{S}_{\mathbf{Y}} = [\mathbf{y}^{(1)}, \ldots, \mathbf{y}^{(n)}]$ (matrix of size $m \times n$).

The PDF of a component Y_i is denoted $f_{Y_i} : D_{Y_i} \rightarrow \mathbb{R}$ and verifies $\mathbb{P}(Y_i \in E_i \subseteq D_{Y_i}) = \int_{E_i} f_{Y_i}(y_i)dy_i$. The *joint* Probability Density Function (PDF) of $\mathbf{Y}$ is denoted $f_{\mathbf{Y}} : D_{\mathbf{Y}} \rightarrow \mathbb{R}$ and verifies $\mathbb{P}(\mathbf{Y} \in E \subseteq D_{\mathbf{Y}}) = \int_E f_{\mathbf{Y}}(\mathbf{y})d\mathbf{y} = \int_E f_{Y_1,\ldots,Y_m}(y_1,\ldots,y_m)dy_1\ldots dy_m$.

Percentiles and Quartiles

The *percentiles* and *quartiles* of PDFs are discrete quantities that can be used to characterize the latter. Percentiles divide a PDF into 100 sub-intervals of equal size. The $k-$th percentile of a random variable Y, denoted $pr(Y,k)$, corresponds to the definition in Equation 2.1.

$$\mathbb{P}(Y \leq pr(Y,k)) = \frac{k}{100} \ , \tag{2.1}$$

where $k \in \{1,\ldots,100\}$. For example, the first percentile $pr(Y,k)$ denotes the value of Y under which 1% of the realizations occur. The 50th percentile is called the *median*. Quartiles divide the PDF into 4 sub-intervals of equal size. The $j-$th quartile of Y is calculated as $qr(Y,k) := pr(Y, j \times 25)$, where $j \in \{1,2,3,4\}$. For example, the first quartile $qr(Y,1)$ denotes the value of Y under which 25% of the realizations occur, and the second quartile is the median.

Statistical moments

Statistical moments can also be used to characterize the PDF. The *$k-$th moments* of a component Y_i are defined as in Equation 2.2.

$$\mathbb{E}[Y_i^k] := \int_{D_{Y_i}} y_i^k f_{Y_i}(\mathbf{y})dy_i \ . \tag{2.2}$$

The first moment is the *Expectation* of Y_i denoted $\mathbb{E}[\mathbf{Y}]$. Its empirical estimate over a sample of size n is the statistical average denoted $\overline{Y_i}$, calculated as in Equation 2.3, where $(\mathcal{S}_{\mathbf{Y}})_i = [y_i^{(1)},\ldots,y_i^{(n)}]$ is line i of matrix $\mathcal{S}_{\mathbf{Y}}$. Expectation of $\mathbf{Y}$ is defined component-wise as $\mathbb{E}[\mathbf{Y}] = [\mathbb{E}[Y_1],\ldots,\mathbb{E}[Y_m]]^T$

$$\mathbb{E}[Y_i] \approx \overline{Y_i} = \frac{1}{n}\sum_{j=1}^{n} Y_i^{(j)} = \frac{1}{n}(\mathcal{S}_{\mathbf{Y}})_i(\mathcal{S}_{\mathbf{Y}})_i^T \ . \tag{2.3}$$

In the same manner, we define the *$k-$th central moments* of Y_i as $\mathbb{E}[(Y_i - \mathbb{E}[Y_i])^k]$. The first central moment equals 0. The second central moment is the *variance* of Y_i denoted $\mathbb{V}[Y_i]$. It can be developed as $\mathbb{V}[Y_i] = \mathbb{E}[Y_i^2] - \mathbb{E}[Y_i]^2$ (Koening-Huygens). Its empirical estimate is written in Equation 2.4.

$$\mathbb{V}[Y_i] \approx \frac{1}{n-1}\sum_{j=1}^{n}(y_i^{(j)} - \overline{Y_i})^2 = \frac{1}{n-1}\left[(\mathcal{S}_{\mathbf{Y}})_i - \overline{Y_i}\right]\left[(\mathcal{S}_{\mathbf{Y}})_i - \overline{Y_i}\right]^T \ , \tag{2.4}$$

A useful statistical estimate is the *standard deviation* defined as $\sigma_{Y_1} := \sqrt{\mathbb{V}[Y_i]}$, which allows to quantify the variance in the variable's unit of measure. This also allows to define a relative estimate $|\sigma_{Y_1}/\mathbb{E}[Y_1]|$, called the *variation coefficient*.

Covariance and correlation

The covariance of two components Y_{i_1} and Y_{i_2} is the bilinear symmetrical operator defined as $cov(Y_{i_1}, Y_{i_2}) = \mathbb{E}[(Y_{i_1} - \mathbb{E}[Y_{i_1}])(Y_{i_2} - \mathbb{E}[Y_{i_2}])]$. As a result $\mathbb{V}[Y_i] = cov(Y_i, Y_i)$. Covariance can be empirically estimated as in Equation 2.5.

$$cov(Y_{i_1}, Y_{i_2}) \approx \frac{1}{n-1} \sum_{j=1}^{n} (y_{i_1}^{(j)} - \overline{Y_{i_1}})(y_{i_2}^{(j)} - \overline{Y_{i_2}}) = \frac{1}{n-1} \left[(\mathcal{S}_{\mathbf{Y}})_{i_1} - \overline{Y_{i_1}} \right] \left[(\mathcal{S}_{\mathbf{Y}})_{i_2} - \overline{Y_{i_2}} \right]^T . \quad (2.5)$$

The variance of $\mathbf{Y}$ is defined as $\mathbb{V}[\mathbf{Y}] = \mathbb{E}[(\mathbf{Y} - \mathbb{E}[\mathbf{Y}])(\mathbf{Y} - \mathbb{E}[\mathbf{Y}])^T]$. It is a matrix of size $m \times m$ called the *covariance matrix*, and can also be developed as $\mathbb{V}[\mathbf{Y}] = \mathbb{E}[\mathbf{Y}\mathbf{Y}^T] - \mathbb{E}[\mathbf{Y}]\mathbb{E}[\mathbf{Y}]^T$. Component of line i_1 and column i_2 is exactly the covariance term $cov(Y_{i_1}, Y_{i_2})$ and hence, diagonal terms i correspond to $\mathbb{V}[Y_i]$ and the matrix is diagonal. The covariance matrix can be empirically estimated as in Equation 2.6.

$$\mathbb{V}[\mathbf{Y}] \approx \frac{1}{n-1} \left(\mathcal{S}_{\mathbf{Y}} - \overline{\mathbf{Y}} \right) \left(\mathcal{S}_{\mathbf{Y}} - \overline{\mathbf{Y}} \right)^T , \quad (2.6)$$

This notion is extended to define the *cross covariance matrix* between two random variables $\mathbf{Y}$ and $\mathbf{X}$ as $cov(\mathbf{Y}, \mathbf{X}) \approx \frac{1}{n-1} \left(\mathcal{S}_{\mathbf{Y}} - \overline{\mathbf{Y}} \right) \left(\mathcal{S}_{\mathbf{X}} - \overline{\mathbf{X}} \right)^T$. Similarly, *auto-correlation matrix* is defined and approximated as in Equation 2.7, and *cross-correlation matrix* reads $\mathbb{C}(\mathbf{Y}, \mathbf{X}) \approx \frac{1}{n-1} \mathcal{S}_{\mathbf{Y}} \mathcal{S}_{\mathbf{Y}}^T$.

$$\mathbb{C}(\mathbf{Y}, \mathbf{Y}) = \mathbb{E}[\mathbf{Y}\mathbf{Y}^T] \approx \frac{1}{n-1} \mathcal{S}_{\mathbf{Y}} \mathcal{S}_{\mathbf{Y}}^T , \quad (2.7)$$

Not to confuse with the *correlation matrix*, denoted $corr(\mathbf{Y})$ and containing component wise Pearson's correlations defined as in Equation 2.8. This gives $corr(\mathbf{Y}) = diag(\mathbb{C}(\mathbf{Y}, \mathbf{Y}))^{-\frac{1}{2}} \mathbb{C}(\mathbf{Y}, \mathbf{Y}) diag(\mathbb{C}(\mathbf{Y}, \mathbf{Y}))^{-\frac{1}{2}}$, where $diag(\mathbf{A})$ contains the diagonal elements of matrix $\mathbf{A}$. *Correlation matrix* is then equivalent to *covariance matrix* if variables are *standardized* (i.e. normalized by their standard deviations), while *auto-correlation matrix* is equivalent to *covariance matrix* if variables are centered around their means.

$$\rho_{Y_1, Y_2} = \frac{\mathbb{E}\left[(Y_1 - \mathbb{E}(Y_1))(Y_2 - \mathbb{E}(Y_2)) \right]}{\sigma_{Y_1} \sigma_{Y_2}} , \quad (2.8)$$

The $\mathcal{L}^2_{\mathbb{R}}$ space

Lastly, the space of real random variables with finite second moments (and finite variances) is denoted $\mathcal{L}^2_{\mathbb{R}}(\Omega, F, \mathbb{P}; \mathbb{R})$, or shortly $\mathcal{L}^2_{\mathbb{R}}$. It is a *Hilbert* space equipped with the inner product in Equation 2.9, where and its induced norm $||Y_i||_{\mathcal{L}^2_{\mathbb{R}}} := \sqrt{\mathbb{E}[Y_i^2]}$.

$$(Y_{i_1}, Y_{i_2})_{\mathcal{L}^2_{\mathbb{R}}} := \mathbb{E}[Y_{i_1} Y_{i_2}] = \int_{\Omega} Y_{i_1}(\omega) Y_{i_2}(\omega) d\mathbb{P}(\omega) = \int_{\Omega} Y_{i_1}(\omega) Y_{i_2}(\omega) f_{Y_1, Y_2}(y_1, y_2) dy_1 y_2 \quad (2.9)$$

2.1.2 Steps of a UQ study

The objective of UQ studies is to determine the impact of modelling uncertainties on a simulated output. Uncertainty can originate from different sources, for example poorly-known physical parameters, closures used within the interest model, Boundary Conditions

(BC), Initial Conditions (IC), modelling simplifications, numerical schemes, etc. These uncertainties are generally classified in three categories: *epistemic uncertainty* that results from poor knowledge of the dynamics, and can be reduced with more observations, *aleatory uncertainty* that is completely random and judged to be irreducible by the modeller [231], and *numerical error* that may concern the choice of modelling system, discretization, interpolation, etc. [183].

In all cases, these variables (or choices) are considered non-deterministic: it is impossible to choose a given value and be certain about it. One can only estimate, hardly, the probability of a value to be accurate. Therefore, uncertainty sources are treated using probabilistic analysis, each source being quantified with a Probability Density Function (PDF), and the model is considered stochastic. Common approach in UQ consists in propagating different values of uncertain inputs through the modelling system, using a sample representative of input PDFs, in order to deduce statistics on the output [240].

Firstly, determining uncertainty sources and characterizing them with PDFs is classically called *quantification of uncertainty sources*. A second step named *uncertainty propagation* consists in transforming input uncertainties through the model to output uncertainties. In an additional step called *sensitivity analysis*, ranking of the inputs as a function of their influence on the output is targeted [240]. Lastly, *uncertainty reduction* consists in correcting the most influencing input PDFs in order to obtain more plausible (less uncertain) outputs. This can be performed through Data Assimilation (DA), in particular balancing *numerial error* with the other types of errors.

UQ steps, i.e. *quantification of uncertainty sources*, *uncertainty propagation* and *sensitivity analysis* are discussed below, while DA is the subject of dedicated Section 2.3.

2.1.3 Quantification of uncertainty sources

This step consists in identifying the potential sources of uncertainty, then constructing adequate stochastic models to express it, consisting in a joint PDF. Uncertainty sources identification is case dependent, and should be performed carefully, with an advanced analysis of involved physics. This is therefore not commented in the following.

Once the uncertain inputs identified, the joint PDF should be determined, based on expert knowledge and/or statistical arguments. In general, this PDF can only be guessed, with more or less confidence, from available information. We therefore speak of *prior* PDF denoted $f_{\boldsymbol{\Theta}}^{prior}(\boldsymbol{\Theta}, \mathbf{s})$, where $\boldsymbol{\Theta}$ are the uncertain inputs and $\mathbf{s}$ are density hyperparameters. Selecting a prior density and corresponding hyperparameters is however known to be difficult, and particularly challenging in the absence of data [231].

Inputs PDF can not be chosen arbitrarily. Indeed, even when the model is perfect, arbitrary inputs PDF leads to arbitrary output's PDF. The UQ study is therefore directly impacted [231]. Hence, for robust density choice, three cases are identified by Soize [231]: (i) if no data are available, then both the density and corresponding hyperparameters $\mathbf{s}$ are highly uncertain, and should be treated as such; (ii) if few data are available then the use of a parametric PDF is advised (e.g. Gaussian, Uniform, etc.), and optimal hyperparameters $\mathbf{s}_{opt}$ are selected with the help of the Maximum Entropy Principle (MEP) (*information theory*) and (iii) if "big data" are available, non-parametric densities can be inferred, for example using KDE [93]. We focus on the case where few (bounds, mean and variance, partial measurements) or ”big” data (complete measurements) are available.

Choice of parametric densities

For the first case of few data, the Maximum Entropy Principle (MEP) is used. It states that the PDF that maximizes the uncertainty (i.e. maximizes $-\mathbb{E}[log(f_{\boldsymbol{\Theta}})]$, *Shannon’s entropy*) should be selected Soize [231]. For example, among all possible PDFs, the one that maximizes the uncertainty while being defined on a bounded subset $K \subset \mathbb{R}^V$ is the Uniform PDF on $\mathbb{R}^V$ with support K [231]. This means that if the only available information consists in interval bounds for the uncertain parameters, then the Uniform PDF should definitely be used as prior. Joint multivariate Uniform PDF is formulated as in Equation 2.10.

$$f_{\boldsymbol{\Theta},K}(\boldsymbol{\theta}) = \frac{1}{|K|}\mathbb{1}_K(\boldsymbol{\theta}) \ , \tag{2.10}$$

where $\mathbb{1}_K$ equals 1 on K and 0 elsewhere, and $|K| = \int_K d\boldsymbol{\Theta}$ (volume of the subspace).

If the first two moments are known (mean and covariance matrix), MEP leads to Gaussian PDF. For the multidimensional input $\boldsymbol{\Theta}$, with mean $\boldsymbol{\mu}_{\boldsymbol{\Theta}}$ and covariance matrix $\boldsymbol{\Sigma}_{\boldsymbol{\Theta}}$, joint multivariate Gaussian PDF is written in Equation 2.11.

$$f_{\boldsymbol{\Theta},\boldsymbol{\mu}_{\boldsymbol{\Theta}},\boldsymbol{\Sigma}_{\boldsymbol{\Theta}}}(\boldsymbol{\theta}) = \frac{1}{\sqrt{(2\pi)^V det[\boldsymbol{\Sigma}_{\boldsymbol{\Theta}}]}} exp\left[-\frac{1}{2\sigma_i^2}(\boldsymbol{\theta}-\boldsymbol{\mu}_{\boldsymbol{\Theta}})^T {\boldsymbol{\Sigma}_{\boldsymbol{\Theta}}}^{-1}(\boldsymbol{\theta}-\boldsymbol{\mu}_{\boldsymbol{\Theta}})\right] \ . \tag{2.11}$$

For one input component Θ_i, with mean μ_i and standard deviation σ_i, Gaussian PDF is written in Equation 2.12.

$$f_{\Theta_i,\mu_i,\sigma_i}(\theta_i) = \frac{1}{\sqrt{2\pi}\sigma_i} exp\left[-\frac{1}{2\sigma_i^2}(\theta_i - \mu_i)^2\right] \ . \tag{2.12}$$

Estimation of hyperparameters

Once a PDF denoted $f_{\boldsymbol{\Theta}}^{prior}(\boldsymbol{\Theta}, \mathbf{s})$ is selected, its hyperparameters denoted $\mathbf{s}$ must be chosen to completely define the stochastic model. Identification of an optimal configuration $\mathbf{s}_n^{opt}$ from a set of observations $\mathbf{y} = \{\mathbf{Y}\}$ can be performed by adequate probability theory formulation, for example using the Maximum Likelihood Estimation (MLE) or the more general *Bayesian inference*.

The MLE is formulated as an optimization problem in Equation 2.13,

$$\mathbf{s}_n^{opt} = \arg\max_{\mathbf{s}} f_{\boldsymbol{\Theta}}^{prior}(\boldsymbol{\theta}^1, \mathbf{s}) \times \ldots \times f_{\boldsymbol{\Theta}}^{prior}(\boldsymbol{\theta}^n, \mathbf{s}) \ , \tag{2.13}$$

where $f_{\boldsymbol{\Theta}}^{prior}(\boldsymbol{\theta}^1, \mathbf{s}) \times \ldots \times f_{\boldsymbol{\Theta}}^{prior}(\boldsymbol{\theta}^n, \mathbf{s})$ is called the *likelihood* PDF, often denoted $\mathcal{L}(\mathbf{s})$, representing the probability of values $\mathbf{y} = \{\mathbf{Y}\}$ to be observed for a given value $\mathbf{s}$ of hyperparameters. The objective is therefore to maximize the latter [231]. In particular, if the MLE is considered as a realization of a random vector $\mathbf{S}_n^{opt}$ from random observations realizations denoted $\mathbf{Y} = \{\mathbf{Y}\}$, it is established that $\mathbf{S}_n^{opt}$ converges to a Gaussian vector whose mean is the true optimum $\mathbf{s}^{(t)}$ given the chosen PDF $f_{\boldsymbol{\Theta}}^{prior}$, with covariance matrix defined as $\mathbf{C} = \left[J_F(\mathbf{s}^{(t)})\right]^{-1}$, where J_F is called the Fisher information matrix and calculated as in Equation 2.14 [231].

$$[\mathbf{J}_F(\mathbf{s})]_{i,j} = \mathbb{E}\left[\frac{\partial\mathcal{L}(\mathbf{s})}{\partial s_i}\frac{\partial\mathcal{L}(\mathbf{s})}{\partial s_j}\right] \tag{2.14}$$

While MLE aims at finding optimal parameterization for a fixed density choice, the objective in *Bayesian inference* is to incorporate information about the observations in the process in order to define a *posterior* PDF denoted $f^{posterior}_{\boldsymbol{\Theta}|\mathbf{Y}=\mathbf{y}}$ from the *prior*, that is more representative of the parameters given the observed data. Firstly, considering the prior PDF parameters and the observations as random variables denoted in capital letter **S** and **Y** respectively, *marginalization* rule is written as in Equation 2.15.

$$f^{posterior}_{\boldsymbol{\Theta}|\mathbf{Y}=\mathbf{y}}(\boldsymbol{\theta}) = \int f_{\boldsymbol{\Theta}|\mathbf{S}=s,\mathbf{Y}=\mathbf{y}}(\boldsymbol{\theta}) f_{\mathbf{S}|\mathbf{Y}=\mathbf{y}}(\mathbf{s})d\mathbf{s}\ . \tag{2.15}$$

The first term can be written $f_{\boldsymbol{\Theta}|\mathbf{S}=s,\mathbf{Y}=\mathbf{y}} = f^{prior}_{\boldsymbol{\Theta}}(\boldsymbol{\theta},\mathbf{s})$, as the probability of $\boldsymbol{\Theta}$ is assumed to be completely determined from the knowledge of **S**, given the definition of parametric distribution. The second term $f_{\mathbf{S}|\mathbf{Y}=\mathbf{y}}$ is however unknown and can be determined using the *Bayes rule* (from which *Bayesian* denomination originates), as in 2.16,

$$f_{\mathbf{S}|\mathbf{Y}=\mathbf{y}}(\mathbf{s}) = \frac{f_{\mathbf{Y}|\mathbf{S}=\mathbf{s}}(\mathbf{y}) f_{\mathbf{S}}(\mathbf{s})}{f_{\mathbf{Y}}(\mathbf{y})}\ , \tag{2.16}$$

where the marginalization rule gives $f_{\mathbf{Y}}(\mathbf{y}) = \int f_{\mathbf{Y}|\mathbf{S}=\mathbf{s}}(\mathbf{y}) f_{\mathbf{S}}(\mathbf{s})d\mathbf{s}$, and the quantity $f_{\mathbf{Y}|\mathbf{S}=\mathbf{s}}$ is no other than the *likelihood* $\mathcal{L}(\mathbf{s})$.

Conversely to MLE, the Bayes rule in Equation 2.16 gives a distribution of the hyperparameters **S** rather than a single estimate. The marginalization rule in Equation 2.15 is then used to correct the prior estimation $f^{prior}_{\boldsymbol{\Theta}}(\boldsymbol{\theta},\mathbf{s})$ in order to obtain a posterior distribution $f^{posterior}_{\boldsymbol{\Theta}|\mathbf{Y}=\mathbf{y}}(\boldsymbol{\theta})$ that is not necessarily of the same shape, using a weighting by the possible values of parameters **S** given the observations. The same concept is for example used in inverse problems, and particularly for Data Assimilation (DA), in order to assimilate data to physics-based models (see Section 2.3).

If the right hand side PDFs of Equation 2.16 are known, then the posterior PDF denoted $f_{\boldsymbol{\Theta}|\mathbf{Y}}$ can be directly estimated from Equations 2.15 and 2.16. However, this requires calculation of integrals that is known to be difficult, and methods as the Markov Chain Monte Carlo (MCMC) are used to avoid such direct calculation [231]. In general, the right hand side PDFs of Equation 2.16 are not known. The posterior PDF is then approximated, either relying on additional assumptions on the involved PDFs (for example Gaussian hypothesis), or consisting on a statistical PDF estimations using sampling techniques. However, the latter remain costly, due to sampling and numerical integration [231].

Non-parametric densities

In case of sufficient measurements ('big' data), Kernel Density Estimates (KDE) can be used [93], which is a continuous approximation of the variables histogram, also called *kernel smoothing*. It consists in a superposition of standard PDFs in the variables space in order to cover all density variations. Kernel designates the used standard PDF, denoted K.

For a random variable X with realizations $[x^{(1)}, \dots, x^{(n)}]$, KDE is written as in Equation 2.17,

$$\widetilde{f_X}(x) = \frac{1}{nh_K} \sum_{i=1}^{n} K\left(\frac{x - x^{(n)}}{h_K}\right) , \tag{2.17}$$

where $\widetilde{f_X}$ is the KDE approximation of the true density f_X, and h_K is a parameter called bandwidth. Using Gaussian Kernels, the optimal bandwidth, defined by Silverman [226], is $h_K = 0.9 \times min\left(\sigma_x, \frac{IQR(X)}{1.349}\right)/(n^{1/5})$, where $IQR(X)$ is the interquartile range ($IQR(X) \coloneqq qr(X,3) - qr(X,1)$), where quartiles are defined with Equation 2.1). The KDE converges to the true PDF with increasing sample size, whatever the chosen Kernel.

2.1.4 Uncertainty propagation

Once uncertainty sources are quantified with adequate PDFs, the idea is to deduce their impact on the output. In particular, one wants to characterize how inputs probabilities propagate to output probabilities. Probabilistic Quantities of Interest (QoI) for the output are therefore studied (moments, percentiles, PDF approximation, etc.). Among the most targeted QoI are the mean and variance, which is called *second moment analysis*.

Two approaches can be used: (i) *sampling techniques* consisting in *direct simulations* with the model $\mathcal{M}(\boldsymbol{\Theta}) = \mathbf{Y}$, that allow providing a set of output realizations $[\mathbf{y}^{(1)}, \dots, \mathbf{y}^{(n)}]$ from a set of input realizations $[\boldsymbol{\theta}^{(1)}, \dots, \boldsymbol{\theta}^{(n)}]$. Probabilistic information are then empirically inferred from data (e.g. Equations 2.3 and 2.4 for statistical moments, and Equation 2.17 for PDF approximation); (ii) *indirect methods*, for example kriging or *spectral stochastic approaches* as PCE and Karhunen-Loève Transfrom (KLT), where the model's output is characterized through a stochastic model, either intrusively (e.g. *Galerkin* scheme) or non-intrusively from $[\mathbf{y}^{(1)}, \dots, \mathbf{y}^{(n)}]$ as a post-processing of sampling techniques, allowing further exploration of the output's space with reasonably low number of simulations [231].

Direct sampling approaches

The most efficient and popular method is Monte Carlo (MC) [231], consisting in fully random sampling with respect to the inputs PDF. Once the Monte Carlo (MC) input sample produced, each input configuration is propagated through the studied model by running a direct simulation. A corresponding sample of output values is therefore obtained, and statistics or PDF can be estimated from the latter, using either parametric or empirical estimates.

Theoretical proof of the convergence of MC empirical estimators for expectation and variance (defined in Equations 2.3 and 2.4 respectively) with the sample size n is provided by the *Central Limit Theorem*. For example, MC estimator of the expectation converges in PDF to Gaussian, with mean corresponding to the true analytical value $\mathbb{E}[Y]$, and variance $\mathbb{V}[Y]/n$. The QoI can therefore be tracked as a function of the sample size n, in order to stop at convergence. MC speed of convergence is $\sqrt{\frac{1}{n}}$. Although independent of inputs dimension (no curse of dimensionality) [231], it remains low. It can be improved using advanced simulation procedures (e.g. Latin Hypercube Sampling (LHS) [53]).

Indirect and spectral stochastic approaches

Three indirect methods were previously mentioned: kriging, and spectral stochastic approaches as PCE and KLT. PCE [113, 139] and kriging [152], allow to build a probabilistic mapping from an input to an output space. In this thesis, PCE is preferred, due to orthonormality properties. The latter allow straightforward calculation of the output's statistical moments from the expansion coefficients, and therefore the study of the output's sensitivity to the input variations without additional cost [103, 241]. PCE is widely used in the UQ community [143, 242, 264, 271, 273], particularly for the study of stochastic behaviors in physics [31, 107, 179, 244]. It is therefore detailed below in Section 2.1.6. Karhunen-Loève Transfrom (KLT), as a Dimensionality Reduction (DR) technique, is discussed in dedicated Section 2.4. In particular, dimensionality of the UQ problem is directly linked to the number V of uncertain inputs $\boldsymbol{\Theta}$, and to the dimension m of output $\boldsymbol{Y}$. High dimension leads to high computational cost for accurate statistical moments estimation. Hence, DR, for example KLT, can be used in this context (also referred to as Proper Orthogonal Decomposition (POD) for spatio-temporal outputs or PCA for multivariate reduction [231]).

2.1.5 Sensitivity analysis

In sensitivity analysis, the quantification of inputs influence on the output variability is of interest. Ranking variables and their interactions according to the impact they have on the model response is usually targeted. This allows to determine the most influencing parameters to calibrate and the least influencing ones to set to fix values, decreasing for example the dimensionality of Data Assimilation (DA) problems.

Local and Global Sensitivity Analysis

Two categories of sensitivity analysis are usually defined: Local Sensitivity Analysis (LSA), where the objective is to study the influence of small input variations around a reference value, and Global Sensitivity Analysis (GSA), where the input variations over the whole support are studied [241]. The second category is of interest in the following. GSA methods are usually grouped in two categories: (i) regression-based and (ii) variance-based methods.

Regression-based GSA

For example, when the model $\mathcal{M}(\boldsymbol{\Theta})$ can be approximated by a multivariate linear regression, the Standard Regression Coefficient (SRC) of each variable Θ_i calculated as in Equation 2.18 can be used to rank the inputs.

$$SRC_i = \frac{Cov[Y, \Theta_i]}{\sigma_Y \sigma_{\Theta_i}} = (\rho_{Y,\Theta_i})^2 \; . \tag{2.18}$$

This is no other than the square of Pearson coefficient, defined in Equation 2.8, for linear dependence.

However, when the model shows non-linearities, such indicators fail to accurately describe the sensitivities. In this case, other indicators can be used if the model is monotonic, for example the Partial Rank Correlation Coefficients (PRCC), defined as $\rho_{Y,\Theta_i|\theta_i}$, where θ_i is a realization of the inputs where only Θ_i is varied.

Variance-based GSA

In general, models are non-monotonic and non-linear. A more convenient approach based on variance decomposition can be used [241]. This consists on calculating the share of output's variance that is due to a given input. For the general case of a multivariate model written as in Equation 2.26, the variance of the output Y can be computed as in Equation 2.19,

$$\begin{array}{rcc} \mathbb{V}[Y] & = & cov\ (Y,Y) \\ & = & cov\ \left(\sum_{\mathcal{I}\subseteq\{1,\ldots,V\}} \mathcal{M}_{\mathcal{I}}(\theta_{\mathcal{I}}), \sum_{\mathcal{J}\subseteq\{1,\ldots,V\}} \mathcal{M}_{\mathcal{J}}(\theta_{\mathcal{J}})\right) \\ & = & \sum_{\mathcal{I}\subseteq\{1,\ldots,V\}} \sum_{\mathcal{J}\subseteq\{1,\ldots,V\}} cov\ \left(\mathcal{M}_{\mathcal{I}}(\theta_{\mathcal{I}}), \mathcal{M}_{\mathcal{J}}(\theta_{\mathcal{J}})\right) \\ & = & \sum_{\mathcal{I}\subseteq\{1,\ldots,V\}} \left(\mathbb{V}\left[\mathcal{M}_{\mathcal{I}}(\theta_{\mathcal{I}})\right] + \sum_{\mathcal{J}\neq\mathcal{I}\subseteq\{1,\ldots,V\}} cov\ \left(\mathcal{M}_{\mathcal{I}}(\theta_{\mathcal{I}}), \mathcal{M}_{\mathcal{J}}(\theta_{\mathcal{J}})\right)\right) \end{array}. \tag{2.19}$$

This is called ANalysis of COVAriance (ANCOVA) decomposition [36, 241]. A normalization of the output's variance results with the general contribution indices proposed in [241] as in Equation 2.20,

$$\begin{array}{rcc} S_{\mathcal{I}}^{(cov)} & := & S_{\mathcal{I}}^{(U)} + S_{\mathcal{I}}^{(C)} \\ & := & \dfrac{\mathbb{V}\left[\mathcal{M}_{\mathcal{I}}(\theta_{\mathcal{I}})\right]}{\mathbb{V}\left[Y\right]} + \dfrac{\sum_{\mathcal{J}\neq\mathcal{I}\subseteq\{1,\ldots,V\}} cov\ \left(\mathcal{M}_{\mathcal{I}}(\theta_{\mathcal{I}}), \mathcal{M}_{\mathcal{I}}(\theta_{\mathcal{J}})\right)}{\mathbb{V}\left[Y\right]} \end{array}, \tag{2.20}$$

where $S_{\mathcal{I}}^{(cov)}$ is called the covariance-based sensitivity index of variables $\boldsymbol{\Theta}_{\mathcal{I}}$, representing both their uncorrelated contributions, denoted $S_{\mathcal{I}}^{(U)}$, and their correlative contributions, denoted $S_{\mathcal{I}}^{(C)}$, to the output's variance.

In the case of independent input variables $\boldsymbol{\Theta}$, the covariance terms in Equation 2.19 vanish. This gives the so called ANOVA decomposition. The correlative indices $S_{\mathcal{I}}^{(C)}$ also consequently vanish, and the covariance-based sensitivity index $S_{\mathcal{I}}^{(cov)} = S_{\mathcal{I}}^{(U)}$ is no other than the so called Sobol' index denoted $S_{\mathcal{I}}$ [230, 241].

Adding Sobol' indices of all different contribution subsets $\mathcal{I} \subseteq \{1,\ldots,V\}$ equals 1. This means that they allow to rank each subset, in terms of relative variance contribution, to the output Y. The contributions can be either analyzed for each subset independently, or used to compute the contribution of a given variable Θ_i. Indeed, the share of subset $\mathcal{I} = \{i\}$ allows to compute the 1^{st} *order contribution* of Θ_i (1^{st} *Sobol' index*, denoted S_i), while adding the shares of all subsets that satisfy $i \in \mathcal{I}$ quantifies the *total contribution* of the variable including its interactions (*total Sobol' index*, denoted S_i^T). Formally, the first Sobol' index can be written as in Equation 2.21,

$$S_i = \frac{\mathbb{V}(\mathbb{E}[Y|\boldsymbol{\Theta}_i])}{\mathbb{V}[Y])}\ , \tag{2.21}$$

where $\mathbb{E}[Y|\boldsymbol{\Theta_i}]$ is the expectation of model values where only Θ_i is varied, and $\mathbb{V}(\mathbb{E}[Y|\boldsymbol{\Theta_i}])$ is called *partial variance*. Similarly, interaction indices, as the *second order sensitivity index* defining the joint influence of parameters Θ_i and Θ_j, is defined in Equation 2.22.

$$S_{ij} = \frac{\mathbb{V}(\mathbb{E}[Y|\boldsymbol{\Theta_i}, \boldsymbol{\Theta_j}])}{\mathbb{V}[Y])} \ . \tag{2.22}$$

Lastly, total index is written in Equation 2.23.

$$S_i^T = S_i + \sum_{j \neq i} S_{ij} + \sum_{j \neq i, k \neq i, j < k} S_{ijk} + \ldots = 1 - \sum_{\mathcal{I} \subseteq \{1,\ldots,V\}, i \notin \mathcal{I}} S_{\mathcal{I}} \ . \tag{2.23}$$

Sobol' indices values can be estimated with MC simulations. For example, Satelli et al. [213] proposes to compute the partial variance $\mathbb{V}(\mathbb{E}[Y|\boldsymbol{\Theta_i}])$ as in Equation 2.24,

$$\begin{aligned} \mathbb{V}(\mathbb{E}[Y|\boldsymbol{\Theta_i}]) \approx \quad & \frac{1}{n} \textstyle\sum_{k=1}^{n} \mathcal{M}(\theta_1^{(k),1}, \ldots, \theta_V^{(k),1}) \mathcal{M}(\theta_1^{(k),2}, \ldots, \theta_i^{(k),1}, \ldots, \theta_V^{(k),2}) \\ & \qquad - \left(\frac{1}{n} \textstyle\sum_{k=1}^{n} \mathcal{M}(\theta_1^{(k),1}, \ldots, \theta_V^{(k),1}) \right)^2 \ , \end{aligned} \tag{2.24}$$

where $(\boldsymbol{\theta}^{(1),1}, \ldots, \boldsymbol{\theta}^{(n),1})$ and $(\boldsymbol{\theta}^{(1),2}, \ldots, \boldsymbol{\theta}^{(n),2})$ are two different samples of inputs $\boldsymbol{\Theta}$, and $V \in \mathbb{N}$ is the dimension of the input space. However, 2^V estimations are necessary with this method for full description of the variances [213] (sensitivity indices at all orders), corresponding to the number of integrals to estimate. Polynomial Chaos Expansion (PCE) can be used as an alternative to estimate the above indices at reasonable cost [36, 103, 241], as described in Section 2.1.6. Additionally, Dimensionality Reduction (DR) techniques can be used to reduce the output to a low dimensional set of representative variables, and generalization of variance-based indices [34, 76, 117] can be found in Section 2.4.

2.1.6 Stochastic spectral approach for metamodelling

As previously explained in Section 2.1.4, both PCE [113, 139], which is a spectral stochastic method, and kriging [152] allow to build efficient probabilistic mapping from an input to an output space. This offers two possibilities for metamodelling. However, PCE is here preferred, due to orthonormality properties, that come with considerable advantages, detailed below.

Polynomial Chaos Expansion (PCE) is a linear expansion on a polynomial basis, that maps the probability space of an interest variable to some random parameters. It offers a convenient theoretical framework to path probabilistic information such as statistical moments or Probability Density Functions (PDFs) [113, 139]. It is part of the broader family of Chaos expansions.

Chaos expansion is a *stochastic spectral representation* for a multidimensional random variable $\mathbf{Y}$ with finite variance, written as in Equation 2.25, where $\{\zeta_j\}_{j=0}^{\infty}$ is a suitable *Hilbertian* basis, and $\{c_j\}_{j=0}^{\infty}$ are real deterministic coefficients. It is classically used to map some functional $\mathbf{Y} = \mathcal{M}(\boldsymbol{\Theta})$ to its inputs. In this case, the basis is written $\{\zeta_j(\boldsymbol{\Theta})\}_{j=0}^{\infty}$.

$$\mathbf{Y} = \sum_{j=0}^{\infty} c_j \zeta_j \ . \tag{2.25}$$

Orthonormality of the basis is a desired property for an efficient representation. In particular, it guarantees a *spectral decay* and therefore fast convergence of the approximation, i.e. reduction of expansion in Equation 2.25 to a finite summation [241]. Polynomial Chaos Expansion (PCE) in this context refers to the case where basis elements are orthonormal polynomials, allowing the stochastic model to capture generally non-linear functions $\mathbf{Y} = \mathcal{M}(\boldsymbol{\Theta})$ of a finite dimension input vector $\boldsymbol{\Theta} = (\theta_1, \ldots, \theta_V)$ [232]. Expansion is then written as in Equation 2.26,

$$\begin{aligned} \mathbf{Y} &= \mathcal{M}(\boldsymbol{\Theta}) = \textstyle\sum_{\mathcal{I} \subseteq \{1,\ldots,V\}} \mathcal{M}_{\mathcal{I}}(\theta_{\mathcal{I}}) \\ &= \mathcal{M}_0 + \textstyle\sum_{i=1}^{V} \mathcal{M}_i(\theta_i) + \sum_{1 \leq i < j \leq V} \mathcal{M}_{i,j}(\theta_i, \theta_j) + \ldots + \mathcal{M}_{1,\ldots,V}(\theta_1, \theta_2, \ldots, \theta_V) \ , \end{aligned} \tag{2.26}$$

where $\mathcal{M}_0$ is the *expectation* of $\mathbf{Y}$ (defined below) and multivariate polynomial $\mathcal{M}_{\mathcal{I} \subseteq \{1,\ldots,V\}}$ represents the common contribution of variables $\mathcal{I} \subseteq \{1, \ldots, V\}$ to the variations of $\mathbf{Y}$.

Two elements are therefore capital for accurate PCE: (i) finding an orthonormal polynomial basis $\{\zeta_j(\boldsymbol{\Theta})\}_{j=0}^{\infty}$ and (ii) choosing $\{c_j\}_{j=0}^{\infty}$ accurately. Corresponding methods are briefly presented hereafter, after a general introduction to the probabilistic framework. Theoretical details, demonstrations and interesting references can be found in [241, 273].

Basis construction: from Wiener to generalized Chaos

Introduction of PCE dates back to 1938 with the *Wiener Chaos* [266], for Gaussian stochastic processes. In particular, it was shown, for a set of Normal and mutually independent inputs $\boldsymbol{\Theta} \in (\mathcal{L}^2_{\mathbb{R}})^V$, that multivariate Hermite polynomials are orthonormal with respect to scalar product $(.\ ,.)_{\mathcal{L}^2_{\mathbb{R}}}$ defined in Equation 2.9 [80]. Hence, any finite variance random variable $Y \in \mathcal{L}^2_{\mathbb{R}} : \Omega \longrightarrow D_Y = \mathbb{R}$ conditioned with Normal and mutually independent inputs, can be expanded on corresponding Hermite basis [80]. Later, extension to other families of input densities was achieved [272], by pairing classical parametric PDFs to corresponding orthonormal Askey-scheme hypergeometric polynomials, as in Table 2.1. This was then referred to as generalized Polynomial Chaos (gPC) for an expansion on inputs with different PDFs. Generalization to arbitrary densities was later developed, either by transforming PDFs to parametric densities from Table 2.1 (*isoprobabilistic transforms*), or by constructing custom orthonormal basis using Gram-Schmidt orthonormalization process in [269] or the Stieltjes three-term recurrence procedure in [265].

PDF	Input support D_{θ_i}	Corresponding orthonormal polynomials
Gaussian	$\mathbb{R}$	Hermite
Uniform	$[-1, 1]$	Legendre
Gamma	$(0, +\infty)$	Laguerre
Ghebyshev	$(-1, 1)$	Chebychev
Beta	$(-1, 1)$	Jacobi

Table 2.1 – Orthonormal Askey-scheme hypergeometric polynomials for parametric PDFs [271]

One of the most important results is provided by Soize and Ghanem [232], who demonstrate the existence of an infinite numerable family of orthonormal polynomials, that form the basis of arbitrary Hilbert space $\mathcal{L}^2_{\mathbb{R}}$ [242]. A mathematical setting to construct a basis for the general case of arbitrary dependent variables (*mixtures of probability measures*) was provided [232]. Hence, exact expansion of arbitrary $Y \in \mathcal{L}^2_{\mathbb{R}}$ on a finite set of random inputs $\boldsymbol{\Theta} \in (\mathcal{L}^2_{\mathbb{R}})^V$ is possible (equality on infinite basis, not approximation), provided that adequate inputs, corresponding densities, and orthonormal polynomials are selected.

General choice of input variables for regression models is an ongoing research question in statistics [87]. However, if all inputs are known, accuracy of the expansion mainly depends on basis choice, crucial to guarantee spectral decay. It is directly related to the choice of input variable marginals, via the inner product $(.,.)_{\mathcal{L}^2_{\mathbb{R}}}$, that should therefore be chosen wisely. Hence, PCE performances can vary with PDFs choice. In the absence of theoretical arguments, the quality of the PCE model can always be verified using adequate measures, discussed below in this Section. If adequate basis is used, convergence rate of the expansion is exponential [272].

In addition to classical set-ups, innovative solutions were identified to apply PCE to challenging cases. For example, when the output's space is characterized with rapid variations or discontinuities (e.g. near a critical point in the inputs space), *adaptive Multi-Element* PCE can be used. This was developed for Legendre polynomials in [264] and extended to arbitrary measures in [265]. The inputs space is decomposed to a union of subsets, and the output variable is locally expanded on each subset. The final solution is then a combination of PCE sub-problems. In case of discontinuity in the inputs $\boldsymbol{\Theta}$, the previous splitting techniques can also be used. For example, the sub-intervals in the inputs space can be constructed in such way to avoid the discontinuity. PCE sub-problems would therefore be treated as usual.

When the inputs $\boldsymbol{\Theta}$ are mutually independent, if orthonormal univariate polynomial basis $\left\{\xi_{\theta_i,\beta}(\theta_i), \beta \in [|0,p|]\right\}$ are known for each component θ_i, where $p \in \mathbb{N}$ is a chosen polynomial degree and $\xi_{\theta_i,\beta}(\theta_i)$ is of degree β, then it is possible to construct a multivariate basis. By defining a multi-index notation $\boldsymbol{\alpha} = (\alpha_1, ..., \alpha_V) \in \mathbb{N}^V$ so that $|\boldsymbol{\alpha}| = \sum_{i=1}^{V} \alpha_i$, the multivariate basis is calculated as $\left\{\zeta_{\boldsymbol{\Theta},\boldsymbol{\alpha}}(\boldsymbol{\Theta}) := \prod_{i=1}^{V} \xi_{\theta_i,\alpha_i}(\theta_i), |\boldsymbol{\alpha}| \in [|0,p|]\right\}$. Therefore, the model in Equation 2.26 can be written as in Equation 2.27, where $c_{\boldsymbol{\alpha}} \in \mathbb{R}$ are the deterministic expansion coefficients that can be estimated with different methods (discussed below).

$$Y = \mathcal{M}(\boldsymbol{\Theta}) = \sum_{|\boldsymbol{\alpha}| \le P} c_{\boldsymbol{\alpha}} \zeta_{\boldsymbol{\Theta},\boldsymbol{\alpha}}(\theta_1, \theta_2, ..., \theta_V) \ , \tag{2.27}$$

In the general case of dependent inputs, the latter can be transformed into independent Gaussian inputs using the *Rosenblatt transformation* as proposed by [232] and discussed in [36], and then the same strategy defined above can be used for basis construction.

For multidimensional variables $\mathbf{Y} \in (\mathcal{L}^2_{\mathbb{R}})^m$, PCE is generally constructed component wise. If the same inputs $\boldsymbol{\Theta}$ are used for all components, the expansion can be written as in Equation 2.28, where $\boldsymbol{\zeta}_{\boldsymbol{\Theta}}$ is a vector containing the basis elements, and each line of matrix $\mathbf{C}$ contains expansion coefficients $c_{Y_i,\boldsymbol{\alpha}}$ of component Y_i.

$$\mathbf{Y} = \mathcal{M}(\boldsymbol{\Theta}) = \mathbf{C}\boldsymbol{\zeta}_{\boldsymbol{\Theta}} \tag{2.28}$$

Orthonormality of the basis with respect to the scalar product $(.\ ,.)_{\mathcal{L}^2_{\mathbb{R}}}$ is particularly convenient for statistical moments estimation as it guarantees:

- $\mathbb{E}\left[\zeta_{\boldsymbol{\Theta},\alpha_1}\zeta_{\boldsymbol{\Theta},\alpha_2}\right] = \delta_{\alpha_1,\alpha_2}$, where $\delta_{\alpha_1,\alpha_2}$ is the Kronecker product;

- Correlation matrix of the PCE basis is $\mathbb{E}\left[\boldsymbol{\zeta}_{\boldsymbol{\Theta}}\boldsymbol{\zeta}_{\boldsymbol{\Theta}}^{T}\right] = \boldsymbol{I}$, where $\boldsymbol{I}$ is the identity matrix (consequence of the previous);
- $\mathbb{E}\left[\zeta_{\boldsymbol{\Theta},\boldsymbol{\alpha}}\right] = \left(\zeta_{\boldsymbol{\Theta},\boldsymbol{\alpha}}, \zeta_{\boldsymbol{\Theta},\boldsymbol{\beta}=(\mathbf{0},\ldots,\mathbf{0})} = 1\right)_{\mathcal{L}^2_{\mathbb{R}}} = 0;$
- $\mathbb{E}\left[Y\right] = \left(\sum_{0\leq|\boldsymbol{\beta}|\leq p} c_{\boldsymbol{\beta}}\zeta_{\boldsymbol{\Theta},\boldsymbol{\beta}}\ , \zeta_{\boldsymbol{\Theta},\boldsymbol{\beta}=(\mathbf{0},\ldots,\mathbf{0})}\right)_{\mathcal{L}^2_{\mathbb{R}}} = c_{\beta=(0,\ldots,0)};$
- $\mathbb{E}\left[Y\zeta_{\boldsymbol{\Theta},\boldsymbol{\alpha}}\right] = \left(\sum_{0\leq|\boldsymbol{\beta}|\leq p} c_{\boldsymbol{\beta}}\zeta_{\boldsymbol{\Theta},\boldsymbol{\beta}}\ , \zeta_{\boldsymbol{\Theta},\boldsymbol{\alpha}}\right)_{\mathcal{L}^2_{\mathbb{R}}} = c_{\boldsymbol{\alpha}}\ ;$
- $\mathbb{V}\left[\zeta_{\boldsymbol{\Theta},\boldsymbol{\alpha}}\right] = \mathbb{E}\left[\left(\zeta_{\boldsymbol{\Theta},\boldsymbol{\alpha}} - \mathbb{E}\left[\zeta_{\boldsymbol{\Theta},\boldsymbol{\alpha}}\right]\right)^2\right] = \mathbb{E}\left[\left(\zeta_{\boldsymbol{\Theta},\boldsymbol{\alpha}}\right)^2\right] = ||\zeta_{\boldsymbol{\Theta},\boldsymbol{\alpha}}||^2_{\mathcal{L}^2_{\mathbb{R}}} = 1\ ;$
- $\mathbb{V}\left[Y\right] = \mathbb{E}\left[(Y - \mathbb{E}\left[Y\right])^2\right] = \left(\sum_{1\leq|\boldsymbol{\beta}|\leq p} c_{\boldsymbol{\beta}}\zeta_{\boldsymbol{\Theta},\boldsymbol{\beta}}\ , \sum_{1\leq|\boldsymbol{\beta}|\leq p} c_{\boldsymbol{\beta}}\zeta_{\boldsymbol{\Theta},\boldsymbol{\beta}}\right)_{\mathcal{L}^2_{\mathbb{R}}} = \sum_{1\leq|\boldsymbol{\beta}|\leq p} c^2_{\boldsymbol{\beta}}\ .$

Hence, in the multidimensional case, first column of matrix $\mathbf{C}$ in Equation 2.28 is the expectation of $\mathbf{Y}$, and $\mathbf{C}\mathbf{C}^T$ its covariance matrix.

Once the orthonormal basis $\left\{\zeta_{\boldsymbol{\Theta},\boldsymbol{\alpha}}, |\boldsymbol{\alpha}| \in [|0, p|]\right\}$ constructed, coefficients $\{c_{|\boldsymbol{\alpha}|}, |\boldsymbol{\alpha}| \in [|0, p|]\}$ should be selected for the PCE model to represent the interest dynamics.

Coefficients choice: intrusive vs. non intrusive methods

Firstly, separation between *intrusive* and *non intrusive* methods is defined in literature. *Intrusive* methods typically refer to the case where an interest field is replaced by expansion 2.27 in a set of governing Partial Differential Equations (PDE). *Galerkin* scheme can for example be used to deduce the coefficients by resolving a new set of equations [80]. This method, although theoretically robust, is however known to be costly and requires, in addition to the model, a supplementary implementation effort [26].

Non intrusive methods consist in finding $\{c_{|\boldsymbol{\alpha}|}, |\boldsymbol{\alpha}| \in [|0, p|]\}$ directly from data, which are considered to be representative of the dynamic system or interest model/equations. Data are classically generated using the interest model, that transforms a sample of input parameters to a sample of studied output. Paired realizations can then be used to estimate adequate values of PCE coefficients. Ideally, the used realizations should be regularly distributed in the inputs space, with respect to their PDFs, therefore offering a *response surface* of the output that is representative of its probabilities. For example, MC sampling can be used, or more sophisticated techniques as LHS for better convergence rates [154]. The model is then considered as a blackbox and the fitted PCE, called *metamodel* (or *surrogate*, *equation-free model*), is usually used as an approximate for statistical estimations.

Spectral projection

Spectral projection is one of the non intrusive PCE techniques, based on the orthonormality of the basis, that gives $\{c_{\boldsymbol{\alpha}} = \mathbb{E}\left[Y\zeta_{\boldsymbol{\Theta},\boldsymbol{\alpha}}\right] = \mathbb{E}\left[\mathcal{M}(\boldsymbol{\Theta})\zeta_{\boldsymbol{\Theta},\boldsymbol{\alpha}}\right], |\boldsymbol{\alpha}| \in [|0, p|]\}$. The expectation can then either be estimated by inputs-model realizations as in Equation 2.3 (*simulation technique*), or by approximating the analytical integral definition of expectation, using appropriate weights and input integration points (*quadrature technique*).

Regression approach

Regression is a second non intrusive PCE approach, where the quadratic distance between PCE and the model is optimized [104], offering an optimal estimate of the coefficients in the least-squares sense. This is recast to minimization of a cost function that could be analytically written, for the PCE probabilistic framework, as in Equation 2.29,

$$\widehat{\mathbf{c}_{(P)}} = \arg\min_{c_{(P)}} J(\mathbf{c}_{(P)}) \coloneqq \mathbb{E}\left[\left(\mathbf{c}_{(P)}^{T}\boldsymbol{\zeta}_{\boldsymbol{\Theta},(P)} - \mathcal{M}(\boldsymbol{\Theta})\right)^{2}\right] , \tag{2.29}$$

where $\mathbf{c}_{(P)} = [c_{\alpha_1}, \dots, c_{\alpha_P}]^T$ and $\boldsymbol{\zeta}_{\boldsymbol{\Theta},(P)} = [\zeta_{\boldsymbol{\Theta},\alpha_1}, \dots, \zeta_{\boldsymbol{\Theta},\alpha_P}]^T$ denote PCE coefficients and basis elements, for expansion 2.27 truncated to a finite number of terms $P \in \mathbb{N}$.

Regression methods generally require numerical approximations of the minimization problem to find an optimum, as discussed in Section 2.2.1. In the PCE case, optimal solution to the minimization problem denoted $\widehat{\mathbf{c}_{(P)}}$ can be analytically calculated by cancelling the gradient of the cost function $\nabla_{\mathbf{c_{(P)}}} J$ as in Equation 2.30.

$$\mathbb{E}\left[\boldsymbol{\zeta}_{\boldsymbol{\Theta},(P)}\boldsymbol{\zeta}_{\boldsymbol{\Theta},(P)}^{T}\right]\widehat{\mathbf{c}_{(P)}} = \mathbb{E}\left[\boldsymbol{\zeta}_{(P)}\mathcal{M}(\boldsymbol{\Theta})\right] \ . \tag{2.30}$$

Theoretically, the orthonormality of the PCE basis guarantees that basis correlation matrix is $\mathbb{E}\left[\boldsymbol{\zeta}_{\boldsymbol{\Theta},(P)}\boldsymbol{\zeta}_{\boldsymbol{\Theta},(P)}^{T}\right] = \boldsymbol{I}_P$, where $\boldsymbol{I}_P$ is the identity matrix of size $P \times P$. Hence, Equation 2.30 therefore shows the equivalence between *regression* and *spectral projection* methods. Empirically, if a number n of inputs realizations provides realizations of basis elements stored in a matrix $\mathcal{S}_{\zeta_{\boldsymbol{\Theta},(P)}}$, and corresponding realizations of the model output are stored in matrix $\mathcal{S}_{\mathcal{M}(\boldsymbol{\Theta})}$, so that line i of each realization matrix contains a sample of component i as $(\mathcal{S}_{\mathbf{Y}})_i = [y_i^{(1)}, \dots, y_i^{(n)}]$, then Equation 2.30 can be estimated as in Equation 2.31

$$\widehat{\mathbf{c}_{(P)}} \approx (\mathcal{S}_{\zeta_{\boldsymbol{\Theta},(P)}}\mathcal{S}_{\zeta_{\boldsymbol{\Theta},(P)}}^{T})^{-1}\mathcal{S}_{\zeta_{\boldsymbol{\Theta},(P)}}\mathcal{S}_{\mathcal{M}(\boldsymbol{\Theta})}^{T} \tag{2.31}$$

Matrix $\mathcal{S}_{\zeta_{\boldsymbol{\Theta},(P)}}\mathcal{S}_{\zeta_{\boldsymbol{\Theta},(P)}}^{T}$ is called *information matrix*. For the well-posedness of the problem, the information matrix of dimension $P \times P$ should be full rank (i.e number of linearly independent column vectors is P). For this, the number of realizations should be at least equal to P. This is a necessary condition for invertiblity.

Dimensionality and sparse basis construction

Cardinality of the number of PCE terms is however factorial with the number of inputs V and chosen polynomial degree p, which is the so called *curse of dimensionality*. It can be calculated as in Equation 2.32. This implies that the dimension of the information matrix, and therefore the inversion computational cost and the number of realizations for a well-posed problem, also suffer from the curse of dimensionality. However, some strategies can be adopted to reduce the number of PCE terms.

$$P = \sum_{k=0}^{p} C^{p}_{V+k-1} = \frac{(V+p)!}{V!p!} \tag{2.32}$$

Firstly, one solution consists in transforming the large set of inputs to a reduced version, for example with the help of Principal Component Analysis (PCA) or KPCA for Dimensionality Reduction (DR), as done by Lataniotis et al. [121] on an ultrahigh-dimensional problems. Discussion about DR can be found in Section 2.4.

Second solution consists in using a truncation strategy. The naive choice consists in considering basis members $\zeta_{\boldsymbol{\Theta},\boldsymbol{\alpha}}$ with a maximal polynomial degree p, which can be written as $|\boldsymbol{\alpha}| \leq p$, and gives the number of terms as in Equation 2.32. Another approach consists in constraining the possible interactions, i.e. the number of non-zero components in $\boldsymbol{\alpha}$ and therefore the number of interacting variables in $\zeta_{\boldsymbol{\Theta},\boldsymbol{\alpha}}$. This is referred to as *low rank expansion*. It can be for example achieved by defining a q-norm constraint as $\|\boldsymbol{\alpha}\|_q := \left(\sum_{i=1}^{V} \alpha_i^q\right)^{1/q} \leq p$, with $0 < q < 1$, as proposed by Blatman and Sudret [27]. With $q = 1$, one obtains the usual truncation by polynomial degree. The smaller the value of q, the less interactions are admitted into the constructed set. This is called an *isotropic hyperbolic index set*.

Lastly, sparse construction strategies for PCE can also be used, for example proposed by [28] using Least Angle Regression Stagewise (LARS). In the PCE case, LARS algorithm begins by finding the polynomial pattern, denoted $\zeta_{\boldsymbol{\Theta},\boldsymbol{\alpha}_i}$, or ζ_i, for simplicity, that is the most correlated to the output $Y = \mathcal{M}(\boldsymbol{\Theta})$. The latter is linearly approximated by $\epsilon_i\zeta_i$, where $\epsilon_i \in \mathbb{R}$. Coefficient ϵ_i is increased starting from 0, until another pattern ζ_j is found to be as correlated to $Y - \epsilon_i\zeta_i$, and so on. In this approach, a collection of possible PCE, ordered by sparsity, is provided and an optimum can be chosen with an accuracy estimate. Blatman and Sudret [28] proposes to use the *corrected* Leave One Out (LOO) indicator, defined below in Equation 2.40. Other sparse construction methods for regression problems are briefly described in Section 2.2.1.

Model accuracy estimation

Firstly, the distance between a random variable Y and its PCE approximate can be evaluated using the appropriate measure in the space of real random variables with finite second moments, which is the $\mathcal{L}^2_{\mathbb{R}}$-norm. This is called the *generalization error* [261], denoted $\delta(Y, \widetilde{Y})$ and defined as in Equation 2.33.

$$\delta(Y, \widetilde{Y}) = \mathbb{E}\left[(Y - \widetilde{Y})^2\right] . \tag{2.33}$$

This error can be estimated as in Equation 2.34, using the statistical approximation of the expectation in Equation 2.3 over a sample of realizations $(y_1, \dots, y_n)$. This approximated version of the *generalization error* is called the *empirical error*.

$$\delta(Y, \widetilde{Y}) \approx \delta_{emp}(Y, \widetilde{Y}) := \frac{1}{n} \sum_{j=1}^{n} \left(y^j - \widetilde{y}^j\right)^2 . \tag{2.34}$$

Its relative estimate denoted $\epsilon(Y, \widetilde{Y})$ is defined in Equation 2.35. It is a measure of the missing variations (distance between the model and reality) relative to the variance of the data. It represents the amount of variance that was not captured by the PCE model (also called "the fraction of unexplained variance" [50]).

$$\epsilon(Y, \widetilde{Y}) := \frac{\delta(Y, \widetilde{Y})}{\mathbb{V}[Y]} = \frac{\mathbb{E}\left[(Y - \widetilde{Y})^2\right]}{\mathbb{E}\left[(Y - \mathbb{E}[Y])^2\right]} \; . \tag{2.35}$$

Empirical estimation can be written as in Equation 2.36, where $\overline{Y} := \frac{1}{n} \sum_{j=1}^{n} y^j$ is the statistical average of Y over the $n-$size sample. This also allows to calculate the well known *determination coefficient* as $R^2 := 1 - \epsilon_{emp}(Y, \widetilde{Y})$.

$$\epsilon(Y, \widetilde{Y}) \approx \epsilon_{emp}(Y, \widetilde{Y}) = \frac{\frac{1}{n} \sum_{j=1}^{n} \left(y^j - \widetilde{y}^j\right)^2}{\frac{1}{n-1} \sum_{j=1}^{n} \left(y^j - \overline{Y}\right)^2} \; . \tag{2.36}$$

However, the empirical approximation in Equation 2.36 can under-estimate the relative generalization error Blatman [26]. Namely, its value decreases with the number of PCE terms P, which may lead to overfitting. Hence, the relative Leave One Out (LOO) error can be used instead. This is a special case of *v-fold cross-validation* [239], where the training set is separated to v sub-sets of quasi-identical sizes. A number of v learnings is then, in turn, performed on $v - 1$ subsets and evaluated on the remaining set, and an average error is calculated. LOO corresponds to the case where $v = n$ and the left subset for each error estimation at iteration j corresponds to singleton of paired realizations $\{\boldsymbol{\theta}^j, y^j\}$. If corresponding fitted model is denoted $\widetilde{\mathcal{M}}^{-i}(\boldsymbol{\Theta})$, then the LOO error is calculated in Equation 2.37.

$$\epsilon_{LOO} := \frac{\frac{1}{n} \sum_{i=1}^{n} \left(y^j - \widetilde{\mathcal{M}}^{-i}(\boldsymbol{\theta}^j)\right)^2}{\frac{1}{n-1} \sum_{j=1}^{n} \left(y^j - \overline{Y}\right)^2}) \; . \tag{2.37}$$

This can also be analytically calculated as in Equation 2.38, according to [26].

$$\epsilon_{LOO} = \frac{\frac{1}{n} \sum_{i=1}^{n} \left(\frac{y^j - \widetilde{y}^j}{1 - h_i}\right)^2}{\frac{1}{n-1} \sum_{j=1}^{n} \left(y^j - \overline{Y}\right)^2} \; , \tag{2.38}$$

where h_i is $i-$th diagonal term of matrix $\mathcal{S}^T_{\zeta_{\boldsymbol{\Theta}}} (\mathcal{S}_{\zeta_{\boldsymbol{\Theta}}} \mathcal{S}^T_{\zeta_{\boldsymbol{\Theta}}})^{-1} \mathcal{S}_{\zeta_{\boldsymbol{\Theta}}}$. This shows that the LOO error is a correction of the empirical error at each prediction $\widetilde{y}^j$ by factor $1/(1 - h_i)^2$. In order to further prevent from overfitting, [26] proposes to penalize the approximation in Equation 2.38 with an additional factor, function of the number of PCE terms P. This is called the *corrected* LOO error, denoted ϵ^*_{LOO} and written as in Equation 2.39,

$$\epsilon^*_{LOO} := \epsilon_{LOO} \times T(P, n) \; , \tag{2.39}$$

where $T(P, n)$ is a penalization term calculated as in Equation 2.40.

$$T(P, n) := \left(1 - \frac{P}{n}\right)^{-1} \left(1 + tr\left(\left(\mathcal{S}_{\zeta_{\boldsymbol{\Theta}}} \mathcal{S}^T_{\zeta_{\boldsymbol{\Theta}}}\right)^{-1}\right)\right) \tag{2.40}$$

PCE-based Global Sensitivity Analysis

As mentioned in Section 2.1.5, PCE can be used as an alternative to Monte Carlo (MC) approaches, in particular to the method proposed by Satelli et al. [213] in Equation 2.24, to estimate ANOVA (Sobol) and ANCOVA based indices at reasonable cost [36, 103, 241]. In this case, the term $\mathcal{M}_{\mathcal{I}}$ in Equation 2.19 corresponds to the polynomial contribution $c_{\boldsymbol{\alpha}} \zeta_{\boldsymbol{\Theta},\boldsymbol{\alpha}}$, where $\boldsymbol{\alpha} = (\alpha_1, \dots, \alpha_V)$ and $\alpha_i \neq 0$ if and only if $i \in \mathcal{I}$. The decomposition of Equation 2.19 can be written as in Equation 2.41.

$$\begin{aligned} \mathbb{V}[Y] &= \sum_{\mathcal{I} \subseteq \{1,\dots,V\}} \left(\mathbb{V}\left[c_{\mathcal{I}} \zeta_{\boldsymbol{\Theta},\mathcal{I}} \right] + \sum_{\mathcal{J} \neq \mathcal{I} \subseteq \{1,\dots,V\}} cov \left(c_{\mathcal{I}} \zeta_{\boldsymbol{\Theta},\mathcal{I}}, c_{\mathcal{J}} \zeta_{\boldsymbol{\Theta},\mathcal{J}} \right) \right) \\ &= \sum_{\mathcal{I} \subseteq \{1,\dots,V\}} \left(c_{\mathcal{I}}^2 \mathbb{V}\left[\zeta_{\boldsymbol{\Theta},\mathcal{I}} \right] + \sum_{\mathcal{J} \neq \mathcal{I} \subseteq \{1,\dots,V\}} c_{\mathcal{I}} c_{\mathcal{J}} cov \left(\zeta_{\boldsymbol{\Theta},\mathcal{I}}, \zeta_{\boldsymbol{\Theta},\mathcal{J}} \right) \right) \end{aligned} . \tag{2.41}$$

Covariance-based indices are then written as in Equation 2.42,

$$\begin{aligned} S_{\mathcal{I}}^{(cov)} &:= S_{\mathcal{I}}^{(U)} + S_{\mathcal{I}}^{(C)} \\ &:= \frac{c_{\mathcal{I}}^2 \mathbb{V}\left[\zeta_{\mathcal{I}}^{\boldsymbol{\Theta}} \right]}{\mathbb{V}[Y]} + \frac{\sum_{\mathcal{J} \neq \mathcal{I} \subseteq \{1,\dots,V\}} c_{\mathcal{I}} c_{\mathcal{J}} cov \left(\zeta_{\mathcal{I}}^{\boldsymbol{\Theta}}, \zeta_{\mathcal{J}}^{\boldsymbol{\Theta}} \right)}{\mathbb{V}[Y]} \end{aligned} . \tag{2.42}$$

With the orthonormal PCE basis, covariance terms vanish, and the output variance simplifies to $\mathbb{V}[Y] = \sum_{\mathcal{I} \subseteq \{1,\dots,V\}} c_{\mathcal{I}}^2$ [241].

Previously presented approaches, in the context of probability theory, allow to efficiently process data for metamodelling and quantitative analysis. They can be used both as data-based techniques, and for physically-based data-driven approaches. These are detailed below respectively.

2.2 Data-based techniques

Data, as measurements or numerically emulated scenarios, can be a valuable source of information if treated wisely. Qualitative analysis, as comparative plots, are an easy to use approach for interpretation. However, they do not use the full potential of data and can easily be outperformed with appropriate tools. In the 21st century, this is generally referred to as *data science* [55], and is fed by the long history of statistics, probability, and information theory.

Data science consists in using mathematical and algorithmic methods to extract knowledge from data. It goes from data analysis [49] that can take various forms as multivariate analysis [88], patterns recognition and interpretation, etc., to predictive data-based models construction, or learning [93], from regression to modern ML and variants [223].

Methods based on probability theory were briefly presented in Section 2.1. This includes Probability Density Function (PDF) construction from data and adequate theorems as the Maximum Entropy Principle (MEP), methods of optimal fitting as the Maximum Likelihood Estimation (MLE), and the Bayesian approach to assimilate data in a PDF construction. Indicators as statistical moments, percentiles, etc., that can be used to describe given data were also presented. Use of such methods for statistical data analysis is described in [49]. In addition, other approaches as *statistical tests* to verify given *hypothesis* about the data, or *unfolding* to correct data distortion due to measurement device error, can also be found in [49], but are not described in this thesis.

Multivariate analysis focuses on finding similarities and differences between different objects. This can for example include pattern recognition and Dimensionality Reduction (DR) techniques as Principal Component Analysis (PCA), described in Section 2.4, where correlations between variables are calculated to reduce the dimension of the multivariate space by spanning it. Other approaches as *clustering* (searching groups within data) or *discriminant analysis* (classification in given groups) can be used [88] but are not of interest in this thesis.

In this section, particular interest is given to construction of predictive purely data-based models. We begin by defining regression in Subsection 2.2.1, before describing ML in Subsection 2.2.2. Section 2.2.3 focuses on NN, which are particularly used in environmental applications as described below.

Use in physics

In physical applications, the complexity of the involved dynamics and phenomena, resulting in a non-unanimity of the modelling approaches in some areas [9, 187], can encourage the use of alternative statistical techniques. This allows exploring new hypothesis, for example with new data. In particular in Geosciences, data sources are in constant increase [109], and some interesting programs can be cited as the new SWOT satellite mission [166, 176], or the Sentinel satellite missions (Copernicus program) [66, 147]. This is of particular interest, in a context of climate change, where the dynamics are changing and ML could help assimilating new data to models [205].

In environmental applications, particular attention is given to NN for example (detailed below), due to its flexibility and adaptability to various non linear cases (meteorology, oceanography, climate and weather, hydrology, etc., as reviewed in [41]). Applications can for example be found (non exhaustive) in [3, 233] for hydrological evolution learning, in [60, 212] for sediment transport, and in [181] for river flow prediction. A recent article [82] gives a complete overview about the use of ML in coastal sediment transport modelling, which is precisely of interest here. The interest variables to approximate can differ from the characterization of various coastal morphological forms, coastlines, wave ripples, bars, to the estimation of suspended sediment concentration. Extraction of quantitative information and forecasting with automated tools, is usually targeted. Data sets can be multivariate, spatio-temporal, and characterized with high dimensionality and high non-linearities. Great majority of applications gravitate around the evolution of shorelines, which is a medium to long term phenomenon (years, decades). An application gap is noticed in the study of artificial channels with a forcing that implies fast dynamics (days, weeks), in a medium spatial scale, as is the case with data at hand. The authors [82] also highlight the importance of probabilistic approaches to enhance prediction accuracy and characterize the confidence intervals, due to movement instability that is intrinsic to morphodynamics.

2.2.1 Regression problems

In regression problems, a classical function is generally chosen to fit a causal input-to-output model. For example, fitting could be univariate or multivariate, and may use different functions in order to capture the involved relationships (identity for linear regression, polynomials, etc). In all cases, hyper-parameters are involved. For example, these could be multiplicative coefficients in front of the input variables for a linear function. The values of such calibration parameters are determined from the data set, in order to fit the observations. Theoretical manner to express this fitting is via a *minimization problem*, also called Ordinary Least Squares (OLS) problem. A squared error function called *Cost function*, measures the distance between the model and the output, and the objective is to find the optimal parameters $\hat{\boldsymbol{\theta}}$ that minimize it [178]. The minimization of this cost function can be written as in 2.43, where $\left\{(x^{(i)}, y^{(i)})\right\}_{i=1,\ldots,m}$ is the paired set of observed input x and output y, $m \in \mathbb{N}$, and $h_{\boldsymbol{\theta}}$ is the regression function (polynomial, linear, etc.) with hyper-parameters θ [178].

$$\hat{\theta} = \arg\min_{\boldsymbol{\theta}} \left[J(\boldsymbol{\theta}) \coloneqq \frac{1}{2m} \sum_{i=1}^{m} (h_\theta(x^{(i)}) - y^{(i)})^2 \right] \tag{2.43}$$

Different manners to find the optimal parameters using the cost function defined in Equation 2.43 can be used. For example, heuristics, meta-heuristics [225] or gradient methods [195] can be employed. The latter may for example rely on iterative descent, as *gradient descent*, that moves in the parameters space, from one configuration to another, until the minimum cost function is reached. As an example, the advanced constrained Broyden-Fletcher-Goldfarb-Shanno Quasi-Newton (c-BFGS-QN) method [276], allows to impose bounds for the parameters to optimize.

Regression algorithms can run into *over-fitting* (high variance of the output), if the space of inputs (or used features for learning) is too high-dimensional compared to the training set size. The cost function is then close to zero, but the model fails to generalize to new examples (poor predictability) [178]. Options to address such problem are: (i) reducing the number of variables manually (ii) using mode selection algorithms that automatically decide which features to keep and which features to get-rid of [182]; (iii) *regularization techniques*, where all features are kept, but the magnitudes of some hyper-parameters θ_i are strongly reduced if not cancelled. This allows to build sparse regressions. Commonly used methods are detailed hereafter

Forward Selection

For example, *Forward Selection* consists in linearizing the output y around the most correlated pattern from the statistical model. If the model can be written as $h_{\boldsymbol{\theta}}(x) = \sum_{j=1}^{V} \theta_j h_j(x)$ where V is the number of patterns, then the target is to find the term $h_j(x)$ that maximizes the correlation to y, then build a linear model $y \approx \widehat{\theta_j} h_j(x)$. Then, the residual $y - \widehat{\theta_j} h_j(x)$ is linearized around the most correlated component $h_{k \neq j}(x)$, and so on iteratively. However, this method is said to be "aggressive" in the sense that it eliminates valuable patterns if they are correlated to already chosen ones. A method called *Forward Stagewise Regression* is an improved version of the previous, where $\widehat{\theta_j}$ is not set to its maximum value but rather considering a smaller contribution in the form $\epsilon_j h_j(x)$. Coefficient ϵ_j should be small enough to avoid "aggressivity" of forward selection, but large enough to avoid increasing the number of necessary iterations. This method is however said to easily accept patterns with low correlations. It is besides unstable, being too sensitive to changes in the training set [96].

Least Absolute Shrinkage and Selection Operator (LASSO)

A more sophisticated regularization, called Least Absolute Shrinkage and Selection Operator (LASSO), can instead be used [254], where a constraint $\sum_{j=1}^{V} |\theta_j| \leq q \in \mathbb{R}$ is added to the minimization problem 2.43. When q is small, only few coefficients θ_j can be non-zero, which then gives a sparse construction. Additionally, if the constructed sparse model gives accurate predictions, then selected variables are considered to be statistically meaningful, allowing interpretation [61]. LASSO can also be formulated by adding a penalization term in the previous minimization [26], and then a new cost function is defined in 2.44 where λ is a regularization parameter. It is important however to note that constraining the problem too much (λ too high or q too low) can lead to under-fit [178]. If an automatic selection of λ is possible, this minimization can be considered as a patterns selection algorithm [178].

$$J(\boldsymbol{\theta}) = \frac{1}{2m} \sum_{i=1}^{m} (h_{\boldsymbol{\theta}}(x^{(i)}) - y^{(i)})^2 + \lambda \sum_{j=1}^{V} |\theta_j| \tag{2.44}$$

Least Angle Regression Stagewise (LARS)

LASSO can however be costly. A more efficient method called Least Angle Regression (LAR) or Least Angle Regression Stagewise (LARS) is proposed in [61]. LARS works on the same principle of *Forward Stagewise Regression*, but regression coefficient ϵ_j that multiplies the most correlated pattern $h_j(x)$ is not selected as a parameter. It is instead iteratively increased starting from 0, until another pattern $h_{k\neq j}(x)$ is found to be as correlated to residual $y - \epsilon_j h_j(x)$. A new term is then added to the approximation as $y \approx \epsilon_j h_j(x) + \epsilon_k h_k(x)$, and procedure continues by jointly increasing ϵ_j and ϵ_k, until a new correlated pattern is found, and so on. A stopping criterion should therefore be used, as the Mallows' statistic suggested in [61]. This method is based on sound theory, as fitting converges to the OLS problem 2.43 when the number of realizations m exceeds the number of terms to fit V. Additionally, it is a generalization of *Forward Stagewise Regression* and LASSO techniques. Lastly, LARS, plays at the same time the role of regularization and selection [61].

Lastly, *under-fitting* can also occur (highly biased model). This can for example be met if the learning set is not sufficient (e.g. not adequate inputs, not diverse enough data), or if the regression function is not appropriate. In some highly non-linear or multidimensional problems, classical functions are not enough. Hence, more complex algorithms have been established, such as Neural Networks (NN) and variants.

2.2.2 Machine Learning

ML is a sub-field of computer science, defined in different manners: a program that is able to learn without explicit instructions, a well-posed statistical learning problem, or an automated detection of meaningful patterns in data [178, 223]. It can be of interest when the problem to model is complex to formalize theoretically (e.g. voice recognition), or when the adaptability of the model to a particular problem is needed [223]. It allows constantly evolving models from constantly evolving knowledge, in a context where data are plentiful. ML algorithms have been widely used in the 80s and 90s, their popularity diminished, then had recent major resurgence due to development of computer calculation capacities and architectures [178]. ML can be viewed as a branch of Artifical Intelligence

(AI), since the ability of recognizing patterns and turning experience to expertise are human/animal. However, the spirit of AI is to mimic human/animal behavior, in contrast with ML, where computer intelligence is considered complementary, and is in particular of interest where the human abilities fail describing the observed [223].

Ingredients of successful learning

In general, ML algorithms learn an output as a function of inputs, as is the case with NN and Genetic Algorithms (GA) for instance. Some exceptions can be noted, for example Bayesian Networks (BN) where the probabilities of occurrence for a given state from knowledge of the inputs is modelled, rather than a deterministic state value [82]. In this case, the interest is to fully characterize the output uncertainties while predicting it. In physics, both approaches are of interest. In all cases, minimum requirements for establishing a ML program are:

- Input's space, also called instance space;
- Output's space
- Training data, composed of inputs-outputs pairs, or eventually a data-generation program (numerical model, probability distribution, etc.)
- Measures of success/failure of the learning (failure probability, generalization error, risk, true error)

The final result is a model (hypothesis, classifier, predictor, etc.) that succeeds in learning the dependencies to be able to predict them [223]. However, ML is not only reproducing the same story, but also having the ability to recognize/predict unseen behavior. A successful learner should be able to progress from individual examples to broader *generalization* [223]. This is called *inductive reasoning* or *inductive inference*, which can be defined as finding general rules from the observation of particular events, on the basis of probabilities. The latter allow to predict the most probable state, based on evidence given by individual examples. The opposite of *inductive reasoning* is *deductive reasoning*, were the hypothesis are clear and conclusions/arguments are certain. This can be linked to the contrast between *statistical inference* and *descriptive statistics*. In *statistical inference*, the properties of a population or an environment are hypothesized from analyzing a finite/small set of data extracted therefrom, supposing it is representative enough of its source. In *descriptive statistics*, the characteristics of the small set are of interest without any assumption or attempt of generalization on the larger set from which it comes.

Data-based prediction algorithms implicitly assume *inductive reasoning*. The resulting model "would potentially be able correctly to predict" [223] a desired behavior given the generalization assumptions that were made on the learning set. However, prior knowledge (assumptions) about the treated problem is often necessary to avoid senseless conclusions (predictions), although it may bias the learning mechanism. The incorporation of *prior knowledge* is inevitable for successful ML, which was formally stated and proved as the *"No-Free-Lunch theorem"* [223]. In every learning process, a bias should be expressed from the application specific expertise, and its effect on the learning must be studied. This is central in the development of ML algorithms, and is called *inductive bias* [223].

Therefore, central points for ML can be summed up as follows:

- Inductive reasoning is unavoidable and is the main principle behind generalization;
- A good application understanding is required to avoid senseless models;

ML algorithms

ML algorithms are generally classified as *supervised* vs. *unsupervised*, and *passive* vs. *active*. Firstly, in supervised learning, the algorithm is directly given with the information to learn, through the provided realizations (e.g. *regression*, *classification*). In unsupervised learning, the ML algorithm may by itself break the data into cohesive groups (*clustering*), with the objective of finding structure in the data, and come up with a compressed version (e.g. POD in Section 2.4.1). Secondly, passive ML consists in learning from the provided data, while in active learning the ML algorithm is given the possibility to point out supplementary designs of experiment that could be helpful [223]. Lastly, learning problems can also be *univariate* or *multivariate*.

Regression and classification are often used in physical problems, sometimes preceded by decomposition/clustering. Regression consists in finding causal input-to-output mode, using linear, polynomial or more complex functions, depending on the treated problem. Classification consists in finding categories of given inputs, the simplest problem being the ”true or false” choice. The border from classification to regression can be crossed using appropriate transforms, which is called *Logistic Regression*. For example, *Sigmoid* function (also called *Logistic*) is used to bound data between 0 and 1, and the output is then interpreted in terms of probability: for example, beyond 0.5 is True. With two inputs, the solution is a line called *decision boundary*, beyond which the output is True and under which the output is False. For more than two inputs, the inputs space is not exactly separated in two regions by a line, and we speak of ”*non-linear decision boundary*” [178].

This is a concise description of the landscape of statistical learning problems, but other set-ups can be met [223]. In this thesis, regression problems are of particular interest for the establishment of measurement-based predictive models. We shall therefore concentrate on this framework henceforth.

2.2.3 Neural Networks

Neural Networks (NN) (also called Artificial Neural Networks (ANN)) are a state of the art technique in modern ML, allowing to fit complex data [216]. Their name comes from an analogy with human/animal brains. Indeed, NN tries to mimic the adaptive biological nervous systems [222]: brain tissues constantly adapt to their new functions, and learn to deal with new tasks from new data. The idea behind NN is therefore to program a structure that is able, as the brain tissues, to adapt to any task, and to learn any function [178]. The algorithm is therefore developed as an ensemble of neurons working together. Each artificial neuron receives inputs (Figure 2.1-(b)), as a brain neuron would catch information via its *dendrites* (Figure 2.1-(a)), and computes outputs that it communicates to its environment, as a brain neuron performs analysis via a *nucleus* and communicates through an *axon*. Groups of artificial neurons are then gathered in *hidden layers*, and communications are performed from one layer to the other (Figure 2.1-(d)) [128, 216]. Analogy it then established with brain neurons, communicating via electricity pulses called spikes, that they send to each other with synapses-dendrites connection (Figure 2.1-(c)).

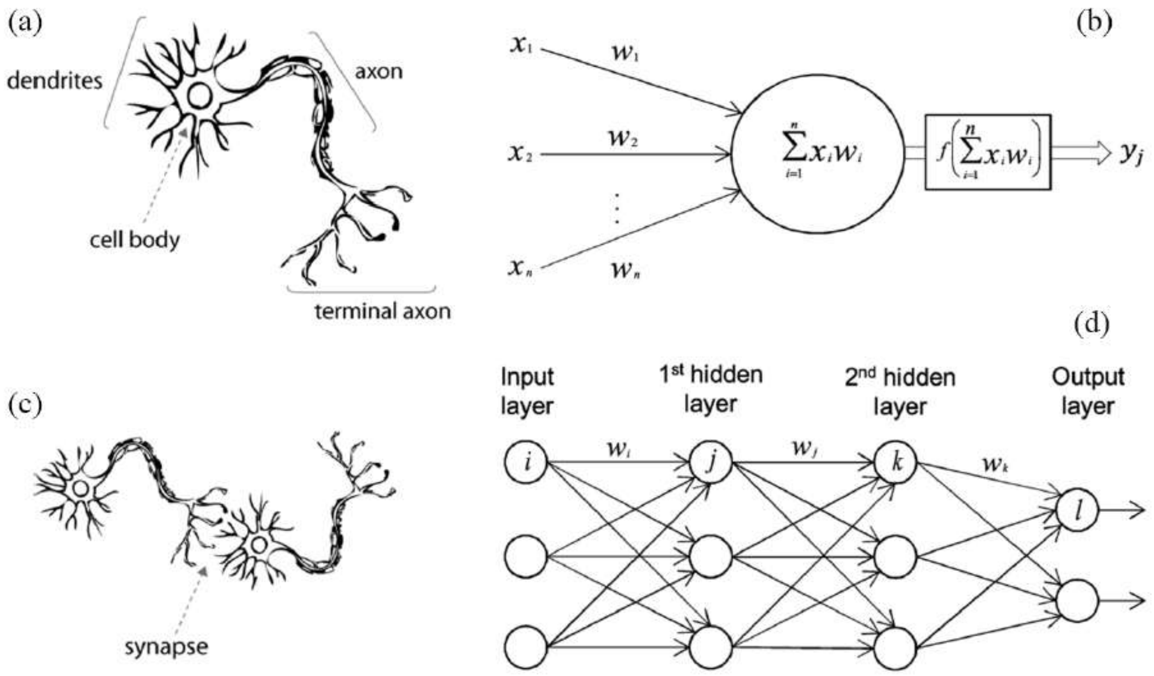

Figure 2.1 – Comparison between NN and human brain. Images (a) vs. (b) for a single artificial vs. human neuron, and images (c) vs. (d) for NN vs. human brain, by Meng et al. [158]

To mimic the information processing performed by brain neurons, each artificial neuron is assigned with a function to transform the inputs, called an Activation Function (AF). A classical linear regression can for example be seen as a single neuron with a linear AF. Hence, more complex NNs function as a network of regression problems working together. The first *input layer* contains the set of inputs $\mathbf{X}$, transformed through the second layer (first *hidden layer*) via AFs, and progressively communicated through the network until the information reaches the last *output layer* to constitute the interest outputs $\mathbf{Y}$ (Figure 2.1-(d)). This succession of layers is called *latent representation*, and can help representing highly non-linear problems [178]. Additionally, each neuron is given a weight through a matrix product from layer k to layer $k+1$, using matrices defined as $\{\mathbf{A}_{k\to k+1} = [w_{i,j}^{k}]_{i,j\in\{0,\dots,l^{(k+1)}\}\times\{0,\dots,l^{(k)}\}}\}_{k\in\{0,\dots,L\}}$, where $L \in \mathbb{N}$ is the number of hidden layers, and $l^{(k)} \in \mathbb{N}$ is the number of neurons for layer k. For example, if a unique AF, denoted $f_{k\to k+1}$, is used for the neurons of each layer k, then the network can be formally written as $\mathbf{Y} \approx \mathbf{A}_{l-1\to l}\ f_{l-1\to l}(\dots f_{1\to 2}(\mathbf{A}_{1\to 2}\ f_{0\to 1}(\mathbf{A}_{0\to 1}\ \mathbf{X}))$.

Many AFs were proposed in literature and their performances in terms of accuracy and computation times were compared. For example, Hermite orthonormal polynomials were proposed in [135] showing that they perform better than sigmoids, and Legendre polynomials in [201]. Hybrid networks using different AFs can also be achieved. However, simple networks can sometimes perform better, as shown for example in [90], where the use of a unique sinusoidal AF achieves better results than merging different types of AFs.

Different types of NN exist. Firstly, a distinction is made between single-layer and multi-layer networks. Secondly, the architecture can also be varied. For example, Feed

Forward Neural Networks (FFNN) consist in successive layers, where every neuron is connected to all (and only) the neurons of the subsequent layer. Other techniques can be met, for example Backward Propagation (BP) in Recursive Neural Networks (RvNN), or layer skipping in Fully Connected Cascade (FCC) [124]. Additionally, complementary techniques are often used, as *Encoding* (mapping the *input layer* to a compressed form) and *Decoding* (mapping compressed output of last hidden layer to interest output) [105].

Popularity of NN is to a large extent due to their powerful modelling and prediction ability. The process is highly adaptive, and allows learning different problems with interactions and non-linearities [2, 222], by various architectural and analytical choices. They are generally accepted in literature as a versatile and powerful tool for non-linear mapping of generic n-dimensional functions [124]. The mapping capabilities of NN are strictly related to the non-linearity of the used AFs. Indeed, without that, NNs would be simple linear interpolators [124]. Additionally, NNs are said to assume little to no prior knowledge or hypothesis about the nature of the data distribution [223]. However, implicit hypothesis are always made when using NN, regarding their ability to approximate any function. Hence, mathematical studies focused on universality of the approach: can any continuous function be approximated arbitrarily well by a FFNN ? [105]

Universal approximation theorem

Mathematical demonstrations of NNs ability to approximate functions find their origins in works from the early 90's [17, 40, 51, 73, 98], with the fundamental "*universal approximation theorem*".

Numerous authors studied the universality property, depending on the inner architecture of the network. The first version of the theorem [51] proved that a single-layer NN, exclusively using sigmoid AFs, can approximate any continuous function defined on a compact subset of $\mathbb{R}^n$, if the number of neurons is allowed to grow. Later works generalized this first version of the theorem to 2-layer FFNN[98] and to the larger class of bounded (non-polynomial) AFs [17, 40, 73, 98, 129]. This shows that universality depends more on the structure of the NN rather on the chosen AF, given mild assumptions about the latter. These versions of the theorem were later called *"shallow and wide"*, in reference to the fact that the NN number of layers limited, while the number of neurons can be increased.

A survey on the theorem's limitations was then given in [255]. In particular, the number of neurons to obtain an approximation with an arbitrary precision, for such depth-limited networks (number of layers), can be exponential. "A reduction in depth results in exponential sacrifice in width" as stated by Lu et al. [142]. Besides, the existence of 3-layer networks that can not be approximated by any 2-layer NN, unless the number of neurons is exponential, has been demonstrated by Eldan and Shamir [65]. As a result, contemporary works focused on the influence of the number of layers (called depth), proving a *"deep and narrow"* versions of the theorem for Lebesgue integrable functions and NNs using ReLu AF (Rectifier Linear Unit: $ReLU(x) = max(x, 0)$) [43, 65, 89, 142, 204]. It is shown in [142] that any *Lebesgue integrable function* on n-dimensional input space can be approximated with a fixed $(n+4)$-width network (where width refers to the number of neurons), if the depth (number of layers) is allowed to grow. The $(n+4)$-width constraint was later relaxed to $(n+1)$-width for convex lipschitz functions on $[0,1]^n$ in [89].

To conclude, and as stated by Hanin [89], "expressivity can be seen both as an effect of both depth and width". The question of narrow vs. shallow networks remains open, in particular about their abilities to approximate each other, without substantially increasing the number of layers and neurons respectively [142]. Indeed, the number of neurons is known to compensate for the number of layers (and vice-versa). The effect of limiting the depth on the exponential growth of width is shown in [43, 65] (importance of depth), while only a polynomial growth of width by depth limitation is shown in [142] (importance of width). Depth is then said to be "more effective for the expressive power of ReLU networks" [142].

Limitations and open research questions

The previously presented works about the universality of NN represent a step towards the understanding of the network's structure role in its expressive power. Some limitations can however still be noted.

Firstly, the *"wide and shallow"* version of the theorem limits the network to 1 or 2 hidden layers, and the *"deep and narrow"* version has only been investigated with ReLu AFs. Additionally, the number of fitting hyper-parameters (e.g. weight matrices, choice of AFs) grows with the number of neurons and layers, which is the so-called *curse of dimensionality*. This generally limits the maximum number of layers and neurons, limiting therefore the interest of NN for highly non-linear problems.

Secondly, on the practical level, no formal indication about the best type of network or the most suitable AF, for an arbitrary data-set, can be given. Consequently, simple networks (one or two layers) [105], with "simple" AFs [124], are often used for physical problems. As stated by Iten et al. [105], the models that are learned from experimental data are selected by their simplicity, and the assumptions on the AFs that are necessary for the validity of the *universal approximation theorem* are often overlooked in favor of efficiency [124]. Common practice consists in selecting AFs or network's architecture to maximize the accuracy and minimize the computational cost of the ML [124]. However, given the large variety of choices, this can be a time consuming task. The main conclusion is that, unfortunately, the outcome of a successful NN is influenced by several aspects, among which: (i) the AF choice; (ii) the architecture and algorithm (e.g. FFNN or BP); (iii) the suitable sizing of the hidden layers and neurons; (iv) prior simplifications of the problem's dimensionality and (v) the use of sparse techniques to remove unimportant patterns from the network. All these choices influence the outcome the learning, making the work too case specific [124]. For example, it has been noticed that spectral similarity between the AFs and the output is desirable for good accuracy [124]. Different papers (summarized in [124]) pointed out advantages and drawbacks of using a particular AF instead of another. The choice is therefore application and data-set dependant, and as highlighted by Laudani et al. [124] "no dealbreaker conclusion can be drawn from the comparative analysis found in literature".

Thirdly, although the universal mapping capabilities of NN have been proven for particular configurations, concerned works unanimously highlight that "a robust theory of why they work so well is in its infancy" [142]. Many developed approaches and architectures are still promoted without proper justification of their theoretical abilities [204].

Lastly, one of the main concerns in ML, specifically for physical problems, is interpretability. Once the algorithms fitted, they could be used to understand what parameters are the most explanatory of the observed dynamics, and in what cases forecasting fails (e.g. extreme events, outliers). To assure this interpretability, minimal uncorrelated and reliable representations are desired. This is still a current research problem [105]. In NNs and variants, the combination of transformations and compositions is far from the desired simplicity, and makes the explicit formulation of inputs-to-outputs relationships difficult. Physical interpretations of the constructed model are therefore tedious. This is why NN have been applied in physics often as a blackbox and rather to optimize the accuracy of the predictions than to extract information about what the network learned, which "limits their utility for scientific discoveries" as highlighted by Iten et al. [105].

2.3 Physically-based data-driven uncertainty reduction: Data Assimilation

As explained in Section 2.1, measurements and process-based models are both characterized with uncertainties. In this context, Data Assimilation (DA) allows reducing the uncertainties, by optimally combining the available sources of information, for robust prediction, design optimization, etc. [231].

As for UQ, geosciences community is increasingly interested in DA. Applications can be found for example in operational storm surge modelling [7], flood forecasting [18, 23, 63], bathymetry optimization in hydrodynamic modelling [118, 185], fire front tracking [203], etc. While use of DA is historical in atmospheric and oceanographic models [149, 177], it is still, in comparison, shyly used in morphodynamic applications, and rarely in coastal morphodynamics as highlighted by Scott and Mason [218]. For example in [218, 229], satellite data are assimilated (inter-tidal land-sea boundary and water depth) in coastal morphodynamic models (currents and sediment transport), in order to reconstruct initial bathymetry, optimize model parameters (sediment transport coefficient of power law in the form of Equation 1.34) and/or correct temporal evolution throughout the assimilation window. Parametric calibration for simulating dike erosion by wave overtopping is performed in [67]. Only few applications of DA on fully coupled coastal wave-hydro-morphodynamics can be found in literature, due to the complexity and computational cost of the systems. Namely, first time use is provided by Garcia et al. [77] (according to the authors), where water depth data from a numerical twin experiment are assimilated into a coupled 5−day flow, wave and morphodynamic model. In particular, due to computational cost in high dimensions, only a single value for three wave parameters (significant wave height, direction and peak period) is optimised.

In the following, DA framework is presented, in order to investigate the possibility of operational use for coastal hydro-morphodynamics.

2.3.1 Introduction to Data Assimilation

DA is a sub-class of inverse problems, where the objective is to estimate an unknown (i.e. state, trajectory, unobserved variable, parameters) using a compromise between two sources of information: observations on the one hand and a dynamic model with physical background on the other hand [11, 29], both characterized with errors (i.e. measurement error, representation error, etc.).

Variables in a DA framework

Three types of information are generally met in DA, with the following notations that will be kept throughout the section: an *interest state/variable* simulated by a model, and that the modeller is interested in correcting or optimizing, is denoted $\mathbf{x}$. Associated parameters, if any, are denoted $\boldsymbol{\Theta}$ and are linked to the state by $\mathbf{x} = \mathcal{M}(\boldsymbol{\Theta})$ (process-based, data-based, stochastic, deterministic, etc.). These are called the *control vector*, in the sense that it controls the *interest state/variable* through the model. If the model is linear, then it is written in matrix form as $\mathbf{x} = \mathbf{M}\boldsymbol{\Theta}$. The observed state is denoted $\mathbf{y}$ and is linked to the simulated state by an operator $\mathbf{y} = \mathcal{H}(\mathbf{x})$ (projection, interpolation, selection, transformation, etc.). Again, if the latter is linear, then the operation is written $\mathbf{y} = \mathbf{H}\mathbf{x}$. Attributes to the different variables are given as superscripts. For example, the true state is denoted $\mathbf{x}^{(t)}$ and associated true parameters are denoted $\boldsymbol{\Theta}^{(t)}$. Truth can designate, depending on the situation, an optimal design, or the perfect output of a model if the latter is calibrated perfectly. It is in general unknown, and the modeller in principle has a prior, or background idea, about its value, denoted $\boldsymbol{\Theta}^{(b)}$ (or $\mathbf{x}^{(b)}$), that is of course uncertain. The objective of DA is therefore to find its best estimate called the analysis and denoted $\boldsymbol{\Theta}^{(a)}$, as an equilibrium between observed values of $\mathbf{y}$ denoted $\mathbf{y}^{(o)}$ and the background, and taken into consideration their respective uncertainties.

The background, observation/model, and analysis, are characterized with errors $\boldsymbol{\epsilon}^{(b)}$, $\boldsymbol{\epsilon}^{(m,o)}$ and $\boldsymbol{\epsilon}^{(a)}$ respectively, defined as in Equation 2.45.

$$\begin{cases}\boldsymbol{\theta}^{(t)} &= \boldsymbol{\theta}^{(b)} + \boldsymbol{\epsilon}^{(b)}\\ \mathbf{y}^{(o)} &= \mathcal{H}(\mathbf{x}^{(t)}) + \boldsymbol{\epsilon}^{(o)} = \mathcal{H}\left(\mathcal{M}\left(\boldsymbol{\theta}^{(t)}\right)\right) + \boldsymbol{\epsilon}^{(m,o)}\\ \boldsymbol{\theta}^{(t)} &= \boldsymbol{\theta}^{(a)} + \boldsymbol{\epsilon}^{(a)}\end{cases} . \tag{2.45}$$

DA problems in physical applications

Different DA problems, depending on the objective, can then be formulated. The unknown truth to approximate can for example concern: (i) the projection of future state denoted $\mathbf{x}^{(t),k+1}$, at time indexed $k+1$, from past and current observations denoted $\mathbf{y}^{(o),1:k}$ (*prediction problem*); (ii) an update of current state $\mathbf{x}^{(t),k}$ from current and past observations $\mathbf{y}^{(o),1:k}$ (*filtering problem*); (iii) or a correction of a series of past and current states $\mathbf{x}^{(t),1:k}$ from a series of past and current observations $\mathbf{y}^{(o),1:k}$ (*smoothing problem*) [39]. The objective can also be to approximate the true value of parameters $\boldsymbol{\Theta}^{(t)}$, referred to as *parameters estimation problem*, inversely deduced from the optimal calibration of state $\mathbf{x}^{(t)}$.

The prior/background can either be: (i) a prior guess of the target itself, for example $\mathbf{x}^{(b),k+1}$ for a prediction problem or $\boldsymbol{\theta}^{(b)}$ for parameters estimation; (ii) a prior guess of the state at previous times or conditioning parameters, linked to the target by a model $\mathcal{M}$ (e.g. initial state $\mathbf{x}^{(b),0}$ and/or parameters $\boldsymbol{\theta}^{(b)}$); (iii) or all at the same time. In general, for a smoothing problem for example, the prior can be written as $\mathbf{x}^{(b),1:k} \approx \mathcal{M}[\mathbf{x}^{(b),0}, \boldsymbol{\theta}^{(b)}]$.

Bayesian Formulation

DA can be formulated using different mathematical frameworks (control, estimation, etc.). Here, the general *Bayesian* viewpoint is adopted (also called statistical, stochastic or sequential, using estimation theory) [11].

Based on the *Bayes* rule previously presented in Equation 2.16 (Section 2.1.3), the objective of Bayesian methods is to characterize the probability of value $\boldsymbol{\theta}^{(b)}$ of parameters, or $\mathbf{x}^{(b)}$ of state, to be true, given a value of the observations $\mathbf{y}^{(o)}$. Hence, all variables are considered random, denoted $\boldsymbol{\Theta}$, $\mathbf{X}$ and $\mathbf{Y}$ respectively. The above values in low case letters are realizations of the latter. For the sake of simplicity, superscripts (o) and (b) are dropped in the following, and random variable $\boldsymbol{\Theta}$ is considered to represent a control variable for the DA problem (parameters, the state itself, previous sate values, etc.). Bayesian DA is then formally expressed as in Equation 2.46,

$$p_{\boldsymbol{\Theta}|\mathbf{Y}=\mathbf{y}}(\boldsymbol{\theta}) = \frac{p_{\mathbf{Y}|\boldsymbol{\Theta}=\boldsymbol{\theta}}(\mathbf{y})p_{\boldsymbol{\Theta}}(\boldsymbol{\theta})}{p_{\mathbf{Y}}(\mathbf{y})} , \tag{2.46}$$

where $p_{\boldsymbol{\Theta}}$ gives probabilities for different background values without information about the observation, and is called *prior* PDF. The target $p_{\boldsymbol{\Theta}|\mathbf{Y}=\mathbf{y}}$ defines the probabilities of different realizations of $\boldsymbol{\Theta}$ to be true when $\mathbf{y}$ is observed, and is called the *posterior* distribution of $\boldsymbol{\Theta}$. It is estimated from the prior distribution, observation distribution $p_{\mathbf{Y}}$, and the *likelihood* PDF $\mathcal{L}(\boldsymbol{\theta}) = p_{\mathbf{Y}|\boldsymbol{\Theta}=\boldsymbol{\theta}}$, representing the probability of observing measurements $\mathbf{y}$ for a given value of the background $\boldsymbol{\Theta} = \boldsymbol{\theta}$ [39].

As the observation $\mathbf{y}^{(o)}$ and the background $\boldsymbol{\theta}^{(b)}$ are considered to be realizations of random variables $\mathbf{Y}$ and $\boldsymbol{\Theta}$ respectively, then the error vectors defined in Equation 2.45 are random. Above densities are then written as in Equation 2.47.

$$\begin{cases} p_{\boldsymbol{\Theta}}(\boldsymbol{\theta}) = p_{\boldsymbol{\epsilon}^{(b)}}\left[\boldsymbol{\theta}^{(t)} - \boldsymbol{\theta}\right] \\ \mathcal{L}(\boldsymbol{\theta}) = p_{\mathbf{Y}|\boldsymbol{\Theta}=\boldsymbol{\theta}}(\mathbf{y}) = p_{\boldsymbol{\epsilon}^{(m,o)}}\left[\mathbf{y} - \mathcal{H}\left(\mathcal{M}\left(\boldsymbol{\theta}\right)\right)\right] \end{cases} . \tag{2.47}$$

As explained in Section 2.1.3, the objective using the *Bayes* rule is to obtain the distribution of possible values with associated probabilities. However, an optimal deterministic choice can be of interest, which is the previously introduced analysis denoted $\boldsymbol{\theta}^{(a)}$. This may correspond to various choices. For example, it can be defined as the expectation $\boldsymbol{\theta}^{(a)} = \mathbb{E}[\boldsymbol{\Theta}|\mathbf{Y} = \mathbf{y}] = \int \boldsymbol{\theta} p_{\boldsymbol{\Theta}|\mathbf{Y}=\mathbf{y}}(\boldsymbol{\theta})d\boldsymbol{\theta}$, which is called Minimum Variance Estimation (MVE). It can also be calculated as the most probable value of $\boldsymbol{\Theta}$ given $\mathbf{Y} = \mathbf{y}$, defined as $\boldsymbol{\theta}^{(a)} = \max_{\boldsymbol{\theta}} p_{\boldsymbol{\Theta}|\mathbf{Y}=\mathbf{y}}(\boldsymbol{\theta})$, referred to as Maximum A Posteriori (MAP). Lastly, it can be selected as the value that maximizes the probability of observing $\mathbf{y}$, written as $\boldsymbol{\theta}^{(a)} = \max_{\boldsymbol{\theta}} p_{\mathbf{Y}|\boldsymbol{\Theta}=\boldsymbol{\theta}}(\mathbf{y})$, which is the Maximum Likelihood Estimation (MLE).

In general, the involved PDFs are not known, and *Bayesian inference* approaches [94] that allow statistical approximations are costly, as explained in Section 2.1.3. Resolving the *Bayesian* problem then requires additional hypothesis, or is based on sampling techniques. For example, analytical solutions as the Best Linear Unbiased Estimator (BLUE) or the Kalman Filter (KF) are defined in Section 2.3.2, and *ensemble methods* based on sampling [70] are briefly described in Section 2.3.3. When all PDFs are Gaussian, resolving the MAP can be written as the minimization of a mismatch function, or *cost function*, which is called *variational* DA [11]. This is presented in dedicated Section 2.3.4.

2.3.2 Analytical solutions of the Bayesian problem

BLUE: Best Linear Unbiased Estimator

Best Linear Unbiased Estimator (BLUE) is a particular analytical solution to the Minimum Variance Estimation (MVE) for the previously presented Bayesian problem under additional hypothesis [29].

Firstly, observation operator $\mathcal{H}$ and model $\mathcal{M}$ are considered linear, which is written $\mathbf{y}^{(o)} = \mathbf{H}\boldsymbol{\theta}^{(t)} + \boldsymbol{\epsilon}^{(m,o)}$ for simplicity. Secondly, background and model/observation errors, defined in Equation 2.45, are considered to have unbiased and independent components. These two conditions are written, for error $\boldsymbol{\epsilon}$, as $\forall i \in [|1, dim(\boldsymbol{\epsilon})|] \quad \mathbb{E}[\epsilon_i] = 0$ and $cov(\epsilon_i, \epsilon_{j\neq i}) = 0$ respectively. Therefore, their covariance matrices denoted $\mathbf{B}$ and $\mathbf{R}$ are diagonal. Lastly, the analysis is also subject to three hypothesis: it is a linear compromise between prior and observation $\boldsymbol{\Theta}^{(a)} = \mathbf{A}\boldsymbol{\Theta}^{(b)} + \mathbf{K}\mathbf{Y}^{(o)}$, unbiased $\mathbb{E}[\boldsymbol{\Theta}^{(a)}] = \boldsymbol{\theta}^{(t)}$ and characterized by minimal variance $\mathbb{V}[\boldsymbol{\Theta}^{(a)}]$ (solution is then defined as MVE), meaning that the estimation does not, in average, fall too far from truth.

The objective becomes then to find $\mathbf{A}$ and $\mathbf{K}$ with the above hypothesis. In the scalar case with identity observation matrix ($\mathbf{H} = 1$), the analytical solution is written in Equation 2.48, with an accuracy of estimation defined in Equation 2.49.

$$\boldsymbol{\theta}^a = \boldsymbol{\theta}^b + \frac{(\sigma^{(b)})^2}{(\sigma^{(b)})^2 + (\sigma^{(m,o)})^2}(\mathbf{y}^{(o)} - \boldsymbol{\theta}^b) \ . \tag{2.48}$$

$$\mathbb{V}[\boldsymbol{\theta}^a] = \frac{1}{(\sigma^{(b)})^2} + \frac{1}{(\sigma^{(m,o)})^2} \ . \tag{2.49}$$

The term $(\mathbf{y}^{(o)} - \boldsymbol{\theta}^b)$ is called *innovation* and $\frac{(\sigma^{(b)})^2}{(\sigma^{(b)})^2+(\sigma^{(m,o)})^2}$ is called *gain factor* [29], where $\sigma^{(b)}$ and $\sigma^{(m,o)}$ are the standard deviations of background and observation errors respectively. In the general multidimensional case, the solution to the problem is defined in Equation 2.50,

$$\begin{cases} \mathbf{K} = \mathbf{B}\mathbf{H}^T(\mathbf{H}\mathbf{B}\mathbf{H}^T + \mathbf{R})^{-1} \\ \boldsymbol{\theta}^{(a)} = \boldsymbol{\theta}^{(b)} + \mathbf{K}(\mathbf{y}^{(o)} - \mathbf{H}\boldsymbol{\theta}^{(b)}) \\ \mathbf{P}^{(a)} = (\mathbf{I} - \mathbf{K}\mathbf{H})\mathbf{B} \end{cases} \tag{2.50}$$

Matrix $\mathbf{K}$ is called the *Kalman gain* or the *gain matrix*, the term $(\mathbf{Y}^{(o)} - \mathbf{H}\boldsymbol{\Theta}^{(b)})$ is the *innovation*, whereas $\mathbf{P}^{(a)}$ defines the covariance matrix of the analysis.

When $p_{\mathbf{Y}|\boldsymbol{\Theta}=\boldsymbol{\theta}}$ and $p_{\boldsymbol{\Theta}}$ are Gaussian PDFs (i.e. the errors $\boldsymbol{\epsilon}^{(b)}$ and $\boldsymbol{\epsilon}^{(m,o)}$ are Gaussian), then it can be shown that BLUE solution, besides being Minimum Variance Estimation (MVE), is also the Maximum A Posteriori (MAP) solution (details in Section 2.3.4). In this case, the first and second moments are both defined by Equations 2.50, providing complete description to the Gaussian PDF, and therefore defining an analytical solution to the Bayesian problem for the linear Gaussian case.

BLUE for temporal problems: Kalman Filter and Smoother

The difference between the Kalman Filter (KF) and Kalman Smoother (KS) on the one hand and the BLUE on the other hand lies in the added temporal dimension. While the objective of BLUE is to identify a general optimal configuration, KF and KS are interested in finding a series of states at different times for a dynamic system. KF designates a solution for filtering problems and KS for smoothing problems. These are not specifically of interest here, but KF is given as an example.

All random variables are considered Gaussian, and model and observation operator are linear. The control variable $\mathbf{\Theta}$ for the problems generally resolved by KF is the initial state of $\mathbf{X}$, denoted $\mathbf{X}^0$. Hence, notation $\mathbf{X}^0$ is here used instead of $\mathbf{\Theta}$, but may concern both initial state and/or conditioning parameters. A linear model, denoted $\mathbf{M}^{k,k+1}$, represents the state evolution from $\mathbf{X}^k$ to $\mathbf{X}^{k+1}$. All errors and associated covariance matrices also evolve in time and are indexed by superscript k. The errors are considered to be independent in time.

KF provides a solution to the filtering problem, focusing on the update of current state $\mathbf{x}^{(t),k}$ from current and past observations $\mathbf{y}^{(o),0:k}$. The temporal modelling system is written in Equation 2.51.

$$\begin{cases} \mathbf{x}^{(t),0} & = & \mathbf{x}^{(b),0} + \boldsymbol{\epsilon}^{(b)} & \\ \mathbf{x}^{(t),i} & = & \mathbf{M}^{i,i-1}\mathbf{x}^{(t),i-1} + \boldsymbol{\epsilon}^{(m),i} & \forall i \in \{1,\ldots,k\} \\ \mathbf{y}^{(o),i} & = & \mathbf{H}^i\mathbf{x}^{(t),i} + \boldsymbol{\epsilon}^{(o),i} & \forall i \in \{0,\ldots,k\} \end{cases} . \tag{2.51}$$

Solution to the problem of finding the posterior PDF $p_{\mathbf{X}^k|\mathbf{Y}^{(o),0:k}}$ for filtering in a linear Gaussian case is established iteratively in two steps: an *analysis step*, and a *forecast step* [29]. The algorithm is initialized by choosing a background value for the initial state as $\mathbf{x}^{(b),0}$ and its associated error covariance matrix $\mathbf{B}$. A first forecast is produced for time 1 and associated error covariance matrix is calculated using the modelling system in Equation 2.52. In particular, $\mathbf{P}^{(a),0} = \mathbf{B}$. The resulting state $\mathbf{x}^{(f),1}$ and error covariance matrix $\mathbf{P}^{(f),1}$, called the forecast, are the ingredients for the analysis step. The latter is first performed using the BLUE Equations 2.50, with observation operator $\mathbf{H}^1$ and error $\mathbf{R}^1$, providing an analyzed state $\mathbf{x}^{(a),1}$ and associated covariance matrix $\mathbf{P}^{(a),1}$. Forecast step is used once again to update the state and its error covariance matrix from time $i = 1$ to time $i = 2$. The resulting state $\mathbf{x}^{(f),i+1}$ and error covariance matrix $\mathbf{P}^{(f),i+1}$, called the forecast, are the background for next iteration $i + 1$. The last forecast $\mathbf{x}^{(f),k}$ and error covariance matrix $\mathbf{P}^{(f),k}$ are the first and second moments of the Gaussian PDF $p_{\mathbf{X}^k|\mathbf{Y}^{(o),0:k}}$. This is performed iteratively for each time indexed by $i \in \{1,\ldots,k-1\}$, until reaching final analysis at $i = k$.

$$\begin{cases} \mathbf{x}^{(f),i+1} = \mathbf{M}^{i,i+1}\mathbf{x}^{(a),i} \\ \mathbf{P}^{(f),i+1} = \mathbf{M}^{i,i+1}\mathbf{P}^{(a),i}(\mathbf{M}^{i,i+1})^T + \mathbf{Q}^i \end{cases} \tag{2.52}$$

The last forecast $\mathbf{x}^{(f),k}$ and error covariance matrix $\mathbf{P}^{(f),k}$ are the first and second moments of the Gaussian PDF $p_{\mathbf{X}^k|\mathbf{Y}^{(o),0:k}}$.

The equations presented above are valid with linear assumptions for the involved models. However, the latter are generally non-linear in physical applications. Hence, they can for example be replaced by their Tangent Linear Model (TLM) in order to use the KF, which is then called Extended Kalman Filter (EKF).

2.3.3 Ensemble methods

In general, analysis and forecast covariance matrices used above can be high-dimensional, and should be calculated at various times, which implies considerable computational cost.

To overcome this, *Ensemble methods* [70] propose an approximate solution based on Monte Carlo (MC) sampling of model realizations, and KF/KS solutions [39], where no direct calculation of covariance matrices is needed. Corresponding approaches are called the Ensemble Kalman Filter (EnKF) and Ensemble Kalman Smoother (EnKS). A brief description is given below, and readers interest in theoretical details can refer to Evensen [70].

For example, EnKF [68] works with an *ensemble* of backgrounds, where each *ensemble member* is independently updated using the classical KF defined above. Analysis covariance matrix $\mathbf{P}^{(a),i}$ is however not calculated according to Equation 2.50, but approximated from the updated ensemble, using the *ensemble-anomaly covariance matrix* [39].

The ensemble-anomaly covariance matrix approximates the analysis covariance matrix as $\mathbf{P}^{(a),i} \approx \mathcal{A}_{\mathbf{x}^{(a),i}}(\mathcal{A}_{\mathbf{x}^{(a),i}})^T$, where $\mathcal{A}_{\mathbf{x}^{(a),i}} := \frac{1}{\sqrt{N-1}}(\mathcal{S}_{\mathbf{x}^{(a),i}} - \mathbb{E}[\mathcal{S}_{\mathbf{x}^{(a),i}}])$ is called the *normalized ensemble-anomaly matrix*, estimated from an ensemble of realizations of size $n \in \mathbb{N}$ stored as $\mathcal{S}_{\mathbf{x}^{(a),i}} = [\mathbf{x}_1^{(a),i}, \dots, \mathbf{x}_n^{(a),i}]$. This is actually the empirical estimate of the covariance matrix from a sample, previously written in Equation 2.6. Furthermore, KF update can be written as $\mathcal{S}_{\mathbf{x}^{(a),i}} = \mathcal{S}_{\mathbf{x}^{(f),i}}\mathbf{T}$, where $\mathcal{S}_{\mathbf{x}^{(f),i}}$ is the result of the previous forecast step $\mathcal{S}_{\mathbf{x}^{(f),i}} = \mathbf{M}^{i-1,i}\mathcal{S}_{\mathbf{x}^{(a),i}}$, and $\mathbf{T}$ is explicitly calculated from the forecast anomaly matrix, the observation operator $\mathbf{H}$, an ensemble of perturbed observations and their associated anomaly matrices [39, 68]. No explicit calculation of error covariance matrices is needed [39]. Besides, it was proven that the EnKF solution converges at a rate of $1/\sqrt{n}$ [127], and that it approaches the analysis $\mathbf{x}^a$ of the KF in the linear case, where error covariances are explicitely calculated.

Although the KF equations are theoretically defined for Gaussian variables, EnKF is usually used on more general cases. The updated ensemble using EnKF is said to inherit the original non-Gaussian properties of the background ensemble [39].

2.3.4 Variational Data Assimilation

Variational methods (first formulated using control theory), can be seen as a particular case of *Bayesian* DA, where all errors PDFs are Gaussian and unbiased. The *Bayesian* formulation in Equation 2.46 can consequently be simplified. The Gaussian errors $\boldsymbol{\epsilon}^{(b)}$ and $\boldsymbol{\epsilon}^{(m,o)}$ are defined by their covariance matrices denoted $\mathbf{B}$ and $\mathbf{R}$ respectively, which then gives the likelihood $\mathcal{L} \sim \mathcal{N}(\mathbf{y} - \mathcal{H}(\mathcal{M}(\boldsymbol{\theta})), \mathbf{R})$ and prior distribution $p_{\boldsymbol{\Theta}} \sim \mathcal{N}(\boldsymbol{\theta}^{(t)} - \boldsymbol{\theta}, \mathbf{B})$, where $\mathcal{N}(\boldsymbol{\mu}, \boldsymbol{\Sigma})$ denotes the Normal/Gaussian distribution with mean $\boldsymbol{\mu}$ and covariance matrix $\boldsymbol{\Sigma}$.

As a consequence, variational DA is expressed as the minimization of an error function, also called mismatch or cost function, whose optimum, or analysis, defines the Maximum A Posteriori (MAP) solution of the *Bayesian* problem. Different cost functions can be defined according to the target. These are summarized below, and the reader can refer to [11] for detailed explanation.

The equations below are presented for a discrete (finite) multidimensional setting, where the information to estimate (state, parameters) and the observations are arranged in vectors (typically, response of a numerical model and spatio-temporal measures). The state vector reads $\mathbf{x} = [\mathbf{x}_1, \dots, \mathbf{x}_{m_x}]^T \in \mathbb{R}^{m_x}$, and observations are arranged as $\mathbf{y}^{(o)} = [\mathbf{y}_1^{(o)}, \dots, \mathbf{y}_{m_y}^{(o)}]^T \in \mathbb{R}^{m_y}$. The model parameters are $\boldsymbol{\theta} = [\theta_1, ..., \theta_V]^T \in \mathbb{R}^V$.

3DVAR formulation and link to Bayesian approach

In three-Dimensional VARiational (3DVAR) formulation, all interest state components are arranged in the same vector $\mathbf{x}$, that may include various spatio-temporal coordinates and multiple variables (same for the observation $\mathbf{y}^{(o)}$). The cost function to minimize is therefore written in Equation 2.53,

$$J(\mathbf{x}, \mathbf{x}^0, \boldsymbol{\theta}) = \frac{1}{2} \left\| \left[\mathbf{x}^0, \boldsymbol{\theta}\right] - \left[\mathbf{x}^{(b),0}, \boldsymbol{\theta}^{(b)}\right] \right\|^2_{\mathbf{B}^{-1}} + \frac{1}{2} \left\| \mathcal{H}(\mathbf{x}) - \mathbf{y}^{(o)} \right\|^2_{\mathbf{R}^{-1}} , \tag{2.53}$$

with the weighted Mahalanobis distance $||\mathbf{v} - \mathbf{w}||_{\mathbf{A}} := (\mathbf{v} - \mathbf{w})^T \mathbf{A} (\mathbf{v} - \mathbf{w})$, parameters $\boldsymbol{\theta}$ and initial state $\mathbf{x}^0$ conditioned by $\mathbf{x} = \mathcal{M}(\mathbf{x}^0, \boldsymbol{\theta})$, vector $\left[\mathbf{x}^0, \boldsymbol{\theta}\right]$ containing, consecutively, the components of $\mathbf{x}^0$ and $\boldsymbol{\theta}$, and observation operator $\mathcal{H}$. Matrices $\mathbf{B} := [cov(\epsilon_i^{(b)}, \epsilon_j^{(b)})]_{i,j \in \{1,\ldots,V\}} \in \mathbb{R}^{m_x \times m_x}$ and $\mathbf{R} := [cov(\epsilon_i^{(m,o)}, \epsilon_j^{(m,o)})]_{i,j \in \{1,\ldots,m_y\}} \in \mathbb{R}^{m_y \times m_y}$ are the symmetrical covariance matrices of the background and state/observation errors $\boldsymbol{\epsilon}^{(b)}$ and $\boldsymbol{\epsilon}^{(m,o)}$, defined by Equation 2.54.

$$\begin{cases} \left[\mathbf{x}^{(t),0}, \boldsymbol{\theta}^{(t)}\right] & = & \left[\mathbf{x}^{(b),0}, \boldsymbol{\theta}^{(b)}\right] + \boldsymbol{\epsilon}^{(b)} \\ \mathbf{y}^{(o)} & = & \mathcal{H}(\mathbf{x}^{(t)}) + \boldsymbol{\epsilon}^{(o)} = \mathcal{H}\left(\mathcal{M}\left(\mathbf{x}^{(t),0}, \boldsymbol{\theta}^{(t)}\right)\right) + \boldsymbol{\epsilon}^{(m,o)} \end{cases} . \tag{2.54}$$

When the initial state $\mathbf{x}^0$ is not of interest or is not uncertain, it disappears from the cost function, and the problem therefore concerns *parametric estimation*.

Using the *Bayes* rule in Equation 2.46 with the Gaussian PDFs, it can be shown that posterior PDF $p_{\boldsymbol{\Theta}|\mathbf{Y}=\mathbf{y}}$ is proportional to the Gaussian PDF $exp(-J)$, where J is the cost function defined in Equation 2.53 [29]. Hence, minimizing J is equivalent to the Maximum A Posteriori (MAP) estimation with the Bayesian formulation. This bridges the gap between variational and Bayesian formulations in the particular case of Gaussian PDFs. The BLUE solution defined in Section 2.3.2 is also an analytical solution for the variational formulation when the operators are linear.

Other formulations: weak vs. strong constraint

Cost function in Equation 2.53 is also sometimes written differently as in Equation 2.55, or as in Equation 2.56, where the errors are dissociated and $\mathbf{Q} := [Cov(\epsilon_i^{(m)}, \epsilon_j^{(m)})]_{i,j \in \{1,\ldots,n\}} \in \mathbb{R}^{n \times n}$ represents pure modelling errors (physical and numerical). However, we will refer to the first version in Equation 2.53 in this thesis.

$$J(\mathbf{x}, \mathbf{x}^0, \boldsymbol{\theta}) = \frac{1}{2} \left\| \mathbf{x} - \mathcal{M}\left(\mathbf{x}^{(b),0}, \boldsymbol{\theta}^{(b)}\right) \right\|^2_{\mathbf{B}^{-1}} + \frac{1}{2} \left\| \mathcal{H}(\mathbf{x}) - \mathbf{y}^{(o)} \right\|^2_{\mathbf{R}^{-1}} , \tag{2.55}$$

$$J(\mathbf{x}, \mathbf{x}^0, \boldsymbol{\theta}) = \frac{1}{2} \left(\left\| \left[\mathbf{x}^0, \boldsymbol{\theta}\right] - \left[\mathbf{x}^{(b),0}, \boldsymbol{\theta}^{(b)}\right] \right\|^2_{\mathbf{B}^{-1}} + \left\| \mathbf{x} - \mathcal{M}\left(\mathbf{x}^0, \boldsymbol{\theta}\right) \right\|^2_{\mathbf{Q}^{-1}} + \left\| \mathcal{H}(\mathbf{x}) - \mathbf{y}^{(o)} \right\|^2_{\mathbf{R}^{-1}} \right) , \tag{2.56}$$

In the previously presented cost functions, all errors, including model error, should be minimized. This problem could be high dimensional, due to the dimension of $\mathbf{x}$. Additionally, model errors $\boldsymbol{\epsilon}^{(m)}$ are in general difficult to define. An additional *perfect model* hypothesis allows to reduce the dimension of the problem by ignoring model errors: the latter vanish and associated terms. The problem is said *strong-constraint* due to the added hypothesis, oppositely to *weak-constraint* problems considering model error.

4DVAR formulation for temporal problems

The 3DVAR solution provides a best fit, or analysis, that reduces the global error over the whole trajectory of the interest variable $\mathbf{x}$. For example when dealing with a smoothing problem, if all temporal numerical states and all temporal observations are arranged in vectors $\mathbf{x}^{1:k} = [\mathbf{x}^1, \dots, \mathbf{x}^k]^T \in \mathbb{R}^{m_x \times k}$ and $\mathbf{y}^{(o)} = [\mathbf{y}^{(o),0}, \dots, \mathbf{y}^{(o),k}]^T \in \mathbb{R}^{m_y \times (k+1)}$, the solution can be formulated in 3DVAR as the minimization of the cost function in 2.57.

$$J(\mathbf{x}^{1:k}, \mathbf{x}^0, \boldsymbol{\theta}) = \frac{1}{2} \left\| \left[\mathbf{x}^0, \boldsymbol{\theta}\right] - \left[\mathbf{x}^{(b),0}, \boldsymbol{\theta}^{(b)}\right] \right\|^2_{\mathbf{B}^{-1}} + \frac{1}{2} \left\| \mathcal{H}(\mathbf{x}^{1:k}) - \mathbf{y}^{(o)} \right\|^2_{\mathbf{R}^{-1}} , \tag{2.57}$$

However, the cost function can also be specifically adjusted for temporal evolution problems, which is called four-Dimensional VARiational (4DVAR). The model is then a time-dependent dynamic system, and in particular, the errors also evolve in time. In general, the goal in 4DVAR is to identify the initial condition for optimal trajectory. Parameters can also be fitted as in Equation 2.57, but this is considered implicitly in the following for the sake of simplicity. The temporal modelling system can be written as in Equation 2.58,

$$\begin{array}{rcll} \mathbf{x}^{(t),i} & = & \mathcal{M}^i \circ \mathcal{M}^{i-1} \circ \dots \circ \mathcal{M}^1(\mathbf{x}^{(b),0}) + \boldsymbol{\epsilon}^{(m),i} & \forall i \in \{1, \dots, k\} \\ \mathbf{y}^{(o),i} & = & \mathcal{H}^i(\mathbf{x}^{(t),i}) + \boldsymbol{\epsilon}^{(o),i} & \forall i \in \{0, \dots, k\} \end{array} , \tag{2.58}$$

and adapted cost function, is then expressed in Equation 2.59.

$$\begin{array}{rcl} J(\mathbf{x}^{1:k}, \mathbf{x}^0) = & & \frac{1}{2} \left\| \mathbf{x}^0 - \mathbf{x}^{(b),0} \right\|^2_{\mathbf{B}^{-1}} + \frac{1}{2} \sum_{i=1}^{k} \left\| \mathbf{x}^i - \mathcal{M}^i \circ \dots \circ \mathcal{M}^1(\mathbf{x}^0) \right\|^2_{(\mathbf{Q}^i)^{-1}} \\ & + & \frac{1}{2} \sum_{i=0}^{k} \left\| \mathcal{H}^i \circ \mathcal{M}^i \circ \dots \circ \mathcal{M}^1(\mathbf{x}^0) - \mathbf{y}^{(o),i} \right\|^2_{(\mathbf{R}^i)^{-1}} \end{array} , \tag{2.59}$$

where model and observation errors are denoted $\boldsymbol{\epsilon}^{(m),i}$ and $\boldsymbol{\epsilon}^{(o),i}$ respectively for each time $i \in \{1, \dots, k\}$, and corresponding covariance matrices are denoted $\mathbf{Q}^i$ and $\mathbf{R}^i$ respectively. Once again, the problem can be transformed to a strong-constraint one with perfect model hypothesis.

Solutions to the variational problems

In case the model and observation operator are linear, the analytical solution corresponds to the BLUE, defined in Section 2.3.2.

In the general non-linear case, the optimal solution (or analysis) can be found by minimizing, depending on the situation, one of the previously presented 3DVAR or 4DVAR cost functions. The minimum corresponds to a null gradient of J. In the general case of non-linear model, where the target state is typically a solution to PDE, a classical approach for gradient calculation is to identify an *adjoint model*, with two classical approaches: the TLM and the Lagrandian Multiplier (LM) [11]. Calculating the gradient is then equivalent to finding a solution for the *adjoint model*, and the computational cost reduces to the resolution of the latter, which is in general equivalent to the resolution time of the direct model (e.g. original PDE) [11]. This method is however intrusive and presents drawbacks: it is conditioned by analytical derivation of the adjoint model, and any update of the direct model and its discretization comes with the supplementary cost of updating the adjoint, which not always trivial and requires resources. Alternatively, algorithmic differentiation [84] can be used (e.g. benchmark of operator overloading and source transformation tools in [236]). In the latter, the modelling system is seen as a composition of elementary functions, to which the chain rule of calculus is applied to obtain analytical derivatives, resulting with an adjoint. This is however not attempted in this thesis for the interest modelling system, and non-intrusive solutions are preferred. As an example of the latter, an approximate optimum can be found using iterative descent methods as explained in Section 2.2.1, where the gradient can be estimated using finite-differences for example.

Due to the involved approximations (cost function definition, error covariance matrices approximation, descent algorithms), the optimal solution to the DA problem as previously formulated is only an approximation (analysis) of the true state (perfect knowledge). It is therefore also characterized with errors, as defined in Equation 2.45.

2.3.5 Error covariance matrices

The quality of DA methods and associated solutions relies, among other things, on a good definition of errors [220]. The latter are capital information, in particular through the use of covariance matrices defined as $\mathbf{B} := [Cov(\lambda_i, \lambda_j)]_{i,j\in\{1,\ldots,V\}}$ and $\mathbf{R} := [Cov(\eta_i, \eta_j)]_{i,j\in\{1,\ldots,m\}}$. These are in general not simple to estimate.

In the absence of alternatives, assumptions and simplifications may be used. For example, when the errors are independent (e.g. spatial independence of errors for a spatial observation $\mathbf{y}^{(o)}$), the corresponding covariance matrix is diagonal, which is the simplest case. Each diagonal element is then the variance of the corresponding error component. Another possibility is to define a parametric correlation length between the errors: only the diagonal and few extra-diagonals are non-zero. This is referred to as *homogeneous* or *second-order stationary* covariance, and can for example concern a spatial measurement of the same variable at neighbouring locations. The error covariance matrix can also be block diagonal, for example when several independent variables are stored in $\mathbf{y}^{(o)}$ and each variable is characterized with dependent error components.

Applications of the above-cited assumptions can be found in literature. For example, the observation error covariance matrix in [202] and [37] are taken as $\sigma^2\mathbf{I}$, where $\mathbf{I}$ is identity and σ is the standard deviation of measurements [131]. The background error covariance matrix is block diagonal in [202], containing the error covariances for four variables. In this particular case, the error dependencies for one variable are modelled with Gaussian functions, using spatial correlation lengths. The dependencies between variables, however existing, are not explicitly modelled in the matrix, but left to the action of the model itself [202]. It is worth mentioning that the Gaussian approximation for correlations is unverified and that the multivariate dependencies should ideally be modelled, which remains difficult [202]. In [37], the background error covariance matrix is diagonal and estimated from the difference between ”truth” and background, because the ”truth” is known since it corresponds to a twin model experiment.

It is important to note however that the above hypothesis are in general far from truth [220]. Hence, as a statistical alternative to parametric definitions, the error covariance matrix can be empirically estimated, inspired from the ensemble based approaches [69], briefly explained above. This is for example used in [252] for the background error covariance matrix estimation in a 4DVAR framework, where a mean estimation of background is perturbed. As an example with the observation vector, if the same physical information can be measured n times, and variations around a mean measurement are stored in a matrix $\mathbf{Y'}$, then the observation error covariance matrix can be estimated as $(\frac{1}{n-1})\mathbf{Y'}(\mathbf{Y'})^T$. This would quantify the measurement device errors.

2.3.6 Metamodelling and Dimensionality Reduction

As in UQ, Dimensionality, and more generally computational cost, is often a bottleneck of DA problems. Matrix inversions and dynamic model evaluations are major consumers of computational resources in a minimization process. Therefore, Dimensionality Reduction (DR) and metamodelling are natural focus points. A number of solutions can be attempted: (i) concerning the state of interest, a representative subspace can be selected instead of the full space, reducing the variable dimension; (ii) metamodelling, which consists in replacing the physics based model by an approximate, can be used; (iii) Sensitivity Analysis can be performed to identify the most influencing parameters, limiting therefore the dimension of the control vector.

Sensitivity analysis has been presented in previous Section 2.1.5. In literature, DR is used with DA for different objectives, namely the development of faster models, the deduction of simpler adjoints, the reduction of control space dimension and the estimation of low dimensional error covariance matrices. This is discussed in details in Section 2.4.

Coupling between DA and metamodelling is generally attempted for the same reasons as DR, i.e. reducing the computational cost. Metamodels are used to replace the full model. For example in [151], PCE is employed to learn states distributions as a function of modelling parameters using a Galerkin scheme, within a Bayesian DA framework. This allows statistical estimations with the posterior distribution much faster than with a MC sampling. Generalization is proposed in [150] for functional outputs (e.g. spatiotemporal fields), by applying KLT prior to PCE learning, in order to reduce computational cost of MCMC estimations. An improvement of the method is extended to highly non linear cases by Birolleau et al. [25]. Indeed, the authors show that when the response of a system lacks smoothness, in particular in the presence of discontinuities, representation problems may occur Birolleau et al. [25]. An iterative PCE method is therefore proposed as a solution. The interest field is first expanded using classical PCE, and the resulting approximation is used as a transform for the generation of a new PCE orthonormal basis. This is repeated iteratively, and remarkably, the resulting expansion performs much better on discontinuous cases.

In other examples, PCE is used to improve accuracy of EnKF, by allowing a considerable increase of ensemble size, as it is known to converge significantly faster than MC sampling. Specifically, accumulation of sampling errors through assimilation cycle is known to impact the accuracy EnKF, particularly for large assimilation windows, and can only be resolved by increasing the ensemble size [133]. Additionally, for highly non-linear cases, the TLM of model and observation operator involved in EnKF can result in loss of accuracy, that PCE may allow to overcome. In a contribution by Li and Xiu [134] uses PCE at three key points of EnKF: (i) at given time step, it replaces the model in producing an ensemble, by generating fairly large samples of inputs ($n \approx 10^5$) and calculating corresponding outputs at low cost; (ii) at forecast step, the temporal dynamics are simulated by making the expansion coefficients evolve, using a Galerkin scheme or stochastic collocation and (iii) error covariance matrices involved in the filter are directly obtained, instead of calculating the ensemble-anomaly [134], by straightforward estimation of statistical moments due to the orthonormality of the basis, as seen in Section 2.1.6. Same strategy is adopted in [203] for fire front tracking application, and in [64] on one-Dimensional (1D) Shallow Water Equations (SWE) for river flows.

It is highlighted however by [141], that use of PCE can have limitations. Namely, when the posterior PDF is significantly different from prior, then a truncated PCE basis may fail in approximating it. For example, posterior distribution can attribute more importance in some regions of the parameter space than the prior, and PCE would result in poor approximation, particularly if the model is non-linear. Identified solution is to increase the expansion number of terms (e.g. polynomial degree), but this comes with a considerable computational cost.

2.4 Dimensionality Reduction

Dimensionality problems are often met in data-based and physically-based data-driven approaches. They can for example occur when dealing with a big amount of data, which may increase the computational cost of statistical analysis and learning. They also concern multidimensional models, for example when using multivariate inputs, and analyzing high-dimensional outputs. As a consequence, interesting approaches as ML, UQ and DA may rapidly become costly when dealing with complex physics.

In particular in Section 2.2.2, it was highlighted that the outcome of ML can be influenced by prior simplifications of the problem's dimensionality before learning [124]. Besides, one may be interested in automated detection of meaningful patterns in data [178, 223]. In Section 2.1, Dimensionality Reduction (DR) techniques were identified as a good pre-processing solution to reduce the dimensionality of the inputs space for UQ [231], and to perform robust Global Sensitivity Analysis (GSA). In Section 2.3, they were also identified in DA framework as an approach for the development of faster models, the reduction of control space dimension, etc. Hence, Modal Decomposition (MD), that can be both used as *pattern recognition* and DR approach, is here of interest.

Use in sediment dynamics

Modal Decomposition (MD) techniques have been actively used in the last years in the sediment dynamics community. In coastal morphodynamics, joint publications by Larson et al. [119] and N. Southgate et al. [175] review the use of linear and non linear decomposition techniques respectively. They are said to be attractive because of the process-based models limitations, as the knowledge of the governing processes is still insufficient [119, 175]. Four objectives are generally targeted in morphodynamics: Dimensionality Reduction (DR), phenomenological study (quantitative), past events analysis, prevision and characterization of global dynamic properties (equilibrium states, degrees of freedom, etc.) [175]. Diverse data are analyzed: profiles, contours, small and big scale forms, etc.

Beginning of use for MD in coastal morphology dates back to middle 70's [119], which is late compared to first publication of such methods and their use in physics (1901 for Principal Component Analysis (PCA)). Until 2003, studies generally focused, as with ML, on shoreline evolution as in [155, 208], study of changes in coastal forms as nearshore dunes in [209], or classification of bed forms with satellite images treatment. Since then, publications on morphodynamic data analysis are becoming more plentiful, and extended to the study of estuarine dynamics (UK [110], Taiwan [100], China [156]) and to fluvial processes [245, 275] (e.g. characterization of sediment fluxes). However, application to coastline dynamics and beach evolution is still largely predominant.

Statistical studies to correlate morphodynamic modes to hydrodynamic variables are also attempted. Evolution of marine bathymetries is for example characterized with MD in [162], then in [163] correlated to waves energy, sediments fall velocity or Froude number using Pearson indicators. Canonical Correlation Analysis (CCA) is used in [97] to correlate MD of bathymetry on the one hand to MD of waves on the other hand.

Some attempts to use MD for prediction can also be found in literature. For example in [97] where CCA regression is also used for forecast. In [110], the authors propose to formulate 2D estuarine dynamics using a diffusion equation with source terms, and the latter are inversely estimated from data and analyzed using MD. In [199], the same authors propose a linear extrapolation of the previously deduced modes for prediction. The predicted source terms are then injected in the diffusion equation to deduce new bathymetries from previous ones. The same approach is proposed in [111], and a comparison between bathymetry modes and corresponding source terms modes is undertaken, showing different temporal scale processes.

Enthusiasm of the community about such techniques is obvious. In the following, we will present Proper Orthogonal Decomposition (POD), that allows efficient and reduced representation based on a linear expansion. POD has shown to be accurate for both linear and non-linear problems [243], combining simplicity and relevance. As detailed below, it was originally applied for spatio-temporal patterns separation, but shares theory with Principal Component Analysis (PCA) from multivariate statistics and Karhunen-Loève Transfrom (KLT) from stochastic processes decomposition [108, 140]. The three expansions are similar, but applied in different frameworks. Therefore, the viewpoint of POD is detailed below, but can be transposed to PCA and KLT.

2.4.1 Proper Orthogonal Decomposition

Proper Orthogonal Decomposition (POD) [144] is part of the broader family of Modal Decomposition (MD) and Dimensionality Reduction (DR), also called Reduced Order Models (ROM) [243]. MD is a mathematical and statistical approach allowing to extract the main components from a variable of interest. These components shed light on typical dynamic behaviors of the observed system. These could be dynamically or energetically important *patterns* (or *modes*), and allow efficient representation of the processed variable. In general, they depend on time, space or stochastic parameters, and are associated to an importance measure, allowing to rank their contribution to the global expansion. By doing so, the objective is to use a minimal number of patterns to accurately represent high-dimensional fields, which is then referred to as DR or ROM. Indeed, physical phenomena are generally subject to complex and non-linear dynamics, and the used governing equations (if existing) can be high-dimensional. MD greatly helps to summarize these systems to finite ROM. The deduced patterns are also simpler sub-structures, allowing a better understanding of the dynamics. The most famous example of MD is most certainly the Fourier transform, where the components have a sinusoidal form, and are associated to determined frequencies and amplitudes [44].

Brief history

In fluid dynamics for example, many MD techniques are used in literature, and generally categorized as linear vs. non-linear [243]. The major techniques can be found in Figure 2.2. Summary of these techniques and their use in literature was presented by Taira et al. [243].

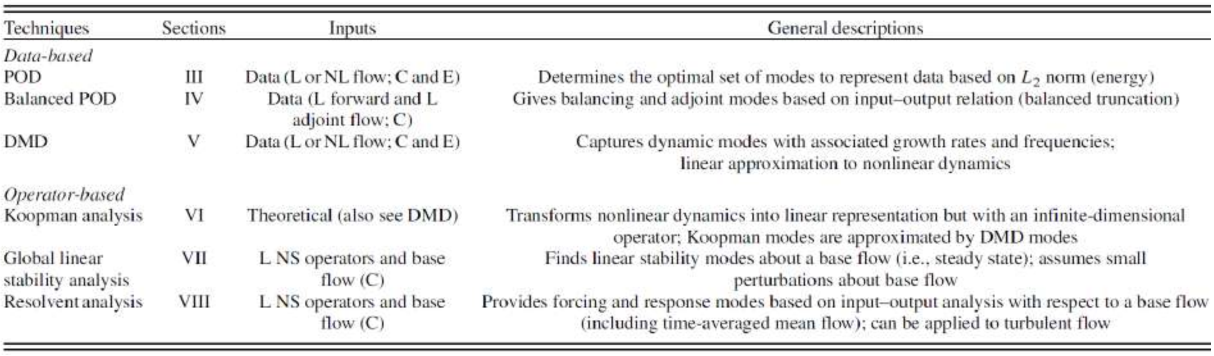

Techniques	Sections	Inputs	General descriptions
Data-based			
POD	III	Data (L or NL flow; C and E)	Determines the optimal set of modes to represent data based on L_2 norm (energy)
Balanced POD	IV	Data (L forward and L adjoint flow; C)	Gives balancing and adjoint modes based on input–output relation (balanced truncation)
DMD	V	Data (L or NL flow; C and E)	Captures dynamic modes with associated growth rates and frequencies; linear approximation to nonlinear dynamics
Operator-based			
Koopman analysis	VI	Theoretical (also see DMD)	Transforms nonlinear dynamics into linear representation but with an infinite-dimensional operator; Koopman modes are approximated by DMD modes
Global linear stability analysis	VII	L NS operators and base flow (C)	Finds linear stability modes about a base flow (i.e., steady state); assumes small perturbations about base flow
Resolvent analysis	VIII	L NS operators and base flow (C)	Provides forcing and response modes based on input–output analysis with respect to a base flow (including time-averaged mean flow); can be applied to turbulent flow

Figure 2.2 – Some major MD techniques, by Taira et al. [243]. L (Linear), NL (Non-Linear), E (Experimental) and NS (Navier-Stokes)

Even though more sophisticated methods have been proposed since POD and variants [215, 256], it remains one of the most widely used decompositions. This is due to its simple linear formulation, and easy extraction from data, with particularly well investigated mathematical properties in literature [5, 47, 173]. Additionally, POD is still the most optimal, compared to other linear techniques, in the sense that it minimizes the number of components, as its orthogonal modes capture more energy than any other decomposition [47, 173]. This is desirable for ML (previously mentioned objective of minimal and uncorrelated representations). Furthermore, POD has shown to be accurate for both linear and non-linear problems, although being a linear process [243], which brings together simplicity and relevance. It is therefore used in the present work to reduce the interest field on an optimal basis, in order to study its variances, by learning them from associated physical inputs.

POD is classically used for spatial patterns recognition and DR of highly-dimensional physical fields to finite linear summations. These spatial patterns, which form an invariant basis, account for spatial correlations in the studied field, and results with interesting possibilities of physical interpretations, in terms of behaviors and energy content [112]. POD finds its origins in the fluid dynamics community, and has first been introduced for the study of turbulent flows [144]. According to [44, 243], it has been constantly rediscovered in the 20th, from different angles and in different scientific research areas, under different names. We may cite, PCA from multivariate statistical analysis, KLT from stochastic processes decomposition [108, 140], Hotelling analysis from economical statistics [99], Empirical Component Analysis [138], Empirical Orthogonal Functions (EOF) [228], etc. Consequently, POD shares theoretical base with these techniques.

For simplicity, POD denomination will be interchangeably used in this thesis for all pattern recognition of continuous bi-variate functions, based on the related theoretical background. This can concern the spatio-temporal case, as classical POD, stochastic vs. deterministic separation with KLT, or extraction of main variation directions from a list of variables as with PCA. In all cases, the objective is to extract the main patterns in terms of variance. These patterns, when added and multiplied by appropriate coefficients, explain the dynamics of the variable of interest.

Theoretical framework

Theory will here be presented for a continuous function $\mathbf{u} : \mathbf{\Omega} \times \mathbb{T} \rightarrow \mathbb{D}$ of two variables $(\mathbf{x}, t) \in \mathbf{\Omega} \times \mathbb{T}$. The following relationships and properties hold for any $\mathbf{\Omega} \times \mathbb{T}$ and Hilbert space $\mathbb{D}$ characterized by its scalar product $(. \, , .)_{\mathbb{D}}$ and induced norm $||.||_{\mathbb{D}}$. However, as is the case for a majority of physical fields, we shall consider $\mathbf{\Omega}$ as a set of spatial coordinates (e.g. $\mathbb{R}^2$ or $\mathbb{R}^3$), $\mathbb{T}$ an event space (e.g. parameters space $\mathbb{R}^V$ with $V \in \mathbb{N}^*$, or a temporal subset $[0, T] \subseteq \mathbb{R}^+$), and $\mathbb{D}$ as a set of scalar real values or vector real values (e.g. $\mathbb{R}$ or $\mathbb{R}^2$).

POD consists in an approximation of $\mathbf{u}$ at a given order $d \in \mathbb{N}$ [144], written as in Equation 2.60,

$$\mathbf{u}(\mathbf{x}, t) \approx \sum_{k=1}^{d} v_k(t) \boldsymbol{\phi}_k(\mathbf{x}) \ , \tag{2.60}$$

where $\{v_k(.)\}_{k=1}^d \subset C(\mathbb{T}, \mathbb{R})$ and $\{\boldsymbol{\phi}_k(.)\}_{k=1}^d \subset C(\mathbf{\Omega}, \mathbb{D})$, with $C(\mathbb{A}, \coloneqq)$ denoting the space of continuous functions defined over $\mathbb{A}$ and arriving at $\coloneqq$. The objective of POD is to identify $\{\boldsymbol{\phi}_k(.)\}_{k=1}^d$ that minimizes the distance of the approximation from the true value $\mathbf{u}(., .)$, over the whole $\mathbf{\Omega} \times \mathbb{T}$ domain, with an orthogonality constraint for $\{\boldsymbol{\phi}_k(.)\}_{k=1}^d$ using the scalar product $(. \, , .)_{\mathbb{D}}$. This can be defined, in the least-squares sense, as the minimization problem in Equation 2.61 for all $d \in \mathbb{N}$, where $\langle . \rangle_{\mathbb{T}}$ is an average defined on $\mathbb{T}$.

$$\forall \mathbf{x} \in \mathbf{\Omega} \qquad \left\langle \left\| \mathbf{u}(\mathbf{x}, t) - \sum_{k=1}^{d} v_k(t) \boldsymbol{\phi}_k(\mathbf{x}) \right\|_{\mathbb{D}}^2 \right\rangle_{\mathbb{T}} = \min_{w_k, \boldsymbol{\Psi}_k} \left\langle \left\| u(x, t) - \sum_{k=1}^{d} w_k(t) \boldsymbol{\Psi}_k(\mathbf{x}) \right\|_{\mathbb{D}}^2 \right\rangle_{\mathbb{T}} . \tag{2.61}$$

As the equality is defined for all orders $d \in \mathbb{N}$, the members $\boldsymbol{\phi}_k$ are ordered according to their importance. In particular, for order 1, $\boldsymbol{\phi}_1$ is the linear generator of the sub-vector space most representative of $\mathbf{u}$ in $\mathbb{D}$. In geometrical terms, this would consist in finding the vector that maximizes the projection of $\mathbf{u}$ in average over $\mathbb{T}$ [47], which can be written as in Equation 2.62.

$$\max \left\langle \left\| \left(\mathbf{u}(\mathbf{x}, t), \frac{\boldsymbol{\phi}(\mathbf{x})}{||\boldsymbol{\phi}(\mathbf{x})||_{\mathbb{D}}} \right)_{\mathbb{D}} \times \frac{\boldsymbol{\phi}(\mathbf{x})}{||\boldsymbol{\phi}(\mathbf{x})||_{\mathbb{D}}} \right\|_{\mathbb{D}}^2 \right\rangle_{\mathbb{T}} . \tag{2.62}$$

One can therefore, by iteratively solving Equation 2.61 or 2.62, find the family $\{\boldsymbol{\phi}_k(.)\}_{k=1}^d$, which is called the POD basis of $\mathbb{D}$ of rank d (if $\mathbb{D} = Im(\mathbf{u})$).

The solution to these problems has already been established in literature [144, 228]: the POD basis of $\mathbb{D}$ of order d is the orthonormal set of eigenvectors of an operator $\mathcal{R} : \mathbb{D} \longrightarrow \mathbb{D}$ defined as $\mathcal{R}\boldsymbol{\phi} = \langle (\mathbf{u}, \boldsymbol{\phi})_{\mathbb{D}} \times \mathbf{u} \rangle_{\mathbb{T}}$, if the eigenvectors are taken in decreasing order of the corresponding eigenvalues $\{\lambda_k\}_{k=1}^{d}$. Indeed, resolving 2.62 is equivalent to maximizing the *Rayleigh Quotient* defined in Equation 2.63,

$$r(\boldsymbol{\phi}) = \frac{(\mathcal{R}\boldsymbol{\phi}, \boldsymbol{\phi})_{\mathbb{D}}}{\|\boldsymbol{\phi}\|_{\mathbb{D}}^2} \ , \tag{2.63}$$

which is then equivalent to cancelling its gradient, calculated as in Equation 2.64 [211].

$$\nabla r(\boldsymbol{\phi}) = \frac{2}{\boldsymbol{\phi}^T \boldsymbol{\phi}} \left[\mathcal{R}\boldsymbol{\phi} - r(\boldsymbol{\phi})\boldsymbol{\phi} \right] \ . \tag{2.64}$$

Hence, this corresponds to $\mathcal{R}\boldsymbol{\phi} = r(\boldsymbol{\phi})\boldsymbol{\phi}$, and shows that $r(\boldsymbol{\phi})$ is an eigenvalue of $\mathcal{R}$. Maximizing it therefore is therefore equivalent to finding the largest eigenvalue, and corresponding eigenvector $\boldsymbol{\Phi}$. Additionally, the spectral theorem implies that the eigenvectors of $\mathcal{R}$ constitute an orthonormal basis of $Im(\mathcal{R})$, which is by definition the vectorial space generated by $\mathbf{u}$. Hence, as previously stated, the iteratively determined POD patterns are the set of eigenvectors of $\mathcal{R}$, arranged in decreasing order of corresponding eigenvalues, and constitute a basis to the space generated by $\mathbf{u}$. Supplementary elements on the theoretical aspects and demonstrations of mathematical properties can, for example, be found in [173, 211].

For this expansion, an accuracy rate, also called the EVR, denoted e_d at rank d, can be calculated as in Equation 2.65 . EVR tends to 1 (perfect approximation) when $d \longrightarrow +\infty$.

$$e_d = \frac{\sum_{k \leq d} \lambda_k}{\sum_{k=1}^{+\infty} \lambda_k} \ . \tag{2.65}$$

Additionally, an approximation error at rank d can be calculated as in Equation 2.66 [47].

$$\epsilon_d = \left\langle \left\| \mathbf{u}(\mathbf{x}, t) - \sum_{k=1}^{d} (\mathbf{u}(\mathbf{x}, t), \boldsymbol{\phi}_k(\mathbf{x}))_{\mathbb{D}} \times \boldsymbol{\phi}_k(\mathbf{x}) \right\|_{\mathbb{D}} \right\rangle_{\mathbb{T}} = \sum_{k=d+1}^{\infty} \lambda_k \ . \tag{2.66}$$

As is the case with Polynomial Chaos Expansion (PCE) presented in Section 2.1.6, POD coefficients can be deduced from a modelling system (e.g. PDE) using an intrusive Galerkin scheme by resolving a new set of equations [48]. However, due to computational cost and supplementary implementation effort, the non-intrusive approach is once again preferred. This consists in finding the expansion coefficients and basis elements directly from data, and is discussed in Section 2.4.2. In particular, this allows deducing a POD basis from measurements, without the need of numerical model.

2.4.2 Data-based POD

As introduced with literature examples, POD can be used to extract patterns directly from data (measurements, outcome of numerical model, etc.). In this case, for $\mathbb{D} = \mathbb{R}$, when $\mathbf{u}(.,.)$ is a discrete sample on a set of $m \in \mathbb{N}$ space coordinates $\boldsymbol{\mathcal{X}} = \{\mathbf{x}_1, \ldots, \mathbf{x}_m\}$ and for $n \in \mathbb{N}$ measurement events $\mathcal{T} = \{t_1, \ldots, t_n\}$ (e.g. realizations of the parameters, time coordinates, etc.), the available data set is arranged in a matrix $\mathbf{U}(\mathcal{X}, \mathcal{T}) = [\mathbf{u}(\mathbf{x}_i, t_j)]_{i,j} \in \mathbb{R}^{m \times n}$, called the *snapshot matrix*, so as to be able to work in a discrete space.

Discrete formulation

The POD problem formulated in Equation 2.60 can be written in its discrete form as $\mathbf{U}(\boldsymbol{\mathcal{X}}, \boldsymbol{\mathcal{T}}) = \boldsymbol{\Phi}^{(d)}(\boldsymbol{\mathcal{X}})\mathbf{V}^{(d)}(\boldsymbol{\mathcal{T}})$, where $\boldsymbol{\Phi}^{(d)}(\boldsymbol{\mathcal{X}}) := [\boldsymbol{\phi}_j(\mathbf{x}_i)]_{i,j} \in \mathbb{R}^{m\times d}$ and $\mathbf{V}^{(d)}(\boldsymbol{\mathcal{T}}) := [v_i(t_j)]_{i,j} \in \mathbb{R}^{d\times n}$. The problem can therefore be viewed as if working with a new function $\mathbf{U}(\boldsymbol{\mathcal{X}}, .) = [\mathbf{u}(\mathbf{x}_i,\ .)]_{i\in\{1,\ldots,m\}} : \boldsymbol{\mathcal{T}} \rightarrow \mathbb{D} = \mathbb{R}^M$. Then, the average over $\mathbb{T}$ can be defined as the statistical mean over the subset $\boldsymbol{\mathcal{T}}$, and the scalar product $(.\ ,.)_{\mathbb{D}}$ as the canonical product over $\mathbb{R}^m$. The POD operator $\mathcal{R}$ can be written as in Equation 2.67,

$$\mathcal{R}\boldsymbol{\phi}(\boldsymbol{\mathcal{X}}) = \frac{1}{n}\sum_{j=1}^{n}\mathbf{U}(\boldsymbol{\mathcal{X}}, t_j)^T\boldsymbol{\Phi}(\boldsymbol{\mathcal{X}})\mathbf{U}(\boldsymbol{\mathcal{X}}, t_j) = \frac{1}{n}\mathbf{U}(\boldsymbol{\mathcal{X}}, \boldsymbol{\mathcal{T}})\mathbf{U}(\boldsymbol{\mathcal{X}}, \boldsymbol{\mathcal{T}})^T\boldsymbol{\Phi}(\boldsymbol{\mathcal{X}}) \ , \tag{2.67}$$

where $\mathbf{U}(\mathcal{X}, t_j) = [\mathbf{u}(\mathbf{x}_i,\ .)]_{i\in\{1,\ldots,m\}}$ is the column number j of the matrix $\mathbf{U}(\boldsymbol{\mathcal{X}}, \boldsymbol{\mathcal{T}})$ (i.e realization t_j of the measurement over $\boldsymbol{\mathcal{X}}$), and $\boldsymbol{\Phi}(\mathcal{X}) = [\boldsymbol{\phi}(\mathbf{x}_i)]_{i\in\{1,\ldots,m\}}$. As finding the POD basis is equivalent to identifying the orthonormal set of eigenvectors of the operator $\mathcal{R}$, then for this discrete representation the problem becomes equivalent to solving the eigen problem of the matrix $\mathbf{R} := \frac{1}{n}\mathbf{U}(\boldsymbol{\mathcal{X}}, \boldsymbol{\mathcal{T}})\mathbf{U}(\boldsymbol{\mathcal{X}}, \boldsymbol{\mathcal{T}})^T$, called the covariance matrix. A number $d \in \mathbb{N}$ of eigenvectors $\boldsymbol{\Phi}(\boldsymbol{\mathcal{X}})$ are identified and stored in the columns of the matrix $\boldsymbol{\Phi}^{(d)}(\boldsymbol{\mathcal{X}})$. For the eigenvalues of the covariance matrix $\mathbf{R}$ denoted $\{\lambda_k\}_{k=1}^{d}$, the expansion in Equation 2.60 can also be written as in Equation 2.68, where $\{\boldsymbol{\phi}_k(.)\}_{k=1}^{d}$ together with $\{a_k(.)\}_{k=1}^{d}$ are bi-orthonormal, and $v_k(.) = a_k(.)\sqrt{n\times\lambda_k}$.

$$\mathbf{u}(\mathbf{x}, t) \approx \sum_{k=1}^{d} a_k(t)\sqrt{n\times\lambda_k}\boldsymbol{\phi}_k(\mathbf{x}) \ . \tag{2.68}$$

By defining the matrix $\mathbf{A}^{(d)}(\boldsymbol{\mathcal{T}}) := [a_i(t_j)]_{i,j} \in \mathbb{R}^{d\times n}$ and the operator $\mathbf{D}^{(d)}(\lambda_1, \ldots, \lambda_d)$ corresponding to the diagonal matrix of elements λ_i, we have:

$$\mathbf{U}(\boldsymbol{\mathcal{X}}, \boldsymbol{\mathcal{T}}) = \boldsymbol{\Phi}^{(d)}(\boldsymbol{\mathcal{X}})\mathbf{D}^{(d)}(\sqrt{n\times\lambda_1}, \ldots, \sqrt{n\times\lambda_d})\mathbf{A}^{(d)}(\boldsymbol{\mathcal{T}}) \ . \tag{2.69}$$

And indeed, thanks to the orthonormality of $\{a_k(.)\}_{k=1}^{d}$, the covariance matrix reads:

$$\mathbf{R} = \frac{1}{n}\boldsymbol{\Phi}^{(d)}(\boldsymbol{\mathcal{X}})\mathbf{D}^{(d)}(n\times\lambda_1, \ldots, n\times\lambda_d)\boldsymbol{\Phi}^{(d)}(\boldsymbol{\mathcal{X}})^T = \boldsymbol{\Phi}^{(d)}(\boldsymbol{\mathcal{X}})\mathbf{D}^{(d)}(\lambda_1, \ldots, \lambda_d)\boldsymbol{\Phi}^{(d)}(\boldsymbol{\mathcal{X}})^T \ , \tag{2.70}$$

which is the eigenvalue decomposition of $\mathbf{R}$.

Link to Singular Value Decomposition

It can also be noticed that Equation 2.69 is the Singular Value Decomposition (SVD) of *snapshot matrix* $\mathbf{U}(\boldsymbol{\mathcal{X}}, \boldsymbol{\mathcal{T}})$ [238]. As a reminder, SVD consists in a matrix factorization in the form $\mathbf{U} = \boldsymbol{\Phi}\boldsymbol{\Sigma}\mathbf{A}^T$, where $\boldsymbol{\Phi}$ and $\mathbf{A}$ are orthogonal (i.e. $\boldsymbol{\Phi}^T = \boldsymbol{\Phi}^{-1}$) and $\boldsymbol{\Sigma}$ is diagonal containing positive real components ranked in decreasing order, called *singular values*. SVD describes the way matrix $\mathbf{U}$, when multiplied by a vector, increases its norm, or changes its direction [243]. For example, if a list of unit-length vectors, geometrically representing a sphere, multiply $\mathbf{U}$, then the sphere transforms to an ellipsoid, whose characteristic lengths are no more than the singular values of $\mathbf{U}$ [44, 243] (see Figure 2.3).

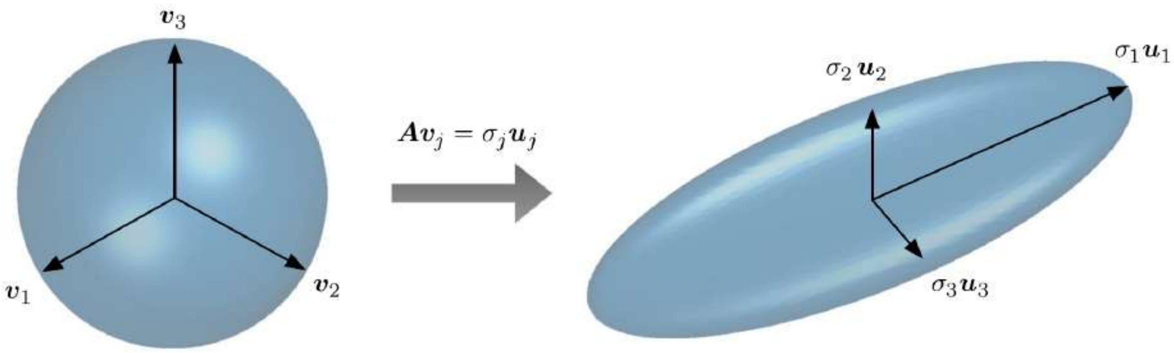

Figure 2.3 – Graphical representation of SVD meaning, by Taira et al. [243].

To solve the SVD problem of **U** it is indeed of common practice to solve the eigenproblem of **R**. However, when $n << m$, it is more computationally efficient to solve the eigenproblem of $\mathbf{R}^T$ instead of the eigenproblem of **R**, as highlighted by Sirovich [228] . This is often the case when a limited number of occurrences is measured for a high-dimensional physical field. When an order $d << min(m,n)$ corresponds to a high EVR as defined in Equation 2.65, we speak of dimensionality reduction, because the data are projected in a sub-space that is of much smaller dimension than $\mathbb{R}^{m\times n}$.

POD as a dynamic basis

When diverse enough records are available for the variable under study, we may consider that the resulting POD basis is a generator of all possible states. Predicting the associated expansion coefficients $\{a_k(t)\}_{k=1}^{d}$ for a given event t would therefore be enough to predict the whole state.

The advantage of POD is that it can be used non-intrusively, on both numerically emulated and field-measurement data. It does not require any prior knowledge about the data or the underlying physics. It is said to be unconditional, in the sense that no predetermined form is chosen for the modes, as they are directly extracted from data (conversely to Fourier for example) [243]. One of the biggest attributes of POD is the orthonormality of the basis, allowing minimal representations, which is desirable for efficient ML. POD is known to be optimal among linear techniques, in the sens that its basis elements "capture more energy per mode than any other set of basis functions" [112]. Additionally, modes are ranked in decreasing order, allowing iterative increase of the complexity of the model, until reaching an arbitrarily small error. POD has also shown to be efficient for non-linear problems, and for data filtering (erroneous or in-homogeneous data are immediately identified) [243].

2.4.3 POD-based Global Sensitivity Analysis

Global Sensitivity Analysis (GSA) was presented in Section 2.1.5 in a UQ framework, as an efficient approach to rank model's inputs by their influence on an interest output denoted. When the studied variable **Y** is multidimensional (e.g.$\mathbf{Y} \in \mathbb{R}^m$), for example a random multivariate spatio-temporal field, sensitivity can be studied for each component Y_i independently (specific spatial coordinate, time, output variable). This allows to analyze the behavior of each component.

However, not only a global view can be desired, but estimating sensitivity indices for each component separately can be costly for high-dimensional outputs. DR techniques can be used to reduce the output to a low dimensional set of representative variables, denoted $\{a_1, \dots a_d\}$, namely using POD, and generalization of Sobol' indices to ROM is the subject of numerous works [34, 78, 117, 192]. In POD case, sensitivity indices are calculated for each a_k independently, and denoted $S_{\mathcal{I}}^k$. Global influence, accounting for the global effect of $\mathcal{I}$ on the multidimensional output $\mathbf{Y}$ is then given in Equation 2.71, with a generalized index denoted $GS_{\mathcal{I}}$ [76],

$$GS_{\mathcal{I}} = \sum_{k=1}^{d} \frac{\lambda_k}{\mathbb{V}[\mathbf{Y}]} S_{\mathcal{I}}^k = \sum_{k=1}^{d} \frac{\lambda_k}{\sum_e^d \lambda_e} S_{\mathcal{I}}^k \tag{2.71}$$

where λ_k is the eigenvalue associated to POD mode k, as detailed in Section 2.4.1. The presented generalized indices show that the contribution of subset $\mathcal{I}$ through a_k is enhanced with the eigenvalue λ_k, that quantifies the share of variance represented by POD mode k. The property $\sum_{\mathcal{I} \subseteq \{1,\dots,V+1\}} GS_{\mathcal{I}} = 1$ holds, allowing to rank the contributions altogether in terms of influence on the multidimensional output $\mathbf{Y}$.

2.4.4 Data Assimilation using POD

As briefly described in Section 2.3, Dimensionality Reduction (DR) is used with Data Assimilation (DA) for different objectives, namely the development of faster models, the deduction of simpler adjoints, the reduction of control space dimension and the estimation of low dimensional error covariance matrices.

POD-based reduced adjoint for variational DA

DR can be applied intrusively in a modelling system and a resulting adjoint can be deduced. In a first example [188], KLT orthogonal basis is deduced from a snapshot of solutions to Boussinesq PDE using a sampling of parameters (here, heat source values). The full solution space is spanned into a reduced subspace, and using a Galerkin scheme, a new model, and a corresponding adjoint are derived. The obtained DA solution is less time consuming, and only characterized with an error of 0.3 % relative to full model use [188]. The latter are used for an inverse problem on a twin experiment (estimation of time-varying heat source from temperature measurements), drastically reducing the evaluation time for each descent iteration, while still providing accurate results compared to the original model. Similar works exist on other applications, for example on 2D tidal equations Qian et al. [196], or 4DVAR ocean modelling Cao et al. [37]. In [37] for example, it is emphasized that although the minimization process is much less costly (two orders of magnitude including POD basis construction), results are less accurate than with the full model. A correction attempt, called adaptive POD-4DVAR, consisting on POD basis update using an outer loop, is performed and gives satisfying results [37]. Absolute errors remain however higher with the reduced model, where the authors point out the possible impact of snapshot sampling method and number of modes choice.

POD-based adjoint approximation for variational DA

Previous contributions are case dependent due to adjoint calculation. A more generic approach is proposed by Vermeulen and Heemink [262] in a 4DVAR framework, where the dynamic model of type $\mathbf{x}^{i+1} = \mathcal{M}^{i+1}(\mathbf{x}^{i+1}, \boldsymbol{\theta})$ is first linearized around the background estimate $\mathbf{x}^{(b)}$ as in Equation 2.72, before applying POD to reduce perturbations of the state $\mathbf{x} - \mathbf{x}^{(b)}$ on the one hand and perturbations of the input parameters denoted $\Delta\theta$ on the other hand. In particular, partial derivatives of the model are estimated using finite differences, and the model and states are replaced by their POD reduced versions. This results with a cost function, where the observation is projected on the spanned space as well, with an easy to implement adjoint due to linearity [262].

$$\mathbf{x}^{i+1} \approx \widetilde{\mathbf{x}}^{i+1} = \mathcal{M}^{i+1}\left(\mathbf{x}^{(b)}, \boldsymbol{\theta}\right)\widetilde{\mathbf{x}}^{i} + \sum_{j=1}^{V+1} \frac{\partial \mathcal{M}^{i+1}\left(\mathbf{x}^{(b)}, \boldsymbol{\theta}\right)}{\partial \theta_j} \Delta\theta_j \ . \tag{2.72}$$

The authors also emphasis the interest of reduction to avoid local minima, with the smoothing inherent to reduction [262]. Their method is successfully applied to Shallow Water Equations (SWE) in [7], for the calibration of bottom elevations from water depth and horizontal velocity components recordings (twin model), with the objective of providing predictive storm surge model. Authors of the last work suggest that a simple improvement is possible if the cost function is estimated using the original model, while the adjoint is approximated in the reduced space [6]. Another application of the same method can be found in [77], on coastal hydro-morphodynamic modelling, with assimilation of bathymetric data by wave properties optimization.

Using POD in a DA framework shows ”superiority of EOFs with regard to the other families of vectors” [202], as shown by Durbiano [59] on SWE application, not only in terms of represented non-linear information, but above all due to the straightforward calculation of error covariance matrices for the reduced vector. Indeed, POD gives a natural estimate of covariances, that is of reduced size, but most importantly diagonal even for highly correlated vectors. As an example, Robert et al. [202] replaces the variation of state variable around background by its reduced form in a 4DVAR cost function, which then implies that the background error covariance matrix is the diagonal eigenvalue matrix resulting from POD. As a result, 4DVAR applied to the reduced model is four to five times faster. Oppositely to the results of Cao et al. [37], Robert et al. [202] conclude to the superiority of POD reduced 4DVAR also in terms of analysis, as the relative error between analysis and truth is found to be smaller than with full model's 4DVAR. This is attributed to POD efficiency in representing complex structures of state variables (spatio-temporal correlations typically) [202]. It is noted however that no reduced form of the adjoint is used oppositely to Cao et al. [37].

POD-based adjoint-free DA: hybrid ensemble-variational approach

The above cited methods however need the calculation of an adjoint or a TLM, even with a reduced model. Conversely, Tian et al. [251] propose a hybrid approach between ensemble and variational methods, called the POD-Ensemble-based 4DVAR (PODEn4DVAR), where neither adjoint nor TLM are needed. Consideration of the model dynamics in the cost function is enforced using POD rather than an adjoint. The spatio-temporal states, at times $\{0, \ldots, k\}$, where each temporal state $\mathbf{x}^j$ is of spatial size m_x are arranged in a single vector $[\mathbf{x}^0, \ldots, \mathbf{x}^k]$ of size $m_x \times k$, and jointly POD reduced around their mean values $\left[\overline{\mathbf{x}}^0, \ldots, \overline{\mathbf{x}}^k\right]^T$. An approximation of dimension d as in Equation 2.69 gives the expression in Equation 2.73. In particular, reduced POD basis of size $(m_x \times k) \times d$ can be written in matricial form as $\boldsymbol{\Phi} := [\boldsymbol{\phi}_j]_{j\in\{1,\dots,d\}}$. Each basis element $\boldsymbol{\phi}_j$ is a vector of size $m_x \times k$, arranged in the same manner as the state vectors, developed as $\boldsymbol{\phi}_j = [\boldsymbol{\phi}_j^0, \dots, \boldsymbol{\phi}_j^k]^T$, where each temporal POD basis vector $\boldsymbol{\phi}_j^i$ is of spatial size m_x.

The full POD basis matrix can therefore be written as a block vector in the form $\boldsymbol{\Phi} = [\boldsymbol{\Phi}^0, \dots, \boldsymbol{\Phi}^k]^T$, where each temporal POD basis denoted $\boldsymbol{\Phi}^i := [\boldsymbol{\phi}_j^i]_{j\in\{1,\dots,d\}}$ is of size $m_x \times d$, and is formed simply by selecting adequate lines of the full matrix.

$$\left[\mathbf{x}^0, \dots, \mathbf{x}^k\right]^T \approx \left[\overline{\mathbf{x}}^0, \dots, \overline{\mathbf{x}}^k\right]^T + \boldsymbol{\Phi}\boldsymbol{\Lambda}^{\frac{1}{2}}\boldsymbol{\beta}\ . \tag{2.73}$$

This provides a linear generator for any state, initial or at time j, by selecting adequate components of the POD basis matrix. Hence, both the initial state and the interest temporal states can be replaced in the 4DVAR cost function $J(\mathbf{x}^{1:k}, \mathbf{x}^0)$ in Equation 2.59. In strong constraint version (perfect model), denoting by $\{\mathbf{H}^i\}_{i\in\{1,\dots,k\}}$ the tangent linear observation operators, a new cost function is written as in Equation 2.74.

$$J(\boldsymbol{\beta}) = \frac{1}{2}\left\|\boldsymbol{\Phi}^0\boldsymbol{\Lambda}^{\frac{1}{2}}\boldsymbol{\beta} - \boldsymbol{\Phi}^0\boldsymbol{\Lambda}^{\frac{1}{2}}\boldsymbol{\beta}^{(b)}\right\|^2_{\mathbf{B}^{-1}} + \frac{1}{2}\sum_{i=0}^{k}\left\|\mathbf{H}^i(\overline{\mathbf{x}}^i + \boldsymbol{\Phi}^i\boldsymbol{\Lambda}^{\frac{1}{2}}\boldsymbol{\beta}) - \mathbf{y}^{(o),i}\right\|^2_{(\mathbf{R}^i)^{-1}}\ . \tag{2.74}$$

The same reduced variables denoted $\boldsymbol{\beta}$ are therefore used to generate both initial and modelled states, and only POD basis members components vary. Cost function becomes linear and explicit, and the gradient can be analytically calculated as in Equation 2.75.

$$\nabla_{\boldsymbol{\beta}} J = (\boldsymbol{\Phi}^0\boldsymbol{\Lambda}^{\frac{1}{2}})^T\mathbf{B}^{-1}(\boldsymbol{\Phi}^0\boldsymbol{\Lambda}^{\frac{1}{2}})\left(\boldsymbol{\beta} - \boldsymbol{\beta}^{(b)}\right) + \sum_{i=0}^{k}(\mathbf{H}^i\boldsymbol{\Phi}^i\boldsymbol{\Lambda}^{\frac{1}{2}})^T(\mathbf{R}^i)^{-1}\left(\mathbf{H}^i(\overline{\mathbf{x}}^i + \boldsymbol{\Phi}^i\boldsymbol{\Lambda}^{\frac{1}{2}}\boldsymbol{\beta}) - \mathbf{y}^{(o),i}\right)\ . \tag{2.75}$$

The analysis is obtained by cancelling the gradient. Straightforward estimation is therefore possible using Equation 2.76.

$$\begin{aligned}\boldsymbol{\beta}^{(a)} &= \left[(\boldsymbol{\Phi}^0\boldsymbol{\Lambda}^{\frac{1}{2}})^T\mathbf{B}^{-1}(\boldsymbol{\Phi}^0\boldsymbol{\Lambda}^{\frac{1}{2}}) + \textstyle\sum_{i=0}^{k}(\mathbf{H}^i\boldsymbol{\Phi}^i\boldsymbol{\Lambda}^{\frac{1}{2}})^T(\mathbf{R}^i)^{-1}\left(\mathbf{H}^i\boldsymbol{\Phi}^i\boldsymbol{\Lambda}^{\frac{1}{2}}\right)\right]^{-1} \\ &\times \left[(\boldsymbol{\Phi}^0\boldsymbol{\Lambda}^{\frac{1}{2}})^T\mathbf{B}^{-1}(\boldsymbol{\Phi}^0\boldsymbol{\Lambda}^{\frac{1}{2}})\boldsymbol{\beta}^{(b)} - \textstyle\sum_{i=0}^{k}(\mathbf{H}^i\boldsymbol{\Phi}^i\boldsymbol{\Lambda}^{\frac{1}{2}})^T(\mathbf{R}^i)^{-1}\left(\mathbf{H}^i\overline{\mathbf{x}}^i - \mathbf{y}^{(o),i}\right)\right]\ .\end{aligned} \tag{2.76}$$

Solution to the minimization is hence straightforward and does not require an iterative algorithm. Using twin experiments, authors show that the misfit of the PODEn4DVAR solution to truth is lower than the misfit of solutions from classical iterative 4DVAR on the one hand and EnKF on the other hand. In particular, TLM is said to be the source of errors for 4DVAR. In a different work [252], POD reduction is performed directly in the observation space on vector $[\mathcal{H}(\mathbf{x}^0), \dots, \mathcal{H}(\mathbf{x}^k)]$. This helps both saving computational time, as the observation space is of lower dimension, and gaining in analysis accuracy [252].

POD reduction in the observation space

Combined advantages of ensemble and variational approaches in PODEn4DVAR [252] gave the latter visibility. It has been applied in Mons et al. [165] to a parameter estimation 3DVAR problem. In this work, the state $\mathbf{x}$ is POD reduced in the observation space, around a background guess of parameters, written as $\mathcal{H}(\mathcal{M}(\boldsymbol{\theta})) \approx \mathcal{H}(\mathcal{M}(\boldsymbol{\theta}^{(b)})) + \boldsymbol{\Phi}\boldsymbol{\Lambda}^{\frac{1}{2}}\boldsymbol{\beta}$. Then, parameters space is spanned using the POD basis as $\boldsymbol{\theta} = \boldsymbol{\theta}^{(b)} + \mathcal{S}_{\boldsymbol{\theta}}\boldsymbol{\beta}$, where

$\mathcal{S}_{\boldsymbol{\theta}} = [\boldsymbol{\theta}^{(1)} - \theta^{(b)}, \ldots, \boldsymbol{\theta}^{(n)} - \theta^{(b)}]$ is a snapshot containing a sample of parameters perturbations. Once again, a new cost function is written, and the analysis explicitly calculated. The method is said to be more stable to the ensemble size than other ensemble DA methods [165]. In this particular case, an iterative procedure is used. After each assimilation cycle, the analysis is perturbed, and a new POD basis is formed, etc. A limited sample of size $n = 20$ is used to generate the POD basis at each step, and is said sufficient up to 10^5 control variables.

Lastly, besides the state and associated parameters, reduction can also be used on the observations. An example can be found in Shenefelt et al. [224] for an inverse estimation of surface heat transfer on a material from temperature measurements. In this application, the model is linear (matrix product). The inverse problem solution is said to be highly sensitive to data noise, resulting in unrealistic heat transfers for small measurement errors. Filtering is therefore applied to the observations using Singular Value Decomposition (SVD) with the objective of both reducing the dimensionality of the problem (simpler matrix inversion), and deleting noise from data.

2.5 Summary

The presented statistical approaches offer a convenient framework for pure measurement-based learning on the one hand, and physically-based data-driven approaches using measurements with process-based models on the other hand. They can be applied to multi-dimensional and non-linear physical system, with complex underlying phenomena. They will therefore be used for constructing a predictive tool and undertaking physical investigations with the process-based modelling system and field measurement data described in Chapter 1.

ML shows adaptability to various applications, by its flexible nature, and used non-linear functions and structures. NN is widely used in physics in general and environmental applications in particular. However, the underlined limitations in Section 2.2.2 can prevent from valuable use for physical investigations, for example due to the complexity of the model, the various algorithmic choices and hyper-parameters and the constrained universality/efficiency.

To overcome the above-mentioned limitations, an alternative ML based on DR and probabilistic modelling is proposed, through coupling between POD and PCE, both based on sound mathematical and probabilistic theory. This approach is proposed for the prediction of spatially-distributed physical fields that vary as a function of forcing parameters, with the additional objective of understanding the underlying dynamics. POD-PCE allows efficient learning and provides a framework for straightforward interpretation and probabilistic investigations. Its use on a purely measurement-based set-up is investigated in the following Chapter 3. Convergence, robustness to training members and noise in the data are demonstrated. Comparison to NN is also provided and physical interpretations are discussed.

Chapter 3

Physically interpretable machine learning algorithm on multidimensional non-linear fields

Dans ce chapitre, une méthode d'apprentissage à base de données, utilisant un couplage entre Décomposition Orthogonale en modes Propres (POD) et Expansion par Polynômes du Chaos (PCE) est proposée. Ce couplage POD-PCE offre un algorithme de Machine Learning (ML) qui peut être interprétée physiquement, et permet une analyse directe de la dynamique. De plus, la méthode POD-PCE est comparée avec succès aux Réseaux de Neurones (NN) classiques. En outre, des investigations de la donnée réalisées en utilisant la POD sont également présentées, en particulier: (i) la détection de mesures de mauvaise qualité et le filtrage de données et (ii) la localisation spatiale de la décomposition pour déduire les emplacements optimaux de mesures.

In this chapter, a data-based learning methodology, using a coupling between Proper Orthogonal Decomposition (POD) and Polynomial Chaos Expansion (PCE) is proposed. This POD-PCE coupling offers a physically interpretable Machine Learning (ML) algorithm, that allows straightforward analysis of the dynamics. Besides, the POD-PCE method is successfully compared to classical Neural Networks (NN). Additionally, data investigations performed using POD are also presented, in particular: (i) detection of bad quality measurements and data filtering and (ii) spatial localisation of the decomposition to deduce optimal measurement locations.

Contents

3.1 Motivations

Previously presented data in Chapter 1, resulting from regular monitoring of the intake over a decade, are a valuable source of information to understand the sediment dynamics. State of the art investigations (Section 1.4) focused on qualitative analysis of the sedimentation and its linear correlations to hydrodynamic and meteorological conditions, and allowed interesting conclusions about the intake dynamics. However, for optimal monitoring, and in order to plan dredging operations and optimize the power plant's functioning, a predictive tool was requested by stakeholders. The objective of this first contribution was therefore to provide a fast running and accurate data-based predictive tool. Furthermore, additional target was to offer deeper analysis and physical interpretation, using advanced statistical tools.

The contribution of this chapter therefore takes place in the general ML framework. However, limitations of classical ML methods, in particular NN that are most widely used in physics, were highlighted in Chapter 2. An alternative approach based on coupling between Proper Orthogonal Decomposition (POD) and Polynomial Chaos Expansion (PCE) was therefore proposed. The previously detailed robustness of both POD and PCE, as well as their linearity, allow to gradually and efficiently add complexity in the model, and offers the possibility of straightforward physical interpretation, as detailed below.

In the following, proposed POD-PCE coupling is presented as a paper in Section 3.2, which is published [172] in Journal of Computational Physics (JCP). Then, complementary investigations of bathymetry data using POD and variants are presented in Section 3.3.

3.2 Published paper in Journal of Computational Physics

Physically interpretable machine learning algorithm on multidimensional non-linear fields

Rem-Sophia Mouradi[1,2], Cédric Goeury[1], Olivier Thual[2,3], Fabrice Zaoui[1], and Pablo Tassi[1,4]

[1]EDF R&D, National Laboratory for Hydraulics and Environment (LNHE), 6 Quai Watier, 78400 Chatou, France
[2]Climate, Environment, Coupling and Uncertainties research unit (CECI) at the European Center for Research and Advanced Training in Scientific Computation (CERFACS), French National Research Center (CNRS), 42 Avenue Gaspard Coriolis, 31820 Toulouse, France
[3]Institut de Mécanique des Fluides de Toulouse (IMFT), Université de Toulouse, CNRS, Toulouse, France
[4]Saint-Venant Laboratory for Hydraulics (LHSV), Chatou, France

3 janvier 2021

Résumé

In an ever-increasing interest for Machine Learning (ML) and a favorable data development context, we here propose an original methodology for data-based prediction of two-dimensional physical fields. Polynomial Chaos Expansion (PCE), widely used in the Uncertainty Quantification community (UQ), has long been employed as a robust representation for probabilistic input-to-output mapping. It has been recently tested in a pure ML context, and shown to be as powerful as classical ML techniques for point-wise prediction. Some advantages are inherent to the method, such as its explicitness and adaptability to small training sets, in addition to the associated probabilistic framework. Simultaneously, Dimensionality Reduction (DR) techniques are increasingly used for pattern recognition and data compression and have gained interest due to improved data quality. In this study, the interest of Proper Orthogonal Decomposition (POD) for the construction of a statistical predictive model is demonstrated. Both POD and PCE have amply proved their worth in their respective frameworks. The goal of the present paper was to combine them for a field-measurement-based forecasting. The described steps are also useful to analyze the data. Some challenging issues encountered when using multidimensional field measurements are addressed, for example when dealing with few data. The POD-PCE coupling methodology is presented, with particular focus on input data characteristics and training-set choice. A simple methodology for evaluating the importance of each physical parameter is proposed for the PCE model and extended to the POD-PCE coupling.

1 Introduction

Deep Learning techniques (DL [36]) and more generally Machine Learning (ML [58]), and their applications to physical problems (fluid mechanics [4] ; plasma physics [49] ; quantum mechanics [42], etc.) have made a promising take-off in the last few years. This has been particularly the case for fields where the measurement potential has dramatically increased (e.g. Geoscience Data [27]). In this context, learning techniques are of interest to establish non-linear physical relationships from the data by a combination of steps, in particular using transformation functions, to capture the complexity of the system [58].

In particular, multi-layer Neural Networks (NN) [55] are widely used for physical applications. Their popularity comes from this complex structure, which makes them adaptable for various applications [1, 57]. However, some limitations prevent the use of NN for physical applications: (i) it is difficult to provide an explicit input-to-output formulation, due to the combinations of steps involved in the learning (*Activation Functions*, *Hidden Layers* [36]). Physical interpretation of the constructed model is therefore tedious [22] ; (ii) too many hyper-parameters and choices are involved, depending on the number of neurons and layers (*curse of dimensionality*) [32] ; (iii) no general proof for the theoretical ability of approximating arbitrary functions is available, except the *Universal Approximation Theorem* and its extensions [18, 21] for particular cases.

To overcome these limitations, we propose an alternative ML method, based on a coupling between Proper Orthogonal Decomposition (POD) [5] and Polynomial Chaos Expansion (PCE) [34, 35]. This approach is proposed for the prediction of spatially-distributed physical fields that vary in time. The idea is to use POD to separate the spatial patterns from the temporal variations, that are related to the conditioning parameters using PCE. To correspond to common NN paradigms, an adequate representation of this idea is given in Figure 1. In particular, POD is used for both *Encoding* and *Decoding* whereas PCE is used as an *Activation Function* in the *Latent Representation* [36].

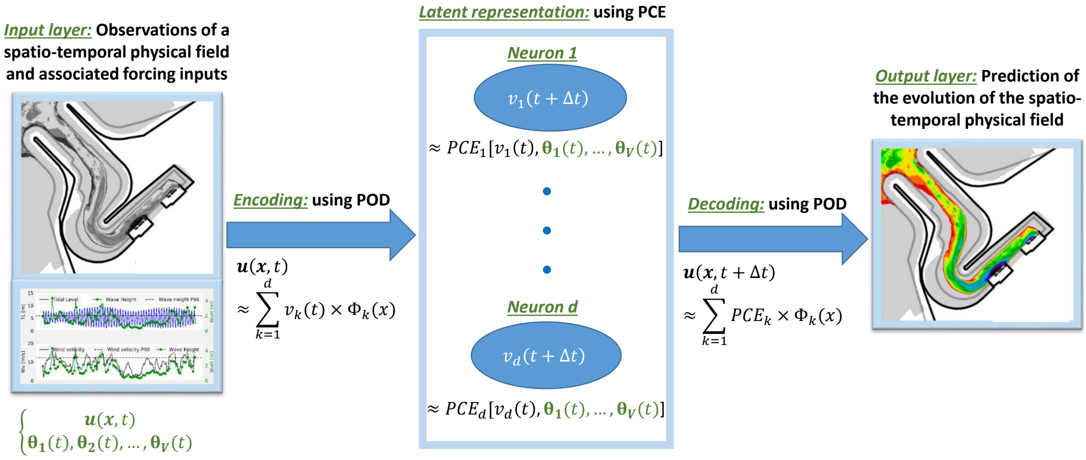

FIGURE 1: Representation of the POD-PCE ML approach.

The proposed POD-PCE addresses these drawbacks of ML.

(*i*) It is explicit and simple to implement, as it consists of the association of two linear decompositions. POD is a linear separation of the spatiotemporal patterns [39], shown to be accurate for both linear and non-linear problems [65], combining simplicity and relevance. PCE is a well-established method in Uncertainty Quantification (UQ) [63, 77], widely used for the study of stochastic behavior in physics [26, 66]. It is a linear polynomial expansion that allows non-linearities to be gradually added to the model by increasing the polynomial degree. The linearity and orthonormality of the POD and PCE components and the probabilistic framework of PCE make the output's statistical moments easier to study [62], enabling straightforward physical interpretation of the model [12].

(*ii*) It only has two hyper-parameters: a number of POD components, and a PCE polynomial degree. Both can be chosen according to quantitative criteria [3, 5]. All other forms of parameterization (choice of the polynomial basis) can be achieved with robust physical and/or statistical arguments [60], as assessed in the present paper. Furthermore, the orthonormality of the POD and PCE bases minimizes the number of components necessary to capture essential variations in data. Additionally, the POD modes capture more energy than any other decomposition [44], PCE is known to exponentially converge with polynomial degree [35], and the cardinality of the latter can be reduced by sparse basis selection [2].

(*iii*) It can be considered as a universal expansion for physical field approximation: a physical field has a finite variance, which implies that it belongs to the Hilbert space of random variables with finite second order moments. There therefore exists a numerable set of orthogonal random variables, that form the basis of this Hilbert space, on which the field of interest can be expanded (strict equality, not approximation) [63]. A mathematical setting for basis construction based on input was established by Soize and Ghanem [60] for the general case of dependent variables with arbitrary density, provided that the set of inputs is finite.

In the literature, associating regression techniques to Reduced Order Models (ROM), that include POD, is not novel [30, 73]. The cited studies, however, focused on dimensionality reduction, whereas the explicit formulation and applicability to complex physical processes are emphasized in the present study. Secondly, coupling PCE to ROM was recently addressed [31, 47] and the use of PCE as ML is consistent with the work of Torre et al. [67], where the authors showed that PCE is as powerful as classical ML techniques. However, neither spatiotemporal fields nor physical interpretability were addressed. The data in these studies were either obtained from numerical experiments, emulated from analytical benchmark functions such as Sobol or Ishigami, or based on one-dimensional data sets [67]. In contrast, the proposed POD-PCE methodology is herein assessed on two-dimensional physical fields. In particular, a toy example where synthetic data are emulated using an analytical function (groundwater perturbations due to tidal loadings [38]), and a real data set (high-resolution field measurements of underwater topography) are used. Although similar from a learning point of view, these two applications are characterized with differences. In particular, the toy problem is purely parametric and controllable, whereas the real data concern temporal dynamics and are of limited size. The cases are therefore complementary, in the sense that they allow demonstrating different properties of the proposed methodology. Hence, using the particularities of each case, the study consists in: i) the evaluation of the combined use of POD and PCE as ML for point-wise prediction ; ii) the robustness of the methodology to noise ; iii) the application to field data with the inherent challenges not encountered with numerical data (e.g. paucity) ; iv) a focus on model explicitness as a key condition for physical understanding and v) the influence of forcing variables study, based on a classical measure of importance (Garson weights [14]) directly computed with the POD-PCE expansion coefficients.

The paper is organized as follows. Section 2 gives a detailed explanation of the methodology, with a proposal for physical importance measures in Subsection 2.2.2. Section 3 deals with the assessment of the methodology on synthetic data, for both prediction and physical interpretation. In particular, the robustness of the approach to noise is evaluated in Subsection 3.3. The model is then deployed on field measurements in Section 4. The study case and data are described in 4.1. POD and PCE performances are then demonstrated independently in 4.2 with a deep physical analysis. The performance of the POD-PCE predictor is discussed in 4.3. A summary of the study and perspectives of the proposed methodology are presented in Section 5.

2 Theoretical framework

In this section, the objective is to define the framework of the proposed POD-PCE Machine Learning methodology, along with physical influence indicators for the inputs. This is the object of Subsection 2.3, but first, a reminder of the existing POD and PCE theoretical bases is presented in 2.1 and 2.2 respectively.

2.1 Proper Orthogonal Decomposition

POD is a dimensionality reduction technique [39] that is well documented in literature [5, 65]. Theoretical details and demonstrations can be found in [7, 44]. For clarity's sake, the essential elements of POD are summarized below.

The goal of POD is to extract the main patterns of continuous bi-variate functions. These patterns, when added and multiplied by appropriate coefficients, explain the dynamics of the variable of interest: a real-valued physical field.

Let $\mathbf{u} : \Omega \times \mathbb{T} \to \mathbb{D}$ be a continuous function of two variables $(\mathbf{x}, t) \in \Omega \times \mathbb{T}$. The following relationships and properties hold for any $\Omega \times \mathbb{T}$ and Hilbert space $\mathbb{D}$ characterized by its scalar product $(.\ ,.)_{\mathbb{D}}$ and induced norm $||.||_{\mathbb{D}}$. However, as is the case for a majority of physical fields, we shall consider Ω as a set of spatial coordinates (e.g. $\mathbb{R}^2$ or $\mathbb{R}^3$), $\mathbb{T}$ an event space (e.g. parameters space $\mathbb{R}^V$ with $V \in \mathbb{N}^*$, or a temporal subset $[0, T] \subseteq \mathbb{R}^+$), and $\mathbb{D}$ as a set of scalar real values or vector real values (e.g. $\mathbb{R}$ or $\mathbb{R}^2$). POD consists in an approximation of $\mathbf{u}(\mathbf{x}, t)$ at a given order $d \in \mathbb{N}$ (Lumley [39]) as in Equation 1,

$$\mathbf{u}(\mathbf{x}, t) \approx \sum_{k=1}^{d} v_k(t)\boldsymbol{\phi}_k(\mathbf{x}) \ , \tag{1}$$

where $\{v_k(.)\}_{k=1}^d \subset \mathcal{C}(\mathbb{T}, \mathbb{R})$ and $\{\boldsymbol{\phi}_k(.)\}_{k=1}^d \subset \mathcal{C}(\Omega, \mathbb{D})$, with $\mathcal{C}(\mathbb{A}, \mathbb{B})$ denoting the space of continuous functions defined over $\mathbb{A}$ and arriving at $\mathbb{B}$. The objective of POD is to identify $\{\boldsymbol{\phi}_k(.)\}_{k=1}^d$ that minimizes the distance of the approximation from the true value $\mathbf{u}(.,.)$, over the whole $\Omega \times \mathbb{T}$ domain, with an orthogonality constraint for $\{\boldsymbol{\phi}_k(.)\}_{k=1}^d$ using the scalar product $(.\ ,.)_{\mathbb{D}}$. This can be defined, in the least-squares sense, as a minimization problem.

The minimization problem is defined for all orders $d \in \mathbb{N}$, so that the members $\boldsymbol{\phi}_k$ are ordered according to their importance. In particular, for order 1, $\boldsymbol{\phi}_1$ is the linear generator of the sub-vector space most representative of $\mathbf{u}(\mathbf{x}, t)$ in $\mathbb{D}$. For $\mathbb{D} = Im(\mathbf{u})$, the family $\{\boldsymbol{\phi}_k(.)\}_{k=1}^{d}$ is called the POD basis of $\mathbb{D}$ of rank d. The solution to this problem has already been established in literature [39, 59]. The theoretical aspects of POD and demonstrations of mathematical properties can, for example, be found in [44]: the POD basis of $\mathbb{D}$ of order d is the orthonormal set of eigenvectors of an operator $\mathcal{R} : \mathbb{D} \to \mathbb{D}$ defined as $\mathcal{R}\boldsymbol{\phi} = \langle (\mathbf{u}, \boldsymbol{\phi})_{\mathbb{D}} \times \mathbf{u} \rangle_{\mathbb{T}}$, if the eigenvectors are taken in decreasing order of the corresponding eigenvalues $\{\lambda_k\}_{k=1}^{d}$.

For this expansion, an accuracy rate, also called the Explained Variance Rate (EVR), denoted e_d at rank d, can be calculated as in Equation 2 . EVR tends to 1 (perfect approximation) when $d \to +\infty$.

$$e_d = \frac{\sum_{k \le d} \lambda_k}{\sum_{k=1}^{+\infty} \lambda_k} \ . \tag{2}$$

In practice, for $\mathbb{D} = \mathbb{R}$, when $\mathbf{u}(.,.)$ is a discrete sample on a set of $m \in \mathbb{N}$ space coordinates $\boldsymbol{\mathcal{X}} = \{\mathbf{x}_1, \dots, \mathbf{x}_m\}$ and for $n \in \mathbb{N}$ measurement events $\mathcal{T} = \{t_1, \dots, t_n\}$ (e.g. realizations of the parameters, time coordinates, etc.), the available data set is arranged in a matrix $\mathbf{U}(\mathcal{X}, \mathcal{T}) = [\mathbf{u}(\mathbf{x}_i, t_j)]_{i,j} \in \mathbb{R}^{m \times n}$, called the snapshot matrix, so as to be able to work in a discrete space. The POD problem formulated in Equation 1 can be written in its discrete form as $\mathbf{U}(\boldsymbol{\mathcal{X}}, \mathcal{T}) = \boldsymbol{\Phi}^{(d)}(\boldsymbol{\mathcal{X}})\mathbf{V}^{(d)}(\mathcal{T})$, where $\boldsymbol{\Phi}^{(d)}(\boldsymbol{\mathcal{X}}) := [\boldsymbol{\phi}_j(\mathbf{x}_i)]_{i,j} \in \mathbb{R}^{m \times d}$ and $\mathbf{V}^{(d)}(\mathcal{T}) := [v_i(t_j)]_{i,j} \in \mathbb{R}^{d \times n}$. The problem can therefore be viewed as if working with a new function $\mathbf{U}(\boldsymbol{\mathcal{X}}, .) = [\mathbf{u}(\mathbf{x}_i,\ .)]_{i \in \{1,\dots,m\}} : \mathcal{T} \to \mathbb{D} = \mathbb{R}^M$. Then, the average over $\mathbb{T}$ can be defined as the statistical mean over the subset $\mathcal{T}$, and the scalar product $(.\ ,.)_{\mathbb{D}}$ as the canonical product over $\mathbb{R}^m$. The POD operator $\mathcal{R}$ can be written as in Equation 3,

$$\mathcal{R}\boldsymbol{\phi}(\boldsymbol{\mathcal{X}}) = \frac{1}{n}\sum_{j=1}^{n} \mathbf{U}(\boldsymbol{\mathcal{X}}, t_j)^T \boldsymbol{\Phi}(\boldsymbol{\mathcal{X}})\mathbf{U}(\boldsymbol{\mathcal{X}}, t_j) = \frac{1}{n}\mathbf{U}(\boldsymbol{\mathcal{X}}, \mathcal{T})\mathbf{U}(\boldsymbol{\mathcal{X}}, \mathcal{T})^T \boldsymbol{\Phi}(\boldsymbol{\mathcal{X}}) \ , \tag{3}$$

where $\mathbf{U}(\mathcal{X}, t_j) = [\mathbf{u}(\mathbf{x}_i,\ .)]_{i \in \{1,\dots,m\}}$ is the column number j of the matrix $\mathbf{U}(\boldsymbol{\mathcal{X}}, \mathcal{T})$ (i.e realization t_j of the measurement over $\boldsymbol{\mathcal{X}}$), and $\boldsymbol{\Phi}(\mathcal{X}) = [\boldsymbol{\phi}(\mathbf{x}_i)]_{i \in \{1,\dots,m\}}$. As finding the POD basis is equivalent to identifying the orthonormal set of eigenvectors of the operator $\mathcal{R}$, then for this discrete representation the problem becomes equivalent to solving the eigen problem of the matrix $\mathbf{R} := \frac{1}{n}\mathbf{U}(\boldsymbol{\mathcal{X}}, \mathcal{T})\mathbf{U}(\boldsymbol{\mathcal{X}}, \mathcal{T})^T$, called the covariance matrix. A number $d \in \mathbb{N}$ of eigen vectors $\boldsymbol{\Phi}(\boldsymbol{\mathcal{X}})$ are identified and stored in the columns of the matrix $\boldsymbol{\Phi}^{(d)}(\boldsymbol{\mathcal{X}})$. For the eigenvalues of the covariance matrix $\mathbf{R}$ denoted $\{\lambda_k\}_{k=1}^{d}$, the expansion in Equation 1 can also be written as in Equation 4, where $\{\boldsymbol{\phi}_k(.)\}_{k=1}^{d}$ together with $\{a_k(.)\}_{k=1}^{d}$ are bi-orthonormal, and $v_k(.) = a_k(.)\sqrt{n \times \lambda_k}$.

$$\mathbf{u}(\mathbf{x}, t) \approx \sum_{k=1}^{d} a_k(t)\sqrt{n \times \lambda_k}\,\boldsymbol{\phi}_k(\mathbf{x}) \ . \tag{4}$$

By defining the matrix $\mathbf{A}^{(d)}(\mathcal{T}) := [a_i(t_j)]_{i,j} \in \mathbb{R}^{d \times n}$ and the operator $\mathbf{D}^{(d)}(\lambda_1, ..., \lambda_d)$ corresponding to the diagonal matrix of elements λ_i, we have $\mathbf{U}(\boldsymbol{\mathcal{X}}, \mathcal{T}) = \boldsymbol{\Phi}^{(d)}(\boldsymbol{\mathcal{X}})\mathbf{D}^{(d)}(\sqrt{n \times \lambda_1}, ..., \sqrt{n \times \lambda_d})\mathbf{A}^{(d)}(\mathcal{T})$. Therefore the transposed form is $\mathbf{U}(\boldsymbol{\mathcal{X}}, \mathcal{T})^T = \mathbf{A}^{(d)}(\mathcal{T})^T\mathbf{D}^{(d)}(\sqrt{n \times \lambda_1}, ..., \sqrt{n \times \lambda_d})\boldsymbol{\Phi}^{(d)}(\boldsymbol{\mathcal{X}})^T$. Thanks to the orthonormality of $\{a_k(.)\}_{k=1}^{d}$, the covariance matrix reads $\mathbf{R} = \frac{1}{n}\boldsymbol{\Phi}^{(d)}(\boldsymbol{\mathcal{X}})\mathbf{D}^{(d)}(n \times \lambda_1, ..., n \times \lambda_d)\boldsymbol{\Phi}^{(d)}(\boldsymbol{\mathcal{X}})^T = \boldsymbol{\Phi}^{(d)}(\boldsymbol{\mathcal{X}})\mathbf{D}^{(d)}(\lambda_1, ..., \lambda_d)\boldsymbol{\Phi}^{(d)}(\boldsymbol{\mathcal{X}})^T$.

When $n << m$, it is more computationally efficient to solve the eigenproblem of $\mathbf{R}^T$ instead of the eigenproblem of $\mathbf{R}$ as highlighted by Sirovich [59] . This is often the case when a limited number of occurrences is measured for a two-dimensional physical field, as is the case encountered for the application described in Section 4.

When an order $d << min(m, n)$ corresponds to a high EVR as defined in Equation 2, we speak of dimensionality reduction, because the data are projected in a sub-space that is of much smaller dimension than $\mathbb{R}^{m \times n}$. When diverse enough records are available for the variable under study, we may consider that $\{\boldsymbol{\phi}_k(\boldsymbol{\mathcal{X}})\}_{k=1}^{d} = \{[\boldsymbol{\phi}_k(\mathbf{x}_i)]_{i \in \{1,\dots,m\}}\}_{k=1}^{d}$, i.e. the resulting POD basis, is a generator of all possible states. Predicting the associated expansion coefficients $\{a_k(t)\}_{k=1}^{d}$ for a given event t would therefore be enough to predict the whole state. Hence, we propose to use the POD as a basis extractor. This would first enable study of the dynamics of the variable of interest and eventually extraction of physical information, as shown in the applications Sections 4 and 3. Then, the basis can be used as a generator for the prediction of diverse states. This implies predicting $\{a_k(t)\}_{k=1}^{d}$, for which we propose to use Polynomial Chaos Expansion (PCE), as described in the following Section 2.2.

2.2 Polynomial Chaos Expansion

A reminder of the theoretical base of PCE is presented in Subsection 2.2.1. Theoretical details, demonstrations and interesting references can be found in [62, 77]. Then, a simple indicator is proposed in Subsection 2.2.2 for the analysis of the variables influence on the output value. The latter is later generalized for POD-PCE in Section 2.3.

2.2.1 Learning

The idea behind Polynomial Chaos Expansion (PCE) is to formulate an explicit model that links a variable of interest (output) to conditioning parameters (inputs), both in a probability space. This enables the propagation path of probabilistic information (uncertainties, occurrence frequencies) to be mapped from the input to the output space. The variable of interest, $\mathbf{Y}$, and the input parameters $\boldsymbol{\Theta} = (\theta_1, \theta_2, ..., \theta_V)$ are therefore considered random variables, characterized by a given Probability Density Function (PDF) denoted $f_{\boldsymbol{\Theta}}$. It should be kept in mind that the outputs of our problem are the POD expansion coefficients $\mathbf{Y} = [a_k(t)]_{k\in\{1,...,d\}}$, and that the inputs correspond to physical forcings, as described later in Section 2.3. The objective is to derive the variations of the POD coefficients as the outcome of the forcings. Let us now recall some fundamentals of the mathematical probabilistic framework, taking the example of a one dimensional real-valued variable. The definitions can be easily extended to $\mathbb{R}^M$.

Let $(\Omega, F, \mathbb{P})$ be a probability space, where Ω is the event space (space of all the possible events ω) equipped with σ-algebra F (some events of Ω) and its probability measure $\mathbb{P}$ (likelihood of a given event occurrence). A random variable defines an application $Y(\omega) : \Omega \to D_Y \subseteq \mathbb{R}$, with realizations denoted by $y \in D_Y$. The PDF of Y is a function $f_Y : D_Y \to \mathbb{R}$ that verifies $\mathbb{P}(Y \in E \subseteq D_Y) = \int_E f_Y(y)dy$. The k^{th} *moments* of Y are defined as $\mathbb{E}[Y^k] := \int_{D_Y} y^k f_Y(y)dy$, the first being the expectation denoted $\mathbb{E}[Y]$. In the same manner, we define the k^{th} *central moments* of Y as $\mathbb{E}[(Y - \mathbb{E}[Y])^k]$, the first being 0 and the second the variance of Y denoted by $\mathbb{V}[Y]$. The covariance of two random variables is defined as $cov(X, Y) = \mathbb{E}[(X - \mathbb{E}[X])(Y - \mathbb{E}[Y])]$ and a resulting property is $\mathbb{V}[Y] = cov(Y, Y)$.

Returning to the PCE construction, inputs $\boldsymbol{\Theta} = (\theta_1, \theta_2, ..., \theta_V)$ are considered to live in the space of real random variables with finite second moments (and finite variances). This space is denoted by $\mathcal{L}^2_{\mathbb{R}}(\Omega, F, \mathbb{P}; \mathbb{R})$ and is a Hilbert space equipped with the inner product $(\theta_1, \theta_2)_{\mathcal{L}^2_{\mathbb{R}}} := \mathbb{E}[\theta_1\theta_2] = \int_\Omega \theta_1(\omega)\theta_2(\omega)d\mathbb{P}(\omega)$ and its induced norm $||\theta_1||_{\mathcal{L}^2_{\mathbb{R}}} := \sqrt{\mathbb{E}[\theta_1^2]}$. The PCE objective is to map the output space from the input space with a model $\mathcal{M}$ as in Equation 5:

$$\begin{aligned} Y &= \mathcal{M}(\boldsymbol{\Theta}) = \textstyle\sum_{\mathcal{I}\subseteq\{1,...,V\}} \mathcal{M}_{\mathcal{I}}(\theta_{\mathcal{I}}) \\ &= \mathcal{M}_0 + \textstyle\sum_{i=1}^{V} \mathcal{M}_i(\theta_i) + \sum_{1\leq i<j\leq V} \mathcal{M}_{i,j}(\theta_i, \theta_j) + ... + \mathcal{M}_{1,...,V}(\theta_1, \theta_2, ..., \theta_V)\ , \end{aligned} \tag{5}$$

where $\mathcal{M}_0$ is the expectation of Y and $\mathcal{M}_{\mathcal{I}\subseteq\{1,...,V\}}$ represents the common contribution of the variables $\mathcal{I} \subseteq \{1, ..., V\}$ to the variation in Y. For the PCE model, these contributions have a polynomial form. We shall define, for each input variable θ_i, an orthonormal univariate polynomial basis $\left\{\xi^{(i)}_\beta(.), \beta \in [|0, p|]\right\}$ where $p \in \mathbb{N}$ is a chosen polynomial degree and $\xi^{(i)}_\beta(.)$ is of degree β. The orthonormality is defined with respect to the inner product $(.,\ .)_{\mathcal{L}^2_{\mathbb{R}}}$. If we introduce the multi-index notation $\boldsymbol{\alpha} = (\alpha_1, ..., \alpha_V) \in \mathbb{N}^V$ so that $|\boldsymbol{\alpha}| = \sum_{i=1}^V \alpha_i$, we can define a multivariate basis $\left\{\zeta^{\boldsymbol{\Theta}}_{\boldsymbol{\alpha}}(.), |\boldsymbol{\alpha}| \in [|0, p|]\right\}$ as $\zeta^{\boldsymbol{\Theta}}_{\boldsymbol{\alpha}}(\theta_1, \theta_2, ..., \theta_V) := \prod_{i=1}^V \xi^{(i)}_{\alpha_i}(\theta_i)$. Therefore, the model in Equation 5 can be written as:

$$Y = \mathcal{M}(\boldsymbol{\Theta}) = \sum_{|\boldsymbol{\alpha}|\leq P} c_{\boldsymbol{\alpha}} \zeta^{\boldsymbol{\Theta}}_{\boldsymbol{\alpha}}(\theta_1, \theta_2, ..., \theta_V)\ , \tag{6}$$

where $c_{\boldsymbol{\alpha}} \in \mathbb{R}$ are deterministic coefficients that can be estimated thanks to different methods. It can be formulated as a minimization problem, and regularization methods can be used when dealing with small data sets. In the present study, we used the Least Angle Regression Stagewise method (LARS) in order to construct an adaptive sparse PCE. It is an iterative procedure, consisting on an improved version of forward selection. The algorithm begins by finding the polynomial pattern, here denoted ζ_i for simplicity, that is the most correlated to the output. The latter is linearly approximated by $\epsilon_i\zeta_i$, where $\epsilon_i \in \mathbb{R}$. Coefficient ϵ_i is not set to its maximal value, but increased starting from 0, until another pattern ζ_j is found to be as correlated to $Y - \epsilon_i\zeta_i$, and so on. In this approach, a collection of possible PCE, ordered by sparsity, is provided and an optimum can be chosen with an accuracy estimate. It was performed in this study using corrected leave-one-out error. The reader can refer to the work of

Blatman and Sudret [3] for further details on LARS and more generally on sparse constructions.

The choice of the basis is crucial and is directly related to the choice of input variable marginals, via the inner product $(.,.)_{\mathcal{L}^2_{\mathbb{R}}}$. Chaos polynomials were first introduced in [74] for input variables characterized by Gaussian distributions. The orthonormal basis with respect to this marginal is the Hermite polynomials family. Later, other Askey scheme hypergeometric polynomial families were associated to some well-known parametric distributions [76]. For example, the Legendre family is orthonormal with respect to the Uniform marginals. This is called *gPC* (generalized Polynomial Chaos) when variables of different PDFs are used as inputs. In practice however, the input distributions of physical variables can be different from usual parametric marginals. In such cases, the marginals can be inferred by empirical methods such as the Kernel Smoother (see [19] for theoretical elements). In this case, an orthonormal polynomial basis with respect to arbitrary marginals can be built with a Gram-Schmidt orthonormalization process as in [75] or via the Stieltjes three-term recurrence procedure as in [72].

To highlight the importance of the marginals and choice of polynomial basis for the learning process, several configurations are attempted in Section 4. Different input sets and distributions (Gaussian, Uniform, inferred by Kernel Smoothing) were tested. The influence of the polynomial basis on the ML is investigated in Section 4.2.2.

2.2.2 Physical importance measures

Once the PCE construction is achieved, a physical interpretation can be performed. It is notable that classical NN indicators can be used [14]. The PCE can be represented in the Feedforward NN paradigm as in Figure 2. Such networks are classically composed, in addition to the input and output layers, of successive *hidden layers*. Each hidden layer is composed of *neurons* that transform the variables of the previous layer (outputs of the previous *neurons*) into a new set of variables. This is done by combining a linear transformation, giving different *weights* to the previous *neurons*, and a transformation function, called *Activation Function* (AF). This succession of layers is called the *latent representation*. For a number of hidden layers $L \geq 1$, the NN can be formally written as $\mathbf{Y} \approx f_{out}(\mathbf{A}_L \ f_L(\ldots \mathbf{A}_2 \ f_2(\mathbf{A}_1 \ f_1(\mathbf{A}_{in} \ \boldsymbol{\Theta}))))$ where $\{\mathbf{A}_k\}_{k\in[|1,L|]}$ and $\{f_k\}_{k\in[|1,L|]}$ are the hidden layer weight matrices and AFs, $\mathbf{A}_{in}$ is the input-to-hidden connection matrix and f_{out} is the final hidden-output transformation [58].

The PCE-based NN represented in Figure 2 is a single layer feedforward, composed of $l \in \mathbb{N}$ neurons, that can be written as $\mathbf{Y} \approx f_{out}(\mathbf{A}_1 \ f_1(\mathbf{A}_{in}\boldsymbol{\Theta}))$. The first matrix $\mathbf{A}_{in}$ is the input-to-hidden connection matrix of dimension $V \times V$, that links the input layer to the PCE hidden layer containing the multivariate polynomials $\left\{\zeta^{\boldsymbol{\Theta}}_{\boldsymbol{\alpha}}, \boldsymbol{\alpha} \in \{\boldsymbol{\alpha}_1, ..., \boldsymbol{\alpha}_l\}\right\}$, where V is the number of inputs and the multivariate indexes $\{\boldsymbol{\alpha}_1, ..., \boldsymbol{\alpha}_l\}$ are conditioned by the chosen polynomial degree p such as $\forall i \in [|1,l|] \ 0 \leq |\boldsymbol{\alpha}_i| \leq p$, and by the number of selected features if a sparse polynomial is constructed, as in the present case using LARS [2]. Matrix $\mathbf{A}_{in}$ represents the contributions of the V variables to the multivariate polynomials $\left\{\zeta^{\boldsymbol{\Theta}}_{\boldsymbol{\alpha}}, \boldsymbol{\alpha} \in \{\boldsymbol{\alpha}_1, ..., \boldsymbol{\alpha}_l\}\right\}$. It is a diagonal matrix such that $[\boldsymbol{A}_{in}]_{j,j\in[|1,V|]^2}$ is 0 if $\forall i \in [|1,l|] \ (\alpha_i)_j = 0$ and 1 if not. The first multi-dimensional AF f_1 is a vector of multivariate functions that transforms the set of selected inputs corresponding to $[\boldsymbol{A}_{in}]_{i,i\in[|1,V|]^2} = 1$ to the multivariate polynomials of the chosen basis (Hermite, Legendre, etc.) by tensor product over the univariate basis. The hidden layer weight matrix $\mathbf{A}_1$ gives different weights to the constructed polynomial features. It is a diagonal matrix composed of the PCE expansion coefficients such as $[\mathbf{A}_1]_{i,j\in[|1,l|]^2} = [c_{\boldsymbol{\alpha}_i}]_{i\in[|1,l|]}$.

The final hidden-output transformation f_{out} is a summation. Figure 2 can also be presented differently: another hidden layer can be added to the PCE latent representation as $\mathbf{Y} \approx f_{out}(\mathbf{A}_2 \ f_2(\mathbf{A}_1 \ f_1(\mathbf{A}_{in} \ \boldsymbol{\Theta})))$. The first AF f_1 would represent a transformation of each input variable to a list of monomials of degrees 1 to p (here, $\mathbf{A}_{in}$ is identity). The second AF f_2 therefore represents the tensor product that transforms the different monomials to multivariate features, with $\mathbf{A}_1$ appropriately filled with zeros and ones, and $[\mathbf{A}_2]_{i,j\in[|1,l|]^2} = [c_{\boldsymbol{\alpha}_i}]_{i\in[|1,l|]}$.

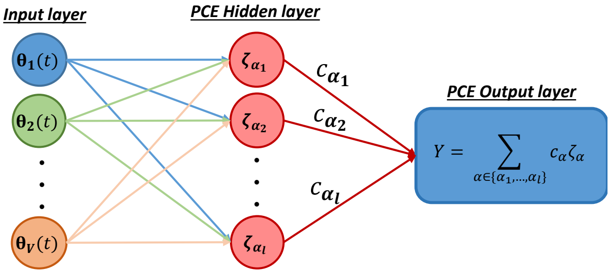

Figure 2: Representation of the PCE learning in the NN paradigm.

To capture the importance of each feature, the Garson relative Weights (GW) defined in Equation 7 are a classical measure to quantify the relative importance of each neuron of the last hidden layer, and therefore of each polynomial pattern, for the output value [14, 68].

$$w_{\zeta_{\boldsymbol{\alpha}}^{\boldsymbol{\Theta}}} = \frac{|c_{\boldsymbol{\alpha}}|}{\sum_{0 \leq \boldsymbol{\beta} \leq 1} |c_{\boldsymbol{\beta}}|} \ . \tag{7}$$

This measure can be used to understand the importance given by the NN algorithm to the variables and their possible interactions, especially when using feature selection algorithms as LARS: ”feature interactions [...] are created at hidden units with nonlinear activation functions, and the influences of the interactions are propagated layer-by-layer to the final output” [68]. In the particular case of a polynomial expansion, the interpretation is straightforward, the importance of each variable alone corresponds to its monomials, and the importance of its interactions with other variables corresponds to the multivariate polynomials in which it is involved.

For the particular case of the orthonormal basis provided by PCE, the GW defined in 7 can be interpreted in terms of Pearson's correlations between output Y and the polynomial basis elements $\zeta_{\boldsymbol{\alpha}}^{\boldsymbol{\Theta}}$ denoted $\rho_{Y,\ \zeta_{\boldsymbol{\alpha}}^{\boldsymbol{\Theta}}}$, with $\alpha \neq (0, ..., 0)$. Indeed, Pearson's correlations $\rho_{Y,\ \zeta_{\boldsymbol{\alpha}}^{\boldsymbol{\Theta}}}$ are defined as in Equation 8,

$$\rho_{Y,\ \zeta_{\boldsymbol{\alpha}}^{\boldsymbol{\Theta}}} = \frac{\mathbb{E}\left[(Y - \mathbb{E}(Y))(\zeta_{\boldsymbol{\alpha}}^{\boldsymbol{\Theta}} - \mathbb{E}(\zeta_{\boldsymbol{\alpha}}^{\boldsymbol{\Theta}}))\right]}{\sqrt{\mathbb{V}(Y)\mathbb{V}(\zeta_{\boldsymbol{\alpha}}^{\boldsymbol{\Theta}})}} = \frac{c_{\boldsymbol{\alpha}}}{\sqrt{\sum_{1 \leq |\boldsymbol{\beta}| \leq p} c_{\boldsymbol{\beta}}^2}} \ , \tag{8}$$

thanks to the orthonormality of the basis with respect to the scalar product $(.\ ,.)_{\mathcal{L}^2_{\mathbb{R}}}$ that guarantees:

- $\mathbb{E}\left[\zeta_{\boldsymbol{\alpha}}^{\boldsymbol{\Theta}}\right] = \left(\zeta_{\boldsymbol{\alpha}}^{\boldsymbol{\Theta}}, \zeta_{\boldsymbol{\beta}=(\mathbf{0},\dots,\mathbf{0})}^{\boldsymbol{\Theta}} = 1\right)_{\mathcal{L}^2_{\mathbb{R}}} = 0\,;$
- $\mathbb{E}\left[Y\right] = \left(\sum_{0 \leq |\boldsymbol{\beta}| \leq p} c_{\boldsymbol{\beta}} \zeta_{\boldsymbol{\beta}}^{\boldsymbol{\Theta}}\ , \zeta_{\boldsymbol{\beta}=(\mathbf{0},\dots,\mathbf{0})}^{\boldsymbol{\Theta}}\right)_{\mathcal{L}^2_{\mathbb{R}}} = c_{\beta=(0,\dots,0)}\,;$
- $\mathbb{E}\left[Y, \zeta_{\boldsymbol{\alpha}}^{\boldsymbol{\Theta}}\right] = \left(\sum_{0 \leq |\boldsymbol{\beta}| \leq p} c_{\boldsymbol{\beta}} \zeta_{\boldsymbol{\beta}}^{\boldsymbol{\Theta}}\ , \zeta_{\boldsymbol{\alpha}}^{\boldsymbol{\Theta}}\right)_{\mathcal{L}^2_{\mathbb{R}}} = c_{\boldsymbol{\alpha}}\,;$
- $\mathbb{V}\left[\zeta_{\boldsymbol{\alpha}}^{\boldsymbol{\Theta}}\right] = \mathbb{E}\left[\left(\zeta_{\boldsymbol{\alpha}}^{\boldsymbol{\Theta}} - \mathbb{E}\left[\zeta_{\boldsymbol{\alpha}}^{\boldsymbol{\Theta}}\right]\right)^2\right] = \mathbb{E}\left[\left(\zeta_{\boldsymbol{\alpha}}^{\boldsymbol{\Theta}}\right)^2\right] = ||\zeta_{\boldsymbol{\alpha}}^{\boldsymbol{\Theta}}||^2_{\mathcal{L}^2_{\mathbb{R}}} = 1\,;$
- $\mathbb{V}\left[Y\right] = \mathbb{E}\left[\left(Y - \mathbb{E}\left[Y\right]\right)^2\right] = \left(\sum_{1 \leq |\boldsymbol{\beta}| \leq p} c_{\boldsymbol{\beta}} \zeta_{\boldsymbol{\beta}}^{\boldsymbol{\Theta}}\ , \sum_{1 \leq |\boldsymbol{\beta}| \leq p} c_{\boldsymbol{\beta}} \zeta_{\boldsymbol{\beta}}^{\boldsymbol{\Theta}}\right)_{\mathcal{L}^2_{\mathbb{R}}} = \sum_{1 \leq |\boldsymbol{\beta}| \leq p} c_{\boldsymbol{\beta}}^2\ .$

Therefore, the weights $w_{\zeta_{\boldsymbol{\alpha}}^{\boldsymbol{\Theta}}}$ can also be computed as $|\rho_{Y,\ \zeta_{\boldsymbol{\alpha}}^{\boldsymbol{\Theta}}}| / \sum_{1 \leq |\boldsymbol{\beta}| \leq p} |\rho_{Y,\ \zeta_{\boldsymbol{\beta}}^{\boldsymbol{\Theta}}}|$. This means that they measure the relative importance of the basis element in the expansion of the output, in terms of linear correlation, regardless of the sign of the latter. These ”relative Pearson's correlations” can be seen as a physical contribution since the PCE model is strictly linear. The sum of the GW $w_{\zeta_{\boldsymbol{\alpha}}^{\boldsymbol{\Theta}}}$ for all the polynomial features equals 1. This means that they allow $\{\zeta_{\boldsymbol{\alpha}}\}_{|\boldsymbol{\alpha}| \leq p}$ to be ranked in terms of relative contribution to the output Y. The contributions can be analyzed either for each polynomial pattern separately, or for a single variable θ_i by adding all the polynomial shares related to this variable alone, or by adding all the polynomial shares related to this variable and its interactions (Sobol' indices analogy [62]).

2.3 POD-PCE based predictor

POD and PCE were introduced separately in Subsections 2.1 and 2.2 respectively. We are now fully equipped with the adequate theoretical basis and mathematical notations, to present the POD-PCE ML methodology for a data-based model learning of a multidimensional physical field. In this Subsection, we will first summarize the proposed approach, then the formal details of the coupling will be given with the definition of adequate accuracy measures. Finally the previously discussed importance measures will be generalized for the POD-PCE physical study.

The proposed POD-PCE ML consists of steps, in a learning and a prediction phase, summed up as follows:

- Learning phase:
  - POD basis construction: given a set of measurements $\mathbf{U}(\mathcal{X}, \mathcal{T}) = [\mathbf{u}(\mathbf{x}_i, t_j)]_{i,j} \in \mathbb{R}^{m \times n}$ (snapshot matrix), construct a spatial POD basis accordingly. Variable t_j can represent time in case of temporal dynamics, or more generally an occurrence of $\mathbf{U}(\mathcal{X}, .)$. Then, in general, $\mathcal{T}$ would be an event space ;
  - PCE learning: construct PCE models that map each POD coefficient, obtained in the previous step along with the spatial basis, to a set of inputs. In the particular case of temporal dynamics, previous values of the physical field, represented by previous POD coefficients, can be part of the learning inputs. For example, one could use an initial field value $\mathbf{U}(\boldsymbol{\mathcal{X}}, t_j)$ to learn a future field $\mathbf{U}(\boldsymbol{\mathcal{X}}, t_{j+1})$ from a set of physical parameters that condition the evolution over $[t_j, t_{j+1}]$. The latter can consist in time series of physical variables, representative statistics of the latter, physical constants, etc. and can be denoted $\boldsymbol{\Theta}(t_j \to t_{j+1})$;
- Prediction phase:
  - Given a new realization of the inputs, predict the new POD coefficients using the learned PCE models, then reconstruct the new estimate $\mathbf{U}(\boldsymbol{\mathcal{X}}, t_k)$ on the POD basis. As previously explained, an initial value to the physical field, denoted $\mathbf{U}(\boldsymbol{\mathcal{X}}, t_{k-1})$, may be part of the inputs for temporal dynamics. In particular, its reduced form, consisting in temporal POD coefficients, is used. In this case, an additional step is needed: $\mathbf{U}(\boldsymbol{\mathcal{X}}, t_{k-1})$ is projected on the constructed POD basis in order to retrieve the values of associated POD coefficients which are then used as PCE inputs.

The learning and prediction set-ups are more complex to establish for temporal evolution problems, because the field information at previous times are required. Therefore, for the sake of clarity, the steps are explicitly developed in the following Subsection 2.3.1. The accuracy of the methodology is later demonstrated on both a parametric toy problem in Section 3, and a field measurements-based temporal problem in Section 4. These two can be considered as complementary applications, and demonstrate that the POD-PCE ML can be applied in different learning set-ups of multi-dimensional physical fields. Similarities in the treatment of both problems can be noticed, but their particularities are also used to demonstrate different properties of the POD-PCE learning, that are shortly described at the beginning of each section.

2.3.1 Machine learning methodology

Here, the formal hypothesis behind the POD-PCE ML reasoning and its mathematical formulation are discussed. Let $\mathbf{U}(\boldsymbol{\mathcal{X}}, .) = [\mathbf{u}(\mathbf{x}_i,\ .)]_{i \in \{1,\ldots,m\}}$ be a field of interest defined on a set of $m \in \mathbb{N}$ space coordinates $\boldsymbol{\mathcal{X}} = \{\mathbf{x}_1, \ldots, \mathbf{x}_m\}$. Let $\boldsymbol{\Theta}\mathbf{(.)} = (\theta_1(.), \theta_2(.), ..., \theta_V(.))$ be a vector of the inputs supposed to condition the evolution of $\mathbf{U}(\boldsymbol{\mathcal{X}}, .)$ over time. The dynamic model, denoted $\mathcal{H}$, that gives an estimation of a future state $\mathbf{U}(\boldsymbol{\mathcal{X}}, t_{j+1})$ from a past state $\mathbf{U}(\boldsymbol{\mathcal{X}}, t_j)$ and an estimation of $\boldsymbol{\Theta}(t_j \to t_{j+1})$ over the time interval $[t_j, t_{j+1}]$, where $t_j < t_{j+1} \in \mathbb{R}^+$, is formulated as in Equation 9 .

$$\mathbf{U}(\boldsymbol{\mathcal{X}}, t_{j+1}) \approx \mathcal{H}\left[\mathbf{U}(\boldsymbol{\mathcal{X}}, t_j), t_{j+1} - t_j, \boldsymbol{\Theta}(t_j \to t_{j+1})\right] \ . \tag{9}$$

If the field of interest has been recorded over a set of past times $\mathcal{T} = \{t_1, \ldots, t_n\} \subset \mathbb{R}^+$, where $t_j < t_{j+1}$, a POD basis can be constructed as in Section 2.1, consisting of $d \in \mathbb{N}$ vectors of dimension m stored in a matrix as $\boldsymbol{\Phi}^{(d)}(\boldsymbol{\mathcal{X}}) = (\boldsymbol{\Phi}_1^{(d)}(\boldsymbol{\mathcal{X}}), \ldots, \boldsymbol{\Phi}_d^{(d)}(\boldsymbol{\mathcal{X}})) \in \mathbb{R}^{m \times n}$, and can be seen as a generator of all possible states if enough records are available. If so, any future state $\mathbf{U}(\boldsymbol{\mathcal{X}}, t_j)$ can be expanded on this POD basis and the associated temporal coefficients are simply the weights of $\mathbf{U}(\boldsymbol{\mathcal{X}}, t_j)$ on the POD basis. They are therefore obtained using the canonical scalar product over $\mathbb{R}^m$, as in Equation 10.

$$\begin{aligned} \mathbf{U}(\boldsymbol{\mathcal{X}}, t_j) &\approx \sum_{k=1}^{d} a_k(t_j) \sqrt{n \times \lambda_k}\, \boldsymbol{\Phi}_k^{(d)}(\boldsymbol{\mathcal{X}}) \\ &\approx \sum_{k=1}^{d} (\mathbf{U}(\boldsymbol{\mathcal{X}}, t_j), \boldsymbol{\Phi}_k^{(d)}(\boldsymbol{\mathcal{X}}))_{\mathbb{R}^m} \boldsymbol{\Phi}_k^{(d)}(\boldsymbol{\mathcal{X}}) \\ &\approx \sum_{k=1}^{d} \mathbf{U}(\boldsymbol{\mathcal{X}}, t_j)^T \boldsymbol{\Phi}_k^{(d)}(\boldsymbol{\mathcal{X}}) \boldsymbol{\Phi}_k^{(d)}(\boldsymbol{\mathcal{X}}) \ . \end{aligned} \tag{10}$$

Hence, the variable part of $\mathbf{U}(\boldsymbol{\mathcal{X}}, t_j)$ is fully expressed in the temporal coefficients $a_k(t_j)$. The field of interest $\mathbf{U}(\boldsymbol{\mathcal{X}}, t_j)$ can be either a field measurement, a laboratory or a numerical experiment. In any-case, it can be considered as being generated by a random process "in the sense that nature happens without consideration of what could be the best realizations for the learning algorithm" [58]. Therefore, the coefficients $a_k(t_j)$ can also be seen as the j^{th} realization of a random variable A_k. We can therefore construct a PCE approximation $\mathcal{H}_k$ that maps A_k from its input space. The latter is taken as a collection of random variables, composed from the set $(A_1, ..., A_d)$ at a previous time, the duration of the dynamic, and the input variables $\mathbf{\Theta}(t_j \to t_{j+1})$. This is formulated as a classical dynamic model in Equation 11 .

$$a_k(t_{j+1}) \approx \mathcal{H}_k\left[a_1(t_j), \ldots, a_d(t_j), t_{j+1} - t_j, \mathbf{\Theta}(t_j \to t_{j+1})\right] \ . \tag{11}$$

The model $\mathcal{H}$ in Equation 9 is approximated as in Equation 12 .

$$\mathcal{H}\left[\mathbf{U}(\boldsymbol{\mathcal{X}}, t_j), t_{j+1} - t_j, \mathbf{\Theta}(t_j \to t_{j+1})\right] \approx \sum_{k=1}^{d} \mathcal{H}_k\left[a_1(t_j), \ldots, a_d(t_j), t_{j+1} - t_j, \mathbf{\Theta}(t_j \to t_{j+1})\right] \sqrt{n \times \lambda_k}\, \mathbf{\Phi}_k^{(d)}(\boldsymbol{\mathcal{X}}) \ . \tag{12}$$

Some limitations to the introduced formulations in Equations 11 and 12 can be highlighted. A first limitation concerns discontinuities that can be met in physical fields. This can occur either in the complete spatial field $\mathbf{U}(.,.)$, in its reduced version represented by the POD coefficients $a_k(.)$, or in the inputs $\mathbf{\Theta}$. In the first case, the classical linear approximations as POD may be inefficient [64]. One solution developed by Taddei [64], called RePOD (Registration POD), consists in a parametric transformation of the interest discontinuous field into a smoother one for linear transformations. In the second case, where discontinuity happens in the POD temporal coefficients, this would impact the learning with PCE. Innovative solutions were identified to apply PCE when the output's space is characterized with rapid variations or discontinuities, for instance near a critical point in the inputs space. As an example, a method called adaptive Multi-Element PCE was developped for Legendre polynomials in [71] and extended to arbitrary measures in [72]. The inputs space is decomposed to a union of subsets, and the output variable is locally expanded on each subset. The final solution is then a combination of PCE sub-problems. In the last discontinuity case that concerns the inputs $\mathbf{\Theta}$, the previous splitting techniques can also be used. For example, the sub-intervals in the inputs space can be constructed in such way to avoid the discontinuity. PCE sub-problems would therefore be treated as usual.

A second limitation concerns the choice of input variables for regression models, and is an ongoing research question in statistics [17]. As a practical illustration, the dynamical problem written in Equation 11 can incorporate additional inputs, for example the information at previous times t_{j-1}, t_{j-2}, etc. However, when a large set of inputs can be used and only a small set of realizations is available for learning, a well-posedness problem occurs. One solution consists in transforming the large set of inputs to a reduced version, for example with the help of PCA [25] for DR. This approach was not studied here and will be the topic of a future study. However, different input configurations will be evaluated, to investigate the influence of variable selection on the proposed learning. For example, the hypothesis of dependence between the random variables $(A_1, \ldots, A_d)$ could be relaxed. This would imply writing the approximation in Equation 11 in a relaxed form as $\mathcal{H}_k\left[a_k(t_j), t_{j+1} - t_j, \mathbf{\Theta}(t_j \to t_{j+1})\right]$. In that case a simpler model $\mathcal{H}$, under the strong independence assumption, can be formulated as in Equation 13.

$$\mathcal{H}\left[\mathbf{U}(\boldsymbol{\mathcal{X}}, t_j), t_{j+1} - t_j, \mathbf{\Theta}(t_j \to t_{j+1})\right] \approx \sum_{k=1}^{d} \mathcal{H}_k\left[a_k(t_j), t_{j+1} - t_j, \mathbf{\Theta}(t_j \to t_{j+1})\right] \sqrt{n \times \lambda_k}\, \mathbf{\Phi}_k^{(d)}(\boldsymbol{\mathcal{X}}) \ . \tag{13}$$

Both alternatives are tested in Section 4. To investigate the influence of input selection on learning accuracy, a quantitative evaluation of the hypothesis is needed. More generally, whether for the above-mentioned simplifications or for the approximated form of the model in general, accuracy estimators are needed. These are presented below.

2.3.2 Accuracy tests for the approximation

There are two determining parts in the POD-PCE learning process. Firstly, the PCE learning $\mathcal{H}_k(.)$ of each mode A_k should be as accurate as possible. Secondly, the reconstructed field $\sum_{k=1}^{d} \mathcal{H}_k(.) \sqrt{n \times \lambda_k}\, \mathbf{\Phi}_k^{(d)}(\boldsymbol{\mathcal{X}})$ for a given rank d should be as close to the real field $\mathbf{U}(\boldsymbol{\mathcal{X}})$ as possible.

The distance between each mode and its PCE approximate can be evaluated using the *generalization error*, denoted $\delta(A_k, \mathcal{H}_k)$ and defined as in Equation 14.

$$\delta(A_k, \mathcal{H}_k) = \mathbb{E}\left[(A_k - \mathcal{H}_k(.))^2\right] \ . \tag{14}$$

For the model defined in Equation 13 , this error can be estimated, on a set of paired realizations $(a_k(t_1), \ldots, a_j(t_n))$ and $(\boldsymbol{\Theta}(t_0 \to t_1), \ldots, \boldsymbol{\Theta}(t_{n-1} \to t_n))$, as in Equation 15 as explained by Blatman [2] . This approximated version of the *generalization error* is called the *empirical error.*

$$\delta(A_k, \mathcal{H}_k) \approx \delta_{emp}(A_k, \mathcal{H}_k) \coloneqq \frac{1}{n} \sum_{j=1}^{n} \left(a_k(t_j) - \mathcal{H}_k\left[a_k(t_{j-1}), t_{j+1} - t_j, \boldsymbol{\Theta}(t_{j-1} \to t_j)\right]\right)^2 \ . \tag{15}$$

Its relative estimate denoted $\epsilon_{emp}(A_k, \mathcal{H}_k)$ can be defined as in Equation 16 .

$$\epsilon_{emp}(A_k, \mathcal{H}_k) \coloneqq \frac{\delta_{emp}(A_k, \mathcal{H}_k)}{\mathbb{V}[A_k]} \ . \tag{16}$$

Once the PCE learnings can be trusted, the distance at time t_j between the true state $\mathbf{U}(\boldsymbol{\mathcal{X}}, t_j)$ and the POD-PCE approximation $\mathcal{H}\left[\mathbf{U}(\boldsymbol{\mathcal{X}}, t_j), t_{j+1} - t_j, \boldsymbol{\Theta}(t_j \to t_{j+1})\right]$ can be defined. It might be estimated using the relative Root Mean Squared Error (relative RMSE), denoted $r[\mathbf{U}, \mathcal{H}](t_j)$ and calculated as in Equation 17 , where $\mathbf{h}(\mathbf{x}_i, t_j)$ refers to the value of the POD-PCE approximation at coordinate $\mathbf{x}_i$ and time t_j.

$$r[\mathbf{U}, \mathcal{H}](t_j) \coloneqq \sqrt{\frac{\sum_{i=1}^{m} \left[\mathbf{u}(\mathbf{x}_i, t_j) - \mathbf{h}(\mathbf{x}_i, t_j)\right]^2}{\sum_{i=1}^{m} \left[\mathbf{u}(\mathbf{x}_i, t_j)\right]^2}} \ . \tag{17}$$

A mean value of the relative RMSE is calculated over a set of realizations corresponding to a set of times $\mathcal{T} = \{t_1, \ldots, t_n\}$. It is denoted $r[\mathbf{U}, \mathcal{H}]^{(\mathcal{T})}$ and estimated as in Equation 18.

$$r[\mathbf{U}, \mathcal{H}]^{(\mathcal{T})} \coloneqq \frac{1}{n} \sum_{j=1}^{n} r[\mathbf{U}, \mathcal{H}](t_j) \ . \tag{18}$$

Once the accuracies of the PCE learnings and the POD-PCE coupling have been evaluated, a final model, which will be the most accurate one, can be chosen. This model would, for our ML set-up, be the best representation of the dependence structure between inputs and outputs. It is used to shed light on the underlying physical relationships. Therefore the inputs are ranked in terms of physical influence, using an appropriate ranking indicator, presented in the following Subsection.

2.3.3 Physical influence of inputs based on the POD-PCE model

The GW influence measures presented for the PCE models in Subsection 2.2 are here extended for the POD-PCE coupling. These indicators are adequate for the analysis of each PCE model $\mathcal{H}_k$, i.e. for interpreting the contribution of the inputs to each random variable A_k separately. However, calculating the contributions to each A_k independently precludes putting them in perspective according to the importance of A_k in the final reconstructed model $\mathcal{H}$ that approximates $\mathbf{U}(\boldsymbol{\mathcal{X}}, .)$. Hence, adapted indicators should be calculated.

Let $\mathbf{U}(\boldsymbol{\mathcal{X}}, .)$ be the random spatiotemporal field approximated by the POD-PCE ML, for prediction from time t_j to time t_{j+1} and let $\mathcal{H}_k$ be the PCE approximation at degree $p^{(k)}$ that maps the random POD temporal coefficient A_k from a set of input variables, using the expansion on the multivariate polynomial basis $\left\{\zeta_{\boldsymbol{\alpha}}^{(k)}(.)\right\}_{|\boldsymbol{\alpha}| \leq p^{(k)}}$. The POD-PCE model formulated in Equation 12 is written as in Equation 19:

$$\mathbf{U}(\boldsymbol{\mathcal{X}}, .) \approx \sum_{k=1}^{d} A_k \sqrt{n \times \lambda_k} \boldsymbol{\Phi}_k^{(d)}(\boldsymbol{\mathcal{X}}) \approx \sum_{k=1}^{d} \left(\sum_{|\boldsymbol{\alpha}| \leq p^{(k)}} c_{\boldsymbol{\alpha}}^{(k)} \zeta_{\boldsymbol{\alpha}}^{(k)}(.) \right) \sqrt{n \times \lambda_k} \boldsymbol{\Phi}_k^{(d)}(\boldsymbol{\mathcal{X}}) \ . \tag{19}$$

Thanks to its linearity, the POD-PCE ML can be represented as a single-layered NN, as shown in Figure 3.

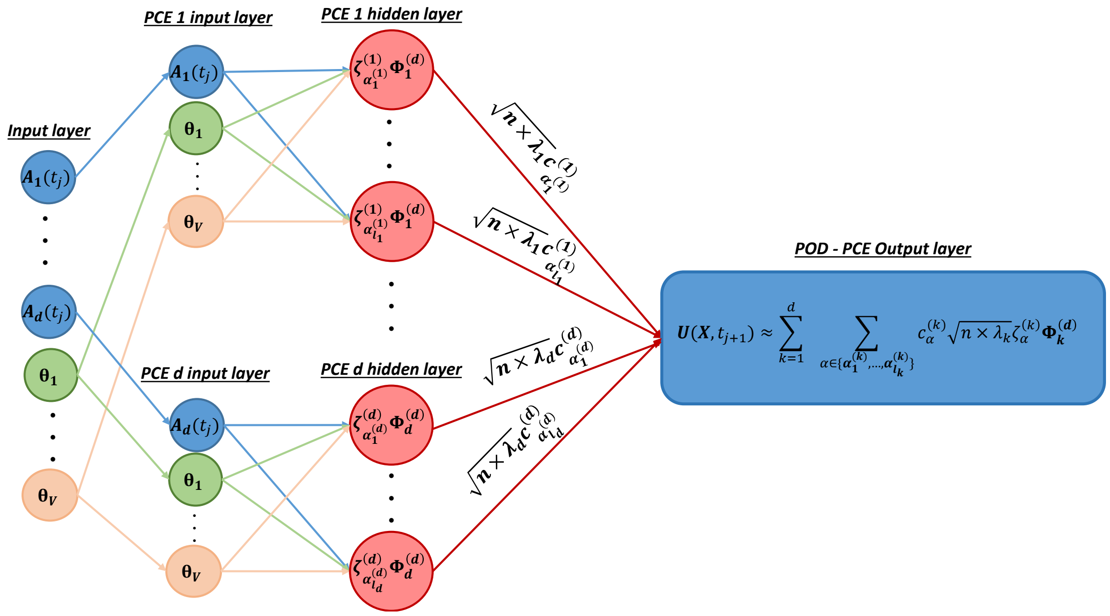

FIGURE 3: Representation of the POD-PCE ML approach in the NN paradigm.

Therefore, a new indicator, *Generalized Garson Weights* (GGW), denoted $W_{\zeta_{\boldsymbol{\alpha}}^{(k)}}$, is computed and simply re-evaluated from the PCE Garson weights (GW), here denoted $w_{\zeta_{\boldsymbol{\alpha}}^{(k)}}$, as in Equation 20.

$$\begin{aligned} W_{\zeta_{\boldsymbol{\alpha}}^{(k)}} \quad &:= \quad \frac{|c_{\boldsymbol{\alpha}}^{(k)}|\sqrt{n\times\lambda_k}}{\sum_{e=1}^{d}\sum_{|\boldsymbol{\beta}|\le p^{(e)}}\left(|c_{\boldsymbol{\beta}}^{(e)}|\sqrt{n\times\lambda_e}\right)} \\ &= \frac{\left(\sum_{|\boldsymbol{\beta}|\le p^{(k)}}|c_{\boldsymbol{\beta}}^{(k)}|\right)w_{\zeta_{\boldsymbol{\alpha}}^{(k)}}\sqrt{\lambda_k}}{\sum_{e=1}^{d}\sum_{|\boldsymbol{\beta}|\le p^{(e)}}\left(|c_{\boldsymbol{\beta}}^{(e)}|\sqrt{\lambda_e}\right)} = \left(\frac{\sum_{|\boldsymbol{\beta}|\le p^{(k)}}\left(|c_{\boldsymbol{\beta}}^{(k)}|\sqrt{\lambda_k}\right)}{\sum_{e=1}^{d}\sum_{|\boldsymbol{\beta}|\le p^{(e)}}\left(|c_{\boldsymbol{\beta}}^{(e)}|\sqrt{\lambda_e}\right)}\right)w_{\zeta_{\boldsymbol{\alpha}}^{(k)}}\ . \end{aligned} \tag{20}$$

These GGW indicators show that the contribution of the polynomials $\{\zeta_{\boldsymbol{\alpha}}^{(k)}\}_{|\boldsymbol{\alpha}|\le p^{(k)}}$ of A_k are enhanced with the eigenvalue λ_k, which is directly linked to the importance of the POD mode $\boldsymbol{\Phi}_k^{(d)}(\boldsymbol{\mathcal{X}})$ (EVR in Equation 2). An analogy can be drawn with the generalized sensitivity indices for a reduced order model [29]. The $\sum_{k=1}^{d}\sum_{|\boldsymbol{\alpha}|\le p^{(k)}}W_{\zeta_{\underline{\alpha}}^{(k)}}=1$ property holds. This means that the indices allow $\{\{\zeta_{\boldsymbol{\alpha}}^{(k)}\}_{|\boldsymbol{\alpha}|\le p^{(k)}}\}_{k\in\{1,\dots,d\}}$ to be ranked altogether in terms of contribution to output $\mathbf{U}$. The influences can be analyzed following the indications of Section 2.2.2.

3 Application on a parametric toy problem

The theoretical framework of the proposed POD-PCE learning was presented in the previous Section 2, including the detailed coupling formulation, accuracy estimators and physical influence measures in Subsection 2.3. In the latter, it was highlighted that there is a slight difference in the learning and prediction steps between temporal problems and parametric problems. In this section, the POD-PCE ML is applied to a parametric toy problem, for which the analytical solution is introduced in Subsection 3.1. The problem is simple and controllable, and allows demonstrating the learning performance, the consistency of physical interpretations in comparison with the analytical information, and the robustness of the learning to noise in the data. Subsection 3.2 therefore deals with the application of the POD-PCE methodology for physical analysis and prediction, while in Subsection 3.3, robustness to different noise levels is investigated.

3.1 Problem description

The chosen toy problem deals with the representation of groundwater flow in a confined aquifer. Such a flow can be complex to describe and is generally represented using the depth-averaged groundwater flow equations [38]. Analytical solutions for these equations can be found for particular configurations. For example, a solution was identified by Li et al. [38] in case of a semi-infinite coastal aquifer subject to oscillating boundary conditions, resulting from oceanic and estuarine tidal loadings. The solution is given for the particular case where the estuary and coastline are perpendicular. The oceanic BC (along coastline) is taken as a single and spatially uniform tidal harmonic constituent $Acos(\omega t)$, where A and ω are the tidal amplitude and pulsation respectively. The corresponding BC along the estuary is a non-uniform tidal loading $Aexp(-\kappa_{er}x)cos(\omega t-\kappa_{ei}x)$, where κ_{er} and κ_{ei} are the estuary's tidal damping coefficient and tidal wave number respectively, that represent changes in the amplitude and phase along the estuary.

This forcing results with fluctuations in the *water table*, that is defined as the level separating the water and saturated ground from the remaining upper unsaturated ground. The fluctuations, denoted f, can be calculated using the analytical solution defined in [38] as in Equation 21.

$$\begin{cases} f(x,y,t) & = & f_0(x,t) + f_1(x,y,t) \\ f_0(x,t) & = & Aexp\left(-\sqrt{\frac{\omega}{2D}}x\right) cos\left(\omega t - \sqrt{\frac{\omega}{2D}}x\right) \\ f_1(x,y,t) & = & A \times Re\left\{\int_0^t \left[g(k_1,x) - g(k_1,-x) - g(k_2,x) + g(k_2,-x)\right] dt_0\right\} \end{cases} \tag{21}$$

where constant D is the diffusivity of the aquifer [38], t is the time variable, and (x,y) are the cartesian cross- and long-shore coordinates, corresponding to the distance from ocean and estuary respectively. The operator $Re\{z\}$ denotes the real part of complex z. Coefficients k_1 and k_2 are defined as $k_1 := -(\kappa_{er}+\kappa_{ei}i)$ and $k_2 := -(\sqrt{\frac{\omega}{2D}} + \sqrt{\frac{\omega}{2D}}i)$, where $i = \sqrt{-1}$. Function f is defined in equation 22, where $erf(z) := \frac{2}{\sqrt{\pi}}\int_0^z e^{-t^2}dt$ is the Gauss error function.

$$\begin{aligned} g(\psi,\xi) \quad = \quad & \frac{y}{4\sqrt{\pi}[D(t-t_0)]^{3/2}} \times exp\left(\psi^2 D(t-t_0) + i\omega t_0 + \psi\xi - \frac{y^2}{4D(t-t_0)}\right) \\ & \times \left[1 + erf\left(\frac{2\psi D(t-t_0)+\xi}{2\sqrt{D(t-t_0)}}\right)\right] \end{aligned} \tag{22}$$

This solution is complex and non-linear due to the presence of an interaction zone where the effects of the ocean and estuary are coupled. This results with complex fluctuation patterns that can extend to several square kilometers [38], depending on the aquifer configuration. For example, the diurnal tide configuration proposed by [38] in Table 1 is used for illustration. The amplitude of the fluctuation calculated at each (x,y) location as $[\max_t(f(x,y,t)) - \min_t(f(x,y,t))]/2$ over $t \in [0,T]$, and the phase calculated at each (x,y) location as the time lag, relative to T, between the time series $f(x,y,t)$ and $f(0,0,t)$ over $t \in [0,T]$, are shown in Figure 4.

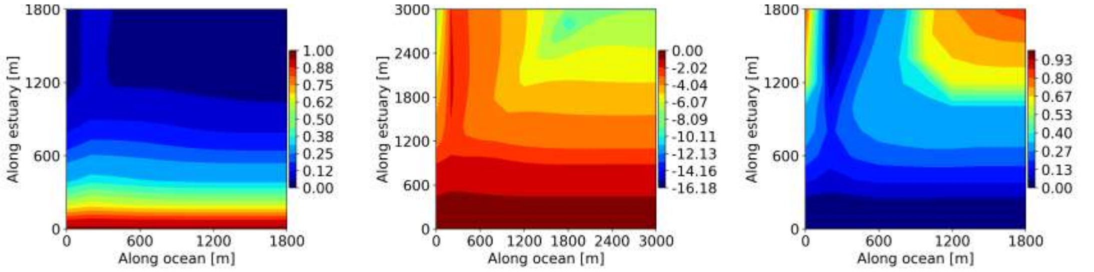

(a) Amplitude (m) (b) log-Amplitude (c) Phase

FIGURE 4: Amplitude and phase of the water table fluctuation, using the parameters proposed by [38] in Table 1.

The amplitude is decreasing through the aquifer (Figures 4-a and 4-b), and a time lag is noticed in the tidal propagation (Figure 4-c). Both the amplitude damping and time lag are increasing through the aquifer and along the estuary. It can therefore be interesting to see if the POD-PCE methodology succeeds in recovering and explaining such patterns, in particular by learning their dependency to the tidal, estuary and aquifer parameters, from a statistical sample of the solution.

In order to apply the POD-PCE methodology on the aquifer case, a statistical sample of the solution and corresponding input sample of parameters are needed. In the presented study, the tidal period T (and therefore pulsation ω) is fixed to the diurnal configuration of Li et al. [38], whereas an ensemble of realizations is generated for the remaining control parameters (A, k_{er}, k_{ei}, D). For this, Gaussian PDFs are used with mean values corresponding to the setting used by Li et al. [38], and a variation coefficient (standard deviation divided by mean) of

20%. This value corresponds to the average variation coefficient associated to optimal fitting of groundwater flow parameters performed by [70] on several cases. Indeed, the maximum variation coefficient was between 12% and 28% depending on the case. A random sample of size $n = 200$ is produced using the Gaussian PDFs (Monte Carlo), and each realization of the inputs denoted $\boldsymbol{\Theta}_{j\in\{1,\dots,n\}}$ is associated to a realization of the output by calculating $f(x, y, t)_{j\in\{1,\dots,n\}}$.

3.2 POD-PCE learning

The methodology is applied on the perturbation amplitude in the aquifer. The objective is to understand how the perturbation propagates from the boundaries, for different tidal, aquifer and estuary characteristics. The perturbations are calculated over a tidal period on a cartesian spatial grid composed of $m \in \mathbb{N}$ points, denoted $(x, y)_{i\in\{1,\dots,m\}}$. The spatial discretization step is 200 m in both directions, and the temporal step is 1 hour. The amplitude of the perturbation, denoted a', is then locally computed on each point of the grid. It depends on both the spatial location in the aquifer and the simulation parameters $\boldsymbol{\Theta}$. The solutions can be stored in a snapshot matrix as $\boldsymbol{A}'(\boldsymbol{\mathcal{X}}, \boldsymbol{\mathcal{T}}) = [a'((x,y)_i, \boldsymbol{\Theta}_j)]_{i,j} \in \mathbb{R}^{m\times n}$, where $\boldsymbol{\mathcal{X}}$ designates the spatial coordinates space and $\boldsymbol{\mathcal{T}}$ designates the parameters space. The snapshot matrix is then POD-processed as explained in Section 2.1. Therefore, at each spatial coordinate (x, y), each realization of the amplitude associated to a given parameterization $\boldsymbol{\Theta}$ can be approximated as $a'(x, y, \boldsymbol{\Theta}) \approx \sum_{k=1}^{d} a_k(\boldsymbol{\Theta})\phi_k(x, y)$, where $d \in \mathbb{N}$ is a chosen POD approximation rank.

The EVR defined in Equation 2 is calculated for each POD approximation rank. More than 99% of the variance is already captured by the first mode, and the problem is therefore highly reducible. The spatial components of the first four POD modes are plotted in Figure 5. The first mode shows a gradual damping of the amplitude in the cross-shore direction. Its spatial values are all positive and the corresponding POD coefficient is strictly positive as well.

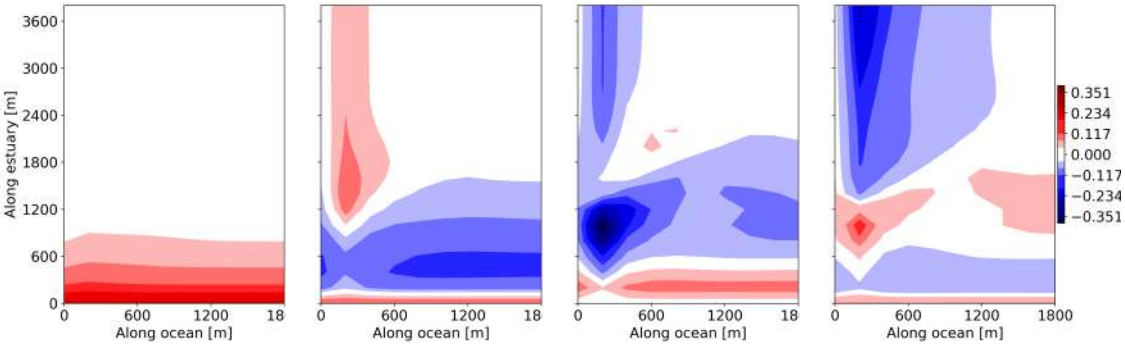

(a) Mode $\Phi_1(x, y)$ (b) Mode $\Phi_2(x, y)$ (c) Mode $\Phi_3(x, y)$ (d) Mode $\Phi_3(x, y)$

FIGURE 5: The first four spatial patterns of the POD applied to aquifer toy problem.

As the coefficient directly multiplies the spatial mode, it plays, at the same time, the role of a magnitude enhancer and a gradient intensification. Indeed, the higher the coefficient, the higher the amplitude at the ocean boundary, and the higher the difference between the latter and the aquifer amplitudes. The second spatial mode plays a regulation role, through a succession of positive and negative spatial values in the cross-shore direction. The corresponding POD coefficients are also either positive or negative. When positive, they enhance the amplitude gradient in the cross-shore direction, and the opposite occurs when they are negative. Added to that is a variation in the longitudinal direction, from the estuary onward. The third modes looks similar to the second with added spatial details, whereas the fourth mode puts more emphasis on the damping in the longitudinal direction, from the estuary onward.

A scatter plot can be used to understand the dependencies between the modes and parameters, as in Figure 6, and confirms the previous interpretations. Namely, a clear linear dependency between Mode 1 and the amplitude A is noticed. The relation of Mode 1 to damping, that is rather related to diffusivity D and estuary coefficient κ_{er}, is however not visible, although a dispersion of the mode around the linear tendency is noticed. This dispersion may be related to D or κ_{er}, even in smaller proportions, or to possible interactions, later clarified using PCE. The dependency of Modes 2 and 3 to the diffusivity D is also obvious, and the shapes indicate existing non-linearities. Mode 4 is highly dependent on the estuary amplitude damping coefficient κ_{er}, and no obvious dependency to the wave number in the estuary κ_{ei}, whatsoever, is noticed.

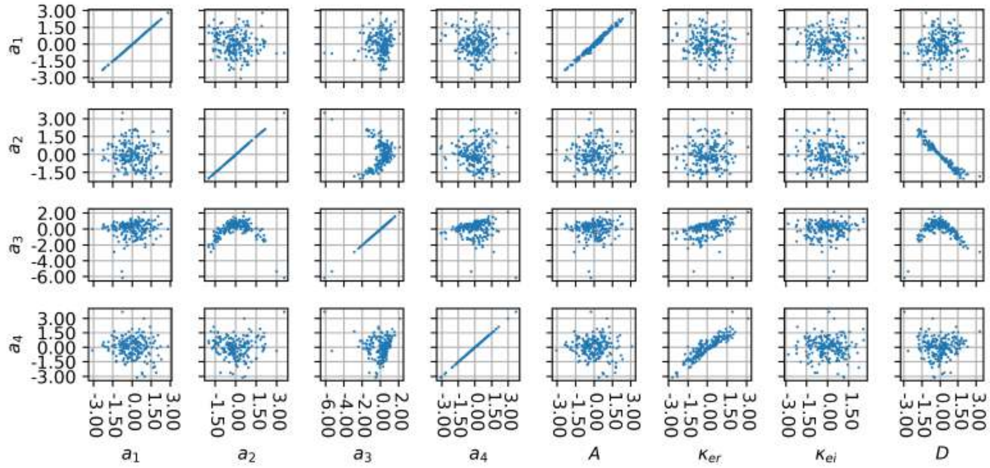

Figure 6: Scatter plot of the first four POD coefficients and control parameters of the aquifer. The variables are centered and reduced.

The dependencies that may explain the dispersion of the clouds around their main shapes need to be investigated. Hence, PCE models (theory in Section 2.2) can be used to detect additional physical relationships. They are learned from the data for each POD coefficient as $a_i = \mathcal{H}_i(\mathbf{\Theta})$, using Hermite polynomials (orthonormal basis with regards to the used Gaussian marginals). The statistical set is separated to a learning set of size 150 and a prediction set of size 50. The PCE polynomial degree is optimized for each mode separately. Degrees from 1 to 7 were tested, and the associated relative empirical errors on the training and prediction sets, respectively denoted ϵ_T and ϵ_P, were calculated as in Equation 16 . The PCE degree that minimized the training and prediction errors for each model was chosen.

The optimal PCE fitting for the first four modes shows good point-wise evaluations on the learning and prediction data-sets. PCE performs better for the modes of higher variance percentages. The smaller the variance rate, the higher the errors. Consequently, in this particular case, PCE succeeds in constructing causal models for the first four modes, but stops at an average evaluation (constant) for modes of higher ranks (smaller variance). For illustration, the prediction relative empirical errors ϵ_P of the first four modes are $6 \times 10^{-5}\%$, $4 \times 10^{-3}\%$, $9 \times 10^{-2}\%$ and $3 \times 10^{-1}\%$ respectively. At least one order of magnitude of precision is lost at each rank. The relative prediction residuals between the POD coefficient and their PCE estimation are also calculated for each sample member. For the first four modes, 90% of the absolute relative residuals are lower than $1 \times 10^{-2}\%$, 6.9%, 5.65% and 37.9% respectively.

The good performance of PCE encourages its use for POD-PCE prediction, as well as for physical interpretation. Firstly, in order to choose the adequate number of POD modes for the full model, the errors generated by the various steps of the algorithm (POD, PCE and coupling) are analyzed. To do so, the mean relative RMSE (averaged over the prediction set, as in Equation 18) was calculated for each step and for each approximation rank d, as follows:

- *Reduction error:* distance between the POD approximation $\sum_{k=1}^{d} a_k \mathbf{\Phi}_k(x, y)$ and the corresponding amplitudes two-dimensional field $\mathbf{a}'(x, y, \mathbf{\Theta})$;
- *Learning error*: distance between the POD approximation $\sum_{k=1}^{d} a_k \mathbf{\Phi}_k(x, y)$ and the prediction using the POD-PCE coupling formulated as $\sum_{k=1}^{d} \mathcal{H}_k(\mathbf{\Theta})\mathbf{\Phi}_k(x, y)$;
- *Prediction error:* the resulting final error between the prediction using POD-PCE coupling and the corresponding amplitudes two-dimensional field $\mathbf{a}'(x, y, \mathbf{\Theta})$.

The results are shown in Figure 7 . Reduction error decreased from 3.8% at rank 1, to $9.5 \times 10^{-2}\%$ at rank 4. The decrease is exponential, with a stabilization starting from rank 4. The learning error increased from $8.8 \times 10^{-3}\%$ at rank 1 to $4.1 \times 10^{-2}\%$ at rank 4, which is related to the increase in the PCE prediction error of the POD modes coefficients. In fact, a prediction of rank $d+1$ has an additional temporal coefficient that is predicted as compared to rank d. It is therefore natural that the distance between the approximation $\sum_{k=1}^{d} a_k(\boldsymbol{\Theta})\phi_k(x,y)$ and its prediction $\sum_{k=1}^{d} \mathcal{H}_k(\boldsymbol{\Theta})\phi_k(x,y)$ increased with increasing rank. The learning error order of magnitude keeps however low. Hence, the prediction error trend is almost identical to reduction error, decreasing from 3.8% at rank 1 (identical to reduction error) to 1×10^{-1}% at rank 4, where it stabilizes. It is the balance of, on the one hand, the increase in accuracy by adding POD modes and, on the other hand, the increase in forecasting error with increasing number of POD coefficients to be predicted. Hence, a 4-Modes POD-PCE model was selected for prediction.

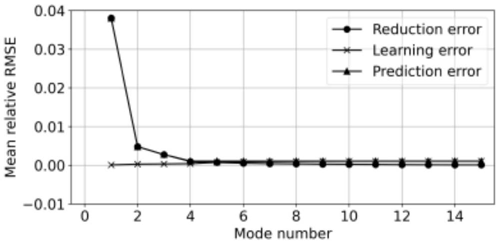

FIGURE 7: Mean relative RMSE generated at different steps of the POD-PCE ML applied to the aquifer case, with different approximation ranks.

An example of prediction is shown in Figure 8. The model gives good qualitative estimation of the two-dimensional amplitude distribution along the estuary and through the aquifer. Slight differences may be noticed however between the analytical solution and POD-PCE prediction. Namely, the absolute residuals can go up to 0.002 m, but this occurs, for example in Figure 8-c, in a zone where the amplitude is 0.3 m, which represents a local error of 0.7%.

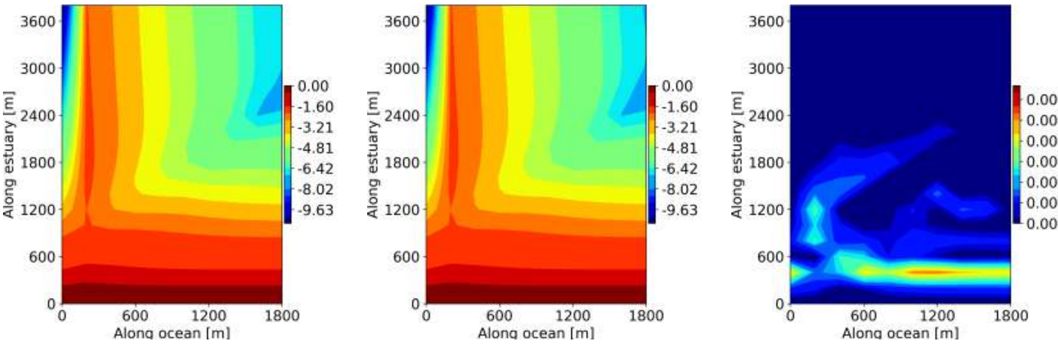

(a) Analytical (b) POD-PCE (c) Absolute residual

FIGURE 8: Analytical solution vs. POD-PCE prediction of the aquifer's log-amplitude in meters, and resulting absolute residual of the amplitude.

The fitted PCE models for the first four POD modes were used to rank and analyze the physical contributions. To do this, the *Garson Weights* (GW) and *Generalized Garson Weights* (GGW), respectively presented in Sections 2.2 and 2.3, were calculated for each polynomial term. The indicators values are shown in Appendix A, Table 1. The GW results confirm the great dependency of Mode 1 on the tidal amplitude A (85%), and a dispersion mainly caused by the diffusivity D (11%). Mode 2 and Mode 3 are principally dependent on the diffusivity D, and the noticed dispersion is related to the interaction of the diffusivity D with the tidal amplitude A in Mode 2 (15%), whereas it is explained by the tidal damping in the estuary κ_{er} for Mode 3 (19%). The main variation of Mode 4 is captured linearly around κ_{er}. The GGW show that the most important parameter is the tidal amplitude, with a total of 80% of influence (without interactions), followed by the diffusivity (more than 15% without interactions). The main dynamics (a total of 93%) are explained by first degree monomials. This means that the non-linearities are represented in the spatial POD patterns. Simple interactions expressed by second degree polynomials are then added to complete the dynamics, as well as other non-linear contributions, for example second to third degree monomials of the diffusivity D.

The same strategy is adopted to learn the phase, or time lag between $p(x, y, t)$ and $p(0, 0, t)$, in Appendix A. The model is optimal when 3 POD modes are used, stabilizing around a 6% prediction error. It gives a good mapping of the two-dimensional time lag distribution in the aquifer, even though more important differences between the analytical solution and the prediction are noticed compared to the amplitude prediction. The error can locally go up to 25%, but the global performance of the model remains satisfying. Lastly, calculation of GW and GGW indicators shows that the phase problem involves higher polynomial degrees, and higher orders of interaction. Additionally, the wave number in the estuary κ_{ei}, which did not appear as an influencing parameter for the amplitude distribution, is necessary for the phase representation.

3.3 Robustness to noise

In this section, three noise levels (1%, 10% and 20%) are added to the data in order to evaluate the POD-PCE methodology. Perturbations are directly added to the $2D$ amplitude distributions in the aquifer. For each realization of the latter, the local value at a given location is perturbed using a zero-mean Gaussian PDF (white noise), with a standard deviation calculated as the average local value over the ensemble, multiplied by the chosen noise level percentage.

The EVR are compared for the different noises in Figure 9-a. The represented variance is smaller with the same approximation rank for the noisiest data. This is natural because the variance of the random Gaussian noise is added, and the highest the noise level, the more it is statistically important. Hence, the POD modes are either impacted with random dispersion, or are totally random. A scatter plot, where the modes at different noise levels are plotted against the original modes without noise, is shown in Figure 10, where dispersion is clearly visible.

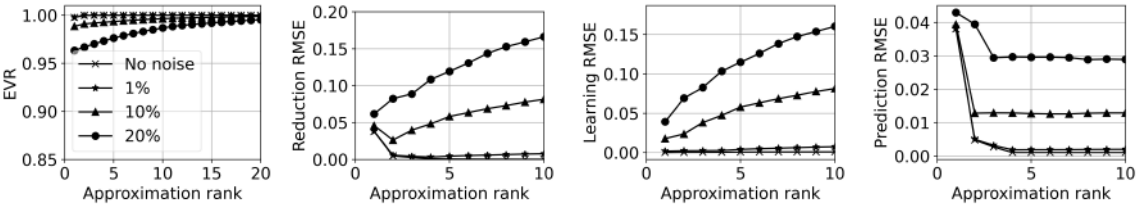

(a) EVR (b) Reduction RMSE (c) Learning RMSE (d) Prediction RMSE

FIGURE 9: EVR and POD-PCE steps RMSE with different noise levels added to the aquifer toy problem.

The perturbed data are then used to evaluate the POD-PCE methodology. The reduction, learning and prediction average RMSE are calculated for each approximation rank as previously described in Section 3.2. The results are shown in Figures 9-b, 9-c and 9-d respectively. A difference in the calculation should be noted however: for the reduction and prediction steps, the RMSE are evaluated between the original field (without noise), and the approximation resulting from the noisy field. For reduction for example, if the original field is denoted $\mathbf{a}'(x, y, \mathbf{\Theta})$ and the noisy field is denoted $\mathbf{b}'(x, y, \mathbf{\Theta})$, the POD approximation $\sum_{k=1}^{d} a_k \mathbf{\Phi}_k(x, y)$ is deduced from realizations of $\mathbf{b}'(x, y, \mathbf{\Theta})$, but the RMSE is calculated between $\sum_{k=1}^{d} a_k \mathbf{\Phi}_k(x, y)$ and the original field $\mathbf{a}'(x, y, \mathbf{\Theta})$ that represents the "truth".

Firstly, it can be noticed in Figure 9-b that the higher the noise, the more difficult the reduction. This is coherent with the previous EVR analysis. Additionally, while reduction error decreases with the mode number up to 1% of noise, it may increase with the mode number for higher noise levels. Indeed, when noise perturbs the modes, adding them to the approximation may move the resulting field away from the "truth" (original field without noise). Secondly, Figure 9-c shows that learning is more difficult with noisy data. In fact, if the higher rank modes are purely random, then it is impossible for PCE to provide a causal model from the inputs. If a given mode contains a physical information and a random perturbation at the same time (dispersion in Figure 10), PCE may succeed in capturing the physical dependencies, and is shown to be robust up to 30% of noise in [67]. However, in both cases, the PCE expansion does not represent pure randomness and the learning error naturally increases with the noise level.

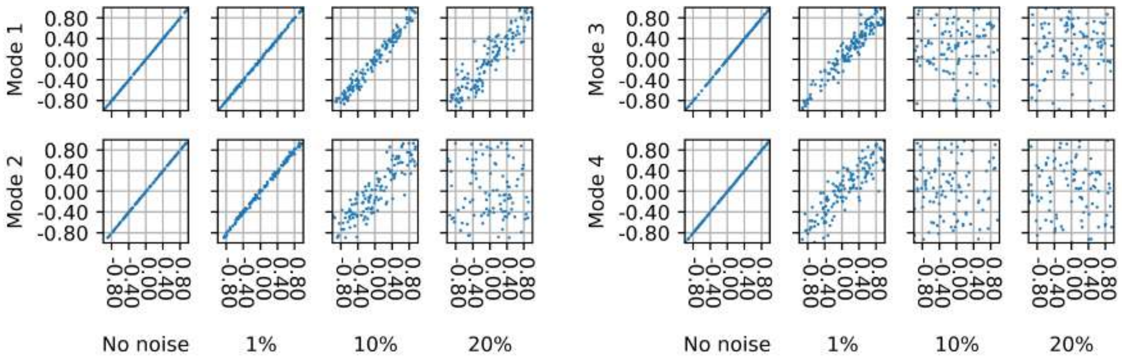

(a) Modes 1 and 2

(b) Modes 3 and 4

FIGURE 10: Original vs. noisy POD modes resulting from $2D$ perturbations. The plotted data are centered and reduced.

Lastly, for the prediction RMSE (Figure 9-d), the 1% and 10% noisy data perform similar to unperturbed ones, where prediction error follows the same decreasing trend as reduction error, then stabilizes to a minimal value where learning is not interesting anymore. Conversely, for the 20% noise level, prediction error decreases from Mode 1 to 3 although reduction error increases. This can be explained by the fact that PCE succeeds in detecting the physical patterns (explainable with inputs), while eliminating the noise from the approximation. Adding the PCE models to the POD-PCE prediction, contribute in the constitution of realistic physical fields (prediction error decrease), while directly adding the noisy POD modes moves the approximation away from the "truth" (reduction error increase).

As a conclusion, even with a maximum of 20% of added noise, a POD-PCE model of rank 1 that could be considered as the simplest approximation, does not exceed an average of 5% RMSE compared to the "truth" for the amplitude prediction. The most optimal model in this case decreases to 3% of RMSE.

3.4 Summary of the POD-PCE ML performances on a toy problem

The proposed POD-PCE ML approach was applied to this toy problem for different motivations. Firstly, the coherence of physical interpretation needed to be confronted to reality for validation, which is here possible due to the availability of analytical solution. Secondly, demonstrating the proposed ML capacity on a parametric problem is complementary with the application to a temporal problem, as in Section 4, and allows at the same time clarifying the learning steps on a simpler case. Lastly, assessing the robustness of the methodology to noise was a capital question to investigate, and here made possible by adding artificial perturbations of different levels to the data.

Firstly, the POD spatial patterns were interpretable, and the associated coefficients show dependencies to the control parameters. The physical analysis was completed using PCE and inputs ranking indicators (GW and GGW). For example, it is noticed that while the wave number in the estuary, denoted κ_{ei}, has no influence on the amplitude distribution, it controls however the time-lag in the aquifer (see Appendix A). This completely makes sense regarding the analytical formula. Next, the errors at the different POD-PCE algorithm steps were analyzed. While a gain in accuracy is established by increasing the POD modes number in the reduction phase, the learning error using PCE is inversely increased with model complexity. However, only a small number of modes is necessary for an accurate prediction, as the average RMSE for the optimal 4-Modes model is around 0.1%, reaching a local maximum of 0.7% for the amplitude. Lastly, robustness to noise was tested using different perturbation levels. The prediction's average RMSE settles around 3% even for a noise level of 20%. PCE with LARS is here of particular interest, as it allows incorporating physical dependencies in the model, while ignoring random perturbations. This assures that the method is trustworthy for an application to a purely measurement-based set-up, as in the following Section 4.

4 Application to a measurement based temporal problem

The POD-PCE ML properties are now investigated on a temporal problem. In particular, the approach is tested on field measurements, introduced with an industrial study case and inherent challenges. As is the case in many measurement based problems, noise can occur due to device errors, and the problem is characterized with data paucity. The noise problematic was treated in Section 3 on the parametric problem. However, the data paucity was not an issue, and supplementary tests are here necessary. They consist in the evaluation of learning choices (selected inputs, marginals, polynomial basis) and thorough analysis of the statistical convergence at different learning stages. The latter is of capital importance to demonstrate the trustworthiness of the physical analysis, as no analytical model is available to confront the conclusions. In particular, convergence as a function of the training set size, with associated confidence intervals, is shown in Subsection 4.2.1 for POD and in Subsection 4.2.2 for PCE. Additionally, different learning set-ups, with different marginals choices and input configurations are compared in Subsection 4.2.2. Lastly, random selection of the training members allows presenting probability distributions of the GW indicators in Subsection 4.2.2. This helps demonstrating the robustness of physical interpretation to the learning set selection.

The physics, data and industrial context are described in Subsection 4.1. Subsection 4.2 deals with application of the POD-PCE learning phase to the data and assessment of accuracy and robustness with respect to the numerical choices (data set, inputs, marginals and polynomial basis). Finally, the prediction phase using POD-PCE is dealt with in Subsection 4.3, and the ability of the proposed ML to predict mean quantities and spatial details is demonstrated.

4.1 Study case

Sedimentation processes in nearshore areas can be responsible for the excessive sediment deposition commonly observed in cooling water intakes in power plants. As a result, the carrying capacity of the water intake can be drastically reduced, by decreasing its effective area of transport [61]. Cooling water intakes usually incorporate jetties, of which the angle with the shoreline and position relative to the direction of the net longshore sediment transport influence the amount of sediments diverted into the channel inlet by waves and tidal currents. Jetties also reduces littoral drift, resulting in localized sediment accretion against the shore-normal structure due to the longshore sediment transport being trapped by the jetty [9]. In addition, a return current is prone to develop, in the form of a swirling vortex at the end of the structure, and can induce sediment deposition in the vicinity of the channel entrance, consequently affecting the amount of sediments delivered into the cooling water intake [6]. Consequently, effective water intake management involves frequent dredging, with high operational costs and usually hindered by a tight schedule. It is then necessary to assess intake sedimentation under different natural forcing and plant operation scenarios in order to optimize dredging operations to help mitigate the potentially adverse impact of the waves, tidal currents, and meteorological forcing combined with plant functioning.

Site characteristics

The study site is located on the eastern English Channel coast in northern France. Tide in the study zone is classified as mega-tidal and is dominated by semi-diurnal circulation, with low-tide water depth of $10 - 15$ m, and a mean tidal range of approximately 8.5 m, reaching 10 m during the spring tide [33]. Hydrodynamics are influenced by asymmetrical current velocities, with flood and ebb currents in the E-NE and W-SW directions, respectively. Current velocity at 2.2 m above seabed vary from 0.70 to 0.98 m/s, depending on flood/ebb phase, respectively [40]. Wave activity in this open exposed environment is moderate, with significant annual and decennial wave height of 3.8 m and 4.7 m, respectively, with maximum values of $4.2 - 5.8$ m, averaged period of $7 - 9$ s and a predominant W direction. Orbital velocities measured during the spring-tide period ranges between 0.5-1.3 m/s. An example of tidal levels, wind direction and velocity and wave height and direction in January 2016 is shown in Figure 11 . In the study area, bed sediment varies from medium to fine silted sands, with a morphology characterized by the presence of mega-rides parallel to the coast. In this zone, rock occupies less than 4% of bed surface [6].

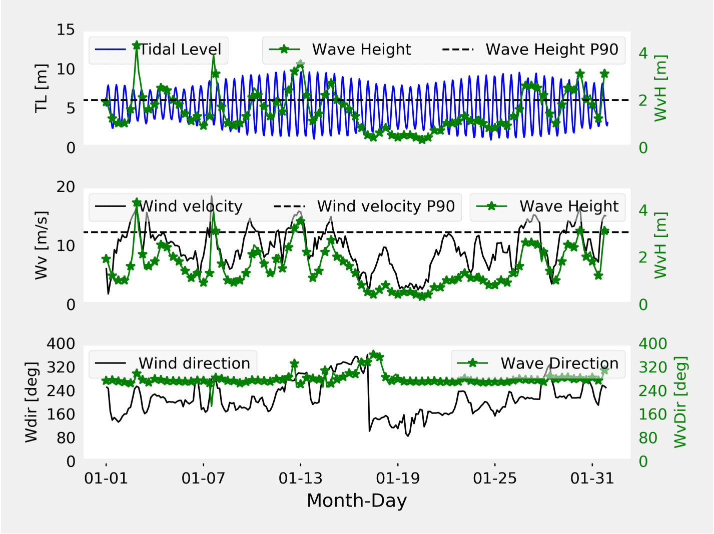

FIGURE 11: Measurements of Tidal Level (TL), Wind velocity (Wv), Wind direction ($Wdir$), Wave Height (WvH) and Wave Direction (WvD) on January 2016. (P: Percentile).

Data

Hydrodynamic and meteorological information comprise wave and wind variables, provided by the VAG prediction model of the sea state [16], using retrospective 3-hourly simulations between 2009 and 2018. Tidal water levels were obtained from the SHOM-REFMAR tide gauge station located in the vicinity of the study zone, with hourly survey frequency [52]. Bathymetric measurements were available from Single-Beam Echo Sounding on 39 cross-sectional profiles of intake measured at 25 m intervals, collected fortnightly between 2005 and 2018. Mean profiles were 100 m long with 0.5 m spatial resolution of bathymetric data. Additional information such as the daily coolant flow rates, and channel dredging volumes and frequency, were provided by the plant operator.

The available measurements of the forcings did not have the same frequencies. One solution to homogenize frequencies consists in reducing the measured data to representative statistics over the sedimentation interval $\Delta t \approx 15\ days$ separating two bed elevations measurements. Hence, the following statistics were used:

- *Tidal level indicators:* average low tide ($TLmean$), minimum low tide ($TLmin$), maximum tidal range ($TLrange$) and standard deviation ($TLstd$) ;
- *Wind indicators:* average wind velocity ($Wmean$) and average direction weighted by velocity ($Wdir$) ;
- *Wave indicators:* average wave height (WvH), standard deviation ($Wvstd$), average wave period and average wave direction weighted by height (*resp.* $Wvper$ and $Wvdir$), average wave height exceeding the 90^{th} percentile (arbitrary storm indicator, $Wv2m$) and percentage occurence ($Wv2m\%$) ;
- *Operational indicators:* average pumping flowrate (Qmean) ; time lapse since last dredging (Dp), and last dredged volume (Dv).

These statistical indicators were calculated for each sedimentation interval, and may be characterized with correlations. For example, a positive correlation was noted between mean low tide $TLmean$ and wave parameters $Wvper$ and WvH. Mean wave periods $Wvper$ and mean wave heights WvH were also positively correlated.

For the learning part, the data overlapped only over a limited period. A maximum of 60 measurements could therefore be used, with up to 15 forcing variables. Obviously, this "small data" configuration is a considerable handicap for the dimension of the problem, especially given that the variable of interest is a two-dimensional bathymetric field. However, permanent intake monitoring ensures that the data set will always grow and can be used to update the learning. This limitation shall not prevent testing the accuracy of the methodology on small sets such as are often encountered in physical applications, as attempted below, where learning and prediction using POD-PCE is applied to the described data. For the learning algorithm, input variables are needed, corresponding to the reduced statistical indicators described above, and denoted $(\theta_1, ..., \theta_V)$, where V is the supposed dimension of the problem.

4.2 Measurement-based learning of a physical field using POD and PCE

This section concerns learning the spatio-temporal bathymetric field using POD and PCE independently. The POD modes are extracted in Subsection 4.2.1 and the temporal patterns are learned from the forcing parameters using PCE in Subsection 4.2.2. Throughout this investigation, particular attention is given to the convergence of the learning and to its robustness with respect to the numerical choices. Trusted POD-PCE learning is immediately used for physical interpretation and the most important physical insights are summarized in Subsection 4.2.3.

4.2.1 Physical analysis and data reduction using POD

First, POD was applied on the bathymetry measurements. The aim was to identify morphodynamic patterns so as to better understand the sediment deposition inside the channel, and to characterize variations in depositions with the external forcing variables. After setting aside poor-quality measurements (e.g. incomplete bathymetries), a total $n = 156$ realizations were used. The bathymetry points were sonar boat measurements on $m_p = 39$ cross-sections inside the intake. Linear interpolation was performed on $m_i = 100$ fixed points for each profile, in order to express all measurements on the same grid, giving a total $m = m_i \times m_p = 3,900$ spatial points. The interpolated realizations were then stored in a snapshot matrix $\boldsymbol{Z}(\boldsymbol{\mathcal{X}}, \mathcal{T}) = [z(x_i, t_j)]_{i,j} \in \mathbb{R}^{m \times n}$ and POD-processed as explained in Section 2.1. The EVR defined in Equation 2 and the mean relative RMSE between the POD approximation and the complete measurement (averaged over the realization set as in Equation 18) were calculated for each POD approximation rank and are plotted in Figure 12.

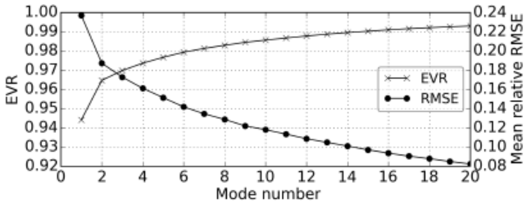

FIGURE 12: Evolution of the EVR and mean relative RMSE with mode number for the POD applied to the intake bathymetries.

The first pattern represents over 94% of the variance, and explains most of the variation in dynamics. The variance percentage reached 99% at rank 14, where the mean error was slightly over 10%, decreasing to 8% at rank 20. Dimensionality reduction is therefore a realistic option for this specific problem

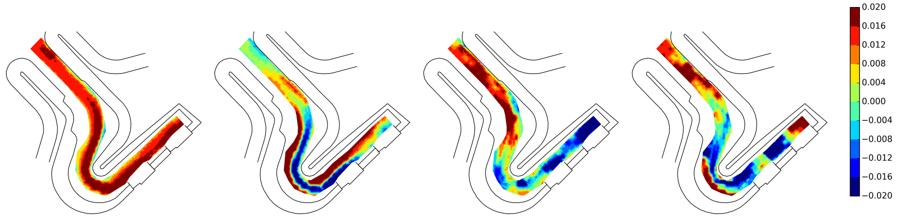

(a) Mode $\Phi_1(x)$ (b) Mode $\Phi_2(x)$ (c) Mode $\Phi_3(x)$ (d) Mode $\Phi_4(x)$ (e)

FIGURE 13: The first four spatial patterns of the POD applied to intake bathymetries.

This encouraged the learning and prediction attempts undertaken in Subsections 4.2.2 and 4.3 respectively. The spatial and temporal components of the first four POD modes corresponding to an EVR higher than 97% are respectively plotted in Figures 13 and 14. The first spatial pattern (Figure 13-a) represents the channel's slope. Its temporal coefficient (Figure 14-a) shows regularity in time that is almost periodicity. When it increased, overall sediment deposition in the channel increased, because the difference between the upstream and the downstream bed elevations, and therefore the slope, diminished. The sediment deposition in the channel might be related to the increasing sediment supply caused by the external forcing influence. Decrease always corresponded to a dredging episode. The apparent periodicity is therefore not natural or seasonal but due to periodicity of operational intervention: sediment deposition in the channel is tolerated up to a certain level and then dredging is always undertaken at a certain point, which corresponds to the maximum of the temporal coefficient.

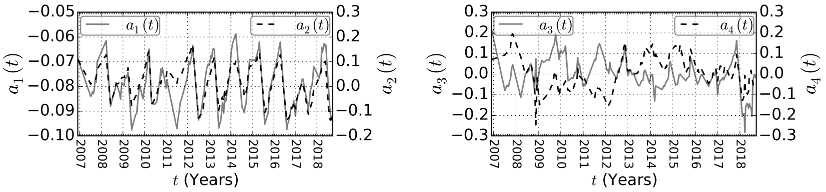

(a) Coefficients $a_1(t)$ and $a_2(t)$ (b) Coefficients $a_3(t)$ and $a_3(t)$

FIGURE 14: The first four temporal coefficients of the POD applied to intake bathymetries.

The second pattern (Figure 13-b) acts as a geometric distribution function of the sediment deposition. In general, when the first temporal coefficient was maximal, the second coefficient was positive, meaning that the sedimentation mainly occurred in the middle of the first portion of the channel (upstream), on the right bank of the bend and on the left bank in front of the pumps. This spatial distribution can be associated to the internal flow characterized by a velocity distribution inside the channel. In fact, the sediments settle where velocity is the lowest, which is probably the case where the banks appear. The computed sediment deposition and erosional patterns are analogous to those commonly observed in meandering rivers [23]. The third pattern (Figure 13-c) shows sediment deposition concentrated in the first portion of the intake, and the fourth pattern (Figure 13-c) emphasizes sediment dynamics, particularly in the downstream part of the channel. This behavior is statistical proof and quantification of finer sediment supply. The finer sediment fraction was transported in suspension and deposited at the end of the intake channel. The temporal coefficients associated with the third and fourth mode (Figure 14-b) were less regular than those of the first and second mode, and seemed to follow a more stochastic dynamic. The peaks may represent unusual sediment supply, probably linked to extreme events (e.g. storms).

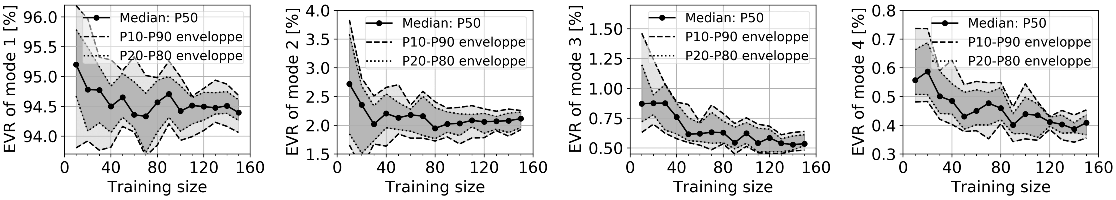

(a) Mode 1 (b) Mode 2 (c) Mode 3 (d) Mode 4

FIGURE 15: EVR convergence of the first four bathymetry POD modes, using a bootstrap of size 20. Plots show median values and confidence intervals (P: Percentile).

To check the robustness of the statistical conclusions deduced from POD, convergence analysis is necessary. This was performed on the EVR values associated with the first four patterns, using bootstrap analysis [11]. The results are shown in Figure 15. The convergence of the mean values and the tightening of the confidence intervals around the mean with increasing matrix size are clear for these first four modes. However, whereas the confidence intervals represent at most an error of ±0.6% around the mean for the first mode, they reached respectively ±12.5%, ±25% and ±12.5% for the second, third and fourth modes.

The analysis proved that the POD results could be used to pursue the learning. Firstly, a high EVR and low RMSE were associated with a small number of modes, guaranteeing optimal data reduction ($d << min(m, n)$ as explained in Section 2.1). The number of POD modes to accurately represent the bathymetry can be chosen accordingly. In the present study, the configuration was $d = 11$ modes (discussed in *Step 3*), guaranteeing EVR $\geq$ 98% and information loss $\leq$ 12% (mean relative RMSE). Secondly, the EVRs were guaranteed to converge statistically at least for the first four modes, with error of ±0.6% around the mean for the most important mode, representing over 94% of the variance. Thirdly, the deduced patterns were physically coherent. Lastly, more than a decade of evolution was used to extract the POD basis, under variable operational and environmental conditions. As long as the operating conditions of the intake remained unchanged, it can be assumed that a wide range of evolutions has been covered, except for extreme events that rarely occur and that are not specifically treated in this study [15]. Hence, the POD basis can be considered as a physically trustworthy and mathematically complete basis to understand past evolutions and to predict future ones. The learning of temporal coefficients is therefore attempted in Subsection 4.2.2.

4.2.2 Learning of the POD patterns using PCE

The temporal coefficients calculated with the POD in Section 4.2.1 (Figure 14) were learned using PCE (theory in Section 2.2). The aim was to learn the way these coefficients evolve over time, as a function of the forcing parameters presented in Section 4.1 , with the ultimate objective of field prediction as explained in Section 2.3 and applied in Section 4.3. The present section focuses strictly on the learning phase and the physical analysis of the learned model, highlighting quality of learning (robustness, convergence, etc.).

The investigation of learning is organized in four steps.

- *Step 1 - Sensitivity of learning to inputs and marginals:* different configurations were tested to practically demonstrate the implications of these choices on the accuracy of fit.
- *Step 2 - Convergence and Robustness of fit:* The best model resulting from Step 1 was studied more deeply. Its convergence and robustness with respect to the choice of training members are were analyzed.
- *Step 3 - Physical interpretation of the best learned model:* the best model was chosen, and the most influential forcings were ranked using the *Garson Weights* (GW) and *Generalized Garson Weights* (GGW) presented in Sections 2.2 and 2.3 respectively.
- *Step 4 - Robustness of the physical interpretation with respect to the learning-set members:* the physical conclusions of the model were shown to be statistically meaningful.

These steps, in the above order, follow the logic of statistical model construction to build a trustworthy prediction algorithm, used in Section 4.3.

Step 1 - Sensitivity of learning to inputs and marginals
Input variable selection is capital, and marginals must be chosen wisely. Below, we demonstrate the influence of these choices on the performance of the learning. Different configurations were tested.

Before introducing the tested configurations, the training steps that are common to all configuration need to be defined. A learning data-set is classically separated into different sub-sets, corresponding to different steps of the learning algorithm. This is commonly referred to as the "Train-Validation-Test Split" [58]: a training set is used for the learning, a validation set is used to check the learning and for further calibration, and a test set is used to assess the prediction capability of the statistical model. However, the data-set used in this study was small: the bathymetry and forcings measurements shown in Subsection 4.1 overlap for the 2012-2017 period only, leaving 64 sedimentation periods to study. Therefore, only a "Train-Predict" split was performed, where the prediction set played the role of both the test set and validation set. Hence, the numerical choices were calibrated on the training set, and validated on the prediction set for both statistical accuracy and physical prediction. The learning was then performed with an arbitrary choice of training-set size at 50, which left a prediction set of 14. The training data were chosen in chronological order (first 50 records), to mimic the learning process in an industrial context. This arbitrary training-set choice had consequences for learning; the sensitivity of learning to training set choice was investigated (*Step 2*). All the model choices presented below (choice of inputs and marginals) were assessed on this training configuration. To assure that comparison is made between models at their best performances, the PCE polynomial degree was optimized for each separately. Degrees from 1 to 7 were tested, and the associated relative empirical errors on the training and prediction sets, respectively ϵ_T and ϵ_P, were calculated as in Equation 16 . The PCE degree that minimized the training and prediction errors for each model was chosen; the corresponding result is referred to as "optimal" learning.

Three different input configurations were used for the learning of each temporal coefficient a_i as generally formulated in Equation 11 .

- $\mathcal{H}_i$-model: a first simple configuration where all the statistical indicators described in Subsection 4.1 were used and an independence hypothesis between the POD temporal coefficients is considered. The model is written as in Equation 13 : $a_i(t_{j+1}) \approx \mathcal{H}_i\left[a_i(t_j), t_{j+1} - t_j, \mathbf{\Theta}(t_j \to t_{j+1})\right]$. This is a model of dimension 17.
- $\mathcal{H}_i^F$-model: a more complex configuration where a "Full" 15-mode POD approximation is considered with possible dependencies between the temporal coefficients. Of course, the choice of the basis size and the dependency structure can be optimized, but the objective here was to make a first step toward a more optimal configuration. The model can be written as: $a_i(t_{j+1}) \approx \mathcal{H}_i^F\left[a_1(t_j), \ldots, a_{15}(t_j), t_{j+1} - t_j, \mathbf{\Theta}(t_j \to t_{j+1})\right]$. This is a model of dimension 31.
- $\mathcal{H}_i^P$-model: a smaller set of inputs, used by the operators to qualitatively evaluate sediment deposition risk, was used. It corresponds to the six variables $TLmean$, WvH, $Wvper$, $Wvdir$, $Wv2m$ and $Wv2m\%$.

This mimics the physical expertise that may be engaged when building a statistical model. It is written as $a_i(t_{j+1}) \approx \mathcal{H}_i^P\left[a_i(t_j), t_{j+1}-t_j, \boldsymbol{\Theta^P}(t_j \to t_{j+1})\right]$, where $\boldsymbol{\Theta^P}$ stands for the "physical". This is a model of dimension 8.

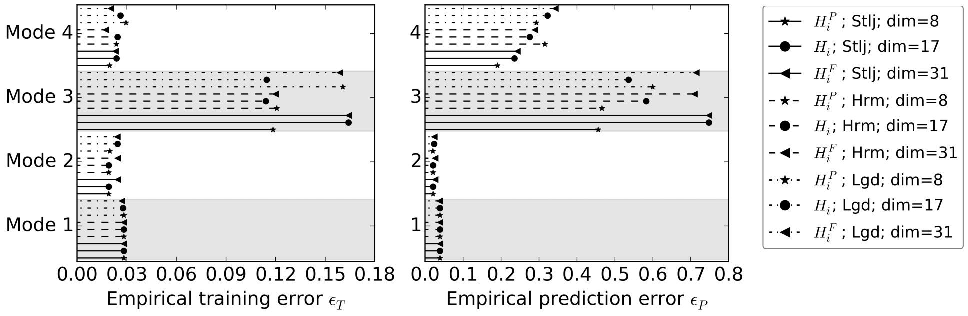

(a) Training error (b) Prediction error

FIGURE 16: The empirical training error ϵ_T and prediction error ϵ_P corresponding to the optimal fitting of models with different dimensions and marginals. The figure is organized as follows: errors are plotted for each mode vertically, separated by a gray band. Each marginal type corresponds to the same line style, and each dimension to the same marker style. The legend is shown in the order of the plots, down to top for each mode.

To these variable choices were associated three choices of marginals, conditioning the choice of the PCE orthonormal polynomial (Section 2.2).

- *Lgd:* all the variables follow a Uniform PDF. The bounds of the marginal were set to the minimum and maximum chronological values ±1% as in [67]. The associated orthonormal polynomial basis is the Legendre family.
- *Hrm:* all the variables have Gaussian marginals characterized by the empirical mean and variance deduced from the data. The associated orthonormal polynomial basis is the Hermite family.
- *Stlj:* the marginals were inferred from the data using Gaussian Kernel density estimates. The orthonormal polynomial basis was constructed from the knowledge of the marginal using a Stieltjes orthogonalization.

The three marginal choices *(Lgd, Hrm, Stlj)* were trained with the three dimension choices ($\mathcal{H}_i^P$ dim=8, $\mathcal{H}_i$ dim=17, $\mathcal{H}_i^F$ dim=31). The empirical errors of the "optimal" learnings are compared in Figure 16 . For Modes 1 and 2, training and prediction errors were almost identical for all configurations, although with a slight advantage with the smallest dimensions for all the marginal types in the learning of Mode 2. Starting from Mode 3, bigger differences emerged. At the learning step of Mode 3, models of dimension 17 and 31 were poorly fitted for the *Stlj* and *Lgd* configurations compared to others. At the prediction step of Mode 3, the errors of models with dimension 31 were much greater than smaller dimensions for all marginal choices. There seemed to be an overfitting of the model by selecting a larger number of inputs. The best models for Mode 3 were those of the smallest dimension, 8, with either the *Stlj* or the *Hrm* model. Lastly, for Mode 4, two orderings were observed for the prediction error. Firstly, for each marginal choice, prediction error increased with dimension, which confirmed the overfitting hypothesis. Secondly, error was the smallest with the *Stlj* model (Kernel density), followed by the *Hrm* model (Gaussian) and lastly by the *Lgd* model (Uniform). Here, Uniform marginals performed worst ; they were probably too different from the real data marginals and did not account for particularities in the inputs. In the parametric family, Gaussian marginals probably fitted real density better.

To conclude this comparison, the best marginal choice was the Kernel density estimate. The smallest dimensions performed the best, with the *Stlj* choice for the polynomial basis. The $\mathcal{H}_i^P; Stlj$ model of dimension 8 was therefore selected. However, the training was performed with an arbitrary split of the available statistical set. The sensitivity of the model to the learning set size and members is performed in the following step.

Step 2 - Convergence and robustness of the fit

Up to this point, an arbitrary number of 50 measurements was used for training, leaving 14 prediction points for testing purposes. In the following, the influence of training set size on the learning and prediction error is assessed. The objective is to check the robustness of the previous best model $\mathcal{H}_i^P; Stlj$ with respect to the data-set size and members. The evolution of the training and prediction empirical errors according to training set size is shown in

Figure 17 and 18 respectively. For comparison, the convergence of the $\mathcal{H}_i^P; Hrm$ model for Mode 3 is also shown for both errors. For each training set size, members were chosen randomly among the full data-set, and the remaining members were used for the prediction phase. For the estimation of the confidence intervals, bootstrap analysis was performed [11].

For the first two modes, the training errors in Figure 17 show a convergence of the median value and a tightening of the confidence intervals. The trainings can be considered as converging from around training size 40.

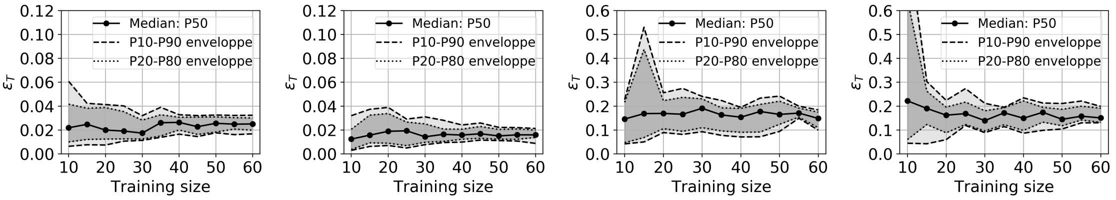

(a) Mode 1 - Stlj (b) Mode 2 - Stlj (c) Mode 3 - Stlj (d) Mode 3 - Hrm

FIGURE 17: Training empirical errors ϵ_T calculated for diverse training sizes with a Bootstrap of size 20. Plots show median value and confidence intervals (P: Percentile).

The associated median prediction errors in Figure 18 globally decreased with increasing training set size. However, although the final median values were lower for the *Hrm* model, the confidence intervals were much larger than for the *Stlj* model. The latter seems much more robust with respect to changes in training scenario.

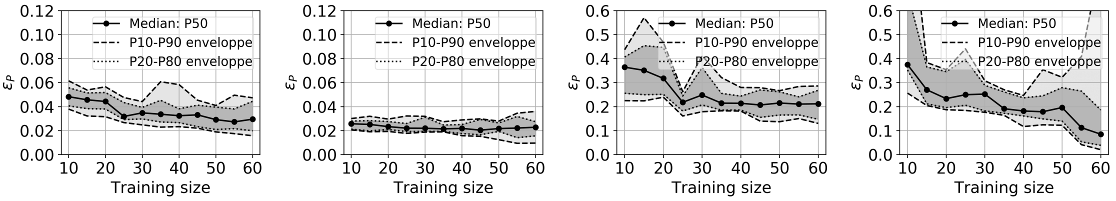

(a) Mode 1 - Stlj (b) Mode 2 - Stlj (c) Mode 3 - Stlj (d) Mode 3 - Hrm

FIGURE 18: The prediction empirical errors ϵ_P calculated for diverse training sizes with a Bootstrap of size 20. Plots show median value and confidence intervals (P: Percentile).

The residuals distributions of the $\mathcal{H}_i^P; Stlj$ model, calculated as $a_i(.) - \mathcal{H}_i^P[.]$ on all the training sizes and Bootstraps, are shown in Figure 19 and Figure 20 for training and prediction, respectively.

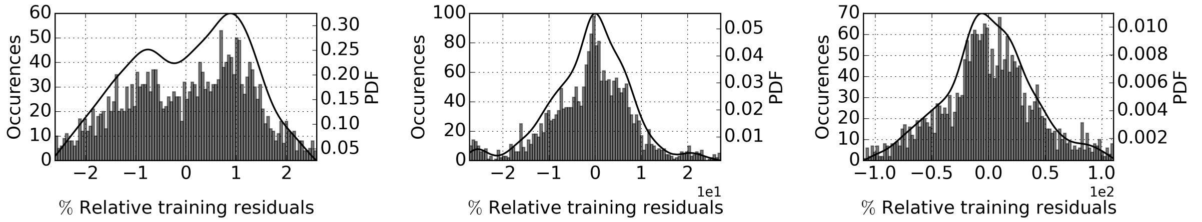

(a) First mode $a_1(t)$ (b) Second mode $a_2(t)$ (c) Third mode $a_3(t)$

FIGURE 19: The training residuals distributions of the $\mathcal{H}_i^P; Stlj$ model calculated for diverse training sizes with a Bootstrap of size 20.

Only the middle 80% portion of the residuals range is plotted, in order to analyze the center of the distribution ; the full residuals distribution was long tailed, because the confidence intervals associated with small training set sizes were too large and produced extreme behaviors of the model. The training residuals were generally centered around zero: i.e., the models are unbiased. A slight asymmetry was, however, observed for Mode 1, which means that $a_1(.)$ was more often overestimated by $\mathcal{H}_i^P; Stlj$. Consequently, the mean elevation in the channel and the mean global sedimentation may be slightly exaggerated. These exaggerations, however, remained within a reasonable range, as most of the residuals fell within the ±2% interval. The training residuals of Modes 2 and 3 were perfectly centered, but percentage error dramatically increased. Most of the residuals fell within the ±10% interval for Mode 2, whereas they reached ±50% for Mode 3. However, this error concerns modes that represent at most 4% of the total bathymetry variance, as more than 96% of the total variance was already captured by the addition of the first two modes.

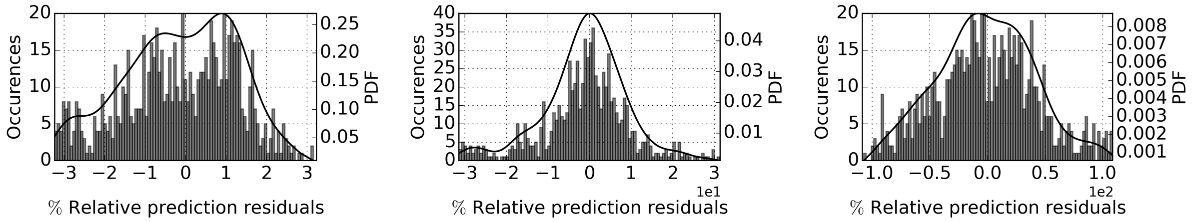

(a) First mode $a_1(t)$ (b) Second mode $a_2(t)$ (c) Third mode $a_3(t)$

FIGURE 20: The prediction residuals distributions using *Stlj* model of dimension 8 calculated for diverse training sizes with a Bootstrap of size 20.

The residuals shapes (i.e. slight overestimation for Mode 1 and perfect centering for Modes 2 and 3) were maintained through the prediction phase. Furthermore, the residuals mostly fell within the ranges identified in the training phase. $\mathcal{H}_i^P; Stlj$ model behavior was stable. The prediction uncertainty could therefore be measured and trusted and the physical interpretation was consequently robust, as discussed below in *Step 3*.

Step 3 - Physical interpretation of the best learned model

The calibrated $\mathcal{H}_i^P; Stlj$ PCE models were considered optimal, as they showed good fit, convergence and robustness with respect to the training choices. Here, they are analyzed to deduce physical information. Firstly, the optimal polynomial degrees selected for each mode and the associated training and prediction empirical errors are shown in Figure 21. Linear models were optimal for Modes 1 and 2 (degree 1), and the associated errors were low for both the training and the prediction sets. For Modes 3 and 4, the optimal polynomial degrees increased, which implies higher-order contributions and/or higher-order interactions for the input variables. For modes of higher ranks, the models were either linear (degree 1) or approximated by a simple average value (degree 0). This means that LARS rejects polynomial terms of higher degrees because they do not significantly improve the learning [2].

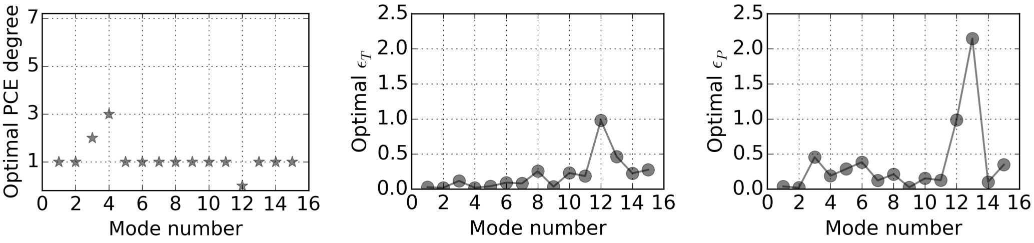

(a) PCE degrees (b) Training errors (c) Prediction errors

FIGURE 21: Optimal PCE degrees for the $\mathcal{H}_i^P; Stlj$ model and associated empirical errors of the training (ϵ_T) and the prediction (ϵ_P) sets.

Prediction relative empirical errors in Figure 21-c (calculated as in Equation 16) increased from Mode 3, but remained under 50% up to mode 11. This must be interpreted according to the meaning of this indicator: it is a measure of the missing variations (distance between the model and reality) relative to the variance of the data. It therefore represents the amount of variance that was not captured by the PCE model (also called "the fraction of unexplained variance" [8]). For example, for mode 12, estimated with a degree 0 PCE model, 100% of the variance is not captured, which is natural because only the average value is accounted for with degree 0. For Modes 3 to 11 with error up 50%, this means that either the training set or the used inputs made it impossible to predict more than 50% of the variance. However, as presented in *Step 2*, this 50% error concerned at most 4% of the total bathymetry variance. Hence, the errors starting from Mode 3 represented at most 2% of missing variance. Beyond Mode 11, prediction with PCE would not be optimal, as the prediction error dramatically increases.

Secondly, PCE models were used to analyze the contribution of each forcing variable to the dynamics. For this, the *Garson Weights* (GW) defined in Equation 7 were used to estimate the influence of the forcings on each temporal coefficient. The global influence on the whole bathymetry field was quantified using the *Generalized Garson Weights* (GGW), as in Equation 20. The ranking of the modes and the impact of the inputs is represented in Figure 22.

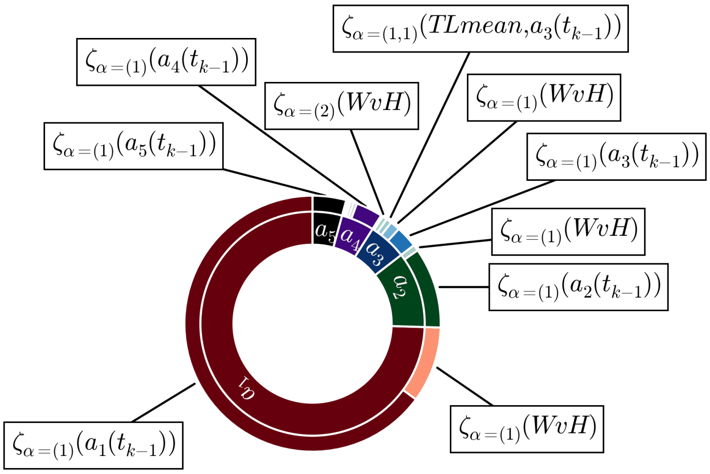

FIGURE 22: Piechart of the most influential parameters, using GW and GGW on the POD-PCE. The inner circle represents the share of each mode. The outer circle represents the share of each polynomial term. The polynomial terms corresponding to GGW higher than 0.5% are shown.

Mode 1 corresponds to a major contribution and the following modes are ranked according to their POD importance. The share of each polynomial term corresponds to the GGW in relation to the global contribution (full circle). When this share is compared to the importance of the corresponding mode, it corresponds to the GW. Lastly, the polynomial terms corresponding to more than 0.5% GGW are indicated. $\zeta_{\boldsymbol{\alpha}=(.)}(.)$ corresponds to the notation introduced in Subsection 2.1, with the multi-index notation for α that represents the polynomial degree of each monomial. For example, $\zeta_{\boldsymbol{\alpha}=(\alpha_1,\alpha_2)}(\theta_1,\theta_2)$ corresponds to a polynomial of degree $\alpha_1+\alpha_2$, where θ_1 contributes as a monomial of degree α_1 and θ_2 as a monomial of degree α_2. The meaning of the variables that appear in Figure 22 can be found in Subsection 4.1 .

For all the temporal coefficients $a_i(.)$, the most influential contributor by far was the value of the previous state $a_i(t_{j-1})$, in the form of a monomial of degree 1. It is followed by contributions involving the mean wave height during the sedimentation period period WvH for all the modes, which makes WvH the most important external forcing, figuring in the third position among all the forcings, with a contribution of 9.6% through the first mode, a total of 12.6% if only WvH monomials are considered, and 13.3% if interactions with other variables are taken into account.

The other forcing contributions also appeared, but with much less importance: e.g., the influence of mean low tide level $TLmean$, which took an interaction form with the previous bathymetry shape for Mode 3. Firstly, this interaction makes sense in terms of physics, as sediment deposition is conditioned by the value of bed shear stress [69], which depends on velocity and water depth. The water depth value is exactly the tidal level minus the bed elevation value, which here appears as a multiplicative interaction between $TLmean$ and Mode 3. Second, the value of this contribution was only 0.7% GGW, which is negligible when compared to the first contribution of WvH. The learned model gave much more importance to waves than to tides. This does not necessarily mean that tides have no influence on sediment deposition, but may simply suggest that, in the present configuration, sediment mobilization by the tide is always more or less the same, and that the forcing that makes a considerable difference is the variation in wave heights. Waves are a determining factor for sediment mobilization in coastal configurations, through the influence they have on bed shear stress [69]. Further more, a noticeable correlation between WvH and $TLmean$ was noticed in the used data-set, which means that the information of low-tide levels is to a certain extent contained in the mean wave height. There is therefore a probable dependency between these variables. In case of dependencies, the iterative process used by LARS may drop a variable that is physically important because the important information is already contained in another variable, due to their dependency.

Lastly, it is important to note that the contribution of less frequent wave events was also present but to a much smaller extent. It is represented by a polynomial term in the form $\zeta_{\alpha=(1,1)(Wv2m,Wv2m\%)}$, where $Wv2m$ and $Wv2m\%$ are respectively mean wave height exceeding $2m$ and the associated frequency of occurrence (arbitrary storm indicator chosen in Subsection 4.1). This term appears in Modes 3 and 4 for a maximum total influence of 0.3%. Higher-order interactions and less frequent events are therefore represented by modes of higher rank, associated with smaller variance percentages.

Step 4 - Robustness of the physical interpretation with respect to the learning-set members
As a last proof of the robustness of the proposed learning algorithm, specifically concerning physical interpretation, a sensitivity analysis with respect to the training set members was performed. The robustness of the calculated *Garson Weights* (GW) with respect to the choice the training members was studied. This is equivalent to studying the robustness of the polynomial basis term selection as produced by LARS, and their associated multiplicative coefficients.

For this, a Bootstrap analysis was again used to construct different learning sets of size 50, instead of choosing the first 50 measurements. This produces a distribution of the GWs rather than a single value, for each polynomial term. The result is shown in Figure 23 for the weights of the $a_k(t_{j-1})$ and WvH monomials.

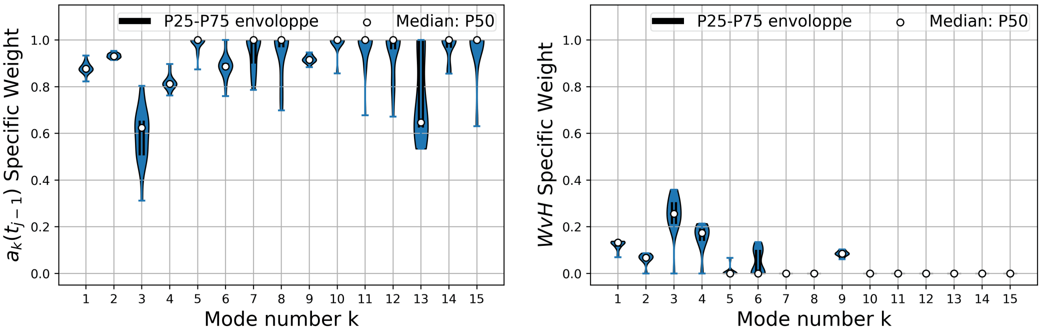

(a) Polynomial term $a_k(t_{j-1})$ (b) Polynomial term WvH

FIGURE 23: Probability density functions of the GWs associated with the degree 1 monomials of variables $a_k(t_{j-1})$ and WvH. The training size is 50 using 20 different random picks for each size.

For modes 1 to 4, the median weights P50 (Percentile 50) of the $a_k(t_{j-1})$ monomials, represented in Figure 23-a, were always over 0.6, but the variation range was strictly less than 1, with density functions centered around the median and a small standard deviation for modes 1, 2 and 4. This means that whatever the training set, the previous state $a_k(t_{j-1})$ value was always predominant but never enough to estimate the evolution of the first four modes. A tendency (in particular linear) using the last state was not sufficient, and additional information was always needed (forcing). In parallel, Figure 23-b shows that this information is certainly the waves, as the median values of the GW for the first four modes were between 10 and 25%, corresponding to the information gap left by the previous value variable $a_k(t_{j-1})$ in the fitted PCE model. Starting from mode 5, the median values of $a_k(t_{j-1})$'s GW had greater chance of falling around 1, which means that the associated polynomial models only rely on the last recorded value of the mode for the future guess. In other terms, the constructed model consists of a linearization around the previous value (tendency capturing) and does not incorporate the correlations between the future-state and the forcing variables (causality model). This can be explained by the small variances of the higher-rank modes and the difficulty of learning the PCE models from statistics averaged over the sedimentation periods. Additionally, the P25-P75 confidence interval moved to the upper bound of the density functions.

4.2.3 Summary of the physical insights from the learning

The spatial patterns as deduced by POD express the spatial correlation in the sediment deposition from the upstream to the downstream part of the channel. The EVR reached 99% with $d = 20$ modes only, where the mean relative RMSE between the approximation and reality was slightly over 10%. This is a statistical proof that the spatial correlations expressed in the POD patterns are explanatory of the physical dynamics over their whole range of variation (at least that observed from 2010 to 2018), with a low approximation rank. In conclusion, the dynamic problem exhibits fairly strong spatial correlations, and the solution to the problem can be expressed on a finite orthonormal basis.

The temporal patterns express the evolution of the sedimentation, as they multiply the spatial patterns. They were learned using PCE as a function of the previously cited inputs (previous states and forcings). The statistical model configuration (dimension and marginals) was chosen after an investigation of different options. The associated training and prediction error converged for the first three modes, and are characterized by tight confidence intervals. The residuals of the selected model were either negligible or centered around zero, demonstrating the unbiased character of the learning and prediction. The fitted models are of lower degree for the low-rank modes 1 and 2 and of higher degrees for modes 3 and 4, which are higher-rank, due to the emergence of interactions between the forcings, namely variables related to extreme behavior (storm events). The model mainly relies on the last state information, showing a strong correlation/continuity in time of the studied physics. Using GW, which measures the forcing influence for the first five modes, the action of waves was highlighted by the PCE model as a determining phenomenon. The first mode influenced the dynamic with a rate of 64.9%, the previous value of the second mode with a rate of 10.2% and, in third position, the mean wave height with a rate of 9.6%. The remaining 15.3% is essentially associated with previous values of higher order modes (10.3%), interactions with tides and contributions of other wave indicators. The GWs show robustness with respect to the choice of the training set members, which makes them trustworthy, at least for temporal correlation and analysis of wave influence. The main physical conclusions are that the dynamic problem is characterized by strong temporal correlations, representing more than 85% of the evolution, with an external sediment source, mainly represented by the waves, representing not more than 15%.

4.3 Prediction of a physical field using POD-PCE coupling

After performing both POD and PCE independently, the accuracy of a Machine Learning process using a POD-PCE coupling was assessed as in Section 2.3. In the continuity with Section 4.2, the first 50 historical bathymetries were used for training and the other 14 for forecasting. First, the impact of the size of the POD basis on the prediction process is assessed in Subsection 4.3.1. Then, the best size was determined and the average prediction behavior is analyzed in Subsection 4.3.2. The accuracy of the POD-PCE ML in predicting spatial details is assessed on cross-section examples in Subsection 4.3.3 and a summary is given in Subsection 4.3.4.

4.3.1 Influence of POD basis size

In order to track the errors generated by the various steps of the algorithm (POD, PCE and coupling), the mean relative RMSE (averaged over the prediction set, as in Equation 18) was calculated for each step (reduction, learning and prediction) and for each approximation rank d, as described in Section 3.2. The results are shown in Figure 24 .

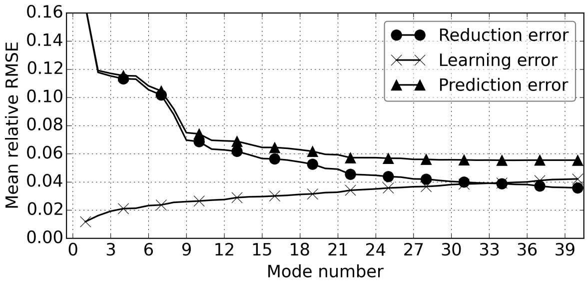

FIGURE 24: Mean relative RMSE generated by the reduction and the learning, and the resulting prediction errors for different approximation ranks.

Reduction error decreased from 16% to 3%, with increasing approximation rank. The error followed a logarithmic trend, with a significant slowdown from rank 9. These errors are coherent with the errors averaged over the full set (rather than the prediction set only) in the POD results Section 4.2.1 (around 8%). The learning error increased from 1% to 5% with increasing approximation rank, which is natural because the complexity of the model is increased. The learning error order of magnitude was consistent with the empirical prediction error of 4% for mode 1 (as calculated in Section 4.2.2), associated with an EVR of over 94%. Lastly, the prediction error decrease is the balance of, on the one hand, the increase in accuracy by adding POD modes and, on the other hand, the increase in forecasting error with increasing number of temporal coefficients to be predicted. Consequently, the prediction error decreased from 16 to 6.9% up to rank 11, following almost the same decreasing trend as the reduction error. However, the decrease rate became slower and increasingly subdued, being overtaken by the learning errors, which dramatically increased starting from mode 12, as seen in Figure 21. Hence, a POD-PCE model of size 11 was selected for prediction.

4.3.2 Average performance of the chosen model

Average sediment deposition was predicted using the POD-PCE model of rank 11, for each of the 14 prediction dates. The average sedimentation rate, denoted S_r, was calculated for time t_j representing the sedimentation over $[t_{j-1}, t_j]$, as in Equation 23. For operational estimation of sediment deposition, only the positive evolutions are of interest; therefore, the erosion points were discarded in calculating rate S_r by cancelling negative evolutions. Indeed, $z(\mathbf{x}_i, t_j) < z(\mathbf{x}_i, t_{j-1})$ implies $(z(\mathbf{x}_i, t_j) - z(\mathbf{x}_i, t_{j-1})) = -|z(\mathbf{x}_i, t_j) - z(\mathbf{x}_i, t_{j-1})|$, and therefore a null contribution to the sedimentation rate S_r. Furthermore, only regions of considerable depth are of interest. Therefore only n_p bathymetry points under $-1\ m$ $(\mathbf{x}_i, i \in \mathcal{N}_p)$ were taken into account. The results are shown in Figure 25

$$S_r = \frac{1}{2n_P} \sum_{i \in \mathcal{N}_p} \frac{(z(\mathbf{x}_i, t_j) - z(\mathbf{x}_i, t_{j-1})) + |z(\mathbf{x}_i, t_j) - z(\mathbf{x}_i, t_{j-1})|}{|z(\mathbf{x}_i, t_j)|} \quad . \tag{23}$$

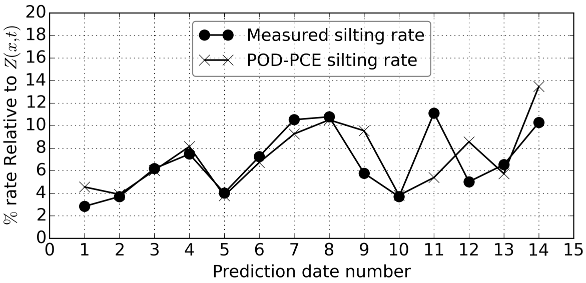

FIGURE 25: A comparison between the real sedimentation rates and the POD-PCE prediction of the sedimentation.

The POD-PCE prediction globally followed the real sedimentation trend, for example from Dates 1 to 8. When it was not equal to the real sedimentation rate, it was generally an overestimation, which is coherent with the asymmetry observed in the distribution of Mode 1 training and prediction residuals (Figure 19 in Subsection 4.2.2).

For the particular Date 11 however, half of the sedimentation was missing. Investigation of the data for this particular measurement showed that the previous record, taken as input, had been made 29 days previously, which is far from the average $\Delta t \approx 15$ days; it is twice the mean interval, thus underestimating sedimentation by half. As measurement intervals were in general around the average, sedimentation time interval Δt was not selected as a key parameter by LARS for the dynamic model, although it was given as an input and is physically significant. For the particular case of the time variable, multiplicative enhancement can be intended as a correction. However, this shows one of the limitations of statistical modeling: statistical significance can be confused with physical importance. Indeed, for the statistical conclusions to be physically significant, the measurements should be diverse enough to account for the variations in the inputs and the impact of these variations on the output. This was unfortunately not guaranteed for sedimentation measurement intervals, as they were often equal to 2 weeks. Additionally, for Dates 12 and 13, a large part of the wave measurements were missing in the sedimentation time interval. Consequently, mean wave height WvH was estimated over only a small portion of the time interval. This may lead to a good prediction (Date 13) if the interval used is representative enough of the full interval, and to bad prediction (Date 12) when not, and highlights the limitations of statistical averaging.

4.3.3 Spatial details of prediction by the chosen model

The spatial details of the prediction were analyzed on cross-sections for specific prediction dates. First, sediment deposition was observed on a cross-section at the entrance of the intake (Figures 26-a, b and c).

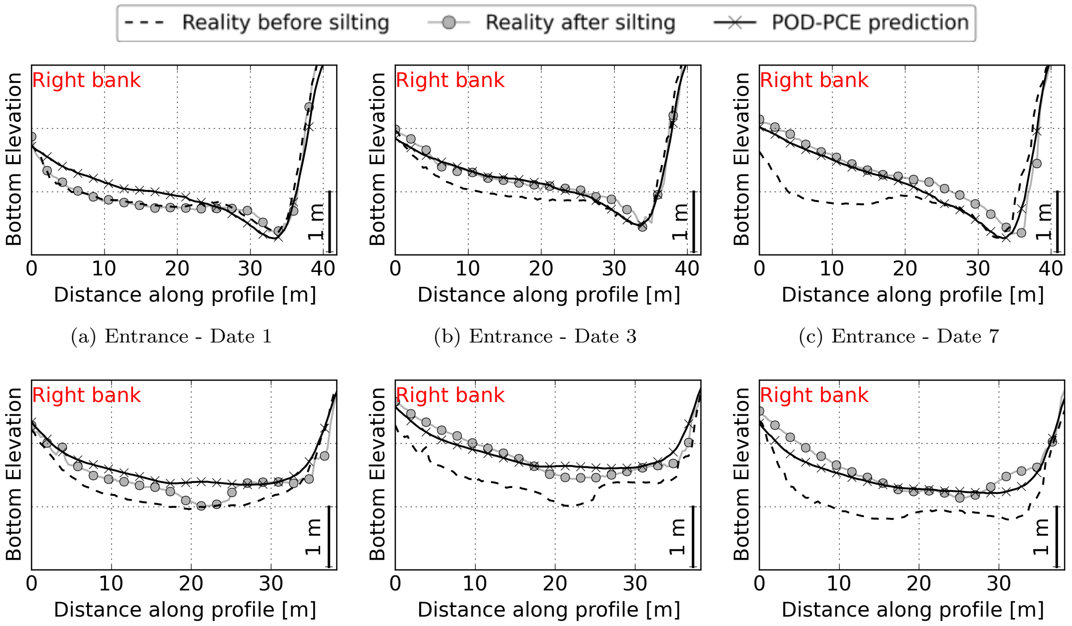

(a) Entrance - Date 1 (b) Entrance - Date 3 (c) Entrance - Date 7

(d) Middle - Date 5 (e) Middle - Date 6 (f) Middle - Date 7

FIGURE 26: POD-PCE prediction vs. reality on cross-sections at the entrance (a, b and c) and middle of the first portion (d, e and f) of the intake.

In accordance with the previous conclusions from Figure 25, the POD-PCE prediction captured various sedimentation ranges, as shown with Dates 2 and 7. However, a slight artificial sedimentation was predicted whereas there was no dynamics in reality, for example for Date 1 (Figure 26-a), due to the fact that the model is continuous, whereas threshold phenomena can occur in reality. Next, sediment deposition was observed on a cross-section at the middle of the first portion of the intake (Figures 26-d, e and f). Mean sedimentation was well captured, but some details of the bathymetry were missing, such as formation of a new feature for Date 5 (distance 20 to 25 m) and Date 7 (distance 30 to 35 m). For Date 6, sediment deposition was slightly underestimated in the right bank and overestimated in the left bank. However, although the details of sediment deposition were not perfectly captured, the value of the sedimentation area corresponds well enough to reality. It can also be concluded that the way the RMSE and relative errors are averaged in space, for example in Figure 24, actually penalizes the accuracy of the algorithm because it does not take account of the oscillation of the prediction around an accurate mean.

Then sediment deposition was observed on a cross-section at the bending part of the intake (Figures 27-a, b and c). It shows that the prediction algorithm understood that the sediment deposition mainly occured in the right bank of the channel, for example for Date 7, even though it was overestimated. Furthermore, considering modes of higher rank from the previous measurement as an input, the algorithm captured the swing in the profile throughout its history, which is here observed from Date 4 to 14. Lastly, a cross-section of the last portion of the channel, in front of the downstream pumping station, is analyzed (Figures 27-d, e and f). Once again, the prediction algorithm understood where the sediment deposition occurs, this time in the left bank of the channel, coherent with the pattern represented by Mode 2 (Figure 13-b). However, it can be seen that unusual sediment deposition occurred for Date 11, which was not captured by the model, and may correspond to the arrival of less frequent fine sediment that appears in Mode 4 (Figure 13-d). This also explains the sediment deposition error observed for Date 11 in Figure 25.

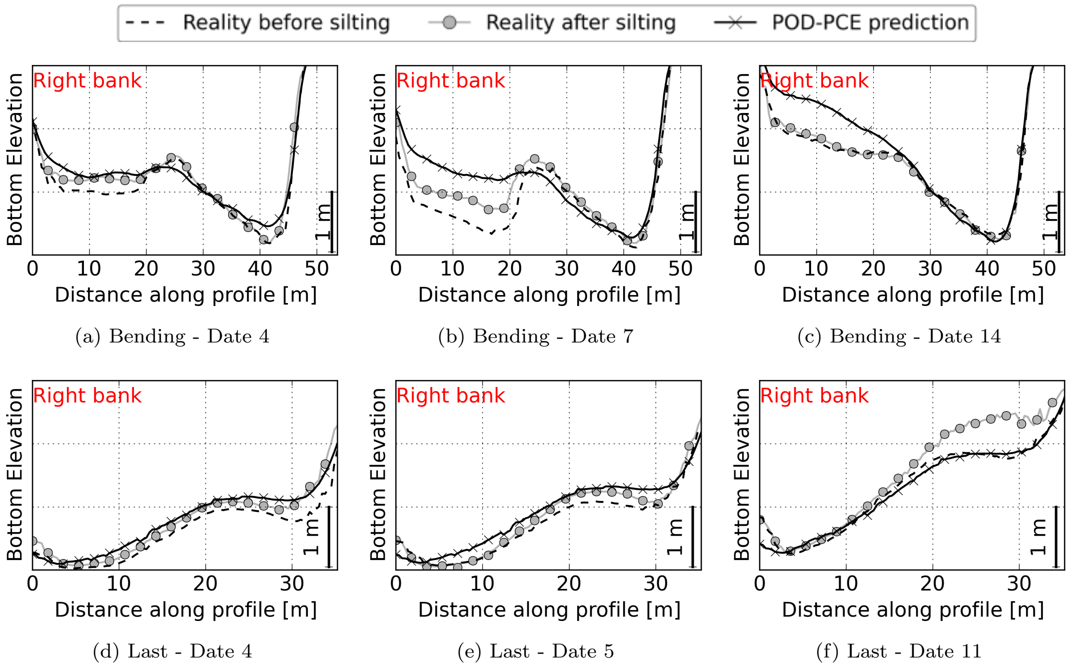

(a) Bending - Date 4 (b) Bending - Date 7 (c) Bending - Date 14

(d) Last - Date 4 (e) Last - Date 5 (f) Last - Date 11

FIGURE 27: POD-PCE prediction vs. reality on cross-sections at the bending (a, b and c) and last portion (d, e and f) of the intake.

4.3.4 Summary of POD-PCE algorithm performance

Overall, the proposed learning algorithm showed interesting prediction characteristics. The model complexity can be increased gradually, by increasing the number of POD modes when accurate. Plotting error against the number of modes shows a convergence that helps in selecting the optimal number of modes. The average RMSE of the predicted field remains reasonably low. It was around 6.9% with the 11 modes selected in the present case.

As a comparison, additional learnings were performed using different NN set-ups in Appendix B. It is shown that POD-PCE gives the best equilibrium between accuracy and fit-time. Among the tested algorithms, only one allowed a RMSE reduction of 0.2%. However, this is of little importance in view of the very large increase in fit-time. Indeed, the latter nearly equals two-hours whereas POD-PCE is fitted in seconds (Table 3 in Appendix B). In addition to fit-time, choosing an algorithmic set-up for NN may be time consuming, as many network architectures are possible, not to mention the numerous choices for the involved hyper-parameters (e.g. Activation Functions).

With the proposed POD-PCE algorithm, the trends are well captured for spatially averaged quantities (here sedimentation rate) and for detailed spatial representations of the field. Good spatial distribution of evolution is guaranteed by the POD modes, even when evolution amplitude is over- or under-estimated.

Nevertheless, some disadvantages should be noted. For example, less frequent events that are represented by modes of higher ranks can be overlooked. Furthermore, sudden changes in features were not sufficiently captured, due to the high temporal correlation between last state and future state that was incorporated in the learning.

5 Summary and discussion

In this study, POD-PCE coupling for field-measurement based Machine Learning was proposed and assessed on a toy problem and a real case. The first one concerns the learning of an analytical solution to groundwater perturbations in an aquifer subject to tidal solicitations, and the second, in an industrial context in the field of geosciences, concerns bathymetry prediction. Both are complex physical phenomena involving non-linear dynamics and various forcings.

POD showed excellent performance on both applications, for dimensionality reduction and physical analysis. This is an important property of POD [28], where the mathematical basis ends up to be physically interpretable, because it efficiently expresses the dynamics. However, adding random perturbations to the toy problem data showed that noise may contaminate the POD patterns (temporal and/or spatial), although modes of high variance are robust. If the noise is significant enough, it may also take more important positions in the decomposition than physical patterns of smaller statistical occurrence. It can then be interesting, for real data, to eliminate modes showing completely stochastic behavior in favor of explainable modes of lower variances. Next, the investigation of POD coefficients is also physically informative: dependency to inputs can sometimes be directly noticed with appropriate plots, and the regularity of the modes can be related either to the representation of different space and time scale physics, or to less frequent events. The potential of POD for detecting biased and missing data was also assessed in the real case. POD was first applied to the whole set of measurements, but discontinuities emerged in the temporal signals of the decomposition. Such a procedure is important because, in most of cases, the data need to be filtered, which is a time-consuming task. The POD enabled fast recognition of elements that react differently from the average. However, many points of improvement are worth mentioning. Firstly, the choice of POD as a decomposition technique was here motivated by its simplicity and the possibility of interpretation when coupled to a linear learning formulation such as PCE. Other decomposition techniques exist, and many authors attempted comparisons, for example with Fourier [50], extensions of POD [20] or other classes of decomposition [54]. For the real case application, other decomposition techniques such as Kernel Principal Component Analysis (KPCA) [41] and Sparse PCA [24] were analyzed, without significant improvements. Secondly, data filtering using POD consisted only in deleting the poor-quality measurements and extracting the spatial zones where data were always measured. POD can however be used to reconstruct missing data, by inverse projection on POD basis elements deduced from qualitative data [53]. This could help to extend the statistical set for the learning. Lastly, a linear interpolation of the bathymetry was used to project all the measurements onto the same grid for POD application. The uncertainty that emerged from this interpolation process was not treated. This, added to the measurement errors, can shed light on model behavior. For example, comparison of mono-beam cross-sections with multi-beam measurements and uncertainty propagation of bathymetry errors through the learning could be attempted, especially because uncertainties in the bathymetric information may impact the flow field computation [37].

PCE was used to learn the POD modes coefficients as 1D data. We showed the importance of the polynomial basis, and therefore of marginals choice, for the learning phase of the real case problem. Indeed, choosing for example uniform distributions, associated with Legendre family, might not be appropriate even though it is widely used when no input information is available [67]. Moreover, the number of inputs can alter the learning. When using LARS, the presence of numerous variables can mislead the algorithm to overfitting. Hence, a good combination between polynomial basis and dimension choice could significantly improve convergence speed, centering of residuals and mean training and prediction errors. The proposed contribution analysis using the PCE coefficients has been successfully tested on the toy problem, resulting with physically coherent conclusions. On the measurements set, it showed that the last-state information is often the most influential input. A robustness test was conducted on the latter by varying the training set, and the observation was stable. Additionally, the noise tests performed on the toy problem showed that LARS selects physically significant polynomial patterns even when the noise contaminates the POD coefficients. PCE and in particular LARS are therefore robust to noise, that propagates from a two-dimensional field to its POD coefficients. This is coherent with the conclusions in [67] about PCE robustness to noise in $1D$ data. In the bathymetry case, for the modes of small ranks associated with the largest variances, wave height was the most influential forcing, whatever the chosen learning set. This is consistent with physical knowledge of sediment mobilization in coastal configurations, where waves are known to be determining through the influence they have on bed shear stress [69]. For modes of higher rank, however, the only selected variable by LARS is the last-state information. Firstly, the forcings that were used as PCE inputs were simple statistical estimators deduced from the data (means, percentiles, etc.). This reduction was used instead of giving all the time series as an input, because the problem would become ultrahigh-dimensional. This unfortunately wastes the richness of the available data as tidal information that are measured on an hourly basis. A more accurate statistical reduction of the inputs could be used. For example, Lataniotis et al. [31] used PCA and KPCA for surrogate modeling with PCE and Gaussian Processes on ultrahigh-dimensional problems. Secondly, dependencies were not specifically modeled. These can be incorporated using the mathematical setting for the construction of the polynomial basis established by Soize and Ghanem [60] . The dependencies, however, indirectly influenced the construction of the model via selection of basis elements by LARS, which avoids redundancy. Thirdly, the choice of tested input configurations for PCE was arbitrary. A more objective variable selection technique is necessary [48]. For example, the information from previous times could also be used as inputs for temporal evolution problems. This may raise other technical questions, such as the number of previous times that should be accounted for (time lag estimation) [10]. Lastly, PCE was chosen for the interpretation possibilities that it allows when combined to POD, thanks to the direct computation of importance measures from the expansion coefficients. Other interesting properties can encourage the use of PCE, for example the developed theoretical frameworks for the treatment of discontinuity [71]. However, some limitations are noted. For example, PCE worked better for modes associated with high than low variances. Although it may be tempting to conclude that modeling of high rank modes is not necessary, it should be noted that their accurate prediction can make the difference between average forecasting and capturing of less frequent events and/or smaller scale features. Therefore, the present ML could be enhanced by improving the learning of high-rank modes. For example, the construction of marginals and the use of random draw with confidence intervals, or extreme statistics models [15], instead of causal models like PCE, could be attempted.

Finally, the robustness and convergence properties added to the physical interpretability supported the choice of POD-PCE coupling as a ML prediction algorithm. It respects the PDR (Predictive, Descriptive, Relevant) framework defined in [45]. It is characterized by both predictive and descriptive accuracy (simplicity) and is stable with respect to data disturbance. It offers the best equilibrium between accuracy and fit-time, compared to other NN configurations tested on the real-case problem. This is consistent with the conclusions by Torre et al. [67], where PCE errors are comparable to the best NN from literature, on classical ML cases, while being much faster. Additionally, POD-PCE is interpretable, as the sparsity, simulatability and modularity defined in [45] are respected by construction. Finally, it is both interpretable at features level (POD components and their PCE) and at multidimensional output level (GW compared to the proposed GGW indicators). The POD-PCE ML was therefore implemented using maximum the first 4 modes for the toy problem, and using the first 11 modes for the real case problem, after sensitivity test to number of modes. Mean information (e.g. sediment deposition rate) was in general well reproduced. Profile-by-profile investigation and $2D$ maps comparisons also showed that POD-PCE coupling was promising, as the spatial distribution of the groundwater perturbation on one hand, and the sediment deposition patch locations and amplitudes on the other hand, were well represented. Some general limitations should be highlighted and could be good perspectives for improving the process. The small data-set was a clear handicap in the measurement based problem. Some events, such as sediment downstream the intake or variation in measurement intervals, were poorly represented. It would be interesting to test the methodology on an enriched data set in order to assess the real potential of POD-PCE Machine Learning. Due to the lack of such data, input distributions were certainly not well approximated. One way of improving POD-PCE coupling would be the development of hybrid measurement-based/process-based data learning [43, 56]. This could be used to enrich the data set, not only by increasing its size (emulated realistic scenarios) but also by adding new input parameters that are not measured but obtained from process-based modeling. Last, the used POD and PCE basis may not always be sufficient for fields whose dependence to conditioning parameters considerably varies over time. Namely, the PDFs of the inputs may evolve, and the number of the basis elements needed for a good representation of the output may increase in time (stochastic drift [13]). Solutions as the Time-Dependent generalized Polynomial Chaos (TD-gPC) [13] could be interesting to explore for long-time learning problems. In particular, an adaptive strategy is used to update the basis elements when needed. Alternatively, the Dynamically Orthogonal (DO) decomposition [46], where both the basis elements and expansion coefficients vary over time in a Karhunen-Loève form, offers a good perspective.

Acknowledgements

This work is funded by the French National Association of Research and Technology (ANRT) through the Industrial Conventions for Training through REsearch (CIFRE) in agreement with EDF R&D. The authors acknowledge their support, and are grateful for data collection and feedback from EDF operators. In particular, we would like to thank D. Rougé for providing the data-set used in this study and for his continuous availability. We also would like to thank Pr. L. Terray (CERFACS) and Dr. M. Rochoux (CERFACS) for constructive discussions on POD and PCE respectively, and Pr. B. Sudret (ETH Zurich) for providing key literature elements on the treatment of ultrahigh dimensional problems and functional inputs using PCE. The authors also gratefully acknowledge the OpenTURNS open source community (An Open source initiative for the Treatment of Uncertainties, Risks'N Statistics). Finally, we would like to thank the anonymous reviewers, whose comments and suggestions helped improve the manuscript.

Appendix A. Complementary results on the parametric toy problem

In addition to the content of Section 3, supplementary materials are herein given for the parametric toy problem. Firstly, *Garson Weights* (GW) and *Generalized Garson Weights* (GGW), respectively presented in Sections 2.2 and 2.3, were calculated for fitted PCE models of the first four POD modes, in the amplitude learning case, as in Table 1.

Secondly, the POD-PCE strategy has also been deployed to learn the time lag between $f(x, y, t)$ and $f(0, 0, t)$ relative to the period T, at each location (x, y). POD was applied to the corresponding snapshot matrix. While 98% of the variance is already represented by Mode 1, a total of 5 modes is needed to approach the 100%. This increase is slow compared to the EVR of the amplitude. As a result, the POD-PCE performances, evaluated at each step of the algorithm, are different, as can be seen in Figure 28.

Polynomial term	GGW	Total	Mode	GW
$\zeta_{\alpha=(1)}(A)$	0.8016	0.80	1	0.84675
$\zeta_{\alpha=(1)}(D)$	0.10138	0.90	1	0.10709
$\zeta_{\alpha=(1)}(D)$	0.03199	0.93	2	0.71521
$\zeta_{\alpha=(1,1)}(A, D)$	0.02115	0.96	1	0.02234
$\zeta_{\alpha=(2)}(D)$	0.0145	0.97	1	0.01532
$\zeta_{\alpha=(1,1)}(A, D)$	0.00667	0.98	2	0.14921
$\zeta_{\alpha=(2)}(D)$	0.00375	0.98	2	0.08373
$\zeta_{\alpha=(1,2)}(A, D)$	0.00316	0.98	1	0.00334
$\zeta_{\alpha=(2)}(D)$	0.00238	0.99	3	0.47515
$\zeta_{\alpha=(1)}(\kappa_{er})$	0.002	0.99	1	0.00211
$\zeta_{\alpha=(1)}(\kappa_{er})$	0.00165	0.99	4	0.46206
$\zeta_{\alpha=(3)}(D)$	0.00118	0.99	1	0.00125
$\zeta_{\alpha=(1)}(\kappa_{er})$	0.00094	0.99	3	0.18655

Table 1: Polynomial terms of PCE models calibrated on the aquifer case, for the 4 first modes ordered by their influence, using the GGWs in Equation 20. Also shown are the GWs calculated as in Equation 7. The contributions are shown up to a total of 99%.

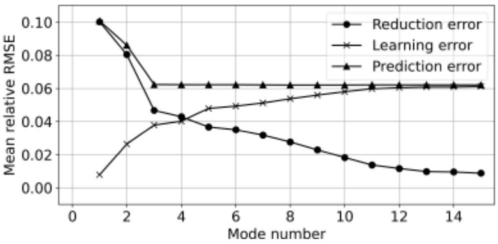

Figure 28: Mean relative RMSE generated at different steps of the POD-PCE ML applied to the time-lag case, with different approximation ranks.

The reduction error equals 10% at rank 1 (compared to 3.8% for the amplitude). It decreases following three slopes, the first one being from 10% at rank 1 to 5% at rank 3. The learning error is here much higher, almost equal to 1% for a 1-Mode approximation, and goes up to 4% for 3-Mode approximation, where it keeps on increasing. The modes coefficients seem more difficult to learn for the phase. Consequently, the prediction error decreases from 10% at rank 1 to 6% rank 3, where it stabilizes. Indeed, even though adding more POD patterns is interesting, learning them with PCE becomes more and more difficult as the represented variance decreases. The gain in accuracy with POD modes is therefore compensated with the loss of precision in PCE learning. Hence, a 3-Modes POD-PCE model was selected for prediction.Examples of phase prediction are shown in Figure 29. The model gives a good mapping of the two-dimensional time lag distribution along the estuary and through the aquifer. However, the residuals are more important compared to the amplitude prediction. For example, an absolute residual of 0.1 T time-lag is noticed in the middle of the aquifer in Figure 29-c, where the analytical time lag (Figure 29-a) is around 0.4 T, representing a local error of 25%. The global performance of the model remains however satisfying.

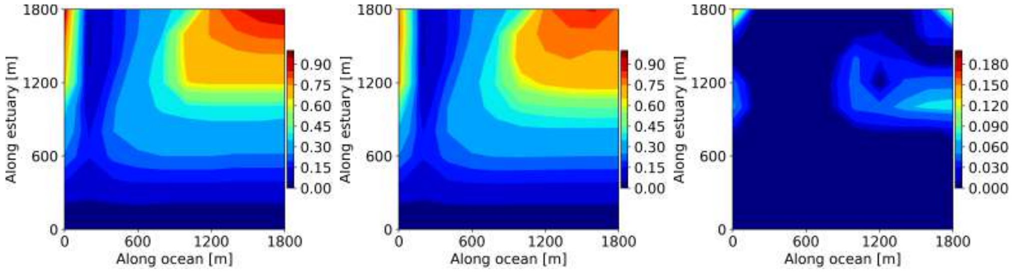

(a) Analytical (b) POD-PCE (c) Absolute residual

Figure 29: Analytical solution vs. POD-PCE prediction of the time-lag, relative to the tidal period T in the aquifer, and resulting absolute residual.

The physical analysis of the latter are therefore performed using the GW and GGW indicators, reported in Table 2. First, the most important polynomial pattern for the coupled POD-PCE model is the diffusivity D at degree 1 (GGW 47%), whereas it was the tidal amplitude A at degree 1 for the amplitude distribtion (GGW 80%). In particular, it barely represents half of the dynamics. It is completed by higher degree monomials of the same parameter D up to 79%. The phase representation exhibits more non-linearities than the amplitude. The contribution of D is followed by an interaction between A, D and the wave number in the estuary κ_{ei}. As a reminder, the latter did not appear as an influencing parameter for the amplitude distribution. Globally, the phase problem involves higher polynomial degrees, and higher orders of interaction.

Polynomial term	GGW	Total	Mode	GW
$\zeta_{\alpha=(1)}(D)$	0.4684	0.47	1	0.54334
$\zeta_{\alpha=(3)}(D)$	0.14637	0.61	1	0.16979
$\zeta_{\alpha=(4)}(D)$	0.0912	0.71	1	0.10579
$\zeta_{\alpha=(2)}(D)$	0.08382	0.79	1	0.09723
$\zeta_{\alpha=(2,1,1)}(A, \kappa_{ei}, D)$	0.03942	0.83	1	0.04572
$\zeta_{\alpha=(1)}(D)$	0.02889	0.86	2	0.35127
$\zeta_{\alpha=(2)}(D)$	0.02066	0.88	3	0.37113
$\zeta_{\alpha=(1)}(D)$	0.01986	0.90	3	0.35668
$\zeta_{\alpha=(1,1)}(\kappa_{er}, D)$	0.01594	0.91	1	0.01849
$\zeta_{\alpha=(3)}(D)$	0.01515	0.93	3	0.27218
$\zeta_{\alpha=(2)}(D)$	0.01389	0.94	2	0.16892
$\zeta_{\alpha=(1,3)}(\kappa_{er}, D)$	0.01288	0.96	1	0.01494
$\zeta_{\alpha=(5)}(D)$	0.00907	0.97	2	0.11024
$\zeta_{\alpha=(2,2)}(A, D)$	0.00658	0.97	2	0.07994
$\zeta_{\alpha=(1,4)}(\kappa_{ei}, D)$	0.0059	0.98	2	0.07178
$\zeta_{\alpha=(2,1,1)}(A, \kappa_{ei}, D)$	0.00531	0.98	2	0.06453
$\zeta_{\alpha=(1,2)}(\kappa_{er}, D)$	0.00405	0.99	1	0.0047

Table 2: Polynomial terms of PCE models calibrated on the aquifer case, for the 3 first modes ordered by their influence, using the GGWs in Equation 20. Also shown are the GWs calculated as in Equation 7

Appendix B. Confronting POD-PCE to NN

As an additional proof for the POD-PCE Machine Learning capacity, multiple NN configurations are tested on the measurement-based problem for confrontation. The latter is a small-data problem, considered as the most challenging case in the presented work. The python library Scikit-learn [51] (`https://scikit-learn.org`) was used for fitting.

A first NN set-up, aiming at learning the bathymetry fields $[z(x_i, t_j)]_{i,j} \in \mathbb{R}^{m \times n}$ directly from their previous values $[z(x_i, t_{j-1})]_{i,j} \in \mathbb{R}^{m \times n}$ and a set of parameters $\mathbf{\Theta}$, was attempted. A simple configuration was tested, where $z(x_i, t_j)$ is learned for each x_i independently, from its own previous value $z(x_i, t_{j-1})$ and the seven physical parameters Δt, $TLmean$, WvH, $Wvper$, $Wvdir$, $Wv2m$ and $Wv2m\%$, as done in the most optimal POD-PCE configuration ($\mathcal{H}_i^P$ described in Subsection 4.2.2). Therefore, m independent learnings are performed (points number), each characterized with an input dimension of $V = 8$, and an output dimension of $o = 1$.

Two learning strategies are adopted. The first one consists in a single-layer NN, where only the *Activation Function* (AF) and the number of *neurons*, denoted l, are varied. The considered AFs are the ones available in Scikit-learn (identity, tanh, logistic and ReLu) [51], and allow to be in the theoretical conditions for the "shallow and wide" *Universal Approximation Theorem* [21]. The second alternative consists in a multi-layer NN using the ReLu AF, where the number of neurons l is fix, and the number of layers, denoted L varies. This allows to be in the framework of the "deep and narrow" version of the theorem [18].

For the single-layer NN, the maximal number of neurons is constrained to $l = 5$. Indeed, the input-to-hidden connection matrix is of size $V \times l$, and the hidden-to-output matrix is of size $l \times o$. In this case, with $l = 5$, a maximum number of 45 matrix coefficients should be estimated from the training sample of size 50. An additional neuron would result with an ill-posed problem. For the multi-layer ReLu NN, the number of neurons is set to $l = 2$ and the maximum number of layers to $L = 9$ (number of coefficients to estimate is $V \times l + (L-1) \times l^2 + l \times o = 50$). Using both configurations, the optimal choices (AF, neurons, layers) are selected for each coordinate x_i, based on the relative empirical error calculated on the test set, as in Equation 16 . The RMSE for each prediction date are then calculated with the whole field $z(., t_j)$ (NN prediction vs. reality), and confronted to POD-PCE in Figure 30-a. The single-layer NN is denoted s-NN and the multi-layer ReLu NN is denoted m-NN.

To account for spatial correlations, a supplementary set-up was tested, where POD is performed before NN. Similarly to the POD-PCE learning set-up, NN is used to learn the first 11 POD coefficients, corresponding to the optimal POD-PCE learning in Section 4.2.2, and a POD-NN coupling is performed. The learning configurations mentioned above (single-layer, and multi-layer ReLu) are tested, and the algorithmic choices corresponding to the minimal relative empirical error are selected for each POD mode independently. The RMSE results are shown in Figure 30-b, where POD-s-NN and POD-m-NN denote the coupling of POD with s-NN and m-NN respectively.

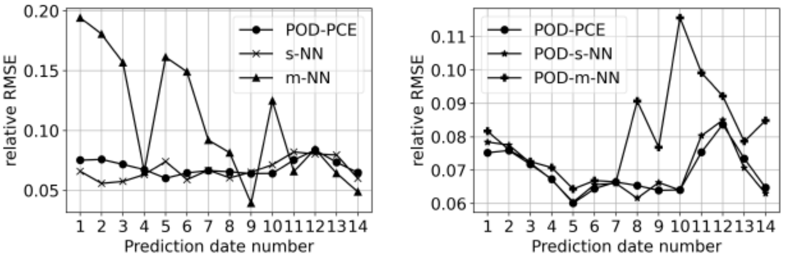

(a) Comparison to NN (b) Comparison to POD-NN

FIGURE 30: Comparison of relative prediction RMSE between the POD-PCE algorithm and different NN set-ups.

A last test is conducted, where an L2-penalty is used to fit sparse POD-NN. This is performed in scikit-learn [51] by adding a constraint to the learning minimization problem, consisting in a regularization term, controlled with an additional hyper-parameter. The values of hyper-parameters that were previously constrained can here be increased: the maximal number of neurons is set to $l = 50$ for POD-s-NN, while the maximal number of layers is set to $L = 10$ for POD-m-NN with a number of neurons fixed to $l = 5$. The L2-penalty coefficient is varied from 10^{-4} (low sparsity) to 10^4 (high sparsity). A comparison of all algorithms in terms of average RMSE and fit-time can be found in Table 3.

Firstly, it can be noticed in Figure 3 that the worst learning is performed with m-NN (average RMSE of 10.8% in Table 3). It might be due to the fact that available data are not sufficient for a deep network fitting. This is followed in terms of worst performance by POD-m-NN (average RMSE of 8.1%), with the same interpretation. The other learning choices (POD-PCE, s-NN and POD-s-NN) have global similar behaviors. Among the last three, it is noted that s-NN performs the best for the three first dates, while it performs the worst for dates 5, 10, and 11 (Figure 3). It scores the lowest average RMSE of 6.7%, but also by far the worst fit-time (Table 3). The performances of POD-PCE and POD-s-NN are very close, their average RMSE are 6.9% and 7%, but POD-PCE is twice faster. Sparsity added to POD-s-NN and POD-m-NN helps reducing the errors by 0.1 and 1.2% respectively. The resulting

RMSE are equivalent to POD-PCE using LARS, which takes much less fit-time.

Algorithm	Sparsity	Average RMSE	Fit-time
POD-PCE	LARS [3]	6.9%	$11s$
s-NN	None	6.7%	$1h47m14s$
m-NN	None	10.8%	$20m16s$
POD-s-NN	None	7%	$25s$
POD-m-NN	None	8.1%	$10s$
POD-s-NN	L2 penalty [51]	6.9%	$11m16s$
POD-m-NN	L2 penalty [51]	6.9%	$2m48s$

Table 3: Summary the performances for all tested learning algorithms.

The POD-PCE coupling methodology offers an interesting alternative to NN in terms of accuracy and fit-time balance. It competes with POD-s-NN which is slightly less accurate, but POD-PCE is here twice-faster. Additionally, the most optimal POD-s-NN is composed of different AFs for the different modes (combinations of logistic and ReLu), which makes the interpretation difficult compared to polynomial patterns, and results with a superiority of POD-PCE for physical analysis. However, these conclusions should be interpreted in light of the learning choices, which can be improved. For example, a combination of the best single-layer networks and best multi-layer ReLu networks can be attempted to optimize the previous set-ups. This can even be further improved by choosing PCE or NN when appropriate. Lastly, as was the case with PCE, limitations to the previous learnings can be noted, among which the physical parameters selection and time-lag choice for the previous field value.

Références

[1] O. I. Abiodun, A. Jantan, A. E. Omolara, K. V. Dada, N. A. Mohamed, and H. Arshad. State-of-the-art in artificial neural network applications : A survey. *Heliyon*, 4(11), 2018. ISSN 2405-8440.

[2] G. Blatman. *Adaptive sparse polynomial chaos expansions for uncertainty propagation and sensitivity analysis.* PhD thesis, 2009.

[3] G. Blatman and B. Sudret. Adaptive sparse polynomial chaos expansion based on least angle regression. *Journal of Computational Physics*, 230(6) :2345 – 2367, 2011. ISSN 0021-9991. doi : https://doi.org/10.1016/j.jcp.2010.12.021. URL `http://www.sciencedirect.com/science/article/pii/S0021999110006856`.

[4] S. L. Brunton, B. R. Noack, and P. Koumoutsakos. Machine learning for fluid mechanics. *Annual Review of Fluid Mechanics*, 52(1) :477–508, 2020. doi : 10.1146/annurev-fluid-010719-060214. URL `https://doi.org/10.1146/annurev-fluid-010719-060214`.

[5] L. Cordier and M. Bergmann. Proper orthogonal decomposition : an overview. In *Lecture series 2002-04, 2003-03 and 2008-01 on post-processing of experimental and numerical data, Von Karman Institute for Fluid Dynamics*, page 46 pages. VKI, 2008.

[6] S. Costa, P. Letortu, and B. Laignel. The hydro-sedimentary system of the upper-normandy coast : Synthesis. *Sediment Fluxes in Coastal Areas*, pages 121–147, 2015.

[7] M. Couplet. *Reduced-order POD-Galerkin modelling for the control of unsteady flows.* Ph.d. thesis, Université Paris-Nord - Paris XIII, Jan. 2005.

[8] G. Cruciani, M. Baroni, S. Clementi, G. Costantino, D. Riganelli, and B. Skagerberg. Predictive ability of regression models. part i : Standard deviation of prediction errors (sdep). *Journal of Chemometrics*, 6(6) : 335–346, 1992.

[9] R. G. Dean and R. A. Dalrymple. *Coastal processes with engineering applications.* Cambridge University Press, 2004.

[10] S. Du, G. Song, and H. Hong. Collective causal inference with lag estimation. *Neurocomputing*, 323 : 299 – 310, 2019. ISSN 0925-2312. doi : https://doi.org/10.1016/j.neucom.2018.09.088. URL `http://www.sciencedirect.com/science/article/pii/S0925231218311792`.

[11] B. Efron and R. Tibshirani. Bootstrap methods for standard errors, confidence intervals, and other measures of statistical accuracy. *Statistical science*, pages 54–75, 1986.

[12] O. Garcia-Cabrejo and A. Valocchi. Global sensitivity analysis for multivariate output using polynomial chaos expansion. *Reliability Engineering & System Safety*, 126 :25–36, 2014.

[13] M. Gerritsma, J.-B. Van der Steen, P. Vos, and G. Karniadakis. Time-dependent generalized polynomial chaos. *Journal of Computational Physics*, 229(22) :8333–8363, 2010.

[14] M. Gevrey, I. Dimopoulos, and S. Lek. Review and comparison of methods to study the contribution of variables in artificial neural network models. *Ecological Modelling*, 160(3) :249 – 264, 2003. ISSN 0304-3800. doi : https://doi.org/10.1016/S0304-3800(02)00257-0. URL `http://www.sciencedirect.com/science/article/pii/S0304380002002570`.

[15] M. Ghil, P. Yiou, S. Hallegatte, B. D. Malamud, P. Naveau, A. Soloviev, P. Friederichs, V. Keilis-Borok, D. Kondrashov, V. Kossobokov, O. Mestre, C. Nicolis, H. W. Rust, P. Shebalin, M. Vrac, A. Witt, and I. Zaliapin. Extreme events : dynamics, statistics and prediction. *Nonlinear Processes in Geophysics*, 18(3) : 295, 2011.

[16] A. Guillaume. *VAG-Modele de prevision de l'etat de la mer en eau profonde*. Dir. de la Meteorologie Nationale, 1987.

[17] I. Guyon and A. Elisseeff. An introduction to variable and feature selection. *Journal of Machine Learning Research*, 3 :1157–1182, 2003.

[18] B. Hanin. Universal function approximation by deep neural nets with bounded width and relu activations. *Mathematics*, 7(10), 2019. ISSN 2227-7390. doi : 10.3390/math7100992. URL `https://www.mdpi.com/2227-7390/7/10/992`.

[19] T. Hastie, R. Tibshirani, and J. Friedman. *The Elements of Statistical Learning : Data Mining, Inference, and Prediction, Second Edition (Springer Series in Statistics)*. 02 2009. ISBN 0387848576.

[20] A. Hekmati, D. Ricot, and P. Druault. About the convergence of pod and epod modes computed from cfd simulation. *Computers & Fluids*, 50(1) :60 – 71, 2011. ISSN 0045-7930. doi : https://doi.org/10.1016/j.compfluid.2011.06.018. URL `http://www.sciencedirect.com/science/article/pii/S0045793011002064`.

[21] K. Hornik. Approximation capabilities of multilayer feedforward networks. *Neural Networks*, 4(2) :251 – 257, 1991. ISSN 0893-6080. doi : https://doi.org/10.1016/0893-6080(91)90009-T. URL `http://www.sciencedirect.com/science/article/pii/089360809190009T`.

[22] R. Iten, T. Metger, H. Wilming, L. del Rio, and R. Renner. Discovering physical concepts with neural networks. *Phys. Rev. Lett.*, 124, Jan 2020.

[23] M. Janocko, M. Cartigny, W. Nemec, and E. Hansen. Turbidity current hydraulics and sediment deposition in erodible sinuous channels : laboratory experiments and numerical simulations. *Marine and Petroleum Geology*, 41 :222–249, 2013.

[24] I. M. Johnstone and A. Y. Lu. On consistency and sparsity for principal components analysis in high dimensions. *Journal of the American Statistical Association*, 104(486) :682–693, 2009.

[25] I. Jolliffe. *Principal Component Analysis*, pages 1094–1096. Springer Berlin Heidelberg, Berlin, Heidelberg, 2011.

[26] B. A. Jones and A. Doostan. Satellite collision probability estimation using polynomial chaos expansions. *Advances in Space Research*, 52(11) :1860 – 1875, 2013. ISSN 0273-1177. doi : https://doi.org/10.1016/j.asr.2013.08.027. URL `http://www.sciencedirect.com/science/article/pii/S0273117713005413`.

[27] A. Karpatne, I. Ebert-Uphoff, S. Ravela, H. A. Babaie, and V. Kumar. Machine learning for the geosciences : Challenges and opportunities. *IEEE Transactions on Knowledge and Data Engineering*, 31(8) :1544–1554, Aug 2019. ISSN 2326-3865. doi : 10.1109/TKDE.2018.2861006.

[28] G. Kerschen and J. Golinval. Physical interpretation of the proper orthogonal modes using the singular value decomposition. *Journal of Sound and Vibration*, 249(5) :849 – 865, 2002. ISSN 0022-460X. doi : https://doi.org/10.1006/jsvi.2001.3930. URL `http://www.sciencedirect.com/science/article/pii/S0022460X01939306`.

[29] M. Lamboni, H. Monod, and D. Makowski. Multivariate sensitivity analysis to measure global contribution of input factors in dynamic models. *Reliability Engineering & System Safety*, 96(4) :450 – 459, 2011. ISSN 0951-8320. doi : https://doi.org/10.1016/j.ress.2010.12.002. URL `http://www.sciencedirect.com/science/article/pii/S0951832010002504`.

[30] M. Larson, M. Capobianco, M. Jansen, G. Różyński, H. Southgate, M. Stive, K. Wijnberg, and S. Hulscher. Analysis and modeling of field data on coastal morphological evolution over yearly and decadal time scales. part 1 : Background and linear techniques. *Journal of Coastal Research*, 19, 09 2003.

[31] C. Lataniotis, S. Marelli, and B. Sudret. Extending classical surrogate modelling to ultrahigh dimensional problems through supervised dimensionality reduction : a data-driven approach. *arXiv preprint :1812.06309*, 12 2018.

[32] A. Laudani, G. M. Lozito, F. R. Fulginei, and A. Salvini. On training efficiency and computational costs of a feed forward neural network : A review. *Computational Intelligence and Neuroscience*, 2015. doi : 10.1155/2015/818243.

[33] S. Le Bot, R. Lafite, M. Fournier, A. Baltzer, and M. Desprez. Morphological and sedimentary impacts and recovery on a mixed sandy to pebbly seabed exposed to marine aggregate extraction (eastern english channel, france). *Estuarine, Coastal and Shelf Science*, 89(3) :221–233, 2010.

[34] O. P. Le Maitre, O. M. Knio, H. N. Najm, and R. G. Ghanem. A stochastic projection method for fluid flow : I. basic formulation. *Journal of Computational Physics*, 173(2) :481 – 511, 2001. ISSN 0021-9991. doi : https://doi.org/10.1006/jcph.2001.6889. URL `http://www.sciencedirect.com/science/article/pii/S0021999101968895`.

[35] O. P. Le Maitre, M. T. Reagan, H. N. Najm, R. G. Ghanem, and O. M. Knio. A Stochastic Projection Method for Fluid Flow : II. Random Process. *Journal of Computational Physics*, 181(1) :9 – 44, 2002. ISSN 0021-9991. doi : https://doi.org/10.1006/jcph.2002.7104. URL `http://www.sciencedirect.com/science/article/pii/S0021999102971044`.

[36] Y. LeCun, Y. Bengio, and G. Hinton. Deep learning. *Nature*, 521 :436–444, 2015. doi : https://doi.org/10.1038/nature14539.

[37] C. J. Legleiter, P. C. Kyriakidis, R. R. McDonald, and J. M. Nelson. Effects of uncertain topographic input data on two-dimensional flow modeling in a gravel-bed river. *Water Resources Research*, 47(3), 2011. doi : 10.1029/2010WR009618. URL `https://agupubs.onlinelibrary.wiley.com/doi/abs/10.1029/2010WR009618`.

[38] L. Li, D. Barry, C. Cunningham, F. Stagnitti, and J.-Y. Parlange. A two-dimensional analytical solution of groundwater responses to tidal loading in an estuary and ocean. *Advances in Water Resources*, 23(8) :825–833, 2000.

[39] J. L. Lumley. The structure of inhomogeneous turbulent flows. *Atmospheric Turbulence and Radio Wave Propagation*, 1967.

[40] C. Michel, S. Le Bot, F. Druine, S. Costa, F. Levoy, C. Dubrulle-Brunaud, and R. Lafite. Stages of sedimentary infilling in a hypertidal bay using a combination of sedimentological, morphological and dynamic criteria (bay of somme, france). *Journal of Maps*, 13(2) :858–865, 2017.

[41] S. Mika, B. Schölkopf, A. J. Smola, K.-R. Müller, M. Scholz, and G. Rätsch. Kernel pca and de-noising in feature spaces. *Advances in neural information processing systems*, pages 536–542, 1999.

[42] K. Mills, M. Spanner, and I. Tamblyn. Deep learning and the Schrödinger equation. *Phys. Rev. A*, 96 :042113, Oct 2017. doi : 10.1103/PhysRevA.96.042113. URL `https://link.aps.org/doi/10.1103/PhysRevA.96.042113`.

[43] A. Mosavi, S. Shamshirband, E. Salwana, K.-w. Chau, and J. H. Tah. Prediction of multi-inputs bubble column reactor using a novel hybrid model of computational fluid dynamics and machine learning. *Engineering Applications of Computational Fluid Mechanics*, 13(1) :482–492, 2019.

[44] M. Muller. *On the POD method : an abstract investigation with applications to reduced-order modeling and suboptimal control.* PhD thesis, 2008.

[45] W. J. Murdoch, C. Singh, K. Kumbier, R. Abbasi-Asl, and B. Yu. Interpretable machine learning : definitions, methods, and applications. *arXiv preprint :1901.04592*, 2019.

[46] E. Musharbash, F. Nobile, and T. Zhou. Error analysis of the dynamically orthogonal approximation of time dependent random pdes. *SIAM Journal on Scientific Computing*, 37(2) :A776–A810, 2015.

[47] J. B. Nagel, J. Rieckermann, and B. Sudret. Principal component analysis and sparse polynomial chaos expansions for global sensitivity analysis and model calibration : Application to urban drainage simulation. *Reliability Engineering & System Safety*, 195 :106737, 2020. ISSN 0951-8320. doi : https://doi.org/10.1016/j.ress.2019.106737. URL `http://www.sciencedirect.com/science/article/pii/S0951832019301747`.

[48] R. Noori, A. Karbassi, A. Moghaddamnia, D. Han, M. Zokaei-Ashtiani, A. Farokhnia, and M. G. Gousheh. Assessment of input variables determination on the svm model performance using pca, gamma test, and forward selection techniques for monthly stream flow prediction. *Journal of Hydrology*, 401(3) :177 – 189, 2011. ISSN 0022-1694. doi : https://doi.org/10.1016/j.jhydrol.2011.02.021. URL `http://www.sciencedirect.com/science/article/pii/S0022169411001363`.

[49] M. S. Parsons. Interpretation of machine-learning-based disruption models for plasma control. *Plasma Physics and Controlled Fusion*, 59(8) :085001, jun 2017. doi : 10.1088/1361-6587/aa72a3. URL `https://doi.org/10.1088%2F1361-6587%2Faa72a3`.

[50] S. Paul and M. K. Verma. Proper orthogonal decomposition vs. fourier analysis for extraction of large-scale structures of thermal convection. *Advances in Computation, Modeling and Control of Transitional and Turbulent Flows*, pages 433–441, 2017.

[51] F. Pedregosa, G. Varoquaux, A. Gramfort, V. Michel, B. Thirion, O. Grisel, M. Blondel, P. Prettenhofer, R. Weiss, V. Dubourg, J. Vanderplas, A. Passos, D. Cournapeau, M. Brucher, M. Perrot, and E. Duchesnay. Scikit-learn : Machine learning in Python. *Journal of Machine Learning Research*, 12 :2825–2830, 2011.

[52] REFMAR. Réseaux de Référence des observations MARégraphiques, 2020.

[53] P. Saini, C. M. Arndt, and A. M. Steinberg. Development and evaluation of gappy-pod as a data reconstruction technique for noisy piv measurements in gas turbine combustors. *Experiments in Fluids*, 57(7) :122, 2016.

[54] P. J. Schmid. Dynamic mode decomposition of numerical and experimental data. *Journal of Fluid Mechanics*, 656 :5–28, 2010. doi : 10.1017/S0022112010001217.

[55] J. Schmidhuber. Deep learning in neural networks : An overview. *Neural Networks*, 61 :85 – 117, 2015. ISSN 0893-6080. doi : https://doi.org/10.1016/j.neunet.2014.09.003. URL `http://www.sciencedirect.com/science/article/pii/S0893608014002135`.

[56] J. Senent-Aparicio, P. Jimeno-Sáez, A. Bueno-Crespo, J. Pérez-Sánchez, and D. Pulido-Velázquez. Coupling machine-learning techniques with swat model for instantaneous peak flow prediction. *Biosystems Engineering*, 177 :67 – 77, 2019.

[57] S. Sengupta, S. Basak, P. Saikia, S. Paul, V. Tsalavoutis, F. Atiah, V. Ravi, and A. Peters. A review of deep learning with special emphasis on architectures, applications and recent trends. *arXiv preprint :1905.13294*, 2019.

[58] S. Shalev-Shwartz and S. Ben-David. *Understanding Machine Learning : From Theory to Algorithms.* Cambridge University Press, 2014.

[59] L. Sirovich. Turbulence and the Dynamics of Coherent Structures : I, II and III. *Quarterly Applied Mathematics*, 45 :561, 1987.

[60] C. Soize and R. Ghanem. Physical systems with random uncertainties : chaos representations with arbitrary probability measure. *SIAM J. Sci. Comput.*, pages 26(2), 395–410, 2004.

[61] T. Sruthi, K. Ranjith, and V. Chandra. Control of sediment entry into an intake canal by using submerged vanes. In *AIP Conference Proceedings*, volume 1875, page 030007. AIP Publishing LLC, 2017.

[62] B. Sudret. Global sensitivity analysis using polynomial chaos expansions. *Reliability Engineering & System Safety*, 93(7) :964 – 979, 2008. ISSN 0951-8320.

[63] B. Sudret. *Polynomial chaos expansions and stochastic finite element methods*, page 624. CRC PressEditors : Kok-Kwang Phoon, Jianye Ching, 12 2014.

[64] T. Taddei. A registration method for model order reduction : data compression and geometry reduction. *SIAM Journal on Scientific Computing*, 42(2) :A997–A1027, 2020.

[65] K. Taira, S. L. Brunton, S. T. M. Dawson, C. W. Rowley, T. Colonius, B. J. McKeon, O. T. Schmidt, S. Gordeyev, V. Theofilis, and L. S. Ukeiley. Modal analysis of fluid flows : An overview. *AIAA Journal*, 55 (12) :4013–4041, 2017. doi : 10.2514/1.J056060. URL `https://doi.org/10.2514/1.J056060`.

[66] A. Tarakanov and A. H. Elsheikh. Regression-based sparse polynomial chaos for uncertainty quantification of subsurface flow models. *Journal of Computational Physics*, 399 :108909, 2019. ISSN 0021-9991. doi : https://doi.org/10.1016/j.jcp.2019.108909. URL `http://www.sciencedirect.com/science/article/pii/S002199911930614X`.

[67] E. Torre, S. Marelli, P. Embrechts, and B. Sudret. Data-driven polynomial chaos expansion for machine learning regression. *Journal of Computational Physics*, 388 :601 – 623, 2019.

[68] M. Tsang, D. Cheng, and Y. Liu. Detecting statistical interactions from neural network weights. *arXiv preprint :1705.04977*, 2017.

[69] L. C. van Rijn. Unified view of sediment transport by currents and waves. i : Initiation of motion, bed roughness, and bed-load transport. *Journal of Hydraulic Engineering*, 133(6) :649–667, 2007. doi : 10.1061/(ASCE)0733-9429(2007)133:6(649). URL `https://ascelibrary.org/doi/abs/10.1061/%28ASCE%290733-9429%282007%29133%3A6%28649%29`.

[70] B. J. Wagner. Simultaneous parameter estimation and contaminant source characterization for coupled groundwater flow and contaminant transport modelling. *Journal of Hydrology*, 135(1) :275 – 303, 1992. ISSN 0022-1694. doi : https://doi.org/10.1016/0022-1694(92)90092-A. URL `http://www.sciencedirect.com/science/article/pii/002216949290092A`.

[71] X. Wan and G. Karniadakis. An adaptive multi-element generalized polynomial chaos method for stochastic differential equations. *Journal of Computational Physics*, 2006.

[72] X. Wan and G. E. Karniadakis. Multi-element generalized polynomial chaos for arbitrary probability measures. *SIAM Journal on Scientific Computing*, 28(3) :901–928, 2006.

[73] Q. Wang, J. S. Hesthaven, and D. Ray. Non-intrusive reduced order modeling of unsteady flows using artificial neural networks with application to a combustion problem. *Journal of Computational Physics*, 384 :289 – 307, 2019. ISSN 0021-9991. doi : https://doi.org/10.1016/j.jcp.2019.01.031. URL `http://www.sciencedirect.com/science/article/pii/S0021999119300828`.

[74] N. Wiener. The homogeneous chaos. *American Journal of Mathematics*, pages 60, 897–936, 1938.

[75] J. A. Witteveen and H. Bijl. Modeling arbitrary uncertainties using gram-schmidt polynomial chaos. *44th AIAA Aerospace Sciences Meeting and Exhibit*, 2006.

[76] D. Xiu and G. E. Karniadakis. The wiener–askey polynomial chaos for stochastic differential equations. *SIAM Journal on Scientific Computing*, 24(2) :619–644, 2002. doi : 10.1137/S1064827501387826. URL `https://doi.org/10.1137/S1064827501387826`.

[77] D. Xiu and G. E. Karniadakis. Modeling uncertainty in flow simulations via generalized polynomial chaos. *Journal of Computational Physics*, 187(1) :137 – 167, 2003. ISSN 0021-9991. doi : https://doi.org/10.1016/S0021-9991(03)00092-5. URL `http://www.sciencedirect.com/science/article/pii/S0021999103000925`.

3.3 Complementary data investigations using POD and variants

As mentioned in the ”Summary and discussion” part of the paper, presented in previous Section 3.2, additional bathymetry data investigations were performed using POD, and attempts with other decompositions for comparison, namely Kernel PCA (KPCA) and Sparse PCA (SPCA), were given. This is therefore detailed in the following, as a complement to previously presented results. Besides, a preliminary study, as perspective for detecting optimal measurement locations using POD, is also given below.

Firstly, POD can serve as a data filtering technique. Indeed, applying it to the full bathymetry data-set, without prior cleaning, allowed noticing outliers. Additionally, analysis of the patterns and associated coefficients has shed light on bad quality and erroneous records. The latter mainly consisted in incomplete profiles inside the intake, which was particularly observed for less recent measurements, previous to 2016. Relying on such records was not an option, as resulting POD patterns were used as a dynamic basis for the data-based model. Hence, to overcome this limitation, a Time-Restrained (T-R) set over 2016-2018 was considered, and resulted with more physically coherent modes. However, by proceeding in such way, too many measurements (2007-2015) had to be put aside, which was limiting for the learning. Another option was therefore considered, called Space-Restrained (S-R) POD, where only the high depths zone of the intake is considered, corresponding to an area where bathymetry was always measured. The three investigation steps, i.e. (i) outliers detection, (iv) T-R POD and (iv) S-R POD are therefore detailed in Section 3.3.1 below.

Secondly, a brief comparison between results provided by POD (or, equivalently Principal Component Analysis (PCA)), KPCA [161] and SPCA [106] is also presented in Section 3.3.2. In particular, the potential of KPCA to provide more efficient decompositions (in terms of reduction), and the possibility of finding more physically coherent patterns with SPCA, are of interest.

Lastly, a comparative study between POD applied to the whole bathymetry of the intake, and POD applied to each single-beam intake profile independently, was undertaken, as presented in Section 3.3.3. This allows determining the most optimal measurement locations in the intake.

3.3.1 POD for data filtering

Besides allowing Dimensionality Reduction (DR), POD can also help detecting noise in the data by smoothing the measurements. Noise can consist in measurement inaccuracies, or processes occurring at smaller scales, which sometimes are not of interest [119] or can make interpretation difficult. Below is an example of noise detection in bathymetry measurements using POD, with an attempt to produce the most meaningful and representative basis of the dynamics.

Outliers detection using POD

At first, all mono-beam bathymetry measurements (a total of 163 measurements) were considered as valuable information. They were POD processed without any filtering or cleaning. The first four temporal coefficients and associated spatial patterns are shown in Figures 3.1 and 3.2 respectively. The first two temporal signals show regularity, except for some extreme points, as circled in red in Figure 3.1-a. Specific dates investigation showed that the latter correspond to incomplete measurements. For example, during significant storm events, sea swell prevents the measuring boat from staying still, making the bathymetry at intake's entrance difficult to measure. Therefore, for these particular dates, bathymetry profiles at the entrance were missing from the data. Due to linear interpolation that precedes POD, performed on $m_i = 100$ fixed points for each profile in order to express all measurements on the same grid and constitute a snapshot matrix (Section 3.2), a bias consisting in artificial dynamics (e.g. extrapolation of bathymetry from downstream to intake's entrance) is therefore created.

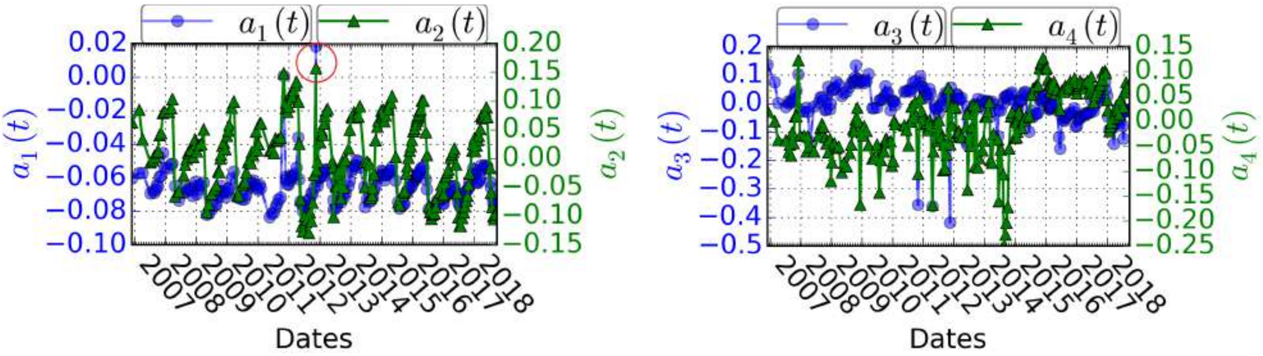

(a) Coefficients 1 and 2 (b) Coefficients 3 and 4

Figure 3.1 – First four temporal coefficients of POD applied to the complete data set. Example of an outlier date circled in red in Figure (a).

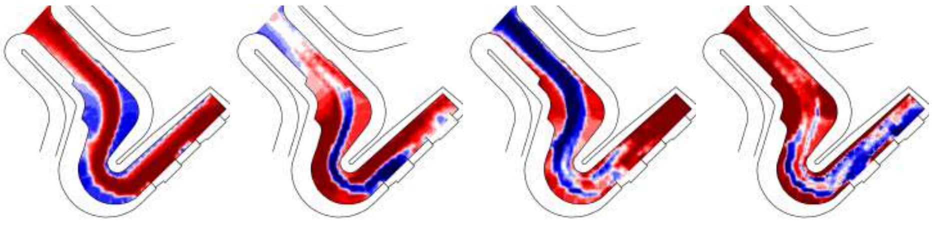

(a) $\Phi_1(x)$ (b) $\Phi_2(x)$ (c) $\Phi_3(x)$ (d) $\Phi_4(x)$

Figure 3.2 – First four spatial patterns of POD applied to the complete data set. Values are positive when red, negative when blue and near-zero when white.

Additionally, it can be noticed that the third and fourth temporal coefficients are irregular. The spatial patterns in Figure 3.2 seem coherent, namely with the upstream silting as can be seen in Figure 3.2-d.

A second POD was therefore performed on a filtered data set, composed of 156 bathymetries, where the incomplete data were deleted from the snapshot matrix. The first four temporal coefficients and associated spatial patterns are shown in Figures 3.3 and 3.4 respectively. The first two show regularity, unlike the third and fourth ones. While the increase and decrease of the former are directly related to sedimentation/dredging, the behavior of the latter is difficult to interpret in terms of physics. Additionally, they easily change by data-set modification, as can be concluded by comparing Figures 3.1 and 3.3. The associated basis components, shown in Figure 3.4, also dramatically changed in comparison with Figure 3.2, while the first two patterns remained almost identical.

After data investigation, this behavior also showed to be generated by missing data. In fact, measured bathymetry profiles before 2016 were not always complete. Starting from 2016, the quality of bathymetric measurements has increased (see Figure 3.5). As a result, bathymetry variance over the 2007-2015 period in Figure 3.5-a shows completely different behavior from variance over 2016-2018 in Figure 3.5-b, which is once again caused by interpolation bias. In fact, the interpolation process fills the gap by extrapolating the values from the middle of the profile to the banks, ending with too low elevations at the latter. The alternating complete and incomplete profile measurements, coupled to interpolation, create artificial dynamics at the banks and therefore result with considerable variances, as shown in Figure 3.5-a. These artificial dynamics end up in the third and fourth POD modes as can be seen in Figure 3.2-c and Figure 3.2-d. The latter are the statistical representation of the occurrence of incomplete measurements.

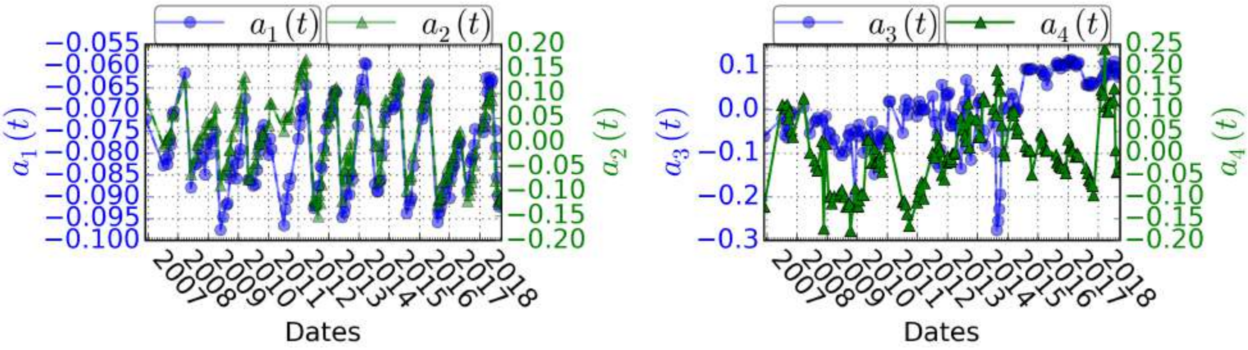

(a) Coefficients 1 and 2 (b) Coefficients 3 and 4

Figure 3.3 – The first four temporal coefficients of the POD applied to the filtered data set.

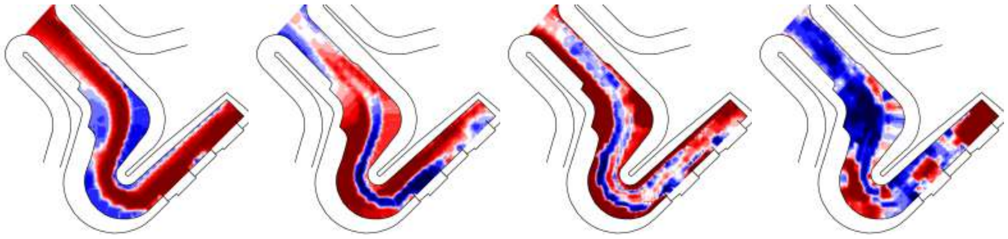

(a) $\mathbf{\Phi}_1(x)$ (b) $\mathbf{\Phi}_2(x)$ (c) $\mathbf{\Phi}_3(x)$ (d) $\mathbf{\Phi}_4(x)$

Figure 3.4 – First four spatial patterns before and after filtering. Values are positive when red, negative when blue and near-zero when white.

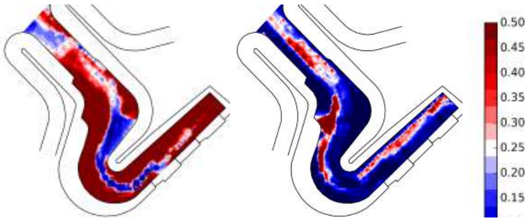

(a) 2007-2015 (b) 2016-2018

Figure 3.5 – Bathymetry variance maps over defined periods.

To limit this bias, two alternatives are considered: (i) using quality data only by considering a Time-Restrained data-set (T-R) on the $2016 - 2018$ period; (ii) using the complete $2007 - 2018$ set but Space-Restrained (S-R) to a limited area where bathymetry is always measured. This area corresponds to the high-depths zone where sediments are most likely to settle (lower velocities). It also corresponds to the zone of considerable siltings where the operational dredgings are usually undertaken.

Time-Restrained POD to maximize data quality

POD is applied to a Time-Restrained (T-R) set, corresponding to good quality $2016 - 2018$ measurements. The resulting temporal coefficients and spatial basis elements are shown in Figures 3.6 and 3.7 respectively.

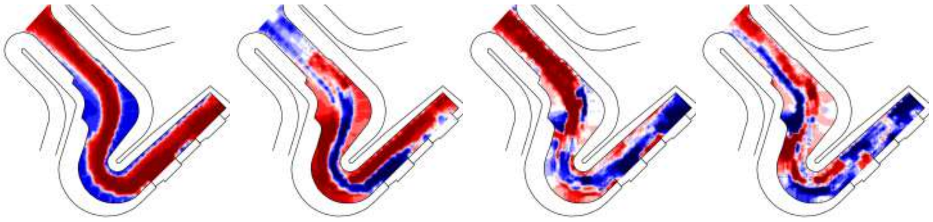

(a) T-R set $\mathbf{\Phi}_1(x)$ (b) T-R set $\mathbf{\Phi}_2(x)$ (c) T-R set $\mathbf{\Phi}_3(x)$ (d) T-R set $\mathbf{\Phi}_4(x)$

Figure 3.6 – First four spatial patterns of the POD applied to the Time-Restrained $2016 - 2018$ set (T-R). Values are positive when red, negative when blue and near-zero when white.

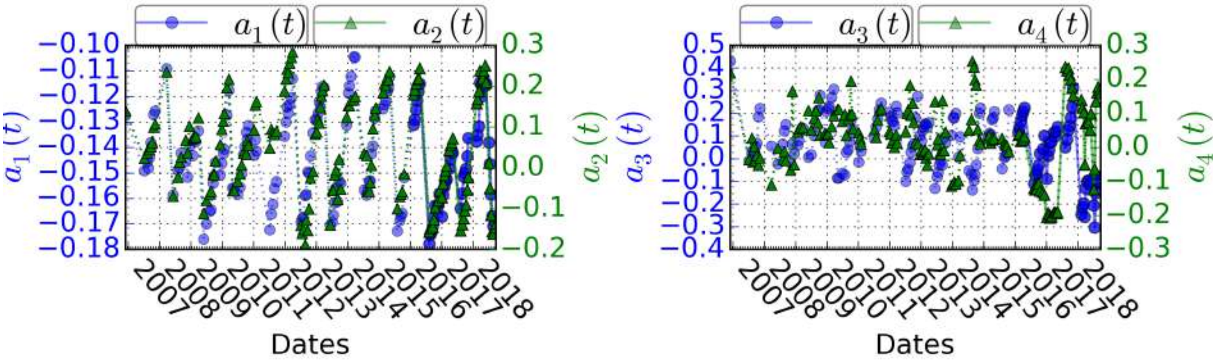

(a) Coefficients 1 and 2 (b) Coefficients 3 and 4

Figure 3.7 – The first four temporal coefficients of POD applied to the Time-Restrained $2016 - 2018$ set (T-R). Lines correspond to the 2016-2018 POD, while dashed lines represent the temporal coefficients obtained by projecting the 2007-2015 measurements on the 2016-2018 basis.

Firstly, while the first pattern remained almost identical to the 2007-2018 POD results (Figure 3.4), the second pattern is impacted upstream and the third and fourth dramatically changed. In particular for Mode 3, previously observed high values at the banks in Figure 3.4-c are no longer present in Figure 3.6-c. Secondly, concerning the temporal coefficients, no considerable change is noticed for the first two modes in Figure 3.7-a. Conversely, the third and fourth coefficients in Figure 3.7-b are less chaotic than previous results of Figure 3.3-b, although some peaks are still observed, probably linked to less frequent events. Lastly, as observed in dashed lines with the projection of Figure 3.7, the T-R POD can allow to reconstruct missing data in older bathymetry, by projecting the latter on the construct basis.

Space-Restrained POD to conserve the learning set size

Next, POD is applied to the Space-Restrained (S-R) bathymetry data-set. The resulting POD basis elements are shown in Figure 3.8. Once again, the first two spatial patterns are almost identical to previous decompositions, while the third and fourth elements dramatically change (although being almost identical for the S-R and the T-R POD).

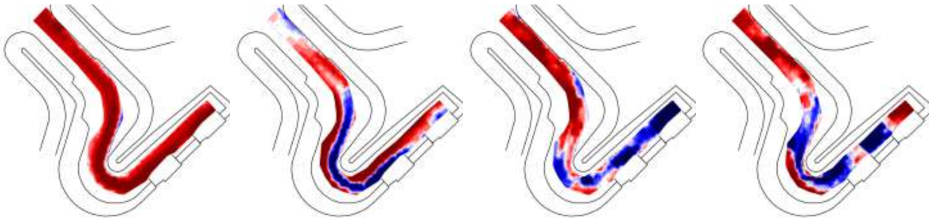
(a) S-R set $\Phi_1(x)$ (b) S-R set $\Phi_2(x)$ (c) S-R set $\Phi_3(x)$ (d) S-R set $\Phi_4(x)$

Figure 3.8 – First four spatial patterns of the POD applied to the Space-Restrained set (S-R). Values are positive when red, negative when blue and near-zero when white.

In order to quantify the loss of information resulting from data-sets restriction (S-R and T-R), the mean relative RMSE between measurements and POD approximations is calculated in the common spatial area (high-depths zone), as shown in Figure 3.9.

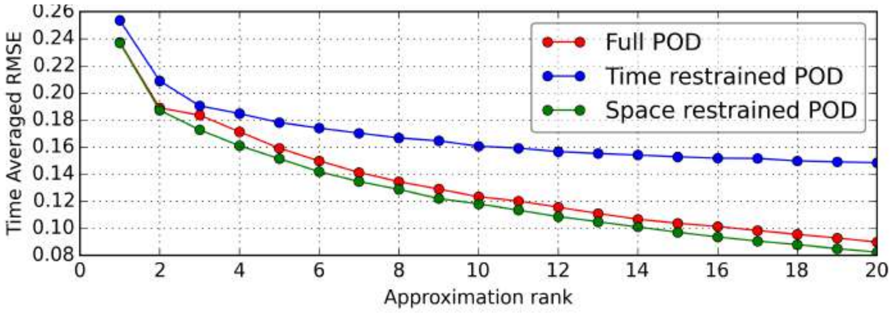

Figure 3.9 – Comparison of the 2007 – 2018 time averaged RMSE using the full, S-R and T-R sets for POD. Approximation rank corresponds to the used POD modes number.

Using three modes only, the RMSE is about 17 to 19 % for the three methods. Performance of the S-R POD is identical to the full set POD for the first two modes. Starting from the third mode, a difference of 1 % arises. Using 20 modes, the RMSE decreases to about 8 % for the S-R POD, 9 % for the full POD and 15 % for the T-R POD. Use of T-R set POD probably alters the adequacy of extracted basis to represent the whole range of bathymetry variations. In fact, ignoring past events puts aside dynamics that did not occur between 2016 and 2018, in particular extreme states that have greater chances being observed over larger time windows.

A comparison between the EVR is also shown in Figure 3.10. About 99 % of EVR is captured with 12 modes only using the S-R set, whereas the same rate requires 20 modes for with the full set.

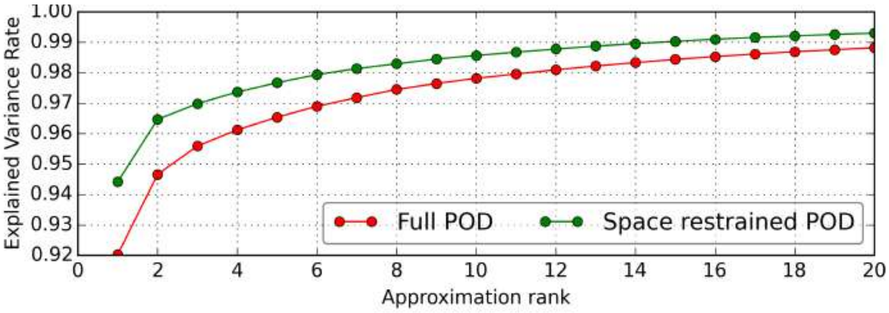

Figure 3.10 – Comparison of EVR resulting from POD on the full, S-R and T-R sets. Approximation rank corresponds to the used POD modes number.

S-R POD was therefore selected for the contribution of Section 3.2, as it is the most accurate (lowest RMSE) in the interest high-depths zone. Additionally, spatial patterns were physically interpreted. Further more, over a decade of evolution has been used to extract the S-R POD basis under variable operational, sea and weather conditions, conversely to the T-R set. The S-R option was therefore the most interesting in terms of data-based learning.

3.3.2 Comparison with other decompositions

Brief comparison between POD, Kernel PCA (KPCA) [161] and Sparse PCA (SPCA) [106] performances was attempted. More precisely, better DR and the possibility of finding more physically coherent patterns were targeted.

Indeed, POD, although efficient as linear decomposition, may present two issues: (i) for some data-sets, Dimensionality Reduction (DR) using linear techniques can be unsatisfactory, in the sense that the number of needed components to reach sufficient representation may be important. Consequently, reduction of the dimensionality, which is the actual objective of such methods, is not achieved. To overcome this, KPCA applies a non-linear transformation (e.g. polynomial, sinusoidal, etc.) to the original data-set before applying POD (or PCA). This sometimes helps spanning the non-reducible subspace (in linear terms, which means that non-linearities are significant), to a linearly reducible space; (ii) POD components are mathematically optimal in terms of data compression. Their interpretation is however not always possible in terms of physics. It may sometimes be interesting to sacrifice Dimensionality Reduction (DR) for physical significance of the patterns. In SPCA, an $L2$ penalty is added to the optimization, which reduces the amplitude of non-significant modes. This helps maximizing the chances of obtaining physically interpretable patterns. Hence, comparison between POD, KPCA [161] and SPCA [106] was attempted. The python library Scikit-learn [190] (`https://scikit-learn.org`) was used for this purpose. It should be noted that while data were not centered before applying POD in previous investigations, the mean was here automatically deduced from the snapshot matrix using Scikit-learn PCA subroutines.

Firstly, relative RMSE between measurements and their transformed versions using Scikit-learn's PCA and KPCA, were compared in Figure 3.11. This allows to evaluate the performance of each decomposition in terms of data compression. In particular, polynomial and cosine kernels where attempted. It can be noticed that KPCA using polynomial kernel, can be more interesting in terms of DR for low rank approximations (up to 6 modes). However, it is later outperformed by PCA, for example for 11-Mode approximations, used in the ML proposed in Section 3.2.

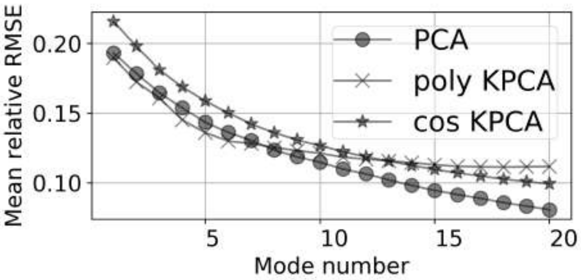

Figure 3.11 – Comparison of time averaged relative RMSE between full field and field reconstruction from reduced vectors, provided by PCA, and KPCA with cosine and polynomial kernels, using Scikit-learn [190].

Secondly, spatial patterns are compared between PCA and SPCA in Figure 3.12.

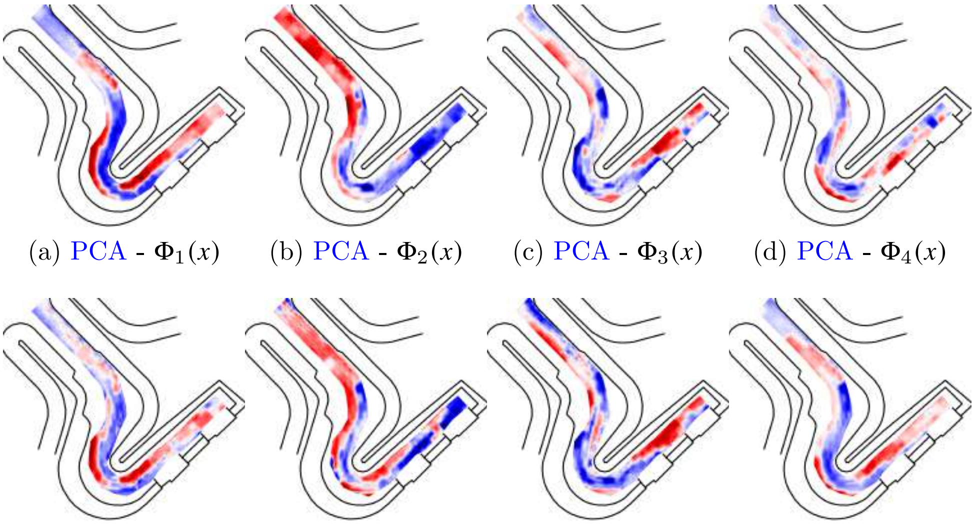

(a) PCA - $\mathbf{\Phi}_1(x)$ (b) PCA - $\mathbf{\Phi}_2(x)$ (c) PCA - $\mathbf{\Phi}_3(x)$ (d) PCA - $\mathbf{\Phi}_4(x)$

(e) SPCA - $\mathbf{\Phi}_1(x)$ (f) SPCA - $\mathbf{\Phi}_2(x)$ (g) SPCA - $\mathbf{\Phi}_3(x)$ (h) SPCA - $\mathbf{\Phi}_4(x)$

Figure 3.12 – Spatial patterns comparison between PCA and SPCA applied to the intake bathymetry, using Scikit-learn [190]. Values are positive when red, negative when blue and near-zero when white.

Slight changes can be noticed, namely emphasis on the sedimentation in front of the pumps in Mode 2, and a less noisy pattern for Mode 4. However, no drastic change or supplement of interpretation could here be made. Therefore, classical POD was selected for the data-based model. Most importantly, it is purely linear and its patterns are orthogonal, which allowed efficient coupling and interpretation with PCE.

3.3.3 Detection of optimal measurement locations using POD

A comparison between POD reduction applied to the whole intake bathymetry on the one hand, and applied to each single-beam intake profile independently on the other hand, was undertaken. The main difference consists in the used snapshot matrix. Columns of the latter are realizations of the whole field for the POD used in the previously presented data-based learning, in Section 3.2. For the independent profile POD, 39 snapshot matrices are set, each of them corresponding to a given profile, and containing realizations of the latter. These snapshot matrices are then POD reduced independently.

The undertaken spatial localisation is not interesting in terms of learning as it dramatically increases the number of POD expansion components. However, it was used as a first attempt to detect optimal measurement locations in the intake. More precisely, correlations between the dynamics of the whole field and the dynamics of single profiles were sought, through comparison of POD patterns.

Hence, Pearson correlations, defined in Equation 2.8, were calculated between the whole bathymetry POD coefficients, and the profiles POD coefficients, using extracted values over the 2007-2018 set. A plot is shown in Figure 3.13 for the first four modes. For example, Profile 18, located in the middle of the intake approximately, maximizes the first and second modes correlations with the whole bathymetry, while the upstream Profile 3 is more interesting to capture Mode 4 variations. However, it should be kept in mid that this is only a basic investigation as Pearson coefficients only detect linear relationships.

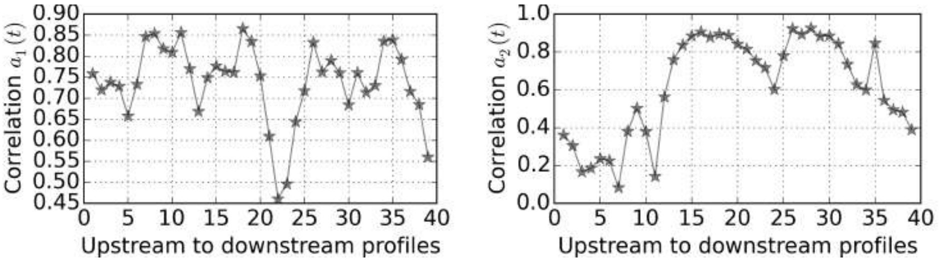

(a) Coefficient 1

(b) Coefficient 2

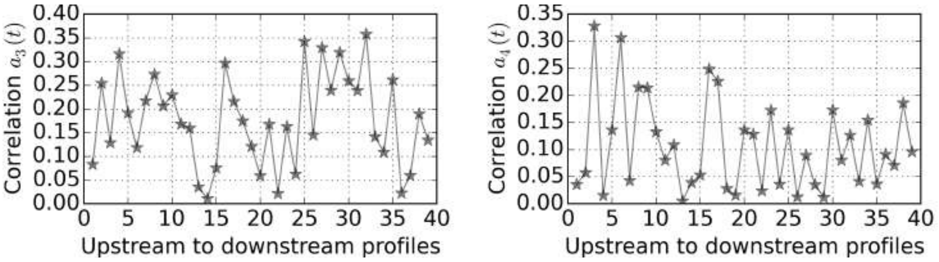

(c) Coefficient 3

(d) Coefficient 4

Figure 3.13 – Pearson correlations between temporal coefficients of the whole intake bathymetry POD, and POD applied to each single-beam profile independently.

This investigation allows to deduce correlations between the dynamics of the whole field and the dynamics of single profiles. By maximizing the correlations, the most informative profiles can be targeted for measurements. As an example, the possibility of installing a permanent device in the intake, in order to track a given profile evolution, was considered by the plant stakeholders. If the spatial location related to maximal correlations, shown in Figure 3.13, can be targeted, then the whole bathymetry field can be reconstituted. This can be performed by providing a first guess of the whole bathymetry POD expansion coefficients, based on previously established correlations (e.g. linear model with dispersion). This first guess would of course be uncertain. However, it can for example be used as a prior for DA with the POD-PCE data-based model, in order to obtain a posterior estimate with reduced uncertainties.

3.4 Summary

Throughout this chapter, it was shown that coupling between POD and PCE techniques is not only valuable as ML, but can also help interpreting the dynamics. Spatial distribution of the sedimentation in the intake was deduced, as well as corresponding EVR that quantify the importance of each sedimentation pattern. Additionally, dependency of the sedimentation to hydrodynamic and meteorological conditions was also quantified using ranking indices.

While POD-PCE helped understanding the dynamics of sedimentation at measurements spatio-temporal scales, other physical questions remain unanswered. For example (i) determining the predominant sediment transport processes (bed-load vs. suspension) can be of importance to design new measurement campaigns and (ii) understanding the dynamics at smaller scales, for example through a given storm event (hours) can be useful to propose a complete predictive tool. For these reasons, a process-based model can complete the data-based exploration.

However, the process-based model at hand (Chapter 1) uses approximations and unknown parameters. In particular, uncertain modelling choices should be made. Hence, Uncertainty Quantificiation (UQ) studies should be undertaken. Hence, the uncertainties of tidal modelling, related to common modelling choices (friction closures, domain extension), were investigated in Chapter 4. POD was used for comparison between numerical and measurement data patterns, and jointly employed with PCE for sensitivity analysis.

Chapter 4

Sensitivity of tidal modelling in coastal configurations

La modélisation numérique de la marée repose sur des équations à base de processus physiques, qui sont sujettes aux incertitudes causées par les choix de modélisations et les lois de fermetures utilisés. Dans ce chapitre, les incertitudes liées au modèle de frottement et au choix de la taille du domaine de calcul sont investiguées. La Réduction de Dimension (DR) et la métamodélisation spectrale stochastique, en particulier la Décomposition Orthogonale en modes Propres (POD) et l'Expansion par Polynômes du Chaos (PCE), sont utilisées pour comparer de manière efficace les résultats numériques aux données de campagne de mesures. Une étude de Quantification d'Incertitudes (UQ) est ainsi proposée.

Numerical modelling of tides relies on physical process-based equations, that are subject to uncertainties caused by modelling choices and used closure relationships. In this chapter, the uncertainties related to the choice of friction closure relationship and computational domain extension are investigated. Dimensionality Reduction (DR) and spectral stochastic metamodelling, and in particular Proper Orthogonal Decomposition (POD) and Polynomial Chaos Expansion (PCE), are used to efficiently compare numerical results to field survey data. An Uncertainty Quantification (UQ) study is hence proposed.

Contents

4.1 Motivations

The process-based model described in Chapter 1 can be of great value for physical investigations concerning the intake's sedimentation. As an example, an objective would be to produce a trustworthy hydro-morphodynamic numerical configuration, where an intake calculation domain, as represented in Figure 4.1, can be used for operational prediction and analysis.

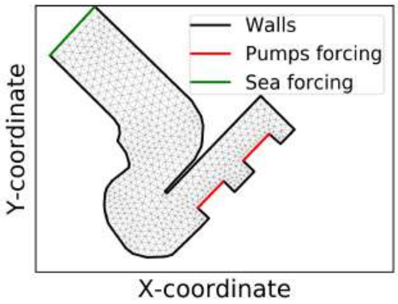

(a) Channel model

Figure 4.1 – Example of meshed calculation domain for the intake with adequate Boundary Conditions (BC).

However, many parameters for such a numerical model are unknown/uncertain (e.g. sediment diameter, Initial Conditions (IC), etc.). For example, the cross-sectional velocity profile at the entrance, corresponding to sea hydrodynamic forcing BC in Figure 4.1, must be determined. To this end, a common practice consists in determining the flow field from large scale models, in order to provide a suitable velocity distribution and water depth at intake's inflow. However, the choice of modelling domain extension is uncertain, and therefore produces uncertain BC at intake's entrance. The objective is therefore to quantify such an uncertainty, that originates from common modelling choices.

In the following, deterministic investigations are first shown in Section 4.2. Sensitivity of the tidal modelling to mesh refinement and domain size extension are discussed. These results allow to design UQ study experiments, conducted in Section 4.3 and presented in the form of a conference article [171] for the Telemac User Conference (TUC) 2020. Lastly, complementary results concerning the uncertainty of intake's sea BC (Figure 4.1) are presented in Section 4.4.

4.2 Deterministic investigations

As a first attempt to numerical modelling of tidal currents at intake's vicinity, deterministic comparisons with different set-ups were undertaken. Mesh convergence study, which is important for the trustworthiness of conclusions, is presented in Section 4.2.1. Sensitivity of the model to computational domain extension is described in Section 4.2.2. A converged mesh and four domain extensions are then selected for UQ study in Section 3.2.

4.2.1 Mesh convergence study

A mesh convergence study is performed on a computational domain, with 2 km offshore distance from the intake, and 2 km longshore distances west and east of the intake. The coarsest mesh configuration is as follows: a mean edge size of 200 m is set at the sea BC, 10 m at the intake's lateral boundaries, and 2 m at the pumps BC. Finer mesh configurations consist in successive divisions of elements sizes by 2 (e.g. 100 m at sea , 5 m at intake's walls and 1 m at pumps). Five mesh configurations are tested, designated according to edge size at sea BC (200, 100, 50, 25 and 12.5 m). To assure smoothness of the spatial discretization, a gradation coefficient is used to provide continuous element size distribution from the pumps to the sea. This coefficient varies from 1.08 to 1.05 and is chosen to guarantee a good quality of the mesh (e.g. avoid degenerate, highly skewed elements). Time step of 0.4 s is selected for the 200 m mesh, in order to keep the Courant–Friedrichs–Lewy (CFL) number below 1. When dividing mesh size by two, the time step is divided by two as well, to guarantee constant CFL for mesh convergence study.

A coarser mesh of size 400 m is used to interpolate raw bathymetry data. This provides a bathymetry map that can be used with either of the above meshes, ensuring that transition from coarser to finer meshes does not imply additional bathymetry details. Indeed, any changes would influence the Shallow Water Equations (SWE) source term as formulated in Equation 1.6, and therefore the modelled physics. For this first investigation, bed shear stress is modelled using the Strickler formulation as shown in Equation 1.9, where a value of $K = 65$ m$^{1/3}$/s is expertly set, based on previous calibrations. Two-days simulations (48 hours) using these configurations are launched. To guarantee the flow initialization, only the last tidal period is analyzed, at key times: High Tide (HT), Half Falling Tide (HFT, or ebb), Low Tide (LT) and Half Rising Tide (HRT, or flood).

Simulated results show no differences on free-surface values. Hence, only velocity values are compared hereafter. Velocity magnitude is extracted at cross-sectional profile located at intake's entrance. Results are shown in Figures 4.2 and 4.3 at HT and LT respectively, where $\overline{u}$ denotes the average magnitude of depth-averaged velocity. The color scale indicates velocity magnitude values, while profile deviation from average illustrates the spatial distribution of velocity. Mesh sizes are ordered along the x-axis.

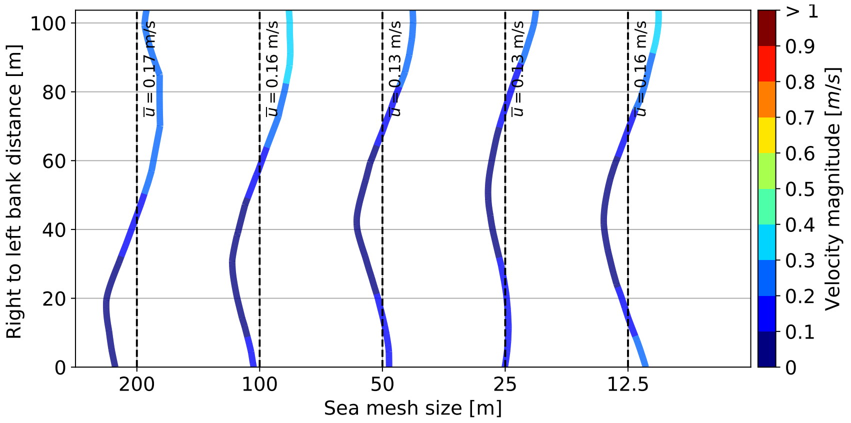

Figure 4.2 – Velocity magnitude at intake's entrance cross-shore profile with different meshes, at HT.

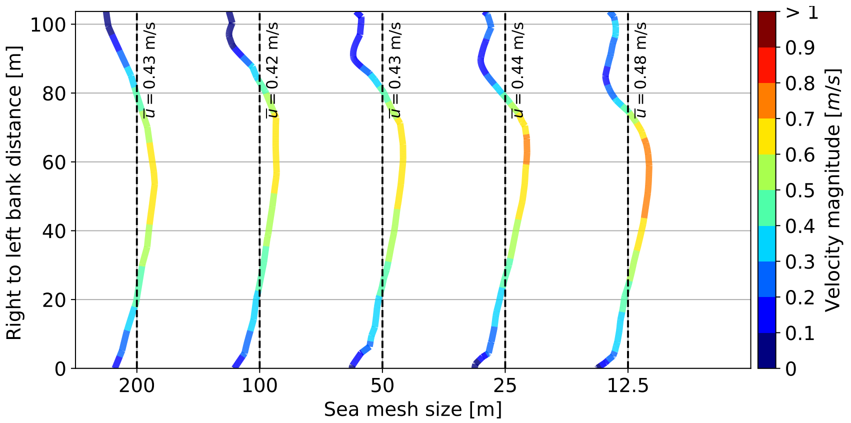

Figure 4.3 – Velocity magnitude at intake's entrance cross-shore profile using different meshes, at Low Tide (LT).

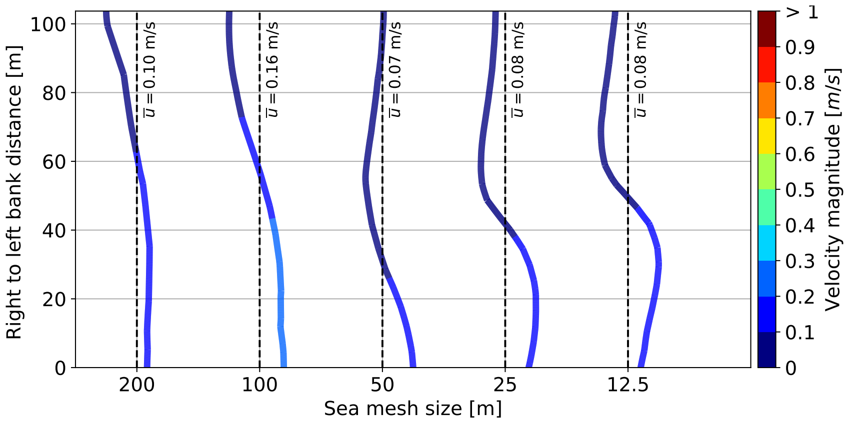

Figure 4.4 – Velocity magnitude at intake's entrance cross-shore profile using different meshes, at Half Falling Tide (HFT).

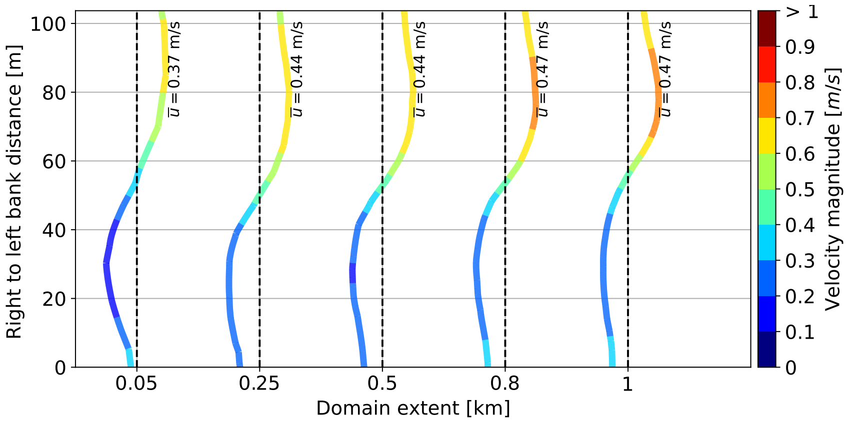

Figure 4.5 – Velocity magnitude at intake's entrance cross-shore profile using different meshes, at Half Rising Tide (HRT).

The velocity profile shape changes from coarser meshes (left hand side of Figures 4.3 and 4.2) to finer meshes. Numerical results obtained with the last three mesh discretizations show similarities, indicating convergence. Average velocity difference between the 50 m mesh and the 12.5 m mesh (considered as a reference) amounts to $-18,75\%$ at HT (lower velocities) and −10.42% at LT (higher velocities). The coarser mesh underestimates, in average, the computed velocities at both characteristic times. Velocity extrema are moving transversely refining the mesh. This is more visible at HT (Figure 4.2), where the average velocity magnitude is lower. Meshes of sizes 50, 25 and 12.5 m give comparable results, namely at LT (Figure 4.3), where velocity distribution differs with meshes of sizes 200 and 100 m at left bank. A similar plot is shown for interest times HFT and HRT, in Figures 4.4 and 4.5 respectively. Same conclusions hold: more similarity is observed for the last three meshes, with a gradual shift in the profiles shape.

This analysis showed that convergence with spatial discretization is observed, for meshes with typical element size of approx. 50 m at sea, 2.5 m at intake's walls and 0.5 m at pumps. This configuration is therefore selected for the remaining investigations below. Nevertheless, slight differences may still be noted with finer mesh discretizations, and should be kept in mind.

4.2.2 Domain size influence study

The domain extension influence is assessed on deterministic simulations, using the 50 m mesh (50 m at sea BC, 2.5 m at intake's walls, and 0.5 m at pumps BC). Domains are denoted by the offshore distance from intake's entrance. For example, domain of size 2 km designates the previously described 2 $km \times 2$ km domain (offshore × longshore distance to east/west). Size 10 km designates a domain of size 10 $km \times 10$ km, constructed in the same manner. It should be highlighted that widening the domain inevitably introduces additional physics, such as the development of bigger flow structures, in addition to modelling larger scale bathymetry patterns. In order to assess the influence of domain size on simulated currents, calculations are first conducted without friction, in order to avoid additional dissipation of energy induced by friction. Simulations without friction are then compared to simulations with a Strickler closure using a coefficient $K = 65$ $\mathrm{m}^{1/3}/\mathrm{s}$, as previously explained.

Firstly, velocity profiles from simulations without friction effect are shown at HT and LT in Figures 4.6 and 4.7 respectively. At HT, a classification of behaviors with domain size ranges is visible. For example, medium scale sizes 2, 3 and 4 km follow an increasing velocity trend in the middle of the profile.

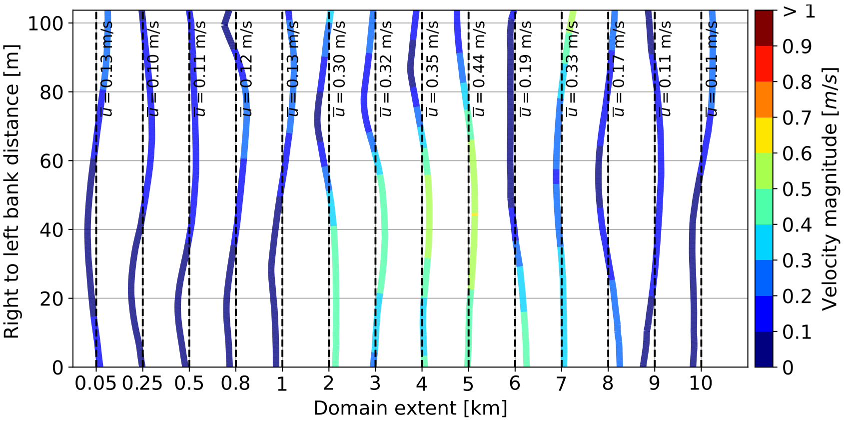

Figure 4.6 – Velocity magnitude at intake's entrance cross-shore profile using different domain extensions, for simulations without Friction, at High Tide (HT).

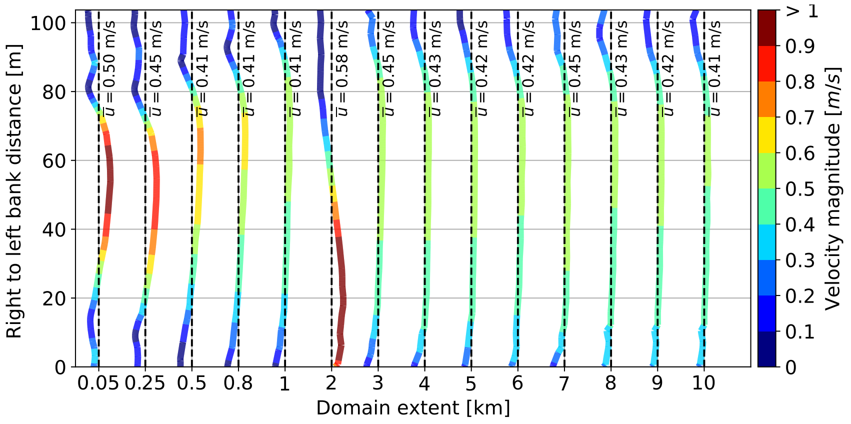

Figure 4.7 – Velocity magnitude at intake's entrance cross-shore profile using different domain extensions, for simulations without Friction, at Low Tide (LT).

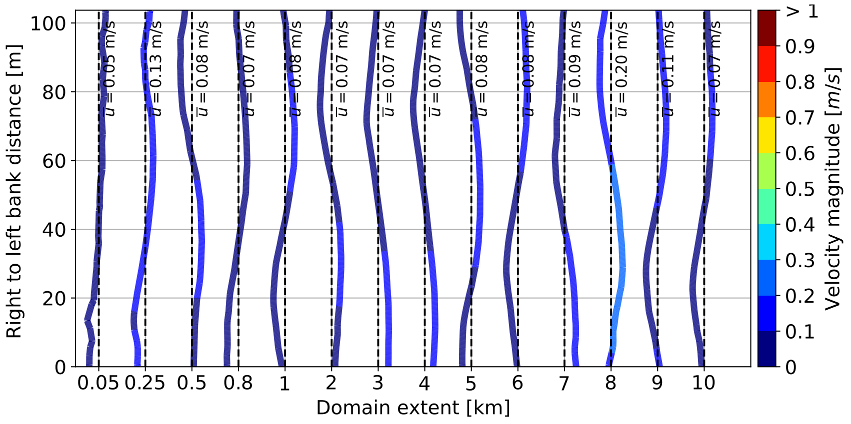

Figure 4.8 – Velocity magnitude at intake's entrance cross-shore profile using different domain extensions, for simulations without Friction, at Half Falling Tide (HFT).

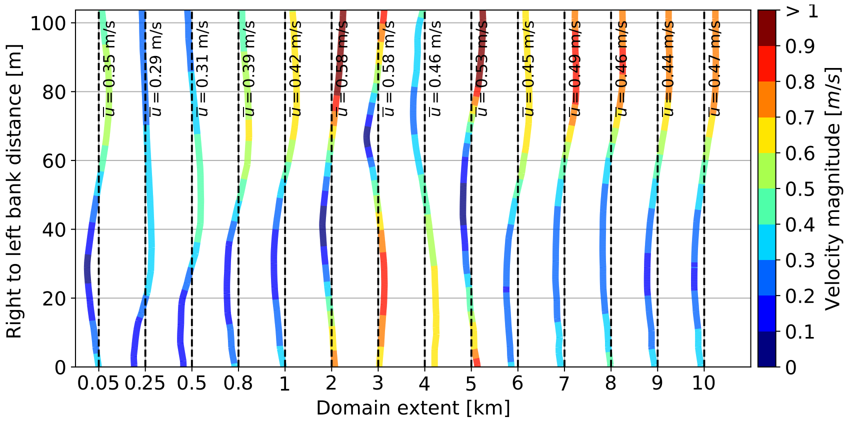

Figure 4.9 – Velocity magnitude at intake's entrance cross-shore profile using different domain extensions, for simulations without Friction, at Half Rising Tide (HRT).

At LT, where velocities are higher, there seems to be a domain size convergence. Indeed, only the first three small smallest (0.05, 0.25 and 0.5 km) differ from the others in terms of average and spatial distribution. Domains of larger extension have the same behavior except for the 2 km one that stands out. Results at HFT and HRT are also shown in Figures 4.8 and 4.9 respectively. Once again, the domains of sizes 2, 3 and 4 km behave the same at HFT, and constitute a transition zone to a convergence at HRT.

Results of simulations using Strickler's formula are for example shown at HT and LT in Figures 4.10 and 4.11 respectively. Friction effect is noticeable on the 2 km domain. Not only it completely changes the shape of the profile, but it also impacts the average velocity, making it nearly identical to the 1 km domain. Friction moderates the velocities from sea BC to intake's entrance. The higher the velocity values, the bigger the influence of friction. Indeed, bed shear stress is a quadratic function of velocity (Equation 1.7).

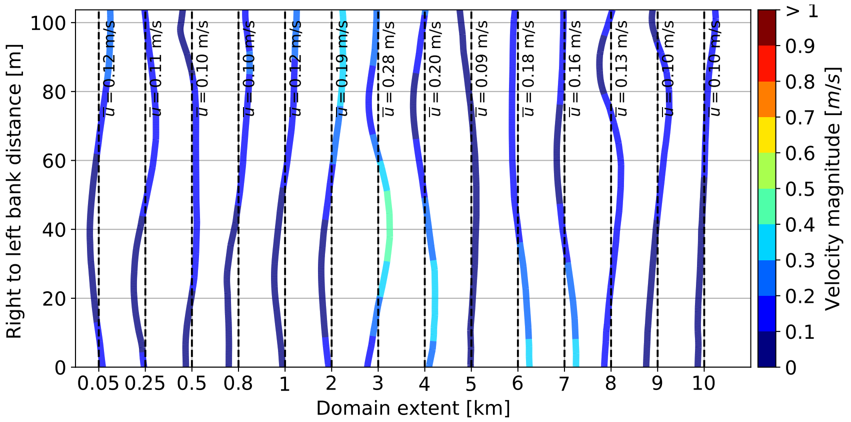

Figure 4.10 – Velocity magnitude at intake's entrance cross-shore profile using different domain extensions, for simulations with Friction, at High Tide (HT).

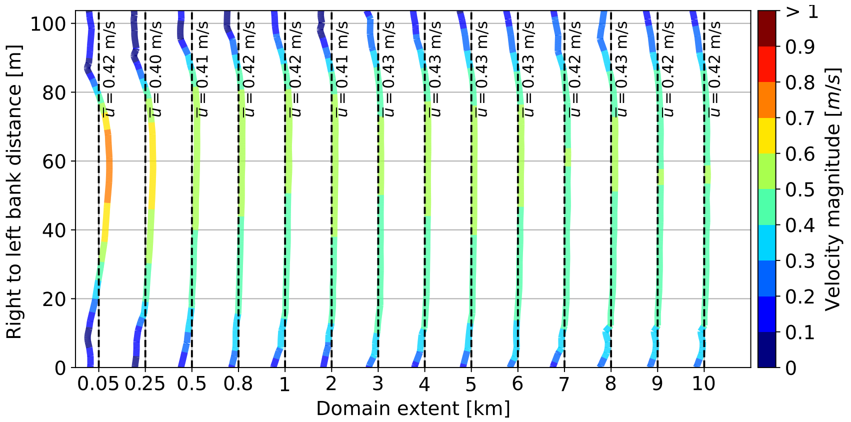

Figure 4.11 – Velocity magnitude at intake's entrance cross-shore profile using different domain extensions, for simulations with Friction, at Low Tide (LT).

As a conclusion, the choice of domain extension might have considerable influence on the velocity magnitude and shape at intake's entrance. Velocities can be controlled using friction. This implies that friction should be calibrated whatever the domain extension. However, same friction value does not imply same result with different domain sizes. This raises questions about the uncertainty implied by domain extension and friction formula choice and calibration. Hence, a UQ study is undertaken in the following, using four representative domains of different extensions: (i) the 800 m domain, considered as small scale; (ii) the 2 km, called medium scale, selected to investigate its particular behavior; (iii) two large scale domains of sizes 7 and 8 km selected for comparison.

4.3 Telemac User Conference article

Sensitivity of tidal modelling in coastal configurations: an uncertainty study based on field-measurement reduction

Rem-Sophia Mouradi[1,2], Cédric Goeury[1], Pablo Tassi[1], Fabrice Zaoui[1]
[1]National Laboratory for Hydraulics and Environment (LNHE)
Electricité De France (EDF) R&D
6 Quai Watier, Chatou, France
remsophia.mouradi@gmail.com

Olivier Thual[2]
[2]Climate, Environment, Coupling and Uncertainties research unit (CECI)
Université de Toulouse, CERFACS/CNRS
Toulouse, France

***Abstract*—Hydrodynamic models are increasingly used in operational industrial contexts for prediction and analysis purposes, including risk assessment and design optimization. In the modelling phase, expertly made choices can have consequences on either computational cost (i.e. mesh resolution, domain size, etc.), or closures to unknowns and their parameters (friction, turbulence, etc.). These choices are examples of epistemic uncertainty in hydrodynamic applications. Simultaneously, in the last few years, field measurements have become more accessible, giving the opportunity to deepen validation processes, and to challenge standard modelling practices based on expert judgement.**

In this study, a sensitivity analysis to modelling choices such as domain extent and friction closure formulas is assessed in the context of tidal forcing in a coastal area. Comparison to field measurements of free surface and velocity components is performed using Dimensionality Reduction (DR), by means of Proper Orthogonal Decomposition (POD).

Firstly, numerical simulations with small, medium and large scale computational domains and two different friction parameterizations (i.e. Strickler and Colebrook-White), are performed and statistically compared. For this purpose, Monte Carlo (MC) simulations are launched for each modelling configuration, using samples of uncertain friction parameters and tidal boundary conditions. The different behaviors are therefore analyzed using comparative statistics on the available measurement points (average, confidence intervals, etc.).

Secondly, using POD, the behavior of each configuration, over the space of all possible events, is reduced to few representative components, commonly called modes or patterns. These modes are mutually compared for the different configurations, as well as to POD modes deduced from a distinct analysis on field measurements. A sensitivity analysis on POD modes using Sobol' indices shows that the chosen configurations can have different sensitivities to the same uncertain input parameters. This suggests that a calibration procedure might respond to different control parameters depending on the modelling choices. Consequently, the optimal estimates found from one configuration to the other, may differ.

I. INTRODUCTION

Shallow Water Equations (SWE) are commonly used in coastal applications as good compromise between precision and computational cost. However, modelling a real case application is not always trivial. For example, the influence of the computation domain extension on the results is in general poorly evaluated, and the uncertainty implied by source terms closures, for example friction, is often overlooked. In the absence of alternatives, these choices are determined by expert opinion. In particular, calibration of the model on measurements is used to justify the model's capacity to provide physically coherent information, and therefore its predictive capability. The fitted model is then used to analyze the flow between calibration points. However, the equivalence between good-fit and accuracy can be questioned. For example, friction is often calibrated to fit measurements at different stream points, spatially or temporally distributed, as in [4, 10]. It is then assumed that the bed and the flow characteristics are uniformly distributed between the calibration points, and that the model is trusted for the other choices, namely domain size. This of course is a strong assumption.

The goal of the present study is to analyze the uncertainty resulting from common modeling choices: domain size and friction closure. For this purpose, four domain extents are compared, and two friction formulas are confronted. Different challenges are however encountered. Firstly, realistic hydrodynamic cases are high dimensional, i.e. they involve numerous parameters, and the response is spatio-temporal, which makes pointwise analysis difficult. Secondly, measurements are also spatio-temporal fields and are sometimes noisy. Proper Orthogonal Decomposition (POD) is therefore used to reduce the dimensionality of the numerical output on one hand, and to reduce and smoothen the observation on the other hand. This makes the comparison of uncertainties resulting from different model choices easier. Indeed, POD is respectively applied on the numerical model results and on observations. The resulting patterns are confronted. Then, the coefficients associated to the numerical POD patterns are learned using PCE (Polynomial Chaos

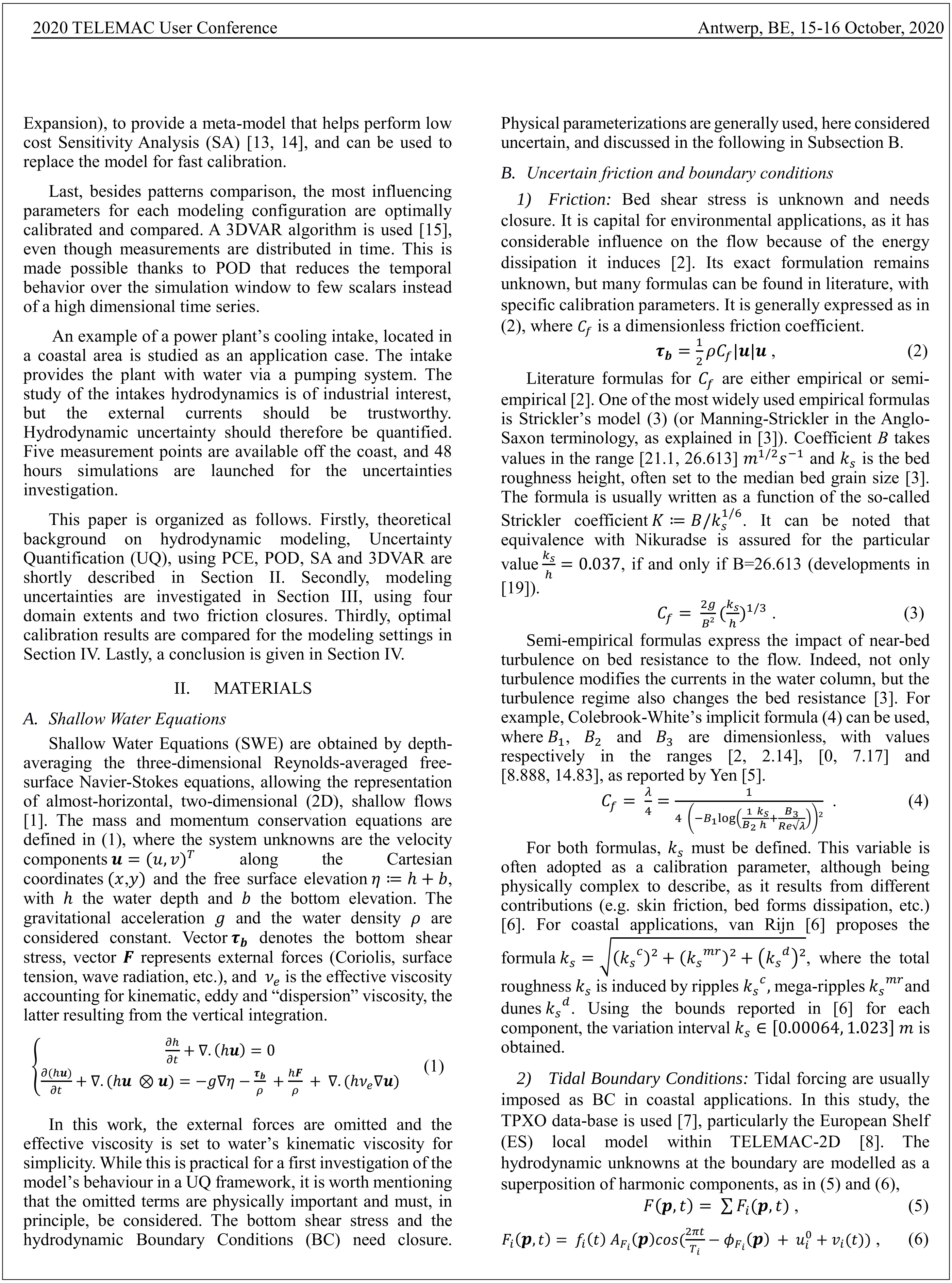

Expansion), to provide a meta-model that helps perform low cost Sensitivity Analysis (SA) [13, 14], and can be used to replace the model for fast calibration.

Last, besides patterns comparison, the most influencing parameters for each modeling configuration are optimally calibrated and compared. A 3DVAR algorithm is used [15], even though measurements are distributed in time. This is made possible thanks to POD that reduces the temporal behavior over the simulation window to few scalars instead of a high dimensional time series.

An example of a power plant's cooling intake, located in a coastal area is studied as an application case. The intake provides the plant with water via a pumping system. The study of the intakes hydrodynamics is of industrial interest, but the external currents should be trustworthy. Hydrodynamic uncertainty should therefore be quantified. Five measurement points are available off the coast, and 48 hours simulations are launched for the uncertainties investigation.

This paper is organized as follows. Firstly, theoretical background on hydrodynamic modeling, Uncertainty Quantification (UQ), using PCE, POD, SA and 3DVAR are shortly described in Section II. Secondly, modeling uncertainties are investigated in Section III, using four domain extents and two friction closures. Thirdly, optimal calibration results are compared for the modeling settings in Section IV. Lastly, a conclusion is given in Section IV.

II. MATERIALS

A. *Shallow Water Equations*

Shallow Water Equations (SWE) are obtained by depth-averaging the three-dimensional Reynolds-averaged free-surface Navier-Stokes equations, allowing the representation of almost-horizontal, two-dimensional (2D), shallow flows [1]. The mass and momentum conservation equations are defined in (1), where the system unknowns are the velocity components $\boldsymbol{u} = (u, v)^T$ along the Cartesian coordinates (x,y) and the free surface elevation $\eta := h + b$, with h the water depth and b the bottom elevation. The gravitational acceleration g and the water density ρ are considered constant. Vector $\boldsymbol{\tau_b}$ denotes the bottom shear stress, vector $\boldsymbol{F}$ represents external forces (Coriolis, surface tension, wave radiation, etc.), and ν_e is the effective viscosity accounting for kinematic, eddy and "dispersion" viscosity, the latter resulting from the vertical integration.

$$\begin{cases} \dfrac{\partial h}{\partial t} + \nabla.(h\boldsymbol{u}) = 0 \\ \dfrac{\partial(h\boldsymbol{u})}{\partial t} + \nabla.(h\boldsymbol{u} \otimes \boldsymbol{u}) = -g\nabla\eta - \dfrac{\boldsymbol{\tau_b}}{\rho} + \dfrac{h\boldsymbol{F}}{\rho} + \nabla.(h\nu_e\nabla\boldsymbol{u}) \end{cases} \tag{1}$$

In this work, the external forces are omitted and the effective viscosity is set to water's kinematic viscosity for simplicity. While this is practical for a first investigation of the model's behaviour in a UQ framework, it is worth mentioning that the omitted terms are physically important and must, in principle, be considered. The bottom shear stress and the hydrodynamic Boundary Conditions (BC) need closure. Physical parameterizations are generally used, here considered uncertain, and discussed in the following in Subsection B.

B. *Uncertain friction and boundary conditions*

1) Friction: Bed shear stress is unknown and needs closure. It is capital for environmental applications, as it has considerable influence on the flow because of the energy dissipation it induces [2]. Its exact formulation remains unknown, but many formulas can be found in literature, with specific calibration parameters. It is generally expressed as in (2), where C_f is a dimensionless friction coefficient.

$$\boldsymbol{\tau_b} = \frac{1}{2}\rho C_f |\boldsymbol{u}|\boldsymbol{u} \, , \tag{2}$$

Literature formulas for C_f are either empirical or semi-empirical [2]. One of the most widely used empirical formulas is Strickler's model (3) (or Manning-Strickler in the Anglo-Saxon terminology, as explained in [3]). Coefficient B takes values in the range [21.1, 26.613] $m^{1/2}s^{-1}$ and k_s is the bed roughness height, often set to the median bed grain size [3]. The formula is usually written as a function of the so-called Strickler coefficient $K := B/k_s^{1/6}$. It can be noted that equivalence with Nikuradse is assured for the particular value $\frac{k_s}{h} = 0.037$, if and only if B=26.613 (developments in [19]).

$$C_f = \frac{2g}{B^2}\left(\frac{k_s}{h}\right)^{1/3} . \tag{3}$$

Semi-empirical formulas express the impact of near-bed turbulence on bed resistance to the flow. Indeed, not only turbulence modifies the currents in the water column, but the turbulence regime also changes the bed resistance [3]. For example, Colebrook-White's implicit formula (4) can be used, where B_1, B_2 and B_3 are dimensionless, with values respectively in the ranges [2, 2.14], [0, 7.17] and [8.888, 14.83], as reported by Yen [5].

$$C_f = \frac{\lambda}{4} = \frac{1}{4\left(-B_1 \log\left(\frac{1}{B_2}\frac{k_s}{h} + \frac{B_3}{Re\sqrt{\lambda}}\right)\right)^2} . \tag{4}$$

For both formulas, k_s must be defined. This variable is often adopted as a calibration parameter, although being physically complex to describe, as it results from different contributions (e.g. skin friction, bed forms dissipation, etc.) [6]. For coastal applications, van Rijn [6] proposes the formula $k_s = \sqrt{({k_s}^c)^2 + ({k_s}^{mr})^2 + \left({k_s}^d\right)^2}$, where the total roughness k_s is induced by ripples ${k_s}^c$, mega-ripples ${k_s}^{mr}$ and dunes ${k_s}^d$. Using the bounds reported in [6] for each component, the variation interval $k_s \in [0.00064, 1.023]\ m$ is obtained.

2) Tidal Boundary Conditions: Tidal forcing are usually imposed as BC in coastal applications. In this study, the TPXO data-base is used [7], particularly the European Shelf (ES) local model within TELEMAC-2D [8]. The hydrodynamic unknowns at the boundary are modelled as a superposition of harmonic components, as in (5) and (6),

$$F(\boldsymbol{p}, t) = \sum F_i(\boldsymbol{p}, t) \, , \tag{5}$$

$$F_i(\boldsymbol{p}, t) = f_i(t)\, A_{F_i}(\boldsymbol{p}) cos\left(\frac{2\pi t}{T_i} - \phi_{F_i}(\boldsymbol{p}) + u_i^0 + v_i(t)\right) , \tag{6}$$

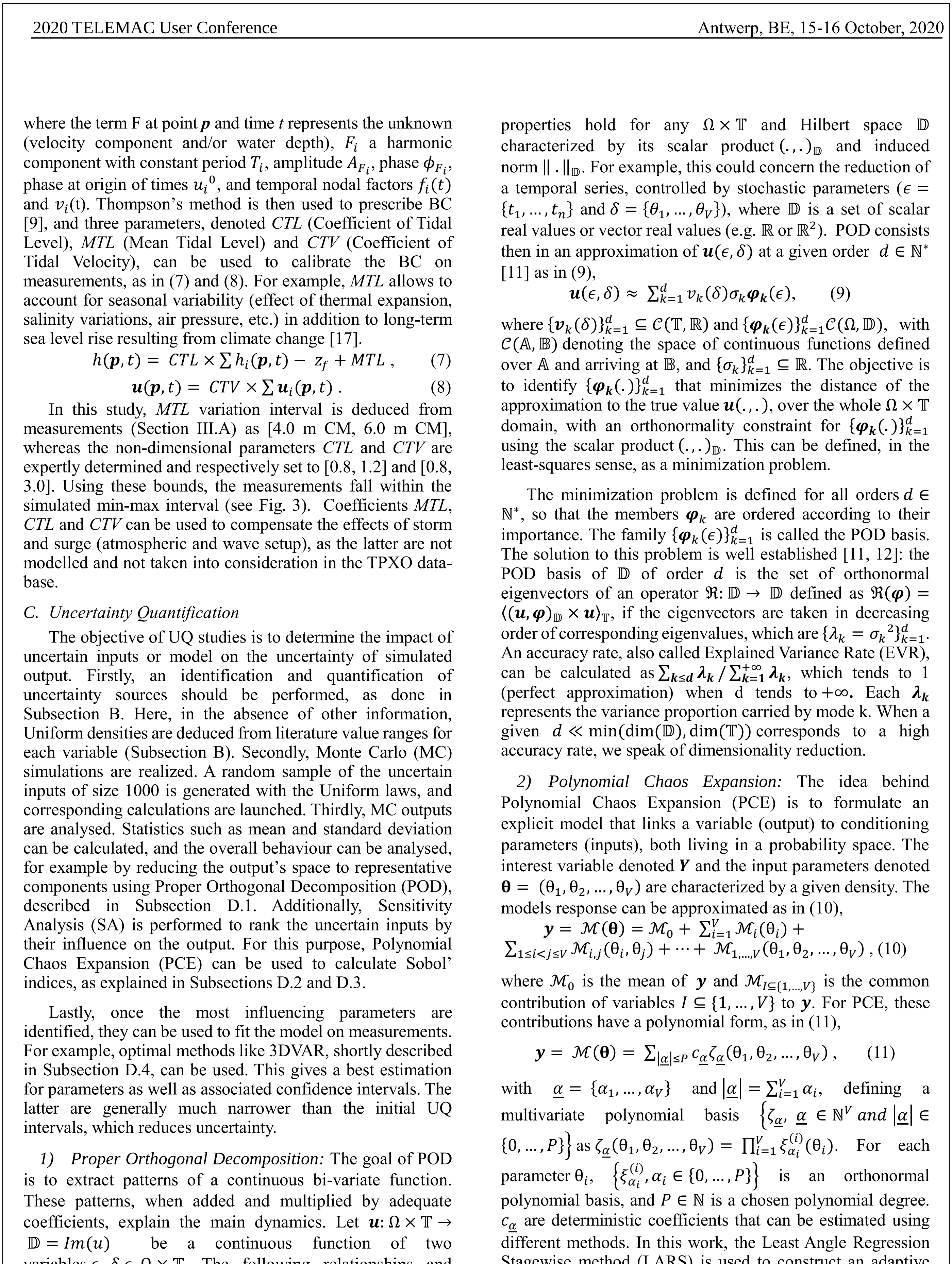

where the term F at point $\boldsymbol{p}$ and time *t* represents the unknown (velocity component and/or water depth), F_i a harmonic component with constant period T_i, amplitude A_{F_i}, phase ϕ_{F_i}, phase at origin of times ${u_i}^0$, and temporal nodal factors $f_i(t)$ and v_i(t). Thompson's method is then used to prescribe BC [9], and three parameters, denoted *CTL* (Coefficient of Tidal Level), *MTL* (Mean Tidal Level) and *CTV* (Coefficient of Tidal Velocity), can be used to calibrate the BC on measurements, as in (7) and (8). For example, *MTL* allows to account for seasonal variability (effect of thermal expansion, salinity variations, air pressure, etc.) in addition to long-term sea level rise resulting from climate change [17].

$$h(\boldsymbol{p},t) = CTL \times \sum h_i(\boldsymbol{p},t) - z_f + MTL\ , \qquad (7)$$

$$\boldsymbol{u}(\boldsymbol{p},t) = CTV \times \sum \boldsymbol{u}_i(\boldsymbol{p},t)\ . \qquad (8)$$

In this study, *MTL* variation interval is deduced from measurements (Section III.A) as [4.0 m CM, 6.0 m CM], whereas the non-dimensional parameters *CTL* and *CTV* are expertly determined and respectively set to [0.8, 1.2] and [0.8, 3.0]. Using these bounds, the measurements fall within the simulated min-max interval (see Fig. 3). Coefficients *MTL*, *CTL* and *CTV* can be used to compensate the effects of storm and surge (atmospheric and wave setup), as the latter are not modelled and not taken into consideration in the TPXO database.

C. Uncertainty Quantification

The objective of UQ studies is to determine the impact of uncertain inputs or model on the uncertainty of simulated output. Firstly, an identification and quantification of uncertainty sources should be performed, as done in Subsection B. Here, in the absence of other information, Uniform densities are deduced from literature value ranges for each variable (Subsection B). Secondly, Monte Carlo (MC) simulations are realized. A random sample of the uncertain inputs of size 1000 is generated with the Uniform laws, and corresponding calculations are launched. Thirdly, MC outputs are analysed. Statistics such as mean and standard deviation can be calculated, and the overall behaviour can be analysed, for example by reducing the output's space to representative components using Proper Orthogonal Decomposition (POD), described in Subsection D.1. Additionally, Sensitivity Analysis (SA) is performed to rank the uncertain inputs by their influence on the output. For this purpose, Polynomial Chaos Expansion (PCE) can be used to calculate Sobol' indices, as explained in Subsections D.2 and D.3.

Lastly, once the most influencing parameters are identified, they can be used to fit the model on measurements. For example, optimal methods like 3DVAR, shortly described in Subsection D.4, can be used. This gives a best estimation for parameters as well as associated confidence intervals. The latter are generally much narrower than the initial UQ intervals, which reduces uncertainty.

1) Proper Orthogonal Decomposition: The goal of POD is to extract patterns of a continuous bi-variate function. These patterns, when added and multiplied by adequate coefficients, explain the main dynamics. Let $\boldsymbol{u}: \Omega \times \mathbb{T} \to \mathbb{D} = Im(u)$ be a continuous function of two variables $\epsilon, \delta \in \Omega \times \mathbb{T}$. The following relationships and properties hold for any $\Omega \times \mathbb{T}$ and Hilbert space $\mathbb{D}$ characterized by its scalar product $(.,.)_{\mathbb{D}}$ and induced norm $\|\,.\,\|_{\mathbb{D}}$. For example, this could concern the reduction of a temporal series, controlled by stochastic parameters ($\epsilon = \{t_1, \dots, t_n\}$ and $\delta = \{\theta_1, \dots, \theta_V\}$), where $\mathbb{D}$ is a set of scalar real values or vector real values (e.g. $\mathbb{R}$ or $\mathbb{R}^2$). POD consists then in an approximation of $\boldsymbol{u}(\epsilon, \delta)$ at a given order $d \in \mathbb{N}^*$ [11] as in (9),

$$\boldsymbol{u}(\epsilon,\delta) \approx \sum_{k=1}^{d} v_k(\delta)\sigma_k \boldsymbol{\varphi_k}(\epsilon), \qquad (9)$$

where $\{\boldsymbol{v}_k(\delta)\}_{k=1}^{d} \subseteq \mathcal{C}(\mathbb{T},\mathbb{R})$ and $\{\boldsymbol{\varphi_k}(\epsilon)\}_{k=1}^{d}\mathcal{C}(\Omega,\mathbb{D})$, with $\mathcal{C}(\mathbb{A},\mathbb{B})$ denoting the space of continuous functions defined over $\mathbb{A}$ and arriving at $\mathbb{B}$, and $\{\sigma_k\}_{k=1}^{d} \subseteq \mathbb{R}$. The objective is to identify $\{\boldsymbol{\varphi_k}(.)\}_{k=1}^{d}$ that minimizes the distance of the approximation to the true value $\boldsymbol{u}(.,.)$, over the whole $\Omega \times \mathbb{T}$ domain, with an orthonormality constraint for $\{\boldsymbol{\varphi_k}(.)\}_{k=1}^{d}$ using the scalar product $(.,.)_{\mathbb{D}}$. This can be defined, in the least-squares sense, as a minimization problem.

The minimization problem is defined for all orders $d \in \mathbb{N}^*$, so that the members $\boldsymbol{\varphi}_k$ are ordered according to their importance. The family $\{\boldsymbol{\varphi}_k(\epsilon)\}_{k=1}^{d}$ is called the POD basis. The solution to this problem is well established [11, 12]: the POD basis of $\mathbb{D}$ of order d is the set of orthonormal eigenvectors of an operator $\mathfrak{R}: \mathbb{D} \to \mathbb{D}$ defined as $\mathfrak{R}(\boldsymbol{\varphi}) = \langle(\boldsymbol{u},\boldsymbol{\varphi})_{\mathbb{D}} \times \boldsymbol{u}\rangle_{\mathbb{T}}$, if the eigenvectors are taken in decreasing order of corresponding eigenvalues, which are $\{\lambda_k = {\sigma_k}^2\}_{k=1}^{d}$. An accuracy rate, also called Explained Variance Rate (EVR), can be calculated as $\sum_{\boldsymbol{k \leq d}} \boldsymbol{\lambda_k} \,/\, \sum_{\boldsymbol{k=1}}^{+\infty} \boldsymbol{\lambda_k}$, which tends to 1 (perfect approximation) when d tends to $+\infty$**.** Each $\boldsymbol{\lambda_k}$ represents the variance proportion carried by mode k. When a given $d \ll \min(\dim(\mathbb{D}), \dim(\mathbb{T}))$ corresponds to a high accuracy rate, we speak of dimensionality reduction.

2) Polynomial Chaos Expansion: The idea behind Polynomial Chaos Expansion (PCE) is to formulate an explicit model that links a variable (output) to conditioning parameters (inputs), both living in a probability space. The interest variable denoted ***Y*** and the input parameters denoted $\boldsymbol{\theta} = (\theta_1, \theta_2, \dots, \theta_V)$ are characterized by a given density. The models response can be approximated as in (10),

$$\boldsymbol{y} = \mathcal{M}(\boldsymbol{\theta}) = \mathcal{M}_0 + \sum_{i=1}^{V} \mathcal{M}_i(\theta_i) + \sum_{1 \leq i < j \leq V} \mathcal{M}_{i,j}(\theta_i, \theta_j) + \dots + \mathcal{M}_{1,\dots,V}(\theta_1, \theta_2, \dots, \theta_V)\ , \qquad (10)$$

where $\mathcal{M}_0$ is the mean of $\boldsymbol{y}$ and $\mathcal{M}_{I \subseteq \{1,\dots,V\}}$ is the common contribution of variables $I \subseteq \{1, \dots, V\}$ to $\boldsymbol{y}$. For PCE, these contributions have a polynomial form, as in (11),

$$\boldsymbol{y} = \mathcal{M}(\boldsymbol{\theta}) = \sum_{|\underline{\alpha}| \leq P} c_{\underline{\alpha}} \zeta_{\underline{\alpha}}(\theta_1, \theta_2, \dots, \theta_V)\ , \qquad (11)$$

with $\underline{\alpha} = \{\alpha_1, \dots, \alpha_V\}$ and $|\underline{\alpha}| = \sum_{i=1}^{V} \alpha_i$, defining a multivariate polynomial basis $\left\{\zeta_{\underline{\alpha}},\ \underline{\alpha} \in \mathbb{N}^V \mathit{and}\ |\underline{\alpha}| \in \{0, \dots, P\}\right\}$ as $\zeta_{\underline{\alpha}}(\theta_1, \theta_2, \dots, \theta_V) = \prod_{i=1}^{V} \xi_{\alpha_i}^{(i)}(\theta_i)$. For each parameter θ_i, $\left\{\xi_{\alpha_i}^{(i)}, \alpha_i \in \{0, \dots, P\}\right\}$ is an orthonormal polynomial basis, and $P \in \mathbb{N}$ is a chosen polynomial degree. $c_{\underline{\alpha}}$ are deterministic coefficients that can be estimated using different methods. In this work, the Least Angle Regression Stagewise method (LARS) is used to construct an adaptive sparse PCE. Further details on PCE in general and LARS in particular can be found in [20].

3) Sensitivity Analysis: PCE can be used with variance decomposition [13, 14] to analyse the influence of the inputs variances on the output's variance [14]. For the general case of a multivariate model written as in (10), the contribution of the polynomial indexed by $\underline{\alpha}$, to the output $\mathbf{y}$ can be computed in terms of variance, as in (12),

$$S_{\underline{\alpha}} = \frac{Var[c_{\underline{\alpha}}\zeta_{\underline{\alpha}}]}{Var[\boldsymbol{y}]} = \frac{{c_{\underline{\alpha}}}^2}{\sum_{|\underline{\beta}| \leq P} {c_{\underline{\beta}}}^2}, \qquad (12)$$

where $S_{\underline{\alpha}}$ are the well-known Sobol' indices [14]. Adding them for all the polynomials that contribute to $\mathbf{y}$ equals 1. They allow to rank all terms by their relative contribution to $\mathbf{y}$. The contributions can either be: (i) analysed for each polynomial; (ii) used to compute the 1st order contribution of a variable θ_i alone (1st Sobol' index denoted S_i) by adding the monomial contributions only; (iii) or used to compute the total contribution of θ_i (total Sobol' index denoted ${S_i}^T$) by adding the contributions of all polynomials involving θ_i.

4) Optimal Calibration using 3DVAR: An automatic algorithm is here used for inverse parameters estimation from observations and a numerical model. On the first hand, observations are not perfect. On the other hand, one may have a first guess for the parameters (physical knowledge, previous simulations, etc.), but the latter is uncertain. In order to find the best compromise between measurements errors and parameters first guess errors, the optimization takes the form of a minimization problem, for the function defined in (13),

$$J(\boldsymbol{\theta}) = \frac{1}{2}(\boldsymbol{\theta} - \boldsymbol{\theta_b})^T \boldsymbol{B}^{-1}(\boldsymbol{\theta} - \boldsymbol{\theta_b}) +$$

$$\tfrac{1}{2}(\boldsymbol{y} - \mathcal{H}(\mathcal{M}(\boldsymbol{\theta})))^T \boldsymbol{R}^{-1}(\boldsymbol{y} - \mathcal{H}(\mathcal{M}(\boldsymbol{\theta}))), \qquad (13)$$

where $\boldsymbol{y}$ is the observation, $\mathcal{M}$ the numerical model, $\mathcal{H}$ an operator from the simulation to the observation space, $\boldsymbol{\theta}$ the set of unknown parameters and $\boldsymbol{\theta_b}$ a background knowledge (or first guess) of the parameters. The background and observation errors are represented by error covariance matrices, respectively denoted $\boldsymbol{B}$ and $\boldsymbol{R}$. This is commonly known as a data assimilation variational problem, where J is called cost function, and minimizing it is referred to as 3DVAR [15, 16].

Here, the observation and simulation are the same variables expressed on the same locations and times, i.e. $\mathcal{H}$ is identity. The observation can be POD reduced and approximated as a matrix product $\boldsymbol{y} \approx \boldsymbol{\Phi_Y \Sigma_Y \tilde{y}}$, where a finite number of POD modes is stored in $\boldsymbol{\Phi_Y}$, the corresponding square roots of eigenvalues are stored in $\boldsymbol{\Sigma_Y}$ and $\boldsymbol{\tilde{y}}$ contains the multiplicative coefficients, which are a reduced form of $\boldsymbol{y}$. Next, the simulation result $\mathcal{M}(\boldsymbol{\theta})$ can be POD reduced and the coefficients learned using PCE as a function of $\boldsymbol{\theta}$, which is written as $\mathcal{M}(\boldsymbol{\theta}) \approx \boldsymbol{\Phi_X \Sigma_X} \widetilde{\mathcal{M}}(\boldsymbol{\theta})$, where $\widetilde{\mathcal{M}}(\boldsymbol{\theta})$ is a vector storing PCE models for the reduced version of simulation result. The cost function can then be approximated as in (14).

$$J(\boldsymbol{\theta}) \approx \frac{1}{2}(\boldsymbol{\theta} - \boldsymbol{\theta_b})^T \boldsymbol{B}^{-1}(\boldsymbol{\theta} - \boldsymbol{\theta_b}) +$$

$$\tfrac{1}{2}\left(\boldsymbol{\tilde{y}} - \boldsymbol{\tilde{H}}\widetilde{\mathcal{M}}(\boldsymbol{\theta})\right)^T \boldsymbol{\tilde{R}}^{-1}\left(\boldsymbol{\tilde{y}} - \boldsymbol{\tilde{H}}\widetilde{\mathcal{M}}(\boldsymbol{\theta})\right), \qquad (14)$$

where $\boldsymbol{\tilde{H}} = (\boldsymbol{\Phi_Y \Sigma_Y})^{-\mathbf{1}}\boldsymbol{\Phi_X \Sigma_X}$ is a new linear operator (matrix) that links the reduced observation to the PCE model of reduced simulation $\widetilde{\mathcal{M}}(\boldsymbol{\theta})$, and $\boldsymbol{\tilde{R}}^{-1} = (\boldsymbol{\Phi_Y \Sigma_Y})^{\boldsymbol{T}}\boldsymbol{R}^{-1}(\boldsymbol{\Phi_Y \Sigma_Y})$. The new minimization problem is an approximation of the original, but is less costly. Indeed, reduction implies that the dimension of $\boldsymbol{\tilde{y}}$ is much lower than the full observation$'s$, and that of $\widetilde{\mathcal{M}}(\boldsymbol{\theta})$ is much lower than the numerical model$'s$. Additionally, PCE performs in seconds while the numerical model needs hours, making the model evaluation time negligible.

In the following, the uncertainties resulting from modelling choices (domain extension, friction closure) are investigated using the previously described theoretical elements.

III. UNCERTAINTIES RELATED TO MODELING CHOICES

Firstly, a description of the study case and available data is given in Subsection A. The case is used to investigate the differences that come from domain extent choice in Subsection B, and friction formula choice in Subsection C.

A. Case study

The study site is located on the eastern English Channel coast in northern France. The study zone is mega-tidal and dominated by a semi-diurnal circulation, with moderate wave activity. In particular, a power plant's cooling intake is of interest. Its upstream boundary is connected to the sea, and a pumping system ensures the plant's cooling. Hydrodynamic models of different extents, as shown in Fig. 1-a, can be used to represent the flow in the intake. The choice of domain extent and other simulation parameters (Section II) is considered uncertain. Consequently, four domain extensions are compared in Subsection B and two friction formulas confronted in Subsection C. For validation, five measurement points (indicated in Fig. 1-a) of $(u, v)^T$ and η over a two-month period are available. In addition to tidal effects, possible occurrence of storms, surges and resulting non-linear interactions with the tides influence these measurements. However, it is difficult to isolate their effect in the measured quantities as highlighted in [17]. The tidal BC coefficients introduced in Subsection B.2 will therefore be used to calibrate the total signal.

Firstly, domains of different sizes, centred on the cooling intake, are created. Four domains in particular, of sizes 800 m, 2 km, 7 km and 8 km, are compared in Section B. These denominations correspond to the distance from the intake entrance to the offshore, and equal distance on either side of the intake, to the east and to the west alongshore. Secondly, mesh convergence is assessed on the 2 km domain, and results in elements of size 50 m at the sea, 2.5 m at the intake walls and 0.5 m at the intake pumps. This configuration is kept for all domain sizes, and the resulting geometries share the same mesh in the common zones. The mesh is shown in Fig. 1-b, where the intake is coloured in red, and the growth of elements size from the intake to the sea is visible. The corresponding meshes contain 28 188, 31 814, 74 079 and 87 617 nodes for the four domain extensions respectively. Thirdly, bathymetries are retrieved from different sources: a Digital Elevation Model (DEM) composed of global and local bathymetries [18], an interpolation of topographic beach profiles and a nearshore multi-beam bathymetry inside the intake and at its vicinity. The same bathymetries are applied for all domain sizes, and the resulting geometries share the same bathymetry in the common zones. It should be mentioned that the used data are not necessarily available at measurement date, and are spatially interpolated. This results in an epistemic uncertainty. Additional sources of uncertainty, namely measurement errors should be noted. However, this is not explicitly dealt with. For the sake of simplicity, calibrating friction is considered to compensate, in average, for the uncertainty in the right hand side terms of SWE.

Lastly, for all domain extensions, the BC are directly interpolated from the TPXO data-based. As all domain sizes keep smaller than a TPXO element size, the differences in the BC only result from linear interpolation due to the distance of boundary elements from the TPXO nodes. The idea is to evaluate the sensitivity of the simulations to pure extension of the calculation domains and not to changes in the BC nature. For the same reasons, BC of the smaller domains are not interpolated from larger domains because this would compensate for the difference of extension, which is exactly what we want to analyse.

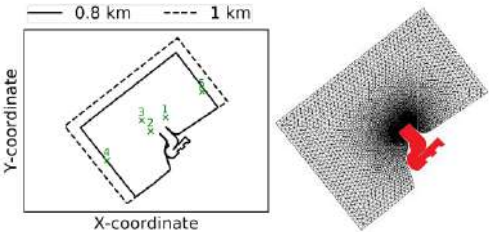

(a) Domain extents *(b) Mesh view*

Figure 1- Examples of domain extents with representation of measurement points outside the intake and view of the mesh.

Measurements of tidal periods are extracted and superposed as in Fig. 2.

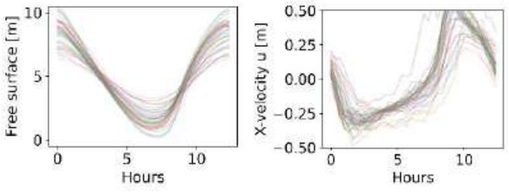

(a) Free surface *(b) X-velocity u*

Figure 2- Superposition of field measurements in front of the intake on point 1, for two hydrodynamic variables.

The different periods are considered as realizations of a temporal series, and POD is performed. The behaviour over two months is therefore reduced to a few components. The associated EVR are shown in Fig. 3. Velocity components u and v show the same behaviour. The two-months measurements, from which 38 periods were extracted for each variable, can therefore be reduced to 2 components, giving 99% of captured variance for free surface, and over 96% for the velocity components.

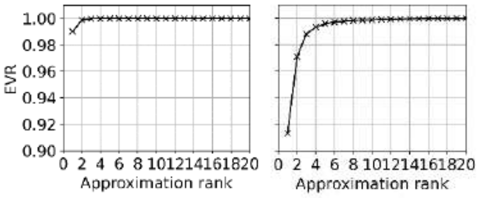

(a) Free surface *(b) X-velocity u*

Figure 3- EVR for the free surface and X-velocity u after measurement based POD reduction on Point 1.

B. *Domain size implications*

As introduced in Section I and represented in Fig. 1, the comparison of hydrodynamic computations with domains of different sizes, centred on the cooling intake, is attempted. The four domains of sizes respectively denoted 800 m, 2 km, 7 km and 8 km, presented in Subsection A, are compared.

In this section the Strickler formula is used for all domain extensions. The following uncertain parameters are considered for UQ: three for BC calibration (*MTL, CLT,* CTV) and two Strickler coefficients at the intake (K_1, red zone in Fig. 1-b) and at sea (K_2). The inputs bounds are described in Section II.B. In particular, the exact calculation for K_1 and K_2 using the formula $K = B/{k_s}^{1/6}$ and the bounds from Section II.B for B and k_s gives the interval $[21.02\,, 90.66\,]\ m^{1/3}s^{-1}$.

A number of 1000 MC simulations is launched on each domain. The min-max values of velocity u and examples of MC realizations are shown in Fig. 4 for two domains. The 2 km domain reaches higher velocities than the 7 km domain, with the same uncertain parameters and bounds. Simulation examples (plots in colours in Fig. 4) show abrupt variations at low tides with the 2 km domain. Conversely, the 7 km one shows a smoother behaviour. For both domains, measurements fall within the modelled interval. Last, whatever the modelling domain, a slight time-lag between measurements and numerical simulations is observed.

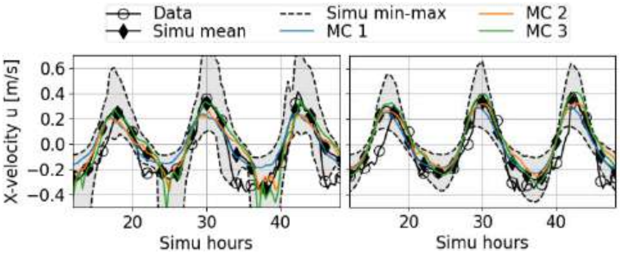

(a) 2 km domain *(b) 7 km domain*

Figure 4- MC min-max envelope of x-velocity u extracted at Point 5, for domains of size 2 km and 7 km, and examples of MC realizations in colours.

Investigation of the 2 km domain shows the presence of tidal flats at BC, which might be the cause of velocity oscillations. Indeed, an extraction of the hydrodynamic variables on the 2 km contour at low tide is performed in Fig. 5. It shows that the velocity extremums are much higher for the 2 km domain (Fig. 5-b) than for bigger extents. These higher velocities are due to the negligible water depths on the same locations (Fig. 5-a). Indeed, the velocity BC provided by the TPXO data base are not directly $(u, v)^T$, but transport fluxes $(uh, vh)^T$. Division by water depth h causes the velocity BC to be infinite when h is negligible. An often used practical engineering solution is to deepen the bathymetry at BC. Nevertheless, this solution is not used to avoid additional uncertainties and the impact of- propagation of this error at BC is studied and compared to other domains.

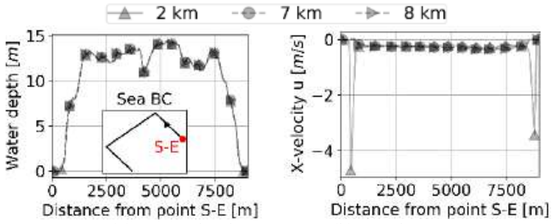

(a) Water depth *(b) X-velocity u*

Figure 5- Hydrodynamic variables extracted on the 2 km sea BC at low tide for three different domain extents.

POD is used in order to analyse the full time series variations at a given point. The EVR is shown for example on Point 1 in Fig. 6. The problem is highly reducible. Free surface elevation reaches 99% variance with two modes, for all domain sizes. The relative RMSE (Root Mean Squared Error) between the simulation results and a 2-Mode POD reduction, averaged over the MC sample, is around 0.3%. Velocity components show different behaviours for different domains. For example, the y-velocity v is much less reducible for the 2 km domain, probably linked to the numerical error at the BC. The average relative RMSE, between the simulations and a 2-Mode POD, is around 5.8% with the 8 km domain, while it reaches 8.4% with the 800 m domain. It can also be noticed that the 800 m, 7 km and 8 km domains EVRs are ordered by domain size and 99% of the variance is captured with 2 modes, except for 2 km.

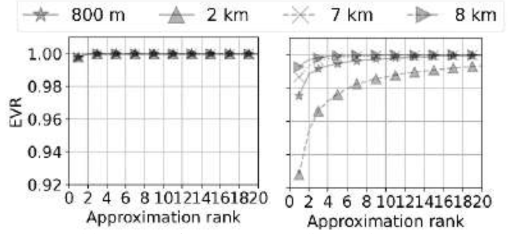

(a) Free surface *(b) Y-velocity v*

Figure 6- EVR for two hydrodynamic variables after MC simulations POD reduction on Point 1.

Next, free surface modes are shown in Fig. 7 for Point 1, where numerical and measurements modes are compared. Both modes are identical for all domains, and their shapes are comparable to measurement modes. However, the amplitudes of numerical Mode 1 are smaller than measurements. This difference can be explained by the represented information. Measurements Mode 1 is characterized by larger amplitudes, because measurements tidal coefficient varies, whereas the numerical Mode 1 only represents MC stochastic variation around the same tide. Furthermore, Mode 1 is always strictly positive, be it for the numerical or real mode. When multiplied by a positive coefficient (corresponding to a given MC realization or a given measurement period), it stays positive and translates vertically, i.e. the mean tidal level changes. Mode 2 oscillates from negative to positive, but not symmetrically. Adding it to Mode 1 corrects both tidal range and mean. It can be noticed that the periods of Mode 1 and 2 are approximately semi-diurnal, which can for example be compared to the principal lunar and solar semidiurnal tidal components (M2 and S2). It should be noted however that POD modes have no theoretical reason to recover the tidal harmonics, as would be the case with a Fourier decomposition. This is rather related to the statistical importance of such harmonics in the global variance of the system. Lastly, a phase shift is observed between simulations and reality, for both modes. This phase is more important at ebb than at flood. It may correspond to the un-modelled effect of tide-surge interactions. Indeed, as explained in [17], the latter can lead to more surge at low than at high tide, resulting in a phase lag where the surge precedes the high water by few hours.

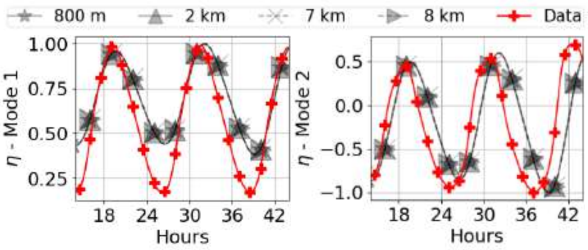

(a) Mode 1 *(b) Mode 2*

Figure 7- Comparison of the first two modes of free surface to reality, after reduction on point 1, for all tested domain sizes.

Comparison of X-velocity modes is shown in Fig. 8. First, differences between domains can be observed, and are bigger in Mode 2 than in Mode 1. Once again, the domain of size 2 km behaves differently even for Mode 1 (oscillations). This is a numerical artefact, as no oscillations are noticed in the measurements.

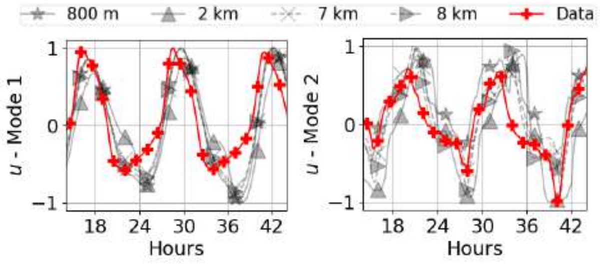

(a) Mode 1 *(b) Mode 2*

Figure 8- Comparison of the first two modes of x-velocity u to reality, after reduction on point 1, for all tested domain sizes.

Secondly, no model succeeds in reproducing the asymmetry observed at the extremums of measurements for Mode 1. Something is missing in the modelling that cannot be corrected by domain extent (Coriolis force, turbulence, waves, storm and atmospheric surges, non-linear interactions of tides with the latter, more precise bathymetry, etc.). For Mode 2, the overall numerical behaviour is comparable to the real one. It seems however that the domain of size 2 km fails at reproducing the sharp minimal peaks (for example at Hour 40 in Fig. 8-b) that the other models capture better. The same conclusions hold for Y-velocity v, with oscillations at the minimum noticed with the numerical simulations, and not present in the real mode. For modes of higher rank, no similarity between the numerical results and the measurements is observed.

Next, Sobol' indices of the inputs are compared for all domain sizes. They are calculated using degree 3 PCE models of the POD temporal coefficients, as explained in Section II.C.3. The MC sample is separated to a training set (80%) and a test set (20%) and PCE models are learned on the training set. For example, with the 8 km model, it can be noted that the 90th percentile of the relative RMSE, between the simulations and a 2-Mode POD-PCE meta-model, calculated on the test set, remains below 0.3% for the free surface, and below 6.1% for the velocities. Sobol' indices results for free surface and X-velocity *u* are shown in Fig. 9. For free surface, the only influencing variable for Mode 1 is *MTL* (Mean Tidal Level). For Mode 2, the influence of coefficient *CTL* is dominant, and *MTL* is in second position. This is coherent with previous interpretation of free surface modes. No differences between domain sizes are noticed. For the velocity components, influences change with domain sizes. For Mode 1, the most influencing variable is *CTV* for all domain extents, followed by the Strickler coefficient K_2. This tendency is inversed for Mode 2. However, *CTV* is more important for the smallest domain of 800 m, whereas K_2 is less important, probably due to the spatial proximity of the BC to the analysed Point 1. For the 2 km domain, K_2 is much more important than for the other extents for both modes. This can be explained by the higher velocity values, as K_2 interacts with velocity in the shear stress formula (2). An interaction between K_2 and CTV is noticed (undashed portion), also explained by the shear stress formula.

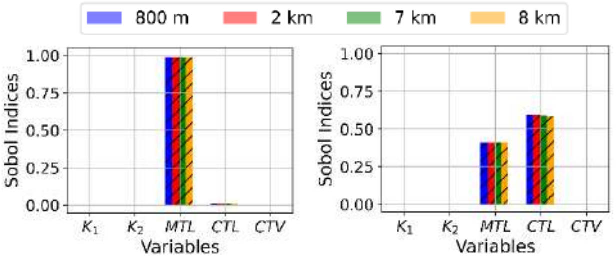

(a) Free-surface - Mode 1 *(b) Free-surface - Mode 2*

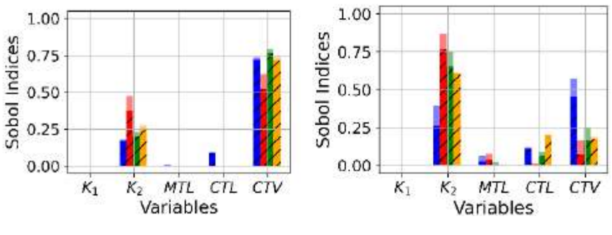

(c) X-velocity u - Mode 1 *(d) X-velocity u - Mode 2*

Figure 9- Sobol' indices for the two first modes of free surface and x-velocity u on Point 1, with the different domain sizes. Full bar plot represents total Sobol' indices. The dashed portion corresponds to the 1st order Sobol' index, and the remaining to the interaction with other variables.

Slight differences are observed between the 7 km and 8 km domains, namely more importance in Mode 1 for K_2 and *CTV* with 7 km, which could be explained by higher proximity of the BC. The differences are larger for Mode 2, but the latter is associated to less variance percentage. Moreover, the Strickler coefficient dominance for Mode 2 means that the observed velocity peaks in Fig. 8 can be moderated by friction, except for the smallest domain, where BC is dominant. The smallest the domain, the more controllable it is with BC only. Last, intake's friction K_1 has no influence outside. Calibration outside can hence be performed without controlling K_1.

C. *Friction closure influence*

The same analysis strategy is adopted to study the Strickler and Colebrook friction formulas, introduced in Section II.B. The same domain of size 8 km with the bathymetry and mesh described in Subsection III.A are used. Eight uncertain parameters are used for Colebrook's UQ: three for BC (*MTL, CLT, CTV*), roughness heights at the intake (${k_s}^1$) and at sea (${k_s}^2$) and three structural uncertainty parameters (B_1, B_2 and B_3). With the Strickler formula, six uncertain parameters are used: three for BC, two roughness heights, and one structural parameter B. All inputs and corresponding bounds are described in Section II.B. Temporal responses at the five measurement points are reduced using POD. No differences can be observed in terms of EVR, all variables can be reduced to 2 modes for over 99% of variance. The modes shapes are compared, and no differences are observed in the free surface first two modes. Slight differences can be seen in the velocity modes, as shown in Fig. 10, particularly for Mode 2 for which small oscillations appear with Strickler's model and not with Colebrook's. No formula succeeds however in reproducing the observed asymmetry of measurements Mode 1, and a phase can be noticed for both modes. Apparently, this lack of asymmetry representation cannot be corrected with friction closure modification either.

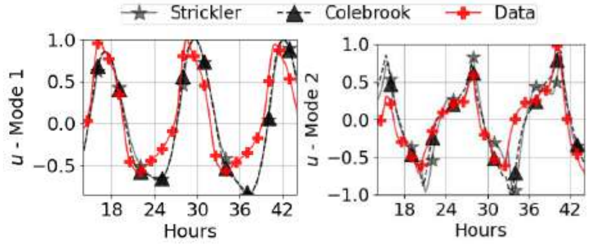

(a) Mode 1 *(b) Mode 2*

Figure 10- Comparison of the first two modes of x-velocity u to reality, after reduction on point 1, for two friction formulas.

SA is performed and no differences are observed for the free surface modes. Sobol' indices of the X-velocity *u* modes are shown in Fig. 11. Naturally, Sobol' indices of B are plotted only for Strickler's model, and those of B_1, B_2 and B_3 are plotted only for Colebrook's. Slight differences are observed in Fig. 11.

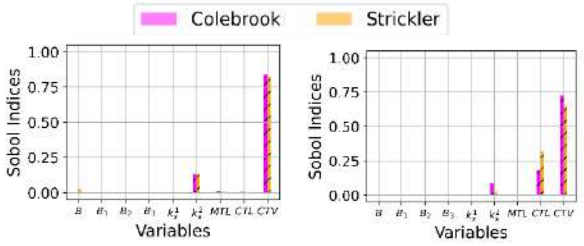

(c) Mode 1 (d) Mode 2

Figure 11- Sobol' indices for the two first modes of free surface and x-velocity u on Point 1, with different friction formulas. Full bar plot represents total Sobol' indices. The dashed portion corresponds to the 1st order Sobol' index, and the remaining to the interaction with other variables.

For Mode 1 there is a slight influence of the structural parameter *B* for the Strickler model, whereas the parameters of Colebrook's model show no influence. Additionally, the velocity BC correction denoted *CTV* gains influence with Colebrook, whereas the sea rugosity $k_s{}^2$ loses impact. The increase of influence for *CTV* with Colebrook's model is more important for Mode 2. The ranking of variables is however the same, even though the proportion of influence changed.

IV. IMPLICATIONS OF EXPERTLY MADE CHOICES ON OPTIMAL CALIBRATION

An example of the uncertainty of optimal calibration is shown on the domain extents variation. A 3DVAR algorithm is used, with the same configurations, parameters and bounds, for all domains. The measurement is reduced to 2 modes, and the calibration is performed on the learned 2-modes POD-PCE meta-models for each numerical simulation, by minimizing the cost function in (14). This allows the observation to be simpler (smoothing) and the problem dimension to be lower (2 coefficients per each variable, instead of 48 hours temporal series). The observation's error covariance matrix $\boldsymbol{R}$ is considered diagonal (no error correlations) and calculated from measurement errors (*5 cm* for free surface and *1 cm/s* for velocity). The background of each input parameter is set to the average of its variation interval, and the background's error covariance matrix $\boldsymbol{B}$, also considered diagonal, is estimated from the interval's variance (squared maximum distance from mean). Calibration results are shown in Fig. 12.

Firstly, it can be noticed that while oscillations are slight with the domain of size 2 km at point 4, they become more and more important when approaching the intake, at Point 3 where they gain amplitude and at Point 1 when the response becomes completely uncontrolled. Without specific correction, this domain is therefore of no interest in operational conditions. Secondly, the velocities represented with size 800 m are of lower amplitudes than with the largest domains of sizes 7 and 8 km. For Point 3 for example in Fig. 12-b, the 800 m domain fits better the minimum velocities than the biggest domains, and vice-versa at the maximum velocities. However, it can be seen in Fig. 12-c that the velocity shapes and amplitudes modelled by the biggest domains are more realistic than with the smallest ones. Lastly, even though domains of sizes 7 and 8 km show similar behaviour, slight differences can be observed. For Point 3 for example in Fig. 12-b, the extrema reached by domain of size 8 km are higher than with the 7 km domain. Hence, even with similar choices for domain extent (7 and 8 km), the best fit could be uncertain. Physical analysis and prediction are therefore also uncertain.

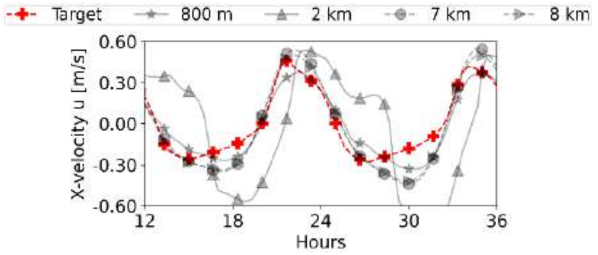

(a) Point 1

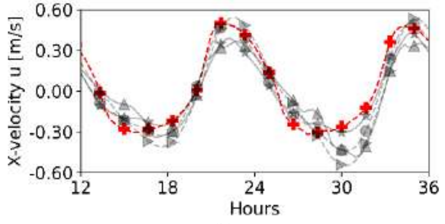

(b) Point 3

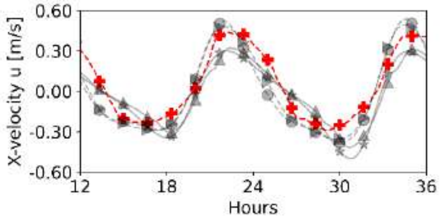

(c) Point 4

Figure 12- Example of optimal calibration with the tested domain extents, for x-velocity u at points 1, 3 and 4.

In particular, a comparison of *X*-velocity *u* profile at the intake's entrance for domains of sizes 7 and 8 km, at half ebb tide, is given in Fig. 13, after 3DVAR calibration. As a reminder, no calibration point is available on this profile. It can be noticed that differences are bigger and analysis is even more uncertain in locations where no measurement is available, even though both domains were calibrated.

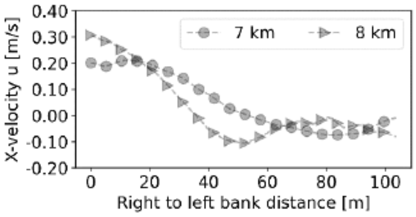

(c) Point 4

Figure 13- Intake's entrance cross-sectional profile of x-velocity at half ebb tide after 3DVAR calibration.

Last, the optimal parameterizations are different with the four domain sizes. For example, the Strickler coefficient at the sea equals 33.9 $m^{1/3}s^{-1}$ for the domain of size 8 km whereas it is equal to 55.85 $m^{1/3}s^{-1}$ for the domain of size 800 m, when *CTV* equals *4.16* for the 8 km domain and *4.38* for the 800 m domain. This shows that, in a coastal configuration, the generalization of such parameters, friction coefficient for

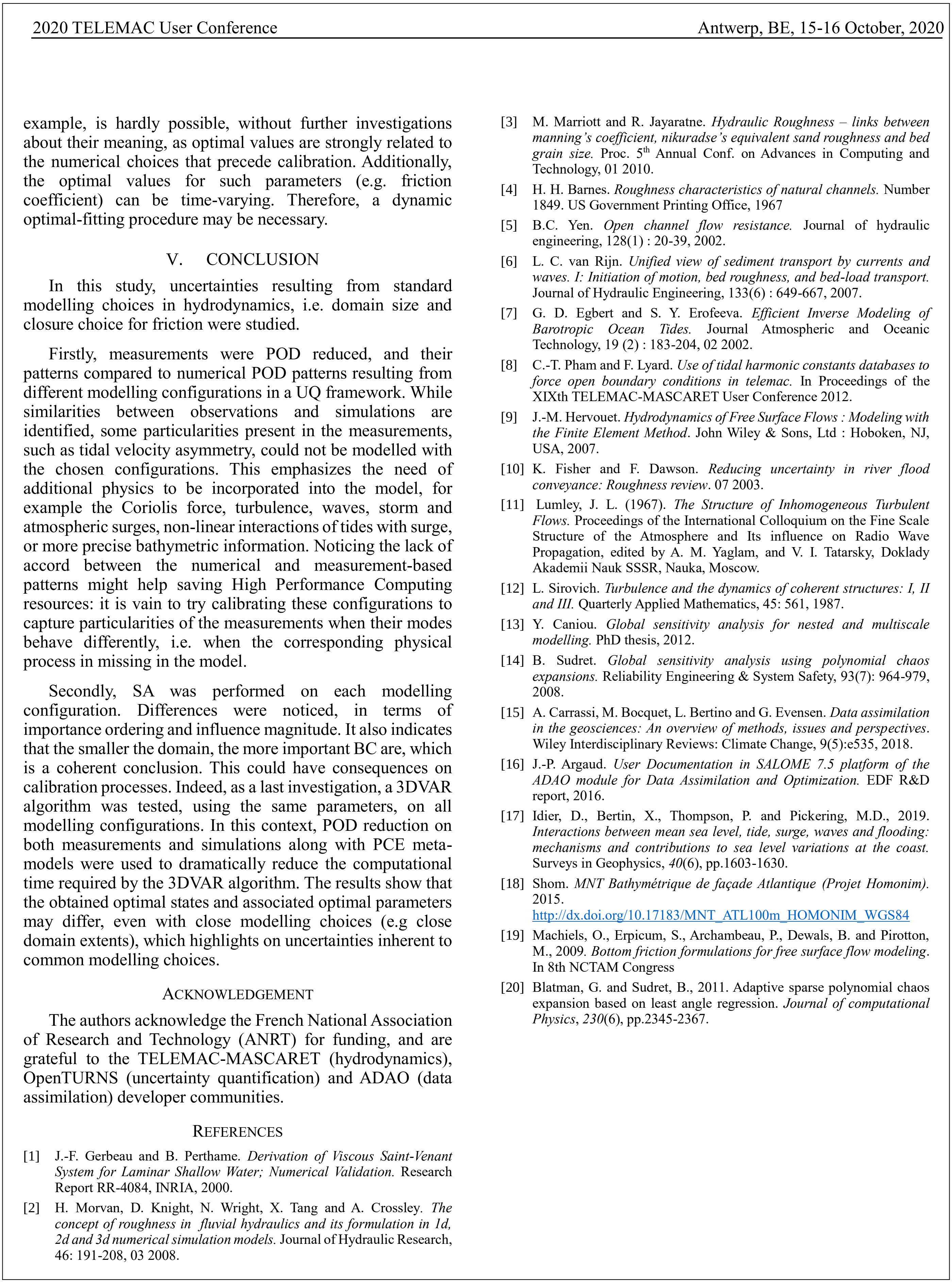

example, is hardly possible, without further investigations about their meaning, as optimal values are strongly related to the numerical choices that precede calibration. Additionally, the optimal values for such parameters (e.g. friction coefficient) can be time-varying. Therefore, a dynamic optimal-fitting procedure may be necessary.

V. CONCLUSION

In this study, uncertainties resulting from standard modelling choices in hydrodynamics, i.e. domain size and closure choice for friction were studied.

Firstly, measurements were POD reduced, and their patterns compared to numerical POD patterns resulting from different modelling configurations in a UQ framework. While similarities between observations and simulations are identified, some particularities present in the measurements, such as tidal velocity asymmetry, could not be modelled with the chosen configurations. This emphasizes the need of additional physics to be incorporated into the model, for example the Coriolis force, turbulence, waves, storm and atmospheric surges, non-linear interactions of tides with surge, or more precise bathymetric information. Noticing the lack of accord between the numerical and measurement-based patterns might help saving High Performance Computing resources: it is vain to try calibrating these configurations to capture particularities of the measurements when their modes behave differently, i.e. when the corresponding physical process in missing in the model.

Secondly, SA was performed on each modelling configuration. Differences were noticed, in terms of importance ordering and influence magnitude. It also indicates that the smaller the domain, the more important BC are, which is a coherent conclusion. This could have consequences on calibration processes. Indeed, as a last investigation, a 3DVAR algorithm was tested, using the same parameters, on all modelling configurations. In this context, POD reduction on both measurements and simulations along with PCE meta-models were used to dramatically reduce the computational time required by the 3DVAR algorithm. The results show that the obtained optimal states and associated optimal parameters may differ, even with close modelling choices (e.g close domain extents), which highlights on uncertainties inherent to common modelling choices.

ACKNOWLEDGEMENT

The authors acknowledge the French National Association of Research and Technology (ANRT) for funding, and are grateful to the TELEMAC-MASCARET (hydrodynamics), OpenTURNS (uncertainty quantification) and ADAO (data assimilation) developer communities.

REFERENCES

[1] J.-F. Gerbeau and B. Perthame. *Derivation of Viscous Saint-Venant System for Laminar Shallow Water; Numerical Validation.* Research Report RR-4084, INRIA, 2000.

[2] H. Morvan, D. Knight, N. Wright, X. Tang and A. Crossley. *The concept of roughness in fluvial hydraulics and its formulation in 1d, 2d and 3d numerical simulation models.* Journal of Hydraulic Research, 46: 191-208, 03 2008.

[3] M. Marriott and R. Jayaratne. *Hydraulic Roughness – links between manning's coefficient, nikuradse's equivalent sand roughness and bed grain size.* Proc. 5th Annual Conf. on Advances in Computing and Technology, 01 2010.

[4] H. H. Barnes. *Roughness characteristics of natural channels.* Number 1849. US Government Printing Office, 1967

[5] B.C. Yen. *Open channel flow resistance.* Journal of hydraulic engineering, 128(1) : 20-39, 2002.

[6] L. C. van Rijn. *Unified view of sediment transport by currents and waves. I: Initiation of motion, bed roughness, and bed-load transport.* Journal of Hydraulic Engineering, 133(6) : 649-667, 2007.

[7] G. D. Egbert and S. Y. Erofeeva. *Efficient Inverse Modeling of Barotropic Ocean Tides.* Journal Atmospheric and Oceanic Technology, 19 (2) : 183-204, 02 2002.

[8] C.-T. Pham and F. Lyard. *Use of tidal harmonic constants databases to force open boundary conditions in telemac.* In Proceedings of the XIXth TELEMAC-MASCARET User Conference 2012.

[9] J.-M. Hervouet. *Hydrodynamics of Free Surface Flows : Modeling with the Finite Element Method*. John Wiley & Sons, Ltd : Hoboken, NJ, USA, 2007.

[10] K. Fisher and F. Dawson. *Reducing uncertainty in river flood conveyance: Roughness review*. 07 2003.

[11] Lumley, J. L. (1967). *The Structure of Inhomogeneous Turbulent Flows.* Proceedings of the International Colloquium on the Fine Scale Structure of the Atmosphere and Its influence on Radio Wave Propagation, edited by A. M. Yaglam, and V. I. Tatarsky, Doklady Akademii Nauk SSSR, Nauka, Moscow.

[12] L. Sirovich. *Turbulence and the dynamics of coherent structures: I, II and III.* Quarterly Applied Mathematics, 45: 561, 1987.

[13] Y. Caniou. *Global sensitivity analysis for nested and multiscale modelling.* PhD thesis, 2012.

[14] B. Sudret. *Global sensitivity analysis using polynomial chaos expansions.* Reliability Engineering & System Safety, 93(7): 964-979, 2008.

[15] A. Carrassi, M. Bocquet, L. Bertino and G. Evensen. *Data assimilation in the geosciences: An overview of methods, issues and perspectives*. Wiley Interdisciplinary Reviews: Climate Change, 9(5):e535, 2018.

[16] J.-P. Argaud. *User Documentation in SALOME 7.5 platform of the ADAO module for Data Assimilation and Optimization.* EDF R&D report, 2016.

[17] Idier, D., Bertin, X., Thompson, P. and Pickering, M.D., 2019. *Interactions between mean sea level, tide, surge, waves and flooding: mechanisms and contributions to sea level variations at the coast.* Surveys in Geophysics, *40*(6), pp.1603-1630.

[18] Shom. *MNT Bathymétrique de façade Atlantique (Projet Homonim).* 2015. http://dx.doi.org/10.17183/MNT_ATL100m_HOMONIM_WGS84

[19] Machiels, O., Erpicum, S., Archambeau, P., Dewals, B. and Pirotton, M., 2009. *Bottom friction formulations for free surface flow modeling*. In 8th NCTAM Congress

[20] Blatman, G. and Sudret, B., 2011. Adaptive sparse polynomial chaos expansion based on least angle regression. *Journal of computational Physics*, *230*(6), pp.2345-2367.

4.4 Intake's Boundary Condition and related uncertainties

The UQ investigations presented in Section 4.3 resulted with interesting conclusions about the tidal currents modelling at intake's vicinity. POD patterns deduced from the numerical model's outcome, were compared to those deduced from the 2010 field measurements. Unfortunately, the used survey did not cover all interest points, and in particular, the cross-sectional velocity profile at intake's entrance, corresponding to sea hydrodynamic forcing BC in Figure 4.1, was not available from measurements. The latter is however a capital information for the targeted hydro-morphodynamic simulations of the intake. It should therefore be determined. The idea here is to extract such an information from the tested modelling configurations. Hence, POD patterns of the interest velocity profile are analyzed in the following, and their sensitivity to the studied uncertain parameters is described. As proposed in the contribution of Section 4.3, the impact of domain extension and friction closure relationship choice are detailed in Section 4.4.1 and 4.4.2 respectively.

4.4.1 Domain size influence

Velocity profiles at intake's entrance are extracted from the tested model configurations at key simulation times. For example, Figure 4.12 shows the profile at HRT with the 8 km domain. With the colored UQ simulation examples, a shift, depending on parameter values, is noticed for the maximum velocity location on the interest profile.

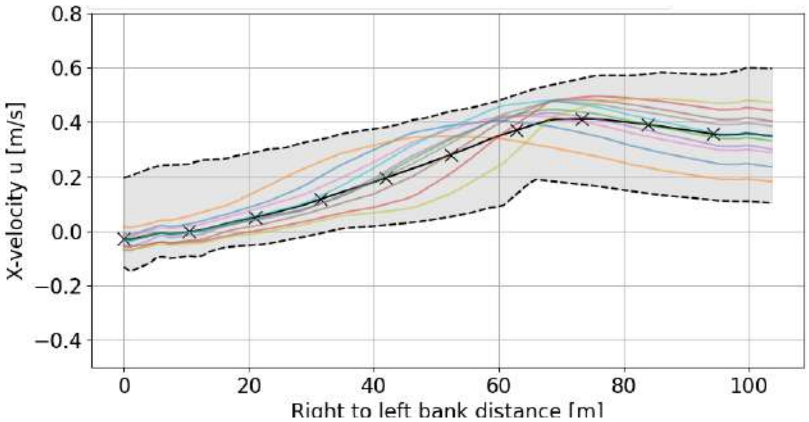

Figure 4.12 – Examples of UQ realizations (in colors) for the X-velocity u profile at intake's entrance, at Half Rising Tide (HRT), for the 8 km domain.

In order to capture this variance, the simulated profiles can be stored in a snapshot matrix as different realizations, and POD reduced accordingly. POD results show that more than 98 % and over 96 % of EVR for the velocity components u and v respectively, can be represented using 2 modes. The first two spatial patterns of the velocity components are compared in Figure 4.13. The first mode of x-velocity u (Figure 4.13-a) is similar for all domains, with slight differences for the smallest 800 m domain. The second mode of x-velocity u (Figure 4.13-b) is identical for the two biggest domains, and differs for domains of sizes 800 m and 2 km. Comparison of the y-velocity components v results with similar conclusions: the first mode is quasi-identical from one domain to the other, and the second mode shows different behaviors from the biggest domains to the smallest ones.

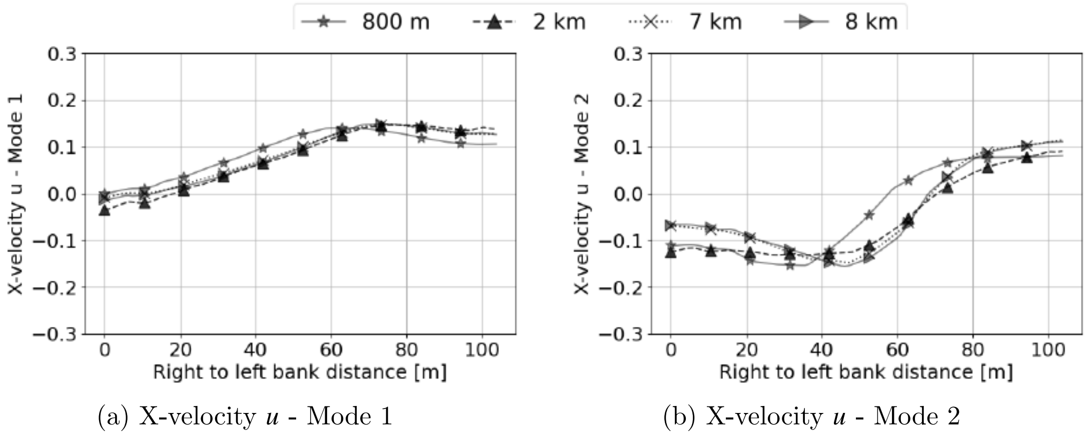

(a) X-velocity u - Mode 1

(b) X-velocity u - Mode 2

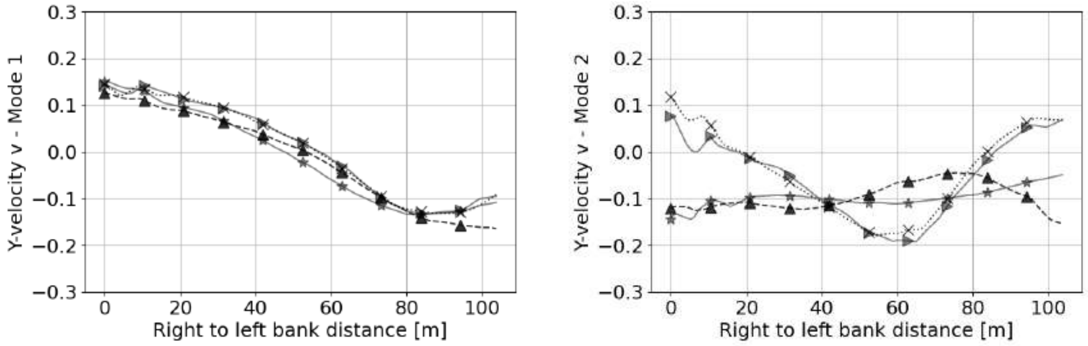

(c) Y-velocity v - Mode 1

(d) Y-velocity v - Mode 2

Figure 4.13 – Comparison of POD patterns of intake's entrance velocity profiles, with the different domain sizes at Half Rising Tide (HRT).

To assess the impact of the interest uncertain parameters on the velocity profile variance, sensitivity analysis is performed. An example with the first mode for velocity components is shown in Figure 4.14.

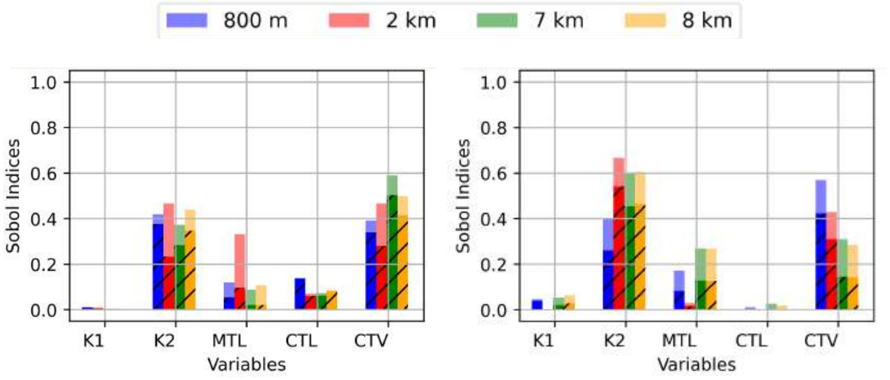

(b) X-velocity u - Mode 1

(c) Y-velocity v - Mode 1

Figure 4.14 – Comparison of Sobol' indices for the two first modes of velocity components, with the different domain sizes at Half Rising Tide (HRT). The full bar plot represents the total Sobol' indices. The dashed portion corresponds to the first Sobol' index, and the remaining to the interaction with other variables.

Sensitivities change with the modelling domain size, meaning that the velocity profile at intake's entrance is controlled by different parameters, depending on the configuration. Results interpretation is identical to the discussions presented in Section 4.3 with temporal signals POD reduction. An additional slight influence of the intake's strickler coefficient, denoted $K1$, is here noticed compared to the signals extracted at sea points outside the intake.

As a main conclusion, the velocity profile at intake's entrance can be reduced to 2 patterns per velocity component, at each characteristic time. The latter represent most of the variability, and can be used to reconstitute adequate BC for numerical investigations of the intake dynamics. The related POD expansion coefficients can be controlled to represent the variances of simulations with larger domain extensions, in particular related to sea Strickler coefficient $K2$ and BC parameters MTL, CTL and CTV. Differences in the patterns, depending on the chosen domain extension, can be noticed. This means that the spatial POD components are also uncertain. Their uncertainty can for example be quantified and simulated with adequate stochastic modelling, in order to represent the randomness related to domain extension choice.

4.4.2 Influence of the friction closure relationship

Simulation outcomes using Strickler and Colebrook friction formulas are also POD processed and compared. Results at HRT are for example shown in Figures 4.15 and 4.16, for velocity components u and v respectively.

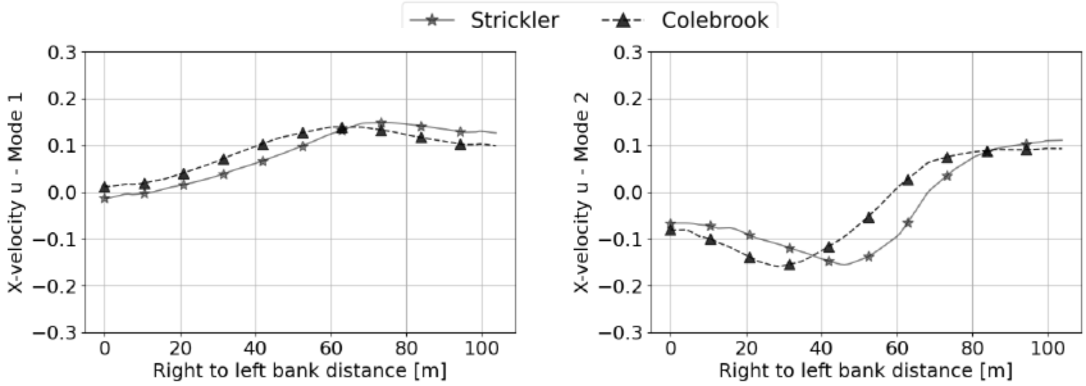

(a) X-velocity u - Mode 1 (b) X-velocity u - Mode 2

Figure 4.15 – Comparison of POD patterns of intake's entrance x-velocity profiles, with two friction formulas, at Half Rising Tide (HRT).

Results with the two formulas have comparable mode shapes, but a shift of the profiles extrema can be noticed. For example, for the first pattern of x-velocity u (Figure 4.15-a), the maximum is located at 70 m with Colebrook, whereas it is located at 60 m with Strickler. The same is observed for Mode 2. For y-velocity v, Mode 1 and 2 (Figures 4.16-a and 4.16-b respectively) show a flattening of the profile at the banks with Colebrook, whereas it shows oscillation with Strickler. The maximum is shifted here as well for Mode 2.

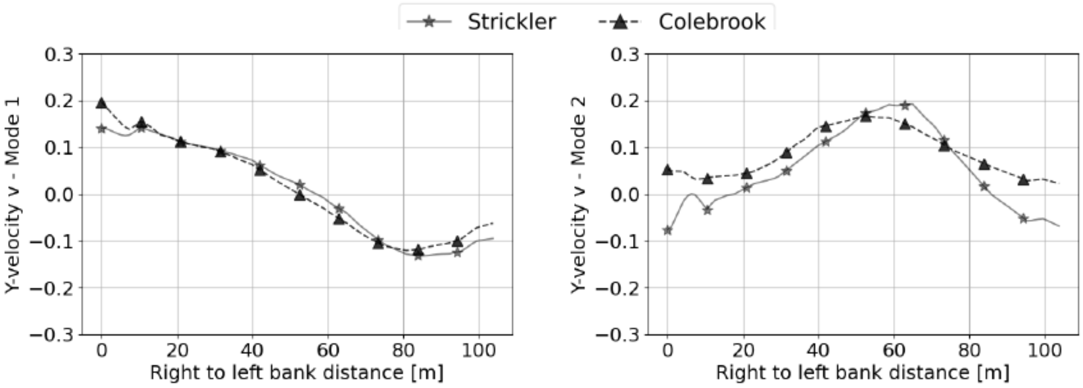

(a) Y-velocity v - Mode 1 (b) Y-velocity v - Mode 2

Figure 4.16 – Comparison of POD patterns of intake's entrance y-velocity profiles, with two friction formulas, at Half Rising Tide (HRT).

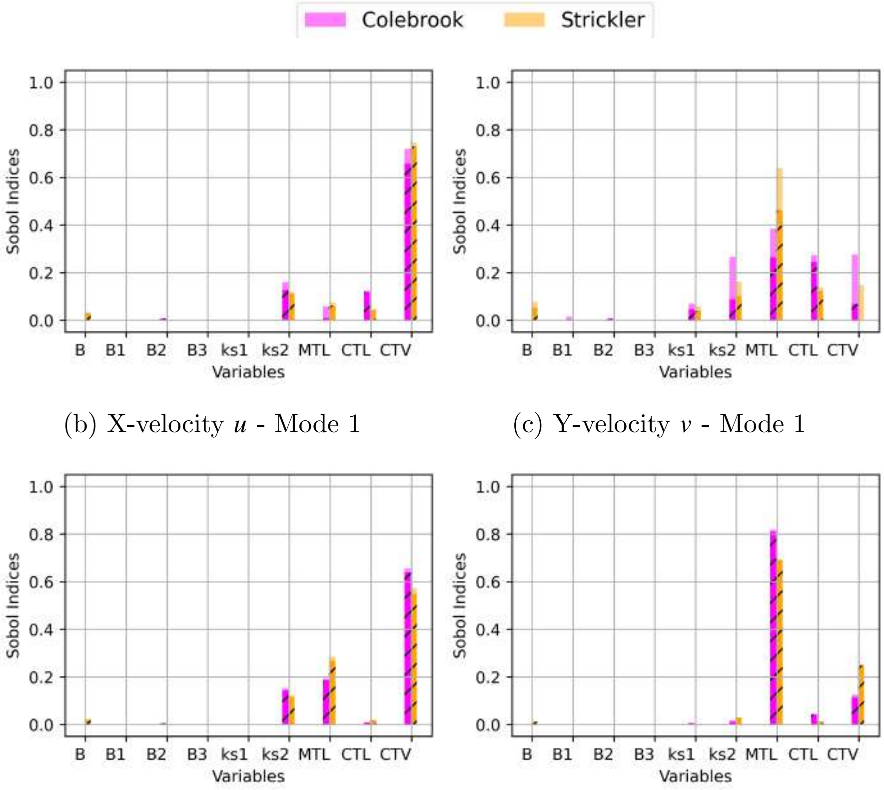

(b) X-velocity u - Mode 1 (c) Y-velocity v - Mode 1

(d) X-velocity u - Mode 2 (e) Y-velocity v - Mode 2

Figure 4.17 – Comparison of Sobol' indices for the two first modes of the velocity components, with different friction formulas at characteristic time HRT. The full bar plot represents the total Sobol' indices. The dashed portion corresponds to the first Sobol' indice, and the remaining to the interaction with other variables.

Corresponding sensitivity analysis is shown in Figure 4.17. For the x-velocity component u, only slight differences are observed, in particular an influence increase for sea rugosity k_{s2} with Colebrook, and decrease for CTV, replaced by an interaction between CTV and k_{s2}. However, if the influence of structural coefficient B for Strickler is added to k_{s2}, the influence of friction is almost equal to Colebrook's. For the y-velocity component

u, differences are more significant. Considerable interaction is added with Colebrook for k_{s2}, MTL and CTV. This can be explained by the presence of the Reynolds number, and therefore of both velocity and water depth, in Colebrook's friction (Equation 1.10). Consequently, correction coefficient of tidal level CTL gains influence as well. Even if y-velocity's Mode 1 (Figure 4.17-c) is almost identical with both formulas, it is controlled differently by the input parameters.

As previously concluded with the domain extension choice experiment, the velocity profile at intake's entrance can be reduced with both friction formulas. The patterns can be used to conduct investigations of the intake dynamics, with slight differences depending on the chosen friction formula. These difference can be accounted for, as an example though a UQ study.

4.5 Summary

In this chapter, tidal modelling uncertainty, related to common modelling choices was investigated. POD patterns resulting from the UQ experiments were compared to patterns extracted from the 2010 field survey. Similarities were observed, as well as particularities in the measurements that were not captured with the selected model. All parameters have shown to be influencing for the currents outside the intake, except the intake's rugosity. However, different rankings for the influence of uncertain parameters on the extracted POD modes were observed, depending on the domain extension and friction closure relationship choice. The outcome of parametric calibration with different modelling configurations was therefore also impacted.

It was shown that this uncertainty can impact the velocities at the intake's entrance. In particular, their POD patterns slightly varied with respect to domain extension and friction closure relationship choice. However, even if uncertain, they still represent valuable information to undertake additional investigations of the intake dynamics. In this case, optimal calibration of the patterns should be set, using adequate observations.

In addition to model uncertainties, observations are also characterized with measurement errors, as described in Chapter 1. Hence, Data Assimilation (DA) can be used to optimally combine the numerical model and observations, and hence reduce the uncertainties. Classical DA can however be costly, and strategies for their reduction through metamodelling are therefore confronted in the following Chapter 5. In particular, a combined input-output DR On the one hand, and previously proposed POD-PCE learning on the other hand, were attempted. This contributes to select the most optimal approach for drastic decrease of computation time, that can be used in operational conditions.

Chapter 5

Model reduction for fast and accurate Data Assimilation

Ce chapitre se concentre sur l'utilisation de techniques de Réduction de Dimension (DR) pour l'accélération d'Assimilation de Données (DA) variationnelle. En particulier, deux méthodes sont confrontées: la décomposition conjointe de l'espace des paramètres et d'état d'une part, et l'apprentissage d'un métamodèle basé sur le couplage POD-PCE précédemment introduit d'autre part. Pour ce dernier, une estimation appropriée de la matrice de covariance d'erreur du méta-modèle est proposée.

This chapter focuses on the use of Dimensionality Reduction (DR) techniques for the acceleration of variational Data Assimilation (DA). In particular, two methods are confronted: joint decomposition of parameters and state spaces on the one hand, and learning of a metamodel based on the previously introduced POD-PCE coupling on the other hand. For the latter, an appropriate estimate of the metamodel error covariance matrix is proposed.

Contents

5.1 Motivations

In order to reduce the uncertainty of hydrodynamic simulations, Data Assimilation (DA) can be attempted for parametric calibration. However, the cost of classical algorithms can be discouraging for use in operational conditions. For example, the cost reduction question arises when the same model should be calibrated for different scenarios, using different measurement campaigns.

In this application, a two-months hydrodynamic field campaign on five measurement points, first presented in Chapter 1, was used in a UQ framework in Chapter 4. It was in particular shown that measurements are POD reducible, if the tidal periods (approx. 12 h 25 mn) are considered as different realizations, and consequently stored in the columns of a snapshot matrix. Using 38 tidal periods realizations, the 2010 campaign measurements could be POD reduced to 2 patterns for over 99 % of EVR for free surface, and over 96 % of EVR for velocity components. The tidal currents at intake's vicinity over a given tidal period can therefore be summarized to few POD components. Hence, if appropriate calibration can be achieved for each tidal period from the 2010 campaign independently, then a dependency structure can be constructed, between the optimally calibrated parameter values on the one hand, and the POD patterns representing each measurement over a tidal period on the other hand. Hence, this would allow calibrating future scenarios more efficiently.

An example of measurements reconstruction using the first two POD modes for each hydrodynamic variable is shown in Figure 5.1. In this example, the free surface is captured almost perfectly, whereas the velocity components can be locally over or under-estimated, which corresponds to the remaining 4 % of EVR. A smoothing of the measurements using POD is also noticed.

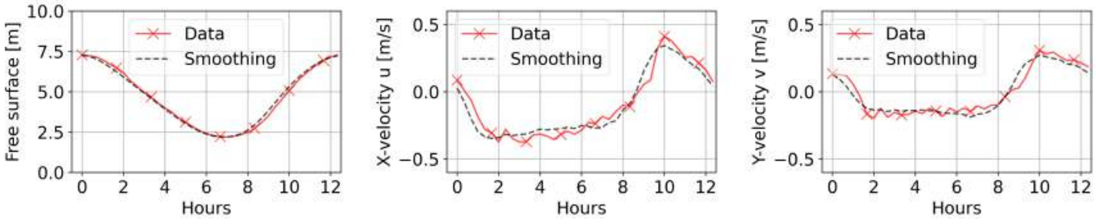

(a) Tidal period 1 - z_s (b) Tidal period 1 - u (c) Tidal period 1 - v

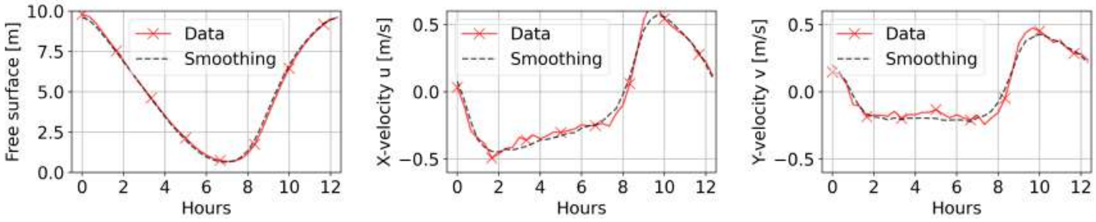

(d) Tidal period 22 - z_s (e) Tidal period 22 - u (f) Tidal period 22 - v

Figure 5.1 – Example of measurement reconstruction on a given tidal period (approx. 12 h 25 mn) for point 1 using 2 POD modes extracted from 38 occurrences.

Efficient reduction also means that the measured free-surface and velocity components show great similarities from one tidal period to another, as they can be projected over the same basis, using few components. It is therefore hypothesised that past/future unmeasured tidal variables, can also be expressed in the constructed POD basis. In particular, measurements at intake's vicinity are in general not available, and the extracted POD components can be used to construct prior hydrodynamic fields for DA calibration of other scenarios. Most importantly, by applying POD to tidal free surface elevations from the nearest harbor (hourly SHOM open source data described in Chapter 1), it can be shown that POD components of the latter are correlated to those of measured points in front of the intake. A scatter plot example of POD expansion coefficients can be seen in Figure 5.2.

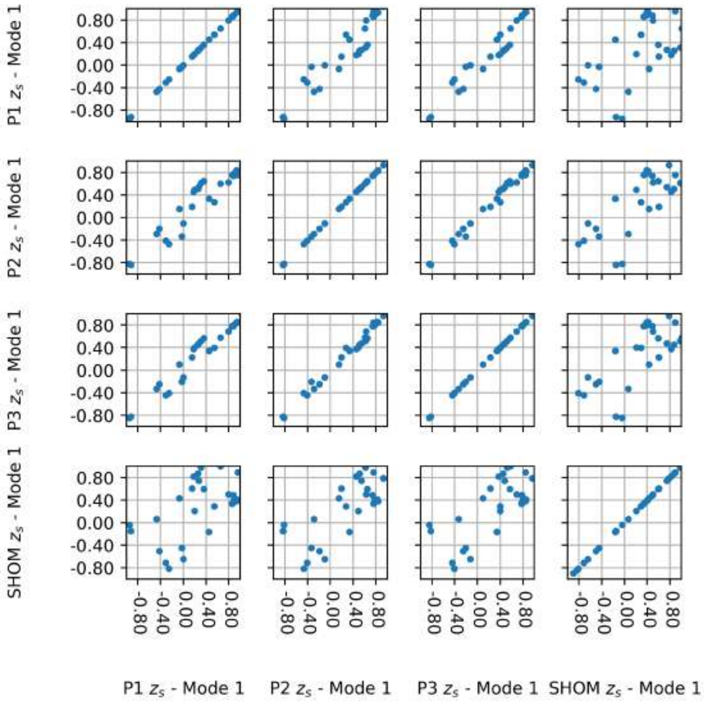

Figure 5.2 – Scatter plot of POD coefficients for Mode 1 of free surface, at points 1, 2 and 3 from the 2010 measurement campaign in front of the intake, and at nearest harbor (SHOM)

This means that tidal information in front of the intake can be reconstructed using the observed tendencies, with a quantifiable degree of uncertainty (dispersions around tendencies from Figures 5.2). It is also shown in Figure 5.3 that POD components of the three hydrodynamic variables are mutually dependent. This implies that reconstructing tidal elevations would allow to reconstruct velocity components as well. Consequently, DA can be attempted for scenarios for which measurements are not specifically available, by coupled correlation analysis and POD projection with SHOM data.

Given this perspective, a metamodel learning, based on numerical simulation results, can be attempted to provide a fast model for DA, in order to allow multiple tidal scenarios calibration. Two approaches are confronted in Section 5.2, presented as preprint for submission: (i) a joint parameter-state POD, which provides a linear model, and (ii) the POD-PCE coupling presented in Chapter 3. For the latter, adapted calculation of model error covariance matrix is proposed.

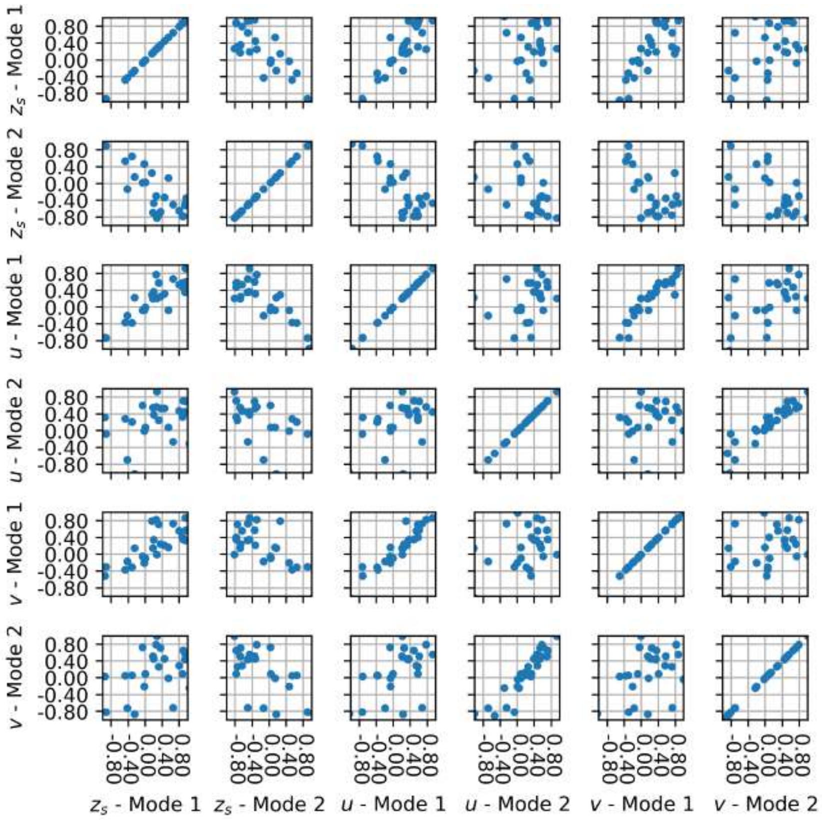

Figure 5.3 – EVR for the three hydrodynamic variables after measurement reduction on point 1.

5.2 Preprint for submission

Model reduction for fast and accurate Data Assimilation

Rem-Sophia Mouradi[1,2], Cédric Goeury[1], Olivier Thual[2,3], Fabrice Zaoui[1], and Pablo Tassi[1,4]

[1]EDF R&D, National Laboratory for Hydraulics and Environment (LNHE), 6 Quai Watier, 78400 Chatou, France
[2]Climate, Environment, Coupling and Uncertainties research unit (CECI) at the European Center for Research and Advanced Training in Scientific Computation (CERFACS), French National Research Center (CNRS), 42 Avenue Gaspard Coriolis, 31820 Toulouse, France
[3]Institut de Mécanique des Fluides de Toulouse (IMFT), Université de Toulouse, CNRS, Toulouse, France
[4]Saint-Venant Laboratory for Hydraulics (LHSV), Chatou, France

13 janvier 2021

Résumé

Data assimilation (DA) methods are widely used to provide trustworthy simulations, by combining physical knowledge and field observations. They are for example employed in geosciences applications to perform parametric calibration. In a context of climate change, old calibrations can not necessarily be used for new scenarios. This raises the question of DA computational cost, as the physical models, which sometimes can be complex and costly, need to be reanalyzed. Reduction and metamodelling represent therefore interesting perspectives. In particular, recent literature contributions focus on hybridization between ensemble and variational methods, in an attempt to benefit from their advantages, in particular efficiency and general non-linear framework. However, Monte Carlo (MC) type sampling can also result in a loss of accuracy, which forces to increase the ensemble size and therefore results in a computational burden for ensemble-based methods as well. To address these issues, two methods are proposed and confronted. The first method, called PODEn3DVAR and directly inspired from PODEn4DVAR, relies on an ensemble-based joint parameter-state Proper Orthogonal Decomposition (POD), injected in the 3DVAR (three-Dimensional VARiational) cost function. This results with a simple cost function whose minimum can be analytically computed. In the second method, called ensemble-POD-PCE-3DVAR, the model states are POD reduced first, and the resulting low dimensional vector is learned using Polynomial Chaos Expansion (PCE). The POD-PCE metamodel replaces the full model in the 3DVAR cost function, making the iterative minimization process much faster. In particular, PCE, widely used in the Uncertainty Quantification (UQ) community, has proven efficiency and fast convergence of statistical moments estimations, compared to MC type methods. For the ensemble-POD-PCE-3DVAR, an updated calculation of the observation error covariance matrix is given, which takes into consideration the metamodelling error. Proposed methods are confronted on a twin experiment, and compared to classical 3DVAR on a measurement-based problem. The results are promising, in particular superior with POD-PCE showing good convergence and trustworthy physical estimations.

1 Introduction

Data assimilation (DA) [3] is a powerful mathematical approach to produce trustworthy simulations, accounting for both measurements and results of physics-based models, while taking into consideration their respective uncertainties. It is applied in geosciences [11], from atmospheric and oceanographic forecasting models (e.g. [29, 41]), to forest fire front tracking [46], hydrodynamics [2, 5, 23], morphodynamics [16, 48, 52], etc. Interest in such methods is enhanced in a context of climate change, where new data constantly need to be accounted for [47], and standard calibrations, specifically optimal values obtained from fitting on old measurements, are not necessarily suitable to be applied for new scenarios [46]. Thus, the same model, which is often complex and computationally costly, has to be reanalyzed for different scenarios. Additionally, a constant increase in data sources is registered [22], as the new SWOT satellite mission [33, 39].

In particular, DA can for example be employed to fit modelling parameters as new data arrive, which is called *parametric calibration* and is the focus of the proposed study. In particular in this context, two DA techniques are commonly used: (i) ensemble methods [17] where a set of parameterizations is studied according to their probabilities, and (ii) variational methods [3], where a mismatch between different data sources, formalized by a *cost function*, is minimized. Each technique has advantages and drawbacks. On the one hand, ensemble-based methods are known to be computationally efficient for moderate control/state dimensions, as they allow faster exploration of the inputs and outputs spaces. They are able to account for non-Gaussian information through sampling, although relying on a Gaussian framework [11]. However, sampling errors accumulate through assimilation cycles and increase with large assimilation windows, which impacts the accuracy of ensemble methods. Small ensembles can overestimate the inter-ensemble correlations, resulting in a single trajectory through assimilation cycles for all members, which is the so-called *filter divergence* [4]. Furthermore, small ensembles are known to systematically underestimate the variances, resulting in underestimated calibration errors [4]. Solutions as *localization* (moderation of covariances) or *inflation* (forced increase of variances) are classically used, but are generally case specific and therefore said unsatisfactory [4]. This problem can only be resolved by increasing the ensemble size [26] which in turn increases the computational cost, and spoils the efficiency advantage. Additionally, ensemble methods rely most of the time on a linearity assumption, or alternatively linearization of the operators, which can result in a loss of accuracy for highly non-linear cases. Conversely, variational methods provide a general non-linear framework which is convenient for complex physical models, and do not rely on sampling. However, they are known to be time consuming for moderate control/state dimensions, oppositely to ensemble methods. This is caused by the classical use of iterative descent for minimization [3]. As a result, both ensemble-based and variational techniques can suffer from computational burden, either caused by sampling size and inefficiency of Monte Carlo (MC) type estimation, or due to iterative descent which only gradually explores the parameters space. Consequently, methods to decrease the cost of DA are desired.

To overcome these limitations, use of Dimensionality Reduction (DR) and input-to-output probabilistic modelling is investigated. Two approaches are proposed and compared: (i) an ensemble of parameters realizations and associated states are jointly reduced using Proper Orthogonal Decomposition (POD). Their covariances are represented through a common orthogonal basis. They are both replaced by their POD projections in a variational cost function. This is referred to as PODEn3DVAR (POD Ensemble-based three-Dimensional VARiational), which is a direct adaptation of PODEn4DVAR originally introduced by Tian et al. [57], to parametric cases ; (ii) model states are first independently reduced using POD. Their variations are therefore represented by a low dimensional vector, whose components are learned as a function of control parameters using Polynomial Chaos Expansion (PCE) [24, 25]. This provides a coupled POD-PCE *metamodel*, replacing the original model in the 3DVAR cost function, and hence called ensemble-POD-PCE-3DVAR.

POD application to increase efficiency of variational DA was given particular attention in recent literature contributions. For example in [42], intrusive Galerkin scheme is used to derive a reduced model and corresponding adjoint, based on orthogonal basis of model states. This was originally proposed for Boussinesq equations in [42], and later applied to ocean modelling in [10] and tidal equations in [44]. Previous contributions are however case dependent due to the use of intrusive approaches and adjoint calculation. Conversely, Vermeulen and Heemink [60] proposed an alternative based on linearization of model responses around a prior, combined to POD reduction and finite differences estimations of partial derivatives. This results with an approximate adjoint derivation, applicable to arbitrary models [60]. Their method was applied to Shallow Water Equations (SWE) for example in [2], and coastal hydro-morphodynamics in [18]. To completely avoid adjoint calculation, Tian et al. [57] propose the so-called PODEn4DVAR, to assimilate temporal states by calibrating a dynamic model's initial condition. POD is used to jointly reduce all spatio-temporal states including initial condition, which produces a common orthogonal basis to generate both the control and state spaces [57]. Using twin experiments, authors show that PODEn4DVAR solution is better than both iterative 4DVAR and Ensemble-based Kalman Filter (EnKF) [17]). Mons et al. [32] adapted PODEn4DVAR for parametric calibration by linearly spanning the parameters space using the model states POD basis. However, by doing so, the relationship between parameters and states is not explicitly modelled.

Use of PCE as metamodel in DA is not novel. It is for example employed by Marzouk et al. [31], within a Bayesian DA framework, also using a Galerkin scheme, to replace the model. This allows efficient approximation of posterior distribution compared to MC sampling. Their method is generalized for functional outputs (e.g. spatiotemporal fields) in [30] using DR prior to PCE learning, in order to reduce computational cost of Markov Chain Monte Carlo (MCMC). In other examples, PCE, known to converge significantly faster than MC sampling, is used to improve accuracy of ensemble methods by generating larger ensembles, as in [27]. It is also used in the latter to obtain error covariance matrices involved in the filter, instead of calculating ensemble-anomaly matrices, by straightforward estimation of statistical moments due to the orthonormality of the basis [27]. Same strategy is adopted in [46] for forest fire front tracking application, and in [15] on 1D SWE for river flows. However, none of the previous ones used PCE in a purely variational framework for functional outputs.

We therefore attempt hereby to: (i) adapt PODEn4DVAR to a purely parametric framework, in such way to capture parameter-state covariances ; (ii) apply PCE as metamodel in a variational framework, and particularly for functional outputs by coupling to POD. In particular in the proposed study, calculation of a new error covariance matrix resulting from model replacement by a POD-PCE surrogate is detailed and allows improving variational estimates. The proposed methods present interesting characteristics for efficient DA. Firstly, joint parameter-state reduction in PODEn3DVAR enforces the model dynamics in the cost function, and avoids learning the non-linear relationships [57]. The resulting cost function linearly depends on a unique reduced vector that represents parameters and states. Its minimum can be analytically calculated, without iterative descent. In particular, POD has shown to be accurate for non-linear problems [56], although being a linear decomposition. Its use in DA shows "superiority [...] with regard to the other families of vectors" [45], not only in terms of representation efficiency, but also due to straightforward calculation of error covariance matrices for the reduced vector [13]. Indeed, POD results with an eigenvalue matrix, that is a reduced size estimate of covariances, diagonal even for highly correlated vectors. Robert et al. [45] for example uses the eigenvalues as a background error covariance matrix, making the variational problem four to five times faster, and the error of DA solution smaller [45]. In addition, Vermeulen and Heemink [60] emphasis the interest of POD to avoid local minima in variational frameworks, with the smoothing inherent to the methods. Secondly, coupled use of POD and PCE benefits from the previously cited advantages of POD, in addition to the *spectral decay* assured by PCE [54]. Indeed, the latter is based on orthogonal polynomials, implying learning efficiency and fast convergence of statistical moments, compared to MC type methods based on sampling. Furthermore, in a previous contribution [37], POD-PCE efficiency to learn complex and non-linear phenomena was demonstrated, in particular for point-wise prediction of multi-dimensional fields.

Both approaches are based on hybridization between ensemble and variational methods. In particular, the variational cost function formulation is used, but the model is replaced with an ensemble-based surrogate. This is performed by generating an ensemble of parameters and related model states that allow to build appropriate emulators. Hybridization is used in an attempt to benefit from the advantages of both variational and ensemble approaches. In particular, while still relying on a cost function with a general non-linear framework, the computational burden of the descent is greatly reduced by the use of a surrogate instead of the full model. Additionally, while still using an ensemble of states, the sample size for convergence is reduced by means of POD that accurately summarizes the variances, and in particular using ensemble-POD-PCE-3DVAR with PCE that is much more efficient than MC sampling. In the presented study, performances of both approaches are investigated on a twin experiment as well as on measurements, applied to tidal modelling in a coastal configuration, using the SWE. Assessment of the robustness to different levels of noise is proposed on the twin experiment. In addition, sensitivity to the considered number of POD basis components is investigated. Hybrid ensemble-POD-PCE-3DVAR and PODEn3DVAR are confronted, and compared to classical 3DVAR on measurements.

The paper is outlined as follows: theoretical elements are introduced in Section 2. In particular, parametric 3DVAR framework is briefly presented in Subsection 2.1, while proposed PODEn3DVar and ensemble-POD-PCE-3DVAR are detailed in Subsections 2.2 and 2.3 respectively, with a focus on metamodel error covariance calculation in the latter. An application case and benchmarks are presented in Section 3, and a summary is proposed in Section 4.

2 Materials

In this Section, two reduction approaches, based on an ensemble generation, are proposed to accelerate parametric calibration using 3DVAR. Firstly, classical 3DVAR framework is briefly reminded in Section 2.1. Then, PODEn3DVAR, which consists in joint parameter-state reduction, is presented in Subsection 2.2 based on Proper Orthogonal Decomposition (POD). Lastly, ensemble-POD-PCE-3DVAR is proposed in Subsection 2.3, based on a coupling between POD and Polynomial Chaos Expansion (PCE). In particular, an appropriate calculation of POD-PCE metamodelling error in order to update the model error covariance matrix is proposed.

2.1 Data Assimilation: parametetric calibration using 3DVAR

Data Assimilation (DA) is a sub-class of inverse problems, where the objective is to estimate an unknown (state, parameters, etc.) using a compromise between observations and a model outputs, with a background idea (or prior knowledge) about the unknown [3, 9]. The most widely used methods are ensemble methods [17] and 3D- or 4DVAR (three- or four-Dimensional VARiational) [3]. Particular attention is here given to hybrid approaches, where variational formulation is used, but the model is replaced with a ensemble-based surrogate. Brief explanation of the framework is given below, and reader interested in details can refer to [3, 17].

This study focuses on *parametric estimation* problems, where the objective is to inversely deduce a set of parameters denoted $\boldsymbol{\theta}$ from optimal calibration of a state denoted $\mathbf{x} \coloneqq \mathcal{M}(\boldsymbol{\theta})$, where $\mathcal{M}$ designates the model [11]. Observed state is denoted $\mathbf{y} \coloneqq \mathcal{H}(\mathbf{x})$, where $\mathcal{H}$ denotes a projection, interpolation, selection, transformation, etc. Attributes are given to variables as superscripts: true state $\mathbf{x}^{(t)}$ and associated true parameters $\boldsymbol{\theta}^{(t)}$ designate a perfect model calibration. It is in general unknown, and the modeller, in principle, has an uncertain idea about its value, denoted $\boldsymbol{\theta}^{(b)}$. The objective is to find the best estimate called analysis and denoted $\boldsymbol{\theta}^{(a)}$, that provides an equilibrium between observed values denoted $\mathbf{y}^{(o)}$ and the background $\mathbf{x}^{(b)} = \mathcal{M}(\boldsymbol{\Theta}^{(b)})$, taking into consideration their respective uncertainties. In variational formulation, finding the analysis consists in minimizing a cost function denoted $J(\boldsymbol{\theta})$.

In a discrete (finite) multidimensional setting, where the parameters, state, and observations are arranged in vectors $\boldsymbol{\theta} = [\theta_1, \dots, \theta_v] \in \mathbb{R}^v$, $\mathbf{x} = [x_1, \dots, x_{m_x}]^T \in \mathbb{R}^{m_x}$ and $\mathbf{y}^{(o)} = [y_1^{(o)}, \dots, y_{m_y}^{(o)}]^T \in \mathbb{R}^{m_y}$ respectively (typically, uncertain parameters, multivariate response of a numerical model and spatio-temporal measures), cost function to minimize [3] can be written as in Equation 1,

$$J(\boldsymbol{\theta}) = \frac{1}{2}\left\|\boldsymbol{\theta} - \boldsymbol{\theta}^{(b)}\right\|^2_{\mathbf{B}^{-1}} + \frac{1}{2}\left\|\mathcal{H}(\mathbf{x}) - \mathbf{y}^{(o)}\right\|^2_{\mathbf{R}^{-1}} \ , \tag{1}$$

where $||\mathbf{v} - \mathbf{w}||_{\mathbf{A}} \coloneqq (\mathbf{v} - \mathbf{w})^T\mathbf{A}(\mathbf{v} - \mathbf{w})$ is the weighted Mahalanobis distance, and matrices $\mathbf{B} \in \mathbb{R}^{m_x \times m_x}$ and $\mathbf{R} \in \mathbb{R}^{m_y \times m_y}$ are the symmetrical covariance matrices of the background and state/observation error respectively. Indeed, the background on the one hand, and the model, observation and its operator on the other hand, are both characterized with errors, denoted $\boldsymbol{\epsilon}^{(b)}$ and $\boldsymbol{\epsilon}^{(m,o)}$ respectively, as expressed in Equation 2.

$$\begin{cases} \boldsymbol{\theta}^{(t)} &= \qquad\qquad \boldsymbol{\theta}^{(b)} + \boldsymbol{\epsilon}^{(b)} \\ \\ \mathbf{y}^{(o)} &= \mathcal{H}(\mathbf{x}^{(t)}) + \boldsymbol{\epsilon}^{(o)} = \mathcal{H}\left(\mathcal{M}\left(\boldsymbol{\theta}^{(t)}\right)\right) + \boldsymbol{\epsilon}^{(m,o)} \end{cases} . \tag{2}$$

In a variational DA framework, errors are considered Gaussian and unbiased (zero expectations), strictly defined by their covariance matrices $\mathbf{B} \coloneqq [cov(\epsilon_i^{(b)}, \epsilon_j^{(b)})]_{i,j \in \{1,\dots,V\}}$ and $\mathbf{R} \coloneqq [cov(\epsilon_i^{(m,o)}, \epsilon_j^{(m,o)})]_{i,j \in \{1,\dots,m_y\}}$. All these errors should be minimized, which sometimes results in a high dimensional problem, principally due to the dimension of model response $\mathbf{x}$. Additionally, model errors $\boldsymbol{\epsilon}^{(m)}$ are in general difficult to define. A *perfect model* hypothesis is therefore added, and resulting problem is said *strong-constraint.*

A minimum corresponds to a null gradient of J. In the general case of non-linear models, classical approach consists in identifying an *adjoint model* [3], whose solution is equivalent to cancelling the gradient [3]. This method is however intrusive and presents drawbacks: it is conditioned by analytical derivation of the adjoint model, not possible for all systems of equations, and any update of the direct model and its discretization comes with the supplementary cost of updating the adjoint, which is not always trivial and requires resources. Non-intrusive solutions are therefore often preferred. For example, iterative descent methods, where the gradient is approximated using finite-differences, can be used [3]. Lastly, due to the numerous approximations (cost function definition, error covariance matrices approximation, descent algorithms), optimal solution is only an approximation (analysis) of the true state (perfect knowledge). It is therefore also characterized with errors, which can be expressed as $\boldsymbol{\theta}^{(a)} = \boldsymbol{\theta}^{(t)} + \boldsymbol{\epsilon}^{(a)}$. An associated error covariance matrix is denoted $\mathbf{P}^{(a)} \coloneqq [cov(\epsilon_i^{(a)}, \epsilon_j^{(a)})]_{i,j \in \{1,\dots,V\}}$.

2.2 Linear Surrogate: PODEn3DVAR

This section is dedicated to the use of Proper Orthogonal Decomposition (POD) as an ensemble based linear surrogate within 3DVAR parametric calibration. POD is briefly presented below. Readers interested in supplementary theoretical details and demonstrations can refer to [38, 51].

2.2.1 Proper Orthogonal Decomposition

POD is a Dimensionality Reduction (DR) technique [28], consisting in a linear variable separation for continuous bi-variate functions denoted $\mathbf{u}(\psi, \omega) : \Psi \times \Omega \rightarrow \mathbb{D}$, where $\mathbb{D}$ is a Hilbert space characterized by its scalar product $(.\,,.)_{\mathbb{D}}$ and induced norm $||.||_{\mathbb{D}}$. This is written as in Equation 3,

$$u(\psi, \omega) = \sum_{k=1}^{\infty} \nu_k(\omega)\sqrt{\lambda_k}\boldsymbol{\phi}_k(\psi) \;, \tag{3}$$

where $\{\lambda_k\}_{k=1}^{\infty} \subset \mathbb{R}$, $\{\nu_k(.)\}_{k=1}^{\infty} \subset \mathcal{C}(\Omega, \mathbb{R})$ and $\{\boldsymbol{\phi}_k(.)\}_{k=1}^{\infty} \subset \mathcal{C}(\Psi, \mathbb{D})$, with $\mathcal{C}(\mathbb{A}, \mathbb{B})$ denoting the space of continuous functions defined over $\mathbb{A}$ and arriving at $\mathbb{B}$. In particular, $\{\boldsymbol{\phi}_k(.)\}_{k=1}^{\infty}$ is called POD basis and is orthonormal with respect to $(.\,,.)_{\mathbb{D}}$. Its members are ordered according to their importance in the interest field representation in terms of variance, which can be calculated as in Equation 4, where e_d is called Explained Variance Rate (EVR). It quantifies the proportion of variance captured by POD at a given rank $d \in \mathbb{N}$, with an approximation $\sum_{k=1}^{d} \nu_k(\omega)\sigma_k\boldsymbol{\phi}_k(\psi)$. When an order $d << min(dim(\Psi), dim(\Omega))$ corresponds to a high EVR, we speak of DR, because u is spanned to a sub-space of much smaller dimension than $\Psi \times \Omega$.

$$e_d = \frac{\sum_{k \leq d} \lambda_k}{\sum_{k=1}^{+\infty} \lambda_k} \;. \tag{4}$$

At given rank d, POD approximation has the lowest error compared to any other linear expansion [28].

In discrete form, POD is usually written as in Equation 5, for a real valued physical variable measured at different coordinates $\{\psi_1, \dots, \psi_m\}$ (e.g. spatio-temporal locations) and for an *ensemble* of events $\{\omega_1, \dots, \omega_m\}$ (e.g. realizations in different configurations), and stored in matrix $\mathbf{U} := [u(\psi_i, \omega_j)]_{i,j} \in \mathbb{R}^{m \times n}$,

$$\mathbf{U} = \overline{\mathbf{U}} + \boldsymbol{\Phi}\boldsymbol{\Lambda}^{1/2}\mathbf{N}^T = \overline{\mathbf{U}} + \boldsymbol{\Phi}\boldsymbol{\Sigma}\mathbf{N}^T \;, \tag{5}$$

where $\boldsymbol{\Phi} := [\phi_k(\psi_i)]_{i,k} \in \mathbb{R}^{m \times e}$, $\mathbf{N} := [\nu_k(\omega_j)]_{j,k} \in \mathbb{R}^{n \times e}$, and $\boldsymbol{\Lambda} := [\lambda_k]_{k,k} \in \mathbb{R}^{e \times e}$, with $e = min(m, n)$, and $\overline{\mathbf{U}}$ the ensemble mean. In particular, matrices $\boldsymbol{\Phi}$ and $\mathbf{N}$ are orthonormal, so that $\boldsymbol{\Phi}\boldsymbol{\Phi}^T = \mathbf{I}_m$ and $\mathbf{N}\mathbf{N}^T = \mathbf{I}_n$, where $\mathbf{I}_m$ is the $m \times m$ identity matrix. The POD basis $\boldsymbol{\Phi}$ corresponds to the eigenvectors of matrix $\mathbf{B}_c := (\mathbf{U} - \overline{\mathbf{U}})(\mathbf{U} - \overline{\mathbf{U}})^T$ decomposed as $\mathbf{B}_c = \boldsymbol{\Phi}\boldsymbol{\Lambda}\boldsymbol{\Phi}^T$, with $\boldsymbol{\Lambda}$ the eigenvalues arranged in decreasing order, or using the equivalent Singular Value Decomposition (SVD) as $(\mathbf{U} - \overline{\mathbf{U}}) = \boldsymbol{\Phi}\boldsymbol{\Sigma}\mathbf{N}^T$, where $\boldsymbol{\Sigma} = \boldsymbol{\Lambda}^{1/2}$ is the singular values matrix. Matrix $\mathbf{N}^T$ is deduced using a projection $\mathbf{N}^T = \boldsymbol{\Sigma}^{-1}\boldsymbol{\Phi}^T\left(\mathbf{U} - \overline{\mathbf{U}}\right)$. Each column j of $\mathbf{N}^T$ is a vector of expansion coefficients that represent a realization ω_j of the decomposed field. When POD approximation is truncated at rank d, it is written as $\mathbf{U} \approx \overline{\mathbf{U}} + \boldsymbol{\Phi}^{(d)}\boldsymbol{\Sigma}^{(d)}\mathbf{N}^{(d)}$, where column j of $\mathbf{N}^{(d)}$ contains reduced vector variable $\boldsymbol{\nu} = [\nu_1(\omega_j), \dots, \nu_d(\omega_j)]^T \in \mathbb{R}^d$.

2.2.2 PODEn4DVAR adapted to parametric 3DVAR

When diverse enough records $\{\omega_1, \dots, \omega_m\}$ are available, resulting POD basis can be considered as a generator of all possible states. Then, any state $u(\psi, \omega_j)$ can be approximated on the same basis $\boldsymbol{\Phi}^{(d)}$ by fitting $\boldsymbol{\nu} = [\nu_1(\omega_j), \dots \nu_d(\omega_j)]^T$. Hence, Tian et al. [57] proposes to replace the model response at any time in a 4DVAR cost function by its POD approximation, which they call PODEn4DVAR. Consideration of the model dynamics is then enforced using POD rather than an adjoint.

We propose the same procedure using a joint parameter-state POD using cost function in Equation 1, where the observation operator $\mathcal{H}$ is considered linear as $\mathbf{H}$ for the sake of simplicity. In particular, n paired realizations of parameters $[\theta_1, \dots, \theta_v]$ and model response $[x_1, \dots, x_{m_x}]$ are arranged in a single vector $[\theta_1, \dots, \theta_v, x_1, \dots, x_{m_x}]$ of size $m_x + k$ and stored in an ensemble matrix of size $(m_x + k) \times n$. The latter is POD reduced which gives an approximation in the form of Equation 6 for each realization. The POD basis matrix can therefore be written as a block vector in the form $\boldsymbol{\Phi}^{(d)} = [\boldsymbol{\Phi}_{\boldsymbol{\theta}}^{(d)}, \boldsymbol{\Phi}_{\mathbf{x}}^{(d)}]^T$, where parameter block denoted $\boldsymbol{\Phi}_{\boldsymbol{\theta}}^{(d)}$ is of size $v \times d$, and state block denoted $\boldsymbol{\Phi}_{\mathbf{x}}^{(d)}$ is of size $m_x \times d$, formed simply by selecting adequate lines of the full matrix $\boldsymbol{\Phi}^{(d)}$.

$$[\theta_1, \dots, \theta_v, x_1, \dots, x_{m_x}]^T \approx \left[\,\overline{\theta_1}, \dots, \overline{\theta_v}, \overline{x}_1, \dots, \overline{x}_{m_x}\right]^T + \boldsymbol{\Phi}^{(d)}\boldsymbol{\Sigma}^{(d)}\boldsymbol{\nu} \;. \tag{6}$$

This provides a common linear generator for parameters and state. Hence, they both can be replaced in the parametric 3DVAR cost function in Equation 1. A new approximate cost function is written as in Equation 7.

$$J(\boldsymbol{\theta}) \approx \widetilde{J}(\boldsymbol{\nu}) := \frac{1}{2}\left\|\boldsymbol{\Phi}_{\boldsymbol{\theta}}^{(d)}\boldsymbol{\Sigma}^{(d)}\left(\boldsymbol{\nu} - \boldsymbol{\nu}^{(b)}\right)\right\|_{\mathbf{B}^{-1}}^2 + \frac{1}{2}\left\|\mathbf{H}\left[\overline{\mathbf{x}} + \boldsymbol{\Phi}_{\mathbf{x}}^{(d)}\boldsymbol{\Sigma}^{(d)}\boldsymbol{\nu}\right] - \mathbf{y}^{(o)}\right\|_{\mathbf{R}^{-1}}^2 \;, \tag{7}$$

The problem becomes linear and explicit, and the gradient can be analytically calculated as in Equation 8.

$$\begin{aligned}\nabla_{\boldsymbol{\nu}}\widetilde{J} &= \left(\boldsymbol{\Phi}_{\boldsymbol{\theta}}^{(d)}\boldsymbol{\Sigma}^{(d)}\right)^T \mathbf{B}^{-1}\left(\boldsymbol{\Phi}_{\boldsymbol{\theta}}^{(d)}\boldsymbol{\Sigma}^{(d)}\right)\left(\boldsymbol{\nu}-\boldsymbol{\nu}^{(b)}\right)\\ &+ \left(\mathbf{H}\boldsymbol{\Phi}_{\mathbf{x}}^{(d)}\boldsymbol{\Sigma}^{(d)}\right)^T\mathbf{R}^{-1}\left(\mathbf{H}\left[\overline{\mathbf{x}}+\boldsymbol{\Phi}_{\mathbf{x}}^{(d)}\boldsymbol{\Sigma}^{(d)}\boldsymbol{\nu}\right]-\mathbf{y}^{(o)}\right)\end{aligned} . \tag{8}$$

The analysis is obtained by cancelling the gradient, as in Equation 9.

$$\begin{aligned}\boldsymbol{\nu}^{(a)} &= \left[\left(\boldsymbol{\Phi}_{\boldsymbol{\theta}}^{(d)}\boldsymbol{\Sigma}^{(d)}\right)^T \mathbf{B}^{-1}\left(\boldsymbol{\Phi}_{\boldsymbol{\theta}}^{(d)}\boldsymbol{\Sigma}^{(d)}\right)+\left(\mathbf{H}\boldsymbol{\Phi}_{\mathbf{x}}^{(d)}\boldsymbol{\Sigma}^{(d)}\right)^T\mathbf{R}^{-1}\left(\mathbf{H}\boldsymbol{\Phi}_{\mathbf{x}}^{(d)}\boldsymbol{\Sigma}^{(d)}\right)\right]^{-1}\\ &\times \left[\left(\boldsymbol{\Phi}_{\boldsymbol{\theta}}^{(d)}\boldsymbol{\Sigma}^{(d)}\right)^T \mathbf{B}^{-1}\left(\boldsymbol{\Phi}_{\boldsymbol{\theta}}^{(d)}\boldsymbol{\Sigma}^{(d)}\right)\boldsymbol{\nu}^{(b)}-\left(\mathbf{H}\boldsymbol{\Phi}_{\mathbf{x}}^{(d)}\boldsymbol{\Sigma}^{(d)}\right)^T\mathbf{R}^{-1}\left(\mathbf{H}\overline{\mathbf{x}}-\mathbf{y}^{(o)}\right)\right]\end{aligned} . \tag{9}$$

If POD is based on an ensemble generated from a perturbation around the background $\boldsymbol{\theta}^{(b)}$ with covariance $\mathbf{B}$, then the cost function can be simply written as in Equation 10, and corresponding analysis formula 12 is simpler.

$$J(\boldsymbol{\theta}) \approx \widetilde{J}(\boldsymbol{\nu}) := \frac{1}{2}\left\|\boldsymbol{\Sigma}^{(d)}\left(\boldsymbol{\nu}-\boldsymbol{\nu}^{(b)}\right)\right\|^2_{\left(\boldsymbol{\Lambda}^{(d)}\right)^{-1}} + \frac{1}{2}\left\|\mathbf{H}\left[\overline{\mathbf{x}}+\boldsymbol{\Phi}_{\mathbf{x}}^{(d)}\boldsymbol{\Sigma}^{(d)}\boldsymbol{\nu}\right]-\mathbf{y}^{(o)}\right\|^2_{\mathbf{R}^{-1}} , \tag{10}$$

$$\nabla_{\boldsymbol{\nu}}\widetilde{J} = \left(\boldsymbol{\nu}-\boldsymbol{\nu}^{(b)}\right) + \left(\mathbf{H}\boldsymbol{\Phi}_{\mathbf{x}}^{(d)}\boldsymbol{\Sigma}^{(d)}\right)^T\mathbf{R}^{-1}\left(\mathbf{H}\left[\overline{\mathbf{x}}+\boldsymbol{\Phi}_{\mathbf{x}}^{(d)}\boldsymbol{\Sigma}^{(d)}\boldsymbol{\nu}\right]-\mathbf{y}^{(o)}\right) . \tag{11}$$

$$\begin{aligned}\boldsymbol{\nu}^{(a)} &= \left[\mathbf{I}_d+\left(\mathbf{H}\boldsymbol{\Phi}_{\mathbf{x}}^{(d)}\boldsymbol{\Sigma}^{(d)}\right)^T\mathbf{R}^{-1}\left(\mathbf{H}\boldsymbol{\Phi}_{\mathbf{x}}^{(d)}\boldsymbol{\Sigma}^{(d)}\right)\right]^{-1}\\ &\times \left[\boldsymbol{\nu}^{(b)}-\left(\mathbf{H}\boldsymbol{\Phi}_{\mathbf{x}}^{(d)}\boldsymbol{\Sigma}^{(d)}\right)^T\mathbf{R}^{-1}\left(\mathbf{H}\overline{\mathbf{x}}-\mathbf{y}^{(o)}\right)\right]\end{aligned} . \tag{12}$$

Solution to the minimization is hence straightforward and does not require an iterative algorithm.

2.3 Hybrid ensemble-POD-PCE-3DVAR

As expected, the proposed ensemble-POD-PCE-3DVAR methodology also relies on POD for building a surrogate. However, instead of relating the parameters and model response by a joint POD, their dependency is modelled using a probabilistic non linear mapping called Polynomial Chaos Expansion (PCE). The latter is briefly presented below, and readers interested in theoretical details can refer for instance to [54, 63].

For the following calculations, we define by $(\Omega, F, \mathbb{P})$ a probability space, where Ω is the event space (space of all the possible events ω) equipped with σ-algebra F (some events of Ω) and its probability measure $\mathbb{P}$ (likelihood of a given event occurrence). A random variable defines an application $Y(\omega) : \Omega \to D_Y \subseteq \mathbb{R}$, with realizations denoted by $y \in D_Y$. The PDF of Y is a function $f_Y : D_Y \to \mathbb{R}$ that verifies $\mathbb{P}(Y \in E \subseteq D_Y) = \int_E f_Y(y)dy$.

The k^{th} *moments* of Y are defined as $\mathbb{E}[Y^k] := \int_{D_Y} y^k f_Y(y)dy$, the first being the expectation denoted $\mathbb{E}[Y]$. In the same manner, we define the k^{th} *central moments* of Y as $\mathbb{E}[(Y-\mathbb{E}[Y])^k]$, the first being 0 and the second the variance of Y denoted by $\mathbb{V}[Y]$. The covariance of two random variables is defined as $cov(X,Y) = \mathbb{E}[(X-\mathbb{E}[X])(Y-\mathbb{E}[Y])]$ and a resulting property is $\mathbb{V}[Y] = cov(Y,Y)$. For a multi-dimensional random denoted $\mathbf{Y} = [Y_1, \ldots, Y_m]^T$, the expectation is defined component-wise as $\mathbb{E}[\mathbf{Y}] = [\mathbb{E}[Y_1], \ldots, \mathbb{E}[Y_m]]^T$, and the variance is defined as $\mathbb{V}[\mathbf{Y}] = \mathbb{E}[(\mathbf{Y}-\mathbb{E}[\mathbf{Y}])(\mathbf{Y}-\mathbb{E}[\mathbf{Y}])^T]$. It is a matrix of size $m \times m$ called the *covariance matrix*, and can also be developed as $\mathbb{V}[\mathbf{Y}] = \mathbb{E}[\mathbf{Y}\mathbf{Y}^T] - \mathbb{E}[\mathbf{Y}]\mathbb{E}[\mathbf{Y}]^T$. Component of line i_1 and column i_2 is exactly the covariance term $cov(Y_{i_1}, Y_{i_2})$ and hence, diagonal terms i correspond to $\mathbb{V}[Y_i]$ and the matrix is diagonal.

In this probabilistic framework, parameters and model response are considered to belong to the space of random variables with finite variances, denoted $\mathcal{L}^2_{\mathbb{R}}$. They are referred to using capital letters $\boldsymbol{\Theta}$ and $\mathbf{X}$ respectively. A realization of these randoms for an event $\omega \in \Omega$, is denoted using lower case letters as $\boldsymbol{\Theta}(\omega) := \boldsymbol{\theta} = [\theta_1, \ldots, \theta_v]^T$ and $\mathbf{X}(\omega) = \mathcal{M}(\boldsymbol{\Theta}(\omega)) := \mathbf{x} = [x_1, \ldots, x_{m_x}]^T$.

The space of real random variables with finite variances $\mathcal{L}^2_{\mathbb{R}}$ is a Hilbert equipped with an inner product $(Y,Z)_{\mathcal{L}^2_{\mathbb{R}}} := \mathbb{E}[YZ] = \int_\Omega Y(\omega)Z(\omega)d\mathbb{P}(\omega) = \int_\Omega yz f_{Y,Z}(y,z)d\omega$ and its induced norm $||Y||_{\mathcal{L}^2_{\mathbb{R}}} := \sqrt{\mathbb{E}[Y^2]}$. In particular, $f_{Y,Z}$ defines the joint PDF of randoms Y and Z, defined as $\mathbb{P}(Y,Z \in E \subseteq D_Y \times D_Z) = \int_E f_{Y,Z}(y,z)dydz$.

A number n of parameters realizations are used to produce n realizations of the model response. Model responses are then stored in an ensemble matrix of size $m_x \times n$, and POD reduced as in Equation 13.

$$\boldsymbol{X}(\omega) \approx \overline{\mathbf{X}} + \mathbf{\Phi}^{(d)}\mathbf{\Sigma}^{(d)}\mathbf{\Upsilon}^{(d)}(\omega)\ . \tag{13}$$

where $\mathbf{\Upsilon}^{(d)}(\omega) := \boldsymbol{\nu}$ is a realization of reduced variable associated to a realization of state $\boldsymbol{X}(\omega)$. PCE is then used to formulate a non-linear model that links random reduced variable $\mathbf{\Upsilon}^{(d)} = [\Upsilon_1, \dots, \Upsilon_d]^T$ to random parameters $\mathbf{\Theta}$.

2.3.1 Polynomial Chaos Expansion

For a component Υ_k or random variable $\mathbf{\Upsilon}^{(d)}$, PCE approximation $\widetilde{\Upsilon}_k(\mathbf{\Theta})$ is written in Equation 14,

$$\Upsilon_k \approx \widetilde{\Upsilon}_k(\mathbf{\Theta}) := \sum_{|\boldsymbol{\alpha}| \leq p} c^k_{\boldsymbol{\alpha}} \zeta_{\mathbf{\Theta},\boldsymbol{\alpha}}(\Theta_1, \Theta_2, ..., \Theta_V)\ , \tag{14}$$

where $c^k_{\boldsymbol{\alpha}} \in \mathbb{R}$ are deterministic coefficients, and $\{\zeta_{\mathbf{\Theta},\boldsymbol{\alpha}}, \boldsymbol{\alpha} := (\alpha_1, \dots, \alpha_v) \in \mathbb{N}^v, |\boldsymbol{\alpha}| := \sum_{i=1}^v \alpha_i \in [|0,p|]\}$ is an orthormal multivariate polynomial basis of maximum degree $p \in \mathbb{N}$. In particular, the orthonormality is defined with respect to the inner product $(.,\ .)_{\mathcal{L}^2_{\mathbb{R}}}$. The multivariate basis is constructed for mutually independent parameters as $\zeta_{\mathbf{\Theta},\boldsymbol{\alpha}}(\mathbf{\Theta}) := \prod_{i=1}^V \xi_{\Theta_i,\alpha_i}(\Theta_i)$, where $\{\xi_{\Theta_i,\beta}, \beta \in [|0,p|]\}$ is an orthonormal univariate polynomial basis for each input variable Θ_i. This is written as $(\xi_{\Theta_i,\beta_j}, \xi_{\Theta_i,\beta_k})_{\mathcal{L}^2_{\mathbb{R}}} = \int_\Omega \xi_{\Theta_i,\beta_j}(\theta_i)\xi_{\Theta_i,\beta_k}(\theta_i) f_{\Theta_i}(\theta_i) d\omega = \delta_{\beta_j\beta_k}$, where $\delta_{\beta_j\beta_k}$ is the Kronecker symbol. The constructed multivariate basis is also orthonormal with respect to joint probability distribution of parameters denoted $f_{\Theta_1,\dots,\Theta_v}$.

The choice of the basis is therefore directly related to the choice of input variable marginals. It has been for example shown that Hermite polynomials are orthonormal with respect to Gaussian distributions, whereas Legendre polynomials are orthonormal with respect to Uniform densities [62].

Coefficients $c^k_{\boldsymbol{\alpha}}$ can be estimated thanks to different methods, and is here performed using the Least Angle Regression Stagewise method (LARS) in order to construct an adaptive sparse PCE. This is an iterative procedure, where the algorithm begins by finding the polynomial pattern, denoted ζ_i for simplicity, that is the most correlated to the output. The latter is linearly approximated by $\epsilon_i\zeta_i$, where $\epsilon_i \in \mathbb{R}$. Coefficient ϵ_i is not set to its maximal value, but increased starting from 0, until another pattern ζ_j is found to be as correlated to $Y - \epsilon_i\zeta_i$, and so on. In this approach, a collection of possible PCE, ordered by sparsity, is provided and an optimum can be chosen with an accuracy estimate. It was performed in this study using corrected leave-one-out error. The reader can refer to the work of Blatman and Sudret [8] for further details on LARS and more generally on sparse constructions.

For multi-dimensional variables $\mathbf{\Upsilon}^{(d)} = [\Upsilon_1, \dots, \Upsilon_d]$, PCE constructed component wise with the same inputs $\mathbf{\Theta}$ can be written as in Equation 15, where $\boldsymbol{\zeta}_{\mathbf{\Theta}}$ is a vector containing the basis elements, and each line of matrix $\mathbf{C}$ contains expansion coefficients $c^k_{\boldsymbol{\alpha}}$ of component Υ_k.

$$\mathbf{\Upsilon}^{(d)} \approx \widetilde{\mathbf{\Upsilon}}^{(d)}(\mathbf{\Theta}) = \mathbf{C}\boldsymbol{\zeta}_{\mathbf{\Theta}} \tag{15}$$

The orthonormality is a particularly convenient property for an efficient representation. In particular, it guarantees *spectral decay* and therefore fast convergence of the approximation, as well as direct estimation of statistical moments [54].

2.3.2 New cost function with updated model error

The model in the parametric 3DVAR cost function 1 is now replaced by an approximate probabilistic POD-PCE metamodel denoted $\widetilde{\boldsymbol{X}}$ for random variable $\mathbf{X}$, written as in Equation 16

$$\boldsymbol{X} \approx \widetilde{\boldsymbol{X}}(\mathbf{\Theta}) := \overline{\mathbf{X}} + \mathbf{\Phi}^{(d)}\mathbf{\Sigma}^{(d)}\widetilde{\mathbf{\Upsilon}}^{(d)}(\mathbf{\Theta})\ . \tag{16}$$

where $\widetilde{\boldsymbol{\Upsilon}}^{(d)}$ is defined in Equation 15 and $\boldsymbol{\Sigma} := \boldsymbol{\Lambda}^{1/2}$. A new cost function is then written (for a given realization) as in Equation 17,

$$J(\boldsymbol{\theta}) \approx \widetilde{J}(\boldsymbol{\theta}) = \frac{1}{2}\left\|\boldsymbol{\theta} - \boldsymbol{\theta}^{(b)}\right\|^2_{\mathbf{B}^{-1}} + \frac{1}{2}\left\|\mathbf{H}\widetilde{\mathbf{x}} - \mathbf{y}^{(o)}\right\|^2_{\widetilde{\mathbf{R}}^{-1}} \ , \tag{17}$$

where $\widetilde{\mathbf{R}}$ is a new error covariance matrix. Indeed, with this surrogate, the model can no longer be considered perfect, even for an originally strong constraint 3DVAR problem. A new error denoted $\boldsymbol{\epsilon}^{(meta,o)}$, resulting from combined POD reduction error $\boldsymbol{\epsilon}^{POD}$, PCE approximation error $\boldsymbol{\epsilon}^{PCE}$ and observation error $\boldsymbol{\epsilon}^{(o)}$, should be considered. The latter then gives a new error covariance matrix written as $\widetilde{\mathbf{R}} = \mathbb{V}\left(\boldsymbol{\epsilon}^{(meta,o)}, \boldsymbol{\epsilon}^{(meta,o)}\right)$.

Firstly, POD basis truncation results in an approximation written in Equation 18, where $\boldsymbol{\epsilon}^{POD}$ is calculated as in Equation 19, and $\underline{\boldsymbol{\Upsilon}^{(d)}}$ designates the POD coefficients not considered in the approximate.

$$\mathbf{X} = \overline{\mathbf{X}} + \boldsymbol{\Phi}^{(d)}\boldsymbol{\Sigma}^{(d)}\boldsymbol{\Upsilon}^{(d)} + \boldsymbol{\epsilon}_{POD} \ , \tag{18}$$

$$\boldsymbol{\epsilon}^{POD} := \underline{\boldsymbol{\Phi}^{(d)}}\ \underline{\boldsymbol{\Sigma}^{(d)}}\ \underline{\boldsymbol{\Upsilon}^{(d)}} \ . \tag{19}$$

Secondly, PCE approximation error, resulting from coefficients fitting and polynomial basis truncation to a given polynomial degree, is defined as in Equation 20.

$$\boldsymbol{\epsilon}^{PCE} := \boldsymbol{\Upsilon}^{(d)} - \widetilde{\boldsymbol{\Upsilon}}^{(d)}(\boldsymbol{\Theta}) \ . \tag{20}$$

Consequently, exact formulation of the metamodel in Equation 16 with error characterization is written in Equation 21, where error $\boldsymbol{\epsilon}^{(meta)}$ is defined in Equation 22.

$$\mathbf{X} = \widetilde{\boldsymbol{X}}(\boldsymbol{\Theta}) + \boldsymbol{\epsilon}^{(meta)} \ . \tag{21}$$

$$\boldsymbol{\epsilon}^{(meta)} = \boldsymbol{\Phi}^{(d)}\boldsymbol{\Sigma}^{(d)}\boldsymbol{\epsilon}^{PCE} + \boldsymbol{\epsilon}^{POD} \ . \tag{22}$$

Lastly, combined metamodel and observation error can be calculated as in Equation 23, where $\mathbf{Y}$ denotes the observation random variable with realizations $\mathbf{y}^{(o)}$.

$$\begin{array}{rcc} \epsilon^{(meta,o)} & = & \mathbf{Y} - \mathbf{H}\widetilde{\mathbf{x}}(\boldsymbol{\theta}^{(t)}) \\ & = & \mathbf{Y} - \mathbf{H}\left(\mathbf{x}^{(t)} - \boldsymbol{\Phi}^{(d)}\boldsymbol{\Sigma}^{(d)}\boldsymbol{\epsilon}^{PCE} - \epsilon^{POD}\right) \\ & = & \boldsymbol{\epsilon}^{(o)} + \mathbf{H}\boldsymbol{\Phi}^{(d)}\boldsymbol{\Sigma}^{(d)}\epsilon^{PCE} + \mathbf{H}\epsilon^{POD} \end{array} \tag{23}$$

2.3.3 POD-PCE metamodel error covariance matrix

In this Subsection, observation errors, POD error and PCE errors for modes 1 to d, are considered mutually independent and unbiased ($\mathbb{E}[\epsilon] = 0$). Independence is assumed in the sense that both methods (patterns extraction and learning) are performed independently. Besides, $\mathbf{H}$ is assumed to be identity for the sake of simplicity. Results below can be easily extended to cases with linear operator $\mathbf{H}$ by simple matrix product, and used for arbitrary non-linear operator $\mathcal{H}$ if replaced with its Tangent Linear Model (TLM). Alternatively, metamodel learning can be directly performed in the observation space by transforming the modelling result using $\mathcal{H}$, as suggested in [58], which helps both gaining in analysis accuracy and saving computational time, as the observation space is generally of lower dimension.

Independence and bilinearity allow to develop the error covariance matrix as in Equation 24.

$$\begin{array}{rcc} \widetilde{\mathbf{R}} & = & \mathbb{V}\left(\boldsymbol{\epsilon}^{(meta,o)}, \boldsymbol{\epsilon}^{(meta,o)}\right) \\ & = & \mathbb{V}\left(\boldsymbol{\epsilon}^{(o)} + \boldsymbol{\Phi}^{(d)}\boldsymbol{\Sigma}^{(d)}\epsilon^{PCE} + \epsilon^{POD}, \epsilon^{(o)} + \boldsymbol{\Phi}^{(d)}\boldsymbol{\Sigma}^{(d)}\epsilon^{PCE} + \epsilon^{POD}\right) \\ & = & \mathbf{R} + \mathbb{V}\left(\boldsymbol{\epsilon}^{POD}, \boldsymbol{\epsilon}^{POD}\right) + \boldsymbol{\Phi}^{(d)}\boldsymbol{\Sigma}^{(d)}\mathbb{V}\left(\boldsymbol{\epsilon}^{PCE}, \boldsymbol{\epsilon}^{PCE}\right)\boldsymbol{\Sigma}^{(d)}\left(\boldsymbol{\Phi}^{(d)}\right)^T \end{array} \tag{24}$$

Firstly, POD error covariance matrix is developed in Equation 25.

$$\begin{array}{rcc} \mathbb{V}\left(\boldsymbol{\epsilon}^{POD}, \boldsymbol{\epsilon}^{POD}\right) & = & \mathbb{V}\left(\underline{\boldsymbol{\Phi}^{(d)}}\ \underline{\boldsymbol{\Sigma}^{(d)}}\ \underline{\boldsymbol{\Upsilon}^{(d)}}, \underline{\boldsymbol{\Phi}^{(d)}}\ \underline{\boldsymbol{\Sigma}^{(d)}}\ \underline{\boldsymbol{\Upsilon}^{(d)}}\right) \\ & = & \underline{\boldsymbol{\Phi}^{(d)}}\ \underline{\boldsymbol{\Sigma}^{(d)}}\ \mathbb{V}\left(\underline{\boldsymbol{\Upsilon}^{(d)}}, \underline{\boldsymbol{\Upsilon}^{(d)}}\right)\ \underline{\boldsymbol{\Sigma}^{(d)}}\ \left(\underline{\boldsymbol{\Phi}^{(d)}}\right)^T \ . \end{array} \tag{25}$$

The covariance matrix $\mathbb{V}\left(\underline{\boldsymbol{\Upsilon}^{(d)}}, \underline{\boldsymbol{\Upsilon}^{(d)}}\right)$ can be estimated as the *ensemble-anomaly covariance matrix* [11], written in Equation 26. Indeed, POD was deduced from an ensemble of realizations of $\mathbf{X}$, which provides n realizations for vector $\underline{\boldsymbol{\Upsilon}^{(d)}}$ stored in the columns of matrix $(\underline{\mathbf{N}^{(d)}})^T \in \mathbb{R}^{(e-d)\times n}$, with $e = min(n,m)$ (details in Section 2.2.1). Covariance is then developped in Equation 26 with unbiased error that cancels $\mathbb{E}\left[\underline{\mathbf{N}^{(d)}}\right] = \left(\underline{\boldsymbol{\Sigma}^{(d)}}\right)^{-1}\left(\underline{\boldsymbol{\Phi}^{(d)}}\right)^T \mathbb{E}\left[\boldsymbol{\epsilon}^{POD}\right]$ and orthonormality of POD coefficients that gives $\left(\underline{\mathbf{N}^{(d)}}\right)^T\left(\underline{\mathbf{N}^{(d)}}\right) = \mathbf{I}_{e-d}$.

$$\begin{array}{rcl} \mathbb{V}\left(\underline{\boldsymbol{\Upsilon}^{(d)}}, \underline{\boldsymbol{\Upsilon}^{(d)}}\right) & \approx & \dfrac{1}{n-1}\left(\underline{\mathbf{N}^{(d)}} - \mathbb{E}\left[\underline{\mathbf{N}^{(d)}}\right]\right)^T\left(\underline{\mathbf{N}^{(d)}} - \mathbb{E}\left[\underline{\mathbf{N}^{(d)}}\right]\right) \\ & = & \dfrac{1}{n-1}\left(\underline{\mathbf{N}^{(d)}}\right)^T\left(\underline{\mathbf{N}^{(d)}}\right) \\ & = & \dfrac{1}{n-1}\mathbf{I}_{e-d} \end{array} . \tag{26}$$

Secondly, PCE error covariance matrix, considering modes fitting errors are independent, can be estimated as:

$$\begin{array}{rcl} \mathbb{V}\left(\boldsymbol{\epsilon}^{PCE}, \boldsymbol{\epsilon}^{PCE}\right) & = & \mathbb{V}\left(\boldsymbol{\Upsilon}^{(d)} - \widetilde{\boldsymbol{\Upsilon}}^{(d)}, \boldsymbol{\Upsilon}^{(d)} - \widetilde{\boldsymbol{\Upsilon}}^{(d)}\right) \\ & = & \begin{pmatrix} \mathbb{V}\left[\Upsilon_1 - \widetilde{\Upsilon_1}\right] & 0 & \dots & 0 \\ 0 & \mathbb{V}\left[\Upsilon_2 - \widetilde{\Upsilon_2}\right] & \dots & 0 \\ \vdots & \vdots & \ddots & \vdots \\ 0 & 0 & \dots & \mathbb{V}\left[\Upsilon_d - \widetilde{\Upsilon_d}\right] \end{pmatrix} \end{array} \tag{27}$$

This independence assumption, that allows to write a diagonal matrix, is possible since each POD mode is learned independently by corresponding PCE model. Then, each variance term can be written in terms of expectation with the Koening-Huygens development. As PCE errors are supposed unbiased (no average over or under estimation), this gives:

$$\begin{array}{rcl} \mathbb{V}\left[\Upsilon_k - \widetilde{\Upsilon_k}\right] & = & \mathbb{E}\left[(\Upsilon_k - \widetilde{\Upsilon_k})^2\right] - \mathbb{E}\left[(\Upsilon_k - \widetilde{\Upsilon_k})\right]^2 \\ & = & \mathbb{E}\left[(\Upsilon_k - \widetilde{\Upsilon_k})^2\right] \end{array} \tag{28}$$

Quantity $\mathbb{E}\left[(\Upsilon_k - \widetilde{\Upsilon_k})^2\right]$ is called *generalization error* [7]. It can be approximated at PCE learning stage with the *empirical error* denoted δ_{emp} defined in Equation 29. This is performed by splitting the ensemble of realizations $(\mathbf{N}^{(d)})^T$ to a training set of size n_t and a validation/prediction set of size $n_p = n - n_t$. The training ensemble is then used to fit the PCE models, and the validation ensemble, with reduced state realizations $\left[\Upsilon_k(\boldsymbol{\theta}^1), \dots, \Upsilon_k(\boldsymbol{\theta}^{n_p})\right]$ associated to parameters realizations $\left[\boldsymbol{\theta}^1, \dots, \boldsymbol{\theta}^{n_p}\right]$, is used to estimate the learned model bias in Equation 29.

$$\mathbb{E}\left[(\Upsilon_k - \widetilde{\Upsilon_k})^2\right] \approx \delta_{emp}(\Upsilon_k, \widetilde{\Upsilon_k}) \coloneqq \frac{1}{n_p}\sum_{j=1}^{n}\left(\Upsilon_k(\boldsymbol{\theta}^{\boldsymbol{j}}) - \widetilde{\Upsilon_k}(\boldsymbol{\theta}^{\boldsymbol{j}})\right)^2 . \tag{29}$$

As explained above, generalization error is used in this study to fit an optimal PCE model for each component Υ_k independently (choice of polynomial degree), by minimization on the prediction set. Consequently, the resulting covariance estimation comes with no additional cost than fitting.

As a result, error $\widetilde{\mathbf{R}}$ can be estimated as in Equation 30.

$$\widetilde{\mathbf{R}} \approx \mathbf{R} + \frac{1}{n-1}\,\underline{\boldsymbol{\Phi}^{(d)}}\,\underline{\boldsymbol{\Lambda}^{(d)}}\left(\underline{\boldsymbol{\Phi}^{(d)}}\right)^T + \boldsymbol{\Phi}^{(d)}\begin{pmatrix} \lambda_1\delta_{emp}(\Upsilon_1 - \widetilde{\Upsilon_1}) & 0 & \dots & 0 \\ 0 & \lambda_2\delta_{emp}(\Upsilon_2 - \widetilde{\Upsilon_2}) & \dots & 0 \\ \vdots & \vdots & \ddots & \vdots \\ 0 & 0 & \dots & \lambda_d\delta_{emp}(\Upsilon_d - \widetilde{\Upsilon_d}) \end{pmatrix}\left(\boldsymbol{\Phi}^{(d)}\right)^T . \tag{30}$$

It is directly calculated from:

- the eigenvalue matrix associated to unused modes $\underline{\boldsymbol{\Lambda}^{(d)}}$ representing an Unexplained Variance Rate (UVR, oppositely to EVR) due to POD truncation;

- the approximation error due to PCE learning of each mode Υ_k, enhanced by the importance of the latter, represented by its eigenvalue λ_k.

For its estimation, no additional computation is necessary, besides POD calculation and PCE fitting by generalization error minimization. New error covariance is therefore directly estimated by transforming reduction and learning errors to the output's space through adequate matrix product using the full POD basis $\mathbf{\Phi} = \left[\mathbf{\Phi}^{(d)}, \underline{\mathbf{\Phi}^{(d)}}\right]$.

3 Numerical experiments with the Shallow Water Equations

The accuracy of the proposed hybrid DA approaches, presented in Section 2, is now assessed on practical examples. In particular, a model $\mathcal{M}$, with uncertain random parameters $\mathbf{\Theta}$ and output $\mathbf{x}$, and observations $\mathbf{y}^{(o)}$, should be specified for cost function defined in Equation 1. The latter are presented in Section 3.1. Then, a twin DA experiment, and a measurement-based DA experiment are presented in Sections 3.2 and 3.3 respectively. In particular in Section 3.3, results with the proposed algorithms are compared to classical 3DVAR.

3.1 Problem setup

The modelling of tidal flow at the vicinity of a power plant's cooling intake is here targeted. The studied intake is located on the eastern English Channel coast in northern France, which is a macro/mega-tidal zone dominated by a semi-diurnal circulation. Few field information about the currents are available, namely a survey of depth-averaged velocity components denoted $(u, v)^T$ and free-surface elevation denoted η at five measurement points, indicated with a schematic drawing of the intake in Figure 1-a.

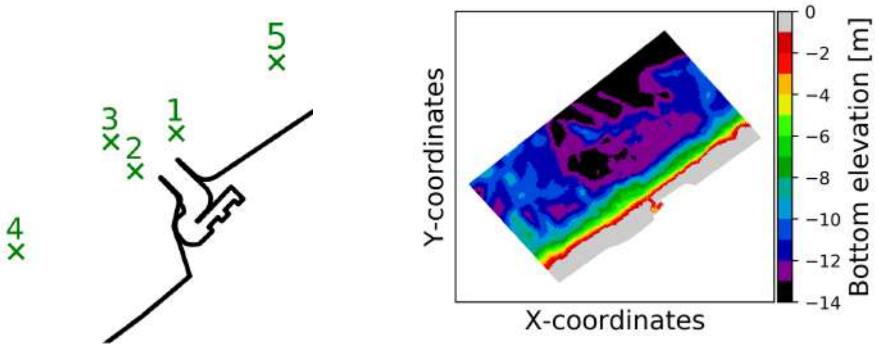

(a) Intake scheme and observation points

(b) Computation domain and bathymetry

FIGURE 1: Locations of measurement points for the two-months survey at intake's vicinity.

A superposition of the measured hydrodynamic variables on tidal periods is shown in Figure 2. The field campaign period is characterized with possible storms and surges.

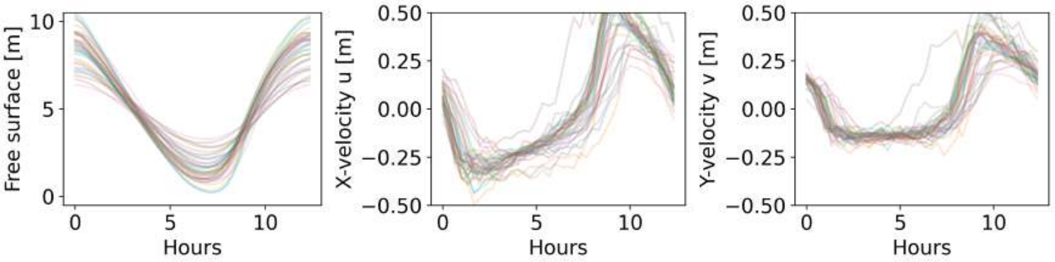

(a) Free surface (b) X-velocity u (c) Y-velocity v

FIGURE 2: Superposition of measurements for the hydrodynamic variables on Point 1.

These data are subject to measurement errors. In particular, Acoustic Wave And Current (AWAC) meters (1 MHz Nortek, Doppler technology) were used for offshore tidal velocities and water depths (through pressure records). Measurements are characterized with absolute errors 1 cm/s for and 5 cm for tidal velocities and free-surface elevations respectively.

In order to numerically reproduce such flow, in particular to obtain a detailed spatio-temporal current distributions for complementary analysis, the Shallow Water Equations (SWE) are used as model. The SWE are a set of non-linear hyperbolic Partial Differential Equations (PDE), obtained by depth-averaging the three-dimensional Reynolds-averaged free-surface Navier-Stokes equations, allowing the representation of almost-horizontal, two-dimensional (2D), shallow flows [19]. The resulting mass and momentum conservation equations are defined in 31.

$$\begin{cases} \dfrac{\partial h}{\partial t} + \dfrac{\partial (hu)}{\partial x} + \dfrac{\partial (hv)}{\partial y} = 0 \\ \dfrac{\partial (hu)}{\partial t} + \dfrac{\partial (hu^2)}{\partial x} + \dfrac{\partial (huv)}{\partial y} = -gh\dfrac{\partial \eta}{\partial x} - \dfrac{1}{\rho}\tau_{bx} + \dfrac{h}{\rho}F_x + \vec{\nabla}\cdot(h\nu_e \nabla u) \\ \dfrac{\partial (hv)}{\partial t} + \dfrac{\partial (huv)}{\partial x} + \dfrac{\partial (hv^2)}{\partial y} = -gh\dfrac{\partial \eta}{\partial y} - \dfrac{1}{\rho}\tau_{by} + \dfrac{h}{\rho}F_y + \vec{\nabla}\cdot(h\nu_e \nabla v) \end{cases} \tag{31}$$

where the system unknowns are the depth-averaged velocity components $u = (u, v)^T$ along the Cartesian coordinates (x, y) and the free surface elevation $\eta := h + b$, with h the water depth and b the bottom elevation. The gravitational acceleration g and the water density ρ are considered as constant values. Vector $\tau_b = (\tau_{bx}, \tau_{by})$ denotes the bottom shear stress, with componenets τ_{bx} and τ_{by} along the Cartesian coordinates (x, y). Vector F represents external forces (in the presented study, only Coriolis effect is considered as external force), and ν_e is the effective viscosity, accounting for kinematic, eddy and "dispersion" viscosity resulting from vertical integration, and here set equal to water's kinematic viscosity for simplicity.

Bed elevation b is here deduced from measurements, represented in Figure 1-b, based on Digital Elevation Model from [50]. This model setup, although characterized with possible approximations (e.g. bottom interpolations), is considered as trustworthy for the ongoing study. However, bottom friction and tidal Boundary Conditions (BC), which are essential elements for tidal modelling with SWE, are unknown, and their uncertainty should be quantified for optimal calibration using DA. In the following, attention is therefore focused on parametric calibration of friction and BC using appropriate variables. However, it should be noted that the developed framework could be used to calibrate other control vectors, as the bathymetry, Initial Conditions (IC), etc.

Firstly, bed shear stress is capital for environmental applications, as it has considerable influence on the flow because of the energy dissipation it induces [34]. Its exact formulation remains unknown, but many formulas can be found in literature, with specific calibration parameters. After sensitivity analysis on the studied case [36], it was concluded that formula choice does not impact the shape of model responses. Consequently in this study, the empirical Strickler's formula [34] is used as written in Equation 32, where K is called Strickler coefficient. The latter is an uncertain calibration parameter, that ranges in $[21.02, 90.66]$ $\mathrm{m}^{1/3}\ \mathrm{s}^{-1}$, as explained in [36]. In particular, two values are set: $K1$ inside the intake and $K2$ outside. Model outputs at measurement points of Figure 1 showed no sensitivity to $K1$ in [36]. Therefore, it is fixed to average interval value, and only $K2$ is calibrated using DA.

$$\vec{\tau}_b = \frac{\rho g}{K^2}\left(\frac{1}{h}\right)^{1/3} |\vec{u}|\vec{u} \tag{32}$$

Secondly, tidal BC are parametrized with the TPXO data-base [14], particularly the European Shelf (ES) local model within TELEMAC-2D software [43]. The hydrodynamic unknowns at the boundary are modelled as a superposition of harmonic components, as in Equation 33,

$$F(\mathbf{p},t) = \sum F_i(\mathbf{p},t) = \sum f_i(t) A_{F_i}(\mathbf{p}) cos\left(2\pi t/T_i - \phi_{F_i}(\mathbf{p}) + u_i^0 + v_i(t)\right) \ , \tag{33}$$

where the term F at point $\mathbf{p}$ and time t represents velocity components or water depth, F_i a harmonic component with constant period T_i, amplitude A_{F_i}, phase ϕ_{F_i}, phase at origin of times u_i^0, and temporal nodal factors $f_i(t)$ and $v_i(t)$. Thompson's method is then used to prescribe BC [20], and three parameters, denoted CTL (Coefficient of Tidal Level), MTL (Mean Tidal Level) and CTV (Coefficient of Tidal Velocity), can be used to calibrate the BC on measurements, as in Equation 34. For example, MTL allows to account for seasonal variability (effect of thermal expansion, salinity variations, air pressure, etc.) in addition to long-term sea level rise resulting from climate change [21], and all three parameters can be used to compensate the effects of storm and surge (atmospheric and wave setup) [21], as the latter are not modelled in the TPXO data-base. Variation interval for MTL is deduced from measurements as $[4.0, 6.0]$ m CM, whereas the non-dimensional parameters CTL and CTV are expertly set to $[0.8, 1.2]$ and $[0.8, 3.0]$ respectively, so that the measurements fall within the simulated min-max interval [36].

$$\begin{array}{rcc} h & = & CTL \times \sum h_i(M,t) - z_f + MTL \\ u & = & CTV \times \sum u_i(M,t) \\ v & = & CTV \times \sum v_i(M,t) \end{array} \tag{34}$$

To conclude, four uncertain parameters are defined for DA calibration: one input for sea friction denoted $K2$, and three BC parameters denoted MTL, CTL and CTV. As the only available information about these variables uncertainties are their variation supports, Uniform PDFs should be used to represent their uncertainty (*Maximum Entropy Principle* [53]). These PDFs are used to produce random ensembles of inputs using Monte Carlo (MC) sampling. Each input configuration is then propagated through the studied model by running a direct simulation. A corresponding ensemble of output values is therefore obtained, which then allows to learn the joint parameter-state POD on the one hand, and the POD-PCE model on the other hand. In particular for the latter, Legendre polynomials are used, and PCE is fitted for each POD pattern independently, by choosing the polynomial degree that minimizes the empirical error calculated in Equation 29. For the variational algorithms however, all variables are characterized by Gaussian errors. In the following, the background parameters are set to the average value from the variation interval, and standard deviation empirically estimated from the bounds, as summarized in Table 1. A great discrepancy is therefore considered for both twin and measurement-based experiments, using the full variation range of parameters, as the latter are generally unknown.

Variable θ_i	θ_i^{min}	θ_i^{max}	$\mathbb{E}[\Theta_i]$	$\sqrt{\mathbb{V}[\Theta_i]}$
$K2$ [m$^{1/3}$s^{-1}]	21.02	90.66	55.84	34.82
MTL [m CM]	4.0	6.0	5.0	1.0
CTL [-]	0.8	1.3	1.05	0.25
CTV [-]	0.8	3.0	1.9	1.1

Table 1: Uncertain parameters bounds and considered standard deviation for the variational DA cost function.

Lastly, previously described equations and closures are used through the open-source TELEMAC-MASCARET SYSTEM (TMS) (`https://www.opentelemac.org/`), in particular with TELEMAC-2D [20] that models hydrodynamics using the SWE. A numerical domain of size 8 × 16 km (offshore × longshore distances) is chosen, resulting from previous sensitivity analysis [36]. After mesh convergence study, elements of maximal size 50 m at the sea and 2.5 m in the intake are selected.

3.2 Robustness investigations on Twin experiment

Before attempting model calibration on complex measurements, one of the randomly produced model states is used to assess the performance of previously presented DA approaches in Section 2 on twin experiments. The model state consists in temporal series of the hydrodynamic variables, registered with a 20 minutes time step, and measured at the five observation points represented in Figure 1-a, over a semi-diurnal tidal period. Model state is arranged in vector form as $\mathbf{x} \coloneqq [u_{P1}(t_1), \ldots, u_{P5}(t_k), \ldots, u_{P5}(t_k), v_{P1}(t_1), \ldots, v_{P5}(t_k), \eta_{P1}(t_1), \ldots, \eta_{P5}(t_k)]$, where $Pi \in \{P1, \ldots, P5\}$ refer to record points and $t_j \in \{t_1, \ldots, t_k\}$ with $k \in \mathbb{N}^*$ to record times. The studied twin experiment model output is considered to be the "true" observation field, denoted $\mathbf{y}^{(t)}$. Perturbed versions denoted $\mathbf{y}^{(o)}$, with different noise levels ranging from 1 % to 20 %, are used to emulate imperfect observations. In particular, each component of $\mathbf{y}^{(t)}$ is perturbed using a white Gaussian noise around the true value, with a variance corresponding to chosen noise percentage. The variance employed for each component is also used to fill the observation error covariance matrix $\mathbf{R}$. Parameters prior values denoted $\boldsymbol{\theta}^{(b)}$ are set to average, and corresponding error covariances stored in $\mathbf{B}$ are calculated from standard deviations, as reported in Table 1. It should also be noted that all states, observations and parameters components are centered and reduced (normalized by their standard deviations) in order to give the same weight to all. Corresponding error covariance matrices are normalized accordingly.

A first confrontation of relative Root Mean Square Error (RMSE) calculated for each hydrodynamic variable and measurement point separately, between true state $\mathbf{y}^{(t)}$ and analyzed model output $\mathbf{x}^{(a)}$, is shown in Figure 3. As an example for this first comparison, 10 % of noise is added to the observation, and a number of POD modes corresponding to 80 % EVR is selected for metamodel construction with both approaches. The evolution of analysis error with the ensemble size can be seen, with a comparison between PODEn3DVAR and POD-PCE. Additionally, a comparison between POD-PCE using original error covariance matrix $\mathbf{R}$, and POD-PCE using metamodel error covariance matrix $\widetilde{\mathbf{R}}$, calculated as in Equation 30, is also provided.

On the one hand, POD-PCE error is globally lower than PODEn3DVAR, in particular for free-surface elevations where the RMSE difference is higher. Convergence is not clearly established with both algorithms for velocity estimation, but is reached much earlier with POD-PCE than with PODEn3DVAR for free surface estimations. For the latter, at about an ensemble of size $n = 200$, POD-PCE analysis error is stable, while it still varies for PODEn3DVAR. This may suggest that joint parameter-state POD, which forms a linear surrogate for PODEn3DVAR, fails at capturing non-linear relationships between the input-output spaces, with the used ensemble sizes. Linearization may indeed not be a good option for such big parameter discrepancies (Table 1), and in this case, POD-PCE is a better option, as non-linearities are efficiently captured by the use of orthogonal multivariate polynomials.

On the other hand, using the new estimation of error covariance matrix greatly reduced the analysis RMSE for all variables and at all measurement points. Additionally, while convergence is not clearly established with both algorithms for velocity estimation, using $\widetilde{\mathbf{R}}$ seems to efficiently stabilize the error at low ensemble sizes.

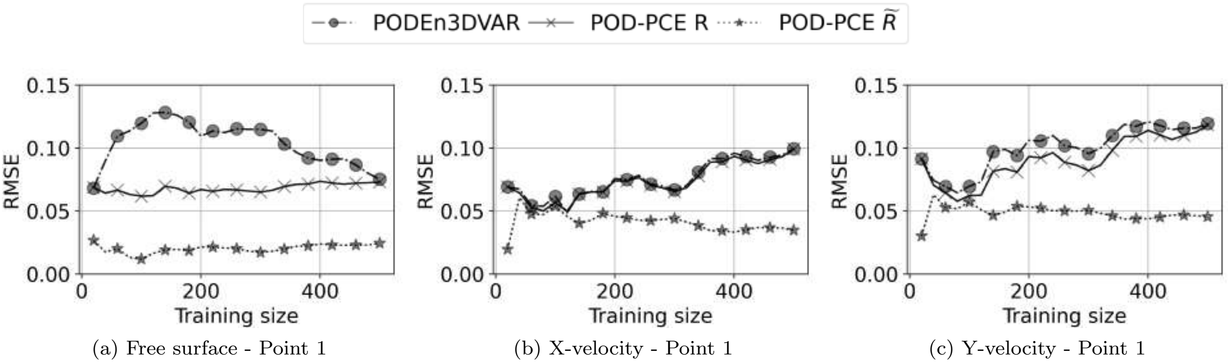

(a) Free surface - Point 1 (b) X-velocity - Point 1 (c) Y-velocity - Point 1

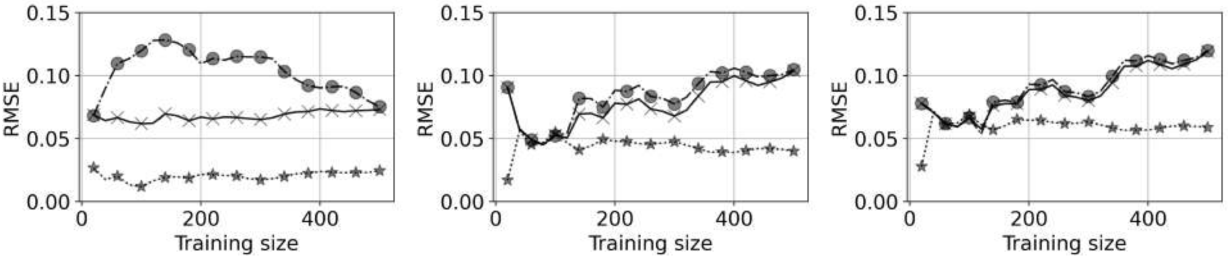

(d) Free surface - Point 4 (e) X-velocity - Point 4 (f) Y-velocity - Point 4

FIGURE 3: Variables RMSE comparison for different calibration algorithms with EVR 80 % and noise 10 %.

Using four different noise levels (1, 5, 10 and 20 %), a comparison of RMSE for the three system unknowns at observation Point 1 (Figure 1), with the POD-PCE approach using $\widetilde{\mathbf{R}}$, is shown in Figure 4. The assimilation seems to be robust to noise, with little RMSE variation from 1% to 10 %, and a maximum of 2% added RMSE with a transition from 10 % to 20 % of observation noise.

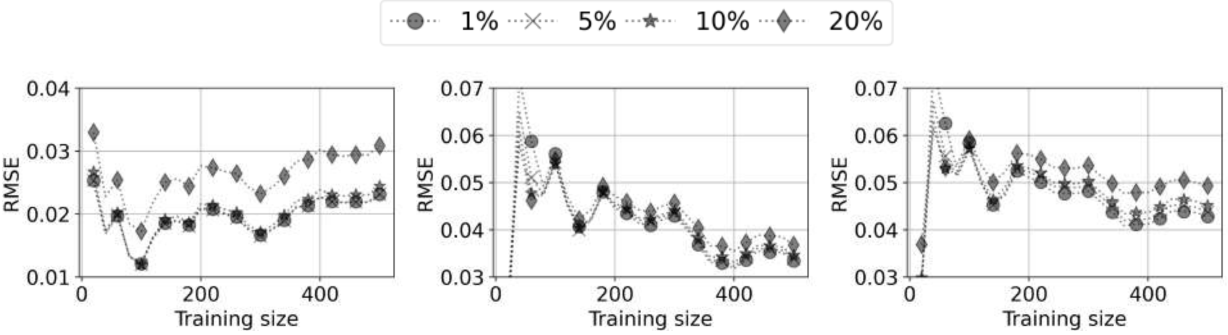

(a) Free surface - Point 1 (b) X-velocity - Point 1 (c) Y-velocity - Point 1

FIGURE 4: Variables RMSE comparison for different noise levels with POD-PCE algorithm using corrected error covariance matrix, for EVR 80 %.

An analysis example with 80 % EVR, on 20 % noisy observation, is shown in Figure 5. Use of POD-PCE with corrected error covariance matrix gives the best fit.

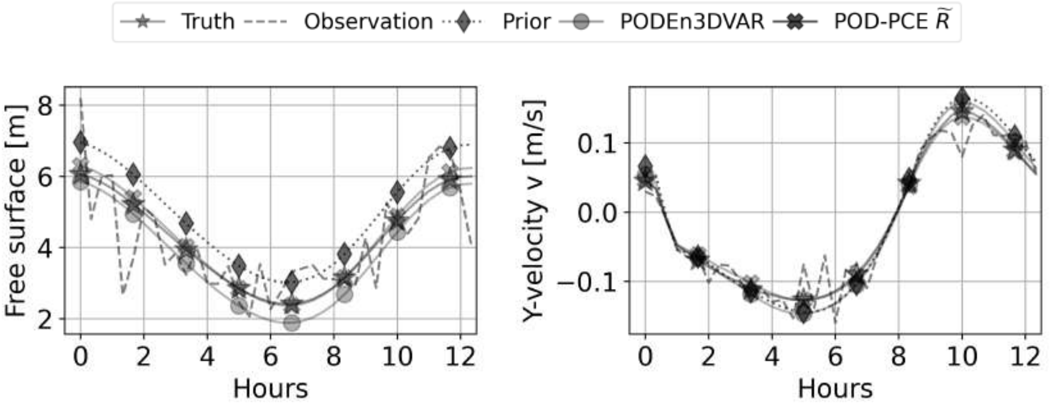

(a) Free surface - Point 1

(b) Y-velocity - Point 1

Figure 5: Examples of fitting with 80 % EVR and 20 % observation noise.

The fitted input values are shown in Table 2. In the first white colored rows, prior is set to variation intervals means, and background errors are set to corresponding variance. It can be noticed that fit errors can be considerable for parameters, for example 34.38% overestimation of CTV with POD-PCE and 12.82% underestimation when using $\widetilde{\mathbf{R}}$. This can be explained by the variables interactions in the model response, showed in previous sensitivity study in [35]. For example $K2$ dissipates the domain velocities while CTV increases them. Consequently, an infinity of paired values can give the same state. This relates to the so-called parameter identifiability issues [40]. Random priors were used in order to investigate the dependency structure between fitted parameter values as shown in Figure 6, which confirms the previous analysis. For example, a great dependency is noticed between fitted CTV values on the one hand and fitted K2 and CTL values on the other hand. As a result, when using a different prior with negligible errors for K2 and CTL, the algorithms has greater chances for fitting the parameters with much smaller errors, as shown in the grey colored rows from Table 2. This is valid even if the errors associated to the remaining parameters (±50 %) are much higher.

Algorithm	K2 [$m^{1/3}s^{-1}$]	MTL [-]	CTL [-]	CTV [-]	field RMSE
Truth	40.73	4.24	0.98	1.68	0.0
Prior	55.84 (37.11%)	5.0 (17.97%)	1.05 (7.0%)	1.9 (12.75%)	17.27 %
PODEn3DVAR	52.07 (27.84%)	3.87 (8.67%)	1.07 (8.83%)	1.76 (4.31%)	8.84 %
POD-PCE	32.81 (19.44%)	4.0 (-5.62%)	1.3 (32.47%)	2.26 (34.38%)	7.35 %
POD-PCE-$\widetilde{R}$	45.65 (12.1%)	4.33 (2.26%)	1.05 (7.0%)	1.47 (-12.82%)	3.05 %
Prior	40.73 (0.01%)	2.12 (-50.0%)	0.98 (0.01%)	2.53 (50.0%)	16.91 %
PODEn3DVAR	54.51 (33.84%)	4.01 (-5.34%)	1.07 (9.04%)	1.89 (12.08%)	5.95 %
POD-PCE	40.73 (0.01%)	4.0 (-5.62%)	0.98 (0.01%)	1.94 (14.84%)	6.09 %
POD-PCE-$\widetilde{R}$	40.73 (0.01%)	4.33 (2.1%)	0.98 (0.01%)	1.62 (-3.88%)	3.0 %

Table 2: Fitted parameter values with different algorithms for noise 20 % and EVR 80 %. The errors relative to true values are mentioned between brackets. Colored in white and grey are two attempts with different priors and their error covariance matrices.

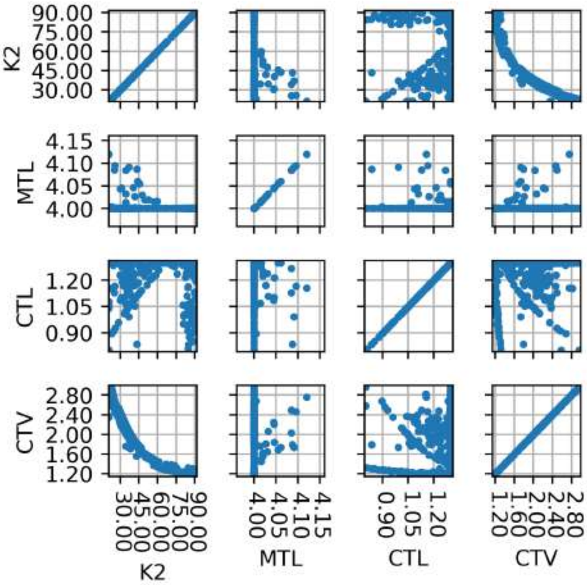

Figure 6: Scatter plot of optimal parameters with random sizes and backgrounds for EVR 80 and noise 20.

Lastly, sensitivity of the proposed algorithms to EVR choice is studied. Comparison of global RMSE, calculated between true state $\mathbf{y}^{(t)}$ and analyzed model output $\mathbf{x}^{(a)}$, is shown in Figure 7 using 10 % noisy twin observations. Error decrease from 80 % to 90 % EVR is more significant for PODEn3DVAR with small ensembles, than for POD-PCE algorithms. However, using $\widetilde{\mathbf{R}}$, the average error decreases from about 3% to 1%. Using the 95 % EVR, the POD-PCE with $\widetilde{\mathbf{R}}$ RMSE seems stable, while it drastically decreases for the other algorithms at small ensemble sizes. However, convergences needs greater sample sizes to be established, and is reached earlier for POD-PCE than for PODEn3DVAR. Perhaps, smaller variance rates need bigger ensemble sizes to be adequately captured. In particular, we showed in previous POD-PCE investigations [37] that PCE performs better for high variance POD patterns learning, than for smaller variance ones.

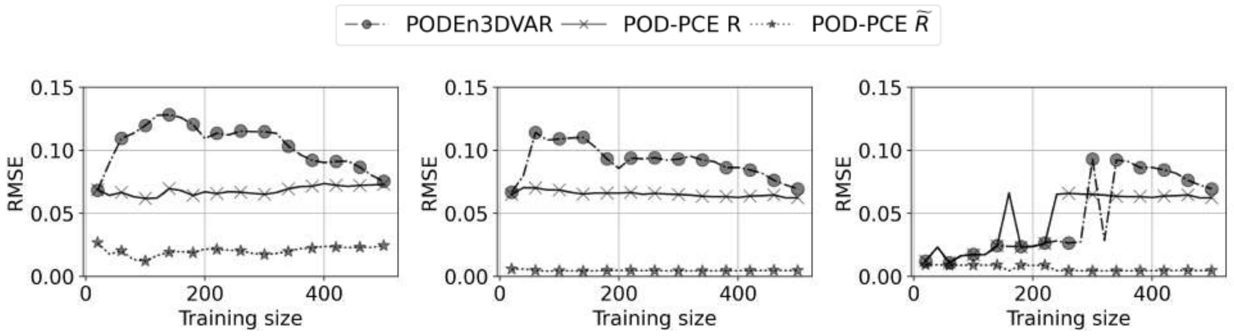

(a) EVR 80 %   (b) EVR 90 %   (c) EVR 95 %

Figure 7: Global RMSE comparison for different calibration algorithms with 10 % noisy twin observations and varying EVR.

3.3 Confrontation to classical 3DVAR on measurements

In this subsection, the proposed PODEn3DVAR and POD-PCE algorithms are used for field measurements based calibration, and confronted to classical 3DVAR using the SWE. In particular, measurements on a tidal period duration are used for fitting.

Comparison of global RMSE with the used approaches for different EVR is shown in Figure 8. Firstly, increasing the EVR generally decreases the RMSE. In particular, transition from 80 % to 90 % allows the POD-PCE metamodel solution to greatly approach the classical 3DVAR solution, as can be seen in in Figure 8-b. However, EVR increase should be performed cautiously as it may lead to slower convergence, for example with the 95 % EVR in Figure 8-c, as also highlighted with the twin experiment. Secondly, PODEn3DVAR and POD-PCE errors are almost identical for the 80 % EVR in Figure 8-a, while POD-PCE using $\widetilde{\mathbf{R}}$ allows slight improvement and faster convergence.

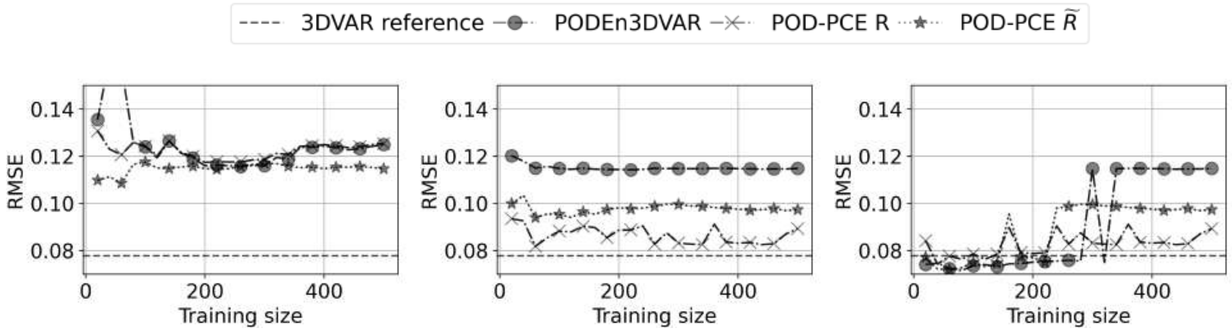

(a) EVR 80 % (b) EVR 90 % (c) EVR 95 %

FIGURE 8: RMSE comparison for different algorithms on calibration measurements with different EVR.

Conversely, for the 90 % and 95 % EVR metamodels, POD-PCE using $\widetilde{\mathbf{R}}$ results with an analysis of higher RMSE, although it allows faster convergence compared to POD-PCE with $\mathbf{R}$. However, it should be kept in mind in this case that the original error covariance matrix $\mathbf{R}$ is not appropriate, because the perfect model assumption is not valid. Indeed, measured variables can show different patterns compared to the model, as can be seen with the fitting example in Figure 9, where a phase shift can be noticed in the free-surface measurements compared to model, as well as an asymmetry in the velocity evolution. However, estimating model errors is not an easy task, and perfect model assumption is used in practice. Therefore, comparison with POD-PCE using $\widetilde{\mathbf{R}}$ can not be conclusive as it only compensates for unconsidered model errors in this case. It can be noted however that even without error covariance matrix correction, the POD-PCE results in Figure 9 are almost identical to classical 3DVAR solution.

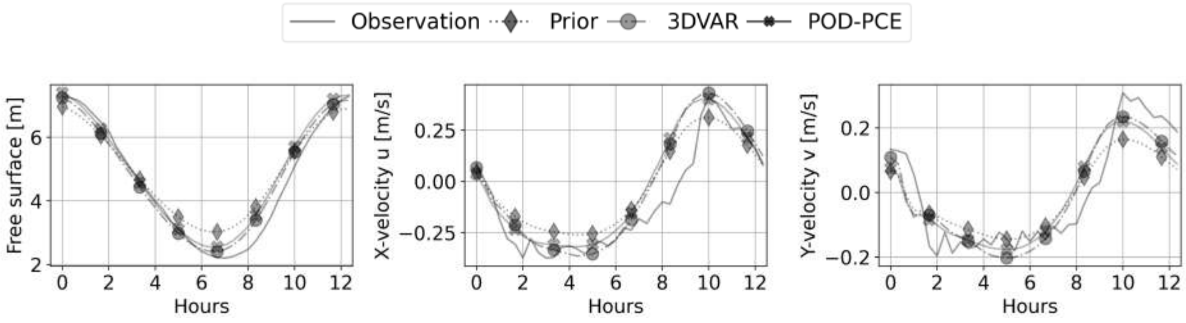

(a) Free surface (b) X-velocity (c) Y-velocity

FIGURE 9: Examples of fitting using the POD-PCE algorithm with 90 % EVR.

RMSE comparisons for different EVR with the POD-PCE metamodel are shown in Figure 10. It can be confirmed that transition from 80 % to 90 % comes with global RMSE decrease in Figure 10-a, in particular for free surface estimation in Figure 10-b. However, use of 95 % EVR, although interesting, does not converge at considered ensemble sizes. Additionally, it can be noticed that RMSE difference between most optimal POD-PCE and 3DVAR is lower than 2% for free surface, while it goes up to 5 % for velocity in Figure 10-c.

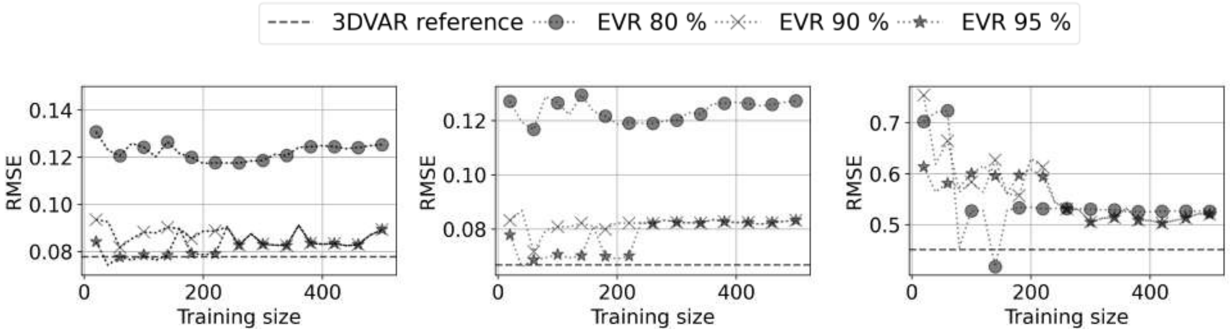

(a) Global (b) Free surface - Point 1 (c) X-velocity - Point 1

Figure 10: RMSE comparison for different EVR with POD-PCE algorithm for calibration on measurements.

Algorithms comparison is shown for the most optimal 90 % EVR in Figure 11. As previously noted, use of $\widetilde{\mathbf{R}}$ for POD-PCE does not come with improvement of RMSE, but rather with faster convergence.

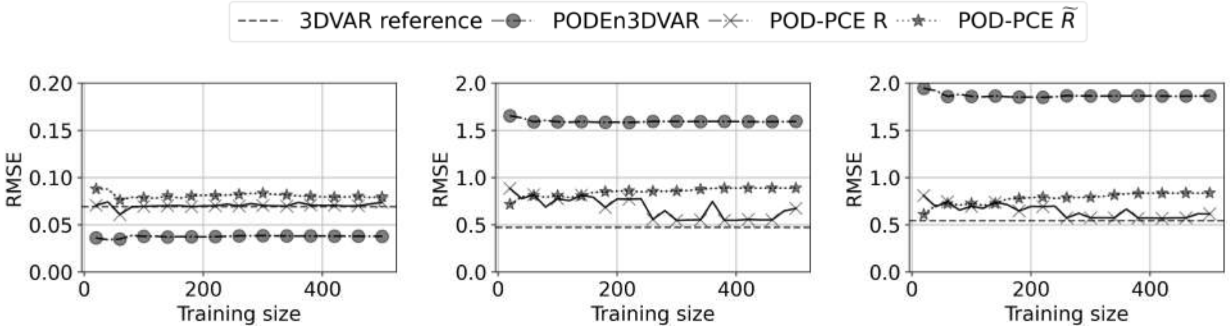

(a) Free surface - Point 1 (b) X-velocity - Point 1 (c) Y-velocity - Point 1

Figure 11: RMSE comparison of interest variables for different algorithms on calibration measurements with EVR 80 %.

PODEn3DVAR gives the worst results for velocity analysis, but seems to provides better results for free-surface. However, analyzing its parameters fitting in Figure 12 shows that it may result with non-physical conclusions. Indeed, parameters values are completely out of range, and sometimes negative, when they must be strictly positive. Use of PODEn3DVAR should therefore be restricted to moderate EVR, for example 80 % EVR giving realistic parameter estimations in 12 for reasonably high ensemble sizes (200 for example). Such limitation also limits the analysis accuracy and results with considerable advantage for POD-PCE.

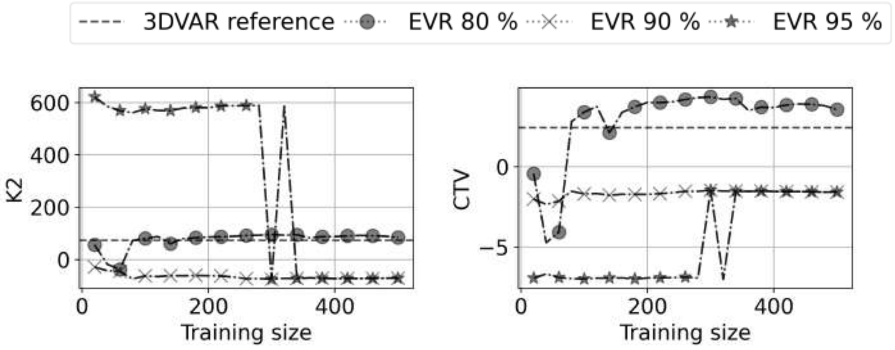

(a) X-velocity - Point 1 (b) Y-velocity - Point 1

Figure 12: Fitting of parameters using PODEn3DVAR with different EVR.

Lastly, as previously highlighted, POD-PCE results are good approximates of classical 3DVAR analysis. They additionally come with the computational time advantage. Indeed, the same computational time required to perform a descent in a given direction with classical 3DVAR, can be used to investigate multiple directions with adequate computational resources. In the studied case for example, 40 simultaneous model runs are possible, where each scenario requires an average run time of 8 hours. Consequently, while 3DVAR with classical descent using the full model gives a single estimation after 8 hours, the ensemble generated for POD-PCE learning can explore 40 parameters configurations, and the learned metamodel, running in seconds, results with an ensemble-based 3DVAR that performs better analysis at the same computational cost (complements in Appendix A). It should be kept in mind however that in terms of number of simulations to reach an optimal analysis, classical 3DVAR is superior, as 40 simulations were already sufficient to reach convergence. Hence, if computational resources are a concern, then classical 3DVAR should be preferred. As a conclusion, choice between classical 3DVAR and hybrid ensemble-POD-PCE 3DVAR could be led by the importance of computational time vs. computational resources.

3.4 Discussion

In the results Sections 3.2 and 3.3, the PODEn3DVAR and ensemble-POD-PCE-3DVAR methods were confronted on a twin and a measurement-driven DA experiments respectively. In the following, the main conclusions from previously presented results are discussed.

Ensemble-POD-PCE-3DVAR vs. PODEn3DVAR

The analysis provided by ensemble-POD-PCE-3DVAR has shown to be more accurate than PODEn3DVAR with the twin experiment, in particular for free-surface elevations, where convergence is reached with ensemble-POD-PCE-3DVAR, while PODEn3DVAR results still vary even for ensembles of size $n = 500$. On the field measurements case, superiority of ensemble-POD-PCE-3DVAR compared to PODEn3DVAR was confirmed. In particular, RMSE was lower with ensemble-POD-PCE-3DVAR, and PODEn3DVAR resulted with unrealistic estimations of parameters, that can be avoided by selecting a lower number of POD components, which in turn decreases the accuracy. Ensemble-POD-PCE-3DVAR therefore gave better estimations, and has shown to be nearly as efficient as classical 3DVAR, with reduced computational cost.

This inadequacy of PODEn3DVAR was interpreted in terms of difficulty of learning with the linear joint parameter-state POD metamodel, particularly for non-linear relationships. In particular, the great discrepancies of the background make linearization difficult. Perhaps, if small perturbations around the background were used to generate the ensemble, then convergence would be faster. However, this does not assure a good coverage of parameters space in case of great uncertainty about prior parameters.

It should be here noted that an improved version called adaptive PODEn4DVAR was proposed in [10], consisting in POD basis update using an outer loop, by iterative perturbation of the sample around the analysis, also performed in [32]. This allows to generate an ensemble based on a small perturbation around the background (analysis of previous iteration), and better succeed in linearizing the relationships. Further more the adaptive PODEn4DVAR is said to be more stable to the ensemble size than other ensemble DA methods [32], and a limited sample of size $n = 20$ is used to generate the POD basis at each step, said sufficient up to 10^5 control variables [32]. Perhaps, an interesting perspective would be to confront PODEn3DVAR and ensemble-POD-PCE-3DVAR, both with an iterative ensemble update.

Additionally, it was suggested in [1] that an improvement is possible if the cost function is estimated using the original model, while the adjoint is approximated in the reduced space [1]. Similarly, one could use the proposed PODEn3DVAR and ensemble-POD-PCE-3DVAR approaches to perform faster calculation of descent directions, while still estimating the cost function and the analysis with the full model.

For now, it is concluded that, at the same computational cost, and without further improvements of the proposed algorithms, ensemble-POD-PCE-3DVAR seems to be superior to PODEn3DVAR. However, this still needs to be confirmed on other test cases.

Robustness to noise

Robustness tests to noise were conducted using the twin experiments. In particular, four noise levels (1, 5, 10 and 20 %) were incorporated to the truth (perfect observation, equal to twin simulation result) in order to simulate measured observation. The tested ensemble-POD-PCE-3DVAR and PODEn3DVAR are both robust to noise in the observations. It is shown in particular that RMSE increase does not exceed 2% even with a noise increase of 10 %.

POD in that sense plays a major role. Indeed, given that the states are simulated with few POD patterns, the resulting analysis is smooth, not characterized with local fluctuations. For example in [49], a Singular Value Decomposition (SVD), on which POD extraction in discrete framework is based, is used as a smoother to delete noise from data, and therefore provide better estimations on a surface heat transfer inverse problem. Additionally, PCE was learned on smooth numerical model results. However, even in the case of perturbed training set, robustness of PCE to noise was demonstrated in [59] in pure Machine Learning setups, and confirmed in [37] in the case of POD-PCE coupling.

POD modes number influence

In both the twin and measurement-based experiments, sensitivity of the results to the choice of POD components number was investigated, through selection of different Explained Variance Rates (EVR).

It was shown that EVR increase (number of POD modes) may be contribute in decreasing the analysis error, for both PODEn3DVAR and ensemble-POD-PCE-3DVAR algorithms. This impact of chosen POD modes number on the performance of POD-based ensemble-variational methods was also highlighted by Cao et al. [10].

However, EVR increase does not systematically result in better analysis. Firstly, convergence issues can be met with ensembles of low size. In particular, the latter may not be sufficient to learn the small variances patterns (high rank modes) efficiently. Adding them to the metamodel may therefore result in uncertain analysis. This difficulty was in particular highlighted in [37] regarding POD expansion coefficients learning using PCE. Secondly, increasing the number of selected patterns has lead to unrealistic parameter estimations using PODEn3DVAR. The algorithm, by controlling too many POD expansion coefficients, results in over-fitting of the analysis on measurements, with the cost of completely unphysical parameter estimations. This also confirms the interest of using POD-PCE as surrogate, since the learned relationships between parameters and POD expansion coefficients prevent from fitting inadequate parameter values.

Impact of metamodel error covariance matrix

With the ensemble-POD-PCE-3DVAR algorithm, an adapted estimation of metamodel error covariance matrix, resulting in an update of observation error covariance matrix $\mathbf{R}$ denoted $\widetilde{\mathbf{R}}$, was proposed and tested. For the twin experiment, use of $\widetilde{\mathbf{R}}$ results with considerable gain in accuracy compared to $\mathbf{R}$, by decreasing RMSE from about 7% to 3%. This may seem counter-intuitive. Indeed, passage from $\widetilde{\mathbf{R}}$ to $\mathbf{R}$ consists in an increase of variances. This should in principle give less weight to the observation, relative to the background, in the cost function defined in Equation 1.

However, two possible interpretations can be given: (i) analysis RMSE is calculated relative to the truth for the twin experiment. For a perfectly defined cost function, in particular with adequate error covariances, minimization should in principle lead to perfect analysis (zero RMSE compared to truth). Hence, $\widetilde{\mathbf{R}}$, which is the adequate definition of error covariances given the metamodelling approximation, leads to better analysis than with $\mathbf{R}$ that only accounts for observation errors (added artificial noise) ; (ii) the shape of $\widetilde{\mathbf{R}}$, as defined in Equation 30, better distributes the errors. This is made both by correcting the variances at adequate spatio-temporal locations for given variables (diagonal update), and by taking into consideration the error covariances, which is performed through matrix product using the POD basis $\mathbf{\Phi}$.

In the measurement-based application, results are different. Use of the new error covariance matrix with ensemble-POD-PCE-3DVAR did not systematically decrease the analysis RMSE, as was the case with the twin experiment. This can be interpreted by the following: (i) perfect model assumption is no longer valid. Observations here are field measurements, that are not necessarily perfectly reproducible with the used Shallow Water Equations

(SWE). This questions the use of $\mathbf{R}$, and lessens the relevance of comparison to $\widetilde{\mathbf{R}}$; (ii) analysis was compared, in terms of RMSE, to the observations that are characterized with measurement errors. A low error does not necessarily mean that the analysis approaches from the truth, but rather that it fits the observations. This is directly related to the used error covariance matrix ($\mathbf{R}$ vs. $\widetilde{\mathbf{R}}$) which indeed impacts the weight given to observations in the cost function. Here, increase of RMSE can be naturally linked to increase of variances in $\widetilde{\mathbf{R}}$.

Ensemble-POD-PCE-3DVAR limitations and proposed perspectives

Firstly, direct POD-PCE coupling may not always be adequate for arbitrary physical problems, for example when dealing with discontinuity or when facing considerable non-linearities. For discontinuity treatment, RePOD (Registration POD) proposed by Taddei [55], consisting in parametric smoothing of the discontinuous field prior to POD, can be used. Furthermore, adaptive Multi-Element PCE in [61] can be attempted, in which sub-learning problems are performed independently on subsets of the inputs space. In a Bayesian DA problem characterized with high non-linearity, Birolleau et al. [6] show that representation problems may occur, with the Karhunen Loève Transform and PCE coupling proposed by Marzouk and Najm [30] for functional outputs. An iterative PCE method is therefore proposed as a solution, where interest field is first expanded using classical PCE, the resulting approximation used as a transform for the generation of a new PCE orthonormal basis, and so on. Remarkably, the expansion resulting from this iterative process performs much better, in particular in the presence of abrupt variations.

Secondly, use of PCE as metamodel may sometimes result with instabilities, which is highlighted by Després et al. [12] where PCE based reduction on the 1D SWE hyperbolic system generates non-physical oscillations that may grow in time, resulting from a loss of hyperbolicity.

Lastly, authors in [10] also mentioned the possible impact of snapshot sampling method on the performance of POD-based ensemble-variational methods. For more efficient PCE learning, in order to reduce the required ensemble size, Gauss-Hermite quadrature rule can be used to learn PCE coefficients instead of random MC sampling, as performed in [15, 46] to accelerate the Ensemble-based Kalman Filter. This however may not be optimal when dealing with high dimensional input spaces.

4 Summary

In the presented study, two approaches for hybrid ensemble-variational parametric calibration were proposed, PODEn3DVAR based on joint parameter-state POD on the one hand, and ensemble-POD-PCE-3DVAR based on POD-PCE metamodel within 3DVAR cost function on the other hand. In particular, calculation of a new error covariance matrix, that accounts for errors resulting from metamodelling, was proposed for the ensemble-POD-PCE-3DVAR approach. PODEn3DVAR and POD-PCE were assessed on a tidal currents modelling case, in a coastal area. A twin and a measurement-based DA experiment were attempted.

Firstly, Robustness of both methodologies to noise was demonstrated on the twin experiment. In particular, POD in both approaches helps providing a smooth analysis. Secondly, analysis provided by ensemble-POD-PCE-3DVAR is characterized by lower RMSE than PODEn3DVAR, compared to the truth for twin experiment, and compared to field data for the measurement-based experiment. It was additionally shown that POD-PCE estimations converge much faster than PODEn3DVAR. In particular, ensemble-POD-PCE-3DVAR using of the updated error covariance matrix results with considerable increase in accuracy (RMSE decrease from 7% to 3% in the twin experiment case) and converges much faster.

Sensitivity of the results to the choice of POD components number was assessed for both ensemble-POD-PCE-3DVAR and PODEn3DVAR. While increasing the complexity can improve the analysis, it may also, beyond a certain degree, result with non-converged metamodel learning and therefore uncertain analysis. Additionally, in the particular case of PODEn3DVAR, increasing the number of selected patterns has lead to unrealistic parameter estimations.

To conclude, with the used setups, POD-PCE is undoubtedly the most interesting choice. It is both accurate and computationally efficient. Convergence is achieved faster than with PODEn3DVAR. Additionally, proposed metamodel error covariance calculation significantly increases the accuracy, when added to an appropriately defined observation error. It gives satisfactory results compared to classical 3DVAR, while needing less run time. However, it was also noted that classical 3DVAR is more interesting in terms of needed number of simulations for convergence. Hence, computational time vs. computational resources could lead the choice between classical 3DVAR and hybrid ensemble-POD-PCE-3DVAR. Finally, POD-PCE metamodel could be adapted for particular cases of discontinuity or [61], considerable non-linearities [6]. Lastly, confrontations to PODEn3DVAR should be attempted in other configurations, for example using an iterative outer loop where the analysis is perturbed to generate a new ensemble, as performed with PODEn4DVAR in [10].

Acknowledgements

This work is funded by the French National Association of Research and Technology (ANRT) through the Industrial Conventions for Training through REsearch (CIFRE) in agreement with EDF R&D. The authors acknowledge their support, and are grateful for data collection and feedback from EDF operators. The authors gratefully acknowledge the TELEMAC-MASCARET (environmental numerical modelling), OpenTURNS (Uncertainties treatment python library) and the ADAO (Data Assimilation python library) open source communities.

Appendix A. Simulation times

Examples of calculation times are given in Figure 13. It can be seen in Figure 13-a that the POD-PCE model calibration time, including POD construction (eigenvalue problem) and PCE fitting for each POD pattern (choice of optimal degree and learning), is at most 10 minutes for the considered ensemble sizes. Effective calibration time for metamodel-based 3DVAR, showed in Figure 13-b, therefore principally consists in computational time required for model runs. As these can be performed 40 at a time, run time increases in stairs.

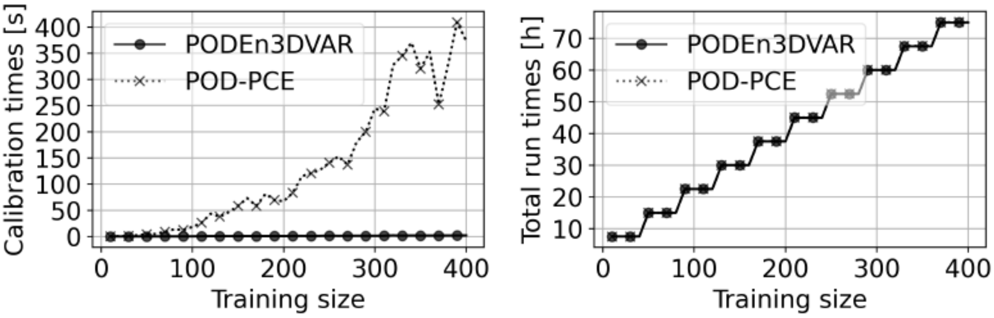

(a) Metamodel learning time

(b) Metamodel-based 3DVAR time

Figure 13: Evolution of calibration and total time (including simulations time) with training size by BLUE-POD and POD-PCE algorithms.

In the end, around 80 hours are necessary for a POD-PCE or PODEn3DVAR calibration, with an ensemble of size 400. In comparison, evolution of RMSE using classical 3DVAR is shown in Figure 14. It can be noticed for example that convergence is reached after 200 hours of descent time, which is already much higher than the used run time with the proposed algorithms.

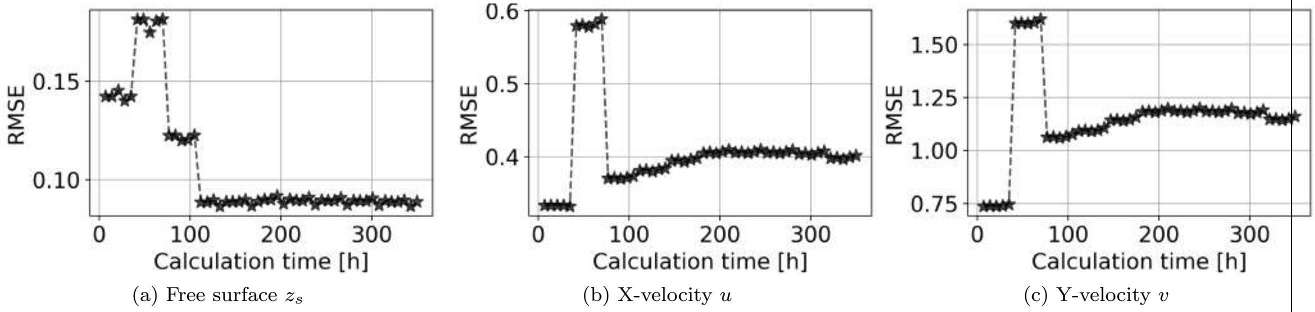

(a) Free surface z_s (b) X-velocity u (c) Y-velocity v

FIGURE 14: Evolution of RMSE with calibration time for the three state variables on point 5 using classical 3DVAR.

However, in terms of needed number of simulations to reach an optimal analysis, classical 3DVAR is superior, as 40 simulations were already sufficient in this particular case, compared to 300 simulations for POD-PCE (Figure 10 for example). As a conclusion, choice between classical 3DVAR and hybrid ensemble-POD-PCE 3DVAR could be led by the importance of computational time vs. computational resources.

Références

[1] M. Altaf, M. E. Gharamti, A. Heemink, and I. Hoteit. A reduced adjoint approach to variational data assimilation. *Computer Methods in Applied Mechanics and Engineering*, 254 :1 – 13, 2013.

[2] M. U. Altaf, A. W. Heemink, and M. Verlaan. Inverse shallow-water flow modeling using model reduction. *International journal for multiscale computational engineering*, 7(6), 2009.

[3] M. Asch, M. Bocquet, and M. Nodet. *Data assimilation : methods, algorithms, and applications.* SIAM, 2016.

[4] R. Bannister. A review of operational methods of variational and ensemble-variational data assimilation. *Quarterly Journal of the Royal Meteorological Society*, 143(703) :607–633, 2017.

[5] L. Bertino, G. Evensen, and H. Wackernagel. Combining geostatistics and kalman filtering for data assimilation in an estuarine system. *Inverse Problems*, 18(1) :1–23, jan 2002.

[6] A. Birolleau, G. Poëtte, and D. Lucor. Adaptive bayesian inference for discontinuous inverse problems, application to hyperbolic conservation laws. *Communications in Computational Physics*, 16(1) :1–34, 2014.

[7] G. Blatman. *Adaptive sparse polynomial chaos expansions for uncertainty propagation and sensitivity analysis.* PhD thesis, 2009.

[8] G. Blatman and B. Sudret. Adaptive sparse polynomial chaos expansion based on least angle regression. *Journal of Computational Physics*, 230(6) :2345 – 2367, 2011.

[9] E. Blayo, E. Cosme, M. Nodet, and A. Vidart. Introduction to data assimilation, 2011.

[10] Y. Cao, J. Zhu, I. M. Navon, and Z. Luo. A reduced-order approach to four-dimensional variational data assimilation using proper orthogonal decomposition. *International Journal for Numerical Methods in Fluids*, 53(10) :1571–1583, 2007.

[11] A. Carrassi, M. Bocquet, L. Bertino, and G. Evensen. Data assimilation in the geosciences : An overview of methods, issues, and perspectives. *Wiley Interdisciplinary Reviews : Climate Change*, 9(5) :e535, 2018.

[12] B. Després, G. Poëtte, and D. Lucor. Robust uncertainty propagation in systems of conservation laws with the entropy closure method. In *Uncertainty quantification in computational fluid dynamics*, pages 105–149. Springer, 2013.

[13] S. Durbiano. *Vecteurs caractéristiques de modèles océaniques pour la réduction d'ordre en assimilation de données.* PhD thesis, 2001.

[14] G. D. Egbert and S. Y. Erofeeva. Efficient Inverse Modeling of Barotropic Ocean Tides. *Journal of Atmospheric and Oceanic Technology*, 19(2) :183–204, 02 2002. ISSN 0739-0572.

[15] N. El Moçayd. *La décomposition en polynôme du chaos pour l'amélioration de l'assimilation de données ensembliste en hydraulique fluviale*. PhD thesis, 2017.

[16] S. Evangelista, G. Giovinco, and S. Kocaman. A multi-parameter calibration method for the numerical simulation of morphodynamic problems. *Journal of Hydrology and Hydromechanics*, 65 :175–182, 06 2017.

[17] G. Evensen. *Data assimilation : the ensemble Kalman filter*. Springer Science & Business Media, 2009.

[18] T. Garcia, G. El Serafy, A. Heemink, and H. Schuttelaars. Towards a data assimilation system for morphodynamic modeling : Bathymetric data assimilation for wave property estimation. *Ocean Dynamics*, 63, 05 2013.

[19] J.-F. Gerbeau and B. Perthame. Derivation of Viscous Saint-Venant System for Laminar Shallow Water ; Numerical Validation. Research Report RR-4084, INRIA, 2000. Projet M3N.

[20] J.-M. Hervouet. *Hydrodynamics of Free Surface Flows : Modelling with the Finite Element Method*. John Wiley & Sons, Ltd. : Hoboken, NJ, USA, 2007.

[21] D. Idier, X. Bertin, P. Thompson, and M. D. Pickering. Interactions between mean sea level, tide, surge, waves and flooding : mechanisms and contributions to sea level variations at the coast. *Surveys in Geophysics*, 40 (6) :1603–1630, 2019.

[22] A. Karpatne, I. Ebert-Uphoff, S. Ravela, H. A. Babaie, and V. Kumar. Machine learning for the geosciences : Challenges and opportunities. *IEEE Transactions on Knowledge and Data Engineering*, 31(8) :1544–1554, Aug 2019.

[23] K. Larnier, J. Monnier, P.-A. Garambois, and J. Verley. River discharge and bathymetry estimations from swot altimetry measurements. working paper or preprint, Oct. 2018.

[24] O. P. Le Maitre, O. M. Knio, H. N. Najm, and R. G. Ghanem. A stochastic projection method for fluid flow : I. basic formulation. *Journal of Computational Physics*, 173(2) :481 – 511, 2001.

[25] O. P. Le Maitre, M. T. Reagan, H. N. Najm, R. G. Ghanem, and O. M. Knio. A Stochastic Projection Method for Fluid Flow : II. Random Process. *Journal of Computational Physics*, 181(1) :9 – 44, 2002.

[26] J. Li and D. Xiu. On numerical properties of the ensemble kalman filter for data assimilation. *Computer Methods in Applied Mechanics and Engineering*, 197(43-44) :3574–3583, 2008.

[27] J. Li and D. Xiu. A generalized polynomial chaos based ensemble kalman filter with high accuracy. *Journal of computational physics*, 228(15) :5454–5469, 2009.

[28] J. L. Lumley. The structure of inhomogeneous turbulent flows. *Atmospheric Turbulence and Radio Wave Propagation*, 1967.

[29] M. J. Martin, M. Balmaseda, L. Bertino, P. Brasseur, G. Brassington, J. Cummings, Y. Fujii, D. Lea, J.-M. Lellouche, K. Mogensen, et al. Status and future of data assimilation in operational oceanography. *Journal of Operational Oceanography*, 8(sup1) :s28–s48, 2015.

[30] Y. M. Marzouk and H. N. Najm. Dimensionality reduction and polynomial chaos acceleration of bayesian inference in inverse problems. *Journal of Computational Physics*, 228(6) :1862–1902, 2009.

[31] Y. M. Marzouk, H. N. Najm, and L. A. Rahn. Stochastic spectral methods for efficient bayesian solution of inverse problems. *Journal of Computational Physics*, 224(2) :560–586, 2007.

[32] V. Mons, L. Margheri, J.-C. Chassaing, and P. Sagaut. Data assimilation-based reconstruction of urban pollutant release characteristics. *Journal of Wind Engineering and Industrial Aerodynamics*, 169 :232 – 250, 2017.

[33] R. Morrow, L.-L. Fu, F. Ardhuin, M. Benkiran, B. Chapron, E. Cosme, F. d'Ovidio, J. T. Farrar, S. T. Gille, G. Lapeyre, P.-Y. Le Traon, A. Pascual, A. Ponte, B. Qiu, N. Rascle, C. Ubelmann, J. Wang, and E. D. Zaron. Global observations of fine-scale ocean surface topography with the surface water and ocean topography (swot) mission. *Frontiers in Marine Science*, 6 :232, 2019.

[34] H. Morvan, D. Knight, N. Wright, X. Tang, and A. Crossley. The concept of roughness in fluvial hydraulics and its formulation in 1d, 2d and 3d numerical simulation models. *Journal of Hydraulic Research*, 46 :191–208, 03 2008.

[35] R.-S. Mouradi, Y. Audouin, C. Goeury, N. Claude, P. Tassi, and K. El Kadi Abderrezzak. Sensitivity analysis and uncertainty quantification in 2d morphodynamic models using a newly implemented api for telemac2d/sisyphe. *Proceedings of the XXIIIrd TELEMAC-MASCARET User Conference 2016, 11 to 13 October 2016, Paris, France*, pages 153–162, 2016.

[36] R.-S. Mouradi, O. Thual, C. Goeury, , P. Tassi, and F. Zaoui. Sensitivity of tidal modelling in coastal configurations : an uncertainty study based on field-measurement reduction. *Proceedings of the TELEMAC-MASCARET User Conference 2020*, 2020.

[37] R.-S. Mouradi, C. Goeury, O. Thual, F. Zaoui, and P. Tassi. Physically interpretable machine learning algorithm on multidimensional non-linear fields. *Journal of Computational Physics*, 428 :110074, 2021. ISSN 0021-9991. doi : https://doi.org/10.1016/j.jcp.2020.110074.

[38] M. Muller. *On the POD method : an abstract investigation with applications to reduced-order modeling and suboptimal control.* PhD thesis, 2008.

[39] NASA (National Aeronautics and Space Administration) and CNES (Centre National d'Etudes Spatiales) in partnership with CSA (Canadian Space Agency) and UKSA (UK Space Agency). Surface water and ocean topography. `https://swot.jpl.nasa.gov/home.htm`, 2021.

[40] I. Navon. Practical and theoretical aspects of adjoint parameter estimation and identifiability in meteorology and oceanography. *Dynamics of atmospheres and oceans*, 27(1-4) :55–79, 1998.

[41] I. M. Navon. Data assimilation for numerical weather prediction : a review. In *Data assimilation for atmospheric, oceanic and hydrologic applications*, pages 21–65. Springer, 2009.

[42] H. Park and W. Jung. The karhunen–loève galerkin method for the inverse natural convection problems. *International Journal of Heat and Mass Transfer*, 44(1) :155 – 167, 2001.

[43] C.-T. Pham and F. Lyard. Use of tidal harmonic constants databases to force open boundary conditions in telemac. In *Proceedings of the XIXth TELEMAC-MASCARET User Conference 2012, 18 to 19 October 2012, St Hugh's College, Oxford*, pages 165–172, 2012.

[44] S. Qian, X. Lv, Y. Cao, and F. Shao. Parameter estimation for a 2d tidal model with pod 4d var data assimilation. *Mathematical Problems in Engineering*, 2016, 2016.

[45] C. Robert, S. Durbiano, E. Blayo, J. Verron, J. Blum, and F.-X. Le Dimet. A reduced-order strategy for 4d-var data assimilation. *Journal of Marine Systems*, 57(1) :70 – 82, 2005.

[46] M. C. Rochoux, S. Ricci, D. Lucor, B. Cuenot, and A. Trouvé. Towards predictive data-driven simulations of wildfire spread–part i : Reduced-cost ensemble kalman filter based on a polynomial chaos surrogate model for parameter estimation. *Natural Hazards and Earth System Sciences*, 14(11) :2951–2973, 2014.

[47] D. Rolnick, P. L. Donti, L. H. Kaack, K. Kochanski, A. Lacoste, K. Sankaran, A. S. Ross, N. Milojevic-Dupont, N. Jaques, A. Waldman-Brown, et al. Tackling climate change with machine learning. *arXiv preprint arXiv :1906.05433*, 2019.

[48] T. Scott and D. Mason. Data assimilation for a coastal area morphodynamic model : Morecambe bay. *Coastal Engineering*, 54(2) :91 – 109, 2007.

[49] J. Shenefelt, R. Luck, R. Taylor, and J. Berry. Solution to inverse heat conduction problems employing singular value decomposition and model-reduction. *International Journal of Heat and Mass Transfer*, 45(1) :67 – 74, 2002.

[50] Shom 2015. MNT Bathymétrique de façade Atlantique (Projet Homonim). 2015. doi : http://dx.doi.org/10.17183/MNT_ATL100m_HOMONIM_WGS84.

[51] L. Sirovich. Turbulence and the Dynamics of Coherent Structures : I, II and III. *Quarterly Applied Mathematics*, 45 :561, 1987.

[52] P. Smith, G. Thornhill, S. Dance, A. Lawless, D. C. Mason, and N. K. Nichols. Data assimilation for state and parameter estimation : Application to morphodynamic modelling. *Quarterly Journal of the Royal Meteorological Society*, 139 :314–327, 01 2013.

[53] C. Soize. *Uncertainty quantification.* Springer, 2017.

[54] B. Sudret. Global sensitivity analysis using polynomial chaos expansions. *Reliability Engineering & System Safety*, 93(7) :964 – 979, 2008. ISSN 0951-8320.

[55] T. Taddei. A registration method for model order reduction : data compression and geometry reduction. *SIAM Journal on Scientific Computing*, 42(2) :A997–A1027, 2020.

[56] K. Taira, S. L. Brunton, S. T. M. Dawson, C. W. Rowley, T. Colonius, B. J. McKeon, O. T. Schmidt, S. Gordeyev, V. Theofilis, and L. S. Ukeiley. Modal analysis of fluid flows : An overview. *AIAA Journal*, 55 (12) :4013–4041, 2017.

[57] X. Tian, Z. Xie, and A. Dai. An ensemble-based explicit four-dimensional variational assimilation method. *Journal of Geophysical Research : Atmospheres*, 113(D21), 2008.

[58] X. Tian, Z. Xie, and Q. Sun. A pod-based ensemble four-dimensional variational assimilation method. *Tellus A : Dynamic Meteorology and Oceanography*, 63(4) :805–816, 2011.

[59] E. Torre, S. Marelli, P. Embrechts, and B. Sudret. Data-driven polynomial chaos expansion for machine learning regression. *Journal of Computational Physics*, 388 :601 – 623, 2019.

[60] P. T. M. Vermeulen and A. W. Heemink. Model-Reduced Variational Data Assimilation. *Monthly Weather Review*, 134(10) :2888–2899, 10 2006.

[61] X. Wan and G. Karniadakis. An adaptive multi-element generalized polynomial chaos method for stochastic differential equations. *Journal of Computational Physics*, 2006.

[62] D. Xiu and G. E. Karniadakis. The wiener–askey polynomial chaos for stochastic differential equations. *SIAM Journal on Scientific Computing*, 24(2) :619–644, 2002.

[63] D. Xiu and G. E. Karniadakis. Modeling uncertainty in flow simulations via generalized polynomial chaos. *Journal of Computational Physics*, 187(1) :137 – 167, 2003.

5.3 Attempt of calibration on different scenarios

As explained in Section 5.1, the 2010 field survey allowed extracting a POD basis to represent the tidal currents at intake's vicinity using few components, over a given tidal period. Two perspectives were highlighted: (i) a dependency structure can be constructed between calibrated parameters, for example using previously presented ensemble-POD-PCE-3DVAR, and the tidal POD expansion coefficients and (ii) hourly SHOM data can be used to provide priors about the tidal currents at intake's vicinity, if an appropriate data-based model is learned from the dependencies shown in Section 5.1. If such learning is successful, this would allow calibrating scenarios outside of the 2010 field campaign.

Consequently in the following, calibration on different scenarios is attempted using the learned POD-PCE metamodel with 90 % EVR, resulting from the contribution of Section 5.2. More precisely, the scenario used in Section 5.2 corresponds to the first tidal period of the two-months 2010 campaign, and an attempt to multi-scenario calibration with other tidal periods from the same survey is given below.

Successful attempts examples are shown in Figure 5.4, while unsuccessful examples are shown in Figure 5.5. In comparison to the tidal period studied in Section 3.2, it can be noticed that the successful attempts of Figure 5.4 correspond to tidal ranges of comparable magnitude. Conversely, failures of Figure 5.5 correspond to much higher tidal amplitudes.

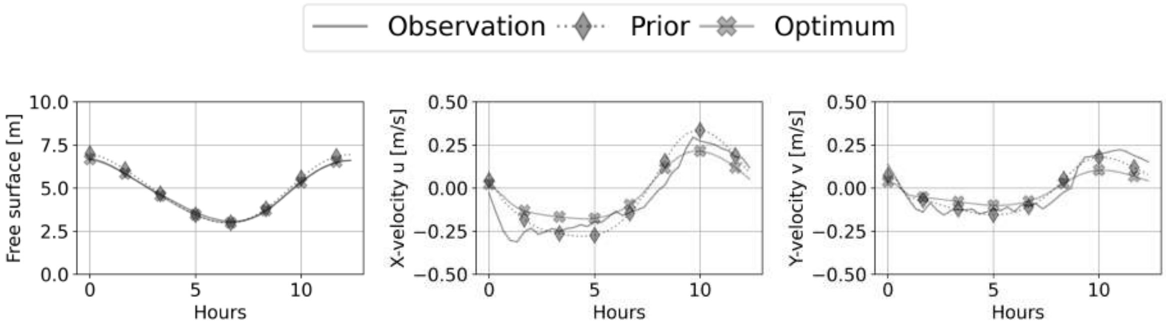

(a) Tidal period 26 - z_s (b) Tidal period 26 - u (c) Tidal period 26 - v

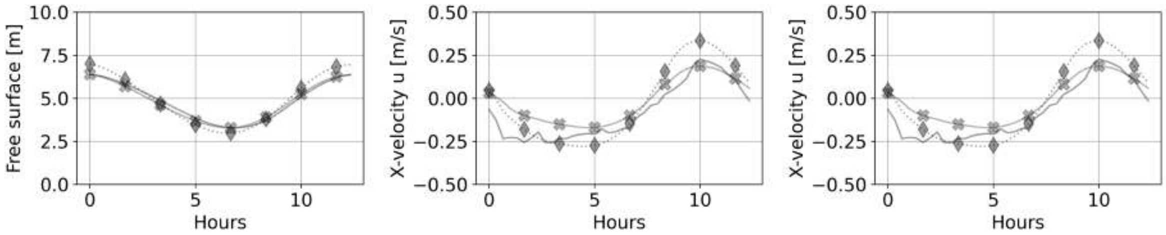

(d) Tidal period 27 - z_s (e) Tidal period 27 - u (f) Tidal period 27 - v

Figure 5.4 – Example of measurement reconstruction on a given tidal period for point 1 using 2 POD modes.

The CTL coefficient for calibration of free-surface BC, that impacts the tidal range in particular, was only varied in ranges that remain close to the reference observation ($CTL \in [0.8, 1.3]$). In the case of Figures 5.5, the POD-PCE metamodel is used to calibrate CTL outside its learned ranges. Although its impact on BC is linear (multiplicative coefficient), the propagation of the latter in the calculation domain is not. Hence, POD-PCE seems to fail at generalizing the effects outside of the learned parameters sub-space.

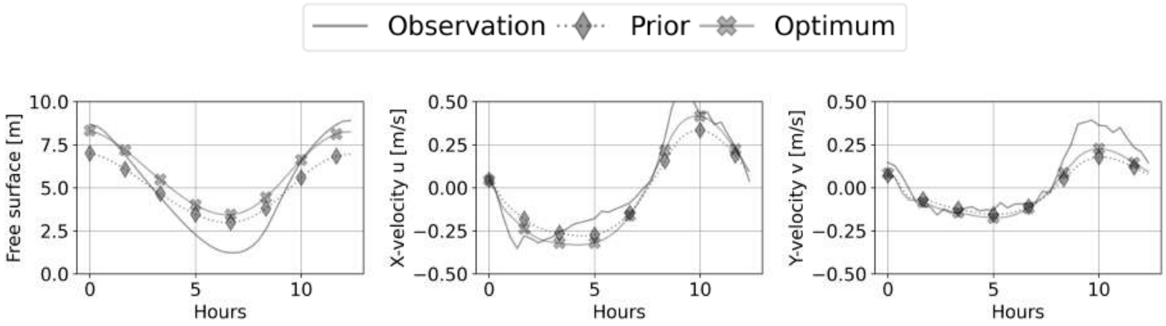

(a) Tidal period 4 - z_s (b) Tidal period 4 - u (c) Tidal period 4 - v

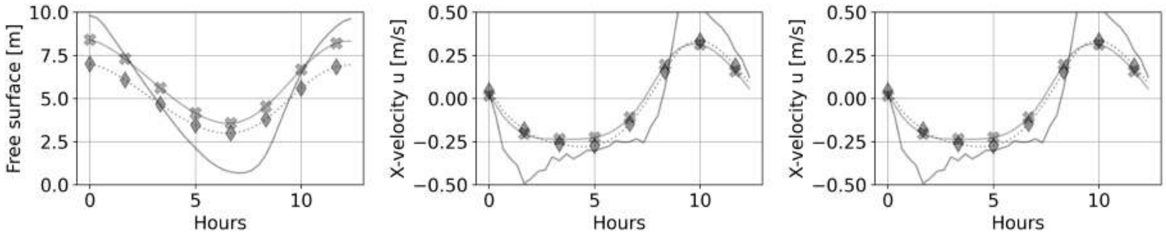

(d) Tidal period 22 - z_s (e) Tidal period 22 - u (f) Tidal period 22 - v

Figure 5.5 – Example of measurement reconstruction on a given tidal period for point 1 using 2 POD modes.

As a conclusion, the projected generalization of the meta-model to other scenarios is not successful in general. It indeed performs poorly in regions of the parameter space where the metamodel was not learned. This is particularly enhanced by the non-linearity of the used SWE, written in Equation 1.6. The same procedure should be attempted with larger variation ranges for the parameters, in order to conclude for the generalization of the POD-PCE metamodel over other scenarios, in order to calibrate other dates outside of the 2010 field campaign, which would be of industrial interest.

5.4 Summary

The POD-PCE methodology has shown to be promising for the acceleration of variational DA. In particular, adapted error covariance matrix calculation, resulting from the metamodelling, was proposed. This opens numerous perspectives for use on coupled hydro-morphodynamic simulations of the intake, in order to calibrate the model on measured bathymetry evolutions.

Before tackling such complex physical coupling, a morphodynamic UQ study should be undertaken, given the highly uncertain hydrodynamic conditions and sediment properties. In particular, POD components of velocity profiles at intake's entrance on the one hand, and POD components of bathymtery fields on the other hand, can be used as low dimensional Boundary Conditions (BC) and Initial Conditions (IC) variables respectively. This is the object of a last contribution in Chapter 6, with a preliminary sediment dynamics UQ.

Chapter 6

Sediment dynamics with uncertain parameters, boundaries and initial conditions

Dans ce chapitre, une étude préliminaire de Quantification d'Incertitude (UQ) appliquée au modèle numérique hydro-sédimentaire du chenal d'amenée est proposée. Dans cette étude, les composantes principales précédemment déduites par Décomposition Orthogonale en modes Propres (POD) appliquée aux mesures bathymétriques d'une part, et aux résultats de simulations hydrodynamiques d'autre part, sont utilisées. En particulier, ces composantes permettent d'investiguer, à coût de calcul réduit, l'incertitude liée aux Conditions Limites (BC) et Conditions Initiales (IC) du modèle hydro-sédimentaire. Ajouté à cela l'incertitude des paramètres liés aux lois de fermeture morphodynamique. Ceci permet de démontrer la faisabilité d'une étude UQ dans un cadre à haute-dimension, avec les outils proposés précédemment.

In this chapter, a preliminary Uncertainty Quantification (UQ) study applied to the hydro-sedimentary numerical model of the water intake is proposed. In this study, the principal components previously deduced by Proper Orthogonal Decomposition (POD) applied to bathymetry measurements on the one hand, and to hydrodynamic simulation results on the other hand, are used. These components allow to investigate, at reduced computational cost, the uncertainty related to Boundary Conditions (BC) and Initial Conditions (IC) of the hydro-sedimentary model. Added to this is the uncertainty of parameters related to closure morphodynamic relationships. This allows the demonstrate the feasibility of a UQ study in a high-dimensional context, with the previously proposed tools.

Contents

6.1 Objective

In the previous chapters, use of Dimensionality Reduction (DR) and spectral stochastic modelling by means of Proper Orthogonal Decomposition (POD) and Polynomial Chaos Expansion (PCE) respectively, allowed investigating the hydro-morphodynamics of the interest water intake. In particular (i) the spatial patterns of sedimentation were analyzed, and a purely data-based predictive tool was provided; (ii) Uncertainty Quantificiation (UQ) study of tidal hydrodynamic modelling in coastal configurations was undertaken, which allowed to deduce the resulting uncertainty of spatio-temporal velocity components at intake's entrance, in the form of POD patterns and (iii) in view of future calibration attempts, an acceleration technique for Data Assimilation (DA) was proposed.

Now, equipped with the previously proposed approaches and undertaken studies, i.e.:

- description of the dynamics in Chapter 1;
- theoretical framework for data-driven approaches in Chapter 2;
- data-based sediment dynamics investigations in Chapter 3;
- tidal hydrodynamics UQ study in Chapter 4;
- speed-up technique for physically-based data-driven DA in Chapter 5;

investigating the unanswered physical questions concerning the intake's sedimentation seems possible. More precisely, it is here of interest to clarify the phenomena that could not be interpreted with the data-based model. As a reminder, the following objectives that could not be resolved were previously evoked: (i) determining the predominant sediment transport processes (bed-load vs. suspension) can be of importance to design new measurement campaigns and (ii) understanding the dynamics at smaller scales, for example through a given storm event (hours) can be useful, as a complement to the data-based model, to propose a complete predictive tool.

The final objective would be to simulate all measured bathymetries using a calibrated hydro-morphodynamic model. For example, the proposed DA acceleration technique could be used for multi-scenario calibration, based on a Monte Carlo (MC) metamodel learning. Then, trustworthy physical interpretations about the unmeasured scales and phenomena would be provided.

The Monte Carlo (MC) hydro-morphodynamic scenarios of the intake can however respond to various forcings: bathymetry as Initial Conditions (IC), hydrodynamic BC, as well as uncertain modelling parameters (friction, grains diameter, etc.) and uncertain solid particles flux at intake's entrance. Given the spatio-temporal nature of hydrodynamic BC and bathymetry IC, this problem is high dimensional.

Fortunately, previously conducted investigations using POD could help providing low dimensional uncertain BC and IC respectively. Demonstrating the feasibility of such an approach for future investigations is the object of a last contribution described hereafter, where a hydro-morphodynamic UQ study is undertaken. It should be noted that this study is used as an algorithmic demonstration. Numerous hypothesis explained below are engaged, and the physical set-up and resulting interpretations could greatly be improved.

6.2 Uncertainty study

The objective of this Section is to apply a POD-based modelling approach of IC and BC related uncertainties, for the reduction of a high dimensional UQ problem. Modelling choices and resulting uncertainty sources are described in Subsection 6.2.1, and preliminary results of uncertainty propagation and sensitivity analysis are shown in Subsection 6.2.2.

6.2.1 Modelling choices and uncertainty sources quantification

The modelling of sediment transport in the interest intake is targeted. For this purpose, a coupled hydro-morphodynamic model is used. In particular, it is hypothesised that the waves influence only takes place outside in the coastal zone in front of the intake, and does not extend inside. Additionally, sediments are supposed to enter the intake as suspended load, due to the wave effect outside, said to be probably predominant in the previously presented literature (Section 1.1). For the presented investigations, simulations over a tidal period (approx. 12 h 25 mn) are launched using the meshed computational domain shown in Figure 6.1. Only the high depth zones, previously considered for measurement-based bathymetry predictions, is studied. The pumping BC of each cooling station is set to average operational flowrate. In principle, this value may be influenced by the sea level that varies, but is here considered constant as first approximation.

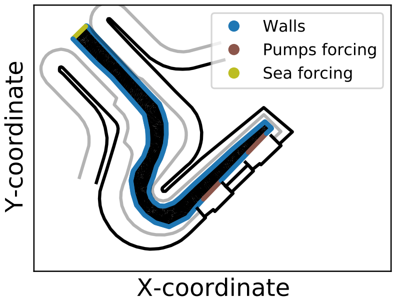

Figure 6.1 – Meshed computational domain for a preliminary UQ study of the intake's hydro-morphodynamics, with prescribed Boundary Conditions (BC).

The used hydro-morphodynamic model relies on the resolution of previously described Shallow Water Equations (SWE) 1.6, coupled to the conservation of sediment concentration in the form of the advection-diffusion Equation 1.25. The latter allows to compute the net sediment flux as $E - D \approx w_s \times (c_{eq} - c_{ref})$. As a reminder, c_{eq} is the equilibrium near bed concentration, here estimated using the empirical Zyserman-Fredsoe formula [278] given in Equation 1.28, parameterized with the median bed grain size d_{50} (see Chapter 1 for details). Reference concentration c_{ref} is estimated by integrating the Rouse profile written in Equation 1.27. Settling velocity is computed as in Equation 1.26, also estimated as a function of d_{50}. Lastly, as in the previous contribution, bed friction is here estimated using Strickler's model 1.9, with a defined friction coefficient K.

In the described model, several uncertainty sources can be highlighted. Firstly, parametric uncertainties mainly result from (i) the median grain size d_{50} and (ii) Strickler's friction coefficient K. Secondly, hydrodynamic sea BC illustrated in Figure 6.1 are also unknown, consisting in tidal elevation temporal variations and spatio-temporal distribution of the velocity components. Thirdly, the morphodynamic sea BC, consisting in entering suspended sediment concentration, is unknown. Lastly, morphodynamic IC, which is the initial bathymetry field, can also vary with the modelled scenario.

Parametric uncertainties

As in the previous contributions, Strickler's coefficient K is estimated from bed roughness height k_s intervals and consequently ranges in $[21.02, 90.66]$ $\text{m}^{1/3}\text{s}^{-1}$.

The variation interval of median grain size d_{50} can be deduced from measurements inside the intake and at its vicinity. In this investigation, data from figures 1.6 and 1.7 allowed to deduce the min-max interval as $[90, 300]$ μm.

As the only available information about K and d_{50} uncertainties are their variation supports, Uniform PDFs are used to represent their uncertainty (*Maximum Entropy Principle* [231]).

Hydrodynamic sea BC uncertainty

Hydrodynamic sea BC consist in tidal level elevations and velocity components. Firstly, temporal evolution of tidal levels can be emulated by a sinusoidal function, using a mean value and a tidal range. The latter are deduced from the hourly 2009-2018 data, obtained from the SHOM-REFMAR at the nearest harbor. Their PDFs are approximated by Gaussian Kernel Density Estimates (KDE) as in Figure 6.2. The distribution of mean sea levels is Gaussian, whereas sea level ranges PDF is bi-modal, ranging from neap to spring tides.

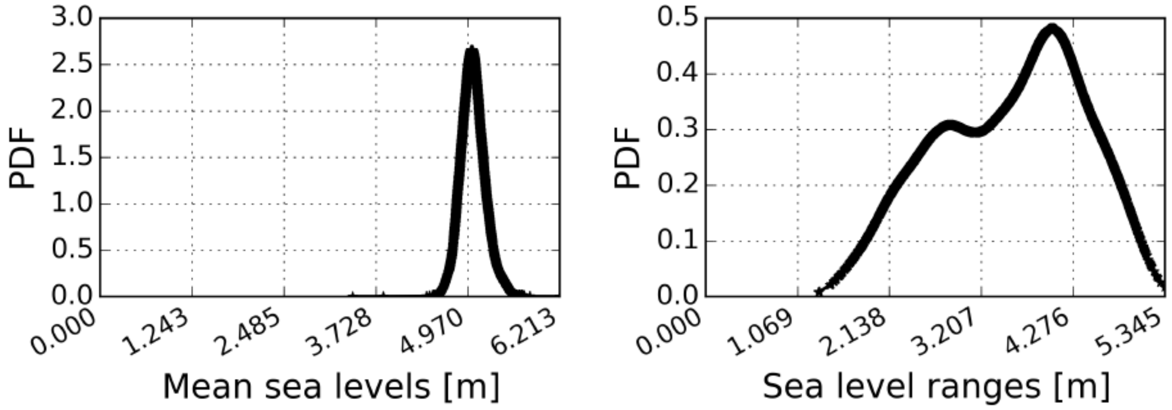

(a) Mean tidal levels

(b) Tidal ranges

Figure 6.2 – Tidal levels characteristics PDFs inferred by Kernel smoothing from the 2007-2018 data.

Secondly, spatio-temporal distributions of the velocity components at intake's entrance are deduced from the previously launched hydrodynamic MC simulations, with the large scale domain of size 8×16 km (offshore × longshore distances). Sea BC of the computational domain in Figure 6.1 corresponds to 19 boundary points. Each velocity component should then be set for the 19 coordinates, in the forms $\mathbf{u}(t) = [u(x_1, t), \ldots, u(x_{19}, t)]$ and $\mathbf{v}(t) = [v(x_1, t), \ldots, v(x_{19}, t)]$, where the time variable t is defined over the simulated tidal period (approx. 12 h 25 mn). Data with the large scale domain are recorded each 10 minutes which corresponds to 12×6+2 = 74 temporal coordinates, resulting in an observed vector of dimension $74 \times 19 = 1368$, in the form $\mathbf{u} = [\mathbf{u}(t_1), \ldots, \mathbf{u}(t_{74})]$. If all these spatio-temporal information at BC should be considered as uncertain inputs, this would result with a high dimensional UQ. However, as previously shown, vector $\mathbf{u}$ can be POD reduced, to deduce deterministic spatio-temporal patterns $\boldsymbol{\Phi}_j = [\Phi_j(x_1, t_1), \ldots, \Phi_j(x_{19}, t_{74})]$ that constitute a basis $\boldsymbol{\Phi} = [\boldsymbol{\Phi}_1, \ldots, \boldsymbol{\Phi}_d]$, with related singular value matrix $\boldsymbol{\Sigma}$ and stochastic coefficients $\mathbf{a} = [a_1, \ldots, a_d]$ that allow to approximate the original vector as $\mathbf{u} \approx \boldsymbol{\Phi}\boldsymbol{\Sigma}\mathbf{a}^T$. In the case of previously cited hydrodynamic simulations, selecting $d = 5$ POD patterns allowed reconstituting measured information for the POD-PCE based DA. Hence, the UQ problem is also reduced to five uncertain parameters.

A multivariate scatter plot of the first four reduced variables is represented in 6.5. These data are obtained from the results of previously launched MC simulations, taking into consideration the uncertainties of large scale domain BC and sea bed friction. Dependencies between the patterns can be observed (e.g. pattern 1 and 3). The PDFs of reduced BC velocity components are approximated by Gaussian KDE, and represented over the diagonal in Figure 6.5.

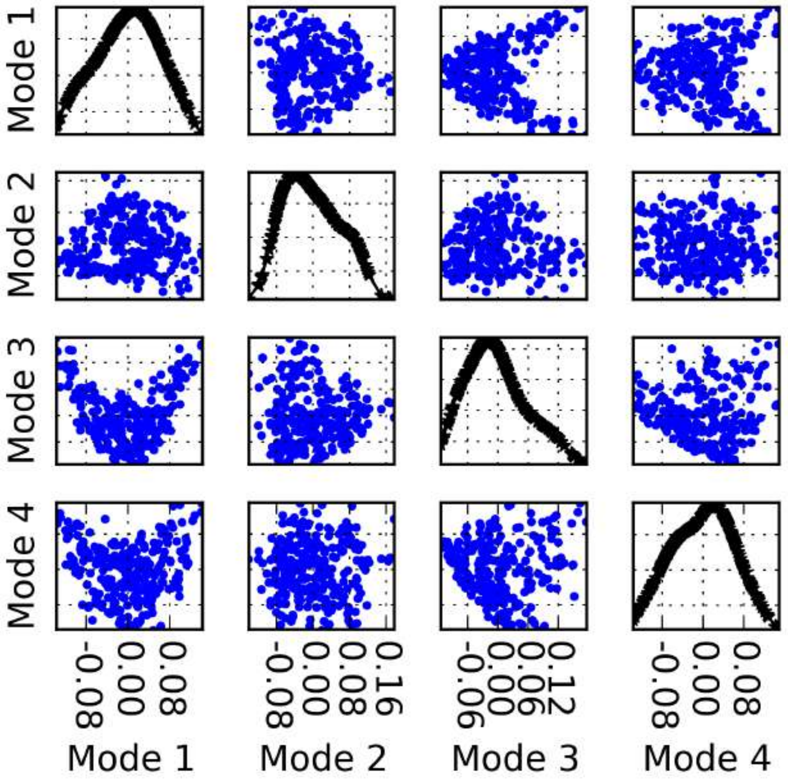

Figure 6.3 – POD expansion coefficients for the first four modes of velocity BC profile at intake's entrance.

As a first approximation, pattern dependencies are not modelled in this UQ study, and previously shown uncertainties of spatio-temporal patterns shapes, resulting from domain size and bed friction formula choice, are not considered.

Morphodynamic sea BC uncertainty

The amount of sediments that enter to the intake through sea BC should be determined, and an attempt for data-based estimation is here given.

Firstly, deposited sediment volume distribution is deduced from the 2007-2018 bathymetries. Each bathymetry is interpolated over the computational domain in Figure 6.1, and a total volume of sand above reference $z = -10$ m CM is calculated, by adding volumes estimated for each triangular element (each triangle results with straight prism volume, if average bottom elevation is considered). Then, deposited volumes are estimated by calculating differences over successive bathymetries. This results with a deposited volume distribution, approximated by Gaussian KDE as in Figure 6.4-a.

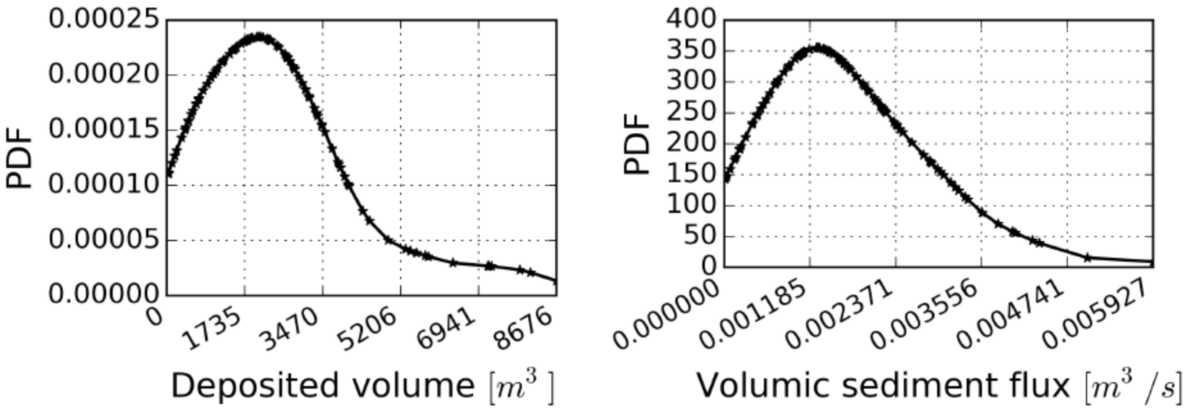

(a) Volume deposit

(b) Sediment flux

Figure 6.4 – Volume deposit and sediment flux PDFs inferred by Kernel smoothing from the 2007-2018 data.

Using the deposited volumes, the average entering sediment flux is deduced dividing the volumes by sedimentation durations, as represented in Figure 6.4-b, where the PDF is once again approximated using Gaussian KDE. Consequently, a sediment concentration in the water column can be imposed at each time of the simulation, dividing the sediment flux by the entering volumic water discharge.

There are underlying assumptions behind the use of an average discharge over the simulated time. Firstly, previously estimated solid flux from deposited volumes is a net flux (entering sediments to the intake, minus leaving). In order to consider it as prescribed BC, it should be supposed that sediments enter to the intake without the possibility of leaving. Secondly, variation of the sediment flux in time is not modelled when imposing an average over the whole simulation window. This is indeed a strong assumption, as previous investigations showed that the first two POD patterns of bathymetry, containing most of sediment volume information, directly depend on average wave height. This result could be extended, as first guess, to produce chronicles of the sediment flux that vary with the instantaneous wave heights. However, this idea is left for future investigations.

Lastly, the undertaken UQ study consisted in simulations over a tidal period, which did not allow observing sedimentation with the previously calculated fluxes (corresponding to 15 days sedimentations in average). Hence, in order to artificially accelerate the dynamics, deposited volumes are considered to be observed over a 3-hours duration, that could correspond to a storm event. This of course is a major assumption, that is not necessarily physical, with the only objective of demonstrating the feasibility of scenarios.

Morphodynamic IC uncertainty

Morphodynamic IC consists in the initial bathymetry of the intake. Measurements of the latter are generally mono-beam, corresponding to 39 profiles inside the intake, with 100 points per profile after interpolation (3900 points field). This bottom state may be uncertain, but considering all bathymetry points as such would result in a high dimensional UQ problem. As explained with BC, this issue can be overcome using POD. The 11 POD patterns, deduced from 2007-2018 measurements, helped establishing a data-based model, and can be good candidates to represent the whole field variability. Hence, the 11 POD patterns are here used as reduced bathymetry variables. The first four modes are represented in Figure 6.4, with Gaussian KDE to estimate the univariate densities. Once again, although dependencies can be noticed, these are not modelled in this preliminary UQ study.

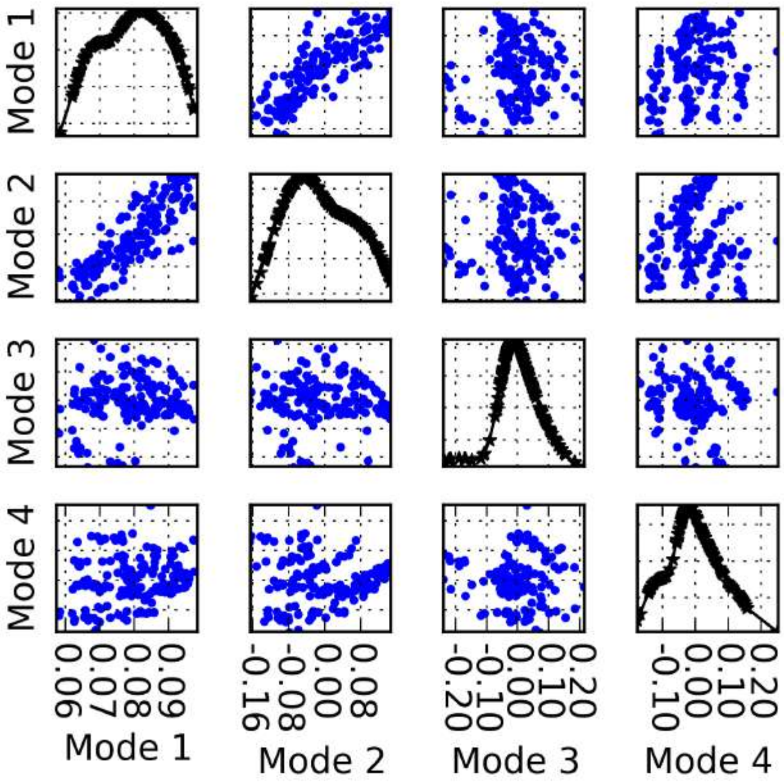

Figure 6.5 – POD expansion coefficients for the first four modes morphodynamic IC (bathymetry) in the intake.

6.2.2 Monte Carlo Results

Previously presented uncertain variations, and associated PDFs, are used to produce a random MC sample of size $n = 1000$. Each input configuration is then propagated through the studied model by running a direct simulation. A corresponding sample of output values is therefore obtained, which then allows to deduce statistics about the morphodynamics inside the intake.

Uncertainty propagation

Statistics of 5 hours bathymetry evolution (final minus initial bathymetry) are for example shown in Figure 6.6. It can be seen that the average dynamics, in Figure 6.6-c, happen in the previously identified zones using POD, i.e. in the middle of the first portion of the channel (upstream), on the right bank of the bend and on the left bank in front of the pumps. Standard deviation in Figure 6.6-d indicates maximal variances at the entrance of the intake, as well as downstream, in front of the pumps. Lastly, the minimum and maximum evolutions, shown in Figures 6.6-a and 6.6-b respectively, indicate that sedimentation can as well not happen at all depending on the configuration, or conversely impact all intake locations. However, it is maximal in the previously identified zones (entrance, right bank then left bank before and after then bend).

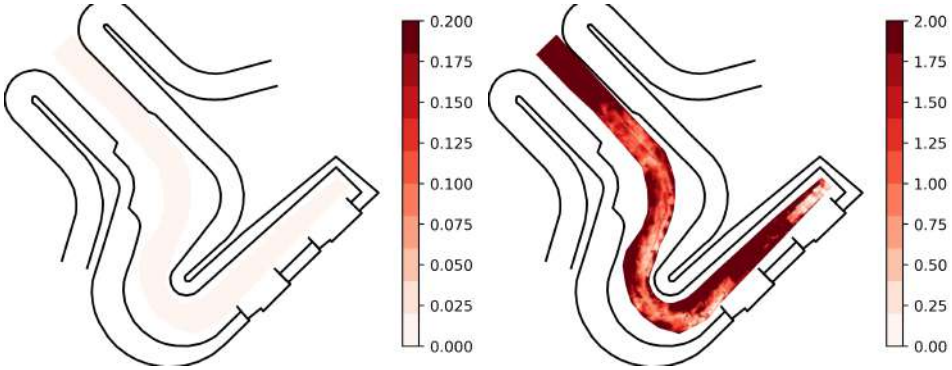

(a) Minimum (b) Maximum

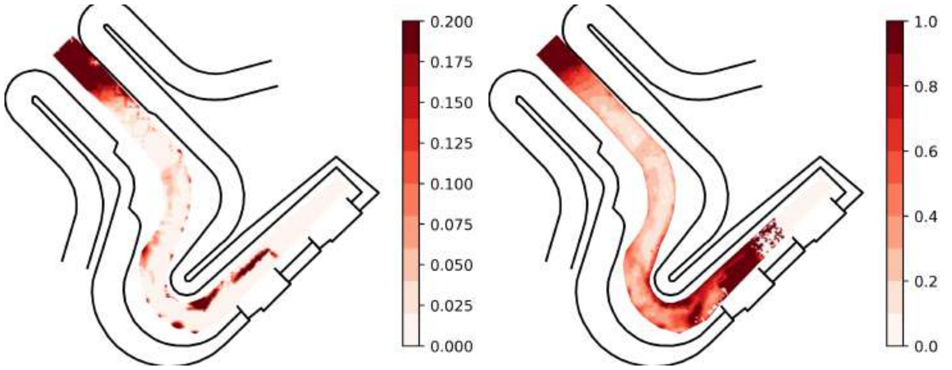

(c) Mean (d) Standard deviation

Figure 6.6 – Statistics of sedimentation in the intake obtained from preliminary UQ investigation. Quantities are expressed in meters.

Sensitivity analysis

In order to measure the impact of the uncertain variables on the simulated sedimentation, first and total Sobol' indices, defined in Equations 2.21 and 2.23 respectively, are computed on interest points of the computational domain, represented in Figure 6.7. Polynomial Chaos Expansion (PCE) of degree 3 is learned for each point independently, in order to estimate the sensitivity indices as in Equation 2.42. In the following, T_M, T_R and q_s denote the mean tidal level, the tidal range and sediment flux respectively, while $B1$ to $B5$ represent the 5 POD reduced variables of hydrodynamic BC, and $I1$ to $I11$ stand for the

POD modes of bathymetry used as IC.

Firstly, sensitivity indices at the entrance of the intake are shown in Figure 6.8.

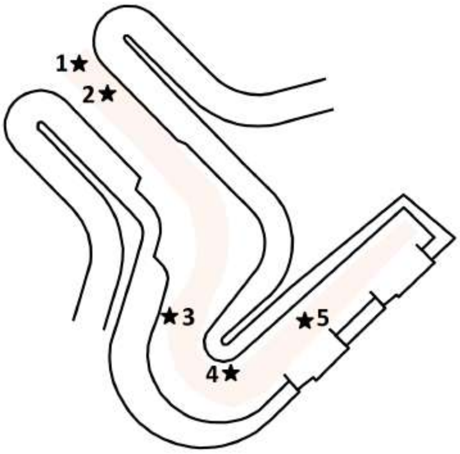

Figure 6.7 – Interest points inside the intake for UQ investigations.

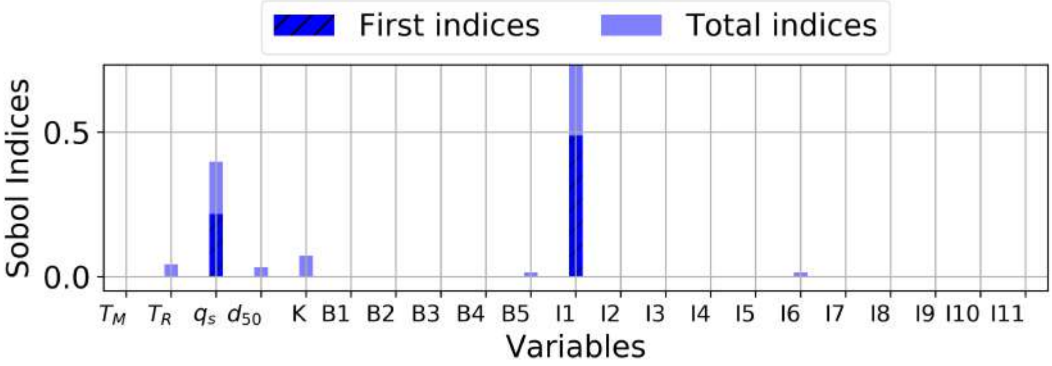

(a) Point 1

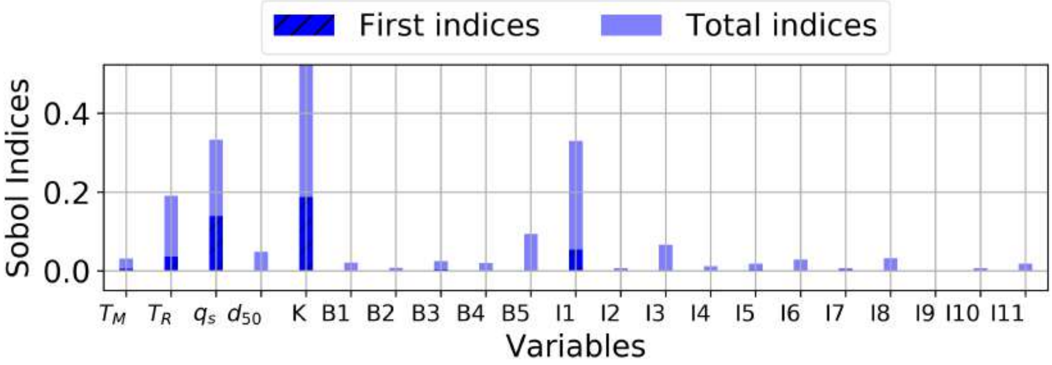

(b) Point 2

Figure 6.8 – First and total Sobol' indices of the studied uncertain parameters at the entrance of the intake.

It can be noticed that the first bathymetry pattern effect is dominant for Point 1 (Figure 6.8-a) while it decreases for Point 2 (Figure 6.8-b) in favor of Strickler coefficient K. Additionally, the entering sediment flux q_s comes in second position for both points, followed by the tidal range T_R for Point 2. This is coherent with conclusions from the data-based model, where the previous bathymetry field was the most important parameter, followed by the wave height that influences the entering sediment load. Interactions between the first bathymetry pattern $I1$ and other variables, namely q_s can be noticed in Figure 6.8 in the form of total sensitivity indices. Lastly, only slight influence of sediment grain size d_{50}, hydrodynamic BC, and high rank bathymetry patterns is noticed.

Secondly, sensitivity indices at the bending part of the intake are shown in Figure 6.8. Here, major changes consist in (i) increasing influence of velocity BC at Point 3 (Figure 6.9-a); (ii) considerable impact of the second bathymetry pattern $I2$ at Point 4 (Figure 6.9-b) and (iii) increase of influence for the remaining bathymetry patterns. In particular, influence of the second bathymetry pattern is coherent with conclusions from the data-based model, as $I2$ contribution was ranked at third position in terms of impact on the observed sedimentations.

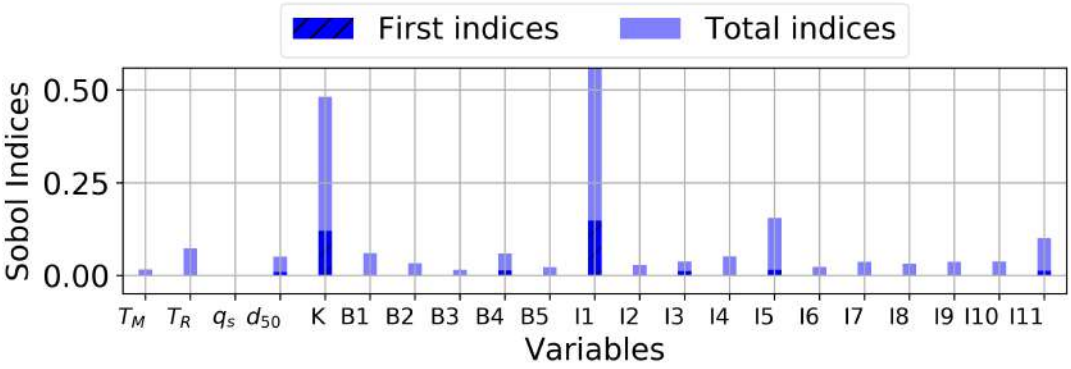

(a) Point 3

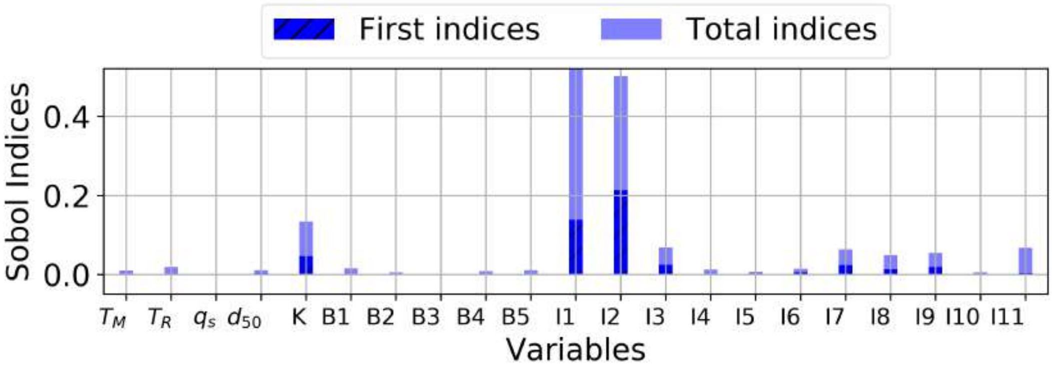

(b) Point 4

Figure 6.9 – First and total Sobol' indices of the studied uncertain parameters at the bending portion of the intake.

Lastly, sensitivity indices downstream the bend, at Point 5, are shown in Figure 6.10. Previous conclusions hold, with no supplementary elements of interpretation.

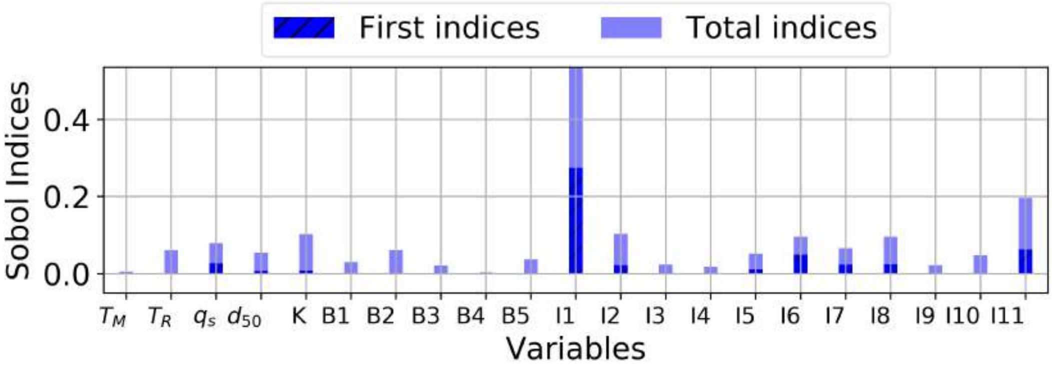

Figure 6.10 – First and total Sobol' indices of the studied uncertain parameters downstream of the intake at Point 5.

It should be noted that Generalized Sensitivity Indices [117], defined in Equation 2.71, can also be calculated to deduce the overall influence of the uncertain parameters on the simulated field. For this, POD patterns of simulated bathymetry evolutions need to be computed, and Sobol' indices of each mode should be estimated. This was not performed above and is left for future investigations.

6.3 Summary

This chapter focused on the reduction of a high-dimensional UQ study, using POD, for both Boundary Conditions (BC) and Initial Conditions (IC). The study concerned the sedimentation of the interest intake using coupled hydro-morphodynamic modelling, and the conclusions were coherent with previously established analysis using a purely measurement-based model.

As previously mentioned, the undertaken study was used as a feasibility demonstration for future investigations. Considerable assumptions detailed throughout the study, were employed. Additionally, no convergence of the statistical results was demonstrated and the PCE models used for the sensitivity indices were not optimized (e.g. degree choice). The deduced physical conclusions are therefore not definitive, but show the interest of POD based data analysis for UQ studies. Indeed, both field measurements and numerical studies outcomes helped setting up a complete UQ framework by means of Dimensionality Reduction (DR). This would allow, in the future, to perform deeper analysis of the intake sedimentation, if further modelling effort is engaged.

Chapter 7

Conclusions and outlook

Cette thèse propose des contributions dans le domaine général de la science des données, avec les outils théoriques présentés dans le Chapitre 2. Sont proposées d'une part une approche efficace pour le Machine Learning (ML) à base de données, et d'autre part une technique d'accélération pour l'Assimilation de Données (AD) basée sur la modélisation physique et guidée par les observations. Pour atteindre ce but, la Réduction de Dimension (DR), et la modélisation stochastique spectrale ont été utilisées, en particulier les méthodes bien connues de Décomposition en modes Propres Orthogonaux (POD) et d'Expansion par Polynômes du Chaos (PCE) ont été couplées pour proposer des solutions optimales. De plus, des études de Quantification des Incertitudes (UQ), basées sur les précédentes techniques, ont été menées.

Ces contributions sont proposées comme tentative de fournir des réponses à des questions physiques soulevées par une problématique industrielle: la sédimentation dans le chenal d'amenée d'une centrale électrique. Une analyse détaillée de la dynamique, et un outil prédictif qui peut être utilisé en conditions opérationnelles, ont été demandés par l'industriel opérant la centrale, afin d'optimiser le fonctionnement de celle-ci. Une revue de littérature de la physique impliquée, en particulier de la dynamique côtière, a été proposée en Chapitre 1, avec une description des données et du modèle à base physique disponibles. Il a été montré que les phénomènes physiques sous-jacents sont hautement complexes et non-linéaires. Ainsi, leur modélisation avec les outils disponibles est généralement coûteuse et incertaine. Ceci est cependant indésirable pour des conditions opérationnelles. La réduction de l'incertitude d'une part, et la diminution du temps de calcul d'autre part, ont donc été des points de départ pour toutes les contributions proposées. Ceci explique un tel intérêt pour la DR et l'apprentissage efficace.

D'abord, une méthode alternative de ML physiquement interprétable, par couplage POD-PCE, a été présentée en Chapitre 3. Cette démarche a permis de répondre à certaines limitations des Réseaux de Neurones classiques (convergence théorique, complexité), tout en se montrant robuste et rapide (quelques secondes) pour des problématiques non-linéaires, avec un cadre théorique probabiliste adapté pour mener des études de UQ.

Dans le Chapitre 4, une étude comparative entre mesures de courants de marée et modélisation à base d'équations physiques a été menée, en utilisant des échantillons de type Monte Carlo (MC) et la réduction POD pour la confrontation des modes. L'impact de l'incertitude liée à des choix communs de modélisation (taille de domaine, modèle de fermeture pour le frottement) sur l'incertitude des vitesses à l'entrée du chenal a été montré.

En Chapitre 5, une stratégie optimale d'AD par méta-modélisation a été introduite, utilisant deux méthodes: un couplage POD-PCE d'une part fournissant un modèle non-linéaire (POD-PCE-3DVAR), et une réduction jointe état-paramètres une utilisant la POD seule (PODEn3DVAR). Ces deux méta-modèles reposent sur la génération d'un ensemble pour leur apprentissage et ainsi, l'approche d'AD proposée est dite hybride ensembliste-variationnelle. La méthode POD-PCE-3DVAR s'est montrée plus rapidement convergente, et fournit une analyse comparable au 3DVAR classique pour un coût de calcul plus intéressant. De plus, une estimation adaptée de la matrice des covariances d'erreur associée au méta-modèle a été proposé et a permis de grandement améliorer l'analyse.

Enfin, dans le Chapitre 6, une étude UQ morphodynamique à haute dimension a été menée, en utilisant les modes POD bathymétriques et hydrodynamiques déduits des précédents travaux. En particulier, les incertitudes concernant à la fois des paramètres, les Conditions Initiales (CI) et Conditions Limites (CL) du modèle ont été étudiées à coût de calcul raisonnable. Les conclusions physiques tirées de cette étude se sont montrées cohérentes vis à vis des analyses établies à partir des données en Chapitre 3.

Plusieurs limitations ont cependant été soulignées dans les travaux résumés ci-dessus. Les perspectives de recherche qui en découlent concernent à la fois des aspects méthodologiques, mathématiques et physiques. Premièrement, la robustesse statistique du ML par POD-PCE pourrait être améliorée en prenant en compte les données récentes. Les incertitudes et biais liées aux dispositifs de mesure et à l'interpolation spatiale des données bathymétriques pourraient être propagées dans ce ML afin de quantifier la confiance en les prédictions. Une sélection plus robuste des paramètres de forçage pourrait être envisagée, notamment concernant la prise en compte d'informations sur des durées temporelles plus longues, ou encore une meilleure extraction des statistiques représentatives pour les chroniques temporelles. La prise en compte des dépendances entre les variables aléatoires dans le modèle PCE, ainsi que le traitement des discontinuités, sont également des perspectives prometteuses. Ces éléments pourraient également être envisagés pour l'amélioration de l'AD par POD-PCE-3DVAR. De plus, pour cette dernière, une génération adaptative de l'ensemble d'apprentissage pourrait être basée sur une exploration itérative des zones paramétriques d'intérêt par perturbation de l'analyse. Deuxièmement, concernant la modélisation hydrodynamique, des particularités dans les mesures, comme l'asymétrie temporelle des vitesses, n'ont pu être simulées. Ceci souligne la nécessité de prendre en compte d'autres phénomènes physiques, par exemple la turbulence, les vagues, les surcotes/décotes et les interactions non-linéaires entre ces éléments. Enfin, s'agissant de la modélisation morphodynamique, les investigations menées en Chapitre 6 constituent une étude exploratoire préliminaire. Plusieurs éléments restent à améliorer, comme la prise en compte de multiples classes de sédiments, ou encore des phénomènes physico-chimiques (e.g. effets cohésifs). De plus, les dépendances entre paramètres doivent être considérées, à la fois pour une analyse de sensibilité fiable, mais également dans la perspective d'un apprentissage efficace de méta-modèle POD-PCE basé sur les simulations, qui permettrait à terme une AD morphodynamique. Ainsi, comme dernière perspective, des scénarios de sédimentation réalistes pourraient être simulés, dans le but d'enrichir le modèle à base de données, et ainsi fournir un outil hybride, complet et rapide, pour une gestion optimale du chenal dans un cadre opérationnel.

This thesis proposes contributions in the general domain of data science, with the theoretical tools presented in Chapter 2. In particular, an efficient approach for data-based Machine Learning (ML) on the one hand, and an acceleration technique for data-driven physically-based Data Assimilation (DA) one the one hand, were developed. For this purpose, Dimensionality Reduction (DR) and stochastic spectral modelling were used, precisely the well-known Proper Orthogonal Decomposition (POD) and Polynomial Chaos Expansion (PCE) that were coupled to propose optimal solutions. Additionally, Uncertainty Quantificiation (UQ) studies, based on the previous techniques, were undertaken.

These contributions were proposed as an attempt to provide answers for physical questions raised by an industrial issue: sedimentation in a coastal power plant's water intake. Comprehensive analysis of the dynamics, and a predictive tool that could be run in operational conditions, were asked by stakeholders in order to optimize the plant's functioning. A literature review of the involved physics, in particular nearshore dynamics in the interest area, was proposed in Chapter 1, with a description of available data and physics-based models. It was shown that the involved physical phenomena are highly complex and non-linear, and that their modelling with the available tools is generally costly and uncertain. This however is not desired in operational conditions. Reduction of the uncertainty on the one hand, and of the computational time on the other hand, were therefore starting points for all proposed contributions, which explains such interest in DR and efficient learning. The following sections therefore present the main achievements and prospects, respectively drawn from previous considerations.

7.1 Main achievements

In this thesis, robust and practical answers for the industrial application were proposed. Resulting approaches can be generalized to other physical frameworks. The main findings of this work, and their impact for the interest industrial application, are summarized below.

Alternative Machine Learning algorithm for non-linear multidimensional fields

In the first contribution of Chapter 3, a physically interpretable ML algorithm, based on POD-PCE coupling, was presented. This approach allowed to overcome the limitations of classical Neural Networks (NN). It has shown to be an accurate and fast non-linear predictive tool, for multidimensional physical fields. Physical interpretation was assured using adequate ranking measures, valid at both POD patterns scale and global output scale. Robustness to noise and training-set variations was demonstrated, and the performance was successfully compared to classical NN. The proposed methodology is adapted for industrial contexts with strong time constraints and physical interpretation needs. Additionally, it gives the possibility of straightforward Uncertainty Quantificiation (UQ) from the probabilistic framework of PCE.

The POD-PCE data-based ML accurately predicts sedimentation in the intake, at low computational cost (seconds). Additionally, given the continuous monitoring of the intake, the training-set size can be continuously increased, and the training members and data can be improved from statistical learning feedback.

Additionally, use of POD allowed quantitative analysis and interpretation of the intake dynamics. Spatio-temporal bathymetry data could be easily filtered (detection of noisy measurements) using the POD patterns and expansion coefficients. Locations for optimal measurements in the intake were identified, for future field surveys.

Dimensionality Reduction for data-based Uncertainty Quantification

In Chapter 4, a comparative study between measurements and physics-based models, concerning numerical scenarios of tidal currents in coastal configurations, was undertaken. Monte Carlo (MC) samples of uncertain numerical scenarios, under different modelling choices (domain size, friction formula choice), were used for POD-based deduction of spatio-temporal patterns. The latter were then compared to patterns independently deduced from field data.

Firstly, in the application context, similarities between observations and simulations POD patterns were identified. However, some particularities present in the measurements, such as tidal velocity asymmetry, could not be modelled with the chosen configurations. Noticing the lack of accord between the numerical and measurement-based patterns might help saving HPC resources: it is vain to try calibrating these configurations to capture particularities of the measurements when their modes behave differently, i.e. when the corresponding physical process is missing in the model.

Secondly, the uncertainty related to common modelling choices impacted the velocities at intake's entrance. Sensitivity of the latter to uncertain parameters changed with the modelling set-ups. As a consequence, optimal measurement-based parametric calibration of the model has shown to be uncertain as well.

A metamodel and associated error calculation for hybrid ensemble-variational Data Assimilation

Optimal strategies for Data Assimilation (DA) based on DR, were studied in Chapter 5. POD-PCE based learning on the one hand, and joint state-parameters POD reduction on the other hand, were proposed as metamodels to accelerate the minimization of a 3DVAR cost function for parametric calibration. This resulted with two approaches for hybrid ensemble-variational DA, called ensemble-POD-PCE-3DVAR and PODEn3DVAR respectively. Additionally, calculation of a new error covariance matrix, that accounts for errors resulting from metamodelling, was proposed for the ensemble-POD-PCE-3DVAR approach.

Robustness of both methodologies to noise was demonstrated. The analysis provided by ensemble-POD-PCE-3DVAR seems to be more efficient than PODEn3DVAR, with faster convergence. This can be explained by PCE ability to efficiently capture non-linear relationships. It provides an analysis that is comparable to classical iterative 3DVAR results, at reduced computational cost. Additionally, proposed metamodel error covariance calculation significantly increases the accuracy, when added to an appropriately defined observation error.

The proposed strategy for DA acceleration provides an adapted approach for costly numerical models calibration under operational conditions. This may help in further physical analysis and generation of realistic synthetic data.

Reduction of High-dimensional Uncertainty Quantification problem

As a last contribution in Chapter 6, previously deduced POD patterns of bathymetry and hydrodynamic conditions at intake's entrance, allowed performing a high-dimensional UQ study at reduced cost. In particular, both IC, BC and parameters, could be considered uncertain.

The physical conclusions drawn from this UQ study were coherent with previously established analysis using a purely measurement-based model. However, this study was based on strong hypothesis, and simply allowed demonstrating the feasibility of setting up such high-dimensional UQ framework for future investigations.

7.2 Perspectives and open questions

In all previously summarized contributions, limitations were highlighted, and resulting perspectives and open questions were identified. These are summarized below.

Improvement of the POD-PCE data-based model

For the proposed POD-PCE ML approach, only 2007-2018 data were used. Since its establishment, two years of bi-monthly bathymetry measurements were recorded. As a first perspective, these data could be used to increase the statistical robustness of the proposed POD-PCE model. The small data-set was indeed a clear handicap for the learning, and due to the lack of such data, input distributions were certainly not well approximated. Consequently, rare events, such as sedimentiation downstream the intake were poorly represented. It would be interesting to test the methodology on an enriched data set in order to assess the real potential of POD-PCE ML.

Additionally, linear interpolation of the bathymetry was used to project all the measurements into the same grid for POD application. Uncertainty related to this interpolation was not treated. For example, comparison of mono-beam cross-sections with multi-beam measurements and uncertainty propagation of bathymetry errors through the learned POD-PCE model can be attempted.

Measurement errors impact on the learning was not specifically studied here. However, a toy problem allowed investigating the impact of noise on the proposed models. For example, by adding random perturbations to the data, it was shown that noise may contaminate the POD patterns (temporal and/or spatial). If noise is significant enough, it may be given more importance in the decomposition than physical patterns of smaller statistical occurrence. Hence, for optimal learning of the dynamics, it can then be interesting to proceed to patterns selection, not necessarily in the eigenvalues order. Mode of high EVR can for example be eliminated, if showing completely stochastic behavior, in favor of explainable modes of lower variances.

The choice of learning input configurations for PCE was arbitrary. Information from previous times could be important, but were not incorporated, as this may raise other technical questions (time lag estimation [58]). A more objective variable selection technique should therefore be attempted [182]. Besides, data used as inputs (time series of wave heights, tidal levels, etc.), were not fully exploited. Indeed, simple statistical indicators (means, percentiles, etc.) were used for PCE learning instead of complete time series, in order to avoid ultrahigh-dimensional learning. This however wastes the richness of available data. A more accurate statistical reduction could be attempted, as PCA or KPCA used in Lataniotis et al. [121]. Dependencies were not modelled either, and could be taken into consideration for optimal construction of the PCE basis Soize and Ghanem [232] .

As for the proposed algorithm, the choice of POD as decomposition was mainly motivated by its linearity, and interpretation possibilities when coupled to PCE. KPCA was also tested in an attempt to reduce the problem's dimensionality, but was not promising enough. Other classes of decomposition [215] should however be attempted. Limitations to PCE can also be noted. For example, PCE worked better for modes associated with high than low variances. Improving the learning of high-rank modes should therefore be investigated. For example, adapted treatment of discontinuity [264] and high non-linearity Birolleau et al. [25], and construction of probabilistic models instead of causal models, can be attempted.

Lastly, data filtering, and optimal measurement locations detection using POD, only consisted in simple approaches (deleting poor-quality measurements, using linear correlation indicators). More robust statistical tools could be used to extend the analysis, for example, reconstructing missing data, by inverse projection on POD basis elements deduced from qualitative data, instead of deleting incomplete measurements [210]. This could help optimizing the learning set size.

Numerical modelling of tidal hydrodynamics

While similarities between observations and simulations are identified, some particularities present in the measurements, such as tidal velocity asymmetry, could not be modelled with the chosen configurations. This emphasizes the need of additional physics to be incorporated into the model, for example turbulence, waves, storm and atmospheric surges, non-linear interactions of tides with surge, or more precise bathymetric information.

For example, as introduced in Chapter 1, waves can be capital for coastal configurations. They imply a change in the flow currents, due to the orbital motion of water particles [248]. This means that velocity values are impacted. Consequently, their impact on sediment transport is also significant. For realistic simulations, they should be taken into consideration. However, computational time was a clear limitation in the operational context. This limitation could be overcome, for example using data bases as ANEMOC or CANDHIS.

Perspectives for the POD-PCE based ensemble-variational DA

Direct improvements of the ensemble-POD-PCE-3DVAR were previously mentioned. Firstly, adaptive algorithm, consisting in POD-PCE learning update using an outer loop, by iterative perturbation of the sample around the analysis, can be attempted as in [37, 165] with PODEn4DVAR. This would allow to decrease the needed ensemble size for accurate estimations. The adaptive PODEn4DVAR is indeed said to be more stable to the ensemble size than other ensemble DA methods [165], and a limited sample of size $n = 20$ is said sufficient up to 10^5 control variables [165].

Secondly, as suggested in [6], the cost function can be estimated using the original model, while still estimating descent directions using the metamodel. This was indeed attempted in [6] with PODEn4DVAR, providing better analysis.

Lastly, previously proposed improvements of POD-PCE ML also hold for the learning of numerical model outcome.

Numerical investigations of the intake sedimentation

As a first step towards realistic morphodynamic scenarios, UQ hydro-sedimentary studies were launched. However, several assumptions were considered and could be overcome.

An obvious model improvement would consist in considering BC and IC patterns dependencies in the launched MC simulations. This also holds for the dependencies between all uncertain inputs, which would allow producing more physically realistic scenarios. For the same reasons, additional physics could be incorporated into the sediment transport. For example, only one class of sediment grain size was considered. It is then possible to extend investigations to two classes. For example, simultaneous presence of sand and silt was observed downstream of the intake (Figure 1.8), giving multi-modal grain size distributions. Based on this observation, physico-chemical cohesive effects, which were not modelled, can also play an important role in the intake's sedimentation.

A constant solid discharge was considered at the entrance as BC. Its temporal variation can be modelled for future investigations, relying on the conclusions deduced from the data-based models. Indeed, the latter showed that the first two POD patterns of bathymetry, containing most of sediment volume information, directly depend on average wave height. Time series of the sediment flux can then be generated in the same shape of wave height time series, for example as a prior to a DA experiment, and corrected in order to obtain realistic bathymetry evolution.

The influence of waves was not considered inside the intake. However, in situ, when participating to the 2018 campaign, their presence upstream was clearly noticed. If spectral modelling of the waves is not possible due to computational time constraints, then a single wave height with a defined spatial distance of action upstream could be imposed as starting point for deeper investigations.

The 2018 campaign results could not be used in this thesis due to lack of time. These are valuable information that could help calibrating the hydrodynamics of the intake. The proposed ensemble-POD-PCE-3DVAR could for example be tested on this configurations. Particularly, the uncertainty of the velocity POD patterns at the entrance of the intake, resulting from modelling choices (domain size, friction formula), could then be considered for optimal calibration.

It should be noted that parallel investigations from stakeholder's research engineers, particularly concerning the calibration of the model on 2018 data, resulted with interesting conclusions. In particular, with calibration effort, SWE were satisfactory, and allowed reproducing the observed flow with Strickler friction law, as long as more sophisticated turbulence closures are used (here, the $k - \epsilon$ model). This insists on the importance of turbulence modelling for realistic flows in the studied configuration. Especially, it was previously highlighted that bad considerations of spatio-temporal turbulence (and waves, 3D flow structures) are often pointed out as a limitation to morphodynamic models, since small eddies, orbital water particle motion, and flow structure may control near-bed mass exchange [9, 187].

For the undertaken investigations, simulations over a tidal period (approx. 12 hours) were launched. To observe numerically emulated sedimentations, the latter were artificially accelerated by exaggerating the sediment flux values. This of course was a major assumption with the only objective of demonstrating the feasibility of scenarios. Scenarios over real sedimentation durations should be launched instead. The final objective would be to simulate all measured bathymetries using a calibrated hydro-morphodynamic model. For example, the proposed DA acceleration technique could be used for multi-scenario calibration, based on hydro-morphodynamic POD-PCE metamodel learning. Then, trustworthy physical interpretations about the unmeasured scales and phenomena would be provided.

As a last perspective, the hydro-morphodynamic POD-PCE metamodel could be used to emulate realistic sedimentation scenarios, in order to enrich the measured that set. This would be a way to improve the data-based POD-PCE model, with a development of hybrid measurement-based/process-based data learning [168, 221]. Additionally, scenarios on smaller temporal and spatial scales (e.g. storm event), could be incorporated. A complete predictive tool would then be provided to the intake stakeholder's for optimal monitoring of the intake.

Appendix A

List of Acronyms

1D one-Dimensional. 88

2D two-Dimensional. 28, 30, 33, 40, 44, 89, 95

2DH 2D-Horizontal. 28

3D three-Dimensional. 25, 26, 29, 33, 40, 44, 45, 224

3D-FS-NS three-Dimensional Free-Surface Navier-Stokes. 28, 30

3DVAR three-Dimensional VARiational. 6, 84, 85, 97, 203, 220, 222, 223

4DVAR four-Dimensional VARiational. 85, 87, 95–97

ADCP Acoustic Doppler Current Profiler. iii, 25–27

AF Activation Function. 75–77

AI Artifical Intelligence. 72, 73

ANCOVA ANalysis of COVAriance. 61, 69

ANEMOC Numerical Atlas for Oceanic and Coastal Sea States. iii, 12–14, 21, 47, 222

ANN Artificial Neural Networks. 74

ANOVA ANalysis Of VAriance. 53, 61, 69

API Application Program Interfaces. 44

AWAC Acoustic Wave And Current. 25

BC Boundary Conditions. iv, vi, 5, 6, 28, 29, 31, 33, 34, 42, 45, 48, 55, 56, 152, 153, 155, 157, 167, 169, 203, 204, 206–212, 214, 215, 221, 223

BLUE Best Linear Unbiased Estimator. 80–82, 84, 85

BN Bayesian Networks. 73

BP Backward Propagation. 76, 77

CANDHIS National In Situ Swell Records Center. 21, 222

c-BFGS-QN constrained Broyden-Fletcher-Goldfarb-Shanno Quasi-Newton. 71

CCA Canonical Correlation Analysis. 89

CFL Courant–Friedrichs–Lewy. 153

DA Data Assimilation. 2, 5, 6, 21, 44, 49, 56, 58, 60, 78–80, 83, 86–88, 95, 96, 98, 149, 171, 174, 175, 204, 206, 209, 219, 220, 223, 224

DNS Direct Numerical Simulations. 34

DR Dimensionality Reduction. 2, 5, 6, 49, 60, 62, 67, 70, 87–90, 95, 98, 142, 147, 171, 206, 215, 219, 220

EKF Extended Kalman Filter. 82

EnKF Ensemble Kalman Filter. 83, 87, 88, 97

EnKS Ensemble Kalman Smoother. 83

EOF Empirical Orthogonal Functions. 91, 96

ES European Shelf. 34

EVR Explained Variance Rate. iv, 92, 94, 146, 147, 150, 167, 174, 203, 221

FCC Fully Connected Cascade. 76

FE Finite Elements. 44

FFNN Feed Forward Neural Networks. 75–77

GA Genetic Algorithms. 73

gPC generalized Polynomial Chaos. 63

GSA Global Sensitivity Analysis. 60, 88, 94

HFT Half Falling Tide. 26

HPC High Performance Computing. 44, 220

HRT Half Rising Tide. 26

HT High Tide. 26

IC Initial Conditions. vi, 5, 6, 45, 56, 152, 204, 206–208, 211, 213, 215, 221, 223

JCP Journal of Computational Physics. 100

KDE Kernel Density Estimates. 53, 57–59, 208–211

KF Kalman Filter. 80–83

KLT Karhunen-Loève Transfrom. 59, 60, 87, 89–91, 95

KPCA Kernel PCA. iv, 67, 142, 147, 148, 222

KS Kalman Smoother. 81–83

LAR Least Angle Regression. 72

LARS Least Angle Regression Stagewise. 67, 72

LASSO Least Absolute Shrinkage and Selection Operator. 72

LHS Latin Hypercube Sampling. 60, 65

LM Lagrandian Multiplier. 85

LOO Leave One Out. 67, 68

LSA Local Sensitivity Analysis. 60

LT Low Tide. 26

MAP Maximum A Posteriori. 80, 81, 83, 84

MC Monte Carlo. 59, 62, 65, 69, 83, 87, 206, 208, 209, 211, 220, 223

MCMC Markov Chain Monte Carlo. 58, 87

MD Modal Decomposition. iv, 88–90

MEP Maximum Entropy Principle. 53, 56, 57, 69

ML Machine Learning. 2, 4–6, 21, 49, 69, 70, 72–74, 77, 78, 88–90, 94, 98, 100, 148, 150, 219, 221, 223

MLE Maximum Likelihood Estimation. 57, 58, 69, 80

MVE Minimum Variance Estimation. 80, 81

NCEP National Centers for Environmental Prediction. iii, 11, 13

NN Neural Networks. iv, 5, 70, 72–78, 98, 100, 219

NS Navier Stokes. 28–31

OLS Ordinary Least Squares. 71, 72

PCA Principal Component Analysis. iv, 60, 67, 70, 89–91, 142, 147, 148, 222

PCE Polynomial Chaos Expansion. 2, 5, 6, 59, 60, 62–69, 87, 88, 92, 98, 100, 148–150, 171, 175, 203, 204, 206, 209, 212, 215, 219–224

PDE Partial Differential Equations. 65, 85, 86, 92, 95

PDF Probability Density Function. 54, 56–59, 63, 69, 80–82, 84, 88, 208, 210

PDFs Probability Density Functions. vi, vii, 53, 54, 56–59, 62–65, 80, 81, 83, 84, 208–211

POD Proper Orthogonal Decomposition. iv–vi, 2, 5, 6, 60, 74, 89–98, 100, 142–150, 167–171, 174, 175, 203, 204, 206, 207, 209–213, 215, 219–224

PODEn4DVAR POD-Ensemble-based 4DVAR. 96, 97

PRCC Partial Rank Correlation Coefficients. 61

QoI Quantities of Interest. 59

RANS Reynolds Averaged NS. 30

REFMAR REFerence network for Tidal observations. 22, 23, 208

ROM Reduced Order Models. 89, 90, 95

RvNN Recursive Neural Networks. 76

SHOM Hydrographic and Oceanographic Marine Service. v, 13, 22, 175, 203, 208

SPCA Sparse PCA. iv, 142, 147, 148

SRC Standard Regression Coefficient. 60

SVD Singular Value Decomposition. iv, 93, 94

SWE Shallow Water Equations. 5, 28, 30–35, 37, 44, 88, 96, 153, 204, 207, 224

TLM Tangent Linear Model. 82, 85, 87, 96, 97

TMS TELEMAC-MASCARET System. iii, 44, 45

TUC Telemac User Conference. 152

UQ Uncertainty Quantificiation. v, vi, 2, 5, 6, 34, 44, 49, 53, 55, 56, 60, 78, 87, 88, 94, 150, 152, 157, 167, 171, 174, 204, 206, 207, 209–213, 215, 219, 221, 223

Bibliography

[1] C. Abernot-Le-Gac, P. Clabaut, L. Drévès, and J. D. Gaffet. Bencaux - may 2008: Bio-morpho-sedimentary study of the marine coastal domain from dieppe to criel-sur-mer (seine-maritime, france). technical report. Technical report, Ifremer, 2011. 9

[2] O. I. Abiodun, A. Jantan, A. E. Omolara, K. V. Dada, N. A. Mohamed, and H. Arshad. State-of-the-art in artificial neural network applications: A survey. *Heliyon*, 4(11), 2018. ISSN 2405-8440. 76

[3] R. J. Abrahart and M. See. Neural network modelling of non-linear hydrological relationships. *Hydrology and Earth System Sciences*, 2007. 70

[4] C. Adam-Bourdarios, G. Cowan, C. Germain, I. Guyon, B. Kégl, and D. Rousseau. The higgs boson machine learning challenge. In *Proceedings of the 2014 International Conference on High-Energy Physics and Machine Learning - Volume 42*, HEPML'14, page 19–55. JMLR.org, 2014. 2

[5] N. Akkari. *Mathematical study of the sensitivity of the POD method (Proper orthogonal decomposition)*. Ph.d. thesis, Dec. 2012. 90

[6] M. Altaf, M. E. Gharamti, A. Heemink, and I. Hoteit. A reduced adjoint approach to variational data assimilation. *Computer Methods in Applied Mechanics and Engineering*, 254:1 – 13, 2013. 96, 223

[7] M. U. Altaf, A. W. Heemink, and M. Verlaan. Inverse shallow-water flow modeling using model reduction. *International journal for multiscale computational engineering*, 7(6), 2009. 78, 96

[8] L. Altarejos García, M. L. Martínez Chenoll, I. Escuder Bueno, and A. J. Serrano Lombillo. Assessing the impact of uncertainty on flood risk estimates with reliability analysis using 1-d and 2-d hydraulic models. *Hydrology and Earth System Sciences and Discussions*, 16(7):1985–1994, 2012. 53

[9] L. O. Amoudry and A. J. Souza. Deterministic coastal morphological and sediment transport modeling: a review and discussion. *Reviews of Geophysics*, 49(2), 2011. doi: 10.1029/2010RG000341. URL `https://agupubs.onlinelibrary.wiley.com/doi/abs/10.1029/2010RG000341`. 4, 28, 39, 40, 41, 42, 43, 44, 45, 70, 224

[10] R. Aris. *Vectors, TTensor and the Basic Equations of Fluid Mechanics*. Prentice Hall, Englewood Cliffs, NJ, 1962. 28, 29

[11] M. Asch, M. Bocquet, and M. Nodet. *Data assimilation: methods, algorithms, and applications*. SIAM, 2016. 79, 80, 83, 85, 86

[12] Y. Audouin, T. Benson, M. Delinares, J. Fontaine, B. Glander, N. Huybrechts, R. Kopmann, A. Leroy, S. Pavan, C.-T. Pham, et al. Introducing gaia, the brand new sediment transport module of the telemac-mascaret system. In *XXVIth TELEMAC-MASCARET User Conference, 15th to 17th October 2019, Toulouse*, 2019. 44

[13] C. Augris, P. Clabaut, and J.-F. Bourillet. Morpho-sedimentary map of the marine coastal domain from dieppe to le tréport (seine-maritime). 1993. 9

[14] C. Augris, P. Clabaut, S. Costa, F. Gourmelon, and B. Latteux. Morpho-sedimentary evolution of the coastal and marine domain of seine-maritime. 2004. 9

[15] F. Ballio, D. Pokrajac, A. Radice, and S. A. H. Sadabadi. Lagrangian and Eulerian Description of Bed Load Transport. *Journal of Geophysical Research: Earth Surface*, 123(2):384–408, 2018. ISSN 2169-9011. doi: 10.1002/2016JF004087. 28

[16] H. H. Barnes. *Roughness characteristics of natural channels*. Number 1849. US Government Printing Office, 1967. 32

[17] A. R. Barron. Approximation and estimation bounds for artificial neural networks. *Mach. Learn.*, 14(1):115–133, Jan. 1994. ISSN 0885-6125. doi: 10.1023/A:1022650905902. URL `https://doi.org/10.1023/A:1022650905902`. 76

[18] S. Barthélémy, S. Ricci, M. C. Rochoux, E. Le Pape, and O. Thual. Ensemble-based data assimilation for operational flood forecasting–on the merits of state estimation for 1d hydrodynamic forecasting through the example of the “adour maritime” river. *Journal of Hydrology*, 552:210–224, 2017. 78

[19] L. A. Bastidas, J. Knighton, and S. W. Kline. Parameter sensitivity and uncertainty analysis for a storm surge and wave model. *Natural Hazards and Earth System Sciences*, 16(10):2195–2210, 2016. doi: 10.5194/nhess-16-2195-2016. URL `https://www.nat-hazards-earth-syst-sci.net/16/2195/2016/`. 2, 53

[20] F. Beckers, M. Noack, and S. Wieprecht. Uncertainty analysis of a 2d sediment transport model: an example of the lower river salzach. *Journal of Soils and Sediments*, 18(10):3133–3144, 2018. 53

[21] M. BENOIT and F. LAFON. A nearshore wave atlas along the coasts of france based on the numerical modeling of wave climate over 25 years. In *Coastal Engineering 2004: (In 4 Volumes)*, pages 714–726. World Scientific, 2005. 21, 47

[22] M. Benoit, F. Marcos, and F. Becq. Development of a third generation shallow-water wave model with unstructured spatial meshing. *Coastal Engineering 1996*, pages 465–478, 1997. 12, 44

[23] L. Bertino, G. Evensen, and H. Wackernagel. Combining geostatistics and kalman filtering for data assimilation in an estuarine system. *Inverse Problems*, 18(1):1–23, jan 2002. 78

[24] J. Besnard. Statistical study of surges at the vicinity of the x nuclear plant. technical report edf-lnhe-he/42/93,43. Technical report, EDF R&D, 1993. 11

[25] A. Birolleau, G. Poëtte, and D. Lucor. Adaptive bayesian inference for discontinuous inverse problems, application to hyperbolic conservation laws. *Communications in Computational Physics*, 16(1):1–34, 2014. 87, 222

[26] G. Blatman. *Adaptive sparse polynomial chaos expansions for uncertainty propagation and sensitivity analysis.* PhD thesis, 2009. 65, 68, 72

[27] G. Blatman and B. Sudret. Anisotropic parcimonious polynomial chaos expansions based on the sparsity-of-effects principle. In *Proc ICOSSAR'09, International Conference in Structural Safety and Relability*, 2009. 67

[28] G. Blatman and B. Sudret. Adaptive sparse polynomial chaos expansion based on least angle regression. *Journal of Computational Physics*, 230(6):2345 – 2367, 2011. 67

[29] E. Blayo, E. Cosme, M. Nodet, and A. Vidart. Introduction to data assimilation, 2011. 79, 81, 82, 84

[30] F. P. Bretherton and C. J. R. Garrett. Wavetrains in inhomogeneous moving media. *Proceedings of the Royal Society of London. Series A. Mathematical and Physical Sciences*, 302(1471):529–554, 1968. 35, 36

[31] L. Bruno, C. Canuto, and D. Fransos. Stochastic aerodynamics and aeroelasticity of a flat plate via generalised polynomial chaos. *Journal of Fluids and Structures*, 25(7):1158 – 1176, 2009. ISSN 0889-9746. doi: https://doi.org/10.1016/j.jfluidstructs.2009.06.001. URL `http://www.sciencedirect.com/science/article/pii/S0889974609000693`. 60

[32] S. L. Brunton, B. R. Noack, and P. Koumoutsakos. Machine learning for fluid mechanics. *Annual Review of Fluid Mechanics*, 52(1):477–508, 2020. doi: 10.1146/annurev-fluid-010719-060214. URL `https://doi.org/10.1146/annurev-fluid-010719-060214`. 2

[33] J. M. Brylinski, Y. Lagadeuc, V. Gentilhomme, J. P. Dupont, R. Lafite, P. A. Dupeuble, M. F. Huault, and A. Y. Le fleuve cotier : Un phenomene hydrologique important en manche orientale. exemple du pas-de-calais, 1991. URL `https://archimer.ifremer.fr/doc/00268/37874/`. 10

[34] K. Campbell, M. D. McKay, and B. J. Williams. Sensitivity analysis when model outputs are functions. *Reliability Engineering & System Safety*, 91(10):1468 – 1472, 2006. ISSN 0951-8320. doi: https://doi.org/10.1016/j.ress.2005.11.049. URL `http://www.sciencedirect.com/science/article/pii/S0951832005002565`. The Fourth International Conference on Sensitivity Analysis of Model Output (SAMO 2004). 62, 95

[35] R. M. Campos and C. Guedes Soares. Comparison and assessment of three wave hindcasts in the north atlantic ocean. *Journal of Operational Oceanography*, 9(1):26–44, 2016. 24

[36] Y. Caniou. *Global sensitivity analysis for nested and multiscale modelling.* PhD thesis, 2012. 61, 62, 64, 69

[37] Y. Cao, J. Zhu, I. M. Navon, and Z. Luo. A reduced-order approach to four-dimensional variational data assimilation using proper orthogonal decomposition. *International Journal for Numerical Methods in Fluids*, 53(10):1571–1583, 2007. 86, 95, 96, 222

[38] J. Carlson, A. Jaffe, and e. A. Wiles. *The Millennium Prize Problems*. AMS, Providence, R.I. (USA), 2006. 30

[39] A. Carrassi, M. Bocquet, L. Bertino, and G. Evensen. Data assimilation in the geosciences: An overview of methods, issues, and perspectives. *Wiley Interdisciplinary Reviews: Climate Change*, 9(5):e535, 2018. 2, 79, 80, 83

[40] J. Castro, C. Mantas, and J. Benitez. Neural networks with a continuous squashing function in the output are universal approximators. *Neural Networks*, 13(6):561 – 563, 2000. ISSN 0893-6080. doi: https://doi.org/10.1016/S0893-6080(00)00031-9. URL `http://www.sciencedirect.com/science/article/pii/S0893608000000319`. 76

[41] V. Cherkassky, V. Krasnopolsky, and J. Solomatine, D. P. abd Valdes. Computational intelligence in earth sciences and environmental applications: Issues and challenges. *Neural Networks*, 2006. 70

[42] P. Clabaut. Sedimentation of the x power plant's intake: Measurements of sediment thickness at the vicinity of the plant. technical report. Technical report, EDF, 2011. 9, 15

[43] N. Cohen, O. Sharir, and A. Shashua. On the expressive power of deep learning: A tensor analysis. In V. Feldman, A. Rakhlin, and O. Shamir, editors, *29th Annual Conference on Learning Theory*, volume 49 of *Proceedings of Machine Learning Research*, pages 698–728, Columbia University, New York, New York, USA, 23–26 Jun 2016. PMLR. URL `http://proceedings.mlr.press/v49/cohen16.html`. 76, 77

[44] L. Cordier and M. Bergmann. Proper orthogonal decomposition: an overview. In *Lecture series 2002-04, 2003-03 and 2008-01 on post-processing of experimental and numerical data, Von Karman Institute for Fluid Dynamics*, page 46 pages. VKI, 2008. 90, 93

[45] S. Cordier, M. Le, and T. M. de Luna. Bedload transport in shallow water models: Why splitting (may) fail, how hyperbolicity (can) help. *Advances in Water Resources*, 34(8):980 – 989, 2011. 44

[46] S. Costa, F. Gourmelon, C. Augris, P. Clabaut, and B. Latteux. Benefits of the systemic and pluridisciplinary approach in the study of the coastal and marine domain of seine-maritime (france). *Norois. Environnement, aménagement, société*, (196):91–108, 2005. iii, 4, 10, 12, 14, 15, 16, 19, 20

[47] M. Couplet. *Reduced-order POD-Galerkin modelling for the control of unsteady flows*. Ph.d. thesis, Université Paris-Nord - Paris XIII, Jan. 2005. 90, 91, 92

[48] M. Couplet, C. Basdevant, and P. Sagaut. Calibrated reduced-order pod-galerkin system for fluid flow modelling. *Journal of Computational Physics*, 207(1):192 – 220, 2005. ISSN 0021-9991. 92

[49] G. Cowan. *Statistical data analysis*. Oxford university press, 1998. 69, 70

[50] G. Cruciani, M. Baroni, S. Clementi, G. Costantino, D. Riganelli, and B. Skagerberg. Predictive ability of regression models. part i: Standard deviation of prediction errors (sdep). *Journal of Chemometrics*, 6(6):335–346, 1992. 68

[51] G. Cybenko. Approximation by superpositions of a sigmoidal function. *Mathematics of Control, Signals and Systems*, 2(4):303–314, Dec 1989. ISSN 1435-568X. doi: 10.1007/BF02551274. URL `https://doi.org/10.1007/BF02551274`. 76

[52] G. L. Dalledonne, R. Kopmann, and T. Brudy-Zippelius. Uncertainty quantification of floodplain friction in hydrodynamic models. *Hydrology and Earth System Sciences,*, 23:373–3385, 2019. doi: 0.5194/hess-23-3373-2019. 53

[53] G. Damblin, M. Couplet, and B. Iooss. Numerical studies of space-filling designs: optimization of latin hypercube samples and subprojection properties. *Journal of Simulation*, 7(4):276–289, 2013. 60

[54] R. G. Dean and R. A. Dalrymple. *Coastal processes with engineering applications*. Cambridge University Press, 2004. 3

[55] P. J. Diggle. Statistics: a data science for the 21st century. *Journal of the Royal Statistical Society: Series A (Statistics in Society)*, 178(4):793–813, 2015. 69

[56] L. Drévès, P. Clabaut, C. Chevalier, and C. Abernot-Le-Gac. Cauxsom - june and july 2004: Bio-morpho-sedimentary study of the marine coastal domain from dieppe to criel-sur-mer (seine-maritime, france). technical report. Technical report, Ifremer, 2006. 9

[57] L. Drévès, C. Abernot-Le-Gac, E. Antajan, P. Clabaut, P. Claquin, M. L. Cochard, P. Monbet, J. Morin, A. Tetard, C. Warenbourg, and H. T. D. Boullay. Hydrobiological overview of the x power plant's site. technical report. Technical report, Ifremer, 2010. 9

[58] S. Du, G. Song, and H. Hong. Collective causal inference with lag estimation. *Neurocomputing*, 323:299 – 310, 2019. ISSN 0925-2312. doi: https://doi.org/10.1016/j.neucom.2018.09.088. URL `http://www.sciencedirect.com/science/article/pii/S0925231218311792`. 222

[59] S. Durbiano. *Vecteurs caractéristiques de modèles océaniques pour la réduction d'ordre en assimilation de données*. PhD thesis, 2001. 96

[60] A. E., S. L., H. A., and W. S. Neural network estimation of suspended sediment: Potential pitfalls and future directions. *Practical Hydroinformatics. Water Science and Technology Library, vol 68.*, 2009. 70

[61] B. Efron, T. Hastie, I. Johnstone, and R. Tibshirani. Least angle regression. *Annals of Statistics*, pages 32, 407–499, 2004. 72

[62] G. D. Egbert and S. Y. Erofeeva. Efficient Inverse Modeling of Barotropic Ocean Tides. *Journal of Atmospheric and Oceanic Technology*, 19(2):183–204, 02 2002. ISSN 0739-0572. 34

[63] N. El Moçayd, S. Ricci, N. Goutal, M. C. Rochoux, S. Boyaval, C. Goeury, D. Lucor, and O. Thual. Polynomial surrogates for open-channel flows in random steady state. *Environmental Modeling & Assessment*, 23(3):309–331, 2018. 78

[64] N. El Moçayd. *La décomposition en polynôme du chaos pour l'amélioration de l'assimilation de données ensembliste en hydraulique fluviale*. PhD thesis, 2017. 88

[65] R. Eldan and O. Shamir. The power of depth for feedforward neural networks. *Conference on Learning Theory*, 12 2015. 76, 77

[66] ESA (European Space Agency) - Copernicus program. Sentinel satellite missions. `https://sentinels.copernicus.eu/web/sentinel/home`, 2000-2020. 2, 70

[67] S. Evangelista, G. Giovinco, and S. Kocaman. A multi-parameter calibration method for the numerical simulation of morphodynamic problems. *Journal of Hydrology and Hydromechanics*, 65:175–182, 06 2017. 78

[68] G. Evensen. The ensemble kalman filter: Theoretical formulation and practical implementation. *Ocean dynamics*, 53(4):343–367, 2003. 83

[69] G. Evensen. Sampling strategies and square root analysis schemes for the enkf. *Ocean dynamics*, 54(6):539–560, 2004. 87

[70] G. Evensen. *Data assimilation: the ensemble Kalman filter*. Springer Science & Business Media, 2009. 80, 83

[71] K. Fisher and F. Dawson. Reducing uncertainty in river flood conveyance: Roughness review, 07 2003. 32, 33

[72] S. J. Fletcher. *Data assimilation for the geosciences: From theory to application*. Elsevier, 2017. 2

[73] K.-I. Funahashi. On the approximate realization of continuous mappings by neural networks. *Neural Networks*, 2(3):183 – 192, 1989. ISSN 0893-6080. doi: https://doi.org/10.1016/0893-6080(89)90003-8. URL `http://www.sciencedirect.com/science/article/pii/0893608089900038`. 76

[74] D. J. Furbish, P. K. Haff, J. C. Roseberry, and M. W. Schmeeckle. A probabilistic description of the bed load sediment flux: 1. theory. *Journal of Geophysical Research: Earth Surface*, 117(F3), 2012. doi: 10.1029/2012JF002352. URL `https://agupubs.onlinelibrary.wiley.com/doi/abs/10.1029/2012JF002352`. 40

[75] M. Garcia. Sedimentation engineering: processes, measurements, modeling, and practice. American Society of Civil Engineers, 2008. 41, 43

[76] T. Garcia. *Towards a data assimilation system for morphodynamic modeling*. PhD thesis, 2014. 62, 95

[77] T. Garcia, G. El Serafy, A. Heemink, and H. Schuttelaars. Towards a data assimilation system for morphodynamic modeling: Bathymetric data assimilation for wave property estimation. *Ocean Dynamics*, 63, 05 2013. 78, 96

[78] O. Garcia-Cabrejo and A. Valocchi. Global sensitivity analysis for multivariate output using polynomial chaos expansion. *Reliability Engineering & System Safety*, 126:25–36, 2014. 95

[79] J.-F. Gerbeau and B. Perthame. Derivation of Viscous Saint-Venant System for Laminar Shallow Water; Numerical Validation. Research Report RR-4084, INRIA, 2000. Projet M3N. 30

[80] R. G. Ghanem and R. M. Kruger. Numerical solution of spectral stochastic finite element systems. *Computer Methods in Applied Mechanics and Engineering*, 129(3):289 – 303, 1996. ISSN 0045-7825. doi: https://doi.org/10.1016/0045-7825(95)00909-4. URL `http://www.sciencedirect.com/science/article/pii/0045782595009094`. 63, 65

[81] C. Goeury, Y. Audouin, and F. Zaoui. Interoperability and computational framework for simulating open channel hydraulics: application to sensitivity analysis and calibration of gironde estuary model, 2020. 44

[82] E. B. Goldstein, G. Coco, and N. G. Plant. A review of machine learning applications to coastal sediment transport and morphodynamics. *Earth-Science Reviews*, 194:97 – 108, 2019. ISSN 0012-8252. doi: https://doi.org/10.1016/j.earscirev.2019.04.022. URL `http://www.sciencedirect.com/science/article/pii/S001282521830391X`. 70, 73

[83] A. Gonoskov, E. Wallin, A. Polovinkin, and I. Meyerov. Employing machine learning for theory validation and identification of experimental conditions in laserplasma physics. *Scientific Reports*, 9:7043, 2019. doi: 10.1038/s41598-019-43465-3. 2

[84] A. Griewank and A. Walther. *Evaluating derivatives: principles and techniques of algorithmic differentiation*. SIAM, 2008. 86

[85] A. Guillaume. *VAG-Modele de prevision de l'etat de la mer en eau profonde*. Dir. de la Meteorologie Nationale, 1987. 22, 23, 24

[86] H. P. Guy, D. B. Simons, and E. V. Richardson. *Summary of alluvial channel data from flume experiments, 1956-61*, volume 462. US Government Printing Office, 1966. iii, 39

[87] I. Guyon and A. Elisseeff. An introduction to variable and feature selection. *Journal of Machine Learning Research*, 3:1157–1182, 2003. 64

[88] J. F. Hair, W. C. Black, B. J. Babin, R. E. Anderson, R. L. Tatham, et al. *Multivariate data analysis*, volume 5. Prentice hall Upper Saddle River, NJ, 1998. 69, 70

[89] B. Hanin. Universal function approximation by deep neural nets with bounded width and relu activations. *Mathematics*, 7(10), 2019. ISSN 2227-7390. doi: 10.3390/math7100992. URL `https://www.mdpi.com/2227-7390/7/10/992`. 76, 77

[90] K. Hara and K. Nakayamma. Comparison of activation functions in multilayer neural network for pattern classification. In *Proceedings of 1994 IEEE International Conference on Neural Networks (ICNN'94)*, volume 5, pages 2997–3002 vol.5, June 1994. doi: 10.1109/ICNN.1994.374710. 75

[91] Y. Hassanzadeh. *Hydraulics of sediment transport*. InTech, 2012. iii, 32, 33

[92] K. Hasselmann, T. P. Barnett, E. Bouws, H. Carlson, D. E. Cartwright, K. Enke, J. Ewing, H. Gienapp, D. Hasselmann, P. Kruseman, et al. Measurements of wind-wave growth and swell decay during the joint north sea wave project (jonswap). *Ergänzungsheft 8-12*, 1973. 37

[93] T. Hastie, R. Tibshirani, and J. Friedman. *The Elements of Statistical Learning: Data Mining, Inference, and Prediction, Second Edition (Springer Series in Statistics).* 02 2009. ISBN 0387848576. 57, 58, 69

[94] W. K. Hastings. Monte carlo sampling methods using markov chains and their applications. 1970. 80

[95] J.-M. Hervouet. *Hydrodynamics of Free Surface Flows: Modelling with the Finite Element Method.* John Wiley & Sons, Ltd.: Hoboken, NJ, USA, 2007. 44

[96] T. Hesterberg, N. H. Choi, L. Meier, C. Fraley, et al. Least angle and l1 penalized regression: A review. *Statistics Surveys*, 2:61–93, 2008. 71

[97] Horillo-Caraballo, J. M., Reeve, D. E. An investigation of the link between beach morphology and wave climate at Duck, NC, USA. *J. Flood Risk Management*, 2008. 89

[98] K. Hornik. Approximation capabilities of multilayer feedforward networks. *Neural Networks*, 4(2):251 – 257, 1991. ISSN 0893-6080. doi: https://doi.org/10.1016/0893-6080(91)90009-T. URL `http://www.sciencedirect.com/science/article/pii/089360809190009T`. 76

[99] Hotelling, H. Analysis of a complex of statistical variables into principal components. *J. of Educational Psychology, 24(6), 417-441 and 498-520*, 1933. 91

[100] T. Hsu, C. Jan, K. Chang, and S. Wang. Ph.d. analysis and prediction of riverbed changes using empirical orthogonal functions. *J. Hydraulic Research*, 2006. 89

[101] R. P. Hunziker and M. N. Jaeggi. Grain sorting processes. *Journal of Hydraulic Engineering*, 128(12):1060–1068, 2002. 43

[102] D. Idier, X. Bertin, P. Thompson, and M. D. Pickering. Interactions between mean sea level, tide, surge, waves and flooding: mechanisms and contributions to sea level variations at the coast. *Surveys in Geophysics*, 40(6):1603–1630, 2019. 34

[103] B. Iooss and P. Lemaître. *A Review on Global Sensitivity Analysis Methods*, pages 101–122. Springer US, Boston, MA, 2015. ISBN 978-1-4899-7547-8. doi: 10.1007/978-1-4899-7547-8_5. URL `https://doi.org/10.1007/978-1-4899-7547-8_5`. 60, 62, 69

[104] S. Isukapalli. Uncertainty analysis of transport-transformation models [ph. d. thesis]. *New Jersey, USA: Rutgers-The State University of New Jersey*, 1999. 66

[105] R. Iten, T. Metger, H. Wilming, L. del Rio, and R. Renner. Discovering physical concepts with neural networks. *Phys. Rev. Lett.*, 124, Jan 2020. 2, 76, 77, 78

[106] I. M. Johnstone and A. Y. Lu. On consistency and sparsity for principal components analysis in high dimensions. *Journal of the American Statistical Association*, 104 (486):682–693, 2009. 142, 147

[107] B. A. Jones and A. Doostan. Satellite collision probability estimation using polynomial chaos expansions. *Advances in Space Research*, 52(11):1860 – 1875, 2013. ISSN 0273-1177. doi: https://doi.org/10.1016/j.asr.2013.08.027. URL `http://www.sciencedirect.com/science/article/pii/S0273117713005413`. 60

[108] Karhunen, K. Zur spektraltheorie stochastischer prozesse. *Ann. Acad. Sci. Fennicae*, 1946. 89, 91

[109] A. Karpatne, I. Ebert-Uphoff, S. Ravela, H. A. Babaie, and V. Kumar. Machine learning for the geosciences: Challenges and opportunities. *IEEE Transactions on Knowledge and Data Engineering*, 31(8):1544–1554, Aug 2019. 2, 70

[110] H. Karunarathna, D. Reeve, and M. Spivack. Long-term morphodynamic evolution of estuaries: An inverse problem. *Estuarine, Coastal and Shelf Science*, 2008. 89

[111] H. Karunarathna, J. Horrillo-Caraballo, and R. D. E. Burningham, Pan S. Two-dimensional reduced-physics model to desribe historic morphodynamic behaviour of an estuary inlet. *Marine Geology*, 2016. 89

[112] G. Kerschen and J. Golinval. Physical interpretation of the proper orthogonal modes using the singular value decomposition. *Journal of Sound and Vibration*, 249(5):849 – 865, 2002. ISSN 0022-460X. doi: https://doi.org/10.1006/jsvi.2001.3930. URL `http://www.sciencedirect.com/science/article/pii/S0022460X01939306`. 90, 94

[113] O. M. Knio and O. P. Le Maître. Uncertainty propagation in CFD using polynomial chaos decomposition. *Fluid Dynamics Research*, 38(9):616–640, sep 2006. doi: 10.1016/j.fluiddyn.2005.12.003. 60, 62

[114] F. Koch and C. Flokstra. *Bed level computations for curved alluvial channels: Prepared for the 19th IAHR Congress, New Delhi, India, February 1981*. Waterloopkundig Laboratorium, 1980. 43

[115] J. Kremer, K. Stensbo-Smidt, F. Gieseke, K. S. Pedersen, and C. Igel. Big universe, big data: Machine learning and image analysis for astronomy. *IEEE Intelligent Systems*, 32(2):16–22, Mar 2017. ISSN 1941-1294. doi: 10.1109/MIS.2017.40. 2

[116] J. N. Kutz. Deep learning in fluid dynamics. *Journal of Fluid Mechanics*, 814:1–4, 2017. doi: 10.1017/jfm.2016.803. 2

[117] M. Lamboni, H. Monod, and D. Makowski. Multivariate sensitivity analysis to measure global contribution of input factors in dynamic models. *Reliability Engineering & System Safety*, 96(4):450 – 459, 2011. ISSN 0951-8320. doi: https://doi.org/10.1016/j.ress.2010.12.002. URL `http://www.sciencedirect.com/science/article/pii/S0951832010002504`. 62, 95, 215

[118] K. Larnier, J. Monnier, P.-A. Garambois, and J. Verley. River discharge and bathymetry estimation from swot altimetry measurements. *Inverse Problems in Science and Engineering*, pages 1–31, 2020. 78

[119] M. Larson, M. Capobianco, M. Jansen, G. Różyński, H. Southgate, M. Stive, K. Wijnberg, and S. Hulscher. Analysis and modeling of field data on coastal morphological evolution over yearly and decadal time scales. part 1: Background and linear techniques. *Journal of Coastal Research*, 19, 09 2003. 88, 89, 142

[120] C. Larsonneur, P. Bouysse, and J.-P. Auffret. The superficial sediments of the english channel and its western approaches. *Sedimentology*, 29(6):851–864, 1982. iii, 15

[121] C. Lataniotis, S. Marelli, and B. Sudret. Extending classical surrogate modelling to ultrahigh dimensional problems through supervised dimensionality reduction: a data-driven approach. *arXiv preprint:1812.06309*, 12 2018. 67, 222

[122] B. Latteux. Assessment of the mechanisms responsible for the water intake's sedimation in x power plant. technical report. Technical report, EDF R&D, 2010. iii, iv, 9, 10, 11, 12, 13, 14, 15, 16, 17, 18, 19, 20, 21, 25, 46, 47, 48, 49

[123] B. Latteux. Reflexions about the water intake's sedimentation in x power plant: analysis of the regional and short term aspects. technical report. Technical report, EDF R&D, 2010. 9

[124] A. Laudani, G. M. Lozito, F. R. Fulginei, and A. Salvini. On training efficiency and computational costs of a feed forward neural network: A review. *Computational Intelligence and Neuroscience*, 2015. doi: 10.1155/2015/818243. 76, 77, 88

[125] A. Laugel. *Climatologie des Etats de mer en Atlantique nord-est : analyse du climat actuelet des Ã©volutions futures sous scénarios de changement climatique par descente d'échelle dynamique et statistique*. PhD thesis, 2013. 37

[126] S. Le Bot, R. Lafite, M. Fournier, A. Baltzer, and M. Desprez. Morphological and sedimentary impacts and recovery on a mixed sandy to pebbly seabed exposed to marine aggregate extraction (eastern english channel, france). *Estuarine, Coastal and Shelf Science*, 89(3):221–233, 2010. 10

[127] F. Le Gland, V. Monbet, and V.-D. Tran. Large sample asymptotics for the ensemble kalman filter. 2009. 83

[128] Y. LeCun, Y. Bengio, and G. Hinton. Deep learning. *Nature*, 521:436–444, 2015. doi: https://doi.org/10.1038/nature14539. 74

[129] M. Leshno, V. Y. Lin, A. Pinkus, and S. Schocken. Multilayer feedforward networks with a nonpolynomial activation function can approximate any function. *Neural Networks*, 6(6):861 – 867, 1993. ISSN 0893-6080. doi: https://doi.org/10.1016/S0893-6080(05)80131-5. URL `http://www.sciencedirect.com/science/article/pii/S0893608005801315`. 76

[130] P. Letortu. *Le recul des falaises crayeuses haut-normandes et les inondations par la mer en Manche centrale et orientale: de la quantification de l'aléa à la caractérisation des risques induits*. Ph.d. thesis, Université de Caen Basse-Normandie, 2013. iii, 9, 10, 11, 12, 13, 14, 18, 19, 46

[131] J. M. Lewis, S. Lakshmivarahan, and S. Dhall. *Dynamic data assimilation: a least squares approach*, volume 13. Cambridge University Press, 2006. 86

[132] J. L'her, G. Goasguen, M. Rogard, et al. Candhis database of in situ sea states measurements on the french coastal zone. In *The Ninth International Offshore and Polar Engineering Conference*. International Society of Offshore and Polar Engineers, 1999. 21

[133] J. Li and D. Xiu. On numerical properties of the ensemble kalman filter for data assimilation. *Computer Methods in Applied Mechanics and Engineering*, 197(43-44): 3574–3583, 2008. 87

[134] J. Li and D. Xiu. A generalized polynomial chaos based ensemble kalman filter with high accuracy. *Journal of computational physics*, 228(15):5454–5469, 2009. 88

[135] Liying Ma and K. Khorasani. Constructive feedforward neural networks using hermite polynomial activation functions. *IEEE Transactions on Neural Networks*, 16(4):821–833, July 2005. ISSN 1941-0093. doi: 10.1109/TNN.2005.851786. 75

[136] A. Loic. Ecological pre-project study on x power plant construction site: benthic environment. technical report. Technical report, EDF R&D, 1976. vii, 9, 10, 11, 16, 18

[137] A. Loic. Ecological pre-project study on x power plant construction site: pelagic environment. technical report. Technical report, EDF R&D, 1977. 9, 18

[138] Lorenz, E. N. Empirical Orthogonal Functions and Statistical Weather Prediction. *Cambrige: MIT, Department of Meteorology, Statistical Forecasting Project*, 1956. 91

[139] T. E. Lovett, F. Ponci, and A. Monti. A polynomial chaos approach to measurement uncertainty. *IEEE Transactions on Instrumentation and Measurement*, 55(3):729–736, June 2006. ISSN 1557-9662. doi: 10.1109/TIM.2006.873807. 60, 62

[140] Loève, M. M. Probability theory. *Princeton, N.J.:VanNostrand*, 1955. 89, 91

[141] F. Lu, M. Morzfeld, X. Tu, and A. J. Chorin. Limitations of polynomial chaos expansions in the bayesian solution of inverse problems. *Journal of Computational Physics*, 282:138–147, 2015. 88

[142] Z. Lu, H. Pu, F. Wang, Z. Hu, and L. Wang. The expressive power of neural networks: A view from the width. In I. Guyon, U. V. Luxburg, S. Bengio, H. Wallach, R. Fergus, S. Vishwanathan, and R. Garnett, editors, *Advances in Neural Information Processing Systems 30*, pages 6231–6239. Curran Associates, Inc., 2017. URL `http://papers.nips.cc/paper/7203-the-expressive-power-of-neural-networks-a-view-from-the-width.pdf`. 76, 77

[143] D. Lucor, C.-H. Su, and G. E. Karniadakis. Generalized polynomial chaos and random oscillators. *International Journal for Numerical Methods in Engineering*, 60(3):571–596, 2004. doi: 10.1002/nme.976. URL `https://onlinelibrary.wiley.com/doi/abs/10.1002/nme.976`. 60

[144] J. L. Lumley. The structure of inhomogeneous turbulent flows. *Atmospheric Turbulence and Radio Wave Propagation*, 1967. 89, 90, 91, 92

[145] M. Ma, J. Lu, and G. Tryggvason. Using statistical learning to close two-fluid multiphase flow equations for bubbly flows in vertical channels. *International Journal of Multiphase Flow*, 85:336 – 347, 2016. ISSN 0301-9322. doi: https://doi.org/10.1016/j.ijmultiphaseflow.2016.06.021. URL `http://www.sciencedirect.com/science/article/pii/S0301932215302226`. 2

[146] O. Machiels, S. Erpicum, P. Archambeau, B. Dewals, and M. Pirotton. Bottom friction formulations for free surface flow modeling. In *8th National Congress on Theoretical and Applied Mechanics, Brussels*, 01 2009. 32, 34

[147] Z. Malenovsky, H. Rott, J. Cihlar, M. E. Schaepman, G. García-Santos, R. Fernandes, and M. Berger. Sentinels for science: Potential of sentinel-1, -2, and -3 missions for scientific observations of ocean, cryosphere, and land. *Remote Sensing of Environment*, 120:91 – 101, 2012. ISSN 0034-4257. doi: https://doi.org/10.1016/j.rse.2011.09.026. URL `http://www.sciencedirect.com/science/article/pii/S0034425712000648`. The Sentinel Missions - New Opportunities for Science. 2, 70

[148] M. Marriott and R. Jayaratne. Hydraulic roughness – links between manning's coefficient, nikuradse's equivalent sand roughness and bed grain size. *Proc. 5th Annual Conf. on Advances in Computing and Technology*, 01 2010. 32, 33

[149] M. J. Martin, M. Balmaseda, L. Bertino, P. Brasseur, G. Brassington, J. Cummings, Y. Fujii, D. Lea, J.-M. Lellouche, K. Mogensen, et al. Status and future of data assimilation in operational oceanography. *Journal of Operational Oceanography*, 8 (sup1):s28–s48, 2015. 78

[150] Y. M. Marzouk and H. N. Najm. Dimensionality reduction and polynomial chaos acceleration of bayesian inference in inverse problems. *Journal of Computational Physics*, 228(6):1862–1902, 2009. 87

[151] Y. M. Marzouk, H. N. Najm, and L. A. Rahn. Stochastic spectral methods for efficient bayesian solution of inverse problems. *Journal of Computational Physics*, 224(2):560–586, 2007. 87

[152] G. Matheron. Principles of geostatistics. *Economic geology*, 58(8):1246–1266, 1963. 60, 62

[153] G. Mattarolo, F. Lafon, and M. Benoit. Wave energy resource off the french coasts: the anemoc database applied to the energy yield evaluation of wave energy converters. *Proceedings of the 8th European wave and tidal energy conference*, pages 247–255, 2009. 12, 47

[154] M. D. McKay, R. J. Beckman, and W. J. Conover. A comparison of three methods for selecting values of input variables in the analysis of output from a computer code. *Technometrics*, 42(1):55–61, 2000. 65

[155] R. Medina, C. Vidal, M. A. Losada, and A. J. Roldan. Three-mode principle component analysis of bathymetric data, applied to"playa de castilla" (huelva, spain). *Coastal Engineering Proceedings*, 1992. 89

[156] X. Mei, Z. Dai, W. Wei, W. Li, J. Wang, and H. Sheng. Secular bathymetric variations of the north channel in the changjiang (yangtze) estuary, china, 1880-2013: Causes and effects. *Geomorphology*, 2018. 89

[157] T. Meile and A. Schleiss. Influence of macro-roughness of walls on steady and unsteady flow in a channel. Technical report, EPFL-LCH, 2007. 32

[158] Z. Meng, Y. Hu, and C. Ancey. Using a data driven approach to predict waves generated by gravity driven mass flows. *Water*, 12, 02 2020. iv, 75

[159] E. Meyer-Peter and R. Müller. Formulas for bed-load transport. In *IAHSR 2nd meeting, Stockholm, appendix 2*. IAHR, 1948. 42, 43

[160] C. Michel, S. Le Bot, F. Druine, S. Costa, F. Levoy, C. Dubrulle-Brunaud, and R. Lafite. Stages of sedimentary infilling in a hypertidal bay using a combination of sedimentological, morphological and dynamic criteria (bay of somme, france). *Journal of Maps*, 13(2):858–865, 2017. 10

[161] S. Mika, B. Schölkopf, A. J. Smola, K.-R. Müller, M. Scholz, and G. Rätsch. Kernel pca and de-noising in feature spaces. *Advances in neural information processing systems*, pages 536–542, 1999. 142, 147

[162] J. Miller and R. G. Dean. Shoreline variability via empirical orthogonal function analysis: Part i temporal and spatial characteristics. *Coastal Engineering*, 2007. 89

[163] J. Miller and R. G. Dean. Shoreline variability via empirical orthogonal function analysis: Part ii relationship to nearshore conditions. *Coastal Engineering*, 2007. 89

[164] K. Mills, M. Spanner, and I. Tamblyn. Deep learning and the Schrödinger equation. *Phys. Rev. A*, 96:042113, Oct 2017. doi: 10.1103/PhysRevA.96.042113. URL `https://link.aps.org/doi/10.1103/PhysRevA.96.042113`. 2

[165] V. Mons, L. Margheri, J.-C. Chassaing, and P. Sagaut. Data assimilation-based reconstruction of urban pollutant release characteristics. *Journal of Wind Engineering and Industrial Aerodynamics*, 169:232 – 250, 2017. 97, 98, 222, 223

[166] R. Morrow, L.-L. Fu, F. Ardhuin, M. Benkiran, B. Chapron, E. Cosme, F. d'Ovidio, J. T. Farrar, S. T. Gille, G. Lapeyre, P.-Y. Le Traon, A. Pascual, A. Ponte, B. Qiu, N. Rascle, C. Ubelmann, J. Wang, and E. D. Zaron. Global observations of fine-scale ocean surface topography with the surface water and ocean topography (swot) mission. *Frontiers in Marine Science*, 6:232, 2019. 2, 70

[167] H. Morvan, D. Knight, N. Wright, X. Tang, and A. Crossley. The concept of roughness in fluvial hydraulics and its formulation in 1d, 2d and 3d numerical simulation models. *Journal of Hydraulic Research*, 46:191–208, 03 2008. 32, 33

[168] A. Mosavi, S. Shamshirband, E. Salwana, K.-w. Chau, and J. H. Tah. Prediction of multi-inputs bubble column reactor using a novel hybrid model of computational fluid dynamics and machine learning. *Engineering Applications of Computational Fluid Mechanics*, 13(1):482–492, 2019. 224

[169] L. Mosser, S. Purves, and E. Z. Naeini. Uncertainty quantification for deep learning in geoscience applications. In *EAGE/AAPG Digital Subsurface for Asia Pacific Conference*, volume 2020, pages 1–3. European Association of Geoscientists & Engineers, 2020. 2

[170] R.-S. Mouradi, Y. Audouin, C. Goeury, N. Claude, P. Tassi, and K. El Kadi Abderrezzak. Sensitivity analysis and uncertainty quantification in 2d morphodynamic models using a newly implemented api for telemac2d/sisyphe. *Proceedings of the XXIIIrd TELEMAC-MASCARET User Conference 2016, 11 to 13 October 2016, Paris, France*, pages 153–162, 2016. 40, 53

[171] R.-S. Mouradi, O. Thual, C. Goeury, , P. Tassi, and F. Zaoui. Sensitivity of tidal modelling in coastal configurations: an uncertainty study based on field-measurement reduction. *Proceedings of the TELEMAC-MASCARET User Conference 2020*, 2020. 152

[172] R.-S. Mouradi, C. Goeury, O. Thual, F. Zaoui, and P. Tassi. Physically interpretable machine learning algorithm on multidimensional non-linear fields. *Journal of Computational Physics*, 428:110074, 2021. ISSN 0021-9991. doi: https://doi.org/10.1016/j.jcp.2020.110074. 100

[173] M. Muller. *On the POD method: an abstract investigation with applications to reduced-order modeling and suboptimal control.* PhD thesis, 2008. 90, 92

[174] E. Muravleva, I. Oseledets, and D. Koroteev. Application of machine learning to viscoplastic flow modeling. *Physics of Fluids*, 30(10):103102, 2018. doi: 10.1063/1.5058127. URL `https://doi.org/10.1063/1.5058127`. 2

[175] H. N. Southgate, K. Wijnberg, M. Larson, M. Capobianco, and H. Jansen. Analysis of field data of coastal morphological evolution over yearly and decadal timescales. part 2: Non-linear techniques. *Journal of Coastal Research*, 19, 09 2003. 88, 89

[176] NASA (National Aeronautics and Space Administration) and CNES (Centre National d'Etudes Spatiales) in partnership with CSA (Canadian Space Agency) and UKSA (UK Space Agency). Surface water and ocean topography. `https://swot.jpl.nasa.gov/home.htm`, 2021. 2, 70

[177] I. M. Navon. Data assimilation for numerical weather prediction: a review. In *Data assimilation for atmospheric, oceanic and hydrologic applications*, pages 21–65. Springer, 2009. 78

[178] A. Ng. Machine learning lecture notes. Stanford Univ. TR, Stanford, CA, 2014. 71, 72, 74, 75, 88

[179] B. T. Nguyen, A. Samimi, and J. J. Simpson. A polynomial chaos approach for em uncertainty propagation in 3d-fdtd magnetized cold plasma. In *2015 IEEE Symposium on Electromagnetic Compatibility and Signal Integrity*, pages 356–360, March 2015. doi: 10.1109/EMCSI.2015.7107714. 60

[180] P. Nielsen. *Coastal bottom boundary layers and sediment transport*, volume 4. World scientific, 1992. 43

[181] R. Noori, A. Khakpour, B. Omidvar, and A. Farokhnia. Comparison of ann and principal component analysis-multivariate linear regression models for predicting the river flow based on developed discrepancy ratio statistic. *Expert Systems with Applications*, 37(8):5856 – 5862, 2010. ISSN 0957-4174. doi: https://doi.org/10.1016/j.eswa.2010.02.020. URL `http://www.sciencedirect.com/science/article/pii/S095741741000059X`. 70

[182] R. Noori, A. Karbassi, A. Moghaddamnia, D. Han, M. Zokaei-Ashtiani, A. Farokhnia, and M. G. Gousheh. Assessment of input variables determination on the svm model performance using pca, gamma test, and forward selection techniques for monthly stream flow prediction. *Journal of Hydrology*, 401(3):177 – 189, 2011. ISSN 0022-1694. doi: https://doi.org/10.1016/j.jhydrol.2011.02.021. URL `http://www.sciencedirect.com/science/article/pii/S0022169411001363`. 71, 222

[183] W. L. Ob, S. M. DeLand, B. M. Rutherford, K. V. Diegert, and K. F. Alvin. Estimation of total uncertainty in modeling and simulation. *Sandia Report SAND2000-0824, Albuquerque, NM*, 2000. 56

[184] B. Oliveira, F. Ballio, and R. Maia. Numerical modelling-based sensitivity analysis of fluvial morphodynamics. *Environmental Modelling & Software*, 135:104903, 2021. 53

[185] H. Oubanas, I. Gejadze, P.-O. Malaterre, and F. Mercier. River discharge estimation from synthetic swot-type observations using variational data assimilation and the full saint-venant hydraulic model. *Journal of Hydrology*, 559:638–647, 2018. 78

[186] C. Paola and V. R. Voller. A generalized exner equation for sediment mass balance. *Journal of Geophysical Research: Earth Surface*, 110(F4), 2005. 40

[187] A. T. N. Papanicolaou, M. Elhakeem, G. Krallis, S. Prakash, and J. Edinger. Sediment transport modeling review - current and future developments. *Journal of Hydraulic Engineering*, 134(1):1–14, 2008. 4, 28, 40, 42, 43, 44, 45, 70, 224

[188] H. Park and W. Jung. The karhunen–loève galerkin method for the inverse natural convection problems. *International Journal of Heat and Mass Transfer*, 44(1):155 – 167, 2001. 95

[189] M. S. Parsons. Interpretation of machine-learning-based disruption models for plasma control. *Plasma Physics and Controlled Fusion*, 59(8):085001, jun 2017. doi: 10.1088/1361-6587/aa72a3. 2

[190] F. Pedregosa, G. Varoquaux, A. Gramfort, V. Michel, B. Thirion, O. Grisel, M. Blondel, P. Prettenhofer, R. Weiss, V. Dubourg, J. Vanderplas, A. Passos, D. Cournapeau, M. Brucher, M. Perrot, and E. Duchesnay. Scikit-learn: Machine learning in Python. *Journal of Machine Learning Research*, 12:2825–2830, 2011. iv, 147, 148

[191] A. Perlin and E. Kit. Apparent roughness in wave–current flow: Implication for coastal studies. *Journal of Hydraulic Engineering*, 128:729–741, 08 2002. doi: 10.1061/(ASCE)0733-9429(2002)128:8(729). 37

[192] T. Perrin, O. Roustant, J. Rohmer, O. Alata, J. Naulin, D. Idier, R. Pedreros, D. Moncoulon, and P. Tinard. Functional principal component analysis for global sensitivity analysis of model with spatial output. *arXiv preprint arXiv:2005.10285*, 2020. 95

[193] O. M. Phillips. The equilibrium range in the spectrum of wind-generated waves. *Journal of Fluid Mechanics*, 4(4):426–434, 1958. 37

[194] F. Pianosi, K. Beven, J. Freer, J. W. Hall, J. Rougier, D. B. Stephenson, and T. Wagener. Sensitivity analysis of environmental models: A systematic review with practical workflow. *Environmental Modelling & Software*, 79:214–232, 2016. 53

[195] B. T. Polyak. Gradient methods for minimizing functionals. *Zhurnal Vychislitel'noi Matematiki i Matematicheskoi Fiziki*, 3(4):643–653, 1963. 71

[196] S. Qian, X. Lv, Y. Cao, and F. Shao. Parameter estimation for a 2d tidal model with pod 4d var data assimilation. *Mathematical Problems in Engineering*, 2016, 2016. 95

[197] G. Radnóti, R. Ajjaji, R. Bubnová, M. Caian, E. Cordoneanu, K. Von Der Emde, J. Gril, J. Hoffman, A. Horányi, S. Issara, et al. The spectral limited area model arpege/aladin. *PWPR report series*, 7:111–117, 1995. 24

[198] A. J. Raudkivi. *Loose boundary hydraulics.* CRC Press, 1998. 33

[199] D. E. Reeve and H. Karunarathna. A statistical-dynamical method for predicting estuary morphology. *Ocean Dynamics*, 2011. 89

[200] REFMAR. Réseaux de Référence des observations MARégraphiques, 2020. 22, 23

[201] A. Rigos, G. E. Tsekouras, A. Chatzipavlis, and A. F. Velegrakis. Modeling Beach Rotation Using a Novel Legendre Polynomial Feedforward Neural Network Trained by Nonlinear Constrained Optimization. In L. Iliadis and I. Maglogiannis, editors, *Artificial Intelligence Applications and Innovations*, pages 167–179, Cham, 2016. Springer International Publishing. ISBN 978-3-319-44944-9. 75

[202] C. Robert, S. Durbiano, E. Blayo, J. Verron, J. Blum, and F.-X. Le Dimet. A reduced-order strategy for 4d-var data assimilation. *Journal of Marine Systems*, 57 (1):70 – 82, 2005. 86, 96

[203] M. C. Rochoux, S. Ricci, D. Lucor, B. Cuenot, and A. Trouvé. Towards predictive data-driven simulations of wildfire spread–part i: Reduced-cost ensemble kalman filter based on a polynomial chaos surrogate model for parameter estimation. *Natural Hazards and Earth System Sciences*, 14(11):2951–2973, 2014. 78, 88

[204] D. Rolnick and M. Tegmark. The power of deeper networks for expressing natural functions, 2017. 76, 77

[205] D. Rolnick, P. L. Donti, L. H. Kaack, K. Kochanski, A. Lacoste, K. Sankaran, A. S. Ross, N. Milojevic-Dupont, N. Jaques, A. Waldman-Brown, et al. Tackling climate change with machine learning. *arXiv preprint arXiv:1906.05433*, 2019. 2, 70

[206] B. Rouet-Leduc, C. Hulbert, N. Lubbers, K. Barros, C. J. Humphreys, and P. A. Johnson. Machine learning predicts laboratory earthquakes. *Geophysical Research Letters*, 44(18):9276–9282, 2017. doi: 10.1002/2017GL074677. URL `https://agupubs.onlinelibrary.wiley.com/doi/abs/10.1002/2017GL074677`. 2

[207] D. Rougé and P. Tassi. Numerical simulation of flow and sediment transport in the vicinity of the x nuclear plant: qualitative validation for the sediment accumulation in the entrance channel. technical report h-p74-2011-03222-fr. Technical report, EDF R&D, 2011. 48, 49

[208] G. Rozynski, M. Larson, and Z. Pruszak. Forced and self-organized shoreline response for a beach in the southern baltic sea determined through singular spectrum analysis. *Journal of Coastal Engineering*, 2001. 89

[209] B. Ruessink. Predictive uncertainty of a nearshore bed evolution model. *Continental Shelf Research*, 25(9):1053 – 1069, 2005. ISSN 0278-4343. doi: https://doi.org/10.1016/j.csr.2004.12.007. URL `http://www.sciencedirect.com/science/article/pii/S0278434305000129`. 89

[210] P. Saini, C. M. Arndt, and A. M. Steinberg. Development and evaluation of gappy-pod as a data reconstruction technique for noisy piv measurements in gas turbine combustors. *Experiments in Fluids*, 57(7):122, 2016. 222

[211] M. Saleh. *Mathematical and numerical study of POD and PGD dimensional reduction methods*. Theses, Université de La Rochelle, May 2015. URL `https://tel.archives-ouvertes.fr/tel-01278980`. 92

[212] S. Samantaray and D. K. Ghose. Evaluation of suspended sediment concentration using descent neural networks. *International Conference on Computational Intelligence and Data Science (ICCIDS 2018)*, 2018. 70

[213] A. Satelli, S. Tarantola, and F. Campolongo. Sensitivity analysis as an ingredient of modelling. *Statistical science*, 15(4):377–395, 2000. 62, 69

[214] M. Schmelter, S. Erwin, and P. Wilcock. Accounting for uncertainty in cumulative sediment transport using bayesian statistics. *Geomorphology*, 175-176:1 – 13, 2012. ISSN 0169-555X. doi: https://doi.org/10.1016/j.geomorph.2012.06.012. URL `http://www.sciencedirect.com/science/article/pii/S0169555X12002966`. 53

[215] P. J. Schmid. Dynamic mode decomposition of numerical and experimental data. *Journal of Fluid Mechanics*, 656:5–28, 2010. doi: 10.1017/S0022112010001217. 90, 222

[216] J. Schmidhuber. Deep learning in neural networks: An overview. *Neural Networks*, 61:85 – 117, 2015. ISSN 0893-6080. doi: https://doi.org/10.1016/j.neunet.2014.09.003. URL `http://www.sciencedirect.com/science/article/pii/S0893608014002135`. 74

[217] P. D. Sclavounos, Y. Ma, P. D. Sclavounos, and Y. Ma. Artificial intelligence machine learning in marine hydrodynamics. In *Proceedings of the ASME 2018 37th International Conference on Ocean, Offshore and Arctic Engineering,17-22 June, Madrid, Spain, ASME, 2018*, 06 2018. doi: 10.1115/OMAE2018-77599. URL `https://doi.org/10.1115/OMAE2018-77599`. 2

[218] T. Scott and D. Mason. Data assimilation for a coastal area morphodynamic model: Morecambe bay. *Coastal Engineering*, 54(2):91 – 109, 2007. 78

[219] L. Scriven. Dynamics of a fluid interface equation of motion for newtonian surface fluids. *Chemical Engineering Science*, 12(2):98 – 108, 1960. ISSN 0009-2509. doi: https://doi.org/10.1016/0009-2509(60)87003-0. URL `http://www.sciencedirect.com/science/article/pii/0009250960870030`. 28, 29

[220] J. Sénégas, H. Wackernagel, W. Rosenthal, and T. Wolf. Error covariance modeling in sequential data assimilation. *Stochastic environmental research and risk assessment*, 15(1):65–86, 2001. 86, 87

[221] J. Senent-Aparicio, P. Jimeno-Sáez, A. Bueno-Crespo, J. Pérez-Sánchez, and D. Pulido-Velázquez. Coupling machine-learning techniques with swat model for instantaneous peak flow prediction. *Biosystems Engineering*, 177:67 – 77, 2019. 224

[222] S. Sengupta, S. Basak, P. Saikia, S. Paul, V. Tsalavoutis, F. Atiah, V. Ravi, and A. Peters. A review of deep learning with special emphasis on architectures, applications and recent trends. *arXiv preprint:1905.13294*, 2019. 74, 76

[223] S. Shalev-Shwartz and S. Ben-David. *Understanding Machine Learning: From Theory to Algorithms*. Cambridge University Press, 2014. 69, 72, 73, 74, 76, 88

[224] J. Shenefelt, R. Luck, R. Taylor, and J. Berry. Solution to inverse heat conduction problems employing singular value decomposition and model-reduction. *International Journal of Heat and Mass Transfer*, 45(1):67 – 74, 2002. 98

[225] P. Siarry. *Metaheuristics*. Springer, 2016. 71

[226] B. W. Silverman. *Density estimation for statistics and data analysis*, volume 26. CRC press, 1986. 59

[227] B. Simon. Les niveaux marins extrêmes le long des côtes de france et leur évolution. *Le changement climatique et les espaces côtiers*, page 7, 2002. 11

[228] L. Sirovich. Turbulence and the Dynamics of Coherent Structures: I, II and III. *Quarterly Applied Mathematics*, 45:561, 1987. 91, 92, 94

[229] P. Smith, G. Thornhill, S. Dance, A. Lawless, D. C. Mason, and N. K. Nichols. Data assimilation for state and parameter estimation: Application to morphodynamic modelling. *Quarterly Journal of the Royal Meteorological Society*, 139:314–327, 01 2013. 78

[230] I. Sobol. Sensitivity estimates for nonlinear mathematical models. *Mat Model*, pages 2, 112 8., 1993. 61

[231] C. Soize. *Uncertainty quantification*. Springer, 2017. 53, 56, 57, 58, 59, 60, 78, 88, 208

[232] C. Soize and R. Ghanem. Physical systems with random uncertainties: chaos representations with arbitrary probability measure. *SIAM J. Sci. Comput.*, pages 26(2), 395–410, 2004. 63, 64, 222

[233] D. P. Solomatine and A. Ostfeld. Data-driven modelling: some past experiences and new approaches. *J. Hydroinformatics*, 2008. 4, 6, 70

[234] R. Soulsby. Dynamics of marine sands: a manual for practical applications. *Oceanographic Literature Review*, 44(9):947, 1997. 4, 19, 20, 37, 42, 43

[235] R. Soulsby. Simplified calculation of wave orbital velocities. 2006. 38

[236] F. Srajer, Z. Kukelova, and A. Fitzgibbon. A benchmark of selected algorithmic differentiation tools on some problems in computer vision and machine learning. *Optimization Methods and Software*, 33(4-6):889–906, 2018. 86

[237] T. Sruthi, K. Ranjith, and V. Chandra. Control of sediment entry into an intake canal by using submerged vanes. In *AIP Conference Proceedings*, volume 1875, page 030007. AIP Publishing LLC, 2017. 3

[238] G. W. Stewart. On the early history of the singular value decomposition. *SIAM Rev.*, 35(4):551–566, Dec. 1993. ISSN 0036-1445. doi: 10.1137/1035134. URL `https://doi.org/10.1137/1035134`. 93

[239] M. Stone. Cross-validation and multinomial prediction. *Biometrika*, 61(3):509–515, 1974. 68

[240] B. Sudret. Uncertainty propagation and sensitivity analysis in mechanical models–contributions to structural reliability and stochastic spectral methods. *Habilitationa diriger des recherches, Université Blaise Pascal, Clermont-Ferrand, France*, 147, 2007. 53, 56

[241] B. Sudret. Global sensitivity analysis using polynomial chaos expansions. *Reliability Engineering & System Safety*, 93(7):964 – 979, 2008. ISSN 0951-8320. 60, 61, 62, 63, 69

[242] B. Sudret. *Polynomial chaos expansions and stochastic finite element methods*, page 624. CRC PressEditors: Kok-Kwang Phoon, Jianye Ching, 12 2014. 60, 63

[243] K. Taira, S. L. Brunton, S. T. M. Dawson, C. W. Rowley, T. Colonius, B. J. McKeon, O. T. Schmidt, S. Gordeyev, V. Theofilis, and L. S. Ukeiley. Modal analysis of fluid flows: An overview. *AIAA Journal*, 55(12):4013–4041, 2017. iv, 89, 90, 93, 94

[244] A. Tarakanov and A. H. Elsheikh. Regression-based sparse polynomial chaos for uncertainty quantification of subsurface flow models. *Journal of Computational Physics*, 399:108909, 2019. ISSN 0021-9991. doi: https://doi.org/10.1016/j.jcp.2019.108909. URL `http://www.sciencedirect.com/science/article/pii/S002199911930614X`. 60

[245] B. Tasar, Y. Z. Kaya, H. Varcin, F. Unes, and M. Demirci. Forecasting of suspended sediment in rivers using artificial neural networks approach. *International Journal of Advanced Engineering Research and Science IJAERS*, 2017. 89

[246] P. Tassi and C. Villaret. Sisyphe user manual. *Telemac Mascaret modleling System.* iii, 45

[247] O. Thual. *Introduction à la mécanique des milieux continus déformables.* Cépaduès-Editions, 1997. 28, 29

[248] O. Thual. Ondes de surface et ressauts. *Article Pédagogique Multimedia*, 2003. URL `http://thual.perso.enseeiht.fr/PagePro/co/rpn.html`. 28, 35, 222

[249] O. Thual. *Des ondes et des fluides.* Cépaduès-Editions, 2005. 35

[250] O. Thual. *Hydrodynamique de l'environnement.* Editions de l'Ecole Polytechnique, 2015. 30, 32, 35

[251] X. Tian, Z. Xie, and A. Dai. An ensemble-based explicit four-dimensional variational assimilation method. *Journal of Geophysical Research: Atmospheres*, 113(D21), 2008. 96

[252] X. Tian, Z. Xie, and Q. Sun. A pod-based ensemble four-dimensional variational assimilation method. *Tellus A: Dynamic Meteorology and Oceanography*, 63(4): 805–816, 2011. 87, 97

[253] A.-L. Tiberi-Wadier, A. Laugel, and M. Benoit. Construction of the numerical wave databases anemoc-2 on the mediterranean sea and the atlantic ocean through hindcast simulations over the period 1979–2010. *Advances in Hydroinformatics*, pages 127–143, 2016. 12

[254] R. Tibshirani, P. Bickel, Y. Ritov, and A. Tsybakov. Least absolute shrinkage and selection operator. 72

[255] D. Tikk, L. T. Kóczy, and T. D. Gedeon. A survey on universal approximation and its limits in soft computing techniques. *International Journal of Approximate Reasoning*, 33(2):185 – 202, 2003. ISSN 0888-613X. doi: https://doi.org/10.1016/S0888-613X(03)00021-5. URL `http://www.sciencedirect.com/science/article/pii/S0888613X03000215`. 76

[256] Y. Tuncer, M. Tanik, and D. Allison. An overview of statistical decomposition techniques applied to complex systems. *Computational Statistics & Data Analysis*, 52:2292–2310, 01 2008. doi: 10.1016/j.csda.2007.09.012. 90

[257] Unesco. *Tenth Report of the Joint Panel on Oceanographic Tables and Standards, Sidney, BC, Canada, 1-5 September 1980.* Unesco, 1981. 45

[258] L. C. van Rijn. Unified view of sediment transport by currents and waves. i: Initiation of motion, bed roughness, and bed-load transport. *Journal of Hydraulic Engineering*, 133(6):649–667, 2007. 19, 20, 27, 33, 37, 38

[259] L. C. van Rijn. Unified view of sediment transport by currents and waves. ii: Suspended transport. *Journal of Hydraulic Engineering*, 133(6):668–689, 2007. 19, 20, 27

[260] J. VanderPlas, A. J. Connolly, Z. Ivezic, and A. Gray. Introduction to astroml: Machine learning for astrophysics. In *2012 Conference on Intelligent Data Understanding*, pages 47–54, Oct 2012. doi: 10.1109/CIDU.2012.6382200. 2

[261] V. Vapnik. The nature of statistical learning theory springer new york google scholar. *New York*, 1995. 67

[262] P. T. M. Vermeulen and A. W. Heemink. Model-Reduced Variational Data Assimilation. *Monthly Weather Review*, 134(10):2888–2899, 10 2006. 95, 96

[263] C. Villaret, J.-M. Hervouet, R. Kopmann, U. Merkel, and A. G. Davies. Morphodynamic modeling using the telemac finite-element system. *Computers & Geosciences*, 53:105–113, 2013. 44

[264] X. Wan and G. Karniadakis. An adaptive multi-element generalized polynomial chaos method for stochastic differential equations. *Journal of Computational Physics*, 2006. 60, 64, 222

[265] X. Wan and G. E. Karniadakis. Multi-element generalized polynomial chaos for arbitrary probability measures. *SIAM Journal on Scientific Computing*, 28(3):901–928, 2006. 63, 64

[266] N. Wiener. The homogeneous chaos. *American Journal of Mathematics*, pages 60, 897–936, 1938. 63

[267] S. Wilkinson, S. Hanna, L. Hesselgren, and V. Mueller. Inductive aerodynamics. In *Proceedings of eCAADe 2013: Computation and Performance. pp.39-48.*, 09 2013. 2

[268] T. Willis, N. Wright, and P. Sleigh. Uncertainty with friction parameters and impact on risk analysis. In *E3S Web of Conferences: Floodrisk2016*, volume 7. EDP Sciences, 2016. 53

[269] J. A. Witteveen and H. Bijl. Modeling arbitrary uncertainties using gram-schmidt polynomial chaos. *44th AIAA Aerospace Sciences Meeting and Exhibit*, 2006. 63

[270] L. Xie, K. Wu, L. Pietrafesa, and C. Zhang. A numerical study of wave-current interaction through surface and bottom stresses: Wind-driven circulation in the south atlantic bight under uniform winds. *Journal of Geophysical Research: Oceans*, 106(C8):16841–16855, 2001. 37

[271] D. Xiu and G. Karniadakis. Modelling uncertainty in steady state diffusion problems via generalized polynomial chaos. *Comput. Methods Appl. Mec. Engrg*, pages 191(43), 4927–4948, 2003. vii, 60, 63

[272] D. Xiu and G. E. Karniadakis. The wiener–askey polynomial chaos for stochastic differential equations. *SIAM Journal on Scientific Computing*, 24(2):619–644, 2002. 63, 64

[273] D. Xiu and G. E. Karniadakis. Modeling uncertainty in flow simulations via generalized polynomial chaos. *Journal of Computational Physics*, 187(1):137 – 167, 2003. 60, 63

[274] B. C. Yen. Open channel flow resistance. *Journal of hydraulic engineering*, 128(1): 20–39, 2002. 32

[275] B. Yilmaz, E. Aras, S. Nacar, and M. Kankal. Estimating suspended sediment load with multivariate adaptative regression spline, teaching-learning based optimization, and artificial bee colony models. *Science of the Total Environment.*, 2018. 89

[276] C. Zhu, R. H. Byrd, P. Lu, and J. Nocedal. Algorithm 778: L-bfgs-b: Fortran subroutines for large-scale bound-constrained optimization. *ACM Transactions on Mathematical Software (TOMS)*, 23(4):550–560, 1997. 71

[277] L. Zhu, W. Zhang, J. Kou, and Y. Liu. Machine learning methods for turbulence modeling in subsonic flows around airfoils. *Physics of Fluids*, 31(1):015105, 2019. doi: 10.1063/1.5061693. URL `https://doi.org/10.1063/1.5061693`. 2

[278] J. A. Zyserman and J. Fredsøe. Data analysis of bed concentration of suspended sediment. *Journal of Hydraulic Engineering*, 120(9):1021–1042, 1994. 41, 207

Abstract

This thesis contributions belong to the general framework of data-based and physically-based data-driven modelling. An efficient approach for Machine Learning (ML), as well as a speed-up technique for Data Assimilation (DA), have been developed. For this purpose, Dimensionality Reduction (DR) and stochastic spectral modelling were used. In particular, a coupling between Proper Orthogonal Decomposition (POD) and Polynomial Chaos Expansion (PCE) is at the center of this thesis contributions.

POD and PCE have widely proved their worth in their respective frameworks, and the idea was to combine them for optimal field measurement based forecasting, and ensemble-based acceleration technique for variational DA. For this purpose, (i) a physically interpretable POD-PCE ML for non-linear multidimensional fields was developed in the Neural Networks (NN) paradigm and (ii) a hybrid ensemble-variational DA approach for parametric calibration was proposed with adapted calculations of POD-PCE metamodelling error covariance matrix.

The proposed techniques were assessed in the context of an industrial application, for the study of sedimentation in a coastal power plant's water intake. Water intakes ensure plant cooling via a pumping system. They can be subject to sediment accumulation, which represents a clogging risk and requires costly dredging operations. For monitoring and safety reasons, the power plant stakeholders asked for a predictive tool that could be run in operational conditions. Data collected during many years of monitoring in the study area were provided. The objective was then to achieve comprehensive analysis of the flow and sediment dynamics, as well as to develop an optimal model in terms of forecasting accuracy, physical meaning, and required computational time. Uncertainty reduction and computational efficiency were therefore starting points for all proposed contributions.

In addition to the previously proposed methods, Uncertainty Quantificiation (UQ) studies were undertaken. Specifically, (i) uncertainties related to tidal hydrodynamic modelling, resulting from common modelling choices (domain size, empirical closures) were investigated. POD patterns resulting from measurements and numerical scenarios were compared; (ii) UQ study of the sediment transport modelling in the intake, in a high-dimensional framework, was achieved. Investigations were based on appropriate DR. In fact, POD patterns of Boundary Conditions (BC) and Initial Conditions (IC), resulting from hydrodynamic simulations outputs and from bathymetry measurements respectively, were used.

A perspective of this work would be to implement a hybrid POD-PCE model, using both measured and numerically emulated data, to better understand and predict complex physical processes. This approach would offer a complete, fast and efficient tool for operational predictions.

Keywords

data-based prediction, physically-based data-driven modelling, statistical learning, data assimilation, uncertainty quantification, sensitivity analysis, geosciences, hydrodynamics, sediment transport, coastal intake.

Résumé

Les contributions de cette thèse figurent dans le cadre général de la modélisation à base de données et des approches physiques guidées par des données. Une méthode d'apprentissage statistique, ainsi qu'une technique d'accélération pour l'Assimilation de Données (AD), ont été développées. Pour cela, la Réduction de Dimension et la modélisation stochastique spectrale sont utilisées. En particulier, un couplage entre Décomposition en modes Propres Orthogonaux (POD) et Expansion par Polynômes du Chaos (PCE), est au centre des différentes contributions.

Les techniques POD et PCE sont toutes deux largement reconnues. L'idée ici est de les combiner pour mettre en place une prédiction optimale à base de données de mesures, et accélérer les techniques d'Assimilation de Données variationnelle sur la base d'une approche d'ensemble. Pour cela, (i) un modèle de Machine Learning POD-PCE, interprétable physiquement, et adapté aux champs multidimensionnels non-linéaires, a été développé dans un paradigme de Réseaux de Neurones et (ii) une approche ensembliste-variationnelle hybride d'AD, pour la calibration paramétrique a été proposée, avec un calcul adapté de la matrice de covariance d'erreur du métamodèle POD-PCE.

Les approches proposées ont été motivées par une problématique industrielle, avec une question physique complexe : la sédimentation dans un chenal d'amenée bord-de-mer d'une centrale électrique. Les chenaux d'amenée assurent le refroidissement des centrales à travers un système de pompage. Ils peuvent être sujets à une accumulation de sédiments, ce qui représente un risque de colmatage et requiert des opérations de dragage coûteuses. Pour des raisons de gestion et de sécurité, l'industriel opérant la centrale d'intérêt demande un outil prédictif pour des conditions opérationnelles. Les données collectées durant plusieurs années de gestion ont été fournies. L'objectif est d'analyser la dynamique observée, ainsi que de développer un modèle optimal, à la fois prédictif, physiquement interprétable, et à coût de calcul limité. La réduction de l'incertitude et la diminution du temps de simulation ont donc été un point de départ pour toutes les contributions proposées.

En supplément des méthodes citées précédemment, des études de Quantification d'Incertitudes (UQ) ont été menées. Plus précisément, (i) les incertitudes liées à la modélisation hydrodynamique de la marée, résultant de choix de modélisation communs (taille de domaine, lois empiriques), ont été investiguées. Les motifs POD des mesures et des scénarios numériques ont été comparés ; (ii) l'étude UQ de la modélisation du transport sédimentaire dans le chenal, dans un cadre à haute-dimension, a été réalisée. Les investigations se sont basées sur une Réduction de Dimension appropriée. En effet, les motifs POD des Conditions aux Limites, et ceux des Conditions Initiales, résultant de simulations hydrodynamiques et de mesures bathymétriques respectivement, ont été utilisés.

Une perspective de ce travail serait d'implémenter un modèle POD-PCE hybride, utilisant à la fois des données de mesures et des données simulées numériquement, pour mieux comprendre et prédire des processus physiques complexes. Cette approche offrirait un outil complet, rapide et efficace pour des prédictions opérationnelles.

Mots-clés

prédiction à base de données, modélisation physique guidée par la donnée, apprentissage statistique, assimilation de données, quantification d'incertitudes, analyse de sensibilité, geosciences, hydrodynamique, transport sédimentaire, chenaux côtiers.